

Physics and Applications of the Josephson Effect

ANTONIO BARONE

*Consiglio Nazionale delle Ricerche
and
Università di Napoli*

GIANFRANCO PATERNÒ

Comitato Nazionale Energia Nucleare



A WILEY-INTERSCIENCE PUBLICATION

JOHN WILEY & SONS

New York • Chichester • Brisbane • Toronto • Singapore

Copyright © 1982 by John Wiley & Sons, Inc.

All rights reserved. Published simultaneously in Canada.

Reproduction or translation of any part of this work beyond that permitted by Section 107 or 108 of the 1976 United States Copyright Act without the permission of the copyright owner is unlawful. Requests for permission or further information should be addressed to the Permissions Department, John Wiley & Sons, Inc.

Library of Congress Cataloging in Publication Data:

Barone, Antonio, 1939-

Physics and applications of the Josephson effect.

“A Wiley-Interscience publication.”

Bibliography: p.

Includes index.

I. Josephson effect. I. Paternò, Gianfranco.

II. Title.

QC176.8.T8B37 530.4'1 81-7554
ISBN 0-471-01469-9 AACR2

Printed in the United States of America

10 9 8 7 6 5 4 3 2 1

*To SVEVA
and
to GIANNA*

Preface

This book surveys all aspects of the Josephson effect—from the underlying physical theory to actual and proposed engineering applications. Both ends of this spectrum are interesting. The physical theory is novel and important for many macroscopic quantum effects, which have a rich and yet untapped potential for technical development. We attempt here to present more than a survey and less than an exhaustive exposition of this wide field. Rather than to cover everything, we have tried to *uncover* those aspects of theory, fabrication technology, and device application that will be of lasting value.

Chapter 1 briefly surveys Josephson junction phenomenology. Although the reader is assumed to have a basic knowledge of superconductivity, we begin with the simplest possible description of Josephson structures and their dynamic behavior. Chapter 2 presents microscopic theory in simple terms. We discuss salient features of the underlying theory that are most useful in appreciating experimental results. To some extent the chapters are self-contained; for example, the reader could skip the microscopic theory (at least on a first reading) without seriously impairing continuity. In Chapter 3 we discuss the dependence of critical current on temperature and on junction parameters. The static (i.e., zero voltage) behavior of “small” and “large” junctions is considered in Chapters 4 and 5. Chapter 6 presents several important results on the current voltage behavior of small weak links, and a variety of weak link structures is described in Chapter 7.

What we discuss in Chapter 8 are those basic technological considerations and certain advanced techniques that have been found useful in several laboratories throughout the world over the past decade. We expect such techniques to continue to be of value, especially for those who are beginning to experiment with Josephson junctions.

Chapters 9 and 10 discuss self-resonant modes in small junctions and the dynamical behavior of extended junctions from the perspective of modern “soliton” theory.

The last three chapters are directed toward applications of Josephson junctions. Chapter 11 discusses the various features of junction interactions with periodic signals and considers such applications as mixing, parametric amplification, and the voltage standard. Chapters 12 and 13 deal with quantum interference loops and their application to measurement of very small magnetic fields. Finally, in Chapter 14, we describe the potential of the Josephson junction as the basic logic and memory element in a very large digital computer system.

Throughout the book our choice of theoretical material has been guided by our later discussions of device applications. In this way we have tried to achieve a large scale coherence in a range of subject matter that at first glance might appear to be rather diffuse. We hope that the book will be useful in graduate courses in the theory and applications of superconductive devices, as well as for research scientists and engineers. Although extensive, the bibliography is not exhaustive, and we apologize to those whose work may have been overlooked.

ANTONIO BARONE
GIANFRANCO PATERNÒ

*Naples, Italy
Rome, Italy
December 1981*

Acknowledgements

It is our pleasure to acknowledge the kind and generous assistance that has been offered throughout the preparation of this book. Without such help our task would not have been possible.

It is hard to adequately express our gratitude to A. C. Scott for his continuous encouragement and advice, and to R. Vaglio and R. D. Parmentier for their careful reading of the manuscript and invaluable contributions.

We warmly acknowledge A. Baratoff for reviewing and suggesting improvements in Chapters 2 and 3; N. F. Pedersen, in Chapter 6; Y. Ovchinnikov and A. L. Aslamazov, in Chapter 7; T. F. Finnegan, in Chapter 11; S. N. Erné and J. E. Zimmerman, in Chapters 12 and 13; and P. Wolf, in Chapter 14.

Thanks are due to M. Russo for his helpful cooperation and suggestions and to L. Solymar for his encouragement during the early stages of preparing this book.

We are indebted to many colleagues for permission to cite and use their published and unpublished results. In particular, we greatly benefited from the preprints and original material of S. Basavaiah, A. N. Broers, P. Carelli, J. Clarke, D. Cohen, C. M. Falco, M. J. Feldman, C. H. Hamilton, R. E. Harris, D. J. Herrel, W. J. Johnson, I. O. Kulik, R. B. Laibowitz, D. N. Langenberg, Li Kong Wang, H. Lübbig, I. Modena, J. E. Nordman, D. E. Prober, M. Ricci, G. L. Romani, N. Sacchetti, R. D. Sandell, I. Schuller, Y. Taur, and I. K. Yanson, to whom we express our deep gratitude.

Discussions with W. Anacker, B. S. Deaver, Jr., S. Callegari, T. A. Fulton, K. Gray, J. Kurkijärvi, J. Matisoo, D. J. Scalapino, E. P. Balsamo, R. Cristiano, O. Natoli, and R. Vitiello are also acknowledged, as well as the useful suggestions given by K. K. Likharev, J. E. Mooij, and M. Tinkham.

Thanks are due to the Landau Institute for Theoretical Physics of the Academy of Sciences of USSR for providing several opportunities to one of us (A. B.) to meet with Soviet scientists during the preparation of the book.

We thank A. M. Mazzarella for her competence, skill, and dedication throughout the preparation of the manuscript and C. Salvia for his invaluable technical assistance.

Finally, we are thankful to L. Crescentini, A. De Feo, M. Izzo, L. Mendaia, S. Piantedosi, C. Salinas for helping with the manuscript in different ways and to A. DeLuca and S. Termini for friendly encouragement and suggestions.

A. B.
G. P.

Contents

CHAPTER 1

WEAK SUPERCONDUCTIVITY—PHENOMENOLOGICAL ASPECTS 1

- 1.1 Macroscopic quantum system, 1
- 1.2 Coupled superconductors, 3
- 1.3 Single electron tunneling, 4
- 1.4 Josephson equations, 9
- 1.5 Magnetic field effects, 14
- 1.6 Barrier free energy, 18
- 1.7 Electrodynamics of the Josephson junction, 19
- 1.8 Other Josephson structures, 22

CHAPTER 2

MICROSCOPIC THEORY 25

- 2.1 Tunneling Hamiltonian formalism, 25
- 2.2 General expression for the total current, 29
 - 2.2.1 *The total current expression in the time domain*, 31
 - 2.2.2 *The total current expression in the frequency domain*, 33
- 2.3 Tunneling current for constant voltage, 35
- 2.4 Expression of I_{qp_1} , I_{qp} , I_{J1} , I_{J2} , 35
 - 2.4.1 *The quasiparticle terms* I_{qp} , I_{qp_1} , 37
 - 2.4.2 *The phase dependent terms* I_{J1} and I_{J2} , 38
- 2.5 Tunneling current in the B.C.S. approximation, 39
- 2.6 The “cos φ ” problem, 47

CHAPTER 3**MAGNITUDE AND TEMPERATURE DEPENDENCE
OF THE CRITICAL CURRENT**

50

- 3.1 Josephson current for $V = 0$, 50
- 3.2 B.C.S. approximation, 51
- 3.3 Strong coupling effects, 56
- 3.4 Effects of paramagnetic impurities, 59
- 3.5 Measurement techniques, 66

CHAPTER 4**“SMALL” JUNCTIONS IN A MAGNETIC FIELD**

69

- 4.1 Josephson penetration depth, 69
- 4.2 Small junctions, 70
- 4.3 Uniform tunneling current distribution, 74
 - 4.3.1 *Rectangular junctions*, 74
 - 4.3.2 *Circular junctions*, 76
 - 4.3.3 *Magnetic field with arbitrary orientation*, 77
- 4.4 Non-uniform tunneling current density, 79
 - 4.4.1 *Various current density profiles*, 80
 - 4.4.2 *Structural fluctuations*, 91

CHAPTER 5**LARGE JUNCTIONS—STATIC SELF-FIELD EFFECTS**

96

- 5.1 Approximate analysis, 96
- 5.2 Analysis of Owen and Scalapino, 100
- 5.3 Effects of the junction geometrical configuration, 112

CHAPTER 6**CURRENT VOLTAGE CHARACTERISTICS**

121

- 6.1 V - I curves of various weak links, 121
- 6.2 Resistively shunted junction model: autonomous case, 122
 - 6.2.1 *Mechanical model*, 123
 - 6.2.2 *Small capacitance limit ($\beta_J \gg 1$)*, 126

6.2.3	<i>Phase plane analysis, 128</i>
6.2.4	<i>D.C. voltage-current characteristics for finite capacitance, 131</i>
6.3	Current biased tunneling junction, 136
6.3.1	<i>Adiabatic approximation, 137</i>
6.3.2	<i>General case, 138</i>
6.4	Effects of thermal fluctuations, 143
6.4.1	<i>Negligible capacitance, 147</i>
6.4.2	<i>Finite capacitance, 153</i>
6.4.3	<i>Large capacitance, 157</i>
6.4.4	<i>Other noise considerations, 158</i>

CHAPTER 7

OTHER SUPERCONDUCTING WEAK LINK STRUCTURES 161

7.1	Metal barrier junctions, 161
7.1.1	<i>Proximity effect, 161</i>
7.1.2	<i>S-N-S junctions, 164</i>
7.1.3	<i>S-I-N-S structures, 166</i>
7.2	Semiconducting barrier junctions, 169
7.2.1	<i>Barrier layers of various semiconductor materials, 170</i>
7.2.2	<i>Light sensitive semiconducting barrier junctions, 172</i>
7.3	Bridge-type junctions, 177
7.3.1	<i>Static behavior, 181</i>
7.3.2	<i>Voltage-current characteristics, 186</i>
7.3.3	<i>Interpretation of voltage carrying states, 187</i>
7.3.4	<i>Aspects of nonequilibrium superconductivity, 193</i>
7.4	Point contact weak links, 196

CHAPTER 8

DEVICE FABRICATION TECHNOLOGY 198

8.1	Josephson tunneling junctions, 198
8.2	Junction electrodes, 199
8.2.1	<i>Soft metals, 199</i>
8.2.2	<i>Soft metal alloys, 200</i>
8.2.3	<i>Hard materials (Transition metals), 204</i>

8.3 Oxide barriers, 205
8.3.1 <i>Thermal oxidation, 206</i>
8.3.2 <i>D.C. glow discharge, 207</i>
8.3.3 <i>R.F. glow discharge, 210</i>
8.4 Junction patterning, 211
8.4.1 <i>Metal masks, 212</i>
8.4.2 <i>Photolithography, 212</i>
8.4.3 <i>Lift-off technique, 214</i>
8.4.4 <i>Electron lithography, 216</i>
8.4.5 <i>X-Ray lithography, 217</i>
8.5 Simple procedures for preparing oxide barrier junctions, 218
8.5.1 <i>Evaporated junctions, 219</i>
8.5.2 <i>Sputtered base layer junctions, 220</i>
8.5.3 <i>Other oxide barrier structures, 221</i>
8.6 Semiconductor barriers, 222
8.6.1 <i>Various semiconductors, 223</i>
8.6.2 <i>Light sensitive barriers, 224</i>
8.6.3 <i>Single crystal barrier junctions, 225</i>
8.7 Bridge-type weak links, 228
8.8 Point contact structures, 232

CHAPTER 9**RESONANT MODES IN TUNNELING STRUCTURES**

235

9.1 Josephson junction as a transmission line, 235
9.2 Resonant modes for low Q junctions, 238
9.3 Junctions of infinite length, 248
9.4 Nonuniform current density distribution, 251
9.5 Resonant modes for high Q Josephson junctions, 256

CHAPTER 10**FLUXON DYNAMICS**

264

10.1 The sine Gordon equation, 264
10.1.1 <i>Traveling wave solutions, 265</i>
10.1.2 <i>Energy functions, 269</i>

10.2	Nonlinear standing waves on a rectangular junction,	271
10.3	Effects of losses and bias,	274
10.4	Zero field steps,	278
10.5	Perturbative analysis of fluxon dynamics,	279
10.5.1	<i>Single fluxon dynamics,</i>	280
10.5.2	<i>Fluxon-antifluxon annihilation,</i>	284
10.6	Effects of flux flow on D.C. voltage-current characteristics,	285
10.7	Two dimensional junctions,	288

CHAPTER 11

HIGH FREQUENCY PROPERTIES AND APPLICATIONS OF THE JOSEPHSON EFFECT

291

11.1	Simple voltage source model,	291
11.1.1	<i>Microwave induced steps,</i>	291
11.1.2	<i>Effect of fluctuations on the induced voltage steps,</i>	293
11.2	Tunneling junctions in external microwave radiation,	294
11.2.1	<i>The “Riedel” peak,</i>	296
11.2.2	<i>Finite dimension effects,</i>	304
11.3	Current source model,	305
11.4	Emission of radiation,	309
11.5	Detection of radiation,	318
11.5.1	<i>Wide band detectors,</i>	318
11.5.2	<i>Narrow band detectors,</i>	324
11.6	Parametric amplification,	330
11.6.1	<i>Parametric amplifiers with externally pumped Josephson elements,</i>	332
11.6.2	<i>Internally pumped parametric amplifiers,</i>	343
11.7	The determination of $2e/h$ and the voltage standard,	344

CHAPTER 12

JOSEPHSON JUNCTIONS IN SUPERCONDUCTING LOOPS

354

12.1	Fluxoid quantization,	354
12.2	Superconducting loop with a single junction,	359

12.2.1	<i>Metastable states, 360</i>
12.2.2	<i>Applied external field, 360</i>
12.2.3	<i>Dynamics of flux transitions for $\beta_e > 1$, 364</i>
12.3	Superconducting interferometer, 369
12.3.1	<i>Zero inductance case, 370</i>
12.3.2	<i>Metastable states, 373</i>
12.3.3	<i>Asymmetric double junction configuration, 375</i>

CHAPTER 13

SQUIDs: THEORY AND APPLICATIONS	383
--	------------

13.1	Radio Frequency SQUID, 383
13.1.1	<i>Effects of the parametric inductance, 384</i>
13.1.2	<i>R.F. SQUID in the dispersive mode, 388</i>
13.1.3	<i>R.F. SQUID in the dissipative mode ($\beta_e > 1$) 398</i>
13.2	D.C. SQUID, 403
13.3	Noise and maximum sensitivity, 409
13.3.1	<i>R.F. magnetometers, 410</i>
13.3.2	<i>D.C. magnetometers, 413</i>
13.3.3	<i>Ultimate sensitivity of practical devices, 415</i>
13.4	Practical superconducting sensor configurations, 416
13.4.1	<i>Single weak link devices, 416</i>
13.4.2	<i>Two weak link configurations, 421</i>
13.5	Measurement techniques, 424
13.5.1	<i>Flux locked configuration, 424</i>
13.5.2	<i>Superconducting transformers, 426</i>
13.6	The resistive SQUID, 429
13.6.1	<i>The resistive loop device in the presence of a D.C. bias, 429</i>
13.6.2	<i>The resistive loop device in the presence of an R.F. bias, 431</i>
13.7	Applications, 434
13.7.1	<i>Measurements of current, voltage and resistance, 435</i>
13.7.2	<i>Magnetic susceptibility measurements, 437</i>
13.7.3	<i>Medical applications, 439</i>
13.7.4	<i>Magnetotellurics, 445</i>

CHAPTER 14	
COMPUTER ELEMENTS	446
14.1 Cryotrons, 446	
14.2 Matisoo's experiments, 449	
<i>14.2.1 Tunneling cryotron, 449</i>	
<i>14.2.2 Flip-flop circuit, 451</i>	
14.3 Operation times, 454	
14.4 Different switching modes, 456	
14.5 Interference switching devices, 459	
14.6 Memory Cells, 461	
<i>14.6.1 Flip-flop memory configuration, 461</i>	
<i>14.6.2 Single flux quantum storage devices, 462</i>	
14.7 Examples of Josephson logic and memory circuits, 465	
14.8 Systems performance and requirements, 470	
14.9 Conclusions and perspectives, 473	
APPENDIX	
SYSTEMS OF UNITS	474
A.1 Comments on systems of units, 474	
A.2 Conversion Tables, 474	
REFERENCES	477
INDEX	525

Every explanation is an hypothesis.

L. W. WITTEGENSTEIN

Remarks on Frazer's Golden Bough

Physics and Applications of the Josephson Effect

CHAPTER 1

Weak Superconductivity— Phenomenological Aspects

In this chapter we briefly review the phenomenology of the Josephson effect, outlining the basic experimental results and providing a qualitative interpretation on the basis of very simple models. However, first let us say a few words about its history.

The discovery of what is usually referred to as the Josephson effect dates back about 20 years (1961–1962). At that time Brian Josephson was a research student at the Royal Society Mond Laboratory in Cambridge under the supervision of Brian Pippard. There is no doubt, as reported by Josephson in his Nobel lecture, that the stimulating oven of the Mond Laboratory, the presence at that time of Phil Anderson, the development of new researches, both on experiments (Giaever, 1960a, b; Nicol, Shapiro, and Smith 1960) and on theory (Cohen, Falicov, and Phillips 1962) of superconductive tunneling, provided an ideal ground for Josephson's intuition and outstanding conclusions. Josephson's prediction and the following experimental confirmation (Anderson and Rowell 1963) opened not only a new important chapter of physics but also new horizons for a wide variety of stimulating applications.

We shall not dwell further on the history of the discovery of the Josephson effect, though it certainly deserves adequate space and a deep analysis. Instead, we prefer to refer the reader to the historical surveys given by Josephson himself (1974) and other protagonists (Anderson 1970; Pippard 1976), thus avoiding any possible deformation of the fascinating atmosphere in which those events took place.

1.1 Macroscopic Quantum System

The interpretation of superconductivity as a quantum phenomenon on a macroscopic scale was introduced by F. London (1935). The theory of Ginzburg and Landau (1950) provided an enormous insight into the nature of superconductivity. They developed a modification of the London theory (F. London and H. London 1935a, b) by introducing a position dependent parameter, ψ , which gives a measure of the order in the superconducting phase. Unlike the earlier two fluid models proposed by Gorter and Casimir (1934), such an order parameter is complex and can be regarded as a wave function

for superconducting electrons. As shown by Gor'kov (1959), ψ is proportional to the local value of the energy gap function Δ . In this framework a single wave function is associated with a macroscopic number of electrons which are assumed to "condense" in the same quantum state. In this sense, the superconductive state can be regarded as a "macroscopic quantum state." Therefore we are dealing with particles, having effective mass and charge m^* and e^* respectively, which can be described as a "whole" by a macroscopic wave function of the form

$$\psi = \rho^{1/2} e^{i\varphi} \quad (1.1.1)$$

where φ is the phase common to all the particles and ρ represents, in this macroscopic picture, their actual density in the macrostate $|s\rangle$:

$$\langle s|\psi^*\psi|s\rangle = |\psi|^2 = \rho$$

The electric current density can be written, in the presence of a vector potential \mathbf{A} :

$$\mathbf{J} = \frac{e^*}{m^*} \left[\frac{j\hbar}{2} (\psi \nabla \psi^* - \psi^* \nabla \psi) - \frac{e^*}{c} \mathbf{A} |\psi|^2 \right]$$

where c is the velocity of the light.

As follows from flux quantization, the charge e^* is twice the electronic charge e , since the "particles" we are dealing with are in fact pairs of coupled electrons. This is contained within the framework of the microscopic theory of superconductivity first derived by Bardeen Cooper and Schrieffer (1957) and usually referred as B.C.S. theory. It is assumed that $m^* = 2m$ (m =electronic mass), but, it is easy to see that the choice of m is arbitrary, since it depends essentially on the normalization assumed for the pair wave function ψ .[†]

Thus with the ψ given by (1.1.1) the expression for \mathbf{J} becomes

$$\mathbf{J} = \rho \frac{e}{m} \left(\hbar \nabla \varphi - \frac{2e}{c} \mathbf{A} \right) \quad (1.1.2)$$

Gauge invariance requires that under the transformations of the vector potential \mathbf{A} and scalar potential U

$$\mathbf{A} \rightarrow \mathbf{A} + \nabla \chi \quad U \rightarrow U - \frac{\partial \chi}{\partial t}$$

the observable physical quantities remain unchanged. This implies the phase transformation

$$\varphi \rightarrow \varphi + \frac{2e}{\hbar c} \chi \quad (1.1.3)$$

[†]See also the microscopic derivation of the Ginzburg Landau theory by Gor'kov (1959).

as can be readily verified for the current density \mathbf{J} by (1.1.2). The choice of constant values for the scalar quantity χ does not affect potentials but just implies different values of the phase factor. This corresponds to the unobservability of ψ .

We can arbitrarily assign a phase value at a given point; however, because of the occurrence of the so-called long range order the value of the phase is fixed in all points. Obviously, as is evident from (1.1.2), spatial variations of the phase φ describe carrying current states of the superconductor.

For a system in equilibrium the required gauge invariance leads necessarily to a time dependent ψ . It is clear in fact that, even assuming a constant ψ in one gauge, any transformation to another gauge would imply a change of φ as in (1.1.3) in which χ is time dependent. The time evolution of ψ in stationary conditions obeys the usual quantum mechanical equation of the form

$$j\hbar \frac{\partial \psi}{\partial t} = E\psi$$

As can be seen from the microscopic theory (Gor'kov 1959) the quantity E is equal to twice the electrochemical potential μ . This value represents the minimum energy required to add a Cooper pair to the system. Thus $\psi(\mathbf{r}, t) = \psi(\mathbf{r})e^{-2\mu t/\hbar}$ (See also Anderson 1963, 1966).

Since the number of pairs N and the phase φ are conjugate variables (Anderson 1963) there is an uncertainty relation, $\Delta N \Delta \varphi \simeq 2\pi$, which corresponds to the circumstance that within an isolated superconductor N will be fixed and, consequently, the phase φ undefined.

1.2 Coupled Superconductors

Let us now consider two superconductors S_L and S_R separated by a macroscopic distance. In this situation, the phase of the two superconductors can change independently. As the two superconductors are moved closer, so that their separation is reduced to about 30 Å, quasiparticles can flow from one superconductor to the other by means of tunneling (single electron tunneling). If we reduce further the distance between S_L and S_R down to say 10 Å, then, as we shall see, also Cooper pairs can flow from one superconductor to the other (Josephson tunneling). In this situation if we assign a given phase in S_L is the possibility of altering independently the phase in S_R still allowed? The answer is no! This degree of freedom is removed, since phase correlation is realized between the two superconductors; that is, the long range order is “transmitted” across the boundary. Therefore we expect that the whole system of the two superconductors separated by a thin (~ 10 Å) dielectric barrier will behave, to some extent, as a single superconductor. Unlike ordinary superconductivity, this phenomenon is often called “weak superconductivity” (Anderson 1963) because of the much lower values of the critical parameters involved. The

above-quoted work by Anderson should be considered a milestone in the development of the field.

Josephson theory (1962a,b, 1964, 1965, 1969, 1974) deals with such systems of weakly coupled superconductors. We devote our attention mostly to tunneling structures although Josephson effects take place in various types of superconducting “weak links” (Dayem bridge, point contacts, etc.; see Section 1.8). To begin, we recall the basic concepts of single electron tunneling within a simple phenomenological approach. An account of both single electron tunneling and Josephson phenomenology can be found in Solymar (1972).

1.3 Single Electron Tunneling

The history of superconductive tunneling began with the experiments performed by Giaever (1960a,b) and by Nicol, Shapiro, and Smith (1960). A tunneling structure consists essentially of two metal films separated by a thin ($\sim 30 \text{ \AA}$) dielectric barrier as sketched in Fig. 1.1. The behavior of such a structure can be investigated by studying the dependence of the tunneling current I on the voltage V across the junction.

To “visualize” the tunneling process, we adopt a simple representation in terms of the energy (E)–momentum (k) diagrams. The normal metal is represented in the E - k plane by the curve of Fig. 1.2a. The dashed line corresponds to the portion of the parabola below the Fermi energy E_F (hole states) which has been reflected across the Fermi level. In this picture the electron hole pair creation is regarded as excitations of two states of energy $E_l = |\epsilon_l|$ and $E_h = |\epsilon_h|$ respectively. That is, all excited states have positive energy measured with respect to E_F . In the case of the superconductor, all the condensed pairs are at the Fermi level and a minimum threshold energy Δ (energy gap) is required by an excitation as shown in Fig. 1.2b. In this case there exists a particle which is “partially” in the hole state and “partially” in the electron state. These are the quasiparticle excitations which have energy

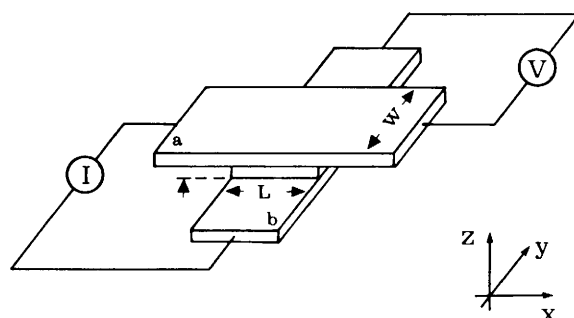


Figure 1.1 Tunneling junction of cross-type geometry. The dimensions are L and W ; a and b are the two superconducting films.

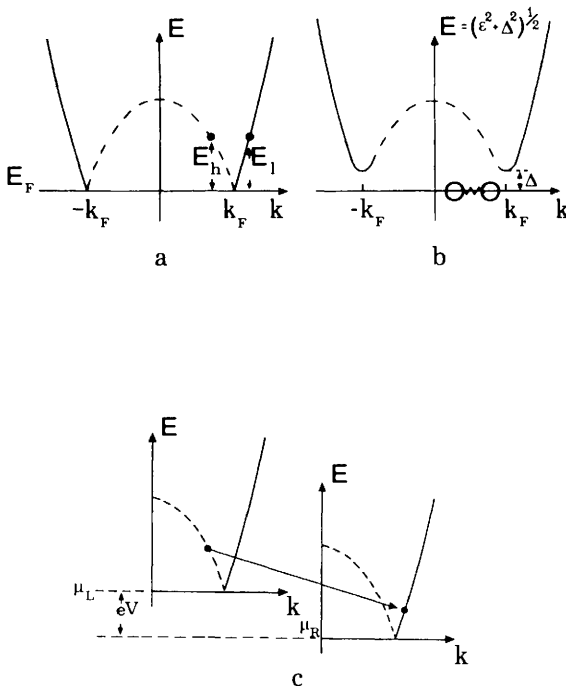


Figure 1.2 Energy momentum diagrams. (a) Normal metal; (b) superconducting metal; (c) electron tunneling process between two normal metal electrodes.

$E=(\epsilon^2 + \Delta^2)^{1/2}$. From this one-to-one correspondence between E and ϵ it follows that $N(E)dE=\mathcal{N}(\epsilon)d\epsilon$ where $N(E)$ and $\mathcal{N}(\epsilon)$ are the density of states in the superconductor and in the normal metal respectively. Thus we have

$$N(E)=N(0)\left[\frac{E}{\sqrt{E^2-\Delta^2(E)}}-\frac{\Delta(E)[d\Delta(E)/dE]}{\sqrt{E^2-\Delta^2(E)}}\right]$$

where we have indicated with $N(0)$ the value of \mathcal{N} for $\epsilon=0$ assumed constant.

In the case of energy independent gap (B.C.S. approximation) we have the following expression for the density of states:

$$\begin{aligned} N(E) &= N(0) \frac{E}{\sqrt{E^2 - \Delta^2}} & |E| \geq \Delta \\ N(E) &= 0 & |E| < \Delta \end{aligned} \quad (1.3.1)$$

Let us outline now the phenomenological theory of tunneling proposed by Giaever and Megerle (1961). In this approach, we assume that we are dealing with normal electrons rather than quasiparticles. The tunneling current $I_{L \rightarrow R}$

from the left to the right electrode is given by

$$I_{L \rightarrow R} = \frac{2\pi}{\hbar} \int_{-\infty}^{+\infty} |T|^2 N_L(E) f_L(E) N_R(E) (1 - f_R(E)) dE \quad (1.3.2)$$

where $f_L(E)$ (f_R) is the Fermi factor $f_L(E) = 1/(1 + e^{\beta_T E})^\dagger$ and N_L (N_R) is the density of states in the left (right) metal; $|T|$ is the tunneling matrix element between states of equal energy. The expression (1.3.2) merely signifies that the current from L to R is proportional to (1) the tunneling probability, (2) the number of electrons “available” on the left (fraction of filled states, $N_L f_L$), and (3) the number of possible states on the right (fraction of empty states $N_R(1 - f_R)$). Changing the subscript L with R we get similarly the current $I_{R \rightarrow L}$ from the right to the left side. The net current I is thus

$$I = I_{L \rightarrow R} - I_{R \rightarrow L} = \frac{2\pi}{\hbar} \int_{-\infty}^{+\infty} |T|^2 N_L(E) N_R(E) [f_L(E) - f_R(E)] dE$$

If we consider an applied voltage V across the junction the Fermi energy levels μ_L and μ_R will be relatively shifted by an energy eV and thus

$$I = \frac{2\pi}{\hbar} |T|^2 \int_{-\infty}^{+\infty} N_L(E) N_R(E + eV) [f_L(E) - f_R(E + eV)] dE$$

where T is assumed to be energy independent.

Let us consider first two normal metals. We make the further hypothesis of considering N_L and N_R to be constant and equal to the densities of states at the Fermi energy level.[‡] Therefore the tunneling current between two normal metals is given by

$$I_{NN} = \text{constant} \times \int_{-\infty}^{+\infty} [f(E) - f(E + eV)] dE$$

which is

$$I_{NN} = \sigma_N V$$

The constant σ_N can be regarded as a normal conductance, that is, a metal-dielectric metal structure behaves for low applied voltage as an ohmic element.

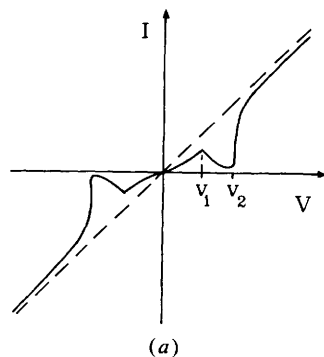
In the E - k plane the tunneling process between normal metals is represented as in Fig. 1.2c. The transfer of an electron from the left to the right metal creates a hole excitation on the left and an electron state on the right.

[†] $\beta_T = 1/k_B T$ where T is the absolute temperature and k_B is the Boltzmann constant.

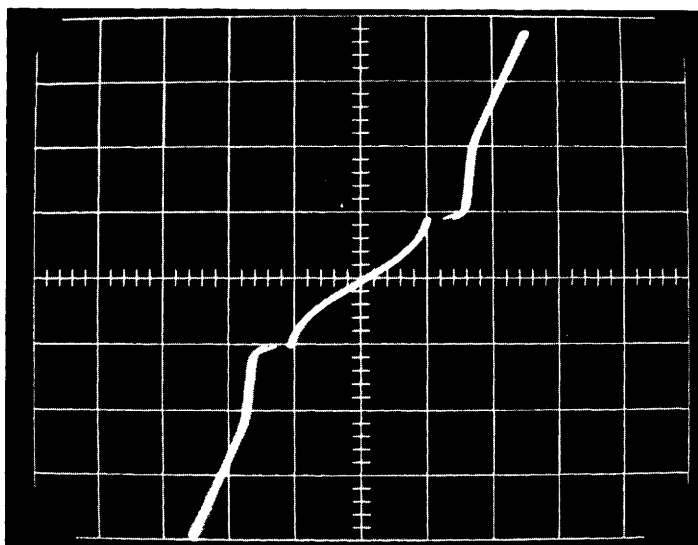
[‡]The assumptions we have made on the energy independence of the tunneling matrix element and of the densities of states can be justified by considering that the quantity $[f_L(E) - f_R(E + eV)]$ in the integral contributes significantly only within an energy range of the order of eV near the Fermi level. On the other hand we are interested in values of eV of the order of a few millivolts whereas the Fermi energy level is of the order of a few electronvolts.

When the two metals are in the superconducting state the situation is greatly altered. In fact the densities of states are now given by the expression (1.3.1). Therefore the tunneling current in a junction with the electrodes both superconductors is given by

$$I_{SS} = \text{constant} \times \int_{-\infty}^{+\infty} \frac{|E|}{|E^2 - \Delta_L^2|^{1/2}} \frac{|E + eV|}{|(E + eV)^2 - \Delta_R^2|^{1/2}} [f(E) - f(E + eV)] dE$$



(a)



(b)

Figure 1.3 (a) Sketch of the theoretical V - I characteristic of a junction with different superconducting electrodes. $V_1 = |\Delta_L - \Delta_R|/e$; $V_2 = \Delta_L + \Delta_R/e$. (b) Observed V - I characteristic for a $\text{Sn}-\text{Sn}_x\text{O}_y-\text{Pb}$ junction.

This integral, solved by numerical calculations, leads, for $T \neq 0$, to a logarithmic singularity for the current I_{SS} at a voltage $V = \pm|\Delta_L - \Delta_R|/e$ and to a finite discontinuity at $V = \pm|\Delta_R + \Delta_L|/e$ (Nicol, Shapiro, and Smith, 1960; Shapiro et al. 1962; Taylor, Burstein, and Langenberg 1962). In Fig. 1.3 is reported the resulting voltage-current (V - I) characteristic (Fig. 1.3a) compared to an experimental one (Fig. 1.3b). The single particle tunneling between two superconductors is illustrated in Fig. 1.4a. The process is shown as the destruction of a pair on the left and creation of an excitation both on the left and on the right. By equating the energies involved in the initial and final state $2eV = E_L + eV + E_R$, the minimum voltage at which the process is possible is given by $eV = \Delta_L + \Delta_R$. For $T > 0$ or in the presence of injected particles in one side of the barrier, a process like that of Fig. 1.4b is also possible. The relation between the applied voltage and the energy of the quasiparticle in the initial and final state (we are assuming specular tunneling) is $eV = E_R - E_L$.

The minimum value of V in this case is zero. When $eV = \pm|\Delta_R - \Delta_L|$ the singularity in the density of states in the two superconductors at $E_R = \Delta_R$ and

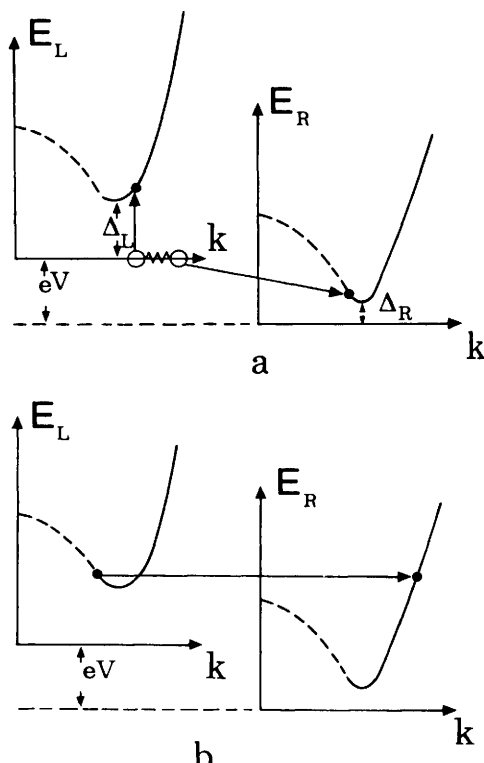


Figure 1.4 Quasiparticle tunneling processes between superconductors for finite d.c. applied bias. Δ_L and Δ_R are the energy gaps of the two electrodes. (a) Process involving the breaking of a pair. (b) Direct tunneling of a thermally excited quasiparticle.

$E_L = \Delta_L$ give rise to the mentioned logarithmic singularity in the V - I characteristics (Fig. 1.3). The finite discontinuity observed at $eV = \Delta_R + \Delta_L$ is also related to the behavior of the density of states near the gap.

1.4 Josephson Equations

It is possible to follow several different approaches in order to obtain the basic Josephson relations. We discuss first a very simple derivation, due to Feynman (Feynman, Leighton and Sands 1965), which is based on a “two level system” picture. This approach, despite its simplicity, offers a powerful key for the understanding of the peculiar features of Josephson phenomena.[†] A discussion of this treatment in the framework of the B.C.S. theory has been given by Rogovin and Scully (1974). In addition Rogovin has extended this kind of analysis to investigate various other aspects of the Josephson effect (Rogovin 1975a, b, c, 1976). Further work has been recently developed by Di Renzo et al. (1977) and Bonifacio, Milani, and Scully (1979), Lugiato and Milani (1980).

Let us consider the tunneling structure superconductor-barrier-superconductor. We call ψ_R (ψ_L) the pair wave function for the right (left) superconductor. As discussed earlier, we are dealing with macroscopic quantum states. Therefore, each superconducting electrode can be described by a single quantum state and the ψ ’s can be regarded as macroscopic wave functions, so that $|\psi|^2$ represents the actual Cooper pair density ρ . Following the notation of Rogovin and Scully we indicate with the ket $|R\rangle$ ($|L\rangle$) the base state for the right (left) superconductor. Then

$$\langle L|\psi_L^*\psi_L|R\rangle = |\psi_L|^2 = \rho_L \quad \langle R|\psi_R^*\psi_R|L\rangle = |\psi_R|^2 = \rho_R$$

If we now take into account the weak coupling existing between the two superconductors, “transitions” between the two states $|R\rangle$ and $|L\rangle$ can occur. This coupling is essentially related to the finite overlap of the two pair wave functions ψ_L and ψ_R . This situation is schematically depicted in Fig. 1.5. A state vector of this two base states system can be described as

$$|\psi\rangle = \psi_R|R\rangle + \psi_L|L\rangle$$

That is, the particle can be either in a “left” or “right” state with amplitude ψ_L or ψ_R respectively. The time evolution of the system is described by the Schrödinger equation:

$$i\hbar \frac{\partial |\psi\rangle}{\partial t} = \mathcal{H}|\psi\rangle \quad (1.4.1)$$

[†]This phenomenological model has been considered extensively by many authors (see for instance Mercereau 1969; De Bruyn Ouboter and De Waele, 1970; De Bruyn Ouboter, 1976).

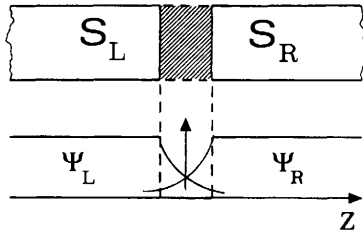


Figure 1.5 Schematic of a Josephson junction. S_L and S_R are the left and right superconductors. ψ_L and ψ_R are the left and right pair wavefunctions.

with the Hamiltonian given by

$$\mathcal{H} = \mathcal{H}_L + \mathcal{H}_R + \mathcal{H}_T$$

where $\mathcal{H}_L = E_L |L\rangle\langle L|$ and $\mathcal{H}_R = E_R |R\rangle\langle R|$ are relative to the unperturbed states $|L\rangle$ and $|R\rangle$.

$$\mathcal{H}_T = K [|L\rangle\langle R| + |R\rangle\langle L|]$$

is the term of interaction (tunneling Hamiltonian) between the two states. E_L and E_R are the ground state energies of the two superconductors. K is the coupling amplitude of the two state system which gives a measure of the coupling interaction between the two superconductors and depends on the specific junction structure (electrode geometry, tunneling barrier, etc.). In the absence of a vector potential \mathbf{A} , the quantity K can be assumed to be real.

Considering the projections on the two base states, (1.4.1) can be written in terms of amplitudes as

$$j\hbar \frac{\partial \psi_R}{\partial t} = E_R \psi_R + K \psi_L$$

$$j\hbar \frac{\partial \psi_L}{\partial t} = E_L \psi_L + K \psi_R$$

As we have seen in the two isolated superconductors, the energy terms are given by $E_R = 2\mu_R$ and $E_L = 2\mu_L$ where μ_R and μ_L are the two chemical potentials. If we consider a d.c. potential difference V across the junction these chemical potentials are shifted by an amount eV and consequently it is $E_L - E_R = 2eV$. We can choose the zero of the energy halfway between the two values on the right and on the left, so that

$$\begin{aligned} j\hbar \frac{\partial \psi_R}{\partial t} &= -eV \psi_R + K \psi_L \\ j\hbar \frac{\partial \psi_L}{\partial t} &= eV \psi_L + K \psi_R \end{aligned} \tag{1.4.2}$$

We can substitute for ψ_L and ψ_R their expressions

$$\psi_L = \rho_L^{1/2} e^{j\varphi_L} \quad \psi_R = \rho_R^{1/2} e^{j\varphi_R}$$

Separating real and imaginary terms in each equation we get

$$\begin{cases} \frac{\partial \rho_L}{\partial t} = \frac{2}{\hbar} K \sqrt{\rho_L \rho_R} \sin \varphi \\ \frac{\partial \rho_R}{\partial t} = -\frac{2}{\hbar} K \sqrt{\rho_L \rho_R} \sin \varphi \end{cases} \quad (1.4.2a)$$

$$\begin{cases} \frac{\partial \varphi_L}{\partial t} = \frac{K}{\hbar} \sqrt{\frac{\rho_L}{\rho_R}} \cos \varphi + \frac{eV}{\hbar} \\ \frac{\partial \varphi_R}{\partial t} = \frac{K}{\hbar} \sqrt{\frac{\rho_L}{\rho_R}} \cos \varphi - \frac{eV}{\hbar} \end{cases} \quad (1.4.2b)$$

where φ now is

$$\varphi = \varphi_L - \varphi_R$$

The pair current density J is given by

$$J \equiv \frac{\partial \rho_L}{\partial t} = -\frac{\partial \rho_R}{\partial t}$$

and, therefore, from (1.4.2) it follows that

$$J = \frac{2K}{\hbar} \sqrt{\rho_L \rho_R} \sin \varphi \quad (1.4.3)$$

If we assume $\rho_L = \rho_R = \rho_1$ where ρ_1 is constant, (1.4.3) becomes

$$J = J_1 \sin \varphi \quad (1.4.4)$$

where $J_1 = 2K/\hbar\rho_1$.

Let us note that although ρ_R and ρ_L are considered constant their time derivative J is not zero. There is no contradiction if we take into account the presence of the current source which continuously replaces the pairs tunneling across the barrier. These feeding currents are not included in the equations; however, this would not change the expressions of the tunnel pair current density. This point has been discussed by Ohta (1976) who gives a self-consistent model that accounts for the role of the external source.

From the two equations (1.4.2b) it follows:

$$\frac{\partial \varphi}{\partial t} = \frac{2eV}{\hbar} \quad (1.4.5)$$

Equations 1.4.4 and 1.4.5 are the constitutive relations of the Josephson effect. Assuming $V=0$ the phase difference φ results, from (1.4.5), to be constant not necessarily zero, so that [from (1.4.4)] a finite current density with a maximum value J_1 can flow through the barrier with zero voltage drop across the junction. This is the essence of the d.c. Josephson effect (Josephson 1962). The first observation was made by Anderson and Rowell in 1963. An experimental evaluation of the voltage across the junction in the d.c. Josephson regime was given by Smith (1965). This author investigated the persistent current in a wholly superconducting loop with a junction inserted and measured an upper bound of 4×10^{-16} V.

In terms of the energy-momentum diagrams, d.c. Josephson tunneling can be described as in Fig. 1.6. In this picture the pairs are located at the Fermi level. A typical voltage-current (V - I) characteristics of a Josephson junction is reported in Fig. 1.7. The zero voltage current is clearly displayed. When the current flowing through the junction exceeds its maximum value I_1 (corresponding to the current density J_1) a finite voltage suddenly appears across the junction. Indeed a switching occurs from the zero voltage state to the quasiparticle branch of the V - I characteristic.

As mentioned in the preceding section, we observe that the existence of a supercurrent (current at $V=0$) suggests that the Josephson effect can be regarded qualitatively as an extension of the superconductive properties over the whole structure including the barrier. In the bulk superconductor the current is related to the gradient of the phase by (1.1.2); in the Josephson junction the pair current is related to the phase difference between the two coupled superconductors by (1.4.4).

If we apply a constant voltage $V \neq 0$, it follows by integration of (1.4.5) that the phase φ varies in time as $\varphi = \varphi_0 + (2e/\hbar)Vt$ and therefore there appears an alternating current

$$J = J_1 \sin\left(\varphi_0 + \frac{2e}{\hbar}Vt\right)$$

with a frequency $\omega = 2\pi\nu = 2eV/\hbar$. This is called a.c. Josephson effect. The

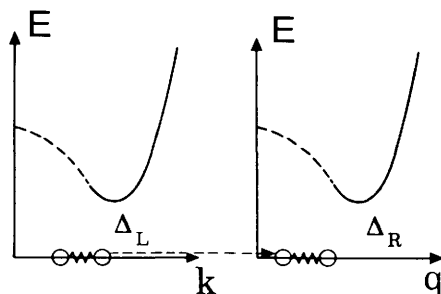


Figure 1.6 Cooper pair tunneling for $V=0$.

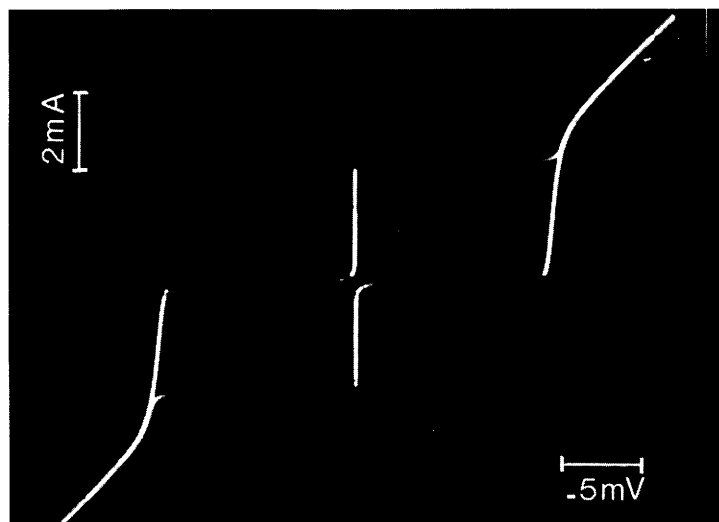


Figure 1.7 Typical voltage-current characteristic for a $\text{Sn}-\text{Sn}_x\text{O}_y-\text{Sn}$ Josephson junction at $T=1.52$ K. Horizontal scale: 0.5 mV/div; vertical scale: 2 mA/div.

ratio between frequency and voltage is given by

$$\frac{\nu}{V} = 483.6 \text{ MHz}/\mu\text{V}$$

Experimental evidence of this phenomenon arises in various situations. One possibility is to observe the effect of microwave irradiation on the d.c. V - I characteristics of the junction. In fact there is an interaction between the a.c. Josephson current and the impressed microwave signal which leads to the appearance of current steps at constant voltages (see Fig. 1.8). The steps occur at voltages

$$V_n = \frac{n\hbar}{2e} \nu_0 \quad (n = \pm 1, \pm 2, \dots)$$

where ν_0 is the frequency of the applied radiation. The first observation of this phenomenon was by Shapiro (1963).

Before proceeding further, let us observe that the derivation of (1.4.4) and (1.4.5), although referred to a tunneling junction, can hold for other kinds of weak links between superconductors. In fact the parameters of the specific structure are essentially included in the coupling factor K , which can be assumed not necessarily as a "tunneling" interaction term. In connection with this point we consider also other weak links in which deviations from the purely sinusoidal current-phase relationship can occur, however (see Chapter 7).

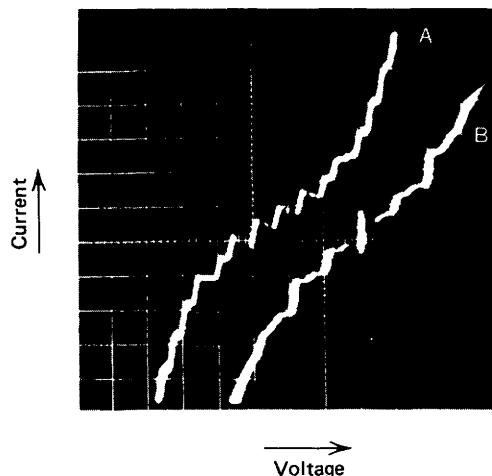


Figure 1.8 Microwave power at 9300 Mc/sec(A) and 24850 Mc/sec(B) produces many zero slope regions spaced at $h\nu/2e$ or $h\nu/e$. For A, $h\nu/e = 38.5$; for B, 103 μ V. For A, horizontal scale is 58.8 μ V/cm and vertical scale is 67 nA/cm; for B, horizontal scale is 50 μ V/cm and vertical scale is 50 μ A/cm. (After Shapiro 1963.)

Let us note finally that the description given for the quasiparticle and Josephson tunneling results from the hybridization of two uncorrelated phenomenological approaches, whereas a unified view of tunneling phenomena can be obtained only by recourse to the microscopic theory. As we see in the chapters that follow, such a theory accounts also for the temperature dependence of the Josephson current.

Finally it is worth mentioning the elegant derivation of Josephson relation due to Bloch (1970).

1.5 Magnetic Field Effects

Let us consider now the effect of a magnetic field H applied to the junction along the y direction[†] (see Fig. 1.9). For this purpose we can calculate the gauge invariant phase difference between two points (with coordinates x and $x+dx$) of the barrier by resorting to (1.1.2):

$$\nabla \varphi_{L,R} = \frac{2e}{\hbar c} \left(\frac{mc}{2e^2\rho} \mathbf{J}_s + \mathbf{A} \right)$$

[†]In the two level picture it is possible to take into account the presence of a vector potential \mathbf{A} as follows. The “coupling amplitude” K is modified by a phase factor as

$$K_A \equiv \langle L | \mathcal{H}_T | R \rangle_A = \langle L | \mathcal{H}_T | R \rangle_{A=0} \exp \left(i \frac{2e}{\hbar c} \int_r' \mathbf{A} \cdot d\mathbf{s} \right)$$

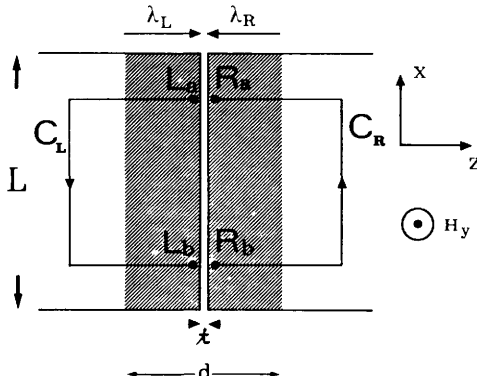


Figure 1.9 Contours of integration C_L and C_R used to derive the magnetic field dependence of the phase difference φ . The field H_y is in the y direction. The dashed zones indicate the regions in which the field penetrates into the superconducting electrodes.

which is valid in each superconductor. \mathbf{A} is the vector potential related to the magnetic field by the usual relation $\nabla \times \mathbf{A} = \mathbf{H}$. By integration along the contours C_L and C_R (see Fig. 1.9) we get

$$\begin{aligned}\varphi_{Ra}(x) - \varphi_{Rb}(x+dx) &= \frac{2e}{\hbar c} \int_{C_R} \left(\mathbf{A} + \frac{mc}{2e^2\rho} \mathbf{J}_S \right) \cdot d\mathbf{l} \\ \varphi_{Lb}(x+dx) - \varphi_{La}(x) &= \frac{2e}{\hbar c} \int_{C_L} \left(\mathbf{A} + \frac{mc}{2e^2\rho} \mathbf{J}_S \right) \cdot d\mathbf{l}\end{aligned}\quad (1.5.1)$$

Assuming the thickness of the superconducting films to be much larger than the London depths we can extend the contours C_L and C_R outside the

The integral is to be taken across the barrier between two points r of the right superconductor and l of the left one. For convenience we assume a constant \mathbf{A} within the barrier and choose the points r and l such that $|r-l|=\delta$, where δ is the barrier thickness. Thus in the presence of a vector potential \mathbf{A} (1.4.2) are modified as follows (de Waele and de Bruyn Ouboter 1969):

$$\begin{aligned}j\hbar \frac{\partial \psi_R}{\partial t} &= eV\psi_R + Ke^{j(2e/\hbar)\mathbf{A}\delta}\psi_L \\ j\hbar \frac{\partial \psi_L}{\partial t} &= -eV\psi_L + Ke^{-j(2e/\hbar)\mathbf{A}\delta}\psi_R\end{aligned}$$

In this case, making the same calculations, we get the Josephson equations in the gauge invariant form:

$$J = J_1 \sin \left(\varphi - \frac{2e}{\hbar c} \int_{\delta} \mathbf{A} \cdot d\mathbf{s} \right)$$

$$\frac{\partial}{\partial t} \left(\varphi - \frac{2e}{\hbar c} \int_{\delta} \mathbf{A} \cdot d\mathbf{s} \right) = \frac{2e}{\hbar} V$$

penetration region where the shielding current density J_S vanishes, thus avoiding also a possible reduction of the pair density ρ which can occur near the barrier. The portions of C_L and C_R in the penetration region can be chosen perpendicular to \mathbf{J}_S . With this assumption the second term in the integrals in (1.5.1) can be neglected and we have

$$\begin{aligned}\varphi(x+dx)-\varphi(x) &= [\varphi_{Lb}(x+dx)-\varphi_{Rb}(x+dx)] - [\varphi_{La}(x)-\varphi_{Ra}(x)] \\ &= \frac{2e}{\hbar c} \left[\int_{C_L} \mathbf{A} \cdot d\mathbf{l} + \int_{C_R} \mathbf{A} \cdot d\mathbf{l} \right]\end{aligned}$$

Furthermore, neglecting the barrier thickness, we can write

$$\varphi(x+dx)-\varphi(x) = \frac{2e}{\hbar c} \oint \mathbf{A} \cdot d\mathbf{l}$$

The line integral can be replaced by the surface integral of the magnetic field

$$\oint \mathbf{A} \cdot d\mathbf{l} = H_y(\lambda_L + \lambda_R + t) dx$$

so that we have, in differential terms,

$$\frac{d\varphi}{dx} = \frac{2e}{\hbar c} (\lambda_L + \lambda_R + t) H_y \quad (1.5.2)$$

where λ_L and λ_R are the London depths in the two superconductors and t the dielectric barrier thickness. By integration (1.5.2) gives

$$\varphi = \frac{2e}{\hbar c} d H_y x + \varphi_0$$

where $d = (\lambda_L + \lambda_R + t)$ is the magnetic penetration. Thus (1.4.4) becomes

$$J = J_1 \sin \left(\frac{2e}{\hbar c} d H_y x + \varphi_0 \right) \quad (1.5.3)$$

which indicates that the tunneling supercurrent is spatially modulated by the magnetic field. Then, due to the periodic character of the expression (1.5.3), situations can be realized in which the net tunneling current is zero. In particular, as is extensively discussed in Chapter 4, a rectangular junction with a uniform zero field tunneling current distribution exhibits a dependence of the maximum supercurrent on the applied magnetic field in the form of a Fraunhofer-like diffraction pattern (see Fig. 1.10a). The first observation of this effect was made by Rowell (1963). It is interesting to consider the close analogy with optical diffraction phenomena produced by a slit of the same shape as the barrier.

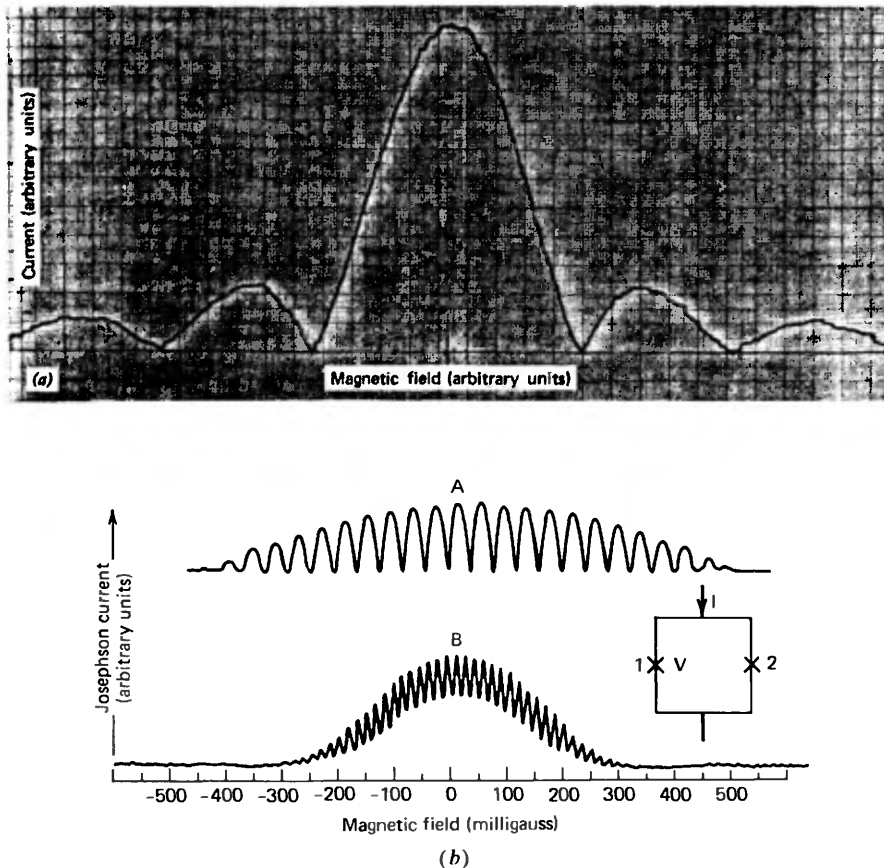


Figure 1.10 (a) Experimental magnetic field dependence of the maximum Josephson current for a Nb-NbO_x-Pb junction. (Barone and Paternó, unpublished.) (b) Experimental trace of the maximum d.c. Josephson current for a double junction configuration like that shown in the inset. The field periodicity is 39.5 and 16 m G for A and B respectively. Approximate maximum currents are 1 mA(A) and 0.5 mA(B). The junction separation is 3 mm and junction width 0.5 mm for both cases. (After Jaklevic et al. 1965.)

The analytical expression of the $I_1(H)$ dependence is given, in terms of magnetic flux Φ threading the junction, by ($H_y \equiv H$)

$$I_1(H) = I_1(0) \left| \frac{\sin \pi \frac{\Phi}{\Phi_0}}{\frac{\Phi}{\pi \frac{\Phi_0}{\Phi}}} \right|$$

where $\Phi = HLd$ and $\Phi_0 = hc/2e$ is the flux quantum (2.07×10^{-7} G cm²). Thus the minima in the pattern occur at values of the magnetic flux which are multiples of the flux quantum. When two Josephson weak links are connected

in parallel by a superconductive path, effects due to quantum interference can be observed (Jaklevic et al. 1964a). Such a two “slit” structure is sketched in the inset of Fig. 1.10b. The relative phase in one junction is related to the relative phase in the other junction through the magnetic flux enclosed in the superconducting loop. The total maximum supercurrent resulting from the interference between the supercurrents in the two links is given by the expression

$$I = 2I_1 \left| \cos \pi \frac{\Phi_e}{\Phi_0} \right|$$

where Φ_e is the flux enclosed in the superconducting loop. This phenomenon is often referred as the “Mercereau effect” (Anderson 1967). The magnetic field dependence of the maximum supercurrent for a double junction configuration is reported in Fig. 1.10b. We observe that the interference modulation is in this case superimposed on the diffraction-like behavior of the single junctions. Let us observe that the characteristic periodicity involved in this phenomenon is given by a flux quantum and that, depending on the experimental circumstances, a rather small fraction of the period can be detected. This extremely high sensitivity of the Josephson current to the magnetic field is the key point to many important applications of the Josephson effects. These aspects are discussed in detail in the following chapters.

1.6 Barrier Free Energy

Let us now make a few remarks on the free energy associated with the junction barrier. This quantity was evaluated by Anderson (1963) on the basis of microscopic theory; we instead follow here the simple thermodynamical derivation due to Josephson (1965). The junction is assumed to have a uniform tunneling current distribution. We consider two separated systems L and R , the former containing the barrier, the other not. Furthermore we imagine these two systems each connected with a current source and assume an equal feeding current I for both parts. The free energy change due to the work done by the current generators is

$$dF_L = IV_L dt \quad \text{and} \quad dF_R = IV_R dt$$

so that the energy associated with the barrier itself is

$$dF = d(F_R - F_L) = I(V_R - V_L) dt$$

$V_R - V_L$ is the voltage across the barrier, and from the Josephson constitutive relations (1.4.4) and (1.4.5) we have

$$dF = \frac{\hbar}{2e} I_1 \sin \varphi d\varphi$$

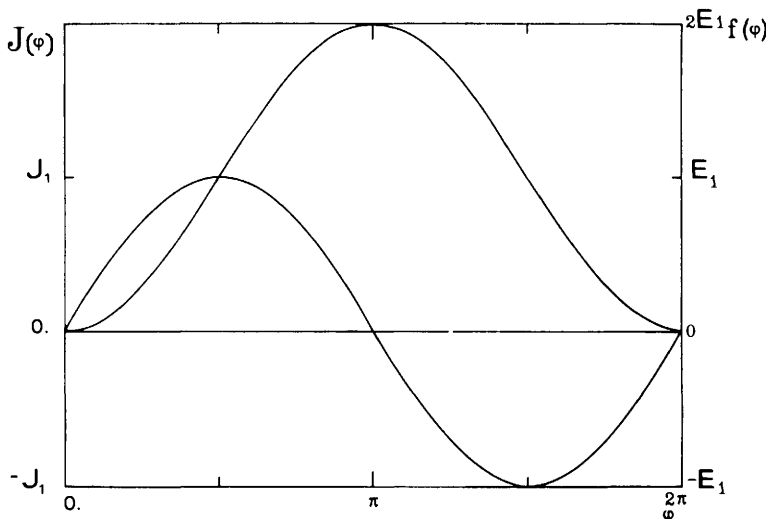


Figure 1.11 Current phase relation $J(\varphi)$ and barrier free energy $f(\varphi)$ for a Josephson junction.

Thus by integration the free energy per unit area is

$$f(\varphi) = -\frac{\hbar}{2e} J_1 \cos \varphi + \text{constant}$$

The constant is chosen by imposing $f=0$ for $\varphi=2n\pi$ ($n=0, 1, 2$) (no current flowing into the junction). Therefore

$$f(\varphi) = E_1(1 - \cos \varphi)$$

where $E_1 = \hbar J_1 / 2e$.

In Fig. 1.11 are sketched both the dependences of the supercurrent and the free energy upon the phase. We see that a given value of the current corresponds to two different values of the phase (for each cycle). The stable state corresponds to the one of minimum energy.

1.7 Electrodynamics of the Josephson Junction

Assuming nonzero magnetic field in both x and y directions we can write

$$\begin{aligned} \frac{\partial \varphi}{\partial x} &= \frac{2e}{\hbar c} H_y d \\ \frac{\partial \varphi}{\partial y} &= -\frac{2e}{\hbar c} H_x d \end{aligned} \quad (1.7.1)$$

These relations together with (1.4.4) can be combined with the Maxwell equation:

$$\nabla \times \mathbf{H} = \frac{4\pi}{c} \mathbf{J} + \frac{1}{c} \frac{\partial \mathbf{D}}{\partial t}$$

which in our case reduces to

$$\frac{\partial H_y}{\partial x} - \frac{\partial H_x}{\partial y} = \frac{4\pi}{c} J_z + \frac{1}{c} \frac{\partial D_z}{\partial t}$$

giving:

$$\frac{\hbar c^2}{8\pi ed} \left(\frac{\partial^2 \varphi}{\partial x^2} + \frac{\partial^2 \varphi}{\partial y^2} \right) = J_1 \sin \varphi + C \frac{dV}{dt}$$

where $C = \epsilon_r / 4\pi t$ is the junction capacitance *per unit area*; ϵ_r is the relative dielectric constant and t the dielectric barrier thickness.

Thus using (1.4.5) we can write

$$\frac{\partial^2 \varphi}{\partial x^2} + \frac{\partial^2 \varphi}{\partial y^2} - \frac{1}{\bar{c}^2} \frac{\partial^2 \varphi}{\partial t^2} = \frac{1}{\lambda_J^2} \sin \varphi \quad (1.7.2)$$

where

$$\bar{c} = c \left(\frac{1}{4\pi Cd} \right)^{1/2} = c \left(\frac{t}{\epsilon_r d} \right)^{1/2} \quad (1.7.3a)$$

and

$$\lambda_J = \left(\frac{\hbar c^2}{8\pi ed J_1} \right)^{1/2} \quad (1.7.3b)$$

Equation 1.7.2 wholly governs the electrodynamics of the junction (Josephson 1965). This equation has the character of a *penetration equation* as evident in the stationary limit of small φ ($\sin \varphi \sim \varphi$). In this case in fact it reduces to a London-type equation; with a one dimensional solution $\varphi \sim e^{-x/\lambda_J}$.

The penetration length λ_J gives a measure of the distance in which d.c. Josephson currents are confined at the edges of the function and for this reason is called “Josephson penetration depth.” It occurs as a consequence of a current screening due to the magnetic field self generated by the supercurrents in the junction. It recalls the Meissner-Ochsenfeld effect in a type 1 superconductor; however the typical values of the London penetration depths, λ_L , are of the order of hundreds of angstroms whereas λ_J is of the order of hundreds of microns. This lower effect of screening is another aspect consistent with the definition of “weak superconductivity.”

As we have mentioned, (1.7.2) describes the phenomenology of a Josephson tunnel junction. An even greater generality can be considered using the results of the microscopic theory. In fact, taking into account the role of quasiparticles, it follows (see Chapter 2) that the expression of the current density is more precisely given by

$$J = J_1(V) \sin \varphi + [\sigma_1(V) \cos \varphi + \sigma_0(V)] V$$

In this relation $\sigma_0(V)V$ represents the quasiparticle tunneling current and $\sigma_1(V)V \cos \varphi$ a quasiparticle pairs interference current. For most cases the last expression can be well approximated by

$$J = J_1 \sin \varphi + \sigma_0(V) V$$

Therefore taking into account the dissipative term, (1.7.2) becomes

$$\frac{\partial^2 \varphi}{\partial x^2} + \frac{\partial^2 \varphi}{\partial y^2} - \frac{1}{\bar{c}^2} \frac{\partial^2 \varphi}{\partial t^2} - \frac{\beta}{\bar{c}^2} \frac{\partial \varphi}{\partial t} = \frac{1}{\lambda_J^2} \sin \varphi \quad (1.7.4)$$

where $\beta = \sigma_0/C$.

This is a rather complicated equation for which general analytical solutions have not been found. It has been widely investigated, and will be discussed in the following chapters, considering special solutions corresponding to specific situations of physical interest.

Let us consider now just the case, first discussed by Anderson (1963), of a spatially independent φ . The general lossless equation (1.7.2) reduces to the ordinary differential equation of the pendulum:

$$\frac{d^2 \varphi}{dt^2} + \omega_J^2 \sin \varphi = 0 \quad (1.7.5)$$

with $\omega_J = \bar{c}/\lambda_J$. The resulting oscillations, in the small amplitude limit ($\sin \varphi \sim \varphi$), occur with a frequency $\nu_J = \omega_J/2\pi$ which is typically of the order of 10^9 – 10^{11} Hz (as is easily verified by assuming realistic values as $\bar{c} = \frac{1}{20}c$ and $\lambda_J \sim 100 \mu\text{m}$). This situation is characterized by the same phase value all over the barrier, that is the magnetic field is zero and the electric field normal to the plane of the barrier. Thus we recognize that such oscillations have the peculiar feature of longitudinal plasma waves (Josephson 1965, 1966). These plasma oscillations come from a pulsating interchange of energy between the barrier and the electrostatic energy terms: $\hbar J_1(1 - \cos \varphi)/2e$ and $\frac{1}{2}(2en)^2/C$. This new excitation, the Anderson plasmon, was observed first by Dahm et al. (1968). From the explicit expressions of \bar{c} and λ_J (1.7.3a,b) we have

$$\omega_J = \frac{\bar{c}}{\lambda_J} = \left(\frac{2eI_1}{\hbar C} \right)^{1/2}$$

Here I_1 and C are the total pair current and the total capacitance respectively.

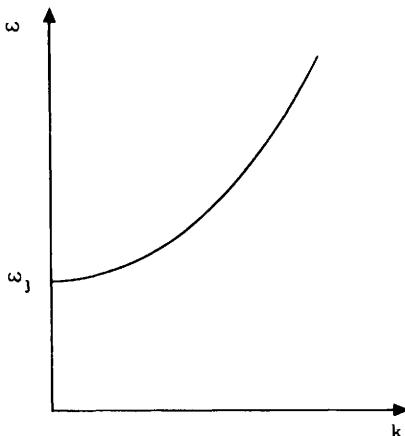


Figure 1.12 Dispersion relation ω vs. k for a Josephson junction in the limit $\varphi \rightarrow 0$. ω_J is the value of the plasma frequency for zero current and in the absence of magnetic field.

We observe that the relatively low frequency of this collective mode is related to the small density of charge carriers in the barrier (peculiar to weak superconductivity). Since the value of ω_J is below the cutoff frequency of the plasma mode in the superconductors the oscillations are confined within the barrier.

In the limit of small variations about the value $\varphi=0$ we can consider solutions of (1.7.2) of the form $\varphi \sim e^{i(\omega t - kx)}$. The resulting dispersion relation between ω and k

$$\omega^2 = \omega_J^2 + k^2 \bar{c}^2$$

is sketched in Fig. 1.12. Therefore ω_J represents the lowest frequency which allows the propagation of electromagnetic waves inside the junction. In terms of circuit parameters the characteristic plasma frequency is given by $\omega_J = 1/\sqrt{LC}$ where $L = \hbar/2eI_1$ is the equivalent inductance of the junction in the zero current limit. The expression of ω_J just derived is strictly valid only in the limit of zero Josephson current. As we see later (Section 11.6) the equivalent inductance (and therefore the plasma frequency) is a function of the total supercurrent flowing in the junction and of the applied magnetic field. Detailed experimental measurements on the plasma frequency have been performed by Pedersen, Finnegan, and Langenberg (1972a,b). These authors have experimentally confirmed the existence of the quasiparticle-pair interference term (see Section 2.6). Experimental and theoretical investigations on nonlinear effects on the plasma resonance have been performed by Dahm and Langenberg (1975).

1.8 Other Josephson Structures

As we have seen, for the occurrence of the Josephson effect it is necessary that the two superconductors be weakly connected by some means. In thin film

junctions the quantum mechanical tunneling considered so far realizes this circumstance. However other configurations of weakly coupled superconductors can be considered, such as those sketched in Fig. 1.13. The first one (Fig. 1.13a) is called the "Dayem bridge" (Anderson and Dayem 1964) and consists of a single superconducting layer in which two regions are linked by a very narrow ($\sim 1 \mu\text{m}$ or less) constriction. The condition required for the coherent transmission of Cooper pairs from one region to the other is roughly given by: $L \lesssim \xi$ where L is the maximum dimension of the link and ξ the coherence length of the specific superconductive material. It is worth pointing out that this condition can be satisfied or not depending on the operating temperature since ξ is a temperature dependent quantity. In the last few years significant progress has been made on these superconducting links regarding both the development of a sophisticated technology and theoretical approaches which account for their behavior. A different kind of film bridge structure has been designed by Notarys and Mercereau (1969). In this case the superconductivity in the bridge region is "weakened" by a proximity effect due to a superimposed normal metal layer. This allows the making of larger bridges and reduces the problem of the geometrical definition (Fig. 1.13b). To date the most promising bridge-type weak link is represented by the variable thickness bridges (see Chapter 7).

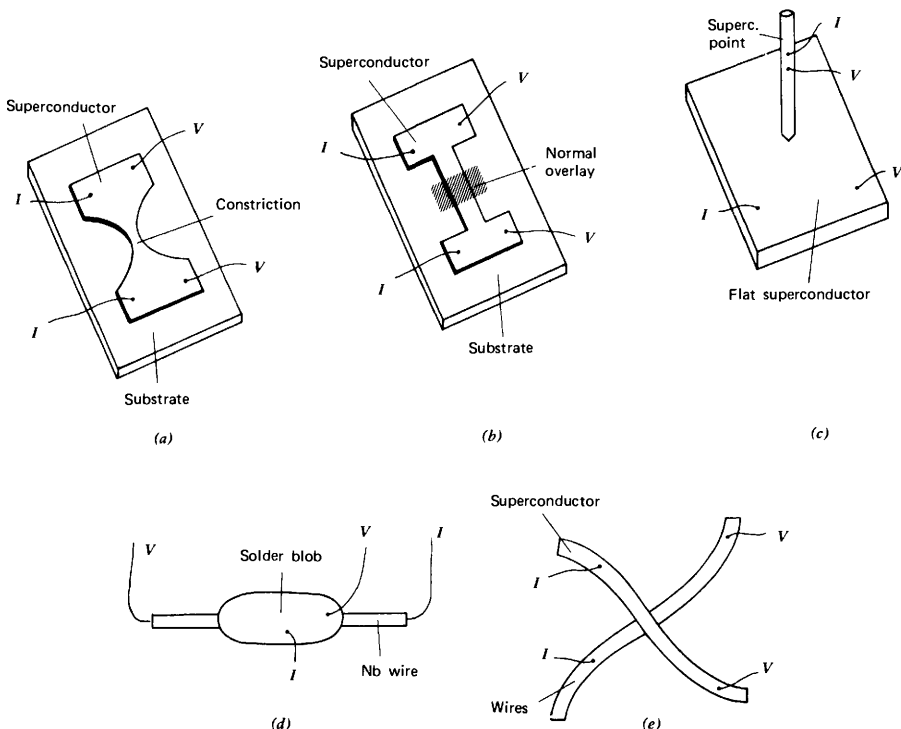


Figure 1.13 Different Josephson structures. (a) Dayem bridge, (b) proximity effect bridge, (c) point contact, (d) Clarke solder blob, and (e) crossed wire weak link.

Another structure of importance is represented by the “point contact” junction (Zimmerman and Silver 1966a; Levinstein and Kunzler 1966). In this case, a very fine superconducting point is pressed onto a flat superconductor as in Fig. 1.13c. It is possible either to establish the link by a direct metal contact between the point and the superconducting layer or to make the contact with a point previously oxidized. In the latter circumstance a structure is realized which falls more properly in the category of tunneling-type junctions. More likely intermediate situations will occur in which the conductance is provided by both mechanisms. In both cases the adjustment of the point contact pressure is extremely critical and this represents in some sense both the advantage (adjustability) and the limit (mechanical instability) of these links over the other structures.

In Fig. 1.13d, e “crossed wire” weak link proposed by Pankove (1966) and the “solder blob” investigated by Clarke (1966) are illustrated. The latter, however, usually behaves as a double junction. It is useful at this stage to make a remark on the nomenclature of the various Josephson structures. It is possible to cover with the definition of “weak links” all kinds of weak coupling between superconductors including tunneling junctions, Dayem bridges, and so on. More often however in the current literature the term “weak link” is intended only for those structures in which the link is not realized by tunneling effect. Here we adopt the expression “weak link” in the more general sense and, whenever necessary, specify the particular structure with which we are concerned.

Finally we remark that other materials rather than dielectrics can be used as barriers in Josephson junctions. The weak coupling can be realized by employing semiconducting layers having thicknesses of a few hundreds of angstroms or metal layers with thicknesses of the order of a few thousand angstroms.

The structures briefly mentioned here are discussed in Chapter 7 and 8 in more detail.

CHAPTER 2

Microscopic Theory

In his original work Josephson (1962a,b) developed the microscopic theory of the superconductive tunnel junction taking into account also pair transfer across the barrier (see also Anderson 1963). He used the transfer Hamiltonian formalism suggested by Bardeen (1961) and by Cohen, Falicov, and Phillips (1962). Later it became evident that the Josephson effect could occur also in other kinds of superconducting weak links. However, to date the tunneling structure seems to be the only one for which there is a complete description in terms of a microscopic theory.

In the present chapter we discuss the basic aspects of the microscopic theory for a Josephson tunneling structure following, basically, the approach given by Ambegaokar and Baratoff (1963). The tunneling process is described by time dependent perturbation theory which involves a properly defined coupling Hamiltonian between the two superconductors.

There exist various excellent articles which consider different theoretical approaches. We recall, among others, the derivations due to De Gennes (1963) and Josephson (1965, 1969). More recently, a theoretical analysis of the tunneling process that avoids the limitations inherent in the transfer Hamiltonian has been developed by Caroli et al. (1971a,b 1972) and with a greater generality by Feuchtwang (1974a,b, 1975, 1976) in several extensive papers. The theory developed by Feuchtwang has been extended to superconducting junctions by Arnold (1978).

Finally we mention the general approach based on the boson method in superconductivity (Leplae, Mancini, and Umezawa 1970; Leplae, Umezawa, and Mancini 1974).

2.1 Tunneling Hamiltonian Formalism

From a quantum mechanical point of view a tunneling junction is usually described by the following Hamiltonian (Cohen, Falicov and Phillips 1962):

$$\mathcal{H} = \mathcal{H}_L + \mathcal{H}_R + \mathcal{H}_T \quad (2.1.1)$$

Here \mathcal{H}_R and \mathcal{H}_L are the complete Hamiltonians of the right and left metal respectively which commute with the particle number of operators N_L and N_R

given by

$$N_L = \sum_{\mathbf{k}, \sigma} c_{\mathbf{k}\sigma}^+ c_{\mathbf{k}\sigma}; \quad N_R = \sum_{\mathbf{q}, \sigma} d_{\mathbf{q}\sigma}^+ d_{\mathbf{q}\sigma} \quad (2.1.2)$$

\mathcal{H}_T is the tunneling interaction term which transfers electrons from one metal to the other:

$$\mathcal{H}_T = \sum_{\mathbf{k}\mathbf{q}\sigma} [T_{\mathbf{k}\mathbf{q}} c_{\mathbf{k}\sigma}^+ d_{\mathbf{q}\sigma} + T_{\mathbf{k}\mathbf{q}}^* d_{\mathbf{q}\sigma}^+ c_{\mathbf{k}\sigma}] \quad (2.1.3)$$

where $c_{\mathbf{k}\sigma}^+$ ($c_{\mathbf{k},\sigma}$) creates (destroys) one electron with momentum \mathbf{k} and spin σ in left metal; $d_{\mathbf{q}\sigma}^+$ ($d_{\mathbf{q}\sigma}$) creates (destroys) one electron with momentum \mathbf{q} and spin σ in the right metal. For clarity we refer to Fig. 2.1. $T_{\mathbf{k}\mathbf{q}}$ is a matrix element connected to the transition probability for an electron from a \mathbf{k} -state on the left to a \mathbf{q} -state on the right. Making the W.K.B. approximation and neglecting the energy dependence of the tunneling probability, one finds that

$$|T_{\mathbf{k}\mathbf{q}}|^2 \propto k_z q_z \exp\left(-\frac{1}{\hbar} \sqrt{2mU} t\right) \delta_{k_y q_y} \delta_{k_x q_x}$$

U and t are the height and the width of the barrier: k_z and q_z are the components of the momenta \mathbf{k} and \mathbf{q} normal to the barrier. The Kronecker symbols account for the conservation of the momentum parallel to the plane of the barrier. As long as one considers voltage up to a few mV (the scale fixed by the energy gap of typical superconductors) and the ratio of the tunneling currents obtained with electrodes in the normal or superconducting state, this approximation is justified.

Let us make a few remarks about the expressions (2.1.1) and (2.1.3). The possibility of writing the total Hamiltonian by adding the Hamiltonians of the two noninteracting metals plus the interaction term \mathcal{H}_T implies the existence of a set of single electron wave functions $\varphi_{\mathbf{k}}$ and $\chi_{\mathbf{q}}$ for the left and right metal respectively. Such functions should have the following properties: as a first $\varphi_{\mathbf{k}}$ and $\chi_{\mathbf{q}}$ should form together a complete orthonormal set and, on the other hand, the wave function for an electron in the left (right) metal should be expressed only in terms of the $\varphi_{\mathbf{k}}$'s ($\chi_{\mathbf{q}}$'s). Unfortunately these two requirements cannot be simultaneously satisfied. However it is possible to proceed in the following way. The states $\varphi_{\mathbf{k}}(\chi_{\mathbf{q}})$ are defined by assuming that the barrier

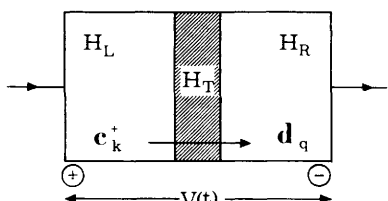


Figure 2.1 Schematic of a tunneling junction. \mathcal{H}_L and \mathcal{H}_R are the left and right Hamiltonians for the two superconducting electrodes. \mathcal{H}_T is the tunneling Hamiltonian. $c_{\mathbf{k}}^+$ and $d_{\mathbf{q}}^+$ are a creation and an annihilation operator for an electron in the left and right metal respectively.

extends to $+\infty$ ($-\infty$) (Bardeen 1961). With this assumption the $\varphi_{\mathbf{k}}$'s and $\chi_{\mathbf{q}}$'s possess an exponential tail in the barrier region and are not orthogonal. Therefore the $c_{\mathbf{k}}$ and $d_{\mathbf{q}}$ operators do not commute in a rigorous sense. As discussed by Prange (1963) under the assumption of specular tunneling between states of equal energy the anticommutation relations $\{c_{\mathbf{k}}^+, d_{\mathbf{q}}\} = \{c_{\mathbf{k}}, d_{\mathbf{q}}\} = 0$ may be assumed to hold to the lowest order in \mathcal{H}_T .

The expression chosen for the tunneling Hamiltonian (2.1.3) neither takes into account the occurrence of processes involving "spin-flip" (coupled creation and annihilation operators of equal spin) nor of tunneling processes accompanied by absorption and emission of energy ($c_{\mathbf{k}\sigma}^+ d_{\mathbf{q}\sigma}$ act at the same time, that is, the tunneling occurs instantaneously). Furthermore, time reversal symmetry implies

$$T_{-\mathbf{k}, -\mathbf{q}}^* = T_{\mathbf{k}, \mathbf{q}} \quad (2.1.4)$$

Let us consider now a voltage $V(t)$ applied to the junction such that the left electrode is positive with respect to the right one (Fig. 2.1). Assuming that the voltage drop occurs entirely across the barrier, the two Fermi levels, μ_L and μ_R will be relatively shifted by $\mu_L - \mu_R = -eV$.[†] This situation can be described assuming an additional energy for the electrons on the left side. Thus the Hamiltonian of that electrode will be

$$\mathcal{H}_L(V) = \mathcal{H}_L(0) - eVN_L$$

where N_L is given by (2.1.2).

Let us denote by $c_{\mathbf{k}\sigma}(t)$ and $\hat{c}_{\mathbf{k}\sigma}(t)$ the destruction operator of an electron in the left metal for $V=0$ and $V \neq 0$ respectively. In the Heisenberg representation the equations of the motion for these two operators are

$$j\hbar \frac{d}{dt} c_{\mathbf{k}\sigma}(t) = [c_{\mathbf{k}\sigma}(t), \mathcal{H}_L(0)]$$

$$j\hbar \frac{d}{dt} \hat{c}_{\mathbf{k}\sigma}(t) = [\hat{c}_{\mathbf{k}\sigma}(t), \mathcal{H}_L(V)] = [\hat{c}_{\mathbf{k}\sigma}(t), \mathcal{H}_L(0)] + eV\hat{c}_{\mathbf{k}\sigma}(t)$$

Therefore (Rickyzen 1965):

$$\hat{c}_{\mathbf{k}\sigma}(t) = e^{j\frac{\Phi(t)}{2}} c_{\mathbf{k}\sigma}(t) \quad (2.1.5a)$$

where

$$\frac{d\Phi}{dt} = \frac{2e}{\hbar} V(t) \quad (2.1.5b)$$

The tunneling current $I(V, T)$ for $T \geq 0$ K and $V \neq 0$ is obtained from the

[†] $e = |e|$ is the absolute value of the electron charge.

expectation value of the rate of change of the electron number of operator N_R :

$$I(V, T) = -e \langle \dot{N}_R \rangle \quad (2.1.6)$$

where \dot{N}_R is the time derivative of N_R and the positive direction for the current is assumed from the left to the right (Fig. 2.1). The expectation value is defined as

$$\langle \dot{N}_R \rangle = \frac{\text{Tr}\{e^{-\mathcal{H}/k_B T} \dot{N}_R\}}{\text{Tr}\{e^{-\mathcal{H}/k_B T}\}}$$

where \mathcal{H} is the total Hamiltonian for the system, k_B is the Boltzmann constant, and $\text{Tr}\{ \cdot \}$ denotes the trace of the operator inside the brackets.

From the equation of the motion for N_R we have

$$\dot{N}_R = \frac{j}{\hbar} [\mathcal{H}, N_R] = \frac{j}{\hbar} [\mathcal{H}_T, N_R]$$

since N_R commute with \mathcal{H}_L and \mathcal{H}_R . The expression (2.1.3) for \mathcal{H}_T yields

$$\dot{N}_R(t) = \frac{j}{\hbar} [T_{\mathbf{kq}} \hat{c}_{\mathbf{k}\sigma}^+ d_{\mathbf{q}\sigma} - T_{\mathbf{kq}}^* d_{\mathbf{q}\sigma}^+ \hat{c}_{\mathbf{k}\sigma}] \quad (2.1.7)$$

where we have used the commutation relations

$$[d_{\mathbf{q}\sigma}^+ d_{\mathbf{q}\sigma}, d_{\mathbf{q}\sigma}] = -d_{\mathbf{q}\sigma}; \quad [d_{\mathbf{q}\sigma}^+ d_{\mathbf{q}\sigma}, d_{\mathbf{q}\sigma}^+] = d_{\mathbf{q}\sigma}^+$$

which follow from the anticommutation relations for $c_{\mathbf{k}}$, $d_{\mathbf{q}}$. Inserting (2.1.7) in (2.1.6) we get for the tunneling current

$$I(V, T) = \frac{2e}{\hbar} \text{Im} \left\{ \sum_{\mathbf{kq}\sigma} T_{\mathbf{kq}} \langle \hat{c}_{\mathbf{k}\sigma}^+ d_{\mathbf{q}\sigma} \rangle \right\} \quad (2.1.8)$$

where we have taken into account that

$$T_{\mathbf{kq}}^* \langle d_{\mathbf{q}\sigma}^+ \hat{c}_{\mathbf{k}\sigma} \rangle = \{ T_{\mathbf{kq}} \langle \hat{c}_{\mathbf{k}\sigma}^+ d_{\mathbf{q}\sigma} \rangle \}^*$$

The expression (2.1.8) is easily evaluated (Ambegaokar and Baratoff 1963) to the first order in \mathcal{H}_T (linear response in \mathcal{H}_T). Since the term \mathcal{H}_T in the Hamiltonian is considered as a perturbation, it is convenient to use the interaction representation in which the time dependence of the operators is determined by the unperturbed Hamiltonian $\mathcal{H}_0 = \mathcal{H}_L(V) + \mathcal{H}_R$, whereas the time evolution of the eigenstates is determined by the perturbation term \mathcal{H}_T .

To first order in \mathcal{H}_T :

$$|\psi(T)\rangle \cong \left(1 - \frac{j}{\hbar} \int_{-\infty}^t d\tau e^{\eta\tau} \mathcal{H}_T(\tau) \right) |\psi(\infty)\rangle$$

where $\eta \rightarrow 0^+$, that is, η tends to zero through positive values; the time argument of \mathcal{H}_T indicates that this operator is taken in the interaction representation. Here $|\psi(t)\rangle$ is an eigenfunction of the total Hamiltonian $\mathcal{H} = \mathcal{H}_0 + \mathcal{H}_T$; $|\psi(\infty)\rangle$ is an eigenfunction of the unperturbed Hamiltonian \mathcal{H}_0 . The factor $e^{\eta\tau}$ implies that the perturbation is “turned on” adiabatically starting from $t = -\infty$. In this approximation relation (2.1.8) becomes

$$I = \frac{2e}{\hbar} \text{Im} \sum_{\mathbf{kq}\sigma} T_{\mathbf{kq}} \left\{ \langle \hat{c}_{\mathbf{k}\sigma}^+ d_{\mathbf{q}\sigma} \rangle_0 - \frac{j}{\hbar} \int_{-\infty}^t d\tau e^{\eta\tau} \langle [\hat{c}_{\mathbf{k}\sigma}^+(t) d_{\mathbf{q}\sigma}(t), \mathcal{H}_T(\tau)] \rangle_0 \right\}$$

where the symbol $\langle \rangle_0$ denotes an expectation value referred to the unperturbed Hamiltonian \mathcal{H}_0 . The first term of this expression vanishes since it represents the current when \mathcal{H}_T is zero. Thus

$$I = -\frac{2e}{\hbar^2} \text{Re} \sum_{\mathbf{kq}\sigma} T_{\mathbf{kq}} \int_{-\infty}^t d\tau e^{\eta\tau} \langle [\hat{c}_{\mathbf{k}\sigma}^+(t) d_{\mathbf{q}\sigma}(t), \mathcal{H}_T(\tau)] \rangle_0 \quad (2.1.9)$$

Inserting (2.1.3) in the last expression we obtain

$$\begin{aligned} I = & \frac{-2e}{\hbar^2} \text{Re} \sum_{\substack{\mathbf{kq}\sigma \\ \mathbf{k}'\mathbf{q}'\sigma'}} T_{\mathbf{kq}} \int_{-\infty}^t d\tau e^{\eta\tau} \left\{ T_{\mathbf{k}'\mathbf{q}'} \langle [\hat{c}_{\mathbf{k}\sigma}^+(t) d_{\mathbf{q}\sigma}(t), \hat{c}_{\mathbf{k}'\sigma'}^+(\tau) d_{\mathbf{q}'\sigma'}(\tau)] \rangle_0 \right. \\ & \left. + T_{\mathbf{k}'\mathbf{q}'}^* \langle [\hat{c}_{\mathbf{k}\sigma}^+(t) d_{\mathbf{q}\sigma}(t), d_{\mathbf{q}'\sigma'}^+(\tau) \hat{c}_{\mathbf{k}'\sigma'}(\tau)] \rangle_0 \right\} \end{aligned}$$

2.2 General Expression for the Total Current

We may use the relations (2.1.5) to extract the dependence on $V(t)$ and write the last expression

$$I = \text{Im} \int_{-\infty}^{+\infty} d\tau e^{\eta\tau} \left\{ e^{-\frac{j}{2}[\phi(t) - \phi(\tau)]} S(t - \tau) + e^{-\frac{j}{2}[\phi(t) + \phi(\tau)]} R(t - \tau) \right\} \quad (2.2.1)$$

where the two functions $S(t - \tau)$ and $R(t - \tau)$ are defined as follows

(Rickayzen 1965):

$$S(t-\tau) = -2j \frac{e}{\hbar^2} \theta(t-\tau) \sum_{\substack{\mathbf{k}\mathbf{q}\sigma \\ \mathbf{k}'\mathbf{q}'\sigma'}} T_{\mathbf{k}\mathbf{q}} T_{\mathbf{k}'\mathbf{q}'}^* \left\{ \langle c_{\mathbf{k}\sigma}^+(t) c_{\mathbf{k}'\sigma'}(\tau) \rangle_0 \langle d_{\mathbf{q}\sigma}(t) d_{\mathbf{q}'\sigma'}^+(\tau) \rangle_0 \right. \\ \left. - \langle d_{\mathbf{q}'\sigma'}^+(\tau) d_{\mathbf{q}\sigma}(t) \rangle_0 \langle c_{\mathbf{k}'\sigma'}(\tau) c_{\mathbf{k}\sigma}^+(t) \rangle_0 \right\} \quad (2.2.2a)$$

$$R(t-\tau) = -2j \frac{e}{\hbar^2} \theta(t-\tau) \sum_{\substack{\mathbf{k}\mathbf{q}\sigma \\ \mathbf{k}'\mathbf{q}'\sigma'}} T_{\mathbf{k}\mathbf{q}} T_{\mathbf{k}'\mathbf{q}'} \left\{ \langle c_{\mathbf{k}\sigma}^+(t) c_{\mathbf{k}'\sigma'}^+(\tau) \rangle_0 \langle d_{\mathbf{q}'\sigma'}(\tau) d_{\mathbf{q}\sigma}(t) \rangle_0 \right. \\ \left. - \langle c_{\mathbf{k}'\sigma'}^+(\tau) c_{\mathbf{k}\sigma}^+(t) \rangle_0 \langle d_{\mathbf{q}\sigma}(t) d_{\mathbf{q}'\sigma'}(\tau) \rangle_0 \right\} \quad (2.2.2b)$$

where $\theta(x)$ is the step function defined as $\theta(x)=1$, $x \geq 0$; $\theta(x)=0$, $x < 0$. Let us observe that the factorization is exact, since the expectation values are in the unperturbed ensemble (Hamiltonian $\mathcal{H}_0 = \mathcal{H}_L + \mathcal{H}_R$) that is, they refer to the two electrodes separately. If we consider these electrodes as two infinite homogeneous superconducting metals, in $S(t-\tau)$ only the diagonal terms ($\mathbf{k}=\mathbf{k}', \mathbf{q}=\mathbf{q}'$) are different from zero.

Introducing the single particle Green functions (Kadanoff and Baym, 1962)

$$G^>(\mathbf{k}, t-\tau) = -j \langle c_{\mathbf{k}}(\tau) c_{\mathbf{k}}^+(t) \rangle; \quad G^<(\mathbf{k}, t-\tau) = j \langle c_{\mathbf{k}}^+(t) c_{\mathbf{k}}(\tau) \rangle \\ G^>(\mathbf{q}, t-\tau) = -j \langle d_{\mathbf{q}}(t) d_{\mathbf{q}}^+(\tau) \rangle; \quad G^<(\mathbf{q}, t-\tau) = j \langle d_{\mathbf{q}}^+(\tau) d_{\mathbf{q}}(t) \rangle$$

The function $S(t-\tau)$ can be written as

$$S(t-\tau) = -4j \frac{e}{\hbar^2} \theta(t-\tau) \sum_{\mathbf{k}, \mathbf{q}} |T_{\mathbf{k}\mathbf{q}}|^2 \left\{ G^<(\mathbf{k}, t-\tau) G^>(\mathbf{q}, t-\tau) \right. \\ \left. - G^<(\mathbf{q}, t-\tau) G^>(\mathbf{k}, t-\tau) \right\}$$

where the summation over the spin has been performed, using the property $\langle c_{\mathbf{k}\uparrow}^+ c_{\mathbf{k}\downarrow} \rangle = \langle c_{\mathbf{k}\downarrow}^+ c_{\mathbf{k}\downarrow} \rangle$. In the expression of $R(t-\tau)$, only the term for which $\mathbf{k}' = -\mathbf{k}$, $\mathbf{q}' = -\mathbf{q}$, $\sigma' = -\sigma$ which describes B.C.S. pairing in bulk superconductors is kept. In terms of the anomalous (pairing) Green functions introduced by Gor'kov (1958):

$$\tilde{F}_{\uparrow\downarrow}^>(\mathbf{k}, t-\tau) = \langle c_{\mathbf{k}\uparrow}^+(t) c_{-\mathbf{k}\downarrow}^+(\tau) \rangle; \quad \tilde{F}_{\uparrow\downarrow}^<(\mathbf{k}, t-\tau) = -\langle c_{-\mathbf{k}\downarrow}^+(\tau) c_{\mathbf{k}\uparrow}^+(t) \rangle \\ F_{\downarrow\uparrow}^>(\mathbf{q}, t-\tau) = \langle d_{-\mathbf{q}\downarrow}(\tau) d_{\mathbf{q}\uparrow}(t) \rangle; \quad F_{\downarrow\uparrow}^<(\mathbf{q}, t-\tau) = -\langle d_{\mathbf{q}\uparrow}(t) d_{-\mathbf{q}\downarrow}(\tau) \rangle$$

$R(t-\tau)$ becomes:

$$R(t-\tau) = 4j \frac{e}{\hbar^2} \theta(t-\tau) \sum_{\mathbf{kq}} |T_{\mathbf{kq}}|^2 \{ \tilde{F}^>(\mathbf{k}, t-\tau) F^<(\mathbf{q}, \tau-t) \\ - \tilde{F}^<(\mathbf{k}, t-\tau) F^>(\mathbf{q}, \tau-t) \}$$

where the summation over the spin has been performed and the relations

$$F_{\uparrow\downarrow}^{\gtrless} = -F_{\downarrow\uparrow}^{\gtrless}; \quad \tilde{F}_{\downarrow\uparrow}^{\gtrless} = -\tilde{F}_{\uparrow\downarrow}^{\gtrless}$$

have been used.

Let us introduce the Fourier transform of the Green functions: $G^{\gtrless}(\mathbf{k}, \omega)$, $\tilde{F}^{\gtrless}(\mathbf{k}, \omega)$, $F^{\gtrless}(\mathbf{k}, \omega)$ defined by

$$G^{\gtrless}(\mathbf{k}, t) = \frac{1}{2\pi} \int_{-\infty}^{+\infty} d\omega e^{-j\omega t} G^{\gtrless}(\mathbf{k}, \omega)$$

and the corresponding spectral functions

$$G^{\gtrless}(\mathbf{k}, \omega) = \mp jA(\mathbf{k}, \omega) f^{\pm}(\omega)$$

$$\tilde{F}^{\gtrless}(\mathbf{k}, \omega) = \pm e^{-j\varphi_L} B_L(\mathbf{k}, \omega) f^{\pm}(\omega)$$

$$F^{\gtrless}(\mathbf{q}, \omega) = \pm e^{j\varphi_R} B_R(\mathbf{q}, \omega) f^{\pm}(\omega)$$

where

$$f^{\pm}(\omega) = (e^{\mp\beta_T \omega} + 1)^{-1} \quad \text{and} \quad f^+(\omega) = 1 - f^-(\omega)$$

with $\beta_T = 1/k_B T$. In the expression for \tilde{F}^{\gtrless} and F^{\gtrless} we have taken out explicitly the phase factors in the spectral functions $B(\mathbf{k}, \omega)$ (Rickayzen 1965). These phase factors have been factorized because otherwise the spectral functions B_R, B_L are proportional to the complex superconducting order parameter Δ_R on the right side and its conjugate Δ_L^* on the left, respectively.

2.2.1 The Total Current Expression in the Time Domain. Let us now make the change in the variable

$$t' = t - \tau$$

Expression (2.2.1) becomes

$$I(t) = \text{Im} \left\{ e^{-j[\phi(t)]/2} \int_{-\infty}^{+\infty} dt' e^{j(t-t')} \left[e^{j[\phi(t-t')]/2} S(t') \right. \right. \\ \left. \left. + e^{-j\phi(t-t')/2} e^{-j(\varphi_L - \varphi_R)} R'(t') \right] \right\} \quad (2.2.3)$$

where we have defined:

$$R(t) = e^{-j(\varphi_L - \varphi_R)} R'(t)$$

the two functions $S(t)$ and $R'(t)$ can be expressed in terms of the real spectral functions introduced above:

$$S(t) = -j \frac{4e}{\hbar^2} \theta(t) \sum_{\mathbf{kq}} |T_{\mathbf{kq}}|^2 \left\{ \iint_{-\infty}^{+\infty} \frac{d\omega d\omega'}{(2\pi)^2} e^{j(\omega - \omega')t} A_L(\mathbf{k}, \omega) \times A_R(\mathbf{q}, \omega') [f^-(\omega) - f^-(\omega')] \right\} \quad (2.2.4a)$$

$$R'(t) = j \frac{4e}{\hbar^2} \theta(t) \sum_{\mathbf{kq}} |T_{\mathbf{kq}}|^2 \left\{ \iint_{-\infty}^{+\infty} \frac{d\omega d\omega'}{(2\pi)^2} e^{-j(\omega - \omega')t} B_L(\mathbf{k}, \omega) \times B_R(\mathbf{q}, \omega') [f^-(\omega') - f^-(\omega)] \right\} \quad (2.2.4b)$$

The phase factor $e^{-j(\varphi_L - \varphi_R)}$ which appears in the expression of $R(t)$ has been introduced in the present derivation in a rather formal way. However, the physics underlying this quantity deserves more attention. Let us recall that a second order transition implies the appearance of a new ordered state characterized by a reduction in symmetry; that is, the system goes into a state which does not exhibit the full symmetry properties of the original Hamiltonian. A convenient example to clarify this concept of broken symmetry is represented by the ferromagnetic transition. The ground state of an isotropic ferromagnet corresponds to a situation in which all the spins are aligned in the same direction. Thus the system has lost the rotational symmetry which is present in the Heisenberg Hamiltonian. The ensemble of all the states of reduced symmetry is called a restricted ensemble. In the case of a superconductor, the situation is less obvious. The symmetry property which is broken in that case is local gauge invariance. That is, the phase of the order parameter cannot be changed arbitrarily at each point since a chosen value at one point fixes the phase at all other points. An excellent discussion of the relation between the concept of broken symmetry in superconductors and the Josephson effect is due to Anderson (1963). From a given restricted ensemble, we can generate another one by applying a unitary transformation that leaves the Hamiltonian invariant. For a homogeneous superconductor: such a transformation is given, for instance, by $e^{jN\varphi}$ where N is the number operator (the total number of electrons) and φ is a real constant. It leaves the Hamiltonian invariant because the Hamiltonian commutes with the operator N , but changes the wave functions by a constant phase factor. This factor is different for states

with different numbers of particles. It is easy to see from the definitions of the Green functions G^{\geq} and F^{\geq} , that the transformation $e^{jN\varphi}$ leaves the G 's invariant because $c_{\mathbf{k}} c_{\mathbf{k}}^+$ and $d_{\mathbf{q}} d_{\mathbf{q}}^+$ couple states with the same number of particles. On the other hand we have

$$\langle e^{jN\varphi} c_{\mathbf{k}}^+ c_{-\mathbf{k}}^+ e^{-jN\varphi} \rangle = e^{-2j\varphi} \langle c_{\mathbf{k}}^+ c_{-\mathbf{k}}^+ \rangle$$

$$\langle e^{jN\varphi} c_{\mathbf{k}} c_{-\mathbf{k}} e^{-jN\varphi} \rangle = e^{2j\varphi} \langle c_{\mathbf{k}} c_{-\mathbf{k}} \rangle$$

because $c_{\mathbf{k}}^+ c_{-\mathbf{k}}^+$ and $c_{\mathbf{k}} c_{-\mathbf{k}}$ couple states of different number of particles (two particles).

Therefore under this transformation we have

$$\tilde{F}(\mathbf{k}, t) \rightarrow e^{-2j\varphi} \tilde{F}(\mathbf{k}, t)$$

$$F(\mathbf{k}, t) \rightarrow e^{2j\varphi} F(\mathbf{k}, t)$$

Thus each restricted ensemble is characterized by a different value of the factor $e^{2j\varphi}$. For a single superconductor one can always choose $\varphi=0$; but this simple assumption is too restrictive when, as in a junction, we consider two different superconductors coupled together. In that case, it is, in fact, imperative to keep the phase factors $e^{j\varphi_L}$ and $e^{j\varphi_R}$ corresponding to the two superconductors although measurable properties can only depend on the phase difference $\varphi_L - \varphi_R$.

2.2.2 The Total Current Expression in the Frequency Domain. Introducing the spectral decomposition (Werthamer 1966):

$$e^{(-j/2)\phi(t)} = \int_{-\infty}^{+\infty} \frac{d\omega}{2\pi} W(\omega) e^{-j\omega t} \quad (2.2.5)$$

and the Fourier transform of $S(t)$ and $R'(t)$

$$S(\omega) = \int_{-\infty}^{+\infty} dt S(t) e^{j\omega t}; \quad R'(\omega) = \int_{-\infty}^{+\infty} dt R'(t) e^{j\omega t}$$

expression (2.2.3) becomes

$$I(t) = \operatorname{Im}_{\eta \rightarrow 0^+} \left\{ \int_{-\infty}^{+\infty} d\omega \int_{-\infty}^{+\infty} d\omega' [W(\omega) W^*(\omega') e^{-j(\omega-\omega')t} S(j\eta-\omega') + e^{-j\alpha} W(\omega) W(\omega') e^{-j(\omega+\omega')t} R'(j\eta+\omega')] \right\} \quad (2.2.6)$$

where $\alpha = \varphi_L - \varphi_R$. Referring to Chapter 1 (Section 1.4) we observe that here $\varphi_L - \varphi_R$ accounts for the time independent part of the relative phase. Let us

assume that the coefficients in the expansion (2.2.5) are real. This condition is satisfied in the cases of physical interest that we shall consider later on. From the expression (2.2.6) it follows:

$$\begin{aligned} I(t) = & \int_{-\infty}^{+\infty} d\omega \int_{-\infty}^{+\infty} d\omega' W(\omega) W(\omega') \{ [I_{qp}(\omega') \cos(\omega - \omega') t \\ & - I_{qp_1}(\omega') \sin(\omega - \omega') t] \\ & + [I_{J2}(\omega') \cos(\alpha + (\omega + \omega') t) + I_{J1}(\omega') \sin(\alpha + (\omega + \omega') t)] \} \quad (2.2.7) \end{aligned}$$

where we have defined

$$\begin{aligned} I_{qp}(\omega) &= \operatorname{Im}_{\eta \rightarrow 0^+} S(j\eta - \omega) \\ I_{qp_1}(\omega) &= \operatorname{Re}_{\eta \rightarrow 0^+} S(j\eta - \omega) \\ I_{J2}(\omega) &= \operatorname{Im}_{\eta \rightarrow 0^+} R'(j\eta + \omega) \\ I_{J1}(\omega) &= -\operatorname{Re}_{\eta \rightarrow 0^+} R'(j\eta + \omega) \quad (2.2.8) \end{aligned}$$

Therefore in the presence of a time varying potential $V(t)$ both real and imaginary parts of $S(\omega)$ and $R'(\omega)$ contribute to the expression for the time dependent current $I(t)$. Since $S(t)$ and $R'(t)$ are both real and vanishing for $t < 0$ the following relations hold:

$$S(-\omega) = S^*(\omega); \quad R'(-\omega) = R'^*(\omega)$$

Furthermore as it has been pointed out first by Werthamer (1966) the real and imaginary parts of $S(\omega)$ and $R'(\omega)$ are correlated by the Kramers-Kronig or dispersion relations (Mathews and Walker 1965):

$$\begin{aligned} \operatorname{Re} S(\omega) &= \frac{1}{\pi} P \int_{-\infty}^{+\infty} d\omega' \frac{\operatorname{Im} S(\omega')}{\omega' - \omega} \\ \operatorname{Im} S(\omega) &= -\frac{1}{\pi} P \int_{-\infty}^{+\infty} d\omega' \frac{\operatorname{Re} S(\omega')}{\omega' - \omega} \quad (2.2.9) \end{aligned}$$

Analogous relations can be written for $\operatorname{Re} R'(\omega)$ and $\operatorname{Im} R'(\omega)$.[†] In the case of slow varying or constant voltage applied the term $I_{J2}(\omega)$ gives no contribution (Larkin and Ovchinnikov 1966). The case of constant voltage is considered in detail in the sections that follow.

[†]P indicates the principal part of the integral.

2.3 Tunneling Current for Constant Voltage

Let us assume $V(t) = V_0 = \text{constant}$. In this case:

$$e^{(j/2)\phi(t)} = e^{(j/2)\omega_f t}$$

where $\omega_f = (2e/\hbar)V_0$. From (2.2.5) it is easy to see that the Fourier coefficients are now

$$W(\omega) = W^*(\omega) = \delta\left(\omega - \frac{\omega_f}{2}\right)$$

Therefore expressions (2.2.6) and (2.2.7) become

$$I(t) = \text{Im} \left\{ S\left(j\eta - \frac{\omega_f}{2}\right) + e^{-j\varphi(t)} R\left(j\eta + \frac{\omega_f}{2}\right) \right\} \quad (2.3.1)$$

and

$$I(t, V_0, T) = I_{qp}(V_0, T) + I_{J1}(V_0, T) \sin \varphi(t) + I_{J2}(V_0, T) \cos \varphi(t) \quad (2.3.2)$$

where $\varphi(t) = \alpha + \omega_f t$ and the dependence of the coefficients on the voltage bias and the temperature has been explicitly indicated. Thus the total tunneling current results from three different contributions. I_{qp} is related to $S(t)$ and therefore represents the quasiparticle tunneling. The phase dependent terms $I_{J1} \sin \varphi$ and $I_{J2} \cos \varphi$ are connected to $R(t)$ and describe processes in which phase coherent tunneling of Cooper pairs occurs. As will be soon apparent, $I_{qp} = I_{J2} = 0$ if $V_0 = 0$, and the only nonvanishing contribution to the total current is given by $I_{J1}(0, T) \sin \varphi$ which represents the d.c. Josephson current. If $V \neq 0$ the phase dependent terms describe a.c. currents of frequency $\omega_f = 2(e/\hbar)V_0$. If we introduce the conductivities defined by

$$\sigma_1(V_0, T)V_0 = I_{J2}(V_0, T); \quad \sigma_0(V_0, T)V_0 = I_{qp}(V_0, T) \quad (2.3.3)$$

(2.3.3) can be written as

$$I(t, V_0, T) = I_{J1}(V_0, T) \sin \varphi(t) + [\sigma_1(V_0, T) \cos \varphi(t) + \sigma_0(V_0, T)] V_0 \quad (2.3.4)$$

This is the expression of the total current as presented for the first time by Josephson (1962).

2.4 Expressions of I_{qp_1} , I_{qp} , I_{J1} , I_{J2}

In this section we derive explicit expressions for the different contributions (2.2.8) in the case of a constant voltage bias V_0 applied to the junction. In order to do this it is necessary to calculate the Fourier transforms of the

quantities $S(t)$ and $R'(t)$ defined by (2.2.4). Assuming specular transmission, integrating over the components of \mathbf{k} and \mathbf{q} parallel to the plane of the barrier, and neglecting the energy dependence in $|T_{kq}|^2$, expressions (2.2.4) can be written as

$$\begin{aligned} S(t) &= -j\theta(t) \frac{\hbar}{\pi e R_N} \int_{-\infty}^{+\infty} d\epsilon \int_{-\infty}^{+\infty} d\epsilon' \\ &\times \left\{ \int_{-\infty}^{+\infty} \frac{d\omega}{2\pi} \int_{-\infty}^{+\infty} \frac{d\omega'}{2\pi} e^{j(\omega-\omega')t} A_L(\epsilon, \omega) A_R(\epsilon', \omega') [f(\omega) - f(\omega')] \right\} \\ R'(t) &= j\theta(t) \frac{\hbar}{\pi e R_N} \int_{-\infty}^{+\infty} d\epsilon \int_{-\infty}^{+\infty} d\epsilon' \\ &\times \left\{ \int_{-\infty}^{+\infty} \frac{d\omega}{2\pi} \int_{-\infty}^{+\infty} \frac{d\omega'}{2\pi} e^{-j(\omega-\omega')t} B_L(\epsilon, \omega) B_R(\epsilon', \omega') [f(\omega') - f(\omega)] \right\} \end{aligned}$$

where we have defined

$$R_N \equiv \frac{\hbar^3}{4\pi} \frac{1}{e^2 N_R(0) N_L(0) \langle |T|^2 \rangle}$$

$N_R(0)$ and $N_L(0)$ are the densities of states at the Fermi level in the right and left metal respectively. We have omitted the minus sign in the Fermi functions. Following Baratoff (1964) we introduce the quasiparticles and pair densities of states:

$$\begin{aligned} n(\omega) &= \frac{1}{2\pi} \int_{-\infty}^{+\infty} d\epsilon A(\epsilon, \omega) \\ p(\omega) &= \frac{1}{2\pi} \int_{-\infty}^{+\infty} d\epsilon B(\epsilon, \omega) \end{aligned} \quad (2.4.1)$$

The expressions of $S(t)$ and $R'(t)$ become

$$\begin{aligned} S(t) &= -j \frac{\theta(t)}{R_N} \frac{\hbar}{\pi e} \int_{-\infty}^{+\infty} d\omega \int_{-\infty}^{+\infty} d\omega' e^{j(\omega-\omega')t} n_L(\omega) n_R(\omega') [f(\omega) - f(\omega')] \\ R'(t) &= j \frac{\theta(t)}{R_N} \frac{\hbar}{\pi e} \int_{-\infty}^{+\infty} d\omega \int_{-\infty}^{+\infty} d\omega' e^{-j(\omega-\omega')t} p_L(\omega) p_R(\omega') [f(\omega') - f(\omega)] \end{aligned} \quad (2.4.2)$$

2.4.1 The Quasiparticle Terms I_{qp}, I_{qp_1} . We have to compute the Fourier transform of $S(t)$ in $j\eta - \omega_f/2$ for $\eta \rightarrow 0^+$. Defining $\omega_0 = \omega_f/2$, it is

$$\begin{aligned} S(j\eta - \omega_0) &= -j \frac{\hbar}{\pi e R_N} \int_{-\infty}^{+\infty} dt \theta(t) e^{-j(\omega_0 - j\eta)t} \int_{-\infty}^{+\infty} d\omega \\ &\quad \times \int_{-\infty}^{+\infty} d\omega' e^{j(\omega - \omega')t} n_L(\omega) n_R(\omega') [f(\omega) - f(\omega')] \end{aligned}$$

Since

$$\int_{-\infty}^{+\infty} dt \theta(t) e^{j(\omega - \omega' - \omega_0 + j\eta)t} = -\frac{1}{j(\omega - \omega' - \omega_0 + j\eta)}$$

and

$$\lim_{\eta \rightarrow 0^+} \frac{1}{x \pm j\eta} = P\left(\frac{1}{x}\right) \mp j\pi \delta(x) \quad (2.4.3)$$

where P indicates the principal part of the remaining integral, we obtain

$$\begin{aligned} S(j\eta - \omega_0) &= \frac{\hbar}{\pi e R_N} \left\{ P \int_{-\infty}^{+\infty} d\omega \int_{-\infty}^{+\infty} d\omega' n_L(\omega) n_R(\omega') [f(\omega) - f(\omega')] \right. \\ &\quad \left. - j\pi \int_{-\infty}^{+\infty} d\omega \int_{-\infty}^{+\infty} d\omega' \delta(\omega - \omega' - \omega_0) n_L(\omega) n_R(\omega') [f(\omega) - f(\omega')] \right\} \end{aligned}$$

That is,

$$\begin{aligned} I_{qp_1} &= \operatorname{Re}_{\eta \rightarrow 0^+} S(j\eta - \omega_0) \\ &= \frac{\hbar}{\pi e R_N} P \int_{-\infty}^{+\infty} d\omega \int_{-\infty}^{+\infty} d\omega' \frac{n_L(\omega) n_R(\omega')}{\omega - \omega' - \omega_0} [f(\omega) - f(\omega')] \quad (2.4.4) \end{aligned}$$

$$\begin{aligned} I_{qp} &= \operatorname{Im}_{\eta \rightarrow 0^+} S(j\eta - \omega_0) \\ &= -\frac{\hbar}{e R_N} \int_{-\infty}^{+\infty} d\omega n_L(\omega) n_R(\omega - \omega_0) [f(\omega) - f(\omega - \omega_0)] \quad (2.4.5) \end{aligned}$$

Note (Werthamer 1966) that $\operatorname{Re} S(j\eta - \omega_0)$ diverges for $\omega_0 \rightarrow 0$ ($V_0 \rightarrow 0$). This can be understood by realizing that the real and the imaginary parts of $S(j\eta - \omega_0)$ are connected by the Kramers-Kronig relations (2.2.9) and that I_{qp} , the quasiparticle current, increases linearly with ω_0 for $\omega_0 \rightarrow \infty$. To overcome this problem we can define $S(j\eta - \omega_0)$ by subtracting $[\operatorname{Re} S(j\eta - \omega_0)]_{\omega_0=0}$. This does not affect the quasiparticle current since it is only related to the imaginary part of $S(j\eta - \omega_0)$.

The expression (2.4.5) is analogous to that derived within the phenomenological theory (Section 1.3).

Let us apply (2.4.5) to the case where both junction electrodes are in the normal state. In this situation:

$$n(\omega) = \int_{-\infty}^{+\infty} d\omega A_0(\epsilon, \omega) = 1$$

Then

$$I_{qp} = I_{NN} = -\frac{\hbar}{eR_N} \int_{-\infty}^{+\infty} d\omega [f(\omega) - f(\omega - \omega_0)]$$

Actually, since

$$\int_{-\infty}^{+\infty} d\omega [f(\omega) - f(\omega - \omega_0)] = -\omega_0$$

and

$$\omega_0 = \frac{\omega_f}{2} = \frac{eV_0}{\hbar}$$

we get

$$I_{NN} = \frac{V_0}{R_N}$$

Therefore the constant R_N , defined at beginning of the section, can be interpreted as the resistance of the junction when both metals are in the normal state. Such an ohmic behavior was also obtained by the simple approach of Section 1.3.

2.4.2 The Phase Dependent Terms I_{J1} and I_{J2} . Let us calculate the Fourier transform of $R'(t)$ in $(j\eta + \omega_0)$. From expression (2.4.b):

$$\begin{aligned} R'(j\eta + \omega_0) &= j \frac{\hbar}{\pi e R_N} \int_{-\infty}^{+\infty} dt \theta(t) e^{i(\omega_0 + j\eta)t} \int_{-\infty}^{+\infty} d\omega \\ &\quad \times \int_{-\infty}^{+\infty} d\omega' e^{-j(\omega - \omega')t} p_L(\omega) p_R(\omega') [f(\omega') - f(\omega)] \end{aligned}$$

Proceeding as in the preceding section, we arrive at

$$\begin{aligned} \lim_{\eta \rightarrow 0^+} R'(j\eta + \omega_0) &= \frac{\hbar}{\pi e R_N} \left\{ P \int_{-\infty}^{+\infty} d\omega \int_{-\infty}^{+\infty} d\omega' \frac{p_L(\omega) p_R(\omega')}{\omega - \omega' - \omega_0} [f(\omega') - f(\omega)] \right. \\ &\quad \left. + j\pi \int_{-\infty}^{+\infty} d\omega \int_{-\infty}^{+\infty} d\omega' \delta(\omega - \omega' - \omega_0) p_L(\omega) p_R(\omega') [f(\omega') - f(\omega)] \right\} \end{aligned}$$

Thus from (2.2.8):

$$\begin{aligned} I_{J1} &= - \operatorname{Re}_{\eta \rightarrow \infty^+} R'(j\eta + \omega_0) \\ &= - \frac{\hbar}{\pi e R_N} P \int_{-\infty}^{+\infty} d\omega \int_{-\infty}^{+\infty} d\omega' \frac{p_L(\omega)p_R(\omega')}{\omega - \omega' - \omega_0} [f(\omega') - f(\omega)] \end{aligned} \quad (2.4.6)$$

$$\begin{aligned} I_{J2} &= \operatorname{Im}_{\eta \rightarrow 0^+} R'(j\eta + \omega_0) \\ &= \frac{\hbar}{e R_N} \int_{-\infty}^{+\infty} d\omega p_L(\omega)p_R(\omega - \omega_0) [f(\omega - \omega_0) - f(\omega)] \end{aligned} \quad (2.4.7)$$

Let us remark that the expressions (2.4.4), (2.4.5), (2.4.6), and (2.4.7) for I_{qp} , I_{qp1} , I_{J1} , and I_{J2} , respectively, hold in general even when strong coupling effects are included. In fact we have not made any specific restriction so far on the expressions for $n(\omega)$ and $p(\omega)$. The case of the B.C.S. approximation is considered in the next section. A few general comments on the different contributions of the total current are in order. The term $I_{J1}\sin\varphi$ describes the coherent tunneling of pairs. The resulting d.c. and a.c. Josephson effects are illustrated in Figs. 1.7 and 1.8.

What is the meaning of the $\cos\varphi$ term? If we compare (2.4.5) with (2.4.7) we notice a close analogy; while (2.4.5) contains the quasiparticle densities of states, (2.4.7) contains the “pair densities” $p(\omega)$. As already observed, both terms, I_{qp} and I_{J2} , vanish for $V=0$. It is possible to interpret the term $I_{J2}\cos\varphi$ as describing a quasiparticle tunneling process which involves a concomitant destruction and creation of pairs on different sides, therefore involving phase coherence effects. Let us again observe that the expression of $R(t-\tau)$, from which both the $\sin\varphi$ and $\cos\varphi$ terms are derived, includes only terms like $c_{\mathbf{k}\uparrow}^+(t)d_{\mathbf{q}\uparrow}(t)c_{-\mathbf{k}\downarrow}^+(\tau)d_{-\mathbf{q}\downarrow}(\tau)$ which manifestly describe such events. The meaning of this term becomes more apparent if the transformation from electron operator to quasiparticle and pairs operators is performed (Stephen 1969a).

2.5 Tunneling Current in the B.C.S. Approximation

For convenience let us summarize the expressions obtained for the various current terms derived in the previous sections:

$$I_{J1}(V_0, T) = \frac{\hbar}{\pi e R_N} P \int_{-\infty}^{+\infty} d\omega \int_{-\infty}^{+\infty} d\omega' \frac{p_L(\omega)p_R(\omega')}{\omega - \omega' - \omega_0} [f(\omega) - f(\omega')] \quad (2.5.1a)$$

$$I_{J2}(V_0, T) = \frac{\hbar}{e R_N} \int_{-\infty}^{+\infty} d\omega p_L(\omega)p_R(\omega - \omega_0) [f(\omega - \omega_0) - f(\omega)] \quad (2.5.1b)$$

$$I_{qp}(V_0, T) = \frac{\hbar}{eR_N} \int_{-\infty}^{+\infty} d\omega n_L(\omega) n_R(\omega - \omega_0) [f(\omega - \omega_0) - f(\omega)] \quad (2.5.1c)$$

$$I_{qp1}(V_0, T) = \frac{\hbar}{\pi eR_N} P \int_{-\infty}^{+\infty} d\omega \int_{-\infty}^{+\infty} d\omega' \frac{n_L(\omega)n_R(\omega')}{\omega - \omega' - \omega_0} [f(\omega) - f(\omega')] \quad (2.5.1d)$$

where $\omega_0 = eV_0/\hbar$; the energies are referred to the Fermi levels and are measured in units of \hbar .

In the B.C.S. approximation:

$$n_i(\omega) = \frac{|\omega|}{\sqrt{\omega^2 - \Delta_i^2}} \theta(|\omega| - |\Delta_i|) \quad (2.5.2a)$$

$$p_i(\omega) = \frac{|\Delta_i|}{\sqrt{\omega^2 - \Delta_i^2}} \operatorname{sgn}(\omega) \theta(|\omega| - |\Delta_i|) \quad i = L, R \quad (2.5.2b)$$

Δ_i is the energy gap and

$$\theta(x) = \begin{cases} 1 & \text{for } x > 0 \\ 0 & \text{for } x < 0 \end{cases} \quad \operatorname{sgn}(x) = \begin{cases} 1 & \text{for } x > 0 \\ -1 & \text{for } x < 0 \end{cases}$$

These expressions are plotted in Fig. 2.2. For $T=0$ Werthamer (1966) has obtained analytical expressions in terms of elliptic integrals using the exchange of variables (Anderson 1963):

$$\omega = \Delta_L \cosh \xi \quad \varepsilon_1 = \Delta_L \sinh \xi$$

$$\omega' = \Delta_R \cosh \xi \quad \varepsilon_2 = \Delta_R \sinh \xi$$

where $\varepsilon_1 = \sqrt{\omega^2 - \Delta_L^2}$ and $\varepsilon_2 = \sqrt{\omega'^2 - \Delta_R^2}$. In the case of a junction with identical electrodes, $\Delta_L = \Delta_R = \Delta$ his expressions reduce to

$$I_{J1}(\omega_0, 0) = \begin{cases} -\frac{\hbar\Delta}{eR_N} K(x) & 0 \leq x \leq 1 \\ -\frac{\hbar\Delta}{eR_N} \frac{1}{x} K(x) & x \geq 1 \end{cases} \quad (2.5.4a)$$

$$I_{J2}(\omega_0, 0) = \begin{cases} 0 & 0 \leq x \leq 1 \\ -\frac{\hbar\Delta}{eR_n} \frac{1}{x} K\left[\left(\frac{x^2 - 1}{x^2}\right)^{1/2}\right] \operatorname{sgn}(\omega_0) & x \geq 1 \end{cases} \quad (2.5.4b)$$

$$I_{qp}(\omega_0, 0) = \begin{cases} 0 & 0 \leq x \leq 1 \\ \frac{\hbar\Delta}{eR_n} \left\{ 2x E\left[\left(\frac{x^2 - 1}{x^2}\right)^{1/2}\right] - \frac{1}{x} K\left[\left(\frac{x^2 - 1}{x^2}\right)^{1/2}\right] \right\} \operatorname{sgn}(\omega_0) & x \geq 1 \end{cases} \quad (2.5.4c)$$

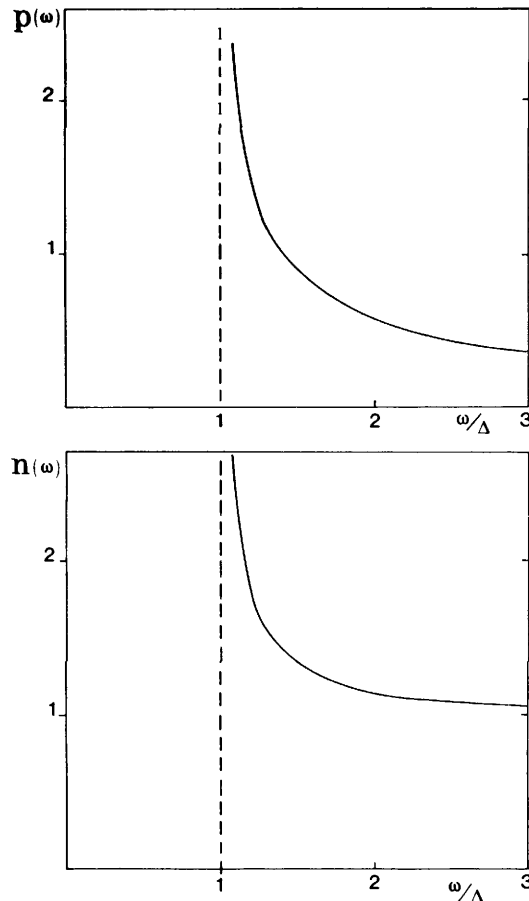


Figure 2.2 Theoretical energy dependence for the pair density $p(\omega)$ and the quasiparticle density $n(\omega)$ in the B.C.S. approximation.

where $x = |\omega_0|/2\Delta$ and $K(z)$ and $E(z)$ are the complete elliptic integral of first and second kind, respectively, and modulus z . The expressions (2.5.4) are plotted in Fig. 2.3. For $T=0$ and $eV \geq \Delta_L + \Delta_R$, as pointed out by Harris (1974a), I_{qp} and I_{J2} have opposite sign whereas I_{J1} and I_{J2} have the same sign.

From Fig. 2.3 the most evident features are the following:

- (a) $|I_{J1}(0,0)| = |I_{J2}(2\Delta,0)| = |I_{qp}(2\Delta,0)| = \pi\hbar\Delta/2eR_N$.
- (b) I_{J1} exhibits a singularity at $V=2\Delta/e$. Analytically this arises from $K(x)$ since $K(1)=\infty$. This singularity, called the Riedel peak after the author who first pointed it out (Riedel 1964), is connected to the singularity of the density of states in the superconductor at $\omega=\Delta$. Indeed $p(\omega)$ has the same singularity at Δ . Harris (1974a) suggests that it could be interpreted as a “resonance” between quasiparticle and pair tunneling.

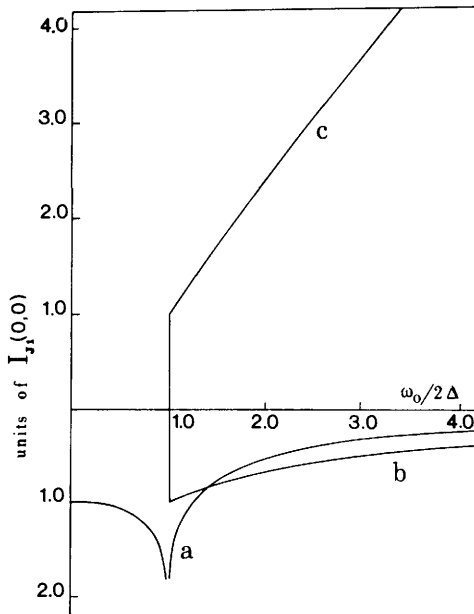
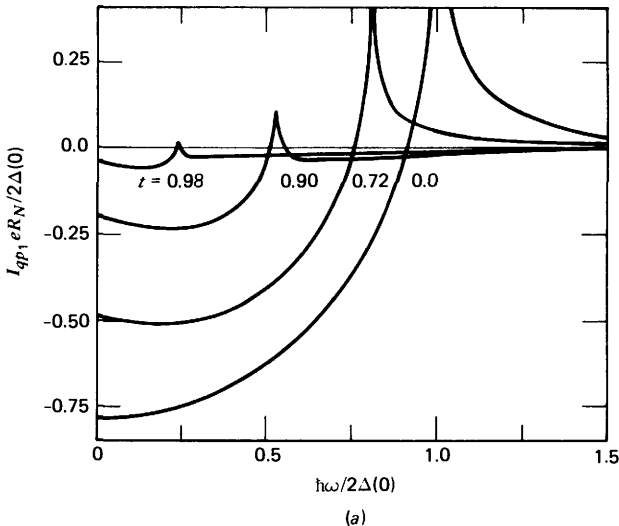


Figure 2.3 Cooper pair term $I_{J1}(\omega_0)$ (a), quasiparticle-pair interference term $I_{J2}(\omega_0)$ (b), and quasiparticle term $I_{qp}(\omega_0)$ (c) computed from (2.5.4a, b, c) derived in the B.C.S. approximation and for $T=0$. The curves are normalized to $I_{J1}(0,0)$.

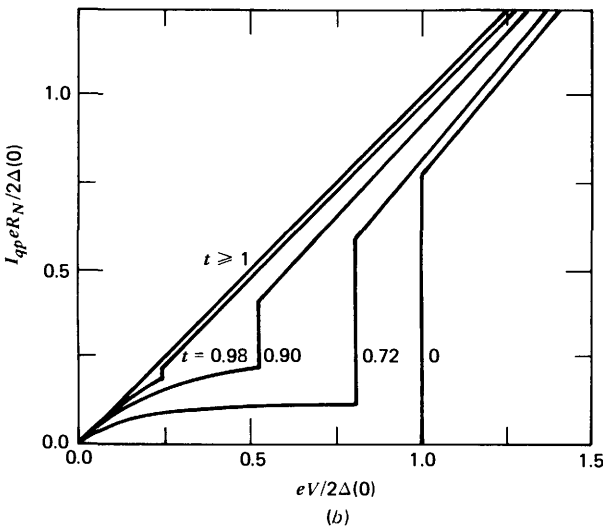
Larkin and Ovchinnikov (1966), by a slightly different formalism, have also derived expressions for the four quantities I_{J1} , I_{J2} , I_{qp} , I_{qp1} , similar to (2.5.1). In particular these authors report for I_{J1} and I_{qp1} , expressions which involve a single rather than a double integral. In the B.C.S. approximation their expressions are

$$\frac{I_{J1}(V_0, T)}{\hbar/eR_N} = \frac{\Delta_L \Delta_R}{2} \int_{-\infty}^{+\infty} d\omega \left\{ \left[\frac{\theta(\Delta_L - |\omega - \omega_0|) \theta(|\omega| - \Delta_R)}{\sqrt{\Delta_L^2 - (\omega - \omega_0)^2} \sqrt{\omega^2 - \Delta_R^2}} \right. \right. \\ \left. \left. + \frac{\theta(|\omega| - \Delta_L) \theta(\Delta_R - |\omega + \omega_0|)}{\sqrt{\omega^2 - \Delta_L^2} \sqrt{\Delta_R^2 - (\omega + \omega_0)^2}} \right] [1 - 2f(|\omega|)] \right\} \quad (2.5.5a)$$

$$\frac{I_{qp1}(V_0, T)}{\hbar/eR_N} = \frac{1}{2} \int_{-\infty}^{+\infty} d\omega \left\{ \left[\frac{(\omega - \omega_0) \theta(\Delta_L - |\omega - \omega_0|) \theta(|\omega| - \Delta_R)}{\sqrt{\Delta_L^2 - (\omega - \omega_0)^2} \sqrt{\omega^2 - \Delta_R^2}} \right. \right. \\ \left. \left. + \frac{(\omega + \omega_0) \theta(|\omega| - \Delta_L) \theta(\Delta_R - |\omega + \omega_0|)}{\sqrt{\omega^2 - \Delta_L^2} \sqrt{\Delta_R^2 - (\omega + \omega_0)^2}} \right] \omega [1 - 2f(|\omega|)] \right\} \quad (2.5.5b)$$



(a)



(b)

Figure 2.4 Real and imaginary components of the functions $S(\omega)$ and $R'(\omega)$ in the B.C.S. approximation for different values of the reduced temperature $t = T/T_c$. (a) Reactive part $I_{qp1}(V_0)$ of the quasiparticle current. (b) Quasiparticle current $I_{qp}(V_0)$. (c) Amplitude of the sine term $I_J(V_0)$. (d) Amplitude of the cosine term $I_{J2}(V_0)$. The data refer to the case of a symmetrical junction ($\Delta_L = \Delta_R = \Delta$). Δ is the energy gap of the superconducting electrodes. (After R. E. Harris 1974a, 1975a.)

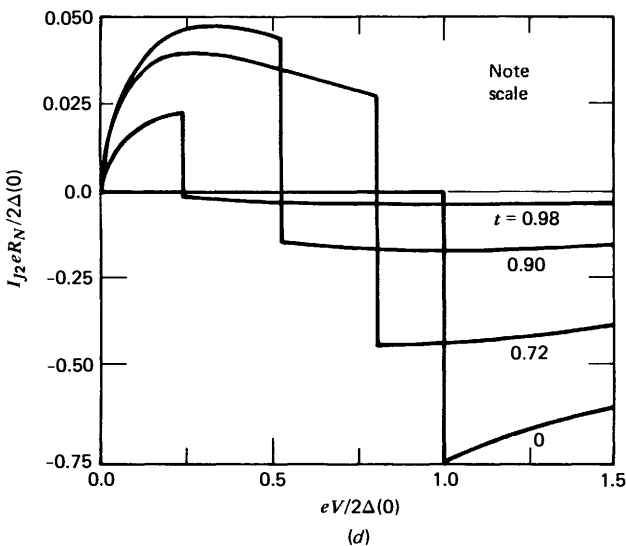
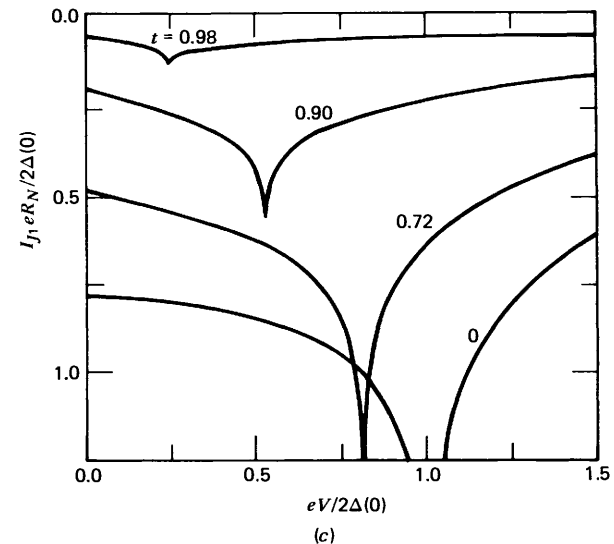
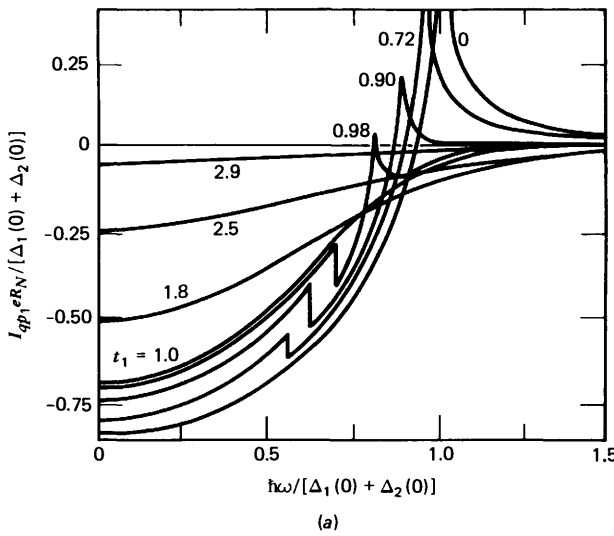
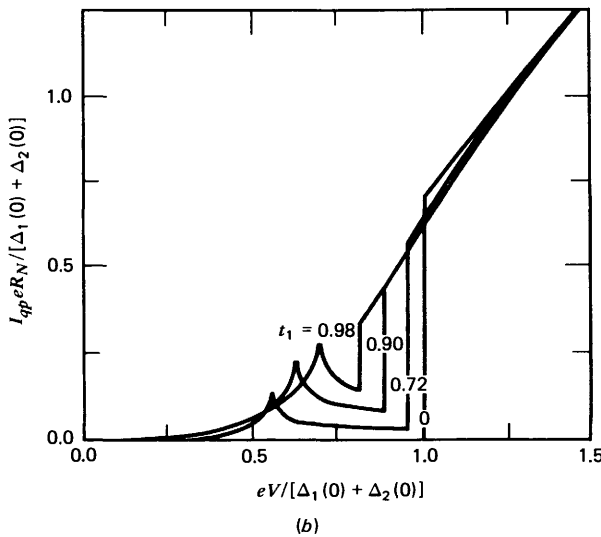


Figure 2.4 (Continued)

At finite temperatures ($T \geq 0$) the expressions (2.5.1) and (2.5.5) must be computed numerically. Analytical solutions are possible only in limiting cases (Larkin and Ovchinnikov 1966). To avoid the problem of the singularities in the calculations, Shapiro et al. (1962) introduced a convenient transformation of the coordinate system. In the same work both numerical values and experimental data for $I_{qp}(V, T)$ are presented. Numerical results for identical



(a)



(b)

Figure 2.5 Real and imaginary components of the functions $S(\omega)$ and $R'(\omega)$ for a junction with different superconducting metals ($\Delta_R = 3\Delta_L$). (a) Reactive part $I_{qp}(V_0)$ of the quasiparticle current. (b) Quasiparticle current $I_{qp}(V_0)$. (c) Amplitude of the sine term $I_{J1}(V_0)$. (d) Amplitude of the cosine term $I_{J2}(V_0)$. $t_1 = T/T_{CR}$ is the reduced temperature ($\Delta_L \equiv \Delta_1$; $\Delta_R \equiv \Delta_2$). (After R. E. Harris 1974a, 1975a.)

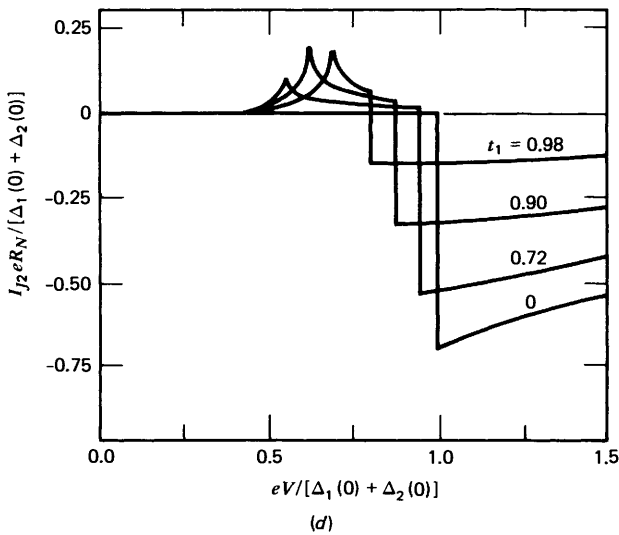
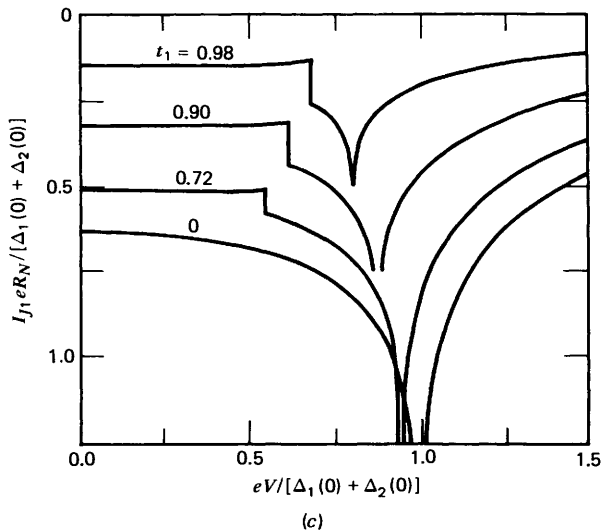


Figure 2.5 (Continued)

metals ($\Delta_L = \Delta_R$) have been reported by Poulsen (1972, 1973a, b) and by Schlup (1973).

An extensive work on the expressions of the total current has been performed by Harris (1974a,b; 1975a). His numerical results are plotted in Figs. 2.4 and 2.5 for the case of symmetrical ($\Delta_L = \Delta_R$) and asymmetrical ($\Delta_L \neq \Delta_R$) junctions respectively. In the computations the expressions (2.5.5) for I_{J1} and I_{qp_2} have been used. In Figs. 2.4 and 2.5 we see that for $T > 0$ both

I_{qp} and I_{J2} are nonzero even for $eV < \Delta_L + \Delta_R$. In the case $\Delta_L = \Delta_R = \Delta$ (Fig. 2.4), I_{qp} and I_{J2} go to zero with infinite slope as $V \rightarrow 0$. In fact for $V_0 \ll \Delta$ or T it can be shown (Larkin and Ovchinnikov 1966) that

$$I_{qp} = I_{J2} = \frac{\hbar}{eR_N} \frac{\Delta}{4\cosh^2(\Delta/2k_B T)} \frac{V_0}{k_B T} \ln\left(\frac{\min(T, \Delta)}{V_0}\right)$$

Therefore in symmetrical junctions the conductances $\sigma_0(V, T)$ and $\sigma_1(V, T)$ defined by the expressions (2.3.3) go to infinity when V goes to zero. This behavior for $\sigma_0(V, T)$ has been experimentally observed by Soerensen (1971). The logarithmic singularity at $eV_0 = \Delta_L + \Delta_R$ is still present at finite temperature. In real samples this singularity is rounded by gap anisotropy and finite quasiparticle lifetime. We return on this point in Section 11.2.1 when we discuss the experimental measurements of the Riedel peak.

In Fig. 2.5a, b, c, d the case of asymmetrical junctions is considered for the particular situation of $\Delta_R(0) = 3\Delta_L(0)$. In this case I_{qp} and I_{J2} do not approach zero for $V \rightarrow 0$ with infinite slope, but they exhibit a logarithmic singularity at $eV = \Delta_R - \Delta_L$. The term $I_{J1}(V)$ shows a jump at $eV = \Delta_R - \Delta_L$ which, (Harris 1974a), is due to the circumstance that I_{J1} is connected through the Kramers-Kronig relations to I_{J2} which has a logarithmic singularity at $eV = \Delta_R - \Delta_L$. As pointed out by Harris (1974a) such a discontinuity in I_{J1} should be observable, possibly with the same technique used for the Riedel peak, but to our knowledge this has not been accomplished so far.

At this point it is worthwhile to make a comment on the expression of I_{qp1} plotted in Figs. 2.4a and 2.5a. As has been already remarked in Section 2.4.1, $\text{Re } S(j\eta - \omega_0)$ diverges as ω_0 goes to zero. Therefore the quantity that is plotted in these figures [i.e., expression (2.5.5)] is more precisely: $I_{qp1} = \lim_{\eta \rightarrow 0^+} \{\text{Re } S(j\eta - \omega_0) - \text{Re } S(j\eta - 0) - \text{Re } S(j\eta - \infty)\}$. This corresponds to a choice for the normalization constant such that I_{qp1} goes to zero as V goes to infinity.

2.6 The "cos φ " Problem

As we have already shown, in the presence of a fixed d.c. voltage bias V the expression of the total current in a Josephson junction is given by the sum of three terms:

$$I(t, V, T) = I_{J1}(V, T) \sin \varphi(t) + V\sigma_0(V, T)[1 + \epsilon(V, T) \cos \varphi(t)]$$

where

$$\epsilon(V, T) = \frac{\sigma_1(V, T)}{\sigma_0(V, T)}$$

and σ_1 and σ_0 are the conductivities defined by the expressions (2.3.3).

Therefore the quasiparticle current contains also a phase dependent term. This is the so called “ $\cos\varphi$ ” term, originally predicted by Josephson (1962a,b). More recently the question has been reexamined in several works (Langenberg 1973; Poulsen 1973a,b; Harris 1974a,b; Schlup 1973). It is interesting to observe that until recently this term has been essentially ignored. The first experimental observations on the “ $\cos\varphi$ ” term have been performed by Pedersen, Finnegan, and Langenberg (1972a,b), by measuring the plasma frequency ω_p in a tunneling junction. Since then there has been a growing interest in the problem (more than 100 papers from 1972 to 1978). One of the main reasons is that since first experiments the observed value for ϵ , for V and $T \rightarrow 0$, was $\epsilon \approx -1$ while the value predicted by the theory is $\epsilon(0,0) = 1$. In Fig. 2.6 numerical data for $\epsilon(V, T)$ computed by Poulsen (1973a,b) for a symmetrical junction in the B.C.S. approximation are reported. Let us observe in passing that the curves reported can be obtained from the ratio between the two quantities displayed in Figs. 2.4d and 2.4b. Subsequent experiments performed by different techniques and using various kinds of samples have also given a value $\epsilon(0,0) \approx -1$ (Vincent and Deaver 1974; Rifkin et al. 1976; Falco, Parker, and Trullinger 1973; Nisenoff and Wolf 1975; Halse and Taunton 1976; Balkashin and Yanson 1976). Measurements of the “ $\cos\varphi$ ” term as a function of the temperature very near to the superconducting transition temperature T_c have been carried out by the group at the Technical University of Denmark (Soerensen, Mygind, and Pedersen 1977; Pedersen, Soerensen, and Mygind 1978) and by Rudner, Claeson, and Wahlsten (1978).

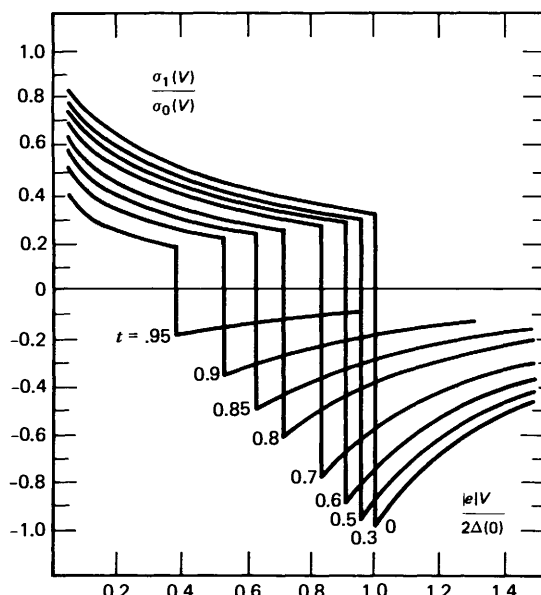


Figure 2.6 The ratio $\sigma_1(V)/\sigma_0(V)$ for the B.C.S. value of the gap parameter $\Delta(T)$ for different values of the reduced temperature $t = T/T_c$; $\sigma_1/\sigma_0 \rightarrow 1$ as $V \rightarrow 0$. (After Poulsen 1973a.)

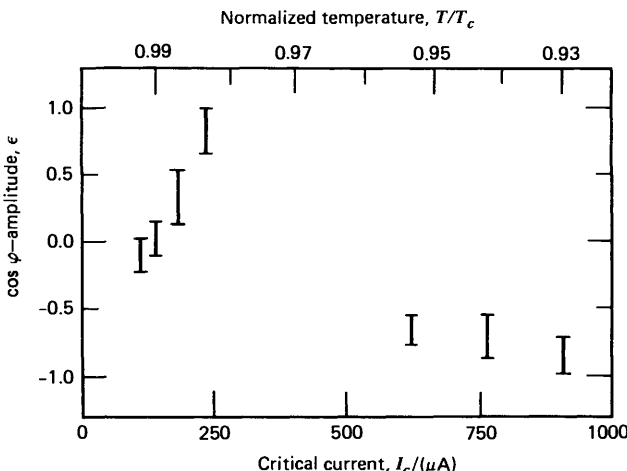


Figure 2.7 The measured $\cos \varphi$ amplitude, ϵ vs. junction critical current or normalized temperature. $T_c = 3.813 \pm 0.0005$ K. (After Soerensen, Mygind, and Pedersen 1977.)

The samples used were tunneling oxide Josephson junctions. Some experimental data on Sn-SnO_x-Sn junctions are reported in Fig. 2.7. By varying the temperature the values of ϵ change from -1 to $+1$. Therefore the microscopic theory for a tunneling junction that we have considered in this chapter seems to predict a sign for the "cos φ " term which is in disagreement with the experiments. Different theoretical approaches based on the time dependent Ginzburg Landau theory (Højgaard, Jensen, and Lindelof 1976; Hida and Ono 1977) which take into account the finite relaxation time of the order parameter (Deaver, Boone, and Rifkin 1976) have given a negative value for the $\cos \varphi$ term. Likharev (1978) has suggested that by introducing a broadening and a linewidth in the Riedel peak it is possible to obtain negative values for the $\cos \varphi$ term. This broadening may arise as a consequence of the finite lifetimes of the quasiparticles (which leads to an imaginary part for the energy gap), of gap anisotropy, and of renormalization. Samuelsen (1978) starting from simple functions that approximate the results of the microscopic theory, has introduced phenomenologically broadening effects. In this way he has shown that any value for $\epsilon(0,0)$ within -1 and $+1$ can be obtained, depending on the degree of broadening. Unfortunately to introduce effects like finite relaxation time or broadening in the Riedel peak in the microscopic theory, based on the tunneling Hamiltonian formalism, appears to be a very difficult task. Thus the sign of the "cos φ " at present is still an unsolved problem in the theory of Josephson tunneling junctions. Very recently the effect of broadening of the Riedel peak on the amplitude of $\cos \varphi$ term has been extensively investigated by Zorin et al. (1979).

CHAPTER 3

Magnitude and Temperature Dependence of the Critical Current

In Chapter 2 the microscopic theory for a Josephson tunneling junction was discussed. In particular we derived the general expressions for the quasiparticle terms I_{qp} and I_{qpl} and the pair dependent terms I_{J1} and I_{J2} as a function of voltage and temperature. We now examine in more detail the expression for the $\sin\varphi$ term I_{J1} in the zero voltage case. As we know, $I_{J1}(0, T)$ is the maximum d.c. Josephson supercurrent observable in the V - I characteristic of a junction. Various assumptions about the superconducting electrodes are considered. We begin by assuming that the two superconductors forming the junction can be described under the simple B.C.S. approximation. In this case expression (2.5.1a) for $V=0$ reduces to the one computed by Ambegaokar and Baratoff (1963). Further effects due to “strong coupling” and to the presence of paramagnetic impurities in the superconductors are examined. The magnitude and temperature dependence of I_{J1} are also investigated in these situations. Finally, effects that can arise from the presence of paramagnetic impurities in the barrier are briefly discussed.

3.1 Josephson Current for $V=0$

Although I_{J1} can be expressed as the single integral (2.5.5a) it was originally evaluated starting from expression (2.5.1a) for $V=0$:

$$I_1(T) = |I_{J1}(0, T)| = \frac{\hbar}{\pi e R_N} P \int_{-\infty}^{+\infty} d\omega \int_{-\infty}^{+\infty} d\omega' \frac{[f(\omega) - f(\omega')]}{\omega - \omega'} p_L(\omega) p_R(\omega') \quad (3.1.1)$$

where P indicates the principal part of the integral. Separating contributions from positive and negative frequencies and using the relation $f(-\omega) = 1 - f(\omega)$ and $p(-\omega) = -p(\omega)$, (3.1.1) becomes

$$\begin{aligned} I_1(T) &= \frac{2\hbar}{\pi e R_N} P \int_0^{+\infty} d\omega \int_0^{+\infty} d\omega' p_L(\omega) p_R(\omega') \\ &\times \left[\frac{f(\omega) - f(\omega')}{\omega - \omega'} + \frac{1 - f(\omega) - f(\omega')}{\omega + \omega'} \right] \end{aligned} \quad (3.1.2)$$

Let us observe that this expression has been derived without assuming pure weak coupling superconductors. This formula can be applied in different situations by choosing for the $p(\omega)$'s the particular expressions that correctly describe the superconducting electrodes.

3.2 B.C.S. Approximation

Let us consider the case in which the two superconductors forming the junction can be described by the B.C.S. theory. In the preceding chapter we reported the expression of $p(\omega)$ valid in this case (2.5.2b): For $\omega > 0$:

$$p_i(\omega) = \frac{|\Delta_i|}{\sqrt{\omega^2 - \Delta_i^2}} \Theta(|\omega| - \Delta_i) \quad (3.2.1)$$

By inserting this expression for $p_i(\omega)$ into (3.1.2) we have

$$\begin{aligned} I_1(T) &= \frac{\hbar}{\pi e R_N} 2\Delta_L \Delta_R P \int_{\Delta_L}^{+\infty} d\omega \int_{\Delta_R}^{+\infty} d\omega' \frac{1}{\sqrt{\omega^2 - \Delta_L^2} \sqrt{\omega'^2 - \Delta_R^2}} \\ &\times \left[\frac{1}{\omega + \omega'} + \frac{2\omega' f(\omega)}{\omega^2 - \omega'^2} - \frac{2\omega f(\omega')}{\omega^2 - \omega'^2} \right] \end{aligned} \quad (3.2.2)$$

Making the change of variables:

$$E_1^2 = \omega^2 = \epsilon_1^2 + \Delta_L^2; \quad E_2^2 = \omega'^2 = \epsilon_2^2 + \Delta_R^2$$

$$d\omega = \frac{\epsilon_1}{\omega} d\epsilon_1 = \frac{\sqrt{\omega^2 - \Delta_L^2}}{\omega} d\epsilon_1; \quad d\omega' = \frac{\sqrt{\omega'^2 - \Delta_R^2}}{\omega'} d\epsilon_2$$

(3.2.2) becomes

$$\begin{aligned} I_1(T) &= \frac{2\hbar \Delta_L \Delta_R}{\pi e R_N} P \int_0^\infty \frac{d\epsilon_1}{E_1} \int_0^\infty \frac{d\epsilon_2}{E_2} \left[\frac{1}{E_1 + E_2} + \frac{2E_2 f(E_1)}{E_1^2 - E_2^2} - \frac{2E_1 f(E_2)}{E_1^2 - E_2^2} \right] \end{aligned} \quad (3.2.3)$$

Thus we recover the expression originally derived by Ambegaokar and Baratoff (1963).

Let us consider (3.2.3) when $T=0$. In this case because the Fermi factors $f(E)$ are zero for $E>0$, both second and third terms of (3.2.3) give no contribution and thus

$$I_1(0) = \frac{2\hbar \Delta_L \Delta_R}{\pi e R_N} \int_0^{+\infty} \frac{d\epsilon_1}{E_1} \int_0^{+\infty} \frac{d\epsilon_2}{E_2} \frac{1}{E_1 + E_2} \quad (3.2.4)$$

Following Anderson (1963) let us make the substitution:

$$E_{1,2} = \Delta_{L,R} \cosh \theta_{1,2} \quad \epsilon_{1,2} = \Delta_{L,R} \sinh \theta_{1,2}$$

The integral in (3.2.4) becomes

$$\int_0^{+\infty} d\theta_1 \int_0^{+\infty} d\theta_2 \frac{1}{\Delta_L \cosh \theta_1 + \Delta_R \cosh \theta_2}$$

which, by the change of variables:

$$u = \frac{\theta_1 + \theta_2}{2} \quad v = \frac{\theta_1 - \theta_2}{2}$$

and using the relations:

$$\cosh \theta_1 \pm \cosh \theta_2 = \frac{2 \cosh u \cosh v}{2 \sinh u \sinh v}$$

reduces, after the integration respect to v , to the expression

$$\pi \int_0^{+\infty} \frac{du}{\sqrt{\Delta_1^2 + \Delta_2^2 + 2\Delta_1 \Delta_2 \cosh 2u}}$$

To do the integration with respect to v the substitution $y = e^v$ has been used. The last integral can be changed into the standard form for the complete elliptic integral of the first kind by the substitution $\cosh 2u = x$; (3.2.4) becomes

$$I_1(0) = \frac{2\hbar}{eR_N} \frac{\Delta_L \Delta_R}{\Delta_L + \Delta_R} K\left(\frac{|\Delta_R - \Delta_L|}{\Delta_R + \Delta_L}\right) \quad (3.2.5)$$

where $K(x)$ is the abovementioned complete elliptic integral of the first kind. If $\Delta_L \approx \Delta_R$ using the asymptotic expression $K(x) \approx \pi/2$ for $x \rightarrow 0$, (3.2.5) becomes

$$I_1(0) \approx \frac{\pi \hbar}{eR_N} \frac{\Delta_L \Delta_R}{\Delta_L + \Delta_R} \quad (3.2.6)$$

This approximate expression can be used as long as Δ_R and Δ_L differ by no more than a factor 2 or 3. For a symmetric junction, in which $\Delta_L = \Delta_R = \Delta$, (3.2.5) reduces to the exact relation

$$I_1(0) = \frac{\pi}{2} \frac{\hbar \Delta}{eR_N} \quad (3.2.7)$$

This expression is very useful in practice. In fact it allows a ready estimation of the expected maximum value for the d.c. Josephson current just by looking at

the V - I characteristic of the junction. It says that the maximum zero voltage current is equal to the one at the voltage $(\pi/2)\hbar\Delta/e$ in the V - I characteristic when both metals are in the normal state^f. Let us observe incidentally that (3.2.7) can be easily obtained from (2.5.4a) by taking $x=0$. In the case $T>0$, as shown by Ambegaokar and Baratoff (1963), the integral in (3.2.3) can be transformed in a sum over the poles of the Fermi function $f(E)$. To show this, we follow a slightly different derivation. Let us start from the single integral expression (2.5.5a). For zero voltage ($\omega_0=0$) introducing the quantities

$$u_i(\omega)=\frac{\omega}{\Delta_i} \quad i=L, R$$

this expression can be written as

$$\frac{I_{J1}(0, T)}{\hbar/eR_N} = - \int_0^{+\infty} d\omega \tanh\left(\frac{\omega}{2k_B T}\right) \text{Im} \left[\frac{1}{\sqrt{u_L^2(\omega)-1}} \cdot \frac{1}{\sqrt{u_R^2(\omega)-1}} \right] \quad (3.2.8)$$

where the following relations have been used:

$$1-2f(\omega)=\tanh\left(\frac{\omega}{2k_B T}\right)$$

and

$$\frac{1}{\sqrt{x^2-1}} = \begin{cases} 1/\sqrt{x^2-1} & x>1 \\ -j/\sqrt{1-x^2} & x<1 \end{cases}$$

The expression in the right side of (3.2.8) is equivalent to (Baratoff 1964)

$$-\frac{1}{2j} \int_{\Gamma_0} dz \frac{f(z)}{\sqrt{u_L^2(z)-1} \sqrt{u_R^2(z)-1}}$$

where the contour Γ_0 is sketched in Fig. 3.1. The Fermi function $f(z)=(e^{\beta z}+1)^{-1}$ has poles at $z_n=j\omega_n=j(\pi/\beta_T)(2n+1)$ with residues $-1/\beta_T$ where $\beta_T=1/k_B T$. Therefore the integral can be computed deforming the contour Γ_0 into the contour Γ to include these poles (see Fig. 3.1). Then (3.2.8) becomes (Baratoff 1964)

$$I_1(T)=\frac{\Delta_L(T)\Delta_R(T)}{eR_N} \frac{\pi\hbar}{\beta_T} \sum_{l=0, \pm 1, \pm 2} \left\{ [\omega_l^2 + \Delta_R^2(T)] [\omega_l^2 + \Delta_L^2(T)] \right\}^{-1/2} \quad (3.2.9)$$

^fLet us recall that here Δ is measured in units of \hbar .

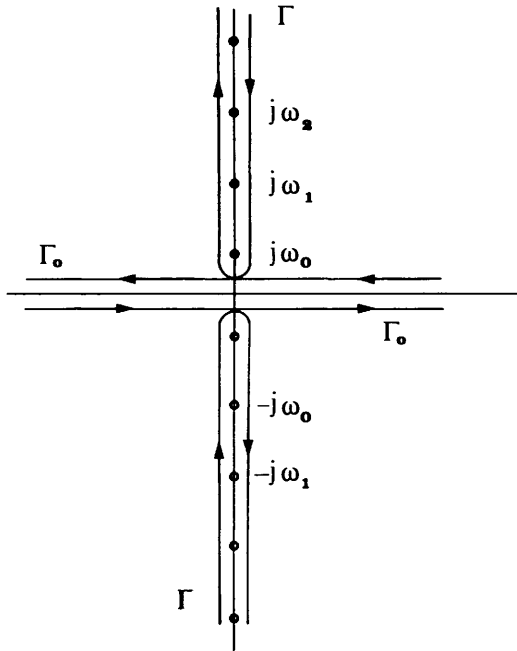


Figure 3.1 The contours Γ_0 and Γ in the complex z plane. Γ encloses the poles of the Fermi function $f(z)$ at $z_n = j(2n+1)\pi k_B T$. (After Baratoff 1964.)

For $\Delta_L = \Delta_R = \Delta$ the last expression reduces to

$$I_l(T) = \frac{\Delta^2(T)}{R_N} \frac{\pi}{\beta_T} \sum_{l=0, \pm 1, \dots} [\omega_l^2 + \Delta^2(T)]^{-1}$$

It can be computed analytically and gives

$$I_l(T) = \frac{\pi}{2} \frac{\Delta(T)}{R_N} \tanh\left(\frac{\Delta(T)}{2k_B T}\right) \quad (3.2.10)$$

The first experimental results on the temperature dependence of the Josephson critical current are due to Fiske (1964) who investigated Sn-Sn and Pb-Sn junctions obtaining a substantial agreement with the theory. Similar agreement was obtained in the results by Yanson, Svistunov and Dmitrenko (1964) on tin-tin samples. Recently, further experiments (Balsamo et al. 1974) performed with a more sophisticated technique have demonstrated an excellent agreement with the Ambegaokar and Baratoff theory. In Fig. 3.2 we present

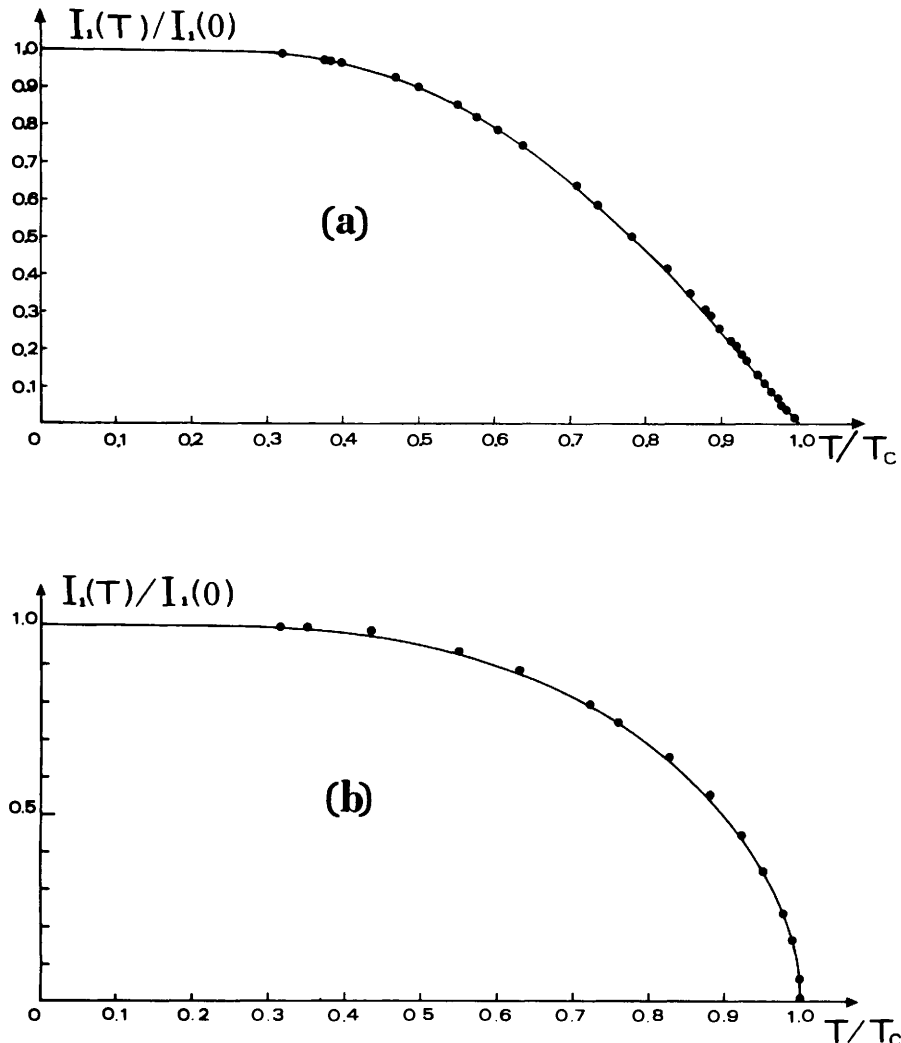


Figure 3.2 Temperature dependence of the maximum (d.c.) Josephson current. (a) Sn-SnO_x-Sn junction; (b) Sn-SnO_x-Pb junction. The experimental data (solid circles) are compared with the theoretical curves (solid lines) calculated using the Ambegaokar and Baratoff results. The maximum error in the data is smaller than the dimensions of the solid circles. (After Balsamo et al. 1974.)

experimental results which refer to (a) symmetric and (b) asymmetric junctions. The data are compared with the Ambegaokar and Baratoff theoretical curves obtained as follows. The dimensionless ratio $I_1(T)/I_1(0)$ is obtained from (3.2.9) and (3.2.5). Expressing the energy gaps in degrees Kelvin, it is useful to rewrite (3.2.9) in terms of reduced gaps $d_i = \Delta_i(T)/\Delta_i(0)$ and temperatures $t_i = T/T_{ci}$ where T_{ci} denotes the critical temperature of either

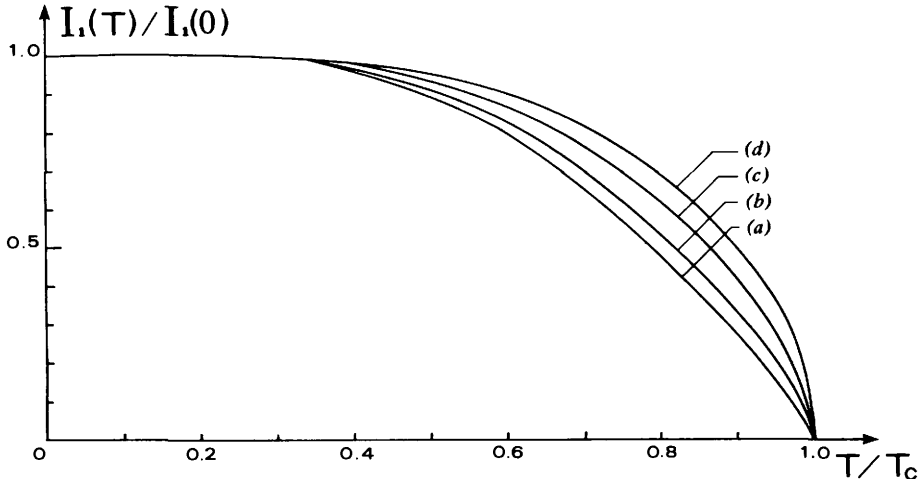


Figure 3.3 Theoretical temperature dependence of the maximum d.c. Josephson current for junctions with different superconducting electrodes computed by using the Ambegaokar and Baratoff results. (a) $\Delta_1/\Delta_2 = 1.00$, $T_{c1}/T_{c2} = 1.00$; (b) $\Delta_1/\Delta_2 = 0.95$, $T_{c1}/T_{c2} = 0.91$; (c) $\Delta_1/\Delta_2 = 1.03$, $T_{c1}/T_{c2} = 0.81$; (d) $\Delta_1/\Delta_2 = 0.43$, $T_{c1}/T_{c2} = 0.41$. $\Delta_1, T_{c1}, \Delta_2, T_{c2}$ are energy gap and critical temperature of the two electrodes. Data are normalized to the zero temperature critical current to T_{ci} . ($L \equiv 1, R \equiv 2$).

electrode ($i=R, L$):

$$\frac{I_i(T)}{I_i(0)} = \frac{2\pi t_L T_{CL} d_L(t_L) d_R(t_R)}{\frac{2\Delta_L(0)\Delta_R(0)}{\Delta_L(0)+\Delta_R(0)} K\left(\frac{|\Delta_L - \Delta_R|}{\Delta_L + \Delta_R}\right)} \\ \times \sum_{i=0,1,2,\dots} \left\{ \prod_{i=1}^2 \frac{(2i+1)^2 \pi^2 t_i^2}{(\Delta_i(0)/T_{ci})^2} + d_i^2(t_i) \right\}^{-1/2}$$

This expression can be computed numerically as a function of the parameters T_{ci} and $\Delta_i(0)$. The gaps ratio $d_i(T)$ were obtained by polynomial interpolation of the numerical results given by Muhschlegel (1959). In Fig. 3.3 we present curves of $I_i(T)$ (normalized) vs. the reduced temperature for different superconducting electrodes. Finally we observe that good agreement with the theory by Ambegaokar and Baratoff has been found in “some” point contact structures. For example, we mention the Ta-Ta point-contacts investigated by Taguchi and Yoshioka (1970).

3.3 Strong Coupling Effects

Let us now consider the influence on the critical current value of so-called strong coupling effects.

A realistic treatment of the electron-phonon interactions in the superconductors leads in fact to a complex energy dependent gap in contrast to the B.C.S. approximation. In this general case the pairing density is given by

$$p_i(\omega) = \text{Re} \left[\frac{\Delta_i(\omega)}{\sqrt{\omega^2 - \Delta_i^2(\omega)}} \right] \quad (3.3.1)$$

where $\Delta_i(\omega)$ is the frequency dependent, complex energy gap. In Fig. 3.4 are reported the real and imaginary parts of $\Delta(\omega)$ for lead which is a markedly strong coupling superconductor. The zero voltage current $I_1(T)$ can be computed by inserting (3.3.1) into (3.1.2).

Fulton and McCumber (1968) have shown that this expression for a symmetric junction, can be transformed into

$$I_1(T) = \frac{\pi}{2} \frac{\hbar \Delta_0}{e R_N} \left[\tanh\left(\frac{\Delta_0}{2k_B T}\right) \right] - \frac{\hbar}{e R_N} \int_{\Delta_0^+}^{+\infty} d\omega \tanh \frac{\omega}{2k_B T} \text{Im} \left[\frac{\Delta^2(\omega)}{\omega^2 - \Delta^2(\omega)} \right] \quad (3.3.2)$$

where

$$\Delta_1(\omega) = \text{Re}[\Delta(\omega)]; \quad \Delta'_1(\omega) = \frac{d\Delta_1(\omega)}{d\omega}$$

and Δ_0 is that value of ω for which $\Delta_1(\omega) = \omega$.

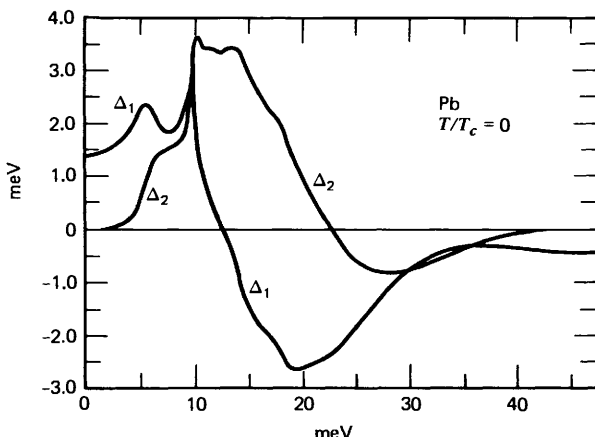


Figure 3.4 Frequency dependence of the real $\Delta_1(\omega)$ and imaginary $\Delta_2(\omega)$ part of the energy gap for $T=0$ K. (After Lim et al. 1970)

The approximation $|\text{Im } \Delta(\Delta_0)| \ll \Delta_0$, which is valid for physical systems, has been used. These authors have performed numerical computations at $T=0$ K for two superconductors, lead and tin, using for $\Delta(\omega)$ values inferred by MacMillan and Rowell (1969) from an inversion of their measurements of $I_{qp}(V)$. They found for Pb and Sn, respectively, values of 78.8 and 91.1% of the values $I_1(0)$ computed using the B.C.S. approximation. For Pb-Pb junctions Lim et al. (1970) have performed both theoretical and experimental investigations of the temperature dependence of the Josephson critical current. These authors have extended the analysis to finite temperature by iteration of the Eliashberg (1962) gap equations at various temperatures using the numerical data of MacMillan and Rowell. In Fig. 3.5 we present their experimental results for the maximum current density versus temperature (both in normalized units) together with their theoretical values. The crosses are strong coupling values calculated from (3.1.5); the solid triangles and circles refer to the values obtained by putting into (3.2.4) the B.C.S. $\Delta(T)$ and the strong coupling $\Delta(T)$, respectively.

In conclusion, strong coupling among other effects reduces the critical current, as confirmed by many careful experiments; see for instance, Schwidtal and Finnegan (1970) and Fulton and Dunkleberger (1974b) for lead-lead and tin-tin junctions respectively. The authors of the present book did not find any reduction other than that predicted by Fulton and McCumber. Recently, Paley, Wilson and Gayley (1975) have reported experimental data on Sn-Sn junctions which exhibit an unusually high maximum d.c. Josephson current, namely in agreement with the B.C.S. rather than strong coupling predictions.

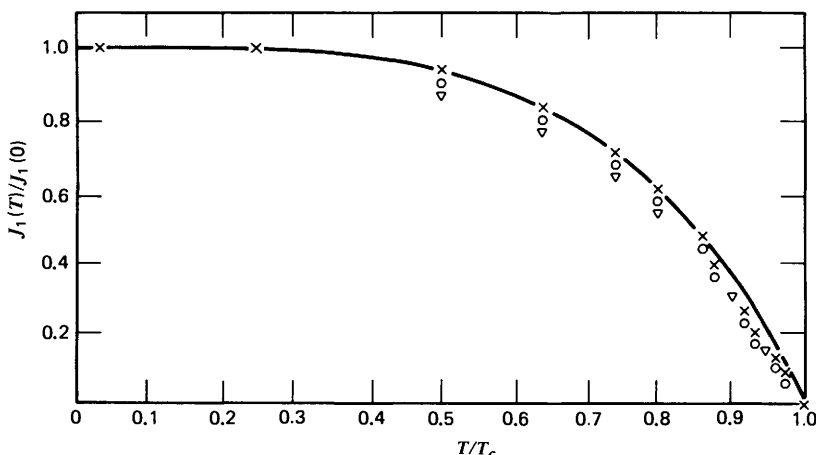


Figure 3.5 Plot of the normalized d.c. Josephson current, $I_1(T)/I_1(0)$ vs. reduced temperature T/T_c . The solid line is the experimental temperature variation observed for Pb-Pb junctions. The crosses are the strong coupling values calculated from (3.3.2). The solid triangles are the predictions of (3.2.10) using the B.C.S. $\Delta(T)$, while the solid circles are the result of putting the strong coupling $\Delta(T)$ into (3.2.10). (After Lim et al. 1970.)

3.4 Effects of Paramagnetic Impurities

Another aspect which deserves great attention is the effect on the behavior of a Josephson junction due to the presence of impurities in the superconductors or in the tunneling barrier. We begin by discussing the former possibility. To find the dependence of the critical current on the concentration of impurities in the superconductor, n_i , it is necessary to introduce the Green functions for impure superconductors whose expressions contain the electron mean free time in the normal state. Baratoff (1964) was the first to discuss the influence of impurities in the superconductors on the Josephson effect. Nonmagnetic impurities were found not to affect the Josephson supercurrent. This is in agreement with Anderson's theorem on dirty superconductors (Anderson 1959) which states that static properties of the superconductor are unaffected by an external perturbation that does not break time reversal symmetry (it should also not produce long range spatial variation of the order parameter (Maki 1969).

Let us observe that this result has an important implication, that is, it legitimizes the use of (3.2.9) [and (3.2.10)] for films of thickness comparable with the superconducting coherence length (Kulik and Yanson 1970).

In the case of superconductors containing paramagnetic impurities there is an exchange interaction (which breaks time reversal symmetry) coupling the spin of the conduction electrons with the magnetic impurity spin. The spin of the impurities polarizes the spins of the electrons and interferes with their tendency for pair formation in a single state.

In the presence of randomly distributed paramagnetic impurities, the expressions for $n(\omega)$ and $p(\omega)$, the quasiparticles and pairing densities are given by

$$n(\omega) = \text{Re} \frac{\tilde{\omega}}{[\tilde{\omega}^2 - \tilde{\Delta}^2(\omega)]^{1/2}} \quad (3.4.1a)$$

$$p(\omega) = \text{Re} \frac{\tilde{\Delta}(\omega)}{[\tilde{\omega}^2 - \tilde{\Delta}^2(\omega)]^{1/2}} \quad (3.4.1b)$$

where in lowest Born approximation (Abrikosov and Gor'kov 1960)

$$\tilde{\omega} = \omega + \frac{1}{2\tau_1} \frac{\tilde{\omega}}{(\tilde{\Delta}^2 - \tilde{\omega}^2)^{1/2}} \quad (3.4.2a)$$

$$\tilde{\Delta} = \Delta + \frac{1}{2\tau_2} \frac{\tilde{\Delta}}{(\tilde{\Delta}^2 - \tilde{\omega}^2)^{1/2}} \quad (3.4.2b)$$

The relaxation times τ_1 and τ_2 differ because of the possibility of scattering. The probability Γ of scattering with spin flip is given by $\Gamma = 1/\tau_S = (1/2\tau_1) -$

$(1/2\tau_2)$. Dividing (3.4.2a) and (3.4.2b) by $\tilde{\omega}$ and $\tilde{\Delta}$ respectively and subtracting (b) from (a) we get

$$\frac{\omega}{\Delta} = \frac{\tilde{\omega}}{\tilde{\Delta}} \left[1 - \frac{\tilde{\Delta}\Gamma}{\Delta} \frac{1}{(\tilde{\Delta}^2 - \tilde{\omega}^2)^{1/2}} \right] \quad (3.4.3)$$

Thus besides being a function of the temperature Δ depends on the concentration of magnetic impurities through Γ . Higher order effects (Kondo anomaly, spin fluctuations) as well as correlations between impurities lead to complications (Maple 1973). Introducing the parameter $Z=(\Gamma/\Delta)^{2/3}$ and substituting (Fulde 1965):

$$Z^{1/2}x = \left[1 - \left(\frac{\tilde{\omega}}{\tilde{\Delta}} \right)^2 \right]^{1/2}$$

Equation (3.4.3) becomes

$$\frac{\omega}{\Delta} = [1 - Zx^2]^{1/2} \left[1 - \frac{Z}{x} \right]$$

or, in equivalent form:

$$x^4 - 2Zx^2 + x^2 \left[\frac{1}{Z} \left(\frac{\omega}{\Delta} \right)^2 - \frac{1}{Z} + Z^2 \right] + 2x - Z = 0 \quad (3.4.4)$$

To find $n(\omega)$ and $p(\omega)$ this fourth order equation has to be solved for a given value of Z .

When a complex conjugate solution, \bar{x} , exists the densities $p(\omega)$ and $n(\omega)$ are different from zero and are given by

$$n(\omega) = \frac{\omega}{\Delta} \frac{1}{Z^{1/2}} \text{Im} \frac{1}{\bar{x} - Z} \quad (3.4.5a)$$

$$p(\omega) = \frac{1}{Z^{1/2}} \text{Im} \frac{1}{\bar{x}} \quad (3.4.5b)$$

Equation 3.4.4 can be solved analytically.[†] An extensive discussion on the way to find the complex conjugate solution is given by Baker and Paternò (1972). In Fig. 3.6 $n(\omega)$ and $p(\omega)$ are plotted for different values of the parameter Γ/Δ . It is interesting to observe that, in the presence of depairing by magnetic impurities, the density of quasiparticles is different from zero also for values of

[†]Let us observe in passing that the pair breaking effect of the paramagnetic impurities is analogous to the one produced by a current flowing into the superconductor and can be treated in the same way (Fulde 1965; Paternò, Ricci, and Sacchetti 1971).

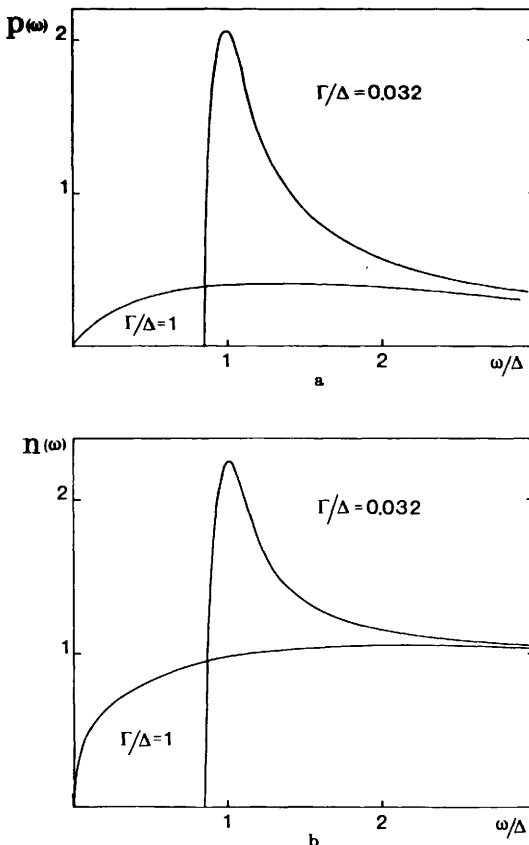


Figure 3.6 Quasiparticle $n(\omega)$ and pair $p(\omega)$ density in the presence of paramagnetic impurities for two different value of the parameter Γ/Δ . For $\Gamma \geq 1$ the superconductor is in the "gapless" state.

the energy ω lower than Δ . The value at which the onset of the quasiparticle density occurs is given as a function of Γ by the expression (Abrikosov and Gor'kov 1960):

$$\omega_g = \Delta(T, \Gamma) \left[1 - \left(\frac{\Gamma}{\Delta(T, \Gamma)} \right)^{2/3} \right]^{3/2}$$

In particular for $\Gamma/\Delta \geq 1$ the sample enters into the so-called gapless region in which the energy gap is equal to zero while the order parameter is still different from zero. With a further increase in Γ , that is, in the impurity concentration, a value is reached at which the superconductivity is destroyed. This critical value for Γ is given by

$$\Gamma_c = \frac{\Delta(0, 0)}{2}$$

$\Delta(0,0)$ being the order parameter for the superconductor at zero temperature in the absence of impurities.

To compute the d.c. Josephson current in the presence of impurities, we have to insert in (3.1.5) the densities of pairs $p_L(\omega)$ and $p_R(\omega)$, evaluated by using (3.4.5b). It is obvious that to solve the integral one has to resort to numerical computation. The first calculations of the effect of paramagnetic impurities were made by Baratoff (1964) who assumed such impurities to be present on the left side of an otherwise symmetric junction. Substituting (3.4.1) and (3.4.3) into the general expression (3.1.1) one finds (see also Kulik and Yanson 1970).

$$I_1(T, \Gamma) = \frac{2\pi\hbar}{eR_N} \sum_{n=0}^{\infty} \frac{\Delta_L(T, \Gamma)\Delta_R(T)}{(\bar{\omega}_n^2 + \Delta_L^2)^{1/2}(\omega_n^2 + \Delta_R^2)^{1/2}}$$

where

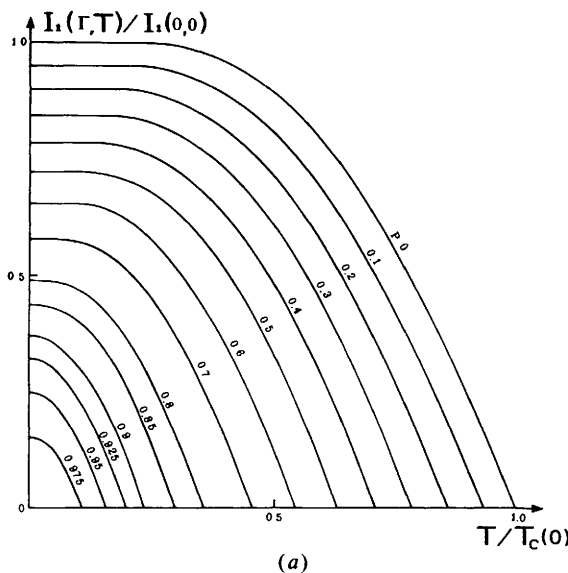
$$\bar{\omega}_n = \omega_n + \Gamma \frac{\omega_n}{(\bar{\omega}_n^2 + \Delta_L^2)^{1/2}}; \quad \omega_n = (2n+1)\pi k_B T$$

Baratoff (1964) also showed how the convergence of such sums can be speeded up by subtracting the corresponding expression with $\Delta_L = \Delta_R = 0$ which can be expressed analytically in terms of polygamma functions. His results for $I_1(\Gamma, T)/I_1(0, 0)$ are shown on Fig. 3.7a as a function of the reduced temperature $t = T/T_c(0)$ and the parameter $p = n_i/n_c = \Gamma/\Gamma_c$.

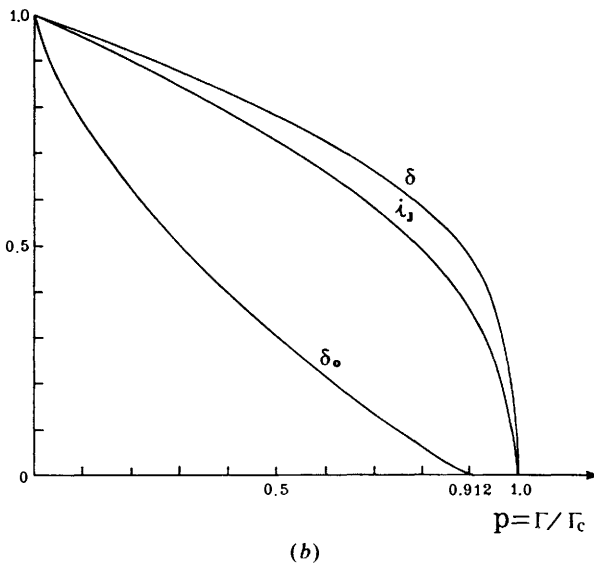
In Fig. 3.7b the maximum supercurrent $i_J = I_1(\Gamma, 0)/I_1(0, 0)$, the order parameter $\delta = \Delta(\Gamma, 0)/\Delta(0, 0)$ as well as the energy gap $\delta_0 = \omega_g(\Gamma, 0)/\Delta(0, 0)$, computed by the above mentioned author are also shown. The case of a symmetrical junction with impurities in both the electrodes has been considered at $T=0$ by Kulik (1966a) and at finite temperatures by Nam (1967a, b).

As discussed above, spin-flip processes reduce the binding of pairs; these acquire finite lifetime τ_s which implies $\Delta E = \hbar/\tau_s$; energy levels originate within the gap which eventually vanishes if $\Delta E \simeq \omega_g$ (see also Claeson 1967). Figure 3.7b implies the existence of Josephson effect also in the region of gapless superconductivity. In fact we see that when the concentration of paramagnetic impurities is such that the parameter Γ reaches the value $0.912\Gamma_c$, the gap ω_g vanishes whereas the Josephson critical current is still nonzero.

Shiba (1968) and Rusinov (1969a, b) have extended the theory to the case of strong exchange interaction between the electrons and the paramagnetic impurity spins. In this case there are states of energy lower than $\Delta(\Gamma, T)$ also for low impurity concentration; that is, $n(\omega)$ and $p(\omega)$ are nonzero for $\omega < \omega_g$ even for values of $\Gamma/\Delta \ll 1$. Lo and Nagi have calculated both the order parameter and the Josephson critical current at finite temperatures in that case (Nagi and Lo 1973; Lo and Nagi 1974). Figure 3.8 summarizes the main results of interest. It shows the temperature dependence of the maximum



(a)



(b)

Figure 3.7 (a) The temperature dependence of the reduced maximum zero voltage current $I_1(\Gamma, T)/I_1(0,0)$ for various values of the parameter $p=\Gamma/\Gamma_c$. (b) The dependence of the reduced order parameter $\delta=\Delta(\Gamma,0)/\Delta(0,0)$, energy gap $\delta_0=\omega_g(\Gamma,0)/\Delta(0,0)$, and maximum d.c. Josephson current $i_J=I_1(\Gamma,0)/I(0,0)$ at $T=0$ K on the parameter $p=\Gamma/\Gamma_c$. $I_1(\Gamma, T)/I_1(0,0)$ refer to a symmetric junction with paramagnetic impurities in one side only. (After Baratoff 1964.)

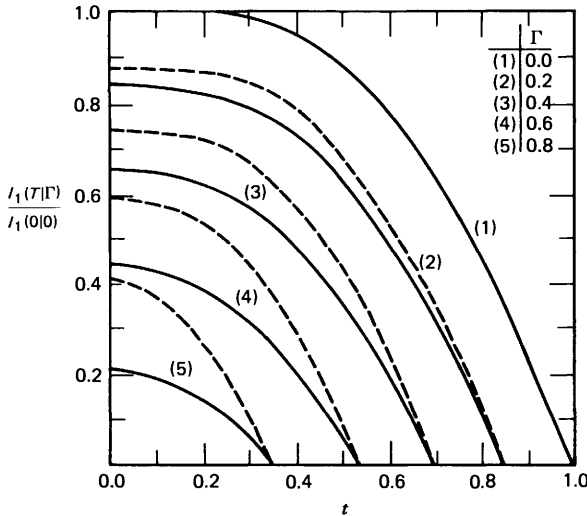


Figure 3.8 Normalized maximum d.c. Josephson current vs. normalized temperature for a symmetric junction with paramagnetic impurities in both electrodes. Solid line: Shiba and Rusinov model; dashed line: Abrikosov-Gorkov model. (After Lo and Nagi 1974.)

Josephson current (in normalized units) taking the impurity concentration as parameter; the dashed curves refer to the Abrikosov and Gor'kov theory.

Experiments on the effect of paramagnetic impurities on the Josephson current have been performed by Hauser (1967). This author, however, instead of dissolving suitable magnetic impurities in the superconducting electrodes realized a gapless configuration by proximity effect with a magnetic element. The samples used were Cr-Pb-PbO-Pb-Cr structures in which, by varying the lead film thickness, it was possible to vary the degree of depairing and, ultimately, the critical supercurrent. These experiments however are not conclusive since, as pointed out by the author, the difficulty of making good quality lead films of thickness less than 800 Å did not allow the observation of marked effects.

We have so far discussed the effect of paramagnetic impurities in the superconducting electrodes. Let us consider now the effect on the critical current of paramagnetic impurities localized within the tunneling barrier. The theory developed in Chapter 2 assumes, among other hypotheses, interaction Hamiltonian \mathcal{H}_T , describing tunneling through the barrier with spin conservation:

$$\mathcal{H}_T = \sum_{\mathbf{kq}\sigma} T_{\mathbf{kq}} (c_{\mathbf{k}\sigma}^+ d_{\mathbf{q}\sigma} + d_{-\mathbf{q}\sigma}^+ c_{-\mathbf{k}\sigma}) + \text{hermitian conjugate}$$

To take into account violations of this hypothesis Kulik (1965b) approached

the problem starting from a different phenomenological Hamiltonian given by

$$\tilde{\mathcal{H}}_T = \mathcal{H}_T^n + \mathcal{H}_T^s$$

in which the two terms

$$\mathcal{H}_T^n = \sum_{\mathbf{kq}} T_{\mathbf{kq}}^n (c_{\mathbf{k}\uparrow}^+ d_{\mathbf{q}\uparrow} + d_{\mathbf{q}\downarrow}^+ c_{-\mathbf{k}\downarrow}) + \text{h.c.}$$

and

$$\mathcal{H}_T^s = \sum_{\mathbf{kq}} T_{\mathbf{kq}}^s (c_{\mathbf{k}\uparrow}^+ d_{-\mathbf{q}\downarrow} + d_{\mathbf{q}\uparrow}^+ c_{-\mathbf{k}\downarrow}) + \text{h.c.}$$

describe, respectively, tunneling with and without spin conservation (arrows clearly indicate spin direction); the matrix elements obey the relations

$$T_{\mathbf{kq}}^{n*} = T_{-\mathbf{k}-\mathbf{q}}^n; \quad T_{\mathbf{kq}}^{s*} = T_{-\mathbf{k}-\mathbf{q}}^s$$

implied by time reversal invariance of \mathcal{H}_T (Anderson 1963). The tunneling processes through the channels are accompanied by spin reversal which can occur either through the presence of paramagnetic impurities in the barrier or as a consequence of the spin-orbit coupling interaction. For the development of the calculations the reader is referred to the work cited above. We here give just the final expression of the Josephson current (at $T=0$) resulting from Kulik's analysis:

$$I(\varphi) = \frac{\pi}{2} \frac{\Delta}{R_N} \frac{\langle |T_n|^2 \rangle - \langle |T_s|^2 \rangle}{\langle |T_n|^2 \rangle + \langle |T_s|^2 \rangle} \sin \varphi$$

Here $\langle |T_n|^2 \rangle$ ($\langle |T_s|^2 \rangle$) is the average of $|T_{\mathbf{kq}}^n|^2$ ($|T_{\mathbf{kq}}^s|^2$) taken over the angles between \mathbf{k} and \mathbf{q} vectors on the Fermi surface. Since

$$\frac{I}{I(0)} = \left| \frac{\langle |T_n|^2 \rangle - \langle |T_s|^2 \rangle}{\langle |T_n|^2 \rangle + \langle |T_s|^2 \rangle} \right| \leq 1$$

the maximum supercurrent is smaller than the value given by (3.2.7).

Other reasons for a reduced critical current are the possibility of tunneling under conditions of no reflection symmetry of the barrier or of trap centers present in the dielectric which make the "in" and "out" channels of the electrons traversing the barrier uncorrelated. These circumstances lead to $T_{\mathbf{kq}}^* \neq T_{-\mathbf{k}-\mathbf{q}}$, that is, breaking of the time reversal invariance assumed in the original expression of $\tilde{\mathcal{H}}_T$.

Recently the effect of magnetic impurities localized into the barrier has been discussed in a different context by Bulaevskii, Kuzii, and Sobyanin (1978).

3.5 Measurement Techniques

So far we have considered theory and experiments on the magnitude of the maximum d.c. supercurrent. Let us now discuss some aspects of the experimental techniques to measure the Josephson critical current and its dependence on external parameters such as temperature and externally applied magnetic field. Usually these measurements involve the observation of the whole d.c. voltage-current characteristics. The simplest procedure to observe a V - I curve of a junction consists of a simultaneous record of both voltage and current on an x - y recorder (Fig. 3.9). In this way one obtains a full V - I curve for a given value of external parameters (e.g., T or H_e). Information about the dependence on these parameters requires iteration of this procedure.

Let us outline another procedure (Lim et al. 1970; Balsamo et al. 1974) which allows also a continuous recording of the variations of the critical current as a function of external parameters. The junction can be current biased by, for example, a triangular wave generator at relatively low frequency ($\sim 50 \div 100$ Hz) and the resulting V - I curve displayed on the oscilloscope (see Fig. 3.10). The current is fed into the junction through a limiting resistor, R_L , and the shunt resistor, R_S , which can be chosen by commutation. The voltage picked up from R_S is proportional to the current. Both voltage and current signals are amplified by low noise low drift differential amplifiers in order to

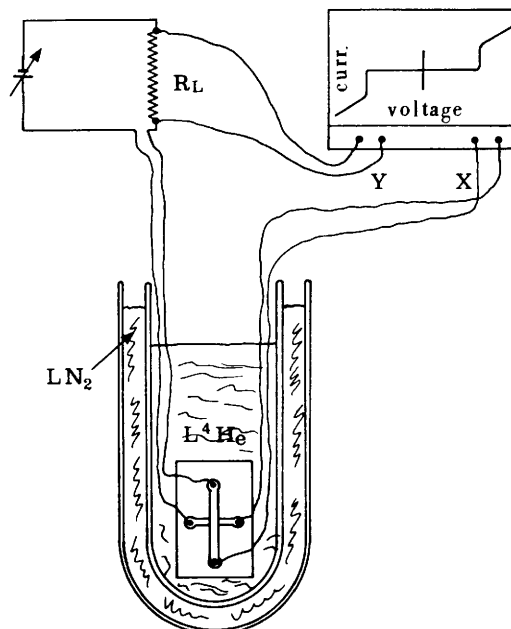
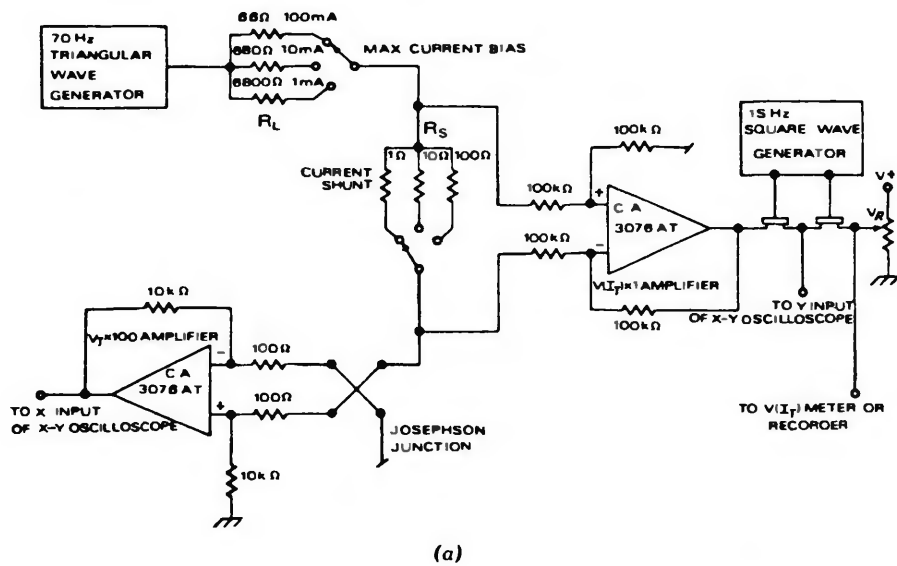


Figure 3.9 Schematic of the experimental apparatus used to measure the voltage-current characteristics of a junction. The inner dewar in which the sample is inserted is filled with liquid helium (L^4He), the outer dewar contains liquid nitrogen (LN_2).



(a)

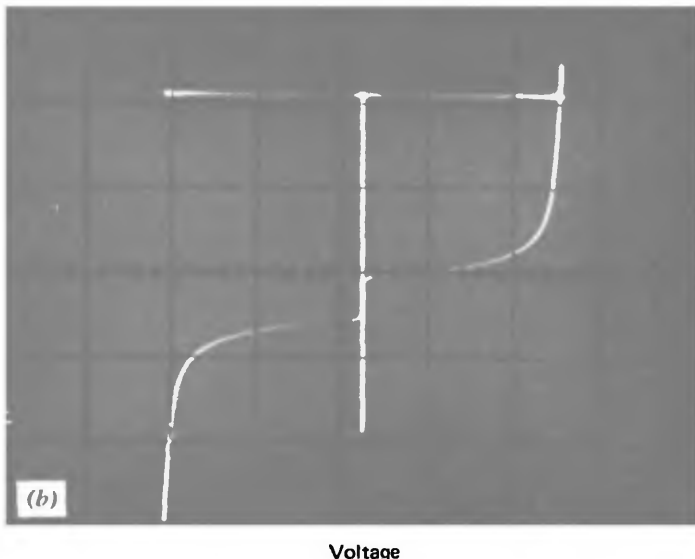


Figure 3.10 (a) Schematic of the circuit used to measure junction V - I characteristic and Josephson current variation. (After Balsamo et al. 1974.) (b) Oscilloscope display. The horizontal line corresponds to the reference voltage V_R .

decouple the sample from the external instrumentation. The voltage across the junction is continuously applied to the x input of an oscilloscope. On the y input is applied the voltage across R_S and a reference voltage V_R which can be manually varied and alternatively displayed. Therefore on the oscilloscope it appears as the V - I curve of the junction and a horizontal line corresponding to V_R . The Josephson current is appreciated by making the V_R line coincident with the top vertical trace of the supercurrent. V_R is measured by a digital voltmeter or by using an x - y plotted. In this procedure since it is not necessary to observe the whole supercurrent on the oscilloscope it is possible to obtain a greater precision. An example of the direct recording of the critical current vs. applied magnetic field by this technique is shown in Fig. 1.10a.

Another simple way to measure the maximum d.c. Josephson current is to use in the y axis of the oscilloscope a differential comparator. The calibrated d.c. voltage V_c supplied by this instrument can be added differentially to the voltage input signal which is proportional to the current. The V - I characteristic on the oscilloscope can be shifted so that the maximum Josephson current corresponds to the zero on the vertical axis. By monitoring V_c , a measure of the d.c. Josephson current is obtained.

CHAPTER 4

“Small” Junctions in a Magnetic Field

One of the most striking features of the behavior of Josephson structures is the occurrence of diffraction and interference phenomena of supercurrents when magnetic fields are applied. This is a consequence of the wavelike nature of Cooper pairs and the phase coherence through Josephson links.

The extremely high sensitivity of the Josephson current to magnetic fields is the key to the most important applications of the Josephson effect. This fact will grow clearer through this and the following chapters. Furthermore, a careful study of the dependence of the maximum d.c. Josephson current on the applied magnetic field represents a very powerful method to investigate important aspects of the junction behavior. In particular, important information can be obtained on the current density distribution inside the junction.

4.1 Josephson Penetration Depth

Let us consider here the basic Josephson relations (1.4.4), (1.4.5) and (1.7.1) in the stationary case:

$$J = J_1 \sin \varphi \quad (4.1.1a)$$

$$\frac{d\varphi}{dt} = 0 \quad (4.1.1b)$$

$$\nabla_{x,y}\varphi = \left(\frac{2e}{\hbar c} d \right) \mathbf{H} \times \mathbf{n} \quad (4.1.1c)$$

where $d = \lambda_{L1} + \lambda_{L2} + t$ and λ_{L1} and λ_{L2} are the effective London penetration depths of the two superconductors forming the junction and t is the physical barrier thickness. \mathbf{H} represents the actual magnetic field in the plane of the junction including both externally applied magnetic field and the field generated by the currents flowing in the junction; \mathbf{n} is the unit vector normal to the plane of the junction. By $\nabla_{x,y}\varphi$ we denote the vector whose components are $\partial\varphi/\partial x, \partial\varphi/\partial y$. Equation 1.7.2 reduces to

$$\frac{\partial^2 \varphi}{\partial x^2} + \frac{\partial^2 \varphi}{\partial y^2} = \frac{1}{\lambda_J^2} \sin \varphi \quad (4.1.2)$$

with λ_J given by

$$\lambda_J = \left(\frac{\hbar c^2}{8\pi e J_1 d} \right)^{1/2} \quad (4.1.3)$$

As already pointed out in Chapter 1, λ_J gives a measure of the length within which d.c. Josephson currents are confined near the edges of the junction. This implies the occurrence of a nonuniform current distribution in junctions with the largest transverse dimension L greater than λ_J , even in the absence of externally applied magnetic field. Thus two classes of junctions can be identified: “small” junctions ($L < \lambda_J$), which have uniform current distribution since self-induced magnetic fields can be neglected, and “large” ($L > \lambda_J$) junctions in which the currents are essentially confined to the edges of the junction. By means of Table 2 of the Appendix we can convert the expression 4.1.3, which is in Gaussian units, to its equivalent in MKSA units:

$$\lambda_J = \left(\frac{\hbar}{2e\mu_0 d J_1} \right)^{1/2}$$

For Nb-NbO_x-Pb junctions typical values for d and J_1 are $d = 1400 \text{ \AA}$, and $J_1 = 5 \text{ A/cm}^2$ (Lacquaiti, Marullo, and Vaglio 1978). Therefore for λ_J we obtain: $\lambda_J = 1.618 \times 10^{-5} (1/1.400 \times 10^{-10} \times 5 \times 10^4)^{1/2} = 0.193 \text{ mm}$ where for the typical constants the values given in the Appendix have been used. From (4.1.3) it can be observed that changes in the barrier thickness t strongly affect λ_J since J_1 depends on t exponentially. Therefore junctions of equal area can be either small or large depending on the value of the current density J_1 . On the other hand, uncertainty about the t value to be used in the expression of d is not relevant since t is negligible compared with the whole value $d = \lambda_{L1} + \lambda_{L2} + t$. It should also be noted that λ_J depends on the temperature through J_1 and the London penetrations (see the next chapter).

4.2 Small Junctions

We now consider junctions with dimensions that are small compared to the Josephson penetration depth. We refer to a coordinate system with the z axis normal to the plane of the junction, Fig. 1.1. Let us consider an external magnetic field \mathbf{H}_e applied in the y direction; inside the junction the magnetic field is constant and equal to the external value (absence of self-fields). Thus (4.1.1c) gives by integration

$$\varphi(x) = \frac{2\pi d}{\Phi_0} H_y x + \varphi_0$$

$\Phi_0 = hc/2e$ is the flux quantum (2.07×10^{-7} G cm 2 ; 2.07×10^{-15} weber) and φ_0 is an integration constant.

The phase shows a linear spatial variation along the x direction, the rate of variation being proportional to the externally applied magnetic field H_y . Furthermore from (4.1.1a) it follows that

$$J(x) = J_1 \sin\left(\frac{2\pi d}{\Phi_0} H_y x + \varphi_0\right)$$

Therefore the Josephson current density exhibits a periodic distribution inside the junction. In Fig. 4.1 spatial variations of $\varphi(x)$ and $J(x)$ are sketched for different values of the external field H_y , assuming a rectangular junction geometry with the origin of the axes in the center of the junction (Fig. 4.2a). We can see that the periodic behavior of $J(x)$ leads, for particular values of the external magnetic field, to situations of zero net current through the junction (see Fig. 4.1c).

The total current in the junction is given by

$$I = \iint dx dy J_1(x, y) \sin\left(\frac{2\pi d}{\Phi_0} H_y x + \varphi_0\right) \quad (4.2.1)$$

where the integral is calculated over the junction area. For a greater generality a spatial dependence ($J_1 = J_1(x, y)$) of the maximum current density has been introduced in order to take into account effects due to nonuniformity in the tunneling barrier (see Section 4.4).

Let us define

$$k = \frac{2\pi d}{\Phi_0} H_y \quad (4.2.2)$$

and

$$\mathcal{G}(x) = \int dy J_1(x, y)$$

where the integral is taken on the junction dimension along the y direction. From (4.2.1) it follows:

$$\begin{aligned} I(k, \varphi_0) &= \int_{-L/2}^{L/2} dx \mathcal{G}(x) \sin(kx + \varphi_0) \\ &= \text{Im} \left\{ e^{j\varphi_0} \int_{-L/2}^{L/2} dx \mathcal{G}(x) e^{j k x} \right\} \end{aligned}$$

where L is the largest junction dimension along x .

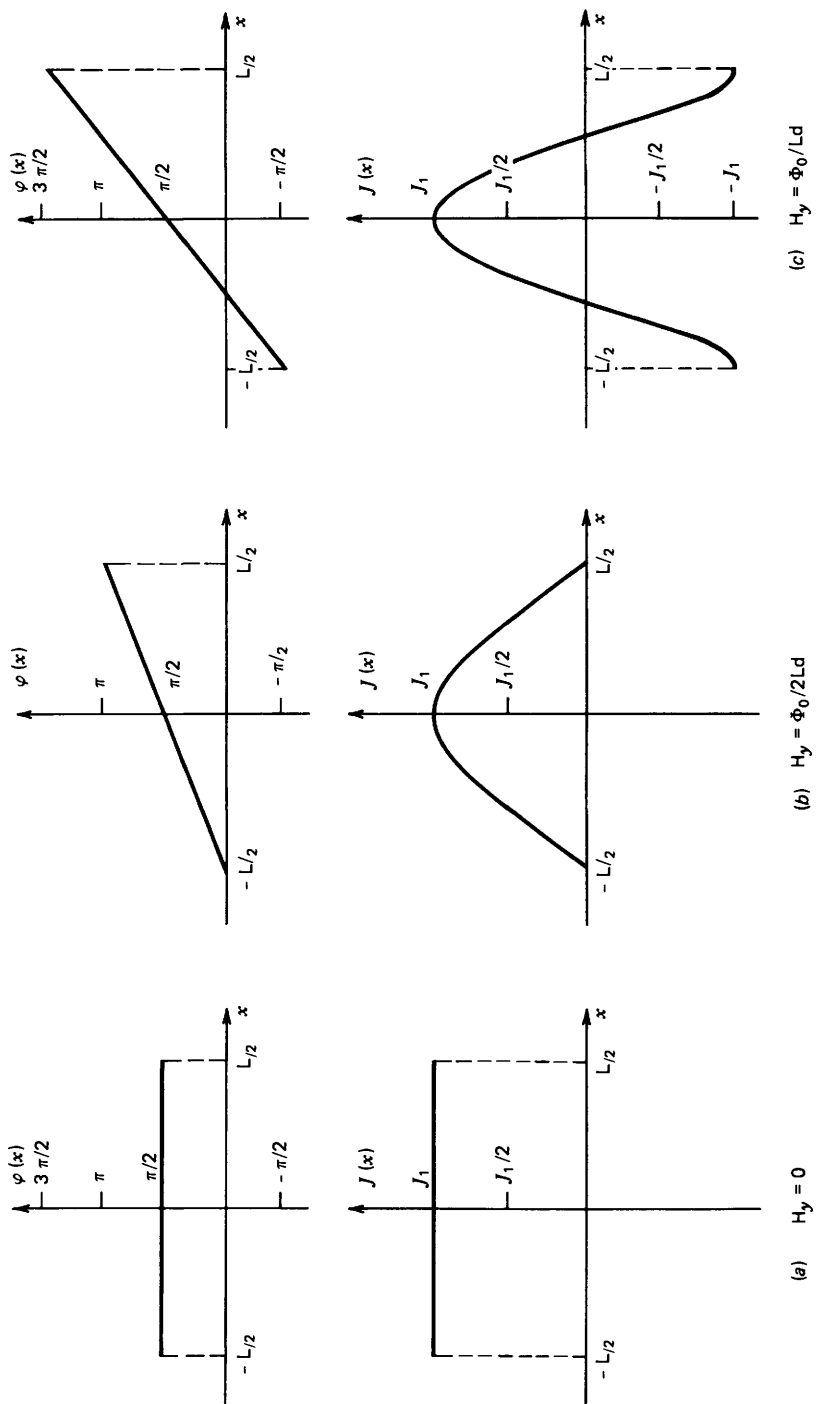


Figure 4.1. Phase $\varphi(x)$ and current density $J(x)$ space variation in the presence of an external magnetic field H_y for a rectangular junction. L is the dimension along the direction perpendicular to the applied field. (a) $H_y = 0$, (b) $H_y = \Phi_0/2Ld$, (c) $H_y = \Phi_0/Ld$.

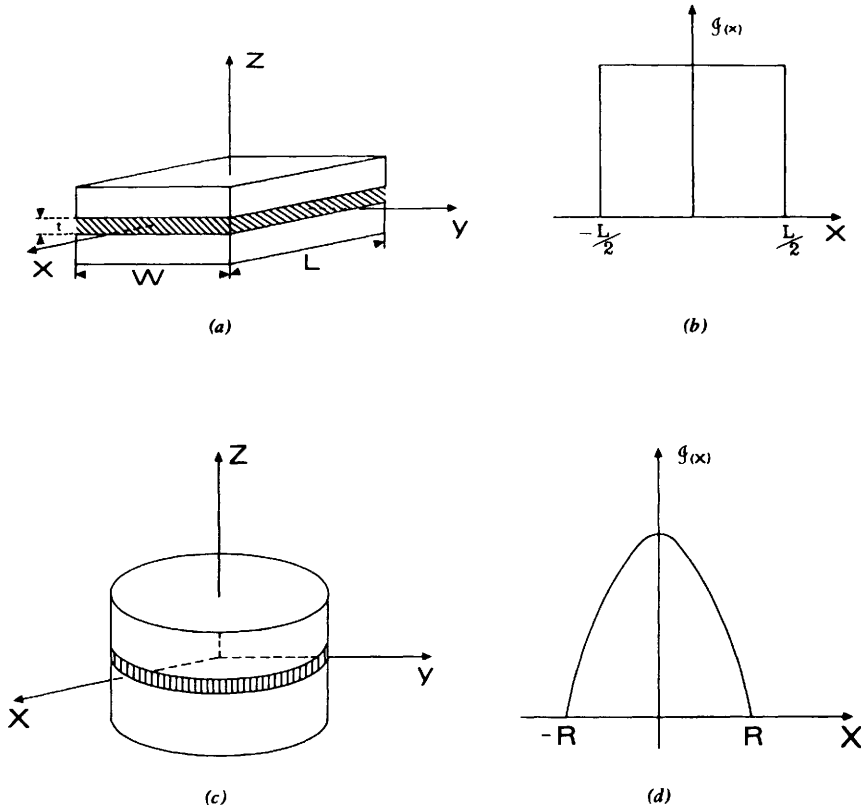


Figure 4.2 Geometrical configurations and the corresponding linear current density $\mathcal{J}(x)$ for uniform current density distribution. (a), (b) Rectangular geometry. (c), (d) Circular geometry.

This expression, maximized with respect to φ_0 , gives the maximum Josephson current $I_1(k)$:

$$I_1(k) = \left| \int_{-L/2}^{+L/2} dx \mathcal{J}(x) e^{jkx} \right|$$

For convenience we can calculate this integral between $-\infty$ and $+\infty$ assuming $\mathcal{J}(x)=0$ for $|x|>L/2$, so that

$$I_1(k) = \left| \int_{-\infty}^{+\infty} dx \mathcal{J}(x) e^{jkx} \right| \quad (4.2.3)$$

Thus the maximum Josephson current, at a given applied magnetic field, is represented by the modulus of the Fourier transform of $\mathcal{J}(x)$ (Dynes and Fulton 1971).

4.3 Uniform Tunneling Current Distribution

We apply the results just obtained to specific junction geometries, assuming in (4.2.1) for the total current a constant tunneling current density J_1 .

4.3.1 Rectangular Junctions. Let us consider now the geometrical configuration of Fig. 4.2a, where the barrier region is defined by $|x| \leq L/2$, $|y| \leq W/2$, $|z| \leq t/2$. Assuming $J_1(x) = J_1 = \text{constant}$, it follows (see Fig. 4.2b) that

$$\mathcal{J}(x) = J_1 W p_{L/2}(x)$$

where

$$p_{L/2} = \begin{cases} 1 & |x| \leq L/2 \\ 0 & |x| > L/2 \end{cases}$$

Thus

$$I_1(k) = \left| J_1 W \int_{-\infty}^{+\infty} dx p_{L/2}(x) e^{jkx} \right|$$

For the Fourier transform of $p_{L/2}(x)$ we find (Papoulis 1962, p. 20)

$$\int_{-\infty}^{+\infty} dx p_{L/2}(x) e^{jkx} = \int_{-L/2}^{+L/2} \cos kx dx + j \int_{-L/2}^{+L/2} \sin kx dx = \frac{2 \sin k(L/2)}{k}$$

Thus

$$I_1(k) = I_1 \left| \frac{\sin k(L/2)}{k(L/2)} \right|$$

where $I_1 = J_1 WL$.

Using (4.2.2) we have

$$I_1 \left(\frac{\Phi}{\Phi_0} \right) = I_1 \left| \frac{\sin \pi \frac{\Phi}{\Phi_0}}{\pi \frac{\Phi}{\Phi_0}} \right| \quad (4.3.1)$$

where $\Phi = H_y L d$ is the magnetic flux through the junction.

Equation 4.3.1 represents a Fraunhofer pattern as shown in Fig. 4.3.

The analogy with the Fraunhofer diffraction pattern produced by a slit of the same shape as the barrier is evident. As shown in Fig. 4.3, the minima symmetric with respect to the origin are evenly spaced and occur at values of the magnetic flux within the barrier equal to multiples of the flux quantum.

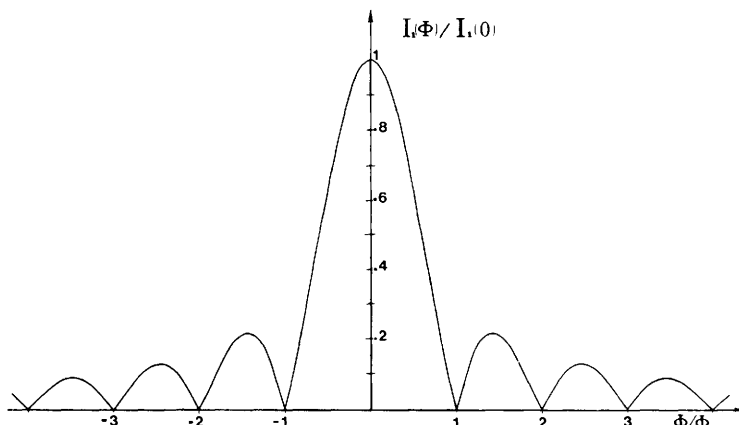


Figure 4.3 Theoretical magnetic field dependence of the maximum Josephson current I_1 (4.3.1) for a rectangular junction.

A first observation of this effect was reported by Rowell (1963). Subsequently, other careful measurements have been performed by various authors (e.g. Fiske 1964; Yamashita, Kunita and Onodera 1968a,b; Schwidtal and Finnegan 1969, 1970; Schwidtal 1972; Balsamo et al. 1976b). Experimental results together with the theoretical fitting by Balsamo et al. 1976b are reported in Fig. 4.4. H_0 is the field value corresponding to the first minimum.

Let us observe that the suppression of the Josephson current occurs for small values of the applied magnetic field (order of a few gauss) and therefore a careful shielding against the earth's magnetic field is required during the measurements. In terms of magnetic field the periodicity of the pattern is given

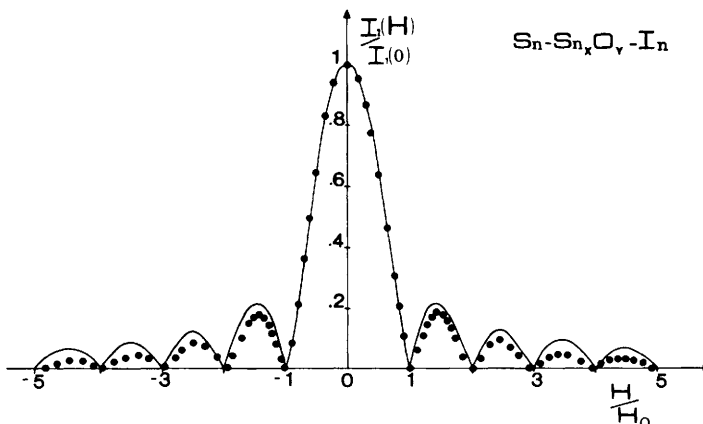


Figure 4.4 Magnetic field dependence of the maximum Josephson current I_1 for an $\text{Sn}-\text{Sn}_x\text{O}_y-\text{In}$ junction. The circles are the experimental data; the solid line is the theoretical dependence computed from (4.3.1). (After Balsamo et al. 1976b.)

by

$$\Delta H = \frac{\Phi_0}{L(\lambda_{L1} + \lambda_{L2} + t)} \quad (4.3.2)$$

When the two superconductors are equal ($\lambda_{L1} = \lambda_{L2}$) this periodicity furnishes a method for the determination of the London penetration depth. It should be remembered, however, that (4.3.2) holds as long as the thicknesses of the superconducting films are large compared with λ_L . When this condition is no longer satisfied, (4.3.2) is modified as

$$\Delta H = \frac{\Phi_0}{L \left(\lambda_{L1} \tanh \frac{d_1}{2\lambda_{L1}} + \lambda_{L2} \tanh \frac{d_2}{2\lambda_{L2}} + t \right)}$$

where d_1 and d_2 are the thicknesses of the superconducting electrodes (Weihnacht 1969).

4.3.2 Circular Junctions. We consider now a junction of circular geometry (Fig. 4.2c, d). In this case

$$\mathcal{J}(x) = \int_{-\sqrt{R^2 - x^2}}^{\sqrt{R^2 - x^2}} dy J_1 = 2 J_1 \sqrt{R^2 - x^2}$$

where R is the radius of the junction. The maximum Josephson current is given by

$$I_1(k) = \left| 2 J_1 \int_{-R}^R dx \sqrt{R^2 - x^2} e^{ikx} \right|$$

Since $\mathcal{J}(x)$ is an even function, one obtains

$$\int_{-R}^R dx \sqrt{R^2 - x^2} e^{ikx} = 2 \int_0^R \sqrt{R^2 - x^2} \cos kx dx$$

Making the substitution: $x = R \cos \theta$, we have

$$\int_0^R \sqrt{R^2 - x^2} \cos kx dx = -R^2 \int_0^{\pi/2} \cos(kR \cos \theta) \sin^2 \theta d\theta$$

This integral can be solved in terms of Bessel functions giving (Matisoo 1969)

$$I_1(k) = I_1 \left| \frac{J_1(kR)}{\frac{1}{2}(kR)} \right|$$

where $I_1 = \pi R^2 J_1$ and $J_1(x)$ is a Bessel function of the first kind. This expression is plotted in Fig. 4.5 with magnetic field values normalized to the first

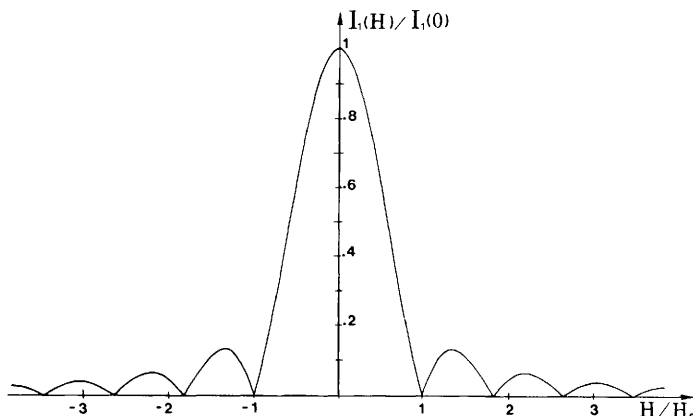


Figure 4.5 Theoretical magnetic field dependence of the maximum d.c. Josephson current I_1 for a circular junction.

minimum. Experimental results on circular tin-tin junctions by Matisoo (1969) are reported in Fig. 4.6.

More recently other measurements on Nb-Pb circular junctions have been also performed by Paternò, Rissman and Vaglio (1975).

4.3.3 Magnetic Field with Arbitrary Orientation. In Section 4.3.1 we considered a rectangular junction with external magnetic field applied in the y direction. Let us now suppose that the magnetic field has components H_x and

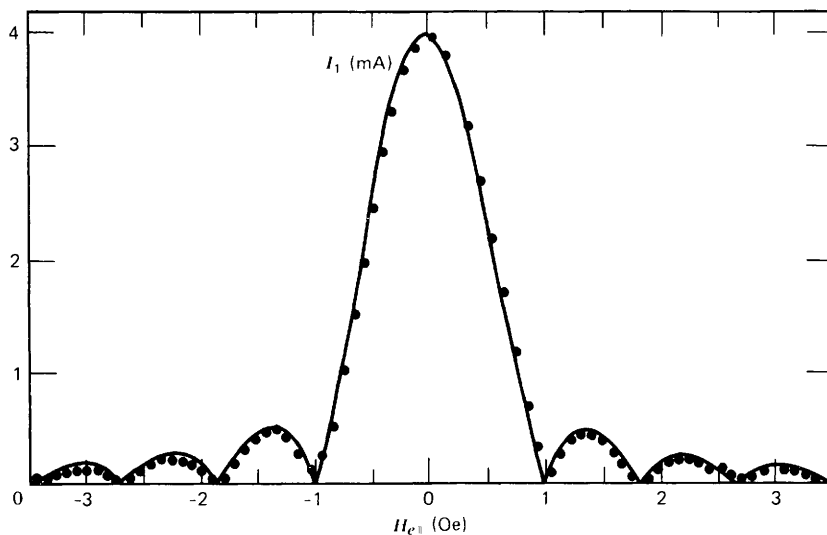


Figure 4.6 Magnetic field dependence of the maximum d.c. Josephson current I_1 for a junction of circular geometry. The points are the experimental data; the solid line is the theoretical dependence. (After Matisoo 1969.)

H_y both nonzero. By integration of (4.1.1c), we have

$$\varphi(x, y) = \frac{2\pi d}{\Phi_0} (H_y x - H_x y) + \varphi_0$$

and from (4.1.1a) the total current in the junction is

$$I = \int \int J_1 \sin(\varphi) dx dy = \text{Im} \left\{ \int \int dx dy J_1 e^{j[2\pi d(H_y x - H_x y)/\Phi_0 + \varphi_0]} \right\}$$

The maximum d.c. Josephson current is therefore:

$$I_1 = \left| \int_{-W/2}^{+W/2} dy \int_{-L/2}^{+L/2} dx J_1 e^{j(k_x x - k_y y)} \right| = I_1 \left| \frac{\sin k_x L/2}{k_x L/2} \right| \left| \frac{\sin k_y W/2}{k_y W/2} \right| \quad (4.3.3)$$

where

$$k_x = \frac{2\pi d}{\Phi_0} H_y \quad k_y = \frac{2\pi d}{\Phi_0} H_x$$

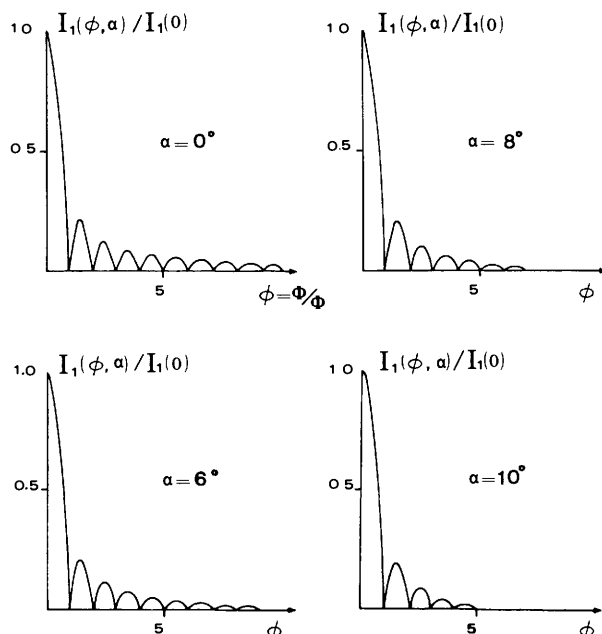


Figure 4.7 Magnetic field dependence of the maximum d.c. Josephson current I_1 for a junction of square geometry and for different orientations of the applied field H_e . α is the angle between H_e and the x direction.

and

$$I_1 = J_1 WL$$

Incidentally, we observe that, in the experimental context, the value of the applied magnetic field is typically calculated directly from the circulating current in the coils producing the field. As a consequence the actual measured quantity is $H_e = \sqrt{H_x^2 + H_y^2}$. Therefore if $H_x = H_e \sin \alpha$, $H_y = H_e \cos \alpha$ where α is the angle between the applied field direction and the y axis, the maximum critical current can be expressed by

$$I_1 \left(\frac{\Phi}{\Phi_0}, \alpha \right) = I_1 \left| \frac{\sin(\pi(\Phi/\Phi_0)\cos\alpha)}{\pi(\Phi/\Phi_0)\cos\alpha} \right| \cdot \left| \frac{\sin[\pi(\Phi/\Phi_0)(W/L)\sin\alpha]}{\pi(\Phi/\Phi_0)(W/L)\sin\alpha} \right|$$

where $\Phi = H_e L d$.

Thus a field, applied to the junction, which has nonzero components along x and y leads to a dependence of I_1 vs. H_e which is given by the product of two Fraunhofer patterns. The resulting behavior for various values of α is reported in Fig. 4.7. The curves refer to a square junction ($W/L = 1$).

4.4 Nonuniform Tunneling Current Density

In actual junctions it is important to take into account effects of the Josephson current density distribution due to nonuniform tunneling barriers. Investigations of the dependence of the maximum Josephson current, on the external magnetic field, provide a useful means to make evident spatial variations of $J_1 = J_1(x, y)$, since these are reflected in peculiar features of the I_1 vs. H patterns. We discuss this aspect in some detail and show that the analysis of the I_1 vs. H dependence has a relevant diagnostic power in the study of Josephson structures (Paternò and Vaglio 1975; Barone et al. 1977).

Dynes and Fulton (1971) have shown the relation between the shape of the $I_1 - H_e$ pattern for a rectangular junction geometry and the corresponding current distribution with the aid of Fourier transform formalism. A different approach to the problem, based on the formalism of information theory, has been discussed by Zappe (1970, 1975c). As pointed out by this author, the procedure for obtaining $\mathcal{J}(x)$ from I_1 vs. H_e experiments is not univocal unless additional physical hypotheses on the peculiar features of the barrier are supplied. For details of the two methods just mentioned the reader is referred to the papers cited above. In Section 4.4.1 we adopt a different point of view: we consider various current density profiles which account for nonuniformities localized in the barrier layer and calculate the corresponding $I_1 - H_e$ patterns. This is performed for simple $\mathcal{J}(x)$ distributions which can be indicative of more realistic situations. In Section 4.4.2 we discuss the effect of nonuniformities assumed to be randomly distributed over the barrier layer. These represent

the so called structural fluctuations (Yanson 1970a) which arise from the unavoidable intrinsic nonuniformity of any real barrier.

4.4.1 Various Current Density Profiles. Let us assume the junction geometry sketched in Fig. 4.2a. The magnetic field is applied in the y direction. The total Josephson current is given by (4.2.3) where

$$J(x) = \begin{cases} 0 & |x| > L/2 \\ \int_{+W/2}^{+W/2} dy J_1(x, y) & |x| \leq L/2 \end{cases}$$

In Section 4.3 we supposed that the Josephson tunneling current density J_1 was spatially constant. Now we consider for $J_1(x, y)$ the profile reported in Fig. 4.8 (variations along x only). The corresponding analytical expression is

$$J_1(x) = J_0 \left[\xi p_{l/2}(x) + p_{s/2} \left(x - \frac{l+s}{2} \right) + p_{s/2} \left(x + \frac{l+s}{2} \right) \right]$$

where ξ is a parameter ($\xi \leq 1$) whose meaning is clarified in Fig. 4.8 and $l = L - 2s$. The meaning of J_0 is clear from the figure.

The function $p_r(x)$ is defined by

$$p_r(x) = \begin{cases} 1 & |x| \leq r \\ 0 & |x| > r \end{cases}$$

The maximum Josephson current is

$$I_1(k) = J_0 W \left| \int_{-\infty}^{+\infty} \left[\xi p_{l/2}(x) + p_{s/2} \left(x - \frac{l+s}{2} \right) + p_{s/2} \left(x + \frac{l+s}{2} \right) \right] dx \right|$$

Since the Fourier transform of $f(x - x_0)$ is given by the Fourier transform of

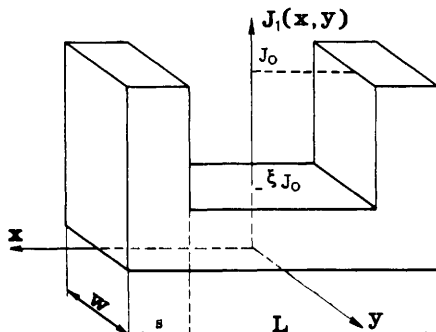


Figure 4.8 Steplike current density profile.

$f(x)$ times a phase factor e^{-jkx_0} , it follows that

$$\begin{aligned} I_l(k) &= \left| J_0 W \left[2\xi \frac{\sin kl/2}{k} + \frac{2 \sin ks/2}{k} (e^{-jk(l+s)/2} + e^{jk(l+s)/2}) \right] \right| \\ &= J_0 WL \left| \xi \frac{l}{L} \frac{\sin kl/2}{kl/2} + 2 \frac{s}{L} \frac{\sin ks/2}{ks/2} \cos\left(\frac{l+s}{2}\right) \right| \end{aligned}$$

For $k=0$ we have the maximum Josephson current

$$I_l(0) = J_0 WL \left(\xi \frac{l}{L} + 2 \frac{s}{L} \right)$$

and, finally,

$$\begin{aligned} I_l\left(\frac{\Phi}{\Phi_0}\right) &= I_l(0) \left(\frac{2s}{\xi l + 2s} \right) \left| \frac{\xi l}{2s} \frac{\sin\left(\pi \frac{l}{L} \frac{\Phi}{\Phi_0}\right)}{\pi \frac{l}{L} \frac{\Phi}{\Phi_0}} \right. \\ &\quad \left. + \frac{\sin\left(\pi \frac{s}{L} \frac{\Phi}{\Phi_0}\right)}{\pi \frac{s}{L} \frac{\Phi}{\Phi_0}} \cos\left[\pi \left(\frac{l+s}{L}\right) \frac{\Phi}{\Phi_0}\right] \right| \end{aligned} \quad (4.4.1)$$

where

$$\Phi = H_y L d.$$

Thus it is evident from (4.4.1) that the higher tunneling current value assumed at the edges of a rectangular junction (see Fig. 4.8) leads to I_l vs. H_e dependence which is markedly different from what obtained assuming uniform current density distribution. In Fig. 4.9 we report the dependence given by (4.4.1) for several values of the parameters ξ and $s' = s/L$. It is clear that s' influences the period of the superimposed modulation (see Fig. 4.9b).

In Fig. 4.10a is reported the experimental I_l vs. H_e dependence for a Sn-Sn_xO_y-Sn junction with the field applied along the direction of the bottom layer. It is interesting to observe the very good agreement between experiments and calculations (Fig. 4.10b) obtained assuming a steplike current density distribution as reported in the inset.

Let us consider now another current distribution peaked at the edges of the junction given by (Fig. 4.11):

$$J_l(x) = J_1 \frac{\cosh(ax)}{\cosh(aL/2)}$$

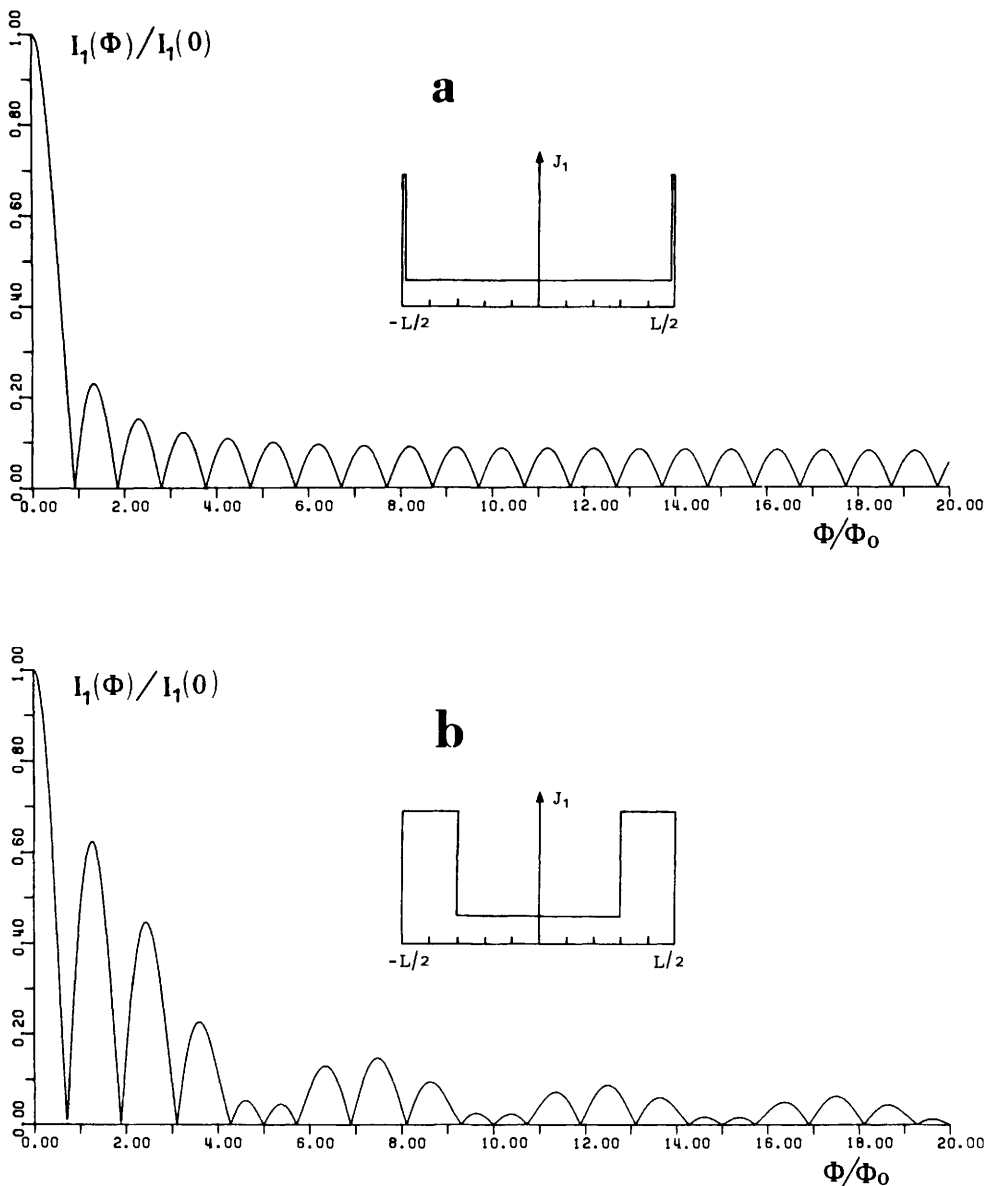


Figure 4.9 Magnetic field dependence of I_1 (4.4.1) for a junction with a steplike current density distribution (see insets) like that of Fig. 4.8. The parameters values are: (a) $\xi=0.20$, $s/L=0.01$; (b) $\xi=0.20$, $s/L=0.20$; (c) $\xi=0.06$, $s/L=0.06$; (d) $\xi=0.06$, $s/L=0.01$.

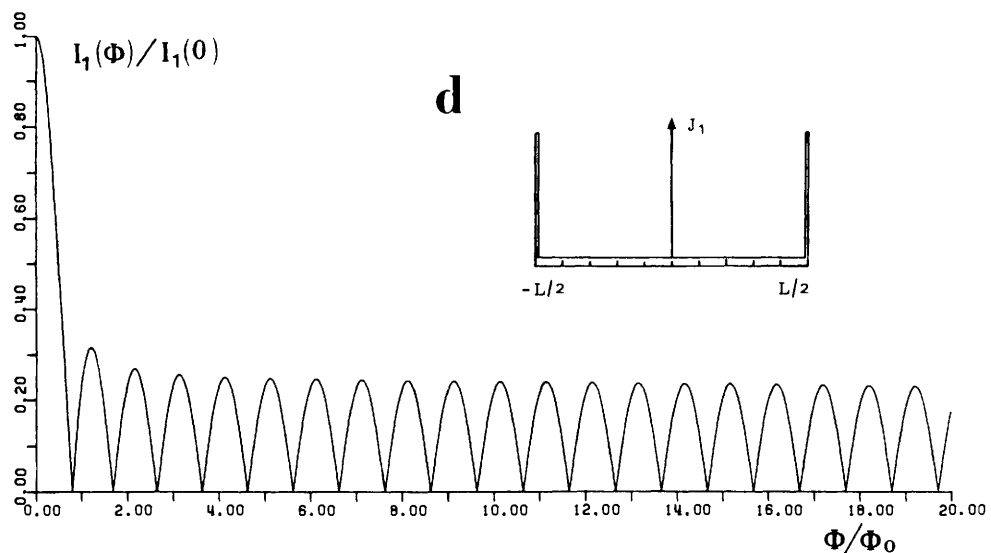
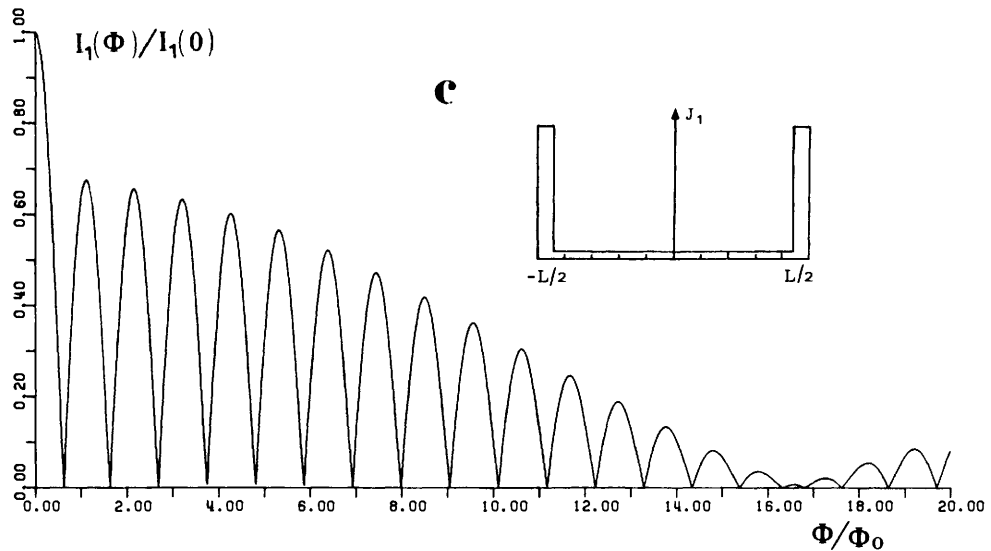
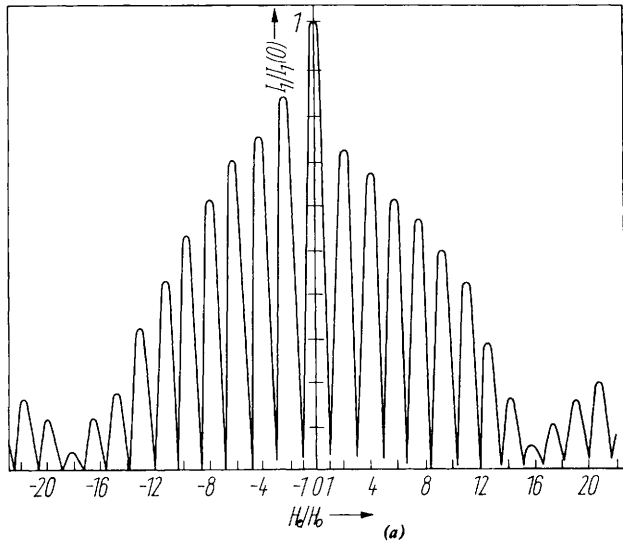
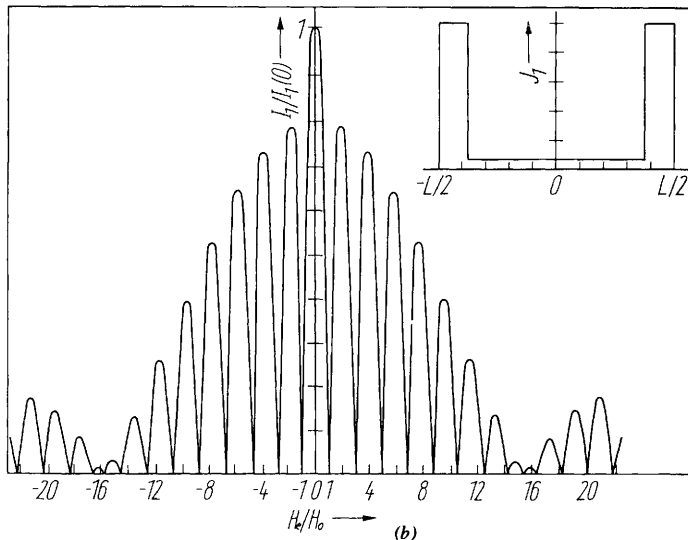


Figure 4.9 (Continued)



(a)



(b)

Figure 4.10 (a) Experimental data for the critical current I_1 vs. applied magnetic field H_e for an Sn-SnO_x-Sn junction. (b) Theoretical I vs. H_e curve corresponding to a steplike current density profile (see inset). The curve has been computed by using (4.4.1) with $\xi=0.06$ and $s/L=0.11$. (After Barone et al. 1977.)

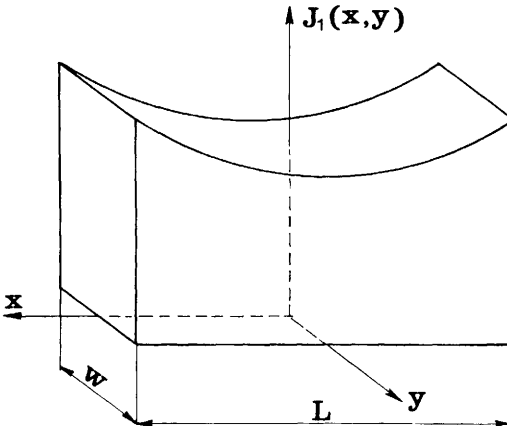


Figure 4.11 Current density profile: one parameter model.

where the parameter a has the dimension of the inverse of a length and gives a measure of the peak to valley ratio in the profile of Fig. 4.11.

In this case we have

$$\begin{aligned} I_1(k) &= \left| \frac{J_1 W}{\cosh\left(\frac{aL}{2}\right)} \int_{-L/2}^{+L/2} \cosh(ax) e^{jkx} dx \right| \\ &= \left| \frac{J_1 W}{\cosh\left(\frac{aL}{2}\right)} \int_{-L/2}^{+L/2} \cosh(ax) \cos(kx) dx \right| \end{aligned}$$

since $\cosh(ax)$ is an even function. By integration, it is easy to show that

$$I_1(k) = I_1(0) \frac{a^2}{a^2 + k^2} \left| \frac{k}{a} \frac{\sin(kL/2)}{\tanh(aL/2)} + \cos\left(\frac{kL}{2}\right) \right| \quad (4.4.2)$$

where

$$I_1(0) = \frac{2J_1}{a} W \tanh\left(\frac{aL}{2}\right)$$

Defining $\chi = (L/2)/(1/a)$, (4.4.2) becomes

$$I_1\left(\frac{\Phi}{\Phi_0}, \chi\right) = I_1(0) \frac{\chi^2}{\chi^2 + \left(\pi \frac{\Phi}{\Phi_0}\right)^2} \left| \frac{\pi \frac{\Phi}{\Phi_0} \sin\left(\pi \frac{\Phi}{\Phi_0}\right)}{\chi \tanh \chi} + \cos\left(\pi \frac{\Phi}{\Phi_0}\right) \right| \quad (4.4.3)$$

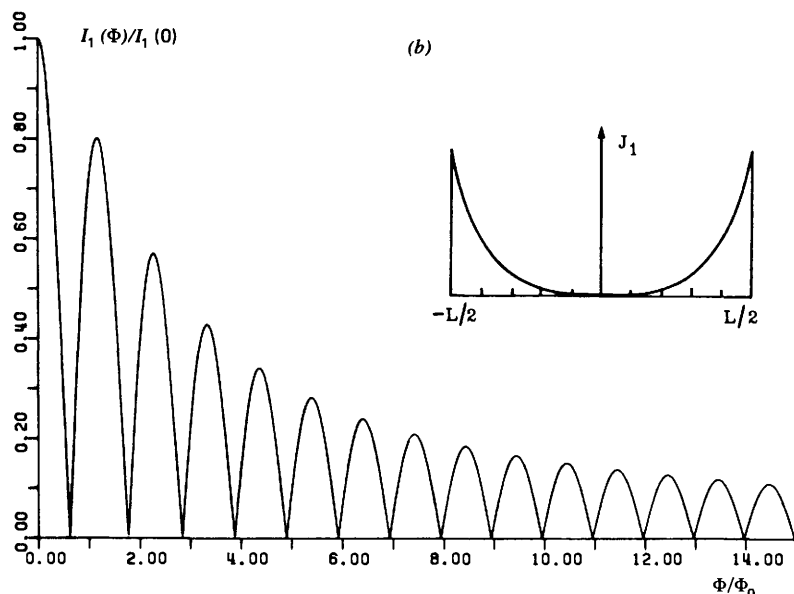
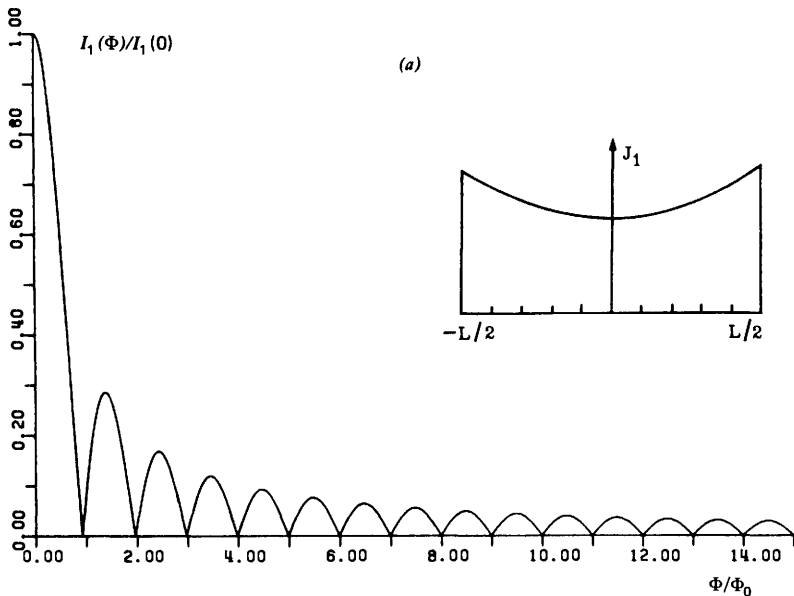


Figure 4.12 Magnetic field dependence of I_1 (4.4.3) for a junction with a “one parameter” current density profile (see insets) like that of Fig. 4.11. The parameter values are: (a) $\chi = 1.00$; (b) $\chi = 5.00$; (c) $\chi = 10.00$; (d) $\chi = 100.00$.

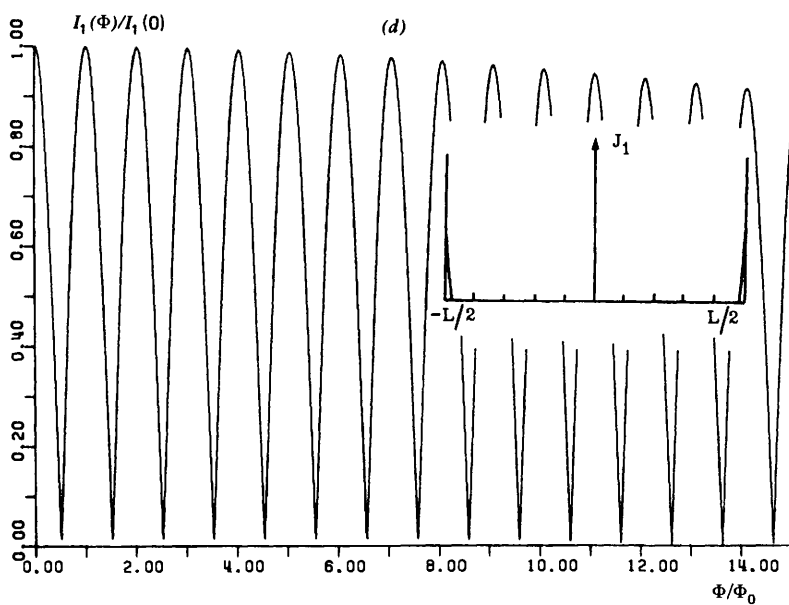
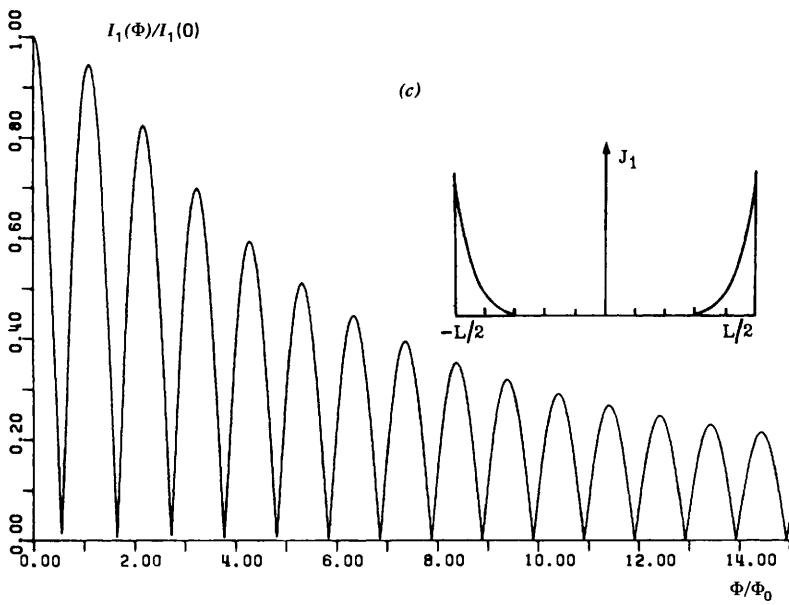


Figure 4.12 (Continued)

This dependence, computed for different values of the parameter χ , is reported in Fig. 4.12. By equating (4.4.3) to zero we get for the minima

$$\pi \frac{\Phi}{\Phi_0} \tan\left(\pi \frac{\Phi}{\Phi_0}\right) = -\chi \tanh(\chi)$$

It is possible to solve this equation by a simple graphical construction (see Fig. 4.13). The minima are given by the intersection of a horizontal line corresponding to a given value of $\chi \geq 0$. Figure 4.13 (top) shows that for $\chi \rightarrow 0$, which is a uniform current density distribution, we find the expected positions for the minima in the Fraunhofer pattern, that is, the distance between the first two minima (symmetric with respect to zero) is twice the distance between consecutive minima. In the limit of large χ , the distance between all the consecutive minima is the same. The latter situation is typical of interference phenomena occurring in the double junction configuration as will be extensively discussed in Chapter 12. Thus we have, as expected, results similar to those obtained assuming the current density profile of Fig. 4.8. However, in order to clarify the passage from “single” to “double” junction behavior, the one free parameter model displayed in Fig. 4.11 is more convenient.

Current density distributions peaked at the edges, like those we have just discussed, can occur in real situations. For instance, in the case of junctions of cross geometry (see the next chapter, Fig. 5.15d) this effect can occur because of possible damage in the oxide barrier at the edges of the bottom film (Schwmidt and Finnegan 1969). In Fig. 4.13b are reported experimental data (dots) which can be interpreted within this framework (Barone et al. 1977). The solid line in the figure is the theoretical curve computed using the current

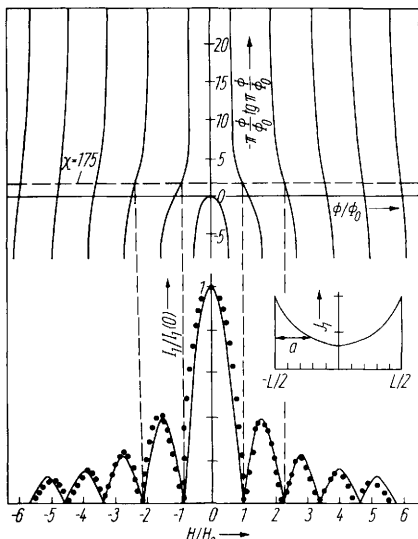


Figure 4.13 *Top:* Graphical determination of the position of the current minima in the “one parameter” model. *Bottom:* Experimental data (dots) for the critical current vs. applied magnetic field for an Nb-NbO_x-Pb junction. The solid line refers to the theoretical dependence corresponding to the exponential current density profile sketched in the inset. (After Barone et al. 1977.)

density distribution sketched in the inset. The experimental measurements shown in Fig. 4.14 refer to a single sample of cross type geometry. The magnetic field was applied either along the upper film direction (Fig. 4.14a) or along the bottom film direction (Fig. 4.14b). In the latter case an edge effect is evident which may be accounted for by a current profile in the x direction such as that of Fig. 4.8 or Fig. 4.11. In the former case a Fraunhofer-like pattern is obtained as a consequence of the uniform current density distribution along the y direction (Fig. 4.14a). A striking evidence of this "double" junction behavior has been reported by Barone et al. (1975) using light sensitive junctions. In this article enhancement of the Josephson current density at the edges of the junction was deliberately induced by light exposure (see Section 7.2.2).

Let us consider now the opposite situation in which the current density distribution is maximum at the center of the junction. Let us assume a simple triangular profile, such that

$$J_1(x) = J_1 a_{L/2}(x) \quad a_{L/2}(x) = \begin{cases} 1 - \frac{|x|}{L/2} & |x| \leq L/2 \\ 0 & |x| > L/2 \end{cases}$$

In this case it is easy to show that

$$I_1(k) = \left| J_1 \frac{WL}{2} \frac{\sin^2(kL/4)}{kL/4} \right|$$

This dependence is shown in Fig. 4.15. When current density distributions decreasing from the center to the edges of the junction are considered, a lowering of the secondary maxima occurs in the I_1 vs. H_e patterns. This agrees with the experimental observation by Dynes and Fulton (1971) who have calculated also the corresponding current density profile. We recall, incidentally, that the lowering of the secondary maxima occurs also in circular junctions with a uniform current density distribution (see Section 4.3.2). This is important, although expected, since the character of the I_1 vs. H_e dependence is essentially related to the quantity $\mathcal{I}(x)$ [see (4.2.3)], so that similar results can be obtained by changing either the form of $J_1(x, y)$ or the junction geometrical configuration (Balsamo et al. 1976a; Cucolo, Pace, and Vaglio 1979; Moser 1979; Broom, Kotyczka, and Moser 1980).

The whole subject of nonuniform current density distribution in the magnetic field patterns has been investigated by Barone et al. (1977) from both theoretical and experimental point of view. More recently, further theoretical work has been reported by Richter and Seidel (1978).

Finally, we remark that when the minima of $I_1(H)$ do not occur at zero current, this can be interpreted as the presence of short circuits or of an asymmetric current density distribution in the junction. In the former case a

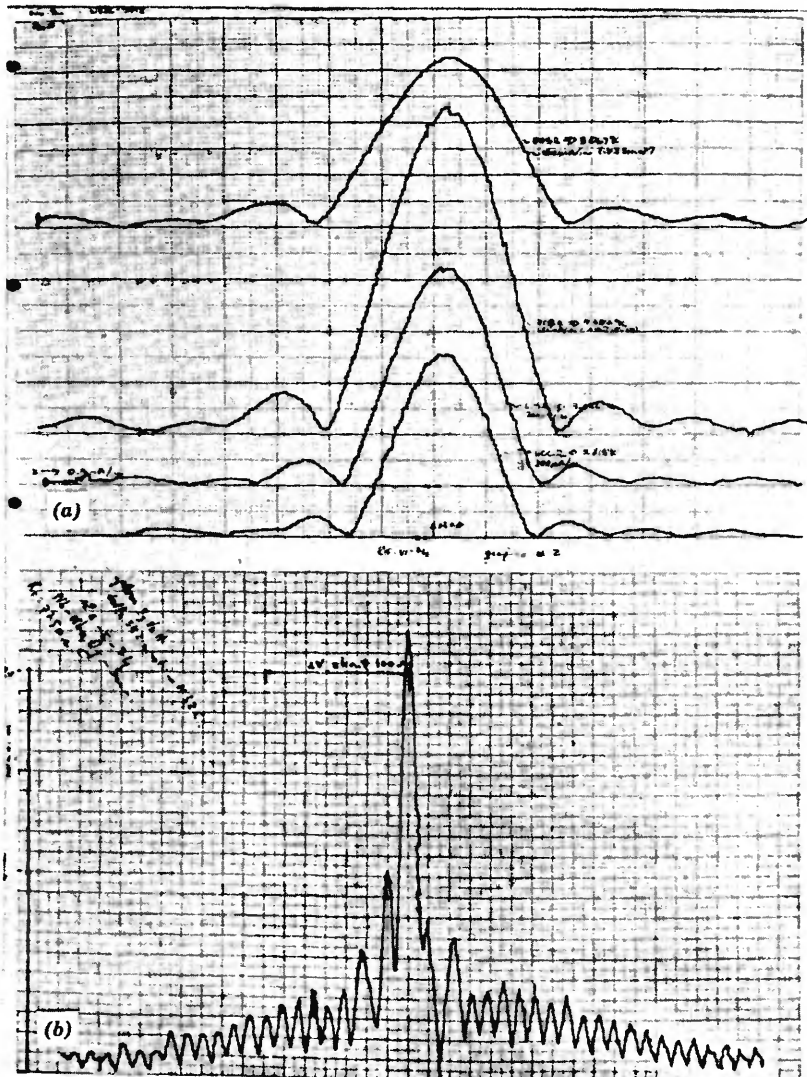


Figure 4.14 Magnetic field dependence for a cross-type Nb-Nb_xO_y-Sn junction showing edge effects (direct recording). Vertical axis current, horizontal magnetic field. (a) The field is along the upper film direction. The curves refer to different temperatures. (b) The field is along the bottom film direction, perpendicular to the direction along which the current density is peaked at the edges.

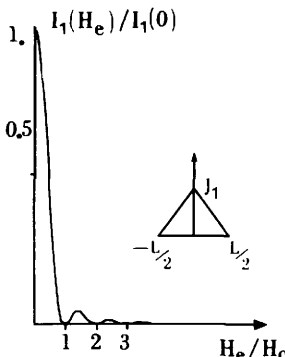


Figure 4.15 Magnetic field dependence of the maximum Josephson current for a junction with a current density profile peaked at the center (see inset).

constant current contribution to the pattern is present whereas in the latter case a field dependent current background is generally observed. As we see in the next section, similar effects can be related to the presence of structural fluctuations.

4.4.2 Structural Fluctuations. So far we have discussed the problem of a nonuniform current density distribution arising from localized nonuniformities in the barrier. Now we consider the effect related to inhomogeneities assumed to be randomly distributed all over the barrier, so-called structural fluctuations (Yanson 1970a, b). Although the stochastic approach to the problem would suggest including this argument within the more general context of fluctuations (thermal, quantum mechanical, etc.), we prefer to discuss here these results to give an overall picture of the effects of the barrier nonuniformities in a Josephson tunnel junction.

To account for the presence of structural fluctuation we follow Yanson's analysis in a slightly modified form.

We assume that the maximum current density can be written in one dimension as

$$J_i(x) = J_i(x) + J_f(x) = J_i(x) + \sum_{n=1}^{\infty} \left(a_n \cos \frac{2\pi n x}{L} + b_n \sin \frac{2\pi n x}{L} \right) \quad (4.4.4)$$

where $J_i(x)$ is the fluctuation free current density and $J_f(x)$ describes the random distribution of the inhomogeneities. This stochastic function is characterized by the properties

$$\overline{J_f(x)} = 0 \quad \text{and} \quad J(\xi) \equiv \overline{J_f(x+\xi)J_f(x)} = \overline{J_f^2} e^{-|\xi|/r} \quad (4.4.5)$$

where the bar indicates spatial averaging over the junction area. $J(\xi)$ is the spatial autocorrelation function, $\overline{J_f^2}$ is the constant mean square amplitude of fluctuations, and r is the correlation radius, which gives a measure of the

nonuniformity. The expression for the autocorrelation function $J(\xi)$ is obtained as follows. We assume that the barrier, along the x direction, consists of a sequence of small sections whose relative average length is r/L so that L/r gives the average number of these sections. The probability of having a number l of sections in the barrier (within L) is given by the Poisson statistics:

$$P_L(l) = \frac{l}{(l-1)!} \left(\frac{L}{r}\right)^{l-1} e^{-L/r}$$

analogously, the probability of having l sections within $|\xi|$ is

$$P_\xi(l) = \frac{l}{(l-1)!} \left(\frac{|\xi|}{r}\right)^{l-1} e^{-|\xi|/r}$$

We assume a Gaussian distribution for the amplitudes of J_f in each section:

$$F[J_F(x)] = \frac{1}{\sqrt{2\pi\bar{J}_f^2}} e^{-J_f^2(\xi)/\bar{J}_f}$$

where \bar{J}_f^2 is the mean square deviation.

We can write:

$$\overline{J_f(x)J_f(x+\xi)} = \sum_{l=1}^{\infty} P_\xi(l) \overline{J_{f,l}(x)J_{f,l}(x+\xi)}$$

whenever $l > 1$ in the interval ξ (length of the section less than ξ), we have:

$$\overline{J_{f,l}(x)J_{f,l}(x+\xi)} = \overline{J_{f,l}(x)} \cdot \overline{J_{f,l}(x+\xi)} = 0$$

that is, no correlation between values of $J_f(x)$ in different sections. For $l=1$ we have

$$\overline{J_{f,1}(x)J_{f,1}(x+\xi)} = \overline{J_f^2(x)} = \bar{J}_f^2 \quad \text{and} \quad P(1) = e^{-|\xi|/r}$$

so that:

$$\overline{J_f(x)J_f(x+\xi)} = \bar{J}_f^2 e^{-|\xi|/r}$$

Let us write the relation between supercurrent and applied magnetic field:

$$I_1(\phi) = W \left| \int_{-L/2}^{+L/2} J_1(x) e^{2\pi j \phi x / L} dx \right|$$

where $\phi = \Phi/\Phi_0$. By inserting (4.4.4) into this expression and using the

properties of J_f we have

$$I_1^2(\phi) = \mathcal{F}^2(\phi) + (I_a^2 + I_b^2) \frac{\sin^2 \pi \phi}{\pi^2 \phi^2}$$

where $\mathcal{F}(\phi)$ is the usual Fourier transform of $J_i(x)$ and

$$\begin{aligned} I_a^2 &= 4W^2 \sum_{m,n=1}^{\infty} (-1)^{m+n} \frac{\phi^2}{\phi^2 - n^2} \frac{\phi^2}{\phi^2 - m^2} \\ &\quad \times \int_{-L/2}^{+L/2} dx_1 \int_{-L/2}^{+L/2} dx_2 J_f(x_1) J_f(x_2) \cos \frac{2\pi n x_1}{L} \cos \frac{2\pi m x_2}{L} \\ I_b^2 &= 4W^2 \sum_{m,i=1}^{\infty} (-1)^{m+n} \frac{n\phi}{\phi^2 - n^2} \frac{m\phi}{\phi^2 - m^2} \\ &\quad \times \int_{-L/2}^{+L/2} dx_1 \int_{-L/2}^{+L/2} dx_2 J_f(x_1) J_f(x_2) \sin \frac{2\pi n x_1}{L} \sin \frac{2\pi m x_2}{L} \end{aligned}$$

The average values of these expressions can be found by introducing the autocorrelation function for $J_F(\xi = x_1 - x_2)$ defined above. By evaluating the integrals one finally obtains:

$$I_1(\phi) = \left\{ \mathcal{F}^2(\phi) + I_0^2 [a(r', \phi) + b(r', \phi)] \frac{\sin^2 \pi \phi}{\pi^2 \phi^2} \right\}^{1/2} \quad (4.4.6)$$

where $I_0 = WL(2r' \overline{J_f^2})$; $r' = \frac{r}{L}$. The functions $a(r', \phi)$ and $b(r', \phi)$ are given by

$$\begin{aligned} a(r', \phi) &= 2 \sum_{n=1}^{\infty} \left(\frac{\phi^2}{\phi^2 - n^2} \right)^2 \frac{1}{1 + (2\pi n r')^2} - r'(1 - e^{-1/r'}) \\ &\quad \times \left[2 \sum_{n=1}^{\infty} \frac{\phi^2}{\phi^2 - n^2} \frac{1}{1 + (2\pi n r')^2} \right]^2 \\ b(r', \phi) &= 2 \sum_{n=1}^{\infty} \left(\frac{n\phi}{\phi^2 - n^2} \right)^2 \frac{1}{1 + (2\pi n r')^2} + r'(1 - e^{-1/r'}) \\ &\quad \times \left[2 \sum_{n=1}^{\infty} \frac{n\phi}{\phi^2 - n^2} \frac{2\pi n r'}{1 + (2\pi n r')^2} \right]^2 \end{aligned}$$

For small fluctuations ($r' \ll 1$) and small applied fields ($2\pi r' \phi \ll 1$) (4.4.7)

become

$$a(r', \phi) = 2 \sum_{n=1}^{\infty} \left(\frac{\phi^2}{\phi^2 - n^2} \right)^2 = \frac{\pi^2 \phi^2}{2 \sin^2 \pi \phi} + \frac{\pi \phi}{2} \cotg \pi \phi - 1$$

$$b(r', \phi) = 2 \sum_{n=1}^{\infty} \left(\frac{n \phi}{\phi^2 - n^2} \right)^2 = \frac{\pi^2 \phi^2}{2 \sin^2 \pi \phi} - \frac{\pi \phi}{2} \cotg \pi \phi;$$

so that

$$I_1(\phi) = \left\{ \mathcal{F}^2(\phi) + I_0^2 \left(1 - \frac{\sin^2 \pi \phi}{\pi^2 \phi^2} \right) \right\}^{1/2} \quad (4.4.8)$$

From the last equation we see that the usual dependence $I_1(\phi) = |\mathcal{F}(\phi)|$ is modified by the presence of fluctuations. In particular we observe that, along with a field modulated contribution, there is present a constant current background of amplitude I_0 . We also see that the zero field current is not modified by the fluctuations. In the more general case of (4.4.6) it is possible to show, by inspection of (4.4.7), that the main difference is the presence of a background current which is no longer constant but vanishes for increasing field.

In the case of small fluctuations it is not possible to decouple the average amplitude of the fluctuation from its average correlation radius. In fact, as follows from (4.4.8), all the information concerning the fluctuations is contained in I_0 . On the other hand, in the large fluctuation limit, the decrease of the background current allows an independent determination of r' and J_f^2 .

Yanson (1970a) has carried out investigations on tin-tin oxide-tin junctions, which indicate that the experimental condition was that of small fluctuations. In this work a value 0.066 for the ratio $\gamma = I_0/I_1(0)$ was found. Recently, investigations on the effect of fluctuations in light sensitive Josephson junctions (see Chapter 7) have been carried out by Barone et al. (1978). In this case the light induced Josephson current vs. the applied field was measured in junctions which did not exhibit zero voltage current in dark conditions. This guarantees the absence of background currents in the $I_1(H)$ patterns due to shorts. Typical experimental results are reported in Fig. 4.16 (dots). It is evident that the presence of a small constant current background which suggests that we are in the small fluctuation limit. The full line in the figure is the theoretical curve obtained by (4.4.8) with $\gamma = 0.06$. Furthermore, using the argument developed in Section 4.4.6 it is possible to take into account also the interferential contributions due to edge effects. In this case a steplike current density profile is assumed with $\xi = 0.01$ and $s' = 0.01$.

As we have seen, this value of γ is similar to the one found by Yanson. However, current measurements at relatively high values of the magnetic field

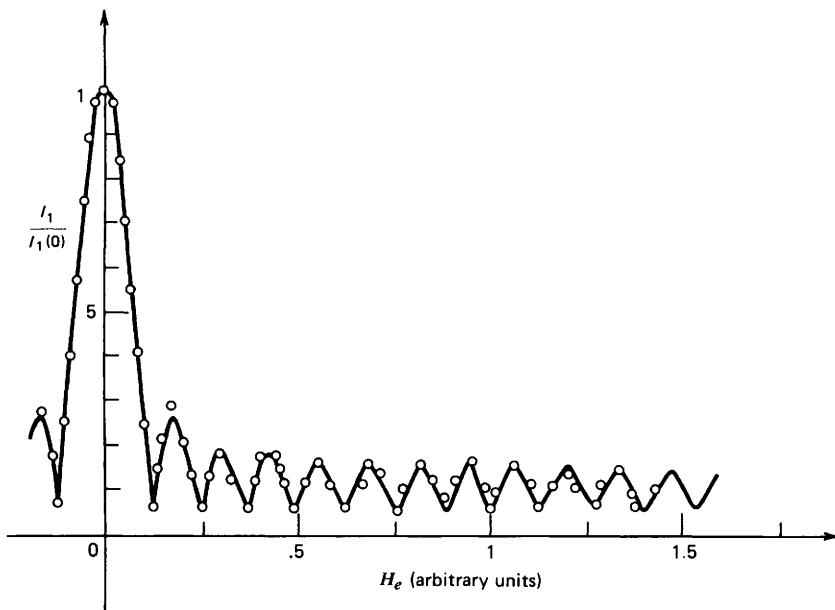


Figure 4.16 Experimental results (dots) for the magnetic field dependence of the photoinduced Josephson current in a Pb-CdS-In junction, exhibiting small scale spatial fluctuations. The solid line is the theoretical dependence computed by (4.4.8) assuming $\gamma = I_0/I_1(0) = 0.06$. $\mathcal{F}(\phi)$ has been computed assuming a steplike current density profile with $\xi = 0.01$ and $s' = s/L = 0.01$. (After Barone et al. 1978.)

permit quantitative inferences regarding r' and $\overline{J_f^2}$. For this purpose the two dimensional nature of the problem should be taken into account. This leads to the same dependence of the Josephson current upon the applied field in which, however $\mathcal{F}(\phi)$ is the Fourier transform of the integral of the current density along the y direction and $I_0 = WL \left(\frac{4a}{WL} \overline{J_f^2} \right)$, where a now gives a measure of the average area of the structural nonuniformities (see the reference above). Large scale fluctuation effects will be mentioned in Chapter 8 in a technological context.

CHAPTER 5

Large Junctions—Static Self-Field Effects

In the preceding chapter we considered the effect of the magnetic field on junctions smaller than the Josephson penetration depth.

In that case, the self field due to the current flowing in the junction electrodes was completely disregarded. We now discuss the I vs. H_e dependence for a junction whose dimensions are of the same order of magnitude as the Josephson penetration depth. Section 5.1 contains an approximate analysis for $L \approx \lambda_J$ designed to give an intuitive feeling of the problem. An exact analysis for the case $L \gg \lambda_J$ is developed in Section 5.2.

5.1 Approximate Analysis

Let us refer to the simple geometry of Fig. 5.1a. If I is the total current flowing into the junction and J_1 is the Josephson current density assumed to be uniform, from current conservation it follows that

$$\frac{d}{dx} \left(\frac{\mathcal{I}(x)}{W} \right) = J_1 \quad (5.1.1)$$

$\mathcal{I}(x)$ is the current at a point x of the junction electrode. In the chosen coordinate system it satisfies the boundary conditions

$$\mathcal{I}\left(-\frac{L}{2}\right) = 0 \quad \mathcal{I}\left(\frac{L}{2}\right) = I$$

From (5.1.1) we get

$$\frac{\mathcal{I}(x)}{W} = J_1 \left(x + \frac{L}{2} \right) \quad (5.1.2)$$

$\mathcal{I}(x)$ is plotted in Fig. 5.1b.

The magnetic field due to $\mathcal{I}(x)$ is directed along the y axis and is given by

$$H_s(x) = \frac{4\pi}{c} \frac{\mathcal{I}(x)}{W} = \frac{4\pi}{c} J_1 \left(x + \frac{L}{2} \right) \quad (5.1.3)$$

To take into account the effect of such a self-field $H_s(x)$ following Yamashita

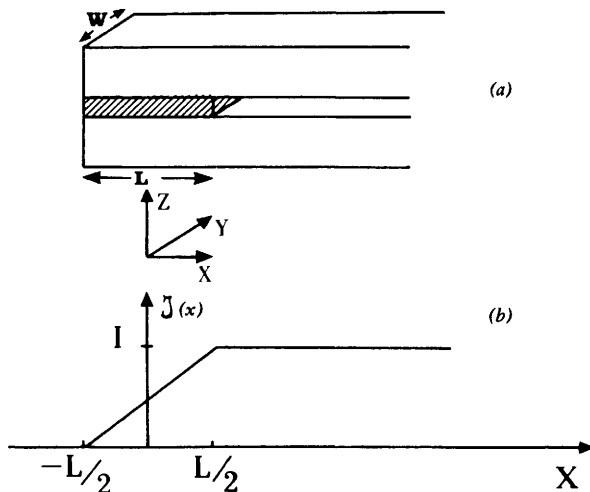


Figure 5.1 (a) Schematic of the simple junction geometry used to evaluate self-field effects. (b) Current distribution $J(x)$ in the superconducting films along the x direction.

and Onodera (1967), we replace (5.1.3) by its mean value $\bar{H}_s = (2\pi/c)(I/W)$. If H_e is the external magnetic field, applied in the y direction, the total field in the junction is $H = H_e + H_s$ and the maximum current is given by (see Section 4.3):

$$I(H_e) = WLJ_1 \left| \frac{\sin \left[\frac{\pi d L}{\Phi_0} \left(H_e + \frac{2\pi}{c} \frac{I(H_e)}{W} \right) \right]}{\frac{\pi d L}{\Phi_0} \left(H_e + \frac{2\pi}{c} \frac{I(H_e)}{W} \right)} \right| \quad (5.1.4)$$

It is easy to see that the maximum value of $I(H)$ is $I_0 = WLJ_1$. Such a maximum does not occur at $H_e = 0$, but at a value of the external field $H_M = -(2\pi/c)(I_0/W)$.

Expression 5.1.4 can be written in terms of flux as

$$\frac{I(\Phi/\Phi_0)}{I_0} = \left| \frac{\sin \pi \left[\frac{\Phi}{\Phi_0} + \frac{\Phi_s^M}{\Phi_0} \frac{I(\Phi/\Phi_0)}{I_0} \right]}{\pi \left[\frac{\Phi}{\Phi_0} + \frac{\Phi_s^M}{\Phi_0} \frac{I(\Phi/\Phi_0)}{I_0} \right]} \right| \quad (5.1.5)$$

where

$$\Phi = dLH_e; \quad \Phi_s^M = dL \frac{2\pi}{c} \frac{I_0}{W}; \quad d = t + \lambda_{L1} + \lambda_{L2};$$

$$\Phi_0 = \frac{hc}{2e} \quad (\text{flux quantum})$$

It is also straightforward to show that in this simple case

$$\frac{\Phi_s^M}{\Phi_0} = \frac{L^2}{4\pi} \left(\frac{8\pi e J_1 d}{\hbar^2 c^2} \right) = \frac{1}{4\pi} \left(\frac{L}{\lambda_J} \right)^2$$

In Fig. 5.2a it is shown I/I_0 vs Φ/Φ_0 for $L/\lambda_J = 2$. For the simple geometry just assumed, we see that the self-field produces a shift of the maxima in the magnetic field pattern. In Fig. 5.2b $I(0)/I_0$ is reported as a function of the

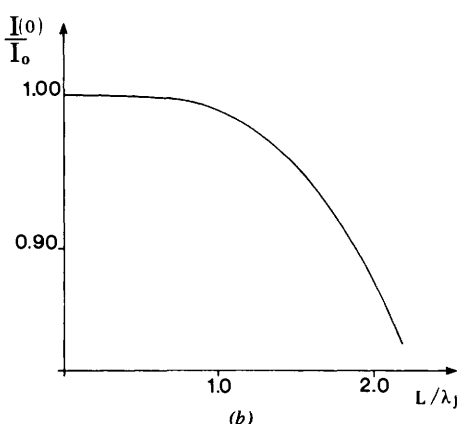
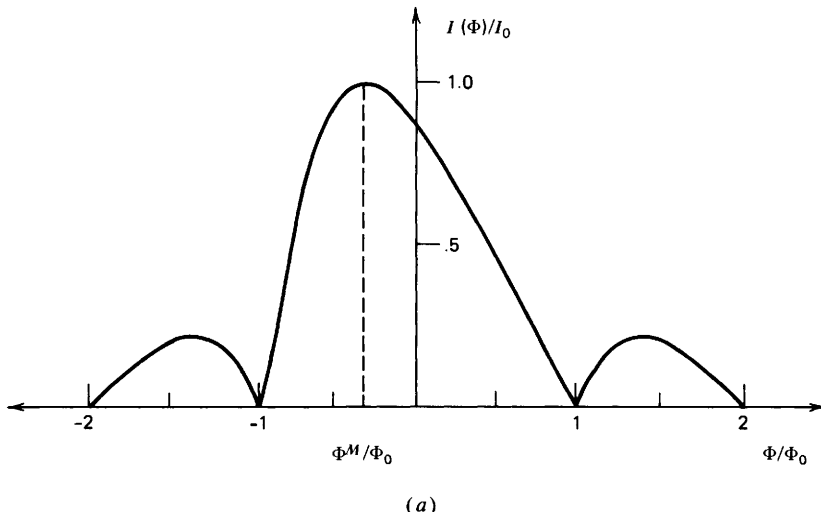


Figure 5.2 (a) Magnetic field dependence of the Josephson current (5.1.5) for a junction of the geometry of Fig. 5.1a. The external field is perpendicular to the x direction. The curve corresponds to the case $L/\lambda_J = 2$. I_0 is the maximum current value that occurs at $\Phi = \Phi_M \neq 0$. (b) The ratio between the zero field current $I(0)$ and the maximum Josephson current I_0 as a function of L/λ_J . L is the junction dimension; λ_J is the Josephson penetration depth.

dimensionless parameter L/λ_J . A two dimensional cross-type geometry was considered by Yamashita and Onodera (1967). The self-field then has nonzero components in both the x and y direction and the I vs. H pattern that results is the product of two Fraunhofer-like factors. The maximum current $I(H_M)$ is no longer given by I_0 but is depressed because of the presence of self-fields in the y direction.

Thus when the dimensions of the junction become larger than λ_J , the effects from the fields associated with the currents in the junction strongly modify its behavior. These effects can be significant even for the ratio L/λ_J near the unity. Furthermore, as we shall see in detail, the geometry of the junction plays a crucial role, since the self-field can be different for different configurations of the junction electrodes.

It is interesting to note that the Josephson penetration length λ_J depends on the temperature through the London penetration depth λ_L and the maximum current density J_1 . In Fig. 5.3 is shown the temperature dependence of λ_J for a junction with equal superconducting electrodes using for $J_1(T)$ the Ambegaokar and Baratoff calculations (see Chapter 3) and for the London depth, $\lambda_L(T)$, the relation

$$\lambda_L(T) = \lambda_L(0) [1 - (T/T_c)^4]^{-1/2} \quad (5.1.6)$$

Thus as long as the reduced temperature is below 0.5 the normalized junction dimension L/λ_J can be assumed to be constant; whereas for $T/T_c >$

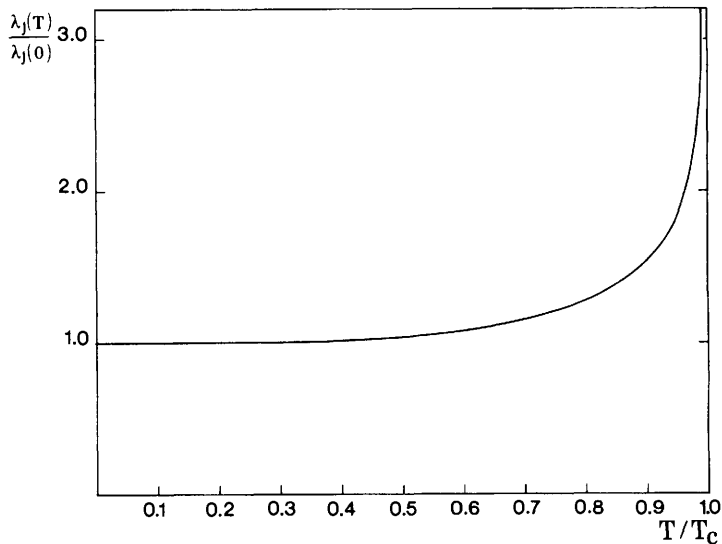


Figure 5.3 Temperature dependence of the Josephson penetration depth $\lambda_J(T)$ for a symmetric junction. T_c is the critical temperature of the superconducting electrodes.

0.5 a junction which is “large” ($L > \lambda_J$) at low temperature becomes smaller and smaller (increasingly λ_J) as T approaches T_c . Incidentally we observe that from this it is easy to deduce how the temperature dependence of I_1 , discussed in Chapter 3, can be affected by the presence of self-field.

5.2 Analysis of Owen and Scalapino

In the simple example considered in Section 5.1 a uniform current density distribution in the junction was assumed. As we will show in detail, this assumption is no longer valid if $L \gg \lambda_J$; in fact, because of the presence of the self-field the current density can be highly nonuniform even in zero external field. Therefore in this case the problem of determining the I vs. H_e dependence requires the solution of (4.1.2) with suitable boundary conditions. This equation, however, cannot be solved analytically in general; therefore one often has to resort to approximate procedures and numerical computation.

Let us confine our attention to the one dimensional case:

$$\frac{d^2\varphi(x)}{dx^2} = \frac{1}{\lambda_J^2} \sin \varphi(x) \quad (5.2.1)$$

The corresponding junction configuration can be realized by a rectangular junction in which one dimension (y) is small compared to λ_J .

Multiplying both sides of (5.2.1) by $2(d\varphi/dx)$ we get

$$\frac{d}{dx} \left(\frac{d\varphi}{dx} \right)^2 = -\frac{2}{\lambda_J^2} \frac{d}{dx} \cos \varphi$$

By integration:

$$\left(\frac{d\varphi}{dx} \right)^2 = \left(\frac{d\varphi}{dx} \right)_{x_0}^2 + \frac{2}{\lambda_J^2} (\cos \varphi_0 - \cos \varphi)$$

where $\varphi_0 = \varphi(x_0)$. Defining

$$C = \cos \varphi_0 + \frac{\lambda_J^2}{2} \left(\frac{d\varphi}{dx} \right)_{x_0}^2$$

we can write

$$\frac{d\varphi}{dx} = \frac{1}{\lambda_J} [2(C - \cos \varphi)]^{1/2} \quad (5.2.2)$$

Let us introduce the parameter κ defined by $C=(2-\kappa^2)/\kappa^2$ so that

$$\frac{d\varphi}{dx} = \frac{1}{\lambda_J} \left[2 \left(\frac{2-\kappa^2}{\kappa^2} \right) - 2 \cos \varphi \right]^{1/2}$$

and since $\cos \varphi = 2 \cos^2 \varphi / 2 - 1$, it becomes

$$\frac{d\varphi}{dx} = \frac{2}{\kappa \lambda_J} (1 - \kappa^2 \cos \varphi / 2)^{1/2} \quad (5.2.3)$$

By integration we have

$$\int_{x_0}^x \frac{dx'}{\kappa \lambda_J} = \int_{\varphi(x_0)}^{\varphi(x)} \frac{d\varphi'/2}{\sqrt{1 - \kappa^2 \cos^2 \varphi'/2}}$$

and by the change of variable

$$\theta = \frac{\varphi'}{2} - \frac{\pi}{2}; \quad d\theta = \frac{d\varphi'}{2}$$

we arrive at (Owen and Scalapino 1967; Scalapino 1967)

$$\frac{x-x_0}{\kappa \lambda_J} = \int_0^{\varphi/2 - \pi/2} \frac{d\theta}{\sqrt{1 - \kappa^2 \sin^2 \theta}} \quad (5.2.4)$$

Furthermore, with the substitution: $\sin \theta = t$, (5.2.4) reduces to

$$\frac{x-x_0}{\kappa \lambda_J} = \int_0^{-\cos \varphi/2} \frac{dt}{(1-t^2)^{1/2} (1-\kappa^2 t^2)^{1/2}} \quad (5.2.5)$$

The last expression for $\kappa \leq 1$ can be solved in terms of the Jacobian elliptic functions, $\text{sn}(u|\kappa^2)$, $\text{cn}(u|\kappa^2)$, $\text{dn}(u|\kappa^2)$, of argument u and modulus κ (Whittaker and Watson 1969). We get

$$\cos \frac{\varphi}{2} = -\text{sn}\left(\frac{x-x_0}{\kappa \lambda_J} \middle| \kappa^2\right) \quad (5.2.6a)$$

and since

$$\sin^2 \frac{\varphi}{2} = 1 - \cos^2 \frac{\varphi}{2} = 1 - \text{sn}^2 = \text{cn}^2$$

it follows that

$$\sin \frac{\varphi}{2} = \text{cn}\left(\frac{x-x_0}{\kappa \lambda_J} \middle| \kappa^2\right) \quad (5.2.6b)$$

If $\kappa > 1$, by the substitution $t = t'/\kappa$ (5.2.5) becomes

$$\frac{x - x_0}{\lambda_J} = \int_0^{-\kappa \cos \varphi / 2} \frac{dt'}{(1 - t'^2/\kappa^2)^{1/2} (1 - t'^2)^{1/2}} \quad (5.2.7)$$

which gives

$$\cos \frac{\varphi}{2} = -\frac{1}{\kappa} \operatorname{sn}\left(\frac{x - x_0}{\lambda_J} \middle| \frac{1}{\kappa^2}\right) \quad (5.2.8a)$$

Using the relation $\sin^2 \varphi/2 = 1 - \cos^2 \varphi/2 = 1 - \operatorname{sn}^2 \varphi/2 = \operatorname{dn}^2$, we have

$$\sin \frac{\varphi}{2} = \operatorname{dn}\left(\frac{x - x_0}{\lambda_J} \middle| \frac{1}{\kappa^2}\right) \quad (5.2.8b)$$

The current density $J(x)$ and the magnetic field $H(x)$ in the junction can be calculated using the Josephson relations:

$$J(x) = J_1 \sin \varphi(x); \quad \frac{d\varphi}{dx} = \frac{2\pi d}{\Phi_0} H(x)$$

Let us consider the case $\kappa \leq 1$. On differentiating (5.2.6a) we have

$$-\frac{1}{2} \left(\frac{d\varphi}{dx} \right) \sin \frac{\varphi}{2} = -\frac{d}{dx} \operatorname{sn}\left(\frac{x - x_0}{\kappa \lambda_J} \middle| \kappa^2\right) = -\frac{1}{\kappa \lambda_J} \operatorname{cn}\left(\frac{x - x_0}{\kappa \lambda_J} \middle| \kappa^2\right) \operatorname{dn}\left(\frac{x - x_0}{\kappa \lambda_J} \middle| \kappa^2\right)$$

which follows from the property of the elliptic function: $(d/dx)\operatorname{sn}(u|\kappa) = \operatorname{cn} \operatorname{dn}$. Considering this expression together with (5.2.6b) it follows that

$$\frac{d\varphi}{dx} = \frac{2}{\kappa \lambda_J} \operatorname{dn}\left(\frac{x - x_0}{\kappa \lambda_J} \middle| \kappa^2\right) \quad (5.2.9)$$

and using (5.2.6a) and (5.2.6b) we have

$$\sin \varphi = -2 \operatorname{sn}\left(\frac{x - x_0}{\kappa \lambda_J} \middle| \kappa^2\right) \operatorname{cn}\left(\frac{x - x_0}{\kappa \lambda_J} \middle| \kappa^2\right)$$

Therefore the expressions for $J(x)$ and $H(x)$ that we obtain (for $\kappa \leq 1$) are

$$H(x) = \frac{H_{c0}}{\kappa} \operatorname{dn}\left(\frac{x - x_0}{\kappa \lambda_J} \middle| \kappa^2\right) \quad (5.2.10a)$$

$$J(x) = -2 J_1 \operatorname{sn}\left(\frac{x - x_0}{\kappa \lambda_J} \middle| \kappa^2\right) \operatorname{cn}\left(\frac{x - x_0}{\kappa \lambda_J} \middle| \kappa^2\right) \quad (5.2.10b)$$

where we have defined

$$H_{c0} = \frac{\Phi_0}{\pi d \lambda_J}$$

It is easy to show that for $\kappa > 1$:

$$H(x) = \frac{H_{c0}}{\kappa} \operatorname{cn}\left(\frac{x-x_0}{\lambda_J} \mid \frac{1}{\kappa^2}\right) \quad (5.2.11a)$$

$$J(x) = -\frac{2J_1}{\kappa} \operatorname{sn}\left(\frac{x-x_0}{\lambda_J} \mid \frac{1}{\kappa^2}\right) \operatorname{dn}\left(\frac{x-x_0}{\lambda_J} \mid \frac{1}{\kappa^2}\right) \quad (5.2.11b)$$

Looking at the behavior of the Jacobian elliptic functions we can see that the solutions obtained for $\kappa \leq 1$ and $\kappa > 1$ are quite different (Ivanchenko, Svidzinskii, and Slyusarev 1966). In particular we observe that for $\kappa \leq 1$, $H(x)$ never reverses sign, since dn is always positive. This behavior is peculiar to situations in which the external applied field (uniform) dominates over the self-field. Since cn goes through both positive and negative values, if $\kappa > 1$, $H(x)$ reverses its sign. Therefore the case $\kappa > 1$ describes situations in which the self-field dominates over the external field. An example of the latter situation is represented by the case $H_e = 0$.

Let us consider the situation in which the self-field is negligible with respect to the external applied field H_e . The solution is given by (5.2.10). If we assume $\kappa \rightarrow 0$ and $\lambda_J \rightarrow \infty$ with the condition that the product $\kappa \lambda_J$ remains finite, we get from (5.2.10a)

$$H(x) = \frac{\Phi_0}{2\pi d} \frac{1}{\kappa \lambda_J} = H_e = \text{constant}$$

because $\operatorname{dn}(u|\kappa^2) \rightarrow 1$ for $\kappa \rightarrow 0$. Therefore

$$\kappa \lambda_J = \frac{\Phi_0}{\pi d H_e} \quad (5.2.12)$$

In the same limit from the asymptotic expressions of sn and cn for $\kappa \rightarrow 0$, (5.2.10b) becomes

$$J(x) = -2J_1 \sin\left(\frac{x-x_0}{\kappa \lambda_J}\right) \cos\left(\frac{x-x_0}{\kappa \lambda_J}\right) \quad (5.2.13)$$

That is,

$$J(x) = -J_1 \sin\left(\frac{2x}{\kappa \lambda_J} + \varphi_0\right)$$

This is a sinusoidal variation of a period given by $X = \pi\kappa\lambda_J$. Using (5.2.12), we get

$$J(x) = -J_1 \sin\left(\frac{2\pi dH_e}{\Phi_0}x + \varphi_0\right)$$

which is just the usual dependence of the maximum supercurrent on the external field for a small junction obtained in Chapter 4.

With respect to the periodicity of the solutions, we observe that cn and sn have periodicity given by $4K(\kappa^2)$ and dn by $2K(\kappa^2)$, where

$$K(\kappa^2) = \int_0^{\pi/2} \frac{d\theta}{\sqrt{1-\kappa^2 \sin^2 \theta}}$$

is the complete elliptic integral of the first kind. However, because of the relations:

$$\text{sn}(u+2K) = -\text{sn}(u); \quad \text{cn}(u+2K) = -\text{cn}(u)$$

the product $\text{sn}(u)\text{cn}(u)$ has periodicity given by $2K(\kappa^2)$. Therefore it is easy to see that the current density $J(x)$ has periodicity given by $2\kappa\lambda_J K(\kappa^2)$ for $0 < \kappa \leq 1$ and $4\lambda_J K(1/\kappa^2)$ for $\kappa > 1$. When $\kappa = 1$ in particular, $K(1) = \infty$ and the period becomes infinite. In (5.2.10) and (5.2.11) we have two parameters x_0 and κ , which can be determined by assuming suitable boundary conditions for the field and the current. Obviously such boundary conditions depend on the specific geometrical configuration of the junction.

Let us begin to consider the simple case of an asymmetric “in-line” junction geometry of infinite length as sketched in Fig. 5.4a. The junction is in the semispace $x \geq 0$ and the transversal dimension W is such that $W \ll \lambda_J$. This model was considered by Ferrel and Prange (1963) who derived a particular

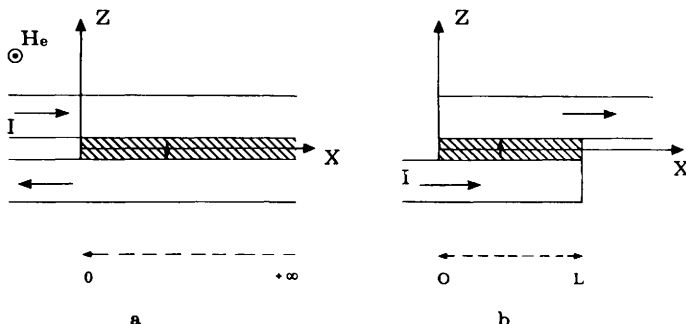


Figure 5.4 Simple one dimensional configurations. (a) Asymmetric in-line junction of infinite length. (b) symmetric in-line geometry.

solution of (5.2.1). They assumed the boundary conditions to be

$$H(+\infty) \sim \frac{d\varphi}{dx} \Big|_{x=+\infty} = 0 \quad \text{and} \quad \varphi = 0 \quad \text{for } x \rightarrow +\infty$$

It is easy to see from (5.2.3) that this corresponds to the particular choice of $\kappa = 1$. From (5.2.6a) and (5.2.6b), using the asymptotic expression for the Jacobian elliptic functions for $\kappa \rightarrow 1$, we get

$$H(x) = H_{c0} \operatorname{sech}\left(\frac{x-x_0}{\lambda_J}\right) \quad (5.2.14a)$$

$$J(x) = -2J_1 \tanh\left(\frac{x-x_0}{\lambda_J}\right) \operatorname{sech}\left(\frac{x-x_0}{\lambda_J}\right) \quad (5.2.14b)$$

The total current carried by the junction is given by

$$\begin{aligned} I &= \left| W \int_0^{+\infty} J(x) dx \right| = 2J_1 W \left| \int_0^{+\infty} \tanh\left(\frac{x-x_0}{\lambda_J}\right) \operatorname{sech}\left(\frac{x-x_0}{\lambda_J}\right) dx \right| \\ &= 2\lambda_J W J_1 \left| \operatorname{sech}\left(\frac{-x_0}{\lambda_J}\right) \right| \end{aligned}$$

The maximum value of the total current is obtained for $x_0 = 0$

$$I_{\max} = 2W\lambda_J J_1 \quad (5.2.15)$$

Thus in zero magnetic field, while the tunneling current density for small junctions (Chapter 4) is uniform over the junction area, in the case of large junctions the tunneling current tends to remain confined within the characteristic distance λ_J from the edge (see Fig. 5.5). Relation 5.2.15 gives the maximum tunneling current that can be carried for a long ($L/\lambda_J \rightarrow \infty$), narrow ($W \ll \lambda_J$) junction. (See also Fig. 5.12.)

Let us consider now the one dimensional junction configuration sketched in Fig. 5.4b. This problem was extensively investigated by Owen and Scalapino (1967). The boundary conditions in this case are

$$\begin{aligned} H(0) &= \frac{\Phi_0}{2\pi d} \left(\left| \frac{d\varphi}{dx} \right|_0 \right) = -\frac{2\pi}{c} \frac{I}{W} + H_e \\ H(L) &= \frac{\Phi_0}{2\pi d} \left(\left| \frac{d\varphi}{dx} \right|_L \right) = H_e + \frac{2\pi}{c} \frac{I}{W} \end{aligned} \quad (5.2.16)$$

where H_e is the external applied field along y and I is the current flowing into the junction. The origin $x=0$ is taken at the left edge of the junction. From

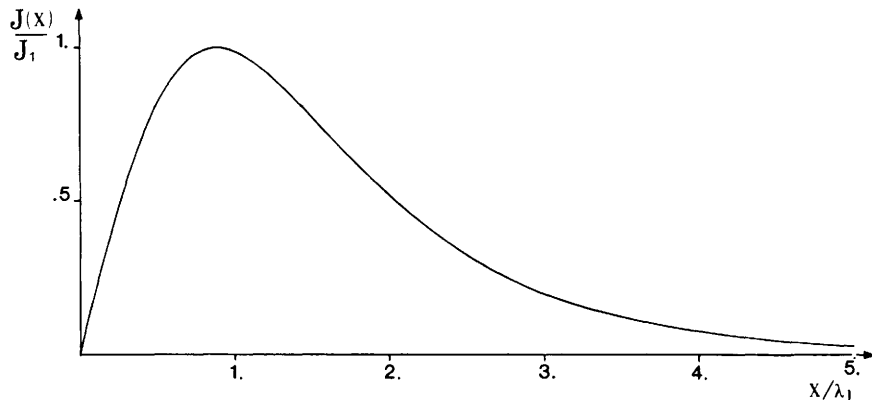


Figure 5.5 Josephson current density along the x direction for a junction of the geometry of Fig. 5.4a.

(5.2.16) we can derive the equivalent relations:

$$\begin{aligned} \frac{\Phi_0}{2\pi d} \left(\left| \frac{d\varphi}{dx} \right|_L - \left| \frac{d\varphi}{dx} \right|_0 \right) &= \frac{4\pi}{c} \frac{I}{W} \\ \frac{\Phi_0}{2\pi d} \left(\left| \frac{d\varphi}{dx} \right|_L + \left| \frac{d\varphi}{dx} \right|_0 \right) &= 2H_e \end{aligned} \quad (5.2.17)$$

From these it is possible, in principle, to determine the parameters κ and x_0 of the general solutions; however, this is not straightforward. The procedure used is to fix the value of the external field and numerically look for values of κ and x_0 that satisfy (5.2.17) and give rise to the maxima for the current I . The results of the magnetic field dependence for a junction with $L/\lambda_J = 10$ are reported in Fig. 5.6. The curve is qualitatively different from that of a small junction, for which the self-field is negligible and the field inside is constant and equal to the external field. If we examine $J(x)$ and $H(x)$, corresponding to the different values of I and H_e , we can distinguish two different behaviors. In the region of Fig. 5.6 from $H_e = 0$; $I = WH_{c0}c/2\pi$ to $H_e = H_{c0}$; $I = 0$ the junction acts as a superconductor of the first type (Meissner region). It tends to shield the external magnetic field. The current is related to the field by the linear relation

$$I_{\max} = \frac{Wc}{2\pi} (H_{c0} - |H_e|)$$

Thus the solutions for $J(x)$ and $H(x)$ describe situations in which both current density and field approach zero inside the junction (Fig. 5.7). The corresponding values of κ are near $\kappa = 1$. The maximum value of the external field that allows this solution is H_{c0} ("lower critical field"). As observed by Anderson (1967), this corresponds to the maximum value of H_e that can be matched by

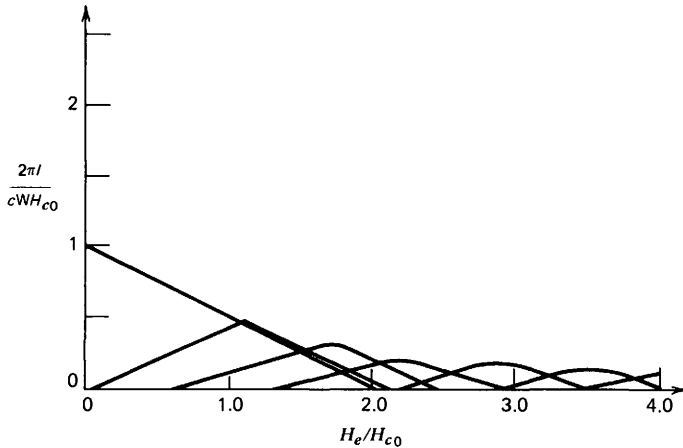


Figure 5.6 Theoretical magnetic field dependence for a large junction of the symmetric in-line geometry (Fig. 5.4b) for $L/\lambda_J = 10$. (After Owen and Scalapino 1967.)

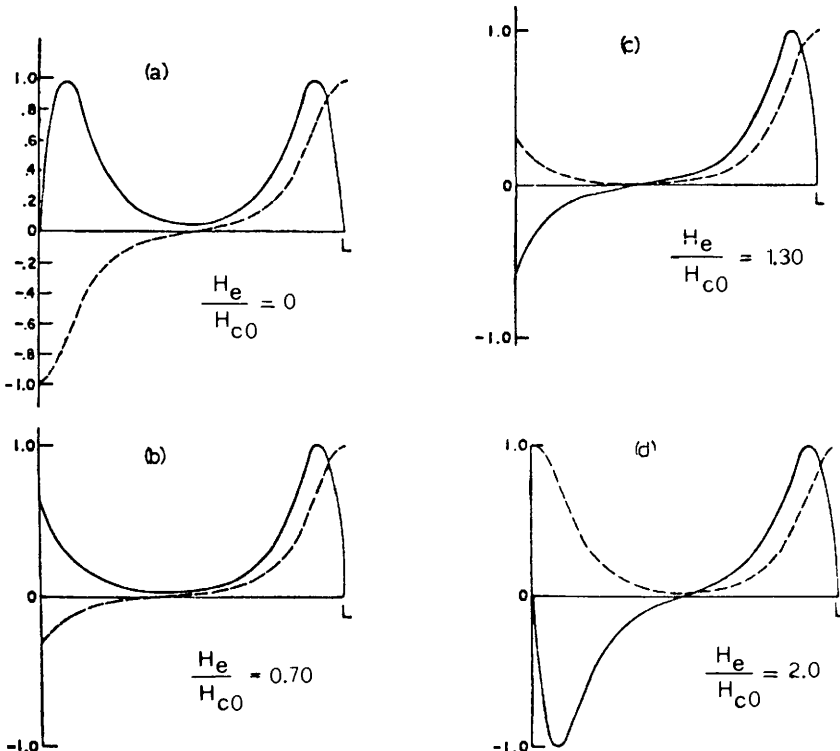


Figure 5.7 Current density (solid) and local magnetic field (dashed) within the junction for various H_e values on the 0-1 mode corresponding to the linear segment running from $(0, 1)$ to $(1, 0)$ in Fig. 5.6. (After Owen and Scalapino 1967.)

the solution $H(x)$ with $\kappa=1$ [see (5.2.10a)]. For $H_e=H_{c0}$ there is one vortex in the junction (Fig. 5.7d). The vortex contains exactly one flux quantum.

Josephson (1965) derived the expression for the lower critical field by a thermodynamic approach. Following Abrikosov (1957) we can write the relation between the “thermodynamic lower critical field” H_{cl} and the free energy F_f per unit length of an isolated flux line as

$$H_{cl} = \frac{4\pi}{\Phi_0} F_f \quad (5.2.18)$$

This relation, which governs the transition to the mixed state, follows when we integrate the equilibrium condition $dF_f = H_{cl} dM$ and recall that $\int_0^{H_{cl}} dM = \Phi_0 / 4\pi$.

Let us observe that, taking into account the magnetic field, the free energy of the barrier per unit area is

$$f = \frac{\hbar J_1}{2e} \left[(1 - \cos \varphi) + \frac{1}{2} \lambda_J^2 \left(\frac{d\varphi}{dx} \right)^2 \right] \quad (5.2.19)$$

The first term is inherent to the barrier and was derived in Chapter 1 (Section 1.6). The second term is the contribution of magnetic energy within the penetration region. This may be calculated from the relation

$$\frac{\partial \varphi}{\partial x} = \frac{2e}{\hbar c} dH_y$$

as

$$\frac{H^2}{8\pi} = \frac{\hbar^2 c^2}{4e^2 d^2} \left(\frac{d\varphi}{dx} \right)^2$$

and using the expression for λ_J (4.1.3).

The expression for F_f corresponding to a single flux line in the barrier is found by using the particular solution φ_f of (5.2.1). From (5.2.2) for $\kappa=1$, $C=1$, and it follows that

$$1 - \cos \varphi_f = \frac{1}{2} \lambda_J^2 \left(\frac{d\varphi_f}{dx} \right)^2$$

Thus from (5.2.19) we get for the free energy per unit length for a flux line

$$F_f = \frac{\hbar J_1}{2e} \int_{-\infty}^{+\infty} dx \left\{ (1 - \cos \varphi_f) + \frac{1}{2} \lambda_J^2 \left(\frac{d\varphi_f}{dx} \right)^2 \right\}$$

$$= \frac{\hbar J_1}{2e} \int_{-\infty}^{+\infty} dx \lambda_J^2 \left(\frac{d\varphi_f}{dx} \right)^2$$

From (5.2.9), using the asymptotic expression for $\kappa=1$ of $\text{dn}[(x-x_0)/\kappa\lambda_J|\kappa^2]$, it follows that

$$\frac{d\varphi_f}{dx} = \frac{2}{\lambda_J} \operatorname{sech} \frac{x}{\lambda_J}$$

where x_0 is assumed to be zero. Hence

$$F_f = \frac{2\hbar J_1}{e} \int_{-\infty}^{+\infty} dx \operatorname{sech}^2 \frac{x}{\lambda_J}$$

which gives

$$F_f = \frac{4\hbar\lambda_J J_1}{e}$$

Therefore the lower critical field H_{c1} given by condition (5.2.18) is

$$H_{c1} = \frac{2}{\pi} \left(\frac{\Phi_0}{\pi\lambda_J d} \right)$$

In Fig. 5.8 is shown the temperature dependence of H_{c1} for symmetrical junctions using for $\lambda_J(T)$ the data reported in Section 5.1 (Fig. 5.3).

It is interesting to observe that the thermodynamic critical field is smaller than H_{c0} and is equal to $(2/\pi)H_{c0}$. H_{c1} represents the lowest field at which the Meissner solution becomes unstable and vortex penetration is energetically favored. For a further increase of the external field the current begins to follow the next branch of the pattern (see Fig. 5.6) which corresponds to a situation of one vortex in the junction (one vortex mode configuration). The various

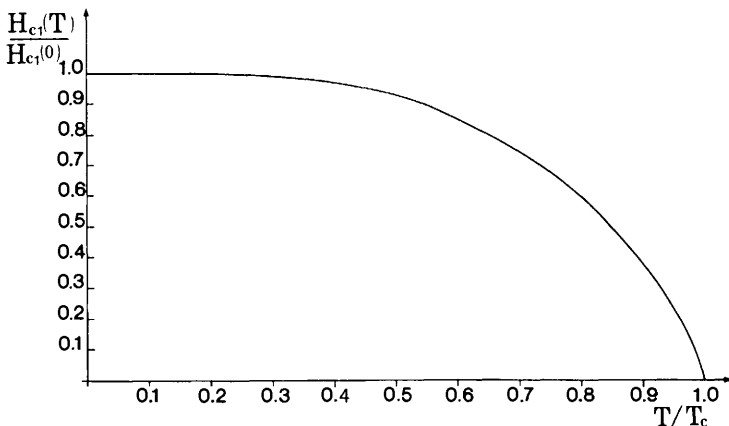


Figure 5.8 The lower critical field H_{c1} as a function of the reduced temperature T/T_c .

branches of the curve correspond to modes that describe configurations from n to $n+1$ vortices. Therefore we see that for magnetic fields exceeding H_{c1} a large junction behaves like a type 2 superconductor allowing vortices to enter. For each vortex entering the junction the relative phase φ across the barrier changes by 2π . Correspondingly the total flux increases by a flux quantum Φ_0 . From the Josephson-relation

$$\frac{\partial \varphi}{\partial x} = \frac{2\pi d}{\Phi_0} H(x)$$

by integration we have

$$\varphi(L) - \varphi(0) = 2\pi \frac{\Phi}{\Phi_0}$$

that is, for $\varphi(L) - \varphi(0) = 2\pi n$ it follows that $\Phi = n\Phi_0$. $J(x)$ and $H(x)$ for

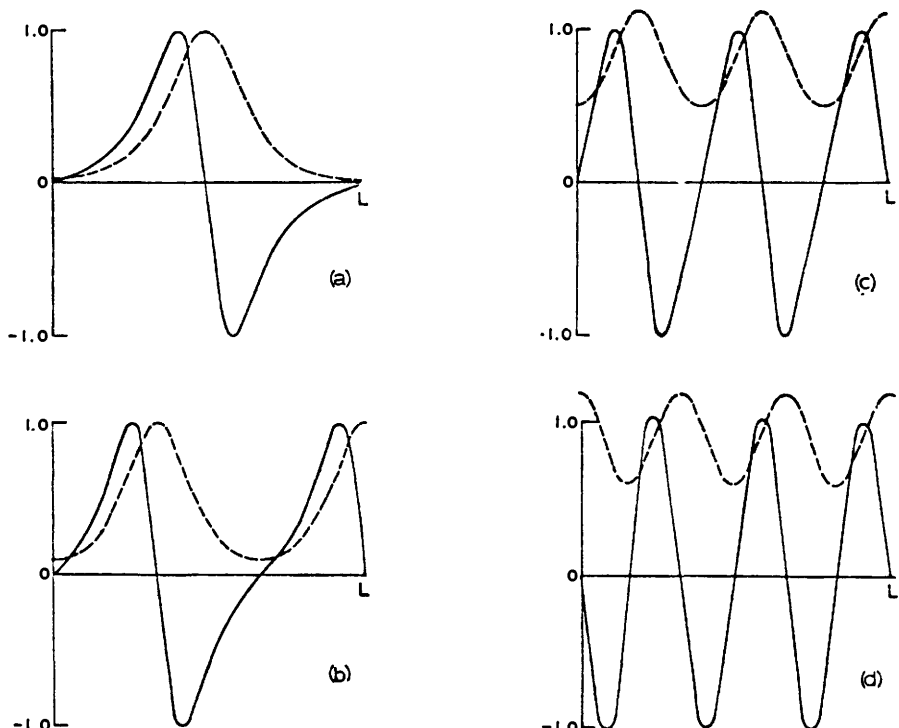


Figure 5.9 Current density $J(x)/J_1$ (solid line) and magnetic field $2H(x)/H_{c0}$ for different values of the normalized field $K = H_e/2H_{c0}$. (a) at $K=0.06$ the one vortex solution at its lowest level. (b) at $K=1.08$ when I_1 is at its maximum for the 1-2 mode of solution. (c) at $K=1.72$ when I_1 is greater for the 2-3 mode. (d) at $K=2.44$ the three vortex solution at its greatest possible K . (After Owen and Scalapino 1967.)

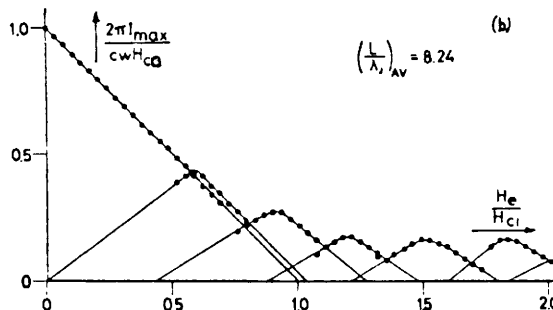


Figure 5.10 Magnetic field dependence of the maximum critical current for an in-line geometry junction (see Fig. 5.4b) for $L/\lambda_J = 8.24$. Dots are the experimental data. The solid lines are the theoretical results of Owen and Scalapino (Fig. 5.6) for $L/\lambda_J = 10$. (After Schwidtal 1970.)

particular values of H_e are sketched in Fig. 5.9. In particular in the branch starting at $H_e/H_{c0} = 0.03$ (Fig. 5.6) the current density distribution goes from a one vortex mode to a two vortex mode. For the second branch the junction goes from a two to a three vortex configuration, and so on. In experiments we expect to observe the envelope of the curve in Fig. 5.6.

The first measurements on large junctions were made by Goldman and Kreisman (1967).[†] They also reported the temperature dependence of the critical field H_{c0} . Experimental results on lead-lead junctions by Schwidtal (1970) are shown in Fig. 5.10. The agreement with the Owen and Scalapino calculations is excellent. Comparing these data with theoretical pattern reported for $L/\lambda_J = 10$ in Fig. 5.6 we see that the spacings between the maxima are slightly different. This can be well accounted for, since the experiments refer to a junction with a ratio $L/\lambda_J = 8.24$. Let us observe that in these measurements the junction geometry was of a cross type; however, the boundary conditions of the theoretical model were provided by a suitable symmetrical current feeding. It is interesting to see in Fig. 5.10 that some "metastable" states (data points under the envelope) are also observable. Such behavior can arise from the interaction between a flux line and the edge of the junction; this gives rise to a sort of potential barrier to overcome in order for a fluxon to get into (or out of) the junction. This "hysteretic" behavior is peculiar to type 2 superconductors.

In conclusion, we have seen in this section that a large Josephson junction behaves in many respects as a type 2 superconductor. However, this analogy cannot be pushed too far; there are some differences between the two systems. There is no upper critical field for a long Josephson junction. H_{c2} can be taken to be that of the superconductive electrodes forming the junction. The vortex structure is in this case one dimensional, whereas in a type 2 superconductor Abrikosov vortices describe a two dimensional lattice. The nature of the vortex

[†]Large junction behavior as predicted by Owen and Scalapino was observed also by Clarke (1968, 1969) on metal barrier junctions.

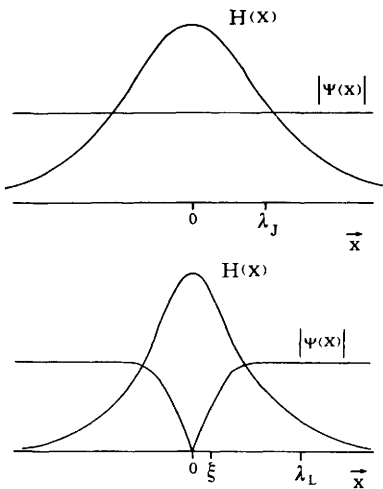


Figure 5.11 The isolated vortex of a Josephson junction compared schematically in one dimension with that of a type 2 superconductor. $H(x)$ and $|\psi(x)|$ are the magnetic field and the amplitude of order parameters, respectively.

is also different, since there is no normal core. In Fig. 5.11 the vortex of a Josephson junction is compared with that one of a superconductor of second type. The analogies between the two systems have been studied by Yamashita and Rinderer (1975), using a mechanical analog model. In particular, they have considered phenomena like pinning effect and magnetization curve.

5.3 Effects of the Junction Geometrical Configuration

As we just saw, the behavior of large Josephson junctions is strongly affected by geometrical factors. Owen and Scalapino in the previously quoted work have solved (5.2.1) for the one dimensional in-line junction geometry (Fig. 5.4b) and reported the saturation curve for the normalized maximum Josephson current versus the normalized length L/λ_J in the absence of external magnetic field (see Fig. 5.12). This curve clearly shows a linear increase of the current (uniform distribution) as long as $L \leq \lambda_J$ and a subsequent saturation (confinement to the edges) for increasing values of L/λ_J . Experimentally, current saturation curves have been obtained by Mahutte et al. (1969), Schroen and Pritchard (1969), and Johnson and Barone (1970). These experiments qualitatively agree with Owen and Scalapino's calculations.

It is important to observe that the actual junction geometries employed in the experiments and in various technological applications are of different types and specific experimental results therefore cannot straightforwardly be matched with such calculations.

In particular, in various experiments an in-line configuration with a “ground plane” is adopted (Matisoo 1969), that is, the bottom film of the junction is placed onto a large superconducting sheet and isolated from it by a suitable dielectric layer of thickness d_i (typically a few thousand angstroms).

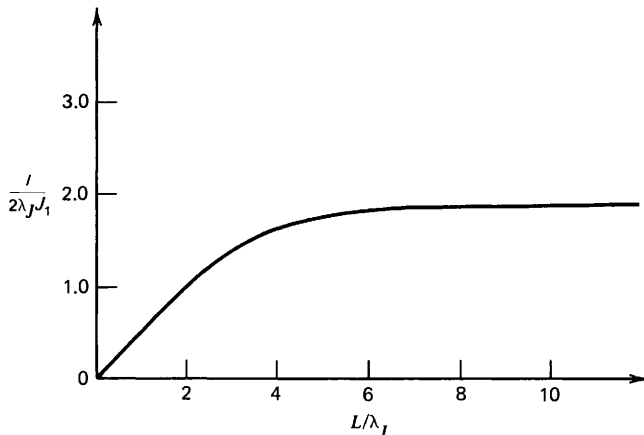


Figure 5.12 Maximum total current vs. junction length L for $H_e = 0$. (After Owen and Scalapino 1967.)

To see the effect of the ground plane, we can consider a film of thickness d_e much smaller than its width W and much larger than the London depth λ_L (i.e., $W \gg d_e \gg \lambda_L$). The surface current density distribution $J_s(y)$ without a ground plane (Newhouse, Bremer, and Edwards 1960) is shown in Fig. 5.13a. The effect of the ground plane is schematically described in Fig. 5.13b (for $d_i \ll W$). We see that the surface current distribution is now almost completely uniform along the y dimension because of an image current line that is formed under the superconducting ground plane in the x direction. The result is a vanishingly small net field above the film. As a consequence of the presence of the ground plane, the boundary conditions are modified. We observe that in the junction region we can assume a uniform current distribution in the superconducting films even in the absence of a ground plane. We can suppose

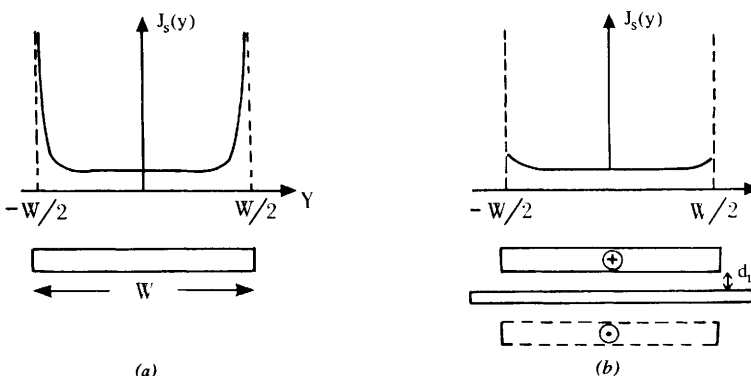


Figure 5.13 Current density distribution $J_s(y)$ in a superconducting film (a) without and (b) with a ground plane.

in fact that the bottom and top films of the junction can perform a reciprocal action of a ground plane. In this case the current is no longer evenly split through both ends of the junction, but is essentially carried by one end only.

Recently Basavaiah and Broom (1974) have carried out an extensive investigation with carefully designed in-line junctions employing a ground plane. They report, among other results, a current saturation curve. In agreement with the argument above, the saturation value in this case was one half of that obtained with Owen and Scalapino boundary conditions. Theoretical works on current and magnetic field distributions in Josephson junctions have been performed more recently by Zharkov and Vasenko (1978) and Vasenko and Zharkov (1978).

An approximate approach to the problem of current flow in junctions of various geometries has been discussed by Barone, Johnson, and Vaglio (1975). A piecewise linear current-phase relationship is assumed and a one dimensional analysis is developed in which rather general boundary conditions are used to account for different kinds of electrode configurations. The starting equation is then

$$\frac{\partial^2 \varphi}{\partial x^2} = \frac{1}{\lambda_J^2} \chi^2 \varphi \quad (5.3.1)$$

where χ is a positive constant. The expression for the linear current-phase relationship can be assumed to be $J(\varphi) = (J_1/4)\varphi$. This and the correct sinusoidal dependence are sketched in Fig. 5.14. This choice for χ together with the condition $J \leq J_1$ fixes the same magnetic energy stored (crosshatched regions with the same area).

To account for various situations of current splitting through the junction edges let us consider (5.3.1) where $\chi = \frac{1}{2}$ with the general boundary conditions

$$H_y(0) = -\alpha \left(\frac{2\pi}{c} \frac{I}{W} \right) + H_e; \quad H_y(L) = +\beta \left(\frac{2\pi}{c} \frac{I}{W} \right) + H_e$$

where α and β are nonnegative constants (for a given current direction) such

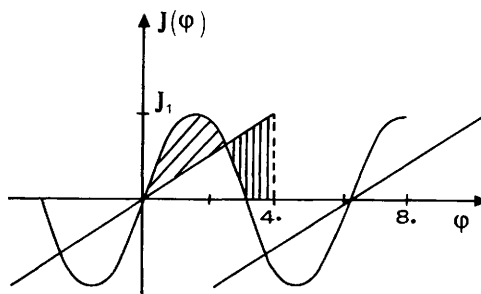


Figure 5.14 Linear and sinusoidal current phase relations. Dashed regions have the same area.

that $\alpha + \beta \leq 1$ as a consequence of Ampere's law. Accordingly, different values of α and β give a measure of the fraction of the current flowing in each edge. The corresponding solution for the current density distribution is

$$J(x) = \frac{I}{2W\lambda_J} \left(\frac{\beta \cosh(x/2\lambda_J) + \alpha \cosh[(L-x)/2\lambda_J]}{\sinh(L/2\lambda_J)} + \frac{1-\alpha-\beta}{L/2\lambda_J} \right) + \frac{c}{4\pi} \frac{H_e}{\lambda_J} \left(\frac{\cosh(x/2\lambda_J) - \cosh[(L-x)/2\lambda_J]}{\sinh(L/2\lambda_J)} \right) \quad (5.3.2)$$

We observe that the quantity $(I/WL)(1-\alpha-\beta)$ that follows from the condition $\int_0^W dy \int_0^L dx J(x) = I$ represents the fraction of the current through the junction that does not produce a field in the y direction. Let us summarize the boundary conditions corresponding to the four geometries sketched in Fig. 5.15a, b, c, d.

- (a) It is easy to show that for the in-line symmetric junction configuration, is $\alpha=\beta=\frac{1}{2}$ and the condition $J_{\max}(x)=J_1$ gives for $H_e=0$

$$\frac{I}{2W\lambda_J J_1} = \frac{2 \sinh(L/2\lambda_J)}{\cosh(L/2\lambda_J) + 1}$$

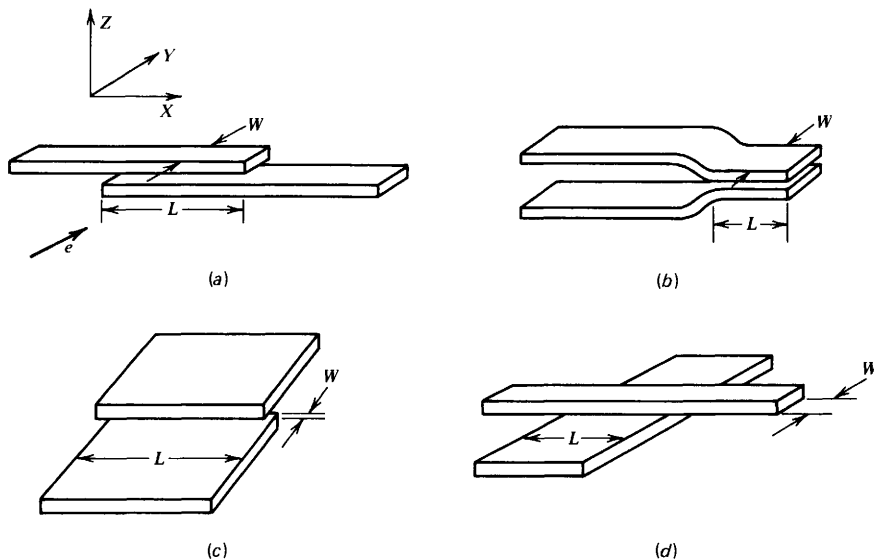


Figure 5.15 Sketch of typical junction geometries. (a) In-line symmetric configuration. (b) In-line asymmetric configuration. (c) Overlap geometry. (d) Cross-type geometry. (After Barone Johnson and Vaglio 1976.)

The normalized supercurrent vs. the normalized junction length is reported in Fig. 5.16 (curve 1). The result agrees with the essential features of the current saturation curve of Owen and Scalapino.

- (b) For the geometry of Fig. 5.15b the boundary conditions (Stuehm and Wilmsen 1974) are $\alpha=1$, $\beta=0$, and we have

$$\frac{I}{2W\lambda_J J_1} = \tanh\left(\frac{L}{2\lambda_J}\right)$$

In this case (Fig. 5.16, curve 2) The saturation of the current occurs at half of the value of the previous case. This, as already mentioned, is also valid for the in-line configuration with a ground plane (Basavaiah and Broom 1974).

- (c) For the overlap geometry of Fig. 5.15c we can assume the boundary conditions $\alpha=\beta=0$ which express the circumstance that the current flows in the y direction. In this case we have (Fig. 5.16, curve 3)

$$\frac{I}{2W\lambda_J J_1} = \frac{L}{2\lambda_J}.$$

That is,

$$I = WLJ_1 = I_1$$

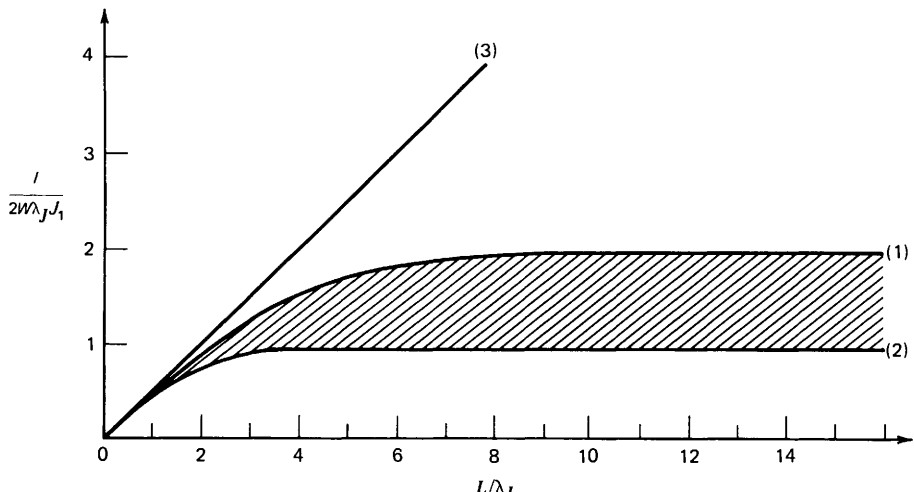


Figure 5.16 Normalized maximum Josephson current vs. normalized junction length. Curves 1–3 correspond to the geometrical configuration of Fig. 5.15a, b, c respectively. Saturation curve for cross-junctions (Fig. 5.15d) should fall in the shaded region. (After Barone, Johnson, and Vaglio 1976.)

Thus we expect that the effect of current saturation should not occur; instead, a linear increase of the normalized Josephson current vs. normalized junction length indicates a uniform current distribution. This is rather consistent with the experimental results of Johnson and Barone (1970) and with the further discussion given by Stuehm and Wilmsen (1971).

- (d) Finally, let us consider the cross geometry configuration. In this case the choice of suitable boundary conditions is not intuitive. We could assume $\alpha + \beta = 1$ and leave a completely free condition $\alpha \geq \beta (\beta \geq \alpha)$ which signifies that, depending on the relative values of the junction dimensions and therefore on the particular current "splitting," $\alpha(\beta)$ could take all values between $\frac{1}{2}$ and 1. Experiments on cross junctions generally reflect situations where one edge carries the current. However, it should be possible for intermediate situations to occur also. Correspondingly the current saturation curves will lie between the two curves a, b (shaded region). We see that if $\alpha > \beta$, for $L/\lambda_J \rightarrow \infty$ we have the limiting condition $I/2W\lambda_J J_1 = 1/\alpha$. The results of Johnson and Barone (1970) probably reflect this situation in which the current is unevenly divided between the two ends. This circumstance can occur also for different reasons, such as the presence of barrier nonuniformities as observed by Mahutte et al. (1969) on in-line symmetric junctions. We should also take into account the effects on cross junctions due to the presence of relatively large films as bottom layers which can play the role of a ground plane (Clarke 1969; Schwidtal 1970).

Using the linearized model we can also have some indications on the I vs. H_e dependence within the Meissner-like region for these various geometries. From the condition $J_{\max}(x) \leq J_1$ it follows that $J(0) \leq J_1$ and $J(L) \leq J_1$. It is easy to show from (5.3.2) in the limit of large junctions that

$$\frac{I}{2W\lambda_J J_1} = \frac{1}{\alpha} \left(1 + \frac{H_e}{H_0} \right); \quad \frac{I}{2W\lambda_J J_1} = \frac{1}{\beta} \left(1 - \frac{H_e}{H_0} \right)$$

where $H_0 = (4\pi/c)\lambda_J J_1$ represents the lower critical field discussed in Section 5.2.

For the symmetric in-line geometry we get (see Fig. 5.17a curve 1)

$$I_1(H_e) = 4\lambda_J J_1 W \left(1 - \frac{|H_e|}{H_0} \right)$$

which agrees with the calculations of Owen and Scalapino. For the asymmetric in-line geometry of Fig. 5.15b or, more generally, whenever $\alpha = 1, \beta = 0$ ($\alpha = 0, \beta = 1$) we obtain the I_1 vs. H_e dependence represented by curve 2 (curve 3) of Fig. 5.17a. In fact, curves 2 and 3 are both also obtained for symmetric in-line

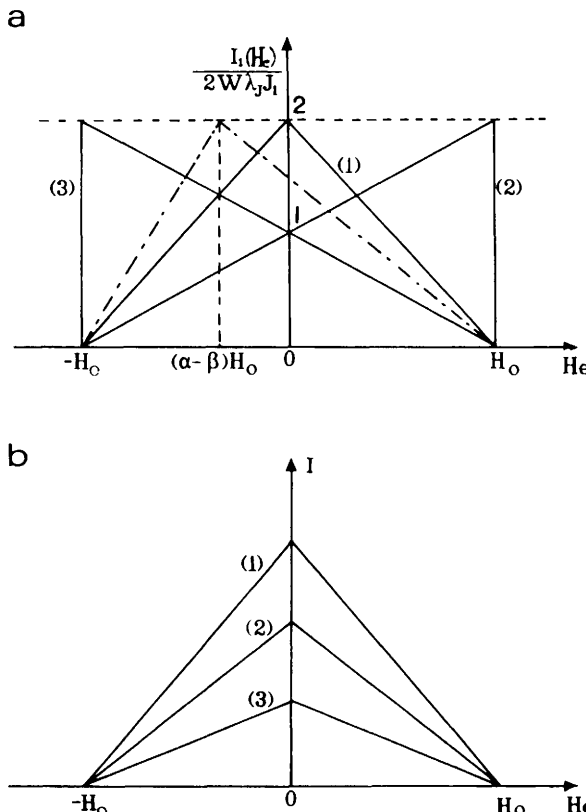


Figure 5.17 Normalized maximum Josephson current vs. external magnetic field for large Josephson junctions. (a) Curve 1 refers to the geometry of Fig. 5.15a (boundary conditions $\alpha=\beta=\frac{1}{2}$); curves 2 and 3 refer to the geometry of Fig. 5.15b ($\alpha=1$, $\beta=0$; $\alpha=0$, $\beta=1$, respectively). For cross-geometries intermediate situations should also occur (dashed curve). (b) The curves are referred to the junction geometry of Fig. 1.15c ($\alpha=\beta=0$) and correspond to three different values of the dimension L. (After Barone, Johnson, and Vaglio 1976.)

junctions with the ground plane (Matisoo 1969; Basavaiah and Broom 1975[†]). Furthermore, let us recall that Schwidtal (1970) obtained experimental results on the cross junction geometry realizing both asymmetric $\alpha=1$, $\beta=0$ ($\alpha=0$, $\beta=1$) and symmetric $\alpha=\beta=\frac{1}{2}$ boundary conditions. In these experiments the values of α and β were controlled by a suitable arrangement of the external current bias. The dashed line in Fig. 5.17a corresponds to an intermediate situation of current splitting. Finally, in Fig. 5.17b is reported I_1 vs. H_e for the junction configuration sketched in Fig. 5.15c. For $\alpha=\beta=0$ we have from

[†]We see that the current has its maximum value $I_1(H_0)$ at $H_c=H_0$, whereas in zero field $I_1(0)=I_1(H_0)/2$. This accounts for the current saturation value in curve 2 of Fig. 5.16 in agreement with the experimental results reported in this reference.

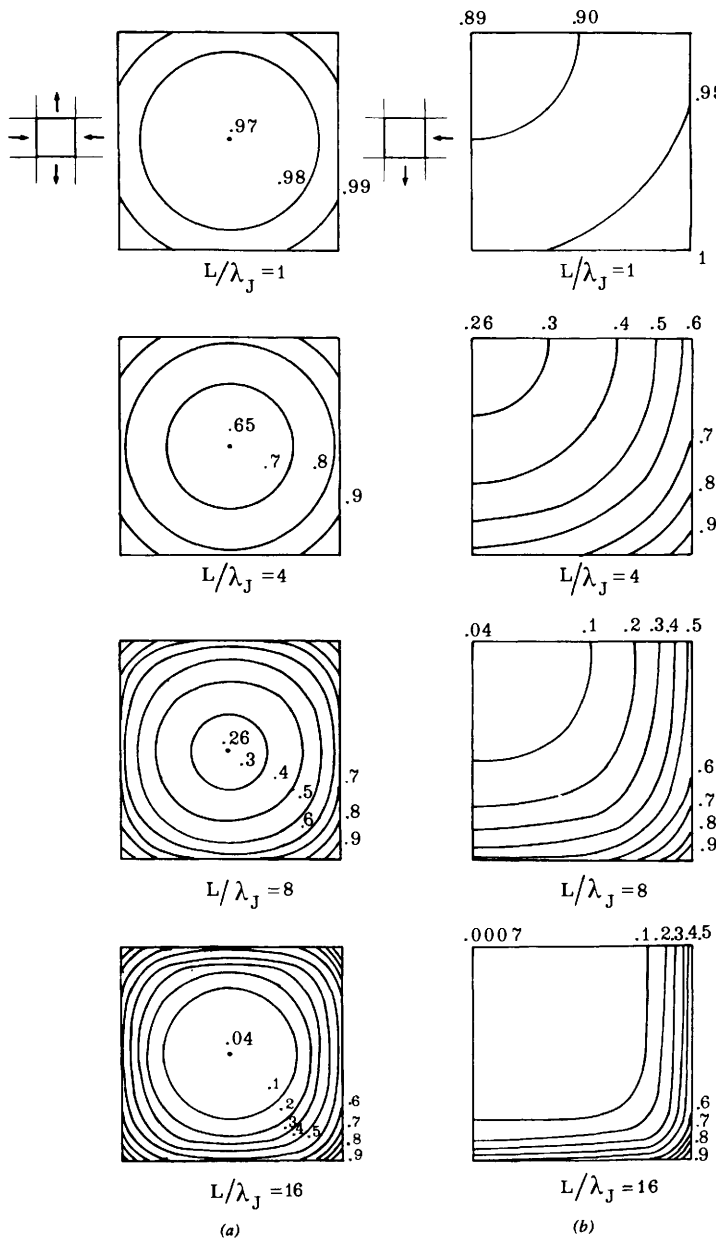


Figure 5.18 Current density maps inside a square junction ($L=W$) for various W/λ_J ratios for zero applied field ($H_e=0$). (a) Symmetric feeding. (b) Asymmetric feeding. The ratio $J(x, y)/J_1$ is constant along each curve (its value is indicated near the corresponding curve). The arrows in (a) and (b) represent the direction of the current in the electrodes. (Courtesy of R. Vaglio.)

(5.3.2)

$$I_1(H_e) = I_1 \left(1 - \frac{|H_e|}{H_0} \right)$$

The various curves correspond to different values of the dimension L. We observe that a similar behavior was also observed in the case of the “window” junction geometry investigated experimentally by Schroen and Pritchard (1969).

In concluding this section we emphasize again the limits of the linearized model used. Obviously in a linear approximation the penetration profile loses its correct structure within the scale of λ_J (namely, the maxima of $J(x)$ occur at $x=0$ and $x=L$; however “integral” results such as the dependences I_1 vs. L/λ_J and I_1 vs. H_e are not significantly affected.

As we have seen, this approximate procedure, although rather crude, can supply useful indications of the behavior of specific junction geometries. The extension of this model in two dimensions has been recently discussed by Vaglio (1976). In particular, the case of square junctions including useful comparisons with available experimental results has been investigated. Some of the results are summarized in Fig. 5.18 in which the current density map inside a square junction is shown.

Finally, we recall for completeness the case of a junction with a circular cross section. If R_0 is the radius, we have a uniform current density $J_1 = I_1 / \pi R_0^2$ as long as the condition $2R_0 \ll \lambda_J$ is satisfied. This is the case discussed in Chapter 4. When $R_0 > \lambda_J$ we must take into account self-field limiting effects which introduce a spatial dependence in J_1 . The two dimensional problem in this case is simplified by the circular symmetry. The phase is just a function of the radial variable R (we are always in the time independent case) and the two dimensional equation $\nabla \varphi = 1/\lambda_J^2 \sin \varphi$ reduces to

$$\frac{\partial^2 \varphi}{\partial r^2} + \frac{1}{r} \frac{\partial \varphi}{\partial r} = \sin \varphi \quad (5.3.3)$$

which is expressed in terms of the dimensionless variable $r = R/\lambda_J$. The total current is

$$I = \int_0^{R_0} 2\pi R J_1 \sin \varphi(R) dR = \lambda_J^2 \int_0^{R_0/\lambda_J} 2\pi J_1 r \sin \varphi(r) dr$$

Taguchi and Yoshioka (1971) have calculated the current density distribution vs. the normalized radius $r = R/\lambda_J$ for different values of the junction dimensions in zero external field. These curves closely reproduce the Owen and Scalapino results for one dimensional in-line junctions. In the present case the current is confined to an annular region of the junction.

CHAPTER 6

Voltage Current Characteristics

In this chapter we examine a simple equivalent circuit model for a Josephson device in order to derive the theoretical voltage-current characteristics. In Section 6.2 the case in which the current in the Josephson element is given by the (1.4.4) is considered. In Section 6.3 we take into account effects due to the frequency dependence of the pair current, resorting to the general expression derived by the microscopic theory (2.2.3) for the time dependent current in a tunneling junction. The effect of fluctuations mainly of thermal nature are considered in Section 6.4, in the simple case of constant quasiparticle conductance G and Josephson current I_1 .

6.1 V - I Curves of Various Weak Links

As we have previously mentioned (Section 1.8), the Josephson phenomena occur in various kinds of structures. A system of two weakly coupled superconductors can in fact be realized by a tunneling junction, as discussed in the previous chapters, a superconducting film with a constriction, a point contact, and so on (see Chapter 7).

Looking at the V - I characteristics of all these devices, a great variety of behaviors is observed. Tunneling junctions can exhibit voltage-current characteristics that are markedly hysteretic (see Fig. 1.7); namely, there are two voltage states ($V=0$ and $V\neq 0$) for current values lower than the maximum current I_1 . In point contacts or bridge structures V - I curves are usually single valued, at least for temperatures not too far from the critical one. As an example, data on an aluminum bridge are reported in Fig. 6.1. The different curves refer to different temperature values. Now the following question arises: are these peculiar differences in the V - I curves of the various weak links inherent in the different physical nature of these structures? The answer is: not completely. In fact many of the features of the V - I characteristics of the weak links can be accounted for in terms of a simple lumped circuit model in which the distributed capacitance and quasiparticle conductance of the device are considered as lumped elements in parallel with a nonlinear Josephson element.

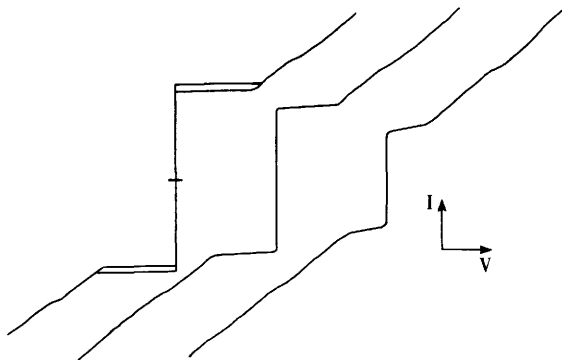


Figure 6.1 Experimental voltage-current characteristics for an aluminum bridge. The three curves refer to different values of the reduced temperature T/T_c . (After P. Carelli and I. Modena, unpublished.)

6.2 Resistively Shunted Junction Model: Autonomous Case

Following McCumber (1968a,b), Stewart (1968), and Johnson (1968), who independently discussed the problem, we can represent a weak link by the simple equivalent circuit of Fig. 6.2. Since for practical devices the impedance is usually much smaller than the source impedance, we assume the circuit to be current biased. We also assume that only a d.c. current I_{dc} is present. The current balance equation for the circuit is

$$I_{dc} = C \frac{dV(t)}{dt} + GV(t) + I_1 \sin \varphi(t) \quad (6.2.1)$$

where $C dV/dt$ is the displacement current through the capacitor C , $GV(t)$ is the current through the resistor $R(G=1/R)$, and $I_1 \sin \varphi$ is the Josephson supercurrent. $V(t)$ is the actual voltage developed across the device and is related to the phase difference $\varphi(t)$ by (1.4.5). We note that this equation refers to situations in which the phase difference φ across the weak link has no spatial variations. By using (1.4.5) the expression (6.2.1) can be transformed into an equation for the phase φ :

$$I_{dc} = \frac{\hbar}{2e} C \frac{d^2\varphi}{dt^2} + \frac{\hbar}{2e} \frac{1}{R} \frac{d\varphi}{dt} + I_1 \sin \varphi \quad (6.2.2)$$

Let us introduce for convenience dimensionless variables. Following Johnson (1968) we define:

$$\tau = \omega_J t$$

$$\beta_J = \frac{1}{\omega_J} \frac{1}{RC}$$

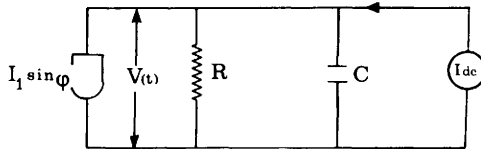


Figure 6.2 Equivalent circuit of a real Josephson junction with a current bias.

and the normalized voltage:

$$\eta(\tau) = \beta_J \frac{d\varphi}{d\tau} = \frac{V}{RI_1}$$

where

$$\omega_J = \left(\frac{2e}{\hbar} \frac{I_1}{C} \right)^{1/2}$$

is the plasma frequency.[†] By this choice (6.2.2) can be written as

$$\alpha = \frac{d^2\varphi}{d\tau^2} + \beta_J \frac{d\varphi}{d\tau} + \sin \varphi \quad (6.2.3)$$

where $\alpha = I_{dc}/I_1$ is the normalized current. Since in the literature different dimensionless variables are used, to facilitate their comparison we report in Table 6.1 the parameters used by McCumber and Stewart together with our parameters used here. Equation 6.2.3 in general is not analytically solvable except in the case in which the second derivative term can be neglected (negligible capacitance $C \rightarrow 0$). In the other cases solutions of (6.2.3) can be studied either by digital computation or by using different types of analog models. A very useful tool is provided also by the phase plane analysis.

6.2.1 Mechanical Model. Let us consider the simple pendulum of mass m and length l sketched in Fig. 6.3 if θ is the angle from the vertical, the equation describing its time variation is

$$\tau_T = M_I \frac{d^2\theta}{dt^2}$$

where τ_T is the total torque and M_I the moment of inertia. τ_T has three components: the applied torque which in our case is $\tau_a = m_w rg$, the restoring torque due to gravity equal to $-mgl \sin \theta$, and the opposing torque due to the friction which we assume to be given by $-D_f(d\theta/dt)$, where D_f is the damping

[†]More correctly ω_J is the plasma frequency value in the small amplitude limit and for $I_{dc} \rightarrow 0$ (Dahm et al. 1968).

TABLE 6.1 Dimensionless variables used in the R.S.J. model by different authors, and their correspondence

Variable	Author		
	Johnson	McCumber	Stewart
Frequency	$\omega_J = \left(\frac{2e}{\hbar} \frac{I_1}{C} \right)^{1/2}$	$\omega_m = \omega_J^2 \frac{C}{G}$	ω_J
Time	$\tau = \omega_J t$	$\theta = \omega_m t$	$\tau_0 = RC$
Current	$\alpha = \frac{I_{dc}}{I_1}$	α	α
Voltage	$\eta = \frac{V}{RI_1}$	η	η
Parameter	$\beta_J = \frac{1}{\omega_J} \frac{1}{RC}$	$\beta_c = \frac{1}{\beta_J^2}$	$\tau_0 \omega_J = \frac{1}{\beta_J}$

coefficient. g as usual is the acceleration due to gravity. Therefore the equation for θ as a function of t is

$$\tau_a = M_1 \frac{d^2\theta}{dt^2} + D_f \frac{d\theta}{dt} + mg l \sin \theta \quad (6.2.4)$$

If we compare this equation with (6.2.2) derived for the electrical model, it is easy to see the close analogy between the simple pendulum and the Josephson weak link. The angle from the vertical θ plays the role of the phase difference φ . Therefore a mechanical analog can be used in order to gain a better insight into the behavior of the Josephson device.

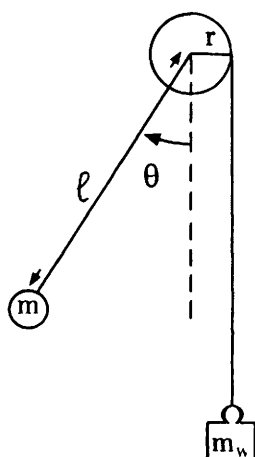


Figure 6.3 The simple pendulum with an applied torque.

The analogy between the Josephson weak link and a rigid pendulum was first pointed out by Anderson (1963). Mechanical models have been constructed and operated by many authors to describe the behavior of long junctions (Scott 1969) and the small junctions described by the R.S.J. model (Sullivan and Zimmerman 1971; Rochlin and Hansma 1973; Pedersen and Soerensen 1977). An excellent review on junction analogs has been given by Fulton (1976). In Table 6.2 the corresponding elements of the electrical and mechanical analogs are reported.

Expression 6.2.4 can be written in dimensionless units:

$$\frac{\tau_a}{mgl} = \frac{d^2\theta}{d\tau^2} + \beta_M \frac{d\theta}{d\tau} + \sin \theta$$

where

$$\tau = \omega_M t$$

$$\beta_M = \frac{D_f}{\sqrt{M_1 mgl}}$$

and

$$\omega_M = \left(\frac{mgl}{M_1} \right)^{1/2}$$

By using typical values, say $m \approx 5 \text{ g}$, $l = 9 \text{ cm}$, $M \approx ml^2$, we get $\omega_M \approx 10 \text{ sec}^{-1}$. This value is a factor $\sim 10^9$ lower than the characteristic values of ω_J , which, as we saw in Section 1.7, ranges in the microwave region (\sim few GHz). Therefore the nonlinearities in the time dependence of θ in the mechanical analog occur sufficiently slowly and are directly observable. In Fig. 6.4 a practical configuration for a mechanical analog is reported. The linear damping is realized by an

TABLE 6.2 Equivalence between physical quantities in the electrical and mechanical analogs

Electrical Analog	Mechanical Analog
D.c. current = I_{dc}	τ_a = applied torque
Capacitance = C	M_1 = moment of inertia
Conductance = $\frac{1}{R}$	D_f = damping coefficient
Maximum Josephson current = I_1	mgl = maximum torque due to gravity
Phase difference = φ	θ = angle from the vertical

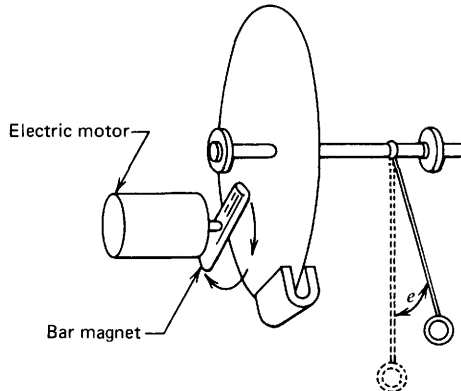


Figure 6.4 The mechanical analog of a simple junction biased by a constant source. The eddy current drive produces a torque on the disk that is proportional to the motor speed. (After Sullivan and Zimmerman 1971.)

aluminum disk and a permanent magnet. The applied torque τ_a in this model is realized by a motor driven bar magnet which rotates near the aluminum disk.

6.2.2 Small Capacitance Limit ($\beta_J \gg 1$). Let us consider the simple case in which the shunt conductance is so large as to short completely the capacitance. The ratio $G/\omega_J C$ is very large and so is the parameter β_J . In the mechanical model this corresponds to a situation in which damping effects dominate inertial effects. This case has been extensively examined also by Aslamazov and Larkin (1968) and Waldram, Pippard, and Clarke (1970). Under this approximation the second derivative term related to the displacement current can be neglected, and (6.2.3) reduces to

$$\alpha = \beta_J \frac{d\varphi}{d\tau} + \sin \varphi \quad (6.2.5)$$

This equation is analytically solvable. By simple integration for $|I_{dc}| > I_1$ we get

$$\varphi(\tau) = 2 \tan^{-1} \left[\left(\frac{\alpha^2 - 1}{\alpha^2} \right)^{1/2} \tan \left(\frac{\pi\tau}{T} \right) - \alpha \right] \quad (6.2.6)$$

where T is the period and is given by

$$T = \frac{2\pi\beta_J}{(\alpha^2 - 1)^{1/2}}$$

The d.c. voltage across the device is proportional to the time average of $d\varphi/d\tau$, that is, to

$$\bar{\dot{\varphi}} = \frac{1}{T} \int_0^T \frac{d\varphi}{d\tau} d\tau = \frac{2\pi}{T}$$

where the dot indicates the derivative with respect to τ . Therefore the relation between normalized voltage and current is

$$\frac{\bar{V}}{RI_1} = \beta_J \dot{\phi} = \sqrt{\alpha^2 - 1} \quad (6.2.7)$$

This dependence is indicated in Fig. 6.5. We see that the time averaged voltage is zero as long as the current I_{dc} does not exceed the critical value I_1 ($\alpha < 1$). A further increase of the driving current brings the junction to finite voltage states. This branch of the curve follows a single valued voltage current correspondence given by (6.2.7). For large current values ($\alpha \gg 1$) the curve approaches asymptotically the normal resistance slope. This behavior is due to the presence of the a.c. Josephson current at finite voltage. It can be understood considering the expression of the voltage $V(\tau)$ as a function of the normalized time τ . Taking the time derivative of $\varphi(\tau)$, from (6.2.6) we get

$$\frac{V(\tau)}{RI_1} = \frac{(\alpha^2 - 1)/\alpha}{\cos^2 \frac{\pi\tau}{T} + \frac{1}{\alpha^2} \left(\sqrt{\alpha^2 - 1} \sin \frac{\pi\tau}{T} - \cos \frac{\pi\tau}{T} \right)^2}$$

This expression is reported in Fig. 6.6 for two different values of the normalized current α . For I_{dc} close to I_1 the voltage time dependence is like a set of periodic pulses and has a high number of harmonics. On increasing the current I_{dc} , the distance between pulses, which is determined by T , decreases. The behavior tends to be closer and closer to a simple sinusoidal oscillation plus a d.c. background nearly equal to $I_{dc}R$. Therefore the time average of the a.c. current tends to zero and gives no significant contribution to the d.c. total

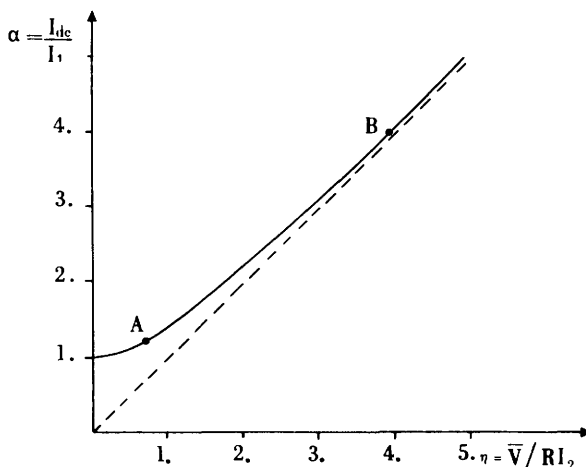


Figure 6.5 Time averaged voltage-current characteristic computed in the R.S.J. model in the limit $\beta_J \gg 1$. (Zero capacitance limit.)

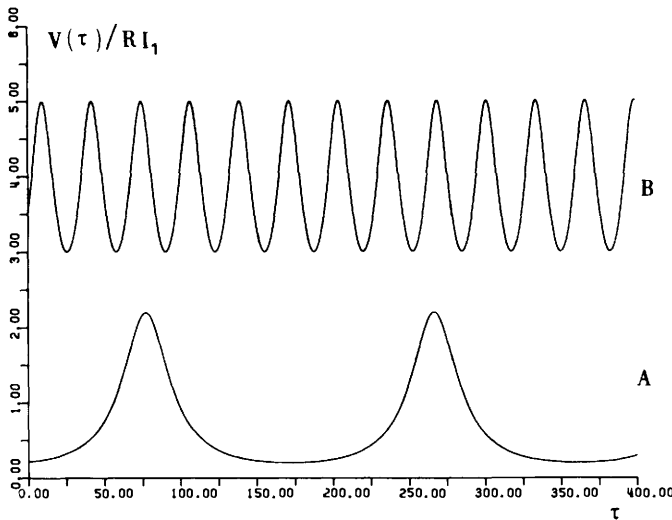


Figure 6.6 The time dependence voltage $V(\tau)$ across the junction for $\beta_J = 20$ and for a d.c. current bias $I_{dc}/I_1 = 1.2$ (A) $I_{dc}/I_1 = 4$. (B). The time averaged voltage corresponds to the points A and B of Fig. 6.6.

current. In terms of a mechanical analog the case $\alpha > 1$ corresponds to an applied torque τ_a sufficiently large to cause rotary rather than oscillatory motion of the pendulum. In particular, the situation described by the curve A of Fig. 6.6 corresponds to an applied torque just slightly larger than the value required to drive the pendulum "over the top" so that the resulting motion is rather nonuniform. The other situation (curve B) corresponds to an applied torque very large with respect to the gravitational restoring torque, so that the resulting rotary motion is almost uniform.

6.2.3. Phase Plane Analysis. Let us go back to (6.2.3), valid for arbitrary values of β_J . As seen in Section 6.2.1, one way to study its solutions is provided by the use of a mechanical analog. Another possibility is offered by an electrical analog (Werthamer and Shapiro 1967; Johnson 1968; Hamilton 1972a; Bak and Pedersen 1973). A very useful technique for a qualitative understanding of the behavior of Josephson system is provided by the study of its motion in an appropriate phase space. This is the so-called phase plane analysis, a well known technique in the theory of oscillating systems (Andronov and Chaikin 1949; Minorsky 1962). Following Johnson (1968), we give a brief outline of the method and apply the results to the study of the solutions of (6.2.3). This equation can be replaced by two equivalent equations of first order:

$$\frac{d\varphi}{d\tau} = Z$$

$$\frac{dZ}{d\tau} = \alpha - \beta_J \frac{d\varphi}{d\tau} - \sin \varphi \quad (6.2.8)$$

Since the time τ appears only as a differential $d\tau$, and not explicitly on the right hand members (there is no external a.c. current), this is called the “autonomous” case. The state of the system is represented at any time by a particular point in the Z, φ plane. As τ varies, this point describes, a trajectory. Each particular trajectory depends on the initial conditions. Therefore for a fixed value of the parameters α and β_J , the system is represented by a set of possible paths in the Z, φ plane. Such a plot is often called a phase space diagram. By inspection of a set of diagrams, obtained for different values of the parameters α and β_J , information about the nature of the possible solutions can be obtained. For instance, a closed curve in the Z, φ plane corresponds to a periodic solution; a point in which $d\varphi/d\tau = dZ/d\tau = 0$ is an equilibrium point; and so on.

Since the variable φ appears in the sine function, and therefore points that differ by 2π in the variable φ are equivalent, it is more convenient to take a cylinder to be the phase space. (Fig. 6.7a). In this cylindrical phase space there are two kinds of closed paths:

- (a) Closed paths of the first kind, encircling an equilibrium point (curve Γ_1 of Fig. 6.7). In terms of the mechanical analog this type of trajectory corresponds to an oscillatory motion of the pendulum.

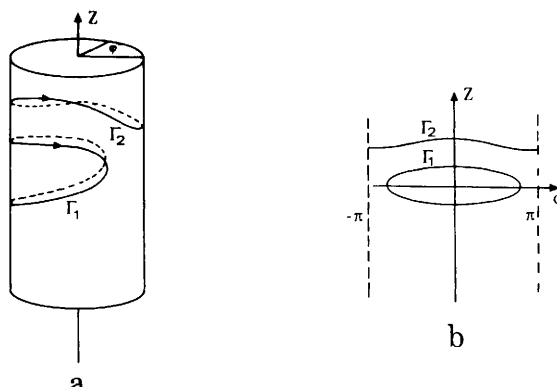


Figure 6.7 (a) Cylindrical phase space. The curves Γ_1 and Γ_2 are closed paths of the first and second kind respectively. (b) The same kind of curves in the unfolded cylinder.

- (b) Closed paths of the second kind, which go around the cylinder without encircling an equilibrium point (curve Γ_2 of Fig. 6.7). In terms of the mechanical analog this type of trajectory corresponds to a rotary motion of the pendulum.

To avoid complications in making the drawings of the phase space diagram, it is more convenient to present the phase space as an unfolded cylinder (see Fig. 6.7b). For the system described by (6.2.8) it can be shown that only one closed path (and therefore a periodic solution) of the second kind can exist lying entirely in the $Z>0$ region. Since $Z=\dot{\phi}$, this solution corresponds to a state in which the mean value of the voltage with respect to the time is different from zero.

In the plane of the parameters β_J and α the situation can be summarized as follows:

- (a) For $\alpha>1$ ($I_{dc}>I_1$) and arbitrary β_J value no equilibrium point exists; there is only a periodic solution of the second kind. Therefore the junction will be in the finite voltage state.
- (b) For $\alpha<1$ ($I_{dc}\leq I_1$) the situation is more complicated. The behavior depends on the particular value of β_J .

In the plane α, β_J , a curve can be identified, denoted by $\alpha_c(\beta_J)$, which divides the plane into two regions corresponding to one or two stable state solutions, respectively. This $\alpha_c(\beta_J)$ dependence calculated by analog computer by Johnson (1968) is reported in Fig. 6.8. Some authors have determined analytical relations that approximate the bifurcation curve $\alpha_c(\beta_J)$ (Stewart 1968; Zappe 1973; Schlup 1974; Zil'berman 1975; Belykh, Pedersen, and Soerensen 1977).

For $\beta_J < 0.2$ the simple relation holds (Stewart 1968):

$$\alpha_c(\beta_J) \approx \frac{4}{\pi} \beta_J \quad (6.2.9)$$

In Fig. 6.9 a typical phase space diagram for a fixed value of β_J and different values of α is shown. It can be seen that for $\alpha < \alpha_c(\beta_J)$ only one equilibrium point exists (Fig. 6.9a). The system has only one stable state corresponding to the zero voltage state. As α increases to the value $\alpha_c(\beta_J)$, the stable separatrix loop appears (Fig. 6.9b). For $\alpha_c(\beta_J) < \alpha < 1$ a stable equilibrium periodic solution appears and coexists with the stable equilibrium point. Therefore the states of zero and finite voltage are both possible. The junction is in either one depending on the initial conditions. A great number of phase space diagrams for the Josephson weak link have been also reported and discussed by Falco (1976).

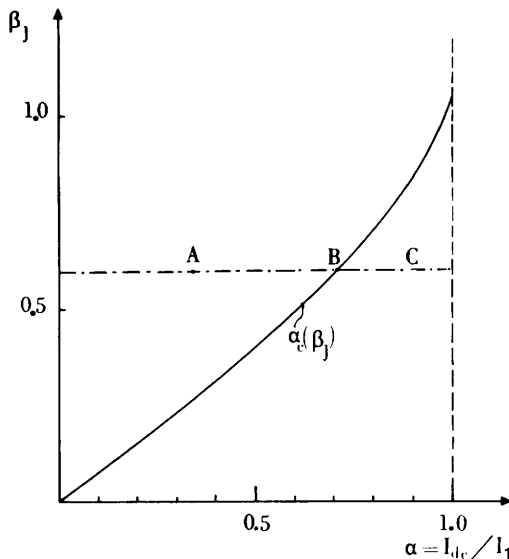


Figure 6.8 Analog computer results for the hysteresis parameter α_c as a function of β_J . In the region above the $\alpha_c(\beta_J)$ curve only one stable solution exists. In the region below the curve two stable solutions exist. (After Johnson 1968.)

6.2.4 D.C. Voltage-Current Characteristics for Finite Capacitance. Let us consider the time averaged value of the voltage V as a function of the normalized current. For $\beta_J < \beta_J(1) \approx 1.15$, a curve like that of Fig. 6.10 is obtained. If we start from $\alpha = 0$, $V = 0$ and increase the current, no voltage drop develops until the critical value $I_1(\alpha = 1)$ is reached. At this point a switch to the finite voltage state occurs and the V - I curve follows this branch of the characteristic. On decreasing the current, the weak link stays in the finite voltage state until I_{dc} is reduced to the value $I_1\alpha_c(\beta_J)$. Comparing the curve of Fig. 6.10 with that of Fig. 6.5 obtained in the zero capacitance limit, we observe that in the present case (finite capacitance) the V - I characteristic is hysteretic. In the limit $\beta_J \rightarrow 0$ ($G \ll \omega_J C$) a full hysteresis is exhibited. Average voltage-current characteristics, which Johnson (1968) obtained by solving

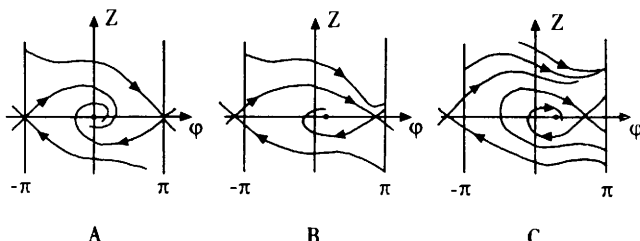


Figure 6.9 Qualitative phase-plane portraits, corresponding to the three different situations (A, B, C) in the β_J - α plane in Fig. 6.8. (After Belykh, Pedersen, and Soerensen 1977a.)

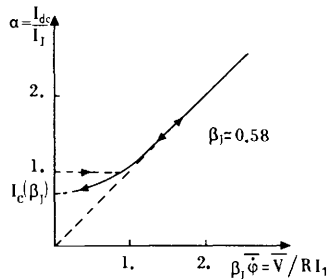


Figure 6.10 Averaged voltage-current characteristic computed by the R.S.J. model for finite capacitance.

(6.2.8) by analog computer, are reported in Fig. 6.11. The values of $\alpha_c(\beta_J)$ at which the junction reaches the zero voltage state agree with the curve of Fig. 6.8. Let us observe that the switching occurs at a finite voltage V_m which is a function of β_J . It is possible to make an estimation valid for $\beta_J < 0.2$ of the maximum theoretical value for V_m . In fact from the V - I curves computed for values of the parameter β_J in this range it is observed that (Johnson 1968)

$$V_m(\beta_J) \lesssim RI_1\alpha_c(\beta_J)$$

From (6.2.9) it follows for $\beta_J < 0.2$ that

$$V_m(\beta_J) \lesssim \frac{4}{\pi} RI_1\beta_J$$

By using the expressions for β_J and ω_J , we have

$$V_m(\beta_J) \lesssim \frac{4}{\pi} \frac{\hbar}{2e} \omega_J$$

This linear dependence of the switching voltage V_m on the plasma frequency has been observed experimentally by Fulton (1973) on tunneling junctions. Recently Pedersen and coworkers (1978a) have performed measurements on the switching voltage in Sn-SnO_x-Sn junctions near the critical temperature for different values of β_J . By independent measurement of ω_J by plasma resonance

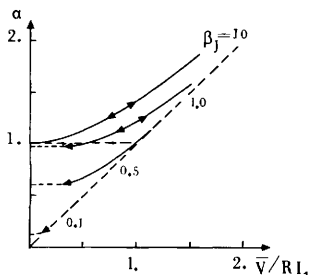


Figure 6.11 Analog computed averaged voltage-current characteristics for different values of the parameter β_J . (After Johnson 1968.)

experiments for each value of β_J , they have observed that the relation: $V_m = k \hbar / 2e \omega_J$ holds, where k is a constant of the order of unity.

Another way to solve (6.3.5) has been to substitute the linear relation GV by a nonlinear form of the kind GV^n and to look for analytical solutions. Pedersen and Saermark (1973) have considered the case $n=2$; Stewart (1974) has examined the case $n=2$ and $n \rightarrow \infty$. In particular, for the case $n=2$ (Pedersen and Saermark 1973) equation (6.2.2) reduces to

$$\frac{d^2\varphi}{dt^2} + k \left(\frac{d\varphi}{dt} \right)^2 + \omega_J^2 \sin \varphi = \omega_J^2 \alpha$$

where it is assumed that $R=\text{const.}/V=k_1/(d\varphi/dt)$ and $k=(k_1 C)^{-1}$. From this equation the solution of the time dependent voltage can be derived. The result is:

$$V(t) = \frac{\hbar}{2e} \frac{d\varphi}{dt} = \frac{\hbar}{2e} \left(\frac{\omega_J}{k^{1/2}} \right) (\alpha + \alpha_0)^{1/2} \operatorname{dn} \left[\frac{1}{2} \frac{\omega_J}{k^{1/2}} (\alpha + \alpha_0)^{1/2} (t - t_0) \right]$$

where $\operatorname{dn}[u]$ is a Jacobian elliptic function and $\alpha_0 = 2k/(1+4k^2)^{1/2}$. Taking

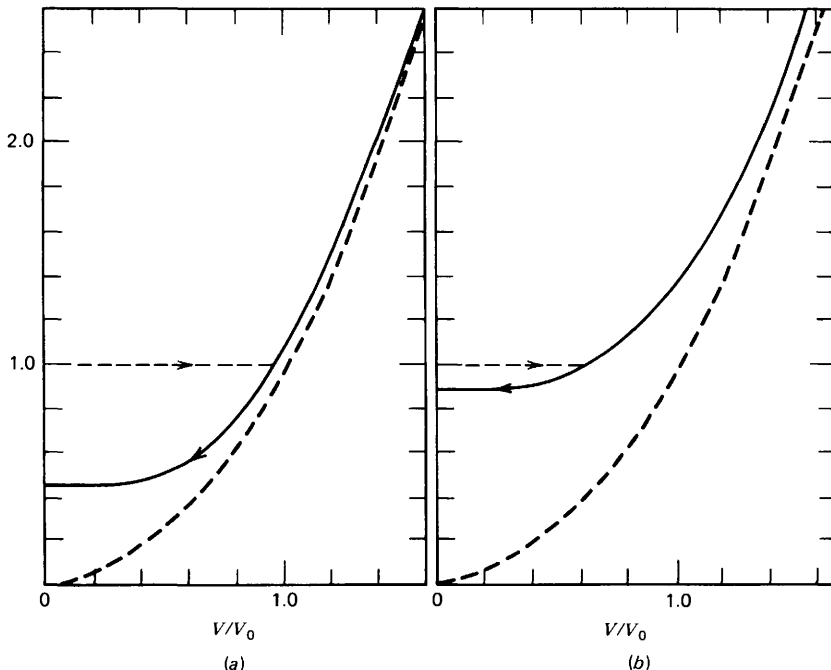


Figure 6.12 The time averaged voltage-current curves (solid lines) obtained by solving (6.2.2) using the nonlinear resistance characteristic $v/v_0 = \alpha^{1/2}$ (dashed lines). (a) $k = \frac{1}{4}$; (b) $k = 1$. (After Pedersen and Saermark 1973.)

the time average of $V(t)$ we have the average V - I characteristics shown in Fig. 6.12. The result is essentially analogous to that obtained with the linear resistance model (Fig. 6.11).

The first difficulty encountered in comparing theoretical V - I curves and experimental data on tunneling junctions is due to the strongly nonlinear voltage dependence of quasiparticle resistance in these samples. In the R.S.J. model a linear voltage dependence has in fact been assumed. Scott (1970a) has numerically solved (6.2.2) by taking into account the actual shape of the quasiparticle conductance. A comparison between experimental V - I curves of

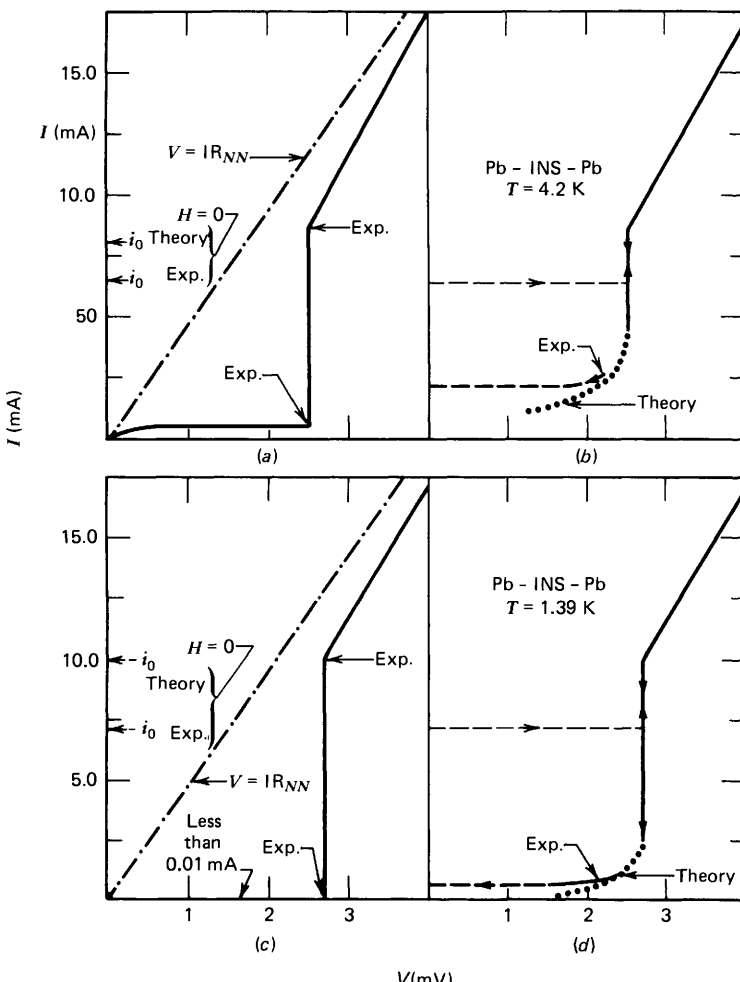


Figure 6.13 (a) Experimental and theoretical quasiparticle tunneling curves at 4.2 K. (b) Experimental and theoretical hysteresis in V - I curve at 4.2 K. (c) Experimental and theoretical quasiparticle tunneling curves at 1.39 K. (d) Experimental and theoretical hysteresis in V - I curve at 1.39 K. (After W. C. Scott 1970a.)

$\text{Sn}-\text{SnO}_x-\text{Sn}$ junctions and theoretical data is reported in Fig. 6.13. It can be observed that the agreement between experimental and numerical data is excellent. A slight discrepancy is related to the “switchback” to zero voltage state which occurs at voltage values higher than those theoretically expected. This point can be related to the effect of thermal fluctuations, as will be discussed in Section 6.4.

The strong nonlinearity in the quasiparticle V - I curve of a tunneling junction can be removed by the use of thin normal film deposited across the electrodes (Hansma, Rochlin, and Sweet 1971; Hansma and Rochlin, 1972; Gundlach and Kadlec 1978). In this case the effective resistance is a parallel combination of the junction and shunt resistance. As pointed out by Fulton (1973), great attention must be given to the effect of the lead inductance between the junction and the shunt. This inductance must be minimized if the

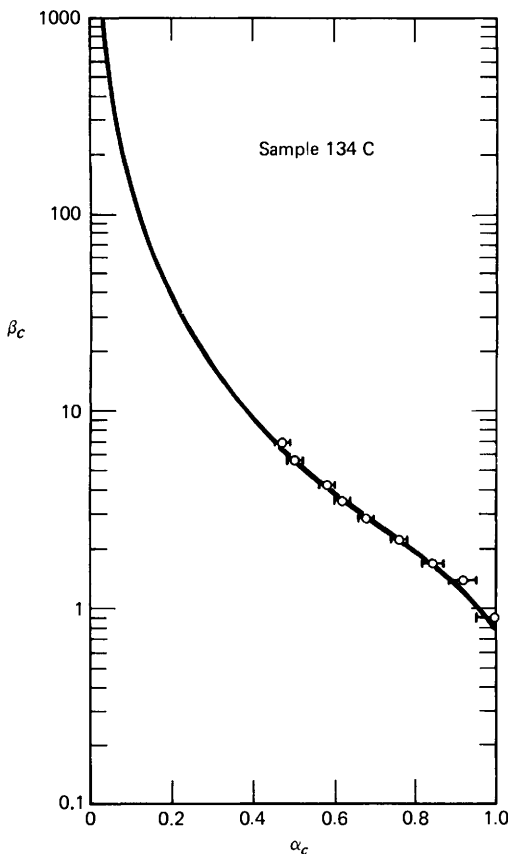


Figure 6.14 Experimental results for the hysteresis parameter α_c as a function of the McCumber parameter β_c for an externally shunted $\text{Sn}-\text{SnO}_x-\text{Sn}$ junction. β_c was varied by decreasing the critical current I_1 with a small magnetic field. Let us note that $\beta_c = 1/\beta_f^2$ (see Table 6.1). (After Hansma and Rochlin 1972.)

R.S.J. model is to be applicable. Experimental data for the hysteresis parameter α_c in an externally shunted Sn-SnO_x-Sn junction are reported in Fig. 6.14 (Hansma and Rochlin 1972). The solid line is the theoretical dependence computed by the R.S.J. model. The data are plotted as a function of the McCumber parameter $\beta_c = 1/\beta_J^2$ (see Table 6.1).

The normal metal shunt was realized by a small silver rectangle deposited on the top of the junction. The parameter β_c , which is directly related to the maximum Josephson current I_1 (see Table 6.1), was varied by changing the latter by applying a magnetic field (as in the data of Fig. 6.14) or by changing the temperature. Let us observe, incidentally, that the use of an external shunt permits employing tunneling junctions in device applications in which nonhysteretic V - I characteristics are required (e.g. in SQUIDs; see Chapter 13).

6.3 Current Biased Tunneling Junction

In the R.S.J. model discussed in the preceding section, the Josephson element was described by the simple sinusoidal current phase relation $I = I_1 \sin \varphi$. The quasiparticle conductance was accounted for by an external parallel resistance. For a tunneling junction, however, we have derived from the microscopic theory a more general expression for the current which includes the effects of both quasiparticles and pairs. This expression is an integrodifferential equation (2.2.3) which, assuming that there are no spatial phase variations, can be written as

$$I(t) = \operatorname{Im}_{\eta \rightarrow 0^+} \left\{ e^{\eta t} e^{-j/2\varphi(t)} \int_{-\infty}^{+\infty} dt' e^{-\eta t'} [e^{j\varphi(t-t')} S(t') + e^{-j\varphi(t-t')/2} R'(t')] \right\} \quad (6.3.1a)$$

or in an equivalent form:

$$I[\varphi(t)] = \int_0^\infty dt' \left[S(t') \sin \frac{\varphi(t-t') - \varphi(t)}{2} - R'(t') \sin \frac{\varphi(t-t') + \varphi(t)}{2} \right] \quad (6.3.1b)$$

$S(t)$ and $R'(t)$ are two real oscillating decaying functions. The frequency of the oscillation is the gap frequency $2\Delta/\hbar$. Their expressions, in the B.C.S. approximation and for a symmetric junction (identical superconducting electrodes), have been computed by Harris (1976a) for $T=0$ and by Schlup (1978a) for finite temperatures. Numerical solutions of (6.3.1) have been considered by Harris (1977) to describe the response of a junction connected to an arbitrary circuit. In Section 2.3 the case of a constant voltage bias was considered. It was shown that the pair current gives no observable contribution to the total current for finite voltage values.

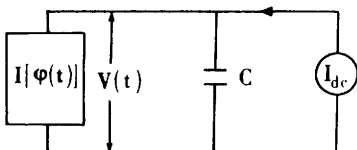


Figure 6.15 Equivalent circuit for a current biased tunneling junction.

Let us now assume that the junction is driven by a constant current I_{dc} and has a capacitance C . The equivalent circuit is sketched in Fig. 6.15. The current balance equation is

$$I_{dc} = \frac{\hbar}{2e} C \frac{d^2\varphi}{dt^2} + I(\varphi) \quad (6.3.2)$$

where $I(\varphi)$ is given by (6.3.1). The phase φ is related to the voltage through (2.1.5b), which can be written as

$$\varphi(t) = \frac{2e}{\hbar} \int_0^t V(t') dt'$$

To get a time averaged V - I characteristic, therefore, (6.3.2) has to be solved.

6.3.1 Adiabatic Approximation. Let us consider the case in which the voltage $V(t)$ is small or has time variations small compared with the gap frequency. The following approximation can be made (Larkin and Ovchinnikov 1966):

$$\int_{t_1}^t V(t') dt' \approx V(t)(t - t_1) + \text{high order terms} \quad (6.3.3)$$

which gives for the phase factors:

$$\varphi(t) = V(t)(t - t_0); \quad \varphi(t - t') = V(t)(t - t_0) - V(t)t'$$

The expression 6.3.1a becomes

$$I(t) = \operatorname{Im}_{\eta \rightarrow 0^+} \left\{ \int_{-\infty}^{+\infty} dt' e^{j(j\eta - V(t)/2)t'} S(t') + e^{-j\varphi(t)} \int_{-\infty}^{+\infty} dt' e^{j(j\eta + V(t)/2)t'} R'(t') \right\}$$

By using the Fourier transform of $S(t)$ and $R'(t')$ (Section 2.2.2) and the definitions 2.2.8, (6.3.2) reduces to:

$$I_{dc} = \frac{\hbar}{2e} C \frac{d^2\varphi}{dt^2} + I_{qp}(V(t)) + I_{J2}(V(t)) \cos \varphi(t) + I_{J1}(V(t)) \sin \varphi(t) \quad (6.3.4)$$

This is the so-called adiabatic approximation. The case $V(t) = V_0 = \text{constant}$ is a special case of this approximation in which (6.3.3) is identically valid.

$I_{qp}(V)$, $I_{J1}(V)$, $I_{J2}(V)$ are related to the Fourier transforms of $S(t)$ and $R'(t)$ and were defined in Section 2.2.2. Their expressions are as discussed for finite voltage (Section 2.4). Current voltage characteristics computed by solving (6.3.4) have been reported by Hahlbohm, Lübbig, and Luther (1975).

A discussion on this kind of approximation has been given by Schlup (1978). If we assume that

$$I_{qp}(V) = GV; \quad I_{J2}(V) = \epsilon GV; \quad I_{J1}(V) = I_1$$

where G and I_1 are constants, (6.3.4) becomes

$$I_{dc} = \frac{\hbar}{2e} C \frac{d^2\varphi}{dt^2} + \frac{\hbar}{2e} G(1 + \epsilon \cos \varphi) \frac{d\varphi}{dt} + I_1 \sin \varphi \quad (6.3.5)$$

For $\epsilon=0$ this equation reduces to (6.2.2) derived for the R.S.J. model discussed in the preceding section. Let us remark that (6.3.5) has been directly deduced from the microscopic theory. Therefore it provides a sort of justification for the use of the R.S.J. model, introduced empirically in Section 6.2. For $\epsilon \neq 0$ (6.3.5) provides an “extension” of the R.S.J. model to include the effect of the quasiparticle-pair interference term (the so-called $\cos \varphi$ term). The extension of the analysis of the R.S.J. model, taking into account the $\cos \varphi$ term ($-1 < \epsilon < 1$), has been performed by Schlup (1974), using perturbation theory and numerical calculations.

An extensive analysis of the general R.S.J. model, including the $\cos \varphi$ term, is given by Belykh, Pedersen, and Soerensen (1977a).

6.3.2 General Case. The complete equations for the current biased junction, (6.3.1) and (6.3.2), have been considered by McDonald, Johnson, and Harris (1976) in the case of zero temperature. Voltage-current characteristics for a symmetric junction numerically computed by these authors are reported in Fig. 6.16. Different curves refer to different values of the parameter RC/τ_g where C is the junction capacitance and $\tau_g = \hbar/\Delta$ is a time constant related to the gap frequency.

The essential features of the V - I curve can be summarized as follows:

- (a) For small values of the parameter RC/τ_g (small capacitance limit) large values of the d.c. current are present at voltages lower than the energy gap voltage. The main contribution to this excess current comes from the pair tunneling term $R(t)$.
- (b) A singularity at $V=2\Delta/e$ is present in the d.c. characteristics, which becomes stronger for junctions of smaller capacitance. Therefore the Riedel peak in the $R'(\omega)$ is directly displayed in the V - I curves.
- (c) Singularities are also observed at voltages given by

$$V_n = \frac{2\Delta}{en}$$

where n is an odd integer.

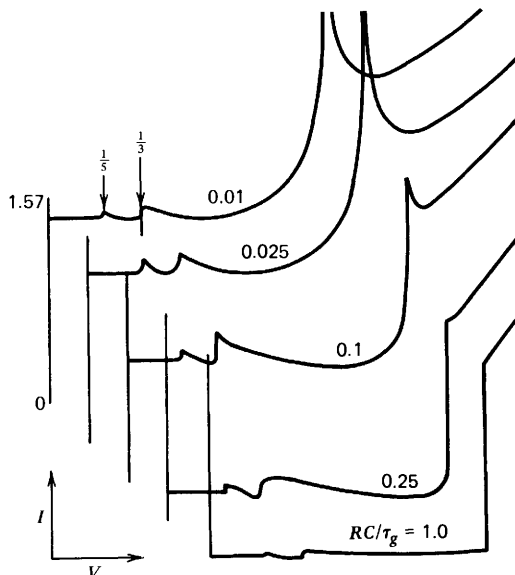


Figure 6.16 Effect of shunt capacitance C on the V - I curve. R is the junction normal state resistance and $\tau_g = h/\Delta$. Each curve is plotted with a displaced origin for clarity and with the zero voltage current going vertically from zero to 1.57 in all cases. (After McDonald, Johnson and Harris 1976.)

These are the subharmonic gap structures observed for the first time by Giaever and Zeller (1970) and subsequently investigated theoretically by Strassler and Zeller (1971) and Hasselberg, Levinsen, and Samuelsen (1974, 1975) and experimentally by Soerensen and coworkers (1974). In the present model the Riedel peak is also responsible for these singularities.

- (d) In the high capacitance limit ($RC/\tau_g \rightarrow 1$) the V - I curves for finite voltage tend to the quasiparticle term and are very similar to those obtained in the voltage biased case.

Zorin and Likharev (1977) have theoretically investigated the zero capacitance limit ($RC/\tau_g = 0$) for finite temperature values. The complete analysis for finite temperature and arbitrary values of the parameter RC/τ_g has been given by Schlup (1978a).

It is interesting to observe that the effect of the Riedel peak had been previously considered in the adiabatic approximation (6.3.4) by Hahlbohm, Lübbig, and Luther (1975) and by Schlup (1978b). In Fig. 6.17 the V - I characteristic obtained in the adiabatic approximation for $T = 0$ and $C = 0$ is compared with that obtained by solving the general equation (6.3.2).

A quantitative comparison between the theoretical results derived for a current biased junction and experiments is not very easy to do. In fact the rounding in the Riedel singularity has not been taken into account in the

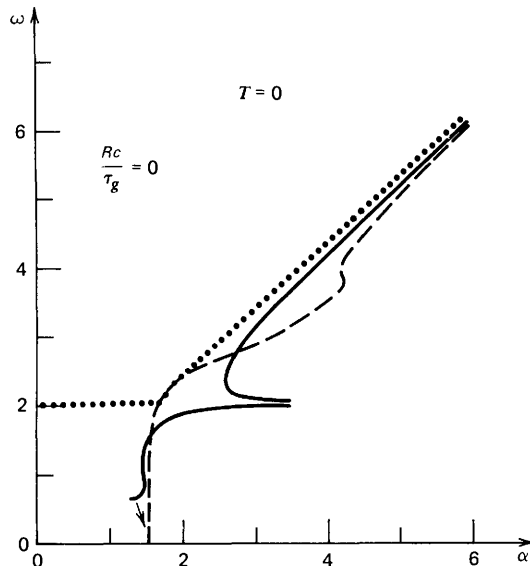


Figure 6.17 Averaged voltage-current characteristic for a current biased tunneling junction computed from the full expression (6.3.2) (full line) compared with the corresponding curve derived in the adiabatic approximation (dashed curve) for $T = 0$ and $RC/\tau_g = 0$ (zero capacitance limit). The result for RC/τ_g (dotted) coincides with the quasiparticle current $I_{qp}(V)$. (After Schlup 1978a.)

theory. Furthermore, for the junctions usually encountered in the literature the parameter RC/τ_g is greater than 0.5 (McDonald, Johnson, and Harris 1976). In this case (see Fig. 6.16) the V - I curves do not differ markedly from the ones obtained when the junction is voltage biased.

Large excess currents have been observed in high current density, current biased Josephson junctions, by Niemeyer and Kose (1976a, b). In fact, by using for the capacitance an expression similar to that of a parallel plate capacitor, it can be shown that

$$\frac{RC}{\tau_g} = \frac{\pi}{h} \frac{\epsilon_r \epsilon_0}{t} \frac{\Delta^2}{J_1} \quad (6.3.6)$$

where ϵ_0 is the vacuum permittivity, ϵ_r and t are relative permeability and thickness of the oxide barrier, Δ the energy gap, and J_1 the maximum Josephson current density. Current voltage characteristics for these high current density junctions are reported in Fig. 6.18. It is interesting that, as usual, both odd and even subharmonic structures (Fig. 6.18a) are observed in the experimental data although the theoretical analysis predicts only the odd series. Furthermore, no singularity is observed at the gap voltage. The effect of the Riedel peak at the gap voltage in the V - I characteristic of current biased tunneling junction has never been observed.

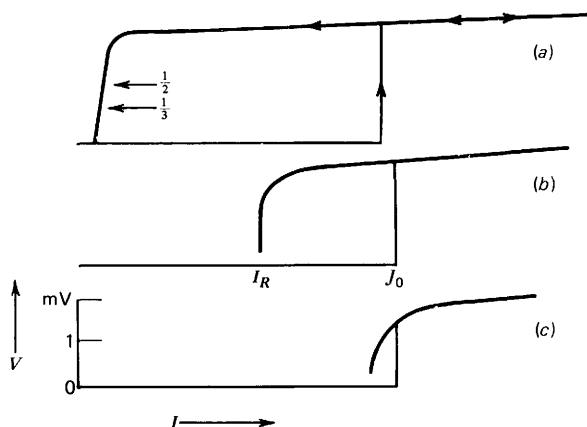


Figure 6.18 Influence of the critical d.c. supercurrent density J_0 on the V - I characteristic of tunnel junctions. The hysteresis is characterized by the ratio of the reverse switching current I_R and the critical d.c. supercurrent J_0 . Temperature $T = 4.2$ K. (a) $J_0 = 3.1 \times 10^3$ A/cm 2 ; $I_0 = 0.68$ mA. (b) $J_0 = 3.4 \times 10^4$ A/cm 2 ; $I_0 = 3.4$ mA. (c) $J_0 = 2.1 \times 10^5$ A/cm 2 ; $I_0 = 6.4$ mA. (After Niemeyer and Kose 1976b.)

In junctions with a niobium base layer an excess current like a “bump” at the gap voltage is often observed (Nordman and Keller 1971, Keller and Nordman 1973, Paternò, Rissman, and Vaglio 1975; Broom et al 1975). Some authors (Zorin and Likharev 1977) claim that this bump is related to the Riedel peak. On the other hand, it seems that such a structure is not related to the excess current at finite voltage in the V - I curves but rather to the physical nature of the niobium film. In fact it is observed in conditions in which a high hysteresis is exhibited in the V - I characteristics and therefore the parameter RC/τ_g is high. Also, it is found to be related to the deposition technique of the base layer. Indeed, a qualitative explanation can be given in term of the presence of a normal layer of “dirty” niobium on the film surface which is proximized (see Chapter 7) by the underlying pure film (Shen 1972). The nature of this normal layer depends strongly on deposition parameters. This explanation is supported by the following experimental observations:

- (a) Shen (1972) has fabricated Nb-NbO_x-Pb junctions using high purity niobium foil. When the niobium foil was carefully outgased at 10^{-11} torr for a few days the samples were showing no bump in the V - I characteristics.
- (b) Proximity effect junctions exhibit V - I curves with the “bump” (Gilabert Romagnan and Guyon 1972). The curve of the temperature dependence of the maximum Josephson current for these structures falls below that predicted by Ambegaokar and Baratoff (1963) and Romagnan et al. (1974). This “lowering” effect has been observed in Nb-NbO_xPb junctions (Paternò, Rissman, and Vaglio 1975), in Nb junctions with and

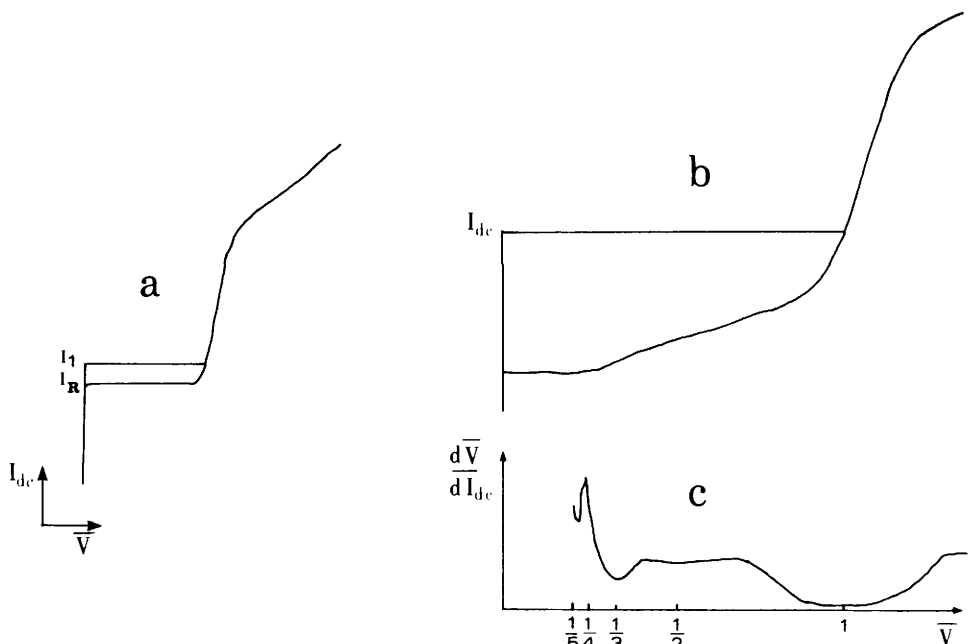


Figure 6.19 (a), (b) Averaged voltage current curves theoretically computed by using an analytical approach for two different values of the junction capacitance. (c) First derivative $d\bar{V}/dI_{dc}$ for the curve of (b) exhibiting multiparticle steps. (After Erné and Lübbig, 1979.)

without aluminum (Cucolo, Pace, and Parmentier 1977), and in Nb-NbO_x-Nb samples (Broom 1976) when the bump was present in the V - I characteristics. Recently extensive work that confirms this behavior for both Nb-NbO_x-Pb and Nb-NbO_x-Nb junctions has been carried out by Matsuda, Inamura, and Yoshikiyo (1980).

The numerical results reported for the solution of the integrodifferential equation (6.3.2) have been usually obtained by the method of subsequent approximations. The limitation of this technique is that the stationary solution can be evaluated only if the frequency of this solution is known. Furthermore, no information is obtained on the transient solution, on its stability, or on the existence condition of the stationary solution.

Recently Erné and Lübbig (1979, 1980a,b) have developed a technique to transform (6.3.2) into a system of differential equations. In this way, although numerically, the complete analytical solution can be computed. A typical V - I curve computed by this method for $T=0$ is shown in Fig. 6.19a. Comparing this curve with those reported in Fig. 6.16, we see that the most striking difference is that in the present case, near the gap voltage, there is no singularity. A further difference that emerges wherever a higher degree of hysteresis is present is that multiparticle steps are observable for both odd and

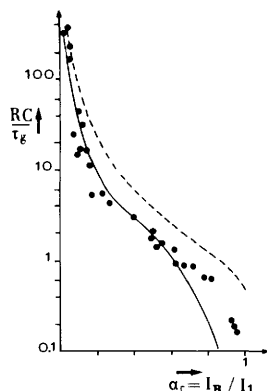


Figure 6.20 The hysteresis parameter α_c as a function of RC/τ_g . The theoretical curve (solid line) computed using an analytical approach is compared with the data of Niemeyer and Kose (1976). The dashed line is the theoretical dependence computed for the R.S.J. model by McCumber (1968). (After Erné and Lubbig 1979.)

even values (Fig. 6.19*b, c*). In Fig. 6.20 the hysteresis parameter α_c is reported as a function of RC/τ_g . The theoretical curve is compared with the experimental data of Niemeyer and Kose (1976); the dashed line is the theoretical dependence computed for the R.S.J. model by McCumber (1968).

In plotting the experimental data, the value of the parameter ε_r/t in (6.3.6) has been chosen to get the best agreement with the theoretical curve.

6.4 Effects of Thermal Fluctuations

Thus far we have discussed the macroscopic voltage-current characteristics from a deterministic point of view (i.e., zero noise case). However, the Josephson junction is a good example of the case where the effects of thermal fluctuations produce a macroscopic effect in the critical region. We now consider the influence of thermal fluctuations on the voltage-current characteristic using, once again, the R.S.J. model for the zero noise limit. As we shall see, the effect of thermal fluctuations results in a “rounding” of the V - I curves (Ivanchenko and Zilberman 1968a, b; Ambegaokar and Halperin 1969). Before embarking on an analysis of thermal fluctuations, a brief review of the basic concepts for analyzing fluctuating phenomena will be instructive (see, for instance, Lee 1960; Stratonovich 1967).

In time the current $I(t)$ undergoes small changes, fluctuating about its mean value which, for simplicity, we take to be zero. The values of $I(t)$ at different times are correlated, so that the value of $I(t)$ has an effect on the value of the current at a later time, $t+\tau$ say. We denote $\langle I(t)I(t+\tau) \rangle$ as the time correlation function where the angular brackets specify an average over the probabilities of all the values that the current can take at the two times. For a stationary process it does not matter at which point in time we begin our observations; the only thing that is of importance is the time interval τ (stationarity). Statistical averaging allows us to obtain the correlation between different values of the current without following their variation in time.

For fluctuating phenomena, can either be given a temporal description or a spectral description. This corresponds to two types of experiments: we can either take readings at close intervals in time or use a frequency analyzer. In the frequency description, the important quantity is power spectrum $P(\omega)$ which is the average power per unit interval of frequency. It is not unexpected that the two descriptions (in the time domain and in the frequency domain) are related, and this is the essence of the well-known Wiener-Khintchine theorem:

$$\langle I(t+\tau)I(t) \rangle = \int_0^\infty P(\omega) \cos \omega \tau d\omega$$

This theorem, expressed in words, states that the power spectrum and the time correlation function are reciprocal Fourier transforms of one another.

For the quasiparticle current, the power spectrum is given by (Scalapino 1967):

$$P(\omega) = \frac{|e|}{\pi} I\left(\frac{\hbar\omega}{|e|}\right) \coth\left(\frac{\hbar\omega}{2k_B T}\right)$$

At a temperature for which $T \gg \hbar\omega/k_B$ we have $\coth(\hbar\omega/2k_B T) \approx 2k_B T/\hbar\omega$, and the power spectrum takes the form

$$P(\omega) = \frac{2k_B T}{\pi} I\left(\frac{\hbar\omega}{|e|}\right) / \frac{\hbar\omega}{|e|}$$

The R.S.J. model assumes that the conductance is frequency independent and consequently the power spectrum reduces to the expression

$$P = \frac{2k_B T}{\pi R}$$

in which Planck's constant has disappeared. This testifies to the fact that the fluctuations are now classical and P is just the Johnson noise associated with the resistor, R . Finally, we can calculate the time correlation function using the Wiener-Khintchine theorem

$$\langle I(t)I(t+\tau) \rangle = \frac{2k_B T}{\pi R} \int_0^\infty \cos \omega \tau d\omega = \frac{2k_B T}{R} \delta(\tau)$$

where we have used the δ function definition $\delta(\tau) = 1/\pi \int_0^\infty \cos \omega \tau d\omega$.[†]

[†]With a greater generality we could start from the relation between the autocovariance and the power spectrum:

$$\text{Re} \overline{\langle I(t+\tau)I(t) \rangle} - \overline{\langle I(t+\tau) \rangle} \langle I(t) \rangle = \int_0^\infty P(\omega) \cos \omega \tau d\omega$$

In our case the second term on the left side is zero because of the thermal equilibrium and the time average (indicated by the bar) does not appear, since the system is stationary (Rogovin and Scalapino 1974).

The effect of thermal fluctuations is accounted for by adding a noise term to the equations of motion describing the junction:

$$\frac{\partial \varphi}{\partial t} = \frac{2e}{\hbar} V \quad (6.4.1a)$$

$$C \frac{\partial V}{\partial t} = I - I_1 \sin \varphi - \frac{V}{R} + \tilde{I}(t) \quad (6.4.1b)$$

Apart from the noise term $\tilde{I}(t)$, the last equation represents the current continuity equation of the R.S.J. model that we have already considered (Equation 6.2.1). Roughly speaking, the reason why the noise term is added only to the second equation is that dissipation goes hand in hand with fluctuations and since there is no dissipative term in the first equation there can be no noise term. $I_1(T)$ is the temperature dependent critical current that we calculated in Chapter 3 in the absence of noise. The resistance R is assumed to have the constant value corresponding to the normal tunneling resistance R_N . This is a good approximation for temperature near the critical T_C . Our interest is confined to precisely this case.

Since the appearance of a term in the governing equations is defined only statistically, we can no longer ask for the solution of the equations (how φ and V change as a function of time), but must content ourselves with knowing the probabilities for the values of these variables at any given instant in time. This requires a knowledge of the probability density, and to determine it we must specify the statistical features of $\tilde{I}(t)$. The quantity $\tilde{I}(t)$ represents the noise due to the resistive flow of the quasiparticle current which is phenomenologically described by V/R . For our purpose, it suffices to consider the high temperature limit and model the stochastic current $\tilde{I}(t)$ after “white noise” which has the following statistical properties:

$$\langle \tilde{I}(t) \rangle = 0 \quad \text{and} \quad \langle \tilde{I}(t+\tau) \tilde{I}(t) \rangle = \frac{2k_B T}{R} \delta(\tau)$$

That the mean value of $I(t)$ be zero is reasonable; indeed, the average behavior of the fluctuations must coincide with the macroscopic behavior described by the deterministic equations. The δ function correlation function means that the values of $\tilde{I}(t)$ are completely uncorrelated; the probability for a value of $\tilde{I}(t)$ at any instant in time is not influenced by any other value that it may have had at an earlier time. This implies that the spectrum is flat like white light or, equivalently, that the correlation function is very sharply peaked.

We now follow the approach of Ambegaokar and Halperin (1969) (see also the work carried out by Ivanchenko and Zilberman 1968a, b) which is based on the original derivation due to Stratonovich (1958) and Tikhonov

(1959)[†] and write (6.4.1) in the form

$$\dot{\varphi} = \frac{p}{M}$$

$$\dot{p} = -\frac{dU}{d\varphi} - \eta_0 p + \tilde{i}(t) \quad (6.4.2)$$

where

$$U(\varphi) = -\frac{1}{2}\gamma k_B T(\alpha\varphi + \cos\varphi)$$

$$p = \left(\frac{\hbar C}{2e}\right)V; \quad M = \left(\frac{\hbar}{2e}\right)^2 C; \quad \tilde{i}(t) = \frac{\hbar}{2e} \tilde{I}(t); \quad \eta_0 = \frac{1}{RC}$$

with the dimensionless parameters

$$\gamma = \frac{\hbar I_1(T)}{ek_B T}; \quad \alpha = \frac{I}{I_1};$$

The reason for writing (6.4.1) in the form (6.4.2) is to capitalize on the analogy with mechanics; that is, φ represents a coordinate and p represents the momentum. Thus (6.4.2) describe the Brownian motion of a particle of mass M in a potential $U(\varphi)$. Carrying the analogy still further, it will be appreciated that C^{-1} is related to the viscosity and the mass M is proportional to the capacitance. The potential $U(\varphi)$ is shown in Fig. 6.21 which is a modification of Fig. 1.11 due to the polarization current. Increasing the current value (i.e., its normalized value, α) causes the average slope of the curve to increase as well.

Equations 6.4.2 are the typical Langevin stochastic differential equations which can be written in the form

$$\dot{\varphi} = f_1(\varphi, V) + L_1(t)$$

$$\dot{V} = f_2(\varphi, V) + L_2(t) \quad (6.4.3)$$

where

$$f_1(\varphi, V) = \frac{p}{M}; \quad L_1(t) = 0$$

$$f_2(\varphi, V) = -\frac{dU}{d\varphi} - \eta_0 p; \quad L_2(t) = \tilde{i}(t)$$

Equations 6.4.3 describe stochastic processes of Markovian type. The mathematical description for our system is given by the Fokker-Planck equation

[†]See also the volume by Kuznetsov, Stratonovich, and Tikhonov (1965).

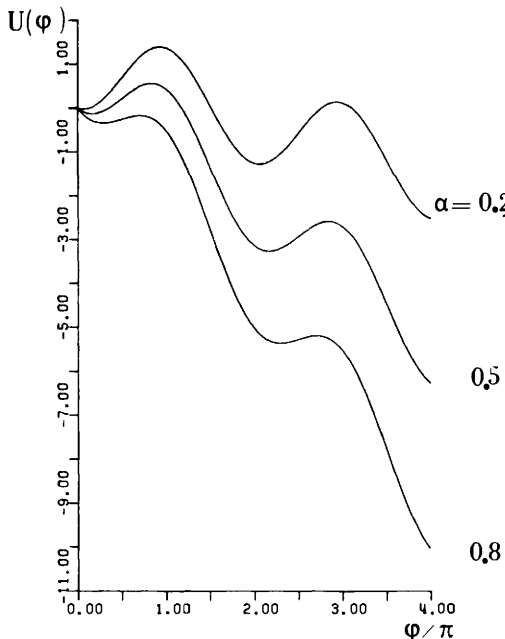


Figure 6.21 Shape of the potential $U(\varphi)$ as in Fig. 1.11 but modified by the polarization current. Current increase corresponds to an increase of the average slope. The curves refer to different values of the parameter $\alpha = I/I_1$ and are shifted so that $U(0)=0$.

(F.P.E.) associated with (6.4.3) for a probability distribution $\mathcal{P}(V, \varphi, t)$. It can be shown (Blaquière 1966) that in our case the F.P.E. is

$$\frac{\partial \mathcal{P}}{\partial t} = -\frac{p}{M} \frac{\partial \mathcal{P}}{\partial \varphi} + \frac{\partial}{\partial p} \left[\left(\frac{\partial U}{\partial \varphi} + \eta_0 p \right) \mathcal{P} + \eta_0 M k_B T \frac{\partial \mathcal{P}}{\partial p} \right] \quad (6.4.4)$$

We consider this equation for the description of three different situations: (1) negligible capacitance, (2) small capacitance, and (3) large capacitance.

6.4.1 Negligible Capacitance. The equations above represent a Markov process in phase space which under appropriate conditions reduces to a Markov process in configuration space. This is simply the Smoluchowski approximation for the relative phase φ . The precise conditions for the validity of the Smoluchowski approximation are obtained by writing (6.4.2) as a single second order equation:

$$\ddot{\varphi} + \frac{1}{M} \frac{dU}{d\varphi} + \eta_0 \dot{\varphi} - \frac{\tilde{i}(t)}{M} = 0$$

which can be considered to be a projection of a Markov process. It reduces to a

Markov process if the junction capacitance happens to be very small. For then we invoke the Smoluchowski approximation on the basis that the external force per unit mass $(1/M)(\partial U/\partial \varphi)$ varies slowly over times much greater than the relaxation time η^{-1} . This means that our imaginary Brownian particle acquires the limiting velocity $(1/\eta_0 M)(dU/d\varphi)$ and suggest the equation:

$$\dot{\varphi} = \frac{1}{\eta_0 M} \frac{dU}{d\varphi} + \frac{1}{\eta_0 M} \tilde{i}(t) \quad (6.4.5)$$

where the last term includes the effects of random fluctuations due to Brownian motion. Defining

$$f(\varphi) = -\frac{1}{\eta_0 M} \frac{dU}{d\varphi} \quad \text{and} \quad L(t) = \frac{1}{\eta_0 M} \tilde{i}(t) \quad (6.4.6)$$

this equation can be cast in the standard form of a Langevin equation:

$$\dot{\varphi} = f(\varphi) + L(t) \quad (6.4.7)$$

which is the basic equation of the Smoluchowski theory (Chandrasekhar 1943).

Assuming the fluctuations to be continuous, it can be described as a diffusion process in φ space using the forward Fokker-Planck equation. The point is that because of the random term in (6.4.5) the best we can do is to determine the probability for a value of φ and the probability density is a solution of the F.P.E. We assume, moreover, that the first two differential moments exist and are given by

$$\lim_{\tau \rightarrow 0} \frac{\langle \varphi(t+\tau) - \varphi(t) \rangle}{\tau} = f(\varphi)$$

$$\lim_{\tau \rightarrow 0} \frac{\langle |\varphi(t+\tau) - \varphi(t)|^2 \rangle}{\tau} = 2D$$

where the angular brackets denote a conditional average, that is, that the value of φ at time t was actually $\varphi(t)$ and D is the diffusion coefficient. Consequently, the probability density function $\sigma(\varphi, t)$, for a single event, satisfies the equation

$$\frac{\partial \sigma}{\partial t} = -\frac{\partial}{\partial \varphi} (\sigma f(\varphi)) + D \frac{\partial^2 \sigma}{\partial \varphi^2} \quad (6.4.8)$$

where we have assumed that we are dealing with a constant diffusion process. This can also be cast in the form of a continuity equation:

$$\frac{\partial \sigma}{\partial t} = -\frac{\partial \mathcal{W}}{\partial \varphi} \quad (6.4.9)$$

where the probability current, \mathfrak{W} is defined as

$$\mathfrak{W} = \left(-\frac{1}{\eta_0 M} \frac{dU}{d\varphi} \sigma - \frac{k_B T}{\eta_0 M} \frac{\partial \sigma}{\partial \varphi} \right) \quad (6.4.10)$$

In defining the probability current, we have reverted to our original notation [cf. (6.4.6)] and have used the Einstein formula which expresses the diffusion coefficient D in terms of the viscosity η_0 , namely, $D = k_B T / \eta_0 M$.

In order to compare theory with experiment, we need to determine some measurable quantity such as the d.c. current-voltage characteristic. What is measured is the average voltage and to obtain an expression for it we proceed as follows. On averaging (6.4.5) we have

$$\langle \dot{\varphi} \rangle = \left\langle \left(-\frac{1}{\eta_0 M} \frac{dU}{d\varphi} \right) \right\rangle = -\frac{1}{\eta_0 M} \int_0^{2\pi} \frac{dU}{d\varphi} \sigma d\varphi$$

which, using the expression of \mathfrak{W} , can be written as

$$\langle \dot{\varphi} \rangle = \int_0^{2\pi} \mathfrak{W} d\varphi + \frac{k_B T}{\eta_0 M} \int_0^{2\pi} \frac{d\sigma}{d\varphi} d\varphi$$

In the stationary case $d\sigma/dt=0$ (i.e., $\mathfrak{W}=\text{const.}$) and using the boundary conditions $\sigma(0)=\sigma(2\pi)$, we have

$$\int_0^{2\pi} \mathfrak{W} d\varphi = 2\pi \mathfrak{W} \quad \text{and} \quad \int_0^{2\pi} \frac{d\sigma}{d\varphi} d\varphi = 0$$

where \mathfrak{W}^{-1} represents the average time in which a 2π phase change occurs.

Thus the relation between the mean voltage and the probability current is

$$\frac{2e}{\hbar} \langle V \rangle = \langle \dot{\varphi} \rangle = 2\pi \mathfrak{W} \quad (6.4.11)$$

An explicit expression for the mean voltage can be found by integrating twice (6.4.8) in the stationary case.

By the first integration we have

$$\frac{\partial \sigma}{\partial \varphi} - \frac{1}{2} \gamma (\alpha - \sin \varphi) \sigma = C'_1$$

By the second integration, imposing the periodicity condition $\sigma(0)=\sigma(2\pi)$ with $C_1=(2/\gamma)C'_1$ we obtain

$$\frac{2}{\gamma} \sigma(\varphi) = C_1 \frac{\exp(\pi\gamma\alpha)}{1 - \exp(\pi\gamma\alpha)} \exp\left[-\frac{\gamma}{2} U_l(\varphi)\right] \int_{\varphi}^{\varphi+2\pi} \exp\left[\frac{\gamma}{2} U_l(\varphi')\right] d\varphi'$$

where $U_1(\varphi) = -(\alpha\varphi + \cos\varphi - 1)$. The constant of integration C_1 is evaluated by the normalization conditions $\int_0^{2\pi} \sigma d\varphi = 1$. The result is:

$$C_1 = \frac{2}{\gamma} \frac{1 - \exp(-\pi\gamma\alpha)}{\exp(\pi\gamma\alpha)} \frac{T_1^{-1}}{2\pi}$$

where

$$T_1 = \int_0^{2\pi} \exp\left(-\frac{\gamma}{2}\alpha\varphi\right) I_0\left(\gamma \sin\frac{\varphi}{2}\right) d\varphi$$

with I_0 modified Bessel function.

Comparing (6.4.10) with the result of the first integration of (6.4.8) it is found that

$$\mathcal{W} = -\frac{\gamma}{2} \frac{k_B T}{\eta_0 M} C_1$$

Substituting the last expression in (6.4.11) we have

$$\langle V \rangle = -\frac{\hbar}{2e} 2\pi \frac{\gamma}{2} \frac{k_B T}{\eta_0 M} C_1$$

and recalling the definitions of C_1 , η_0 , and M we finally have

$$\langle V \rangle = \frac{2}{\gamma} R I_1 \frac{\exp(\pi\gamma\alpha) - 1}{\exp(\pi\gamma\alpha)} T_1^{-1} \quad (6.4.12)$$

Here the average symbol stands for double averaging (ensemble and time averages). There are various limiting cases. At high temperature, for instance, $\gamma \rightarrow 0$, $V \rightarrow IR_N$. When the temperature goes to zero, $\gamma \rightarrow \infty$, the zero noise case is reproduced: $V=0$ for $I < I_1$; $V = I_1 R \sqrt{\alpha^2 - 1} = R \sqrt{I^2 - I_1^2}$ for $I > I_1$.

The voltage-current characteristics obtained by a numerical computation of (6.4.12) are shown in normalized units in Fig. 6.2.2. As a result of thermal fluctuations a “rounding” effect is present in the V - I curve, and at finite temperature the average voltage across the junction is nonvanishing no matter how small the current. We can discuss our results by referring to the curve of $U(\varphi)$ in Fig. 6.21. For $T=0$ the stable state for the system corresponds to one of the relative minima of $U(\varphi)$, say at φ_0 . The necessary condition $(dU/d\varphi)_{\varphi=\varphi_0}=0$ corresponds to the Josephson relation $I=I_1 \sin\varphi_0$. At finite temperature, the system undergoes thermal noise and the phase can “slip” from one potential well to the next. The resulting time phase variation produces ultimately a nonzero mean voltage across the junction. Thus in the absence of noise the switching from the zero voltage to a finite voltage state occurs at $I=I_1$, whereas in the presence of fluctuations the transition occurs at

random values of the current smaller than I_1 . It is clear that in the mechanical analogy the zero current condition corresponds to the situation in which the particle remains (oscillates) in a valley of $U(\varphi)$. As α is continuously increased, the particle "sees" a lower and lower barrier until it escapes from the throat and begins to move down the slope.[†] Actually, the character of the motion is governed by dissipative factors. High or low viscosity, that is, small or large capacitance, depicts the two limiting cases of overdamped and underdamped conditions respectively. The analysis previously developed refers to the former situation ($C=0$). Of course to obtain the complete V - I curve the current is progressively reduced, that is, the average slope of $U(\varphi)$ decreases and our "particle" slows down—the voltage goes continuously to zero (nonhysteretic path in the V - I characteristics).

The voltage-current curves obtained by the theory discussed above have been very closely reproduced by a numerical approach based on pseudorandom-number generation techniques (Tesche and Clarke 1977). They observe that the phase fluctuates around the equilibrium positions (minima of $U(\varphi)$) and randomly performs jumps of 2π to another equilibrium position, as previously discussed. The corresponding variations of the voltage appear as marked spikes even in the region of small variations of the phase, since the voltage is related to the derivative of φ .

The first experimental results that confirm, at least qualitatively, the theoretical calculations discussed above are due to Anderson and Goldman (1969a,b) (see also Galkin et al. 1968, 1971). These authors have reported voltage-current characteristics, comparing experiments and theory, for small Sn-SnO_x-Sn junctions. The various curves obtained correspond to different values of the parameter γ within a range of temperatures very near the critical. In the theoretical fitting an effective noise temperature of 10 K was considered. Among other factors, such as the external noise, the discrepancy can be due to the assumption $\Omega=1/\beta_J \ll 1$ stated in the theory which was not satisfied to a sufficient degree in these experiments. In fact, junction capacitance and resistance were $C=245$ pF and $R=1.3$ Ω, respectively. This implies that the theory becomes adequate only for extremely small values for the critical current ($I_1 < 10^{-6}$ – 10^{-7} A).

The situation is markedly different for other kinds of superconducting weak links as point contacts, Dayem bridges, or metal barrier junctions. These structures, in fact, display much lower values of the capacitance with respect to tunneling structures with dielectric barriers and therefore better fit into the picture of the overdamped regime. As an example we recall the work by Simmonds and Parker (1970) on Dayem bridges with a capacitance of ~ 3 pF. The agreement with the theory is in this case fairly close. As mentioned in

[†]We do not consider here quantum processes, that is, transition from one metastable state to another (at $T=0$) via tunneling with conservation of energy [see, for instance, early works by Anderson (1963) and Ivanchenko and Zilberman (1968b)]. In connection with fluctuation phenomena, a quantum field theory of a long ($L>\lambda_J$) Josephson junction has been developed by Fetter and Stephen (1968).

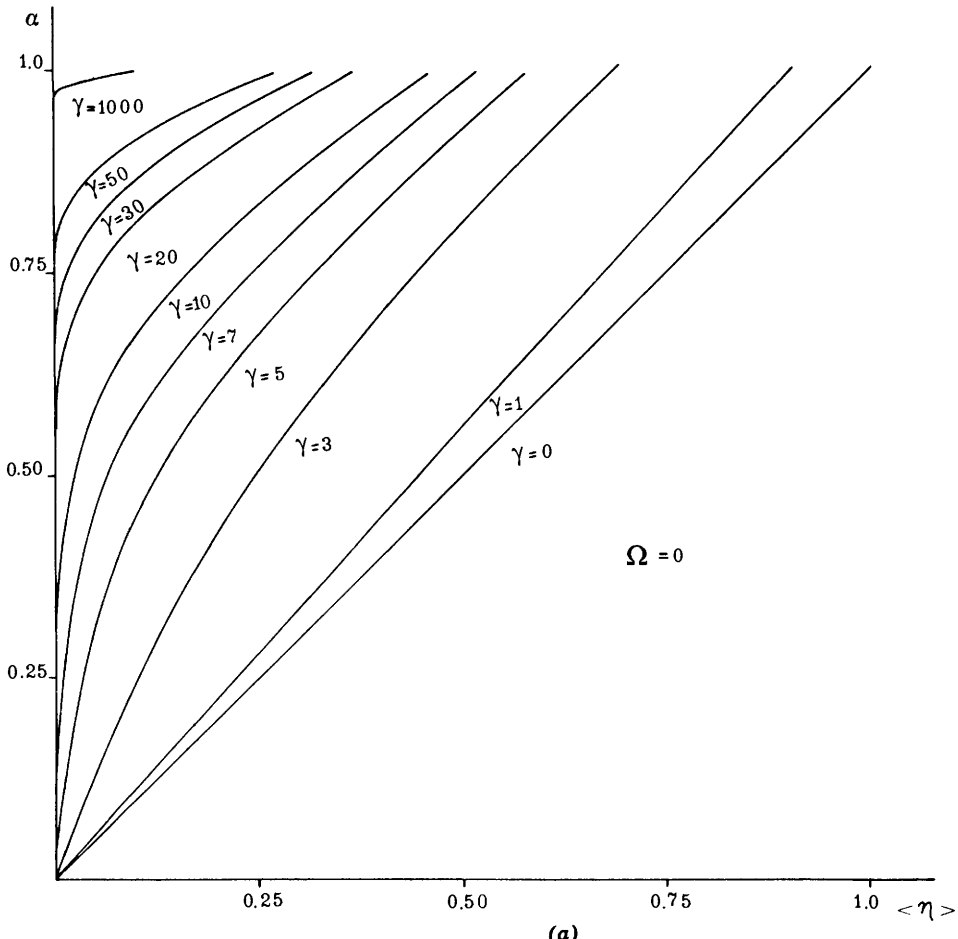


Figure 6.22 Voltage-current characteristics in the presence of thermal fluctuations obtained by numerical integration of (6.4.12) (zero capacitance case). The various curves correspond to different values of the parameter $\gamma = \hbar I_1(T)/(ek_B T)$. Voltage and current are in reduced units: $\alpha = I/I_1$ and $\langle \eta \rangle = \langle V \rangle / I_1 R$. (a) and (b) correspond to the same values of γ but in different scales.

Chapter 1 and discussed in Chapter 7, for this category of weak links deviations of the current phase relation from the purely sinusoidal can occur. This deserves some attention in the context of fluctuations, since the shape of $U(\varphi)$ is modified.[†] In the fitting of the experimental results just mentioned the authors have carefully considered this point. Other measurements have been performed by Falco, Parker, and Trullinger (1973) on weak link structures made by the Notarys-Mercereau normal-metal underlay technique (see the

[†]An extensive discussion of this effect for a variety of current phase relations is given by Auracher and Van Duzer (1972a).

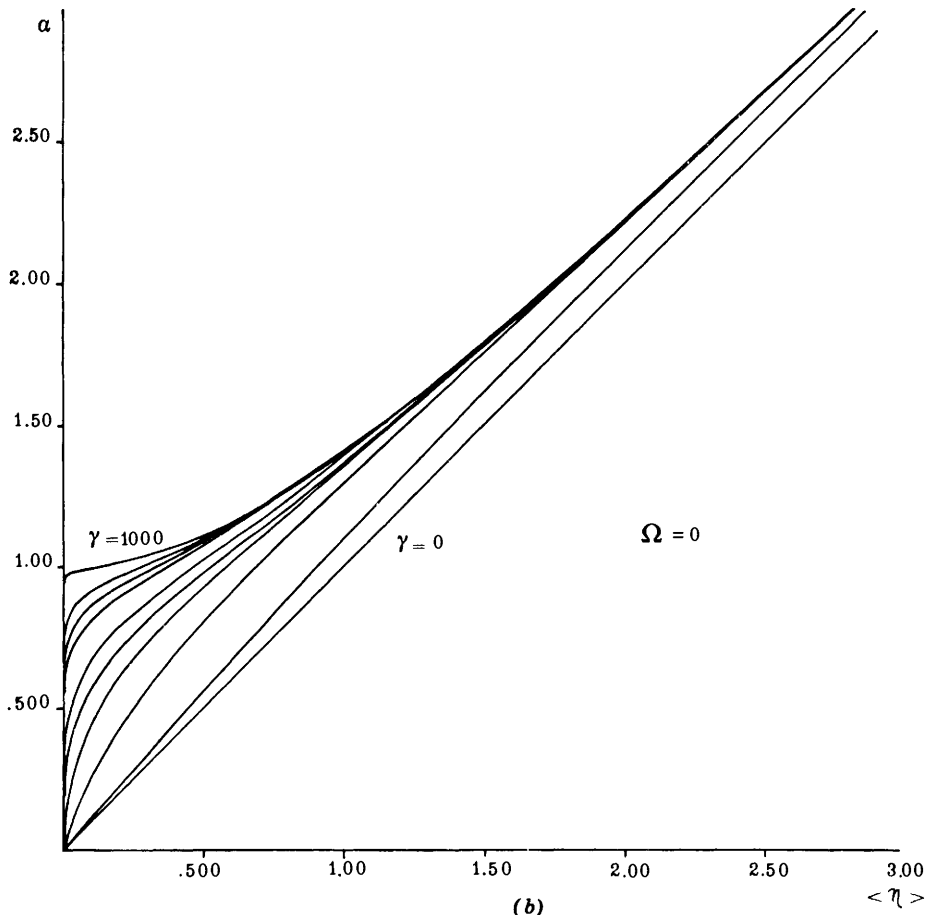


Figure 6.22 (Continued)

next chapter).[†] In that reference, an extension of the theory that accounts for the effect of the $\cos \varphi$ term was also given. It has been also investigated the noise effect on externally shunted tunnel junctions. In this way the results agreed very well with the theory (Falco et al. 1974).

6.4.2 Finite Capacitance. Thus far we have restricted our discussion to the case where the capacitance of the junction is zero. It is important to know under what conditions we may neglect the capacitance. This requires that we return to our original set of equations in the form (6.4.2) and find a proper expansion parameter that will allow us to obtain the lowest order correction for a junction with finite capacitance. This was first treated correctly by Lee

[†]See also the detailed works by Kirschman and Mercereau (1971) and by Decker and Mercereau (1974, 1975).

(1971), whose treatment we follow, using a result obtained by Stratonovich (1967) (see also Ivanchenko and Zil'berman 1968b).

Let $\mathcal{P}(\varphi, V, t)$ be the probability density in phase space, that is, φ and V spaces. It is easily shown that the phase space probability density satisfies the two dimensional F.P.E. (6.4.4).

By introducing the dimensionless parameters

$$v = \frac{2e}{\hbar I_1} p \eta_0 \quad \text{and} \quad \hat{\tau} = \frac{2e}{\hbar} I_1 R_N t$$

The F.P.E. can be written in the dimensionless form

$$\frac{\partial \mathcal{P}}{\partial \hat{\tau}} = -\frac{1}{\Omega} (\alpha - \sin \varphi) \frac{\partial \mathcal{P}}{\partial v} + \frac{1}{\Omega^2} \frac{\partial(v \mathcal{P})}{\partial v} - \frac{1}{\Omega} \frac{\partial(v \mathcal{P})}{\partial \varphi} + \frac{1}{\Omega^2} \frac{\partial^2}{\partial v^2} \left(\frac{2}{\gamma} \mathcal{P} \right) \quad (6.4.13)$$

To evaluate this equation in the case of a small, but finite capacitance we use an expansion technique proposed by Stratonovich (1967). The idea is that for large viscosity, or equivalently for small Ω , the "velocity" distribution should not be very different from the equilibrium one (Maxwell-Boltzmann distribution). In this case, the velocity space is orthogonal to the configuration space and we need only consider the Markov process for the phase φ . Lee (1971) has found that when the phase space probability density $\mathcal{P}(\varphi, v, t)$ is expanded in terms of Hermite polynomials, which is the only expansion consistent with an integrable and everywhere finite probability density, Ω^2 emerges as the natural expansion parameter and not $\Omega(4/\gamma)^{1/2}$, as has been attributed to a physical argument of Kramers (1940) by Ambegaokar and Halperin (1969). That is, defining $A(\varphi) = \alpha - \sin \varphi$ as

$$\Omega^2 \left(\frac{dA}{d\varphi} \right) \ll 1 \quad (6.4.14a)$$

and not

$$\Omega \left(\frac{4}{\gamma} \right)^{1/2} \ll 1 \quad (6.4.14b)$$

should be the criterion that permits us to neglect the capacitance. The interesting point is that Lee's criterion (6.4.14a) corresponds to the condition that is necessary to apply the Smoluchowski approximation, which we discussed earlier. More precisely, the condition for the Smoluchowski approximation is that for time intervals of the order of the relaxation time, η_0^{-1}

$$\frac{\Delta t}{\eta_0 M} \left(\frac{d^2 U}{d\varphi^2} \right) \ll 1 \quad (6.4.15)$$

permits a description of phase fluctuations as a diffusion process in configuration space. Physically speaking, inequality (6.4.15) states that a Fokker-Planck description of phase fluctuations is valid when the external force varies very slowly over fluctuating path trajectories of the order of the relaxation time. This aspect was clarified by B. Lavenda (1979). The same physical content is contained in Lee's condition (6.4.14a).

Thus, to first order in the small expansion parameter Ω^2 , the following F.P.E. in configuration space is obtained:

$$\frac{\partial \sigma}{\partial t} = - \frac{\partial}{\partial \varphi} \left[1 - \Omega^2 \frac{dA}{d\varphi} \right] \left[A(\varphi) - \frac{2}{\gamma} \frac{\partial}{\partial \varphi} \right] \sigma \quad (6.4.16)$$

where σ is the probability density in configuration space, that is,

$$\sigma = \int dv \mathcal{P}(\varphi, v, \tau) \quad (6.4.17)$$

It will now be appreciated that in the limit $\Omega \rightarrow 0$, the case of zero capacitance, the F.P.E. (6.4.16) reduces to the F.P.E. (6.4.8). Following the same mathematical procedure as for $\Omega=0$ we can evaluate the modified current-voltage characteristic due to the first order effects of a finite capacitance:

$$\langle V \rangle = \frac{2}{\gamma} R_N I_1 \frac{\exp(\pi \gamma \alpha) - 1}{\exp(\pi \gamma \alpha)} T_2^{-1} \left(1 + \Omega^2 \frac{T_2}{T_1} \right) \quad (6.4.18)$$

where

$$\begin{aligned} T_1 &= \int_0^{2\pi} d\varphi I_0 \left(\gamma \sin \frac{\varphi}{2} \right) \exp \left[- \left(\frac{\gamma}{2} \alpha \right) \varphi \right] \\ T_2 &= \int_0^{2\pi} d\varphi \sin \frac{\varphi}{2} I_1 \left(\gamma \sin \frac{\varphi}{2} \right) \exp \left[\left(- \frac{\gamma}{2} \alpha \right) \varphi \right] \end{aligned} \quad (6.4.19)$$

and $I_0(x)$ and $I_1(x)$ are modified Bessel functions.

For $\Omega^2 = 0$, the current-voltage characteristic (6.4.18) reduces to (6.4.12). Thus the correction for the finite capacitance is given by $\Omega^2 T_2 / T_1$. The ratio T_2 / T_1 as function of the normalized current is shown in Fig. 6.23 for various values of γ .[†] The effect on the V - I characteristics, due to this correction, leads to a closer agreement with the experiments previously reported.

Among the contributions to the problem of fluctuations in the case of finite capacitance we recall the pioneering work by Ivanchenko and Zil'berman (1968b). It is also worth recalling the theoretical investigation by Kurkijarvi and Ambegaokar (1970) in which the montecarlo method was employed. The underlying physics of their approach, roughly speaking, lies in a description of

[†]Such specific curves, as well as those reported in Fig. 6.22, are computed by F. Esposito (1978).

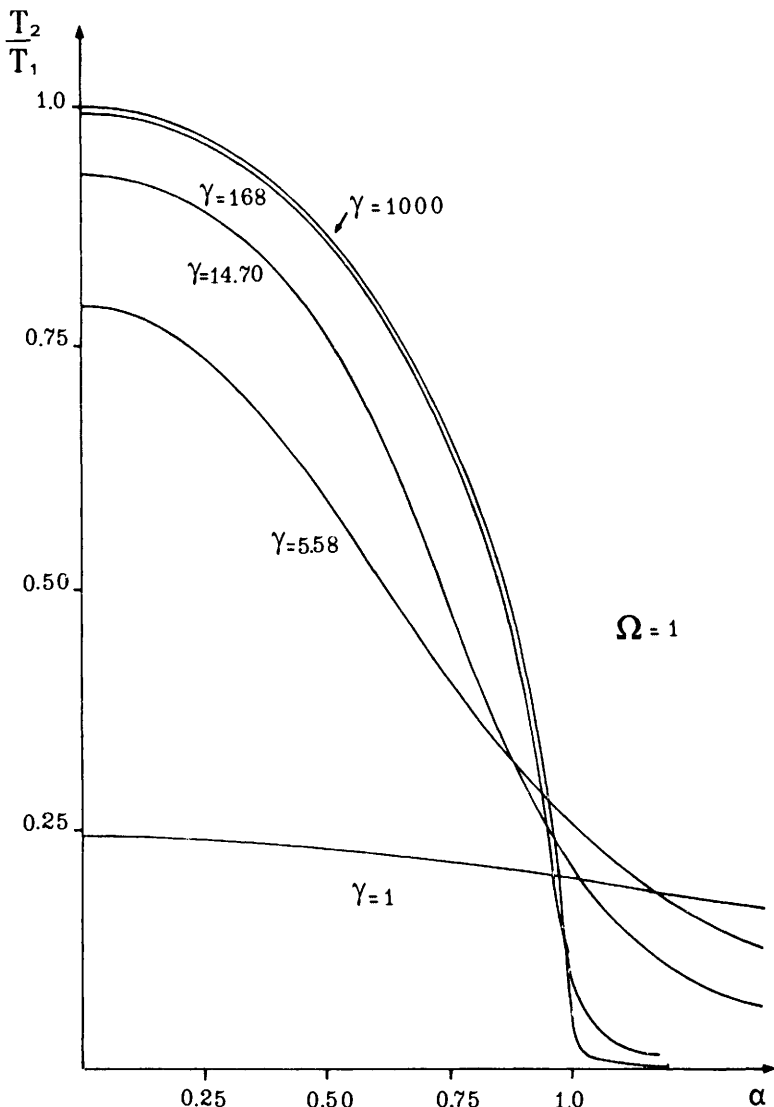


Figure 6.23 Ratio T_2/T_1 (6.4.19) vs. normalized current, α , obtained by numerical integration (finite capacitance case, $\Omega=1$). The various curves correspond to different values of the parameter γ .

the fluctuating term $L(t)$ by random pulses corresponding to collisions with a gas of particles assumed to be in equilibrium. In this work several important features of the V - I curves (For $\Omega \neq 0$) were indicated. The most important are the faster approach to the $v = V/I_1 R$ line with respect to the curves corresponding to $\Omega = 0$ and the crossing of the curves including noise with those in absence of noise (for equal values of Ω). Detailed calculations have been also given in the work of Biswas and Jha (1970). Experimental results in good

agreement with the Kurkijarvi and Ambegaokar analysis have been obtained in the detailed work by Falco et al. (1974).

6.4.3 Large Capacitance. As far as the phenomenology is concerned, we have already mentioned that the main feature of the voltage-current characteristics of large capacitance junctions is the presence of the hysteresis. Referring once more to the mechanical analogy, we can say that this corresponds to the case of small friction. Starting with a “zero average slope” in the curve of $U(\varphi)$ (zero current) let us gradually increase the slope up to a value (critical current) such that the “particle” begins to move down the curve (appearance of finite voltage across the junction). In regard to our hypothesis of small friction, we can assume that the particle can freely run down the slope without being retrapped in a following valley. To describe the full V - I curve we have to go backward, that is, we reverse the slope which is significant in continually decreasing the current. To account for the presence of hysteresis in the V - I curve, we can make the following qualitative argument. We have seen that when the current increases and approaches I_1 , the transition from the zero voltage to a finite voltage state can be “switched on” by the noise that supplied the residual amount of energy necessary to escape from the trough. Conversely, as soon as we begin to reduce the current, we expect the motion of the particle with finite average velocity (finite voltage state) to be much more stable against noise, since a trapping in a valley as a consequence of random fluctuations is unlikely to occur. Thus when the slope is reduced the particle “tends” to remain in motion, that is, when the current is reduced the junction tends to remain in the finite voltage state (hysteretic behavior).

In the case of large capacitance, (6.4.13) in the limit $\Omega \gg 1$ must be considered (Stratonovich 1967). We just mention the result. It is found that the time in which the particle remains in a valley is given by (Lee 1971):

$$\mathfrak{T} = RC \frac{\exp(\gamma|E_m|/2)}{\frac{\gamma}{2}|E_m|}$$

where

$$E_m = \left[\alpha(\pi - 2 \sin^{-1} \alpha) - 2(1 - \alpha^2)^{1/2} \right]$$

is the value of the potential barrier height as function of α . From this we see that as long as γ is large, that is, the temperature is low, the zero voltage current step is extremely stable even at current values rather close to the critical value; in fact, the lifetime \mathfrak{T} depends exponentially on the ratio $|E_m|/k_B T$. Fulton and Dunkleberger (1974b) have performed detailed measurements on Sn-Sn_xO_y-Sn tunnel junctions, in underdamped regime, which led to the evaluation of the lifetime for the metastable zero voltage state as a function of the current bias I_B . Values were found ranging within $\frac{1}{10}$ second and $\frac{1}{10}$ microsecond decreasing roughly exponentially by increasing I_B . To the same extent, this work can be considered to be complementary to those by Jackel et al. (1972, 1974b), which refer to the overdamped case and show good

agreement with theoretical predictions due to Kurkijarvi (1972). We mention that the problem of thermal fluctuations in extended ($L > \lambda_J$) junctions has been approached theoretically (e.g. Zil'berman and Ivanchenko 1970). The analogy between the mean thermal-noise voltage near the critical current and an order parameter for a classical mean-field phase transition has been discussed in a recent interesting paper by Bishop and Trullinger (1978).

6.4.4 Other Noise Considerations. The problem of the noise effect on the properties of Josephson weak links (tunnel junctions, point contacts, bridges, etc.) has attracted and still deserves great attention both in theoretical and in experimental contexts. The reason lies not only in the interest of the underlying physics, which cannot be considered to be completely understood in all aspects, but also in the paramount importance of noise in determining the ultimate limits of the sensitivity in actual devices based on the Josephson effect.

Several detailed studies have been developed taking into account the effects of the intrinsic and or the extrinsic noise in Josephson structures (e.g. Dahm et al. 1969; Zil'berman and Ivanchenko 1971; Likharev and Semenov 1972, 1973; Kalashnik et al. 1972). Among the experiments we recall, besides those already quoted in this section, early works on various types of noise effects carried out by Vant-Hull and Mercereau (1966), Vant-Hull (1968), Buckner, Chen and Langenberg (1970a, b), Kanter and Vernon (1970a, b, c), Vernet and Adde (1971), Henkels and Webb (1971), Vystavkin et al. (1973) Likharev and Ulrich (1978), the recent study on flicker noise due to Clarke and Voss (1974), Kurdyumov (1976), Voss and Clarke (1976), and Clarke and Hawkins (1976).

All the problems concerning fluctuations cannot be considered completely solved. The interested reader going through the papers listed so far and further literature reported therein will find not only detailed explanations and convincing experimental results but also some open questions and stimulating problems.

Before concluding the chapter we outline some results and considerations concerning the expressions of the power spectra related to various noise contributions (see the extensive paper by Rogovin and Scalapino 1974).

The effect of the single particle tunneling to the current noise spectrum has been investigated by various authors (Scalapino 1967; Larkin and Ovchinnikov 1967; Rogovin and Scalapino 1968; Dahm et al. 1969). The expression of this power spectrum is

$$P_{qp}(\omega) = \frac{e}{2\pi} \left\{ I_{qp} \left(V_0 + \frac{\hbar\omega}{e} \right) \coth \left[\frac{1}{k_B T} \left(\frac{eV_0 + \hbar\omega}{2} \right) \right] \right. \\ \left. + I_{qp} \left(V_0 - \frac{\hbar\omega}{e} \right) \coth \left[\frac{1}{k_B T} \left(\frac{eV_0 - \hbar\omega}{2} \right) \right] \right\} \quad (6.4.20)$$

which in the limit of $V_0 \rightarrow 0$ (unbiased junction) reduces to the Johnson-Nyquist formula used at the beginning of this section. When a d.c. bias V_0 is applied across the junction, the system is no longer in equilibrium but just in a steady-state regime. Therefore (6.4.20) has to be regarded as an extension of the Callen-Welton (1951) fluctuations-dissipation theorem (see Rogovin and Scalapino 1974). In the limit $eV_0 \gg \hbar\omega$ expression (6.4.20) reduces to the shot noise formula

$$P_{qp}(\omega) = \frac{e}{\pi} I_{qp}(V_0) \coth \frac{eV_0}{2k_B T} \quad (6.4.21)$$

When eV_0 exceeds $k_B T$ (let us observe that $k_B T/e \approx 360 \mu\text{V}$ at 4.2K) we have the usual expression of shot noise in a diode

$$P_{qp}(\omega) = \frac{e}{\pi} I_{qp}$$

such a temperature-independent noise is related to a random motion of quasiparticle crossing the barrier junction independently. In the limit $k_B T \gg eV_0$ (in addition to the condition $eV_0 \gg \hbar\omega$ which is inherent in the validity of 6.4.21) the power spectrum (6.4.21) gives a classical Johnson noise expression $P(\omega) = 2k_B T/\pi R_N$, since thermal fluctuations dominate. This is an approximate result in that it assumes very small voltage values so that a linear current-voltage relation holds (i.e., a constant value for the differential resistance $R_D = R_N$ is taken).

There is also a contribution to the current power spectrum that arises from the dissipative quasiparticle pair interference term I_{J2} . It is found for unbiased junctions that

$$P_{J2}(\omega) = \frac{e}{2\pi} \left(\frac{\hbar\omega}{e} \right) \sigma_1 \left(\frac{\hbar\omega}{e} \right) \cos \varphi_0 \coth \left(\frac{1}{2} \frac{\hbar\omega}{k_B T} \right)$$

which in the limit $\hbar\omega \ll k_B T$ reduces to

$$P_{J2}(\omega) = \frac{4k_B T}{R_D} \cos \varphi_0$$

with R_D differential resistance for quasiparticles, and for biased junctions

$$\begin{aligned} P_{J2}(\omega) = & \frac{2e}{2\pi} \left\{ I_{J2} \left(V_0 + \frac{\hbar\omega}{2e} \right) \coth \left[\frac{1}{k_B T} \left(\frac{2V_0 + \hbar\omega}{2} \right) \right] \right. \\ & \left. + I_{J2} \left(V_0 - \frac{\hbar\omega}{2e} \right) \coth \left[\frac{1}{k_B T} \left(\frac{2V_0 - \hbar\omega}{2} \right) \right] \right\} \end{aligned}$$

Another contribution is that arising from the Cooper pair current (see the pioneering works by Anderson 1963; Stephen 1968, 1969b, c). The corresponding power spectrum can be written in general as (Rogovin and Scalapino 1969)

$$P_{J1}(\omega) = \frac{2e}{2\pi} \left\{ I_{J1}\left(V_0 + \frac{\hbar\omega}{2e}\right) \coth\left[\frac{1}{k_B T}\left(\frac{2eV_0 + \hbar\omega}{2}\right)\right] + I_{J1}\left(V_0 - \frac{\hbar\omega}{2e}\right) \right. \\ \times \left. \coth\left[\frac{1}{k_B T}\left(\frac{2eV_0 - \hbar\omega}{2}\right)\right]\right\}$$

We observe that this expression is, as in the previous case, in the form of a Callen-Welton fluctuation dissipation relation. This circumstance is extensively discussed by Rogovin and Scalapino (1974) using the nonequilibrium thermodynamic approach given by Bernard and Callen (1951).[†] The similarity with relation (6.4.20) for the quasiparticle current noise is complete except for the charge $2e$, which accounts for the Cooper pair current. In the low frequency limit, $\hbar\omega \ll eV_0$ the expression of $P_{J1}(\omega)$ is just

$$P_{J1}(\omega) = 4|e|I_{J1}(V_0) \coth\left(\frac{|e|V_0}{k_B T}\right)$$

whereas for $k_B T \ll eV_0$ is $P_{J1}(\omega) = 4|e|I_{J1}(V_0)$. The origin of this noise lies in the coupling of coherent pair tunneling to stochastic fluctuations in the thermal photon field.

Another contribution relative to a nonequilibrium steady-state process is due to the coupling of coherent pair tunneling to low density charge fluctuations into the barrier (Anderson plasmons). The corresponding power spectrum is given by

$$P_p = (J_1 \cos \varphi_D)^2 \frac{\hbar\omega_J}{2E_1} \frac{\Gamma/\pi}{[\omega - \tilde{\omega}_J] + \Gamma^2} \coth \frac{\hbar\omega_J}{2k_B T}$$

where $\Gamma = \omega_J/2Q$ is a damping term.

We observe that the supercurrent is not dissipative and coherent that is, pairs cannot fluctuate independently and so cannot be intrinsically a source of noise. However, the contribution to the power spectrum results from the interaction of pairs with barrier excitations: thermal photon field and plasma modes for biased and unbiased junctions, respectively.

[†]It is worth observing that the d.c. pair current process is indeed a nonequilibrium process, although steady state. Equilibrium in fact would imply a minimum junction energy which corresponds to a zero relative phase and thus to the absence of driven supercurrent through the barrier.

CHAPTER 7

Other Superconducting Weak Link Structures

In this chapter we consider Josephson structures that are different from dielectric barrier junctions. We present only the basic ideas rather than an exhaustive discussion of their behavior and the underlying physics.

As we pointed out at the beginning of this book, the Josephson effect occurs in a variety of weakly coupled superconducting structures. The whole phenomenology takes the general definition of “weak superconductivity” (Anderson 1963) which reflects the circumstance that relatively low values of some critical parameters are involved with respect to those in the ordinary superconductivity.

7.1 Metal Barrier Junctions

Let us discuss first a sandwich-type junction which is made by a normal metal barrier layer (S–N–S structure).

Since the first “historical” experiments due to Meissner (1958, 1960), in which measurements were performed on the resistance between two copper-plated tin wires held tightly together at right angles, many investigations have been carried out on normal-superconductor contacts (e.g. Smith et al. 1961; Hilsh 1962; Minnigerode 1966). Some theoretical works to recall are the paper by Parmenter (1960) and among others, those by Fulde and Maki (1965), De Gennes and Mauro (1965), and McMillan (1968a).[†]

7.1.1 Proximity Effect. In a superconductor-normal metal sandwich the two adjacent layers (providing a good electrical contact) influence each other, reducing the superconductive character of the superconductor, that is, of the Cooper pair density near the boundary and, conversely, “extending” the superconducting properties across the boundary into the normal metal.[†] This is roughly the essence of the so-called proximity effect. It is clear, therefore, that this peculiar behavior implies that both the density of states and the effective electron-electron interaction are varying parameters across the N–S structure. Such inhomogeneous systems cannot be described in the framework of the

[†]The reader is referred to the extensive discussions of the proximity effect given by Deutscher and De Gennes (1969) and by Gilabert (1977) and to the references cited there.

B.C.S. theory which assumes translational invariance for the gap. Rather, this problem can be treated by using the theory developed by Gor'kov (1958, 1959). In such a theory the statistical Green functions G and F^+ are used, which are defined as

$$G(\mathbf{r}, \mathbf{r}', t) = -j\langle T\{\psi(\mathbf{r}; 0)\psi^+(\mathbf{r}'; t)\} \rangle$$

$$F^+(\mathbf{r}, \mathbf{r}', t) = \langle T\{\psi_\uparrow^+(\mathbf{r}; 0)\psi_\downarrow^+(\mathbf{r}'; t)\} \rangle$$

where $\psi(\mathbf{r}; t)(\psi^+(\mathbf{r}; t))$ is the usual destruction (creation) operator of an electron at point \mathbf{r} and time t . T is the time ordering operator. G is a single particle Green function in the normal state, and F^+ is related to the existence of the Cooper pairs. In Chapter 2 we considered the Green functions G and F in terms of momentum and energy. Moreover, it can be defined the quantity

$$\Delta(\mathbf{r}) = V(\mathbf{r})F(\mathbf{r})$$

which represents a spatially dependent generalization of the order parameter. $V(\mathbf{r})$ is the effective electron-electron interaction and $F(\mathbf{r}) = \langle \psi_\uparrow(\mathbf{r})\psi_\downarrow(\mathbf{r}) \rangle$ is the pair condensation amplitude. $|F(\mathbf{r})|^2$ represents the probability amplitude of finding a pair at point \mathbf{r} . $F(\mathbf{r})$ is thus related to the local density of pairs and therefore is a actual parameter that gives a measure of the "degree of superconductivity."

On the basis of the Gor'kov results De Gennes, Guyon, and Werthamer (De Gennes and Guyon 1963; Werthamer 1963; De Gennes 1963, 1964, 1966) have developed an extensive theory of the proximity effect.

The spatially dependent order parameter is the solution of Gor'kov's self-consistent linear equation:

$$\Delta(\mathbf{r}) = \int K(\mathbf{r}, \mathbf{r}') \Delta(\mathbf{r}') d^3 r'$$

which is valid for small $\Delta(\mathbf{r})$, that is, when the system is sufficiently close to its critical temperature $T_{C_{NS}}$. More precisely, it is assumed that at $T = T_{C_{NS}}$ ($T_{C_{NS}}$ being the critical temperature of the sandwich) a second order phase transition occurs so that when $T \rightarrow T_{C_{NS}}$ $\Delta(\mathbf{r})$ is small for all \mathbf{r} . Figure 7.1a shows a qualitative picture of the order parameter near the S-N interface. The coherence length is

$$\xi_{N,S} = \left(\frac{\hbar D_{N,S}}{2\pi k_B T} \right)^{1/2}$$

[†]If we consider a sandwich structure of two superconductors S_1 and S_2 having critical temperatures T_{c1} and T_{c2} , respectively, with $T_{c1} < T_{c2}$, then the critical current of the whole system is expected to have a transition temperature higher than T_{c1} .

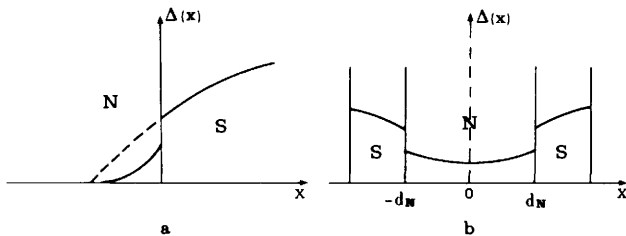


Figure 7.1 Qualitative sketch of the order parameter behavior at temperature close to the critical (see, for instance De Gennes 1964.) (a) N - S system; (b) S - N - S junction.

where $D_{N,S} = \frac{1}{3}v_{F_{N,S}}l_{N,S}$ is the diffusion coefficient with $v_{F_{N,S}}$ the Fermi velocity and $l_{N,S}$ the electron mean free path. N and S refer to the normal and superconductor respectively. In the De Gennes-Werthamer theory it is assumed that $l_{N,S} \ll \xi_{N,S}$ (dirty limit) and that the films are relatively thick. With this assumption the actual details of the structure at the interface $N-S$ become less important and the motion of superconducting electrons can be well described by a diffusion process.[†]

For a semiinfinite normal region $N(-\infty < x < 0)$ the condensation amplitude “transmitted” across the boundary into the normal metal is

$$F_N(x) \simeq F_N(0_-) e^{-K_N|x|} \quad \text{for large } |x|$$

where

$$K_N^{-1} = \left(\frac{\hbar D_N}{2\pi k_B T} \right)^{1/2} = \xi_N$$

represents the penetration depth of pairs into the normal metal. When the “normal” metal N is itself a superconductor ($V_N > 0$) with a relatively low transition temperature T_{cN} ($T_{cN} < T_{cS}$), the exponential dependence for $F_N(x)$ is retained and K_N takes the form ($T \ll T_{cN}$):

$$K_N^{-1} = \left(\frac{\hbar D_N}{2\pi k_B T} \right)^{1/2} \left(1 + \frac{2}{\log(T/T_{cN})} \right)$$

In the general case of arbitrary $|x|$, F_N should be written as $F_N(x) = \sum_{K_N} A_{K_N} e^{-K_N|x|}$ where K_N are the roots of the equation

$$\log\left(\frac{T_{cN}}{T}\right) = \psi\left(\frac{1}{2} - \hbar D_N K_N^2 / 4\pi k_B T\right) - \psi\left(\frac{1}{2}\right)$$

[†]As an alternative to the diffusion theory, it has been also considered a variational theory approach (see Silvert 1974 and references reported).

The function ψ is the logarithmic derivative of the Γ function, that is, of Euler's integral of the second kind (Ryzhik and Gradsteyn 1965).

In the dirty limit, to which we are confined, the boundary conditions for F are (De Gennes 1964) at a metal vacuum (or metal-insulator) surface at the normal-superconductor interface ($x=0$)

$$\frac{F_N(0_-)}{N_N} = \frac{F_S(0_+)}{N_S} \quad \text{and} \quad D_N \left(\frac{dF_N}{dx} \right)_{0_-} = D_S \left(\frac{dF_S}{dx} \right)_{0_+} \quad (7.1.1)$$

The problem of the boundary conditions has been discussed in detail also by Zaitsev (1965, 1966) and more recently by Ivanov et al. (1978) and by Barone and Ovchinnikov (1979).

In concluding this brief discussion on the $N-S$ sandwich it is worth recalling the theory by McMillan (1968a) which assumes the existence of a potential barrier at the $N-S$ interface and films, in the clean limit, of thickness small compared to ξ_S thus preserving the uniformity of the superconductor properties. The passage of electrons across such a barrier is treated by a tunneling Hamiltonian approach. In this model the pair current is governed by the low transmission across the barrier. For experimental verification of the theory we can mention, among others, the work by Gilabert, Romagnan, and Guyon (1971) (see also below).

7.1.2 $S-N-S$ Junctions. Let us consider a superconductor-normal metal-superconductor sandwich ($S-N-S$) with the two $N-S$ boundaries at $|x|=d_N$ (i.e., metal thickness equal to $2d_N$) (Fig. 7.1b). The analysis based on the diffusion approximation previously discussed and the boundary condition 7.1.1. lead to the same current phase relation $I = I_1 \sin \varphi$ as for dielectric barrier junctions ($S-I-S$). The expression of $I_1(T)$, valid for temperatures near the critical T_{cS} ($T_{cS} - T \ll T_{cS}$) in the dirty limit and for both S and N metal layers larger than the coherence length, can be written in the form (De Gennes 1964):

$$I_1(T) \propto (T_{cS} - T)^2 \exp(-2d_N K_N) \quad (7.1.2)$$

Aslamazov, Larkin, and Ovchinnikov (1968) have considered extensively the problem of metal barrier junctions and have found a full solution, assuming a small transparency at the $N-S$ boundary. In their work the current is obtained by perturbation theory for all temperatures and normal metal layer thicknesses. Among other results they found limiting behaviors, including the one reported above.[†]

It is instructive to give a brief outline of the approach proposed by Clarke (1969) which is an oversimplified version of De Gennes analysis. This model assumes that $N_S = N_N$ and $\xi_S = \xi_N$ which implies through 7.1.1 conservation of

[†]For the theory of $S-N-S$ junctions the reader is also referred to the papers by Galaiko, Svidzinskii, and Slyusarev (1969), Svidzinskii, Antsygina, and Bratus (1971), and Ishii (1970, 1972).

F and dF/dx at the $N-S$ boundaries. It is also assumed that $T_{cN}=0$ so that $K_N^{-1}=\xi_N$. Moreover, a simple linear variation of $F_N(x)$ near the boundary, as sketched in Fig. 7.2a, is adopted. The final expression for the maximum supercurrent is found to be

$$I_1(T) \propto |F_0(T)|^2 \left(\frac{\xi_N(T)}{\xi_{GL}^2(T)} \right) \exp[-2d_N/\xi_N(T)]$$

On the other hand, $F_0(T)$, the condensation amplitude inside the bulk superconductors, and $\xi_{GL}(T)$ vary as $(T_{cS}-T)^{1/2}$ and $(T_{cS}-T)^{-1/2}$ respectively, so that the expression of $I_1(T)$ reproduces that by De Gennes (7.1.2) (here ξ_N has replaced K_N^{-1} because of the assumption $T_{cN}=0$). The temperature dependence of ξ_N is neglected since in our hypothesis near T_{cS} the $T^{1/2}$ dependence of ξ_N is rather small with respect to those of F_0 and ξ_{GL} . Let us recall that in the case of dielectric barrier ($S-I-S$ structures) the critical current $I_1(T)$ can be written near the critical temperature T_{cS} as $I_1(T) \propto |F_0(T)|^2$ (De Gennes 1966). Thus for a $S-I-S$ junction I_1 depends on the temperature as $I_1(T) \propto (T_{cS}-T)$ whereas, as we have seen, for a $S-N-S$ structure it is $I_1(T) \propto (T_{cS}-T)^2$.

From the experimental point of view the first and most extensive investigation on $S-N-S$ structures was carried out by Clarke and reported in the reference quoted above. The junctions were lead-copper-lead sandwiches made by a simple evaporation technique. The choice of the metals that form the $S-N$ interface is limited by various stringent requirements such as a very low mutual solubility to avoid interdiffusion and the necessity of not forming intermetallic compounds. The thickness of the metal (Cu) layer was of the order of several thousand angstroms; alloying with about 3% of aluminum provided a shortening of the electron mean free path (see below). Typically the corresponding junction resistance is in the range of 10^{-7} ohms. Such low

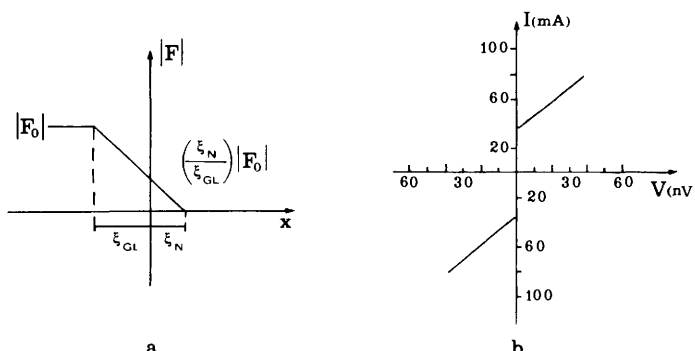


Figure 7.2 (a) Clarke's simple model for the condensation amplitude at the $N-S$ interface. (b) Voltage-current characteristics of an SNS junction at $T=2.98$ K. Normal metal thickness-5520 Å; mean free path $l=140$ Å. (After Clarke 1969.)

values of the resistance require very accurate voltage measurements to indicate whether the sample is in the zero or a finite voltage ($\sim 10^{-10}$ V) state and thereby to detect the critical current value. This is clear from the current-voltage characteristic reported in Fig. 7.2b. For the purpose the voltage drop across the sandwich was measured by a superconducting galvanometer in series with a 10^{-7} ohms resistance (Clarke 1966) with a sensitivity of 10^{-13} V and a time constant of 0.3 second. In Clarke's work are also reported measurements of the maximum critical current density J_1 vs. the barrier thickness in the range of $3 \times 10^3 - 7 \times 10^3$ Å and its temperature dependence. These data are compared with the results of the simplified theory mentioned above which in spite of its crudeness, allows a reasonable fitting. It is found both that the critical current I_1 near T_{cS} depends on $(T_{cS} - T)^2$ and decreases exponentially with increasing thickness of the copper layer. Moreover, it is found that at low temperatures the exponential factor dominates the $I_1(T)$ dependence, that is, $I_1(T) \propto \exp(-\text{const.}\sqrt{T})$. The effect of the electron mean free path l_N is also clearly observed (I_1 decreases with decreasing l_N). Furthermore, the supercurrent magnetic field pattern (I_1 vs. H_a) was investigated, showing the peculiar shape expected for "large" tunneling junctions (see Chapter 5). The finite voltage current carrying states have been also investigated in detail (Clarke 1971).

A Josephson $S-N-S$ junction behavior can be also observed in more complex structures. It is possible in fact to realize by directional solidification, lamellar eutectic alloys as Pb-Sn (Dupart and Baixeras 1975, 1977) or In-Bi-In (Bi) (Truong and Baixeras 1978). These structures are formed in a $S-N-S$ periodic configuration. These series of metal barrier junctions exhibit different behaviors depending on the working temperature T , namely the two situations $S-N-S$ or $S-S'-S$ can be realized for $T > T_{cN}$ and $T < T_{cN}$ respectively. Finally we recall, among others, the careful work on the effect of impurities in the normal barrier layer performed by Niemeyer and Minnigerode (1979) and the very recent paper by Hsiang and Finnemore (1980) (see also references reported therein).

7.1.3 $S-I-N-S$ Structures. An interesting structure, which is related to that previously discussed, consists of a superconductor-insulator-normal-superconductor sandwich (Greenspoon and Smith 1971). In this $S-I-N-S$ structure the coupling of the pair wave function in the superconductor S with that in the proximized sandwich ($N-S$) is realized through a dielectric barrier.[†] Since the Josephson supercurrent is indeed given by the product of the two wave functions in the two sides of the barrier (De Gennes 1966), such structures appear to be particularly useful in studying the proximity effect in the normal region. From the experimental point of view the $S-I-N-S$ junction configuration allows the investigation of the proximity effect by Josephson tunneling, avoiding the problems due to the extremely low resistance of $S-N-S$ structures. From a theoretical point of view this circumstance permits a greater consistency with the theoretical analysis developed

[†]SNINS structures have also been considered (e.g., Zaikin and Zharkov 1978).

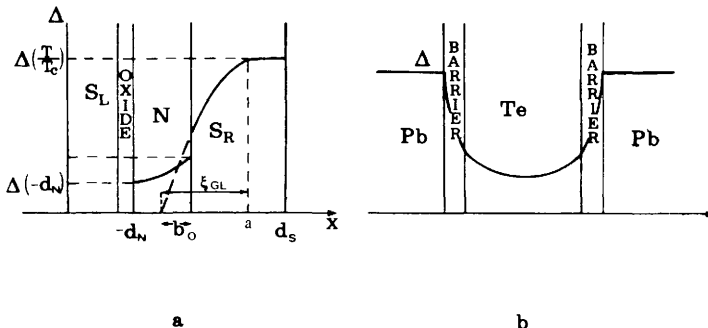


Figure 7.3 (a) Sketch of a $S-I-N-S$ structure with the assumed order parameter throughout the left superconducting layer and the $N-S$ sandwich. (After Rowell and Smith 1976.) (b) Qualitative model of a superconductor-semiconductor-superconductor junction with the assumed position dependent pair potential. (After Seto and Van Duzer 1972.)

within the assumption of low transparency. Theoretical implications of the analysis of these sandwiches are important also in the context of semiconductor barrier junctions.

We outline here the simplified picture given by Rowell and Smith (1976). (The system is that sketched in Fig. 7.3a.) As before, the x axis is taken to be normal to the sandwich structure, with its origin at the $N-S$ boundary. It is assumed that the order parameter in the superconducting layer S_R (i.e., $0 < x < d_s$) is described by the linear Ginzburg-Landau equation $\Delta = \Delta_0(T/T_c)\sin \pi[(x+b)/2\xi_{GL}]$ within the region $0 < x < a$ and by the B.C.S. theory $\Delta = \Delta_0(T/T_c)$ within the region "far" from the $N-S$ interface. The expression for the order parameter in the normal metal (i.e., $-d_N < x < 0$) is that of Werthamer for a finite layer previously discussed. Moreover, the boundary conditions used in this analysis are those of De Gennes (7.1.1). The final expression of the d.c. supercurrent is then found in which I_1 is proportional to the product of the two order parameters: one holds throughout the superconductor layer S_L and the other is in the N region at the free surface of the normal metal ($x = -d_N$). (For details see Rowell and Smith 1976.)

In spite of the simplicity of this scheme, the experimental results obtained by Rowell and Smith (1976) on the temperature dependence of the d.c. Josephson current can be well fitted by the theoretical calculations as shown in Fig. 7.4. The data refer to $\text{Sn}-\text{Sn}_{x}\text{O}_y-\text{Zn}-\text{Sn}$ structures. The full lines are the theoretical behaviors. Dots indicate experimental data. The figure is self-explanatory; we might just point out that the curves a to f correspond to increasing values of the ratio d_N/l_N . For smaller values of this ratio, that is, as long as $d_N \sim l_N$, a behavior close to that predicted by Ambegaokar and Baratoff for $S-I-S$ structures, is found. At larger values the depression of the order parameter emerges. Details of these experiments and various theoretical aspects on the generalized Ginzburg-Landau equation in the context of the proximity effect can be found in the paper by Blackburn, Smith, and Rowell (1975).

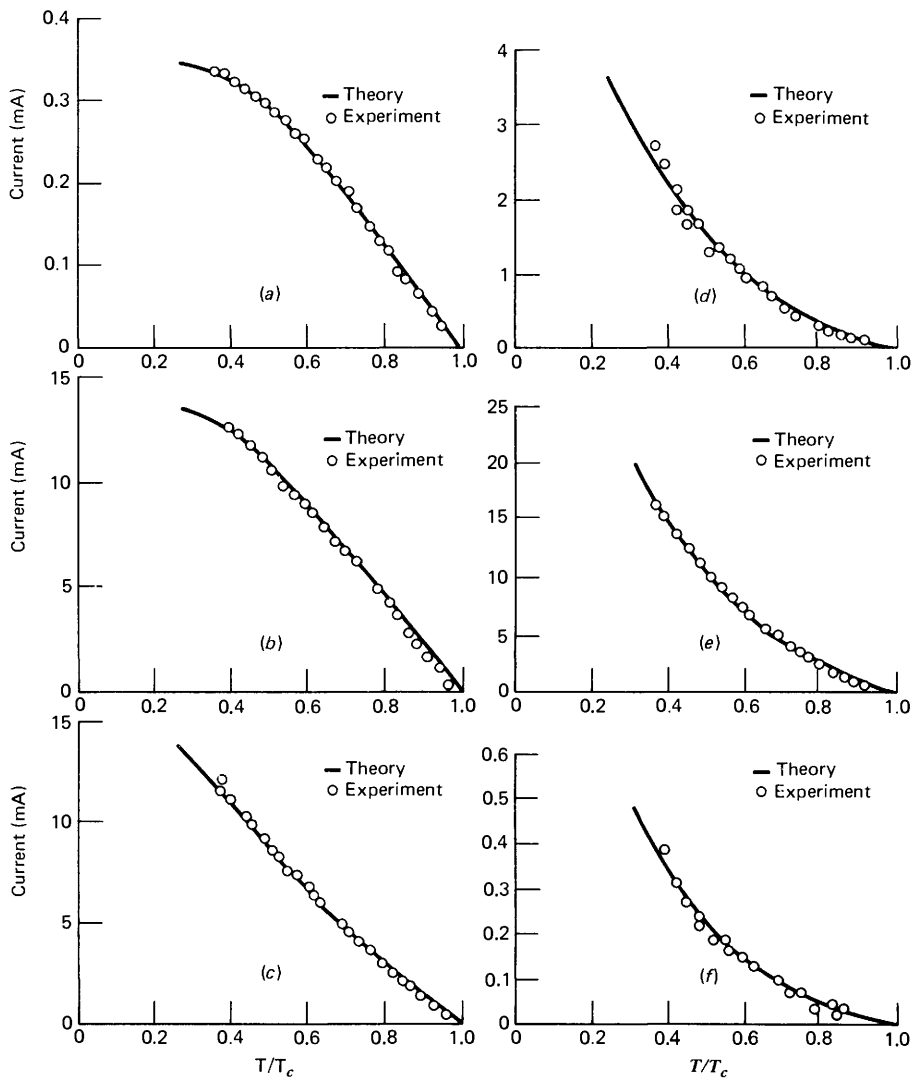


Figure 7.4 The Josephson current vs. reduced temperature for S-I-N-S structures. Data refer to Sn-Sn_x0_y-Zn-Sn structures. (a) $T_c = 3.68$ K, $d_N = 600$ Å, $I_N = 845$ Å. (b) $T_c = 3.60$ K, $d_N = 1200$ Å, $I_N = 1180$ Å. (c) $T_c = 3.34$ K, $d_N = 2400$ Å, $I_N = 916$ Å. (d) $T_c = 3.43$ K, $d_N = 3600$ Å, $I_N = 1130$ Å. (e) $T_c = 3.44$ K, $d_N = 3600$ Å, $I_N = 1110$ Å. (f) $T_c = 3.32$ K, $d_N = 3600$ Å, $I_N = 725$ Å. (After Rowell and Smith 1976.) (Reproduced by permission of the National Research Council of Canada.)

Regarding the investigations of these inhomogeneous sandwich structures $S - I - N - S$ we recall the work, previously mentioned by Greenspoon and Smith (1971), on Pb-PbO-Cu-Pb junctions[†] and by Romagnan et al. (1974) in which the proximity occurs between a superconductor ($N = S_N$) and a "stronger" superconductor ($S = \text{Pb}$) in a Pb-PbO-Sn-Pb sandwich. Aluminum-lead superimposed films ($N = \text{Al}$, $S = \text{Pb}$) have been employed as counterelectrodes in niobium based junctions. A detailed investigation on these structures has been carried out by Folens, Schwidtal, and Bruynseraeede (1976).[‡] It is also worth recalling the results obtained by Hauser (1967) on structures in which N is magnetic. The actual samples were in this case CrPb-I-PbCr and Pb-I-Pb (see also Chapter 3).[§]

So far we have considered experiments on the temperature dependence of the critical current in $S - I - N - S$ junctions whose results were interpreted essentially in the framework of the Ginzburg-Landau theory. Such a theory stems from the hypothesis that the temperatures are near the critical and that the dirty limit conditions are verified. However, in actual experiments with proximized structures these assumptions are not, or are only to some extent, verified. It is interesting therefore to resort to the McMillan theory (1968a) which does not require these conditions. It is worth observing that the two types of theories, although different in nature and starting from the opposite limits of "clean" and "dirty" conditions, lead essentially to the same qualitative features of the $I_c(T)$ dependence (see, for instance, recent calculations by Mori, Kodama, and Ozaki 1978). In a recent detailed work on $\text{Nb-Nb}_x\text{O}_y - \text{Al}/\text{Pb}$ and $\text{Nb-Nb}_x\text{O}_y - \text{Cu}/\text{Pb}$ proximized structures (Gilabert et al. 1979) the experimental dependence of the Josephson critical current was investigated and the results were found in good agreement with the McMillan theory.

Finally, we mention a peculiar effect expected in $S - I - N - S$ structures by some theoretical considerations (McMillan 1968b). This model in fact assumes that the discontinuity of the pair potential at $N - S$ produces spatial oscillations of the pair amplitude $F(x)$ that invert the sign at $x = -d_N$ when the temperature changes. This in turn would lead to an anomalous behavior of the critical current. This effect has not been experimentally confirmed. There are some results that could be interpreted in this framework (e.g., Clarke and G. A. Hawkins 1974); however, the extensive experiments by Van den Dries et al. (1979) seem to exclude unambiguously any anomaly.

7.2 Semiconducting Barrier Junctions

Another class of sandwich-type junctions employs semiconductors as a barrier layer. One of the reasons why such structures have been investigated is the

[†]See also Vrba and Woods (1971a,b) for Cu-Pb and Al-Sn proximized electrodes.

[‡]See also Cucolo, Pace, and Parmentier (1977) and the recent paper by Matsuda, Inamura and Yoshiakiyo (1980).

[§]Other features that can be interpreted in the framework of the proximity effect are often observed in niobium based junctions (see also Section 6.3.2).

inherently large capacitance of the oxide barrier junctions, which can be viewed as a drawback in some applications. In the case of a semiconductor because of the reduced barrier height, it is expected to get reasonable values of the maximum current density without critically decreasing the junction barrier thickness. The results collected so far are, however, not yet satisfying enough to make such structures competitive with oxide junctions. Nevertheless, devices using deposited semiconductor barrier have potential.

7.2.1 Barrier Layers of Various Semiconductor Materials. The semiconductors that have been employed as a tunneling barrier include CdS, CdSe, C, Te, Ge, InSb, Tl, ZnS, PbTe, GaAs, and PbS. Josephson tunneling was observed using CdS, Te, PbTe, Ge, InSb and Si. We point out here the main features and performances of these structures and postpone to Chapter 8 the various aspects of their preparation.

As will be discussed, devices of particular physical interest are obtained using photosensitive semiconductor materials, which are also the first semiconducting barrier junctions ever investigated (Giaever 1968; Giaever and Zeller 1970).

In semiconducting barrier junctions both their performance and a suitable interpretation of their behavior are limited by such problems as interdiffusion at the barrier boundaries, existence of surface states, uncontrolled doping, the amorphous-polycrystalline structure of many deposited semiconductor films, and the presence of pinholes even in films as thick as 1000 Å. These pinholes in turn lead to parallel shunting paths for the current. To avoid this problem, an oxidation step after the semiconductor layer deposition can be performed. However, this procedure for filling the pinholes is not innocuous; the oxygen in fact can produce drastic modifications in the structure, such as doping and a series of oxide barriers either by oxidation of the semiconductor layer or by oxidation of the top electrode (this would be caused by the underlying oxygen adsorbed by the semiconductor). These and other problems lead us to conclude that the knowledge of various parameters, such as the effect of the doping in bulk materials and the values of the work function in semiconductors and superconducting electrodes, is only relatively significant, since the behavior of the whole junction drastically depends on the structure of the film, which is mainly related to the specific deposition technique, the actual details of the semiconductor-superconductor interface, and so on.

Leaving aside the CdS barrier junctions, which are extensively discussed in the next section, let us consider now the most common semiconductors employed in the context of the Josephson effect. By using germanium in very thin layers (~ 50 Å), junctions that exhibit critical current density above 30 A/cm² can be obtained. We recall the earlier observations by Lipson and Stupel (1970) on Sn-Ge-Sn junctions. Keller and Nordman (1971) realized niobium based junctions (with Pb or Sn counterelectrode) which exhibit rather clean voltage-current characteristics with a defined gap structure and a current-magnetic field periodicity. Similar results were also obtained by these

investigators using indium antimonide barriers. Another semiconductor material that has been investigated in this context is tellurium (Cardinne, Marti, and Renard 1971; Cardinne, Manhes, and Renard 1972; Seto and Van Duzer 1971, 1972). It is interesting to observe that in the work by Cardinne et al. the quasiparticle structures in the V - I characteristics was evident though with the presence of a leakage current; the gap value however appears to be smaller than that expected from the lead superconducting electrodes. These authors suggest that this effect is related to the interdiffusion between lead and tellurium which leads to a PbTe layer in the structure. The corresponding barrier shape can be modeled as in Fig. 7.5. In the same figure proposed barrier models for surface state dominated semiconductors are also sketched (Cardinne, Nordman, and Renard 1973).

An extensive investigation of tellurium barrier junctions from both experimental and theoretical points of view was reported by Seto and Van Duzer (1971, 1972). They performed experiments on Sn-Te-Sn evaporated junctions which employ semiconducting barrier thickness up to 800 Å. The theoretical model assumes that tellurium can be considered to be a degenerate p -type semiconductor and that two Schottky barriers are formed at the semiconductor-lead interfaces (see Fig. 7.3b). The corresponding barrier shape is sketched in Fig. 7.5d. The dependence of the critical current on the temperature and the tellurium barrier thickness is discussed in the light of De Gennes theory following arguments similar to those in the preceding sections. The coherence length for the degenerate semiconductor layer in the framework of the free

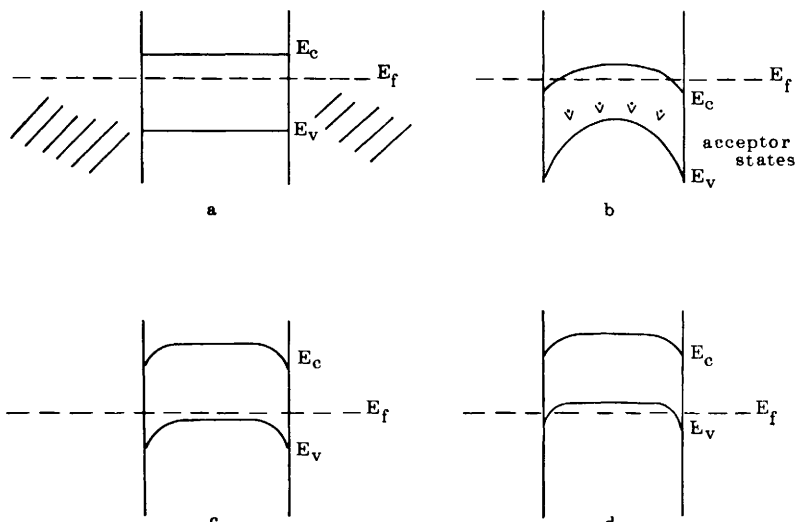


Figure 7.5 Qualitative sketch of the energy barrier models. (a) Ideal barriers; (b) barrier model without surface states; (c) and (d) barrier models with surface states; amorphous material (Ge, InSb) and degenerate p -type Te respectively. E_f is the Fermi level, E_v is the top of the valence band and E_c the bottom of the conduction band. (After Cardinne, Nordman, and Renard 1973.)

electron model can be defined as

$$K_N^{-1} \simeq \xi_N = \left(\frac{\hbar^3 \mu}{6\pi k_B T_{cm^*}} \right)^{1/2} (3\pi^2 n)^{1/3}$$

where μ is the temperature independent electron mobility, m^* is the electron effective mass, and n the carrier density. As before, it is assumed that T is higher than the transition temperature of the semiconductor. The barrier is supposed to be thick enough so that the pair potentials can be assumed to be constant inside the superconductors. The resulting I_1 vs. T dependence obtained by Seto and Van Duzer appears to be characterized by three different behaviors. The first recalls the Ambegaokar and Baratoff dependence of the oxide barrier junctions and corresponds to the Schottky barrier dominated region. The second consists of an exponential decrease of the current and corresponds to the region in which it is the bulk semiconductor that "drives" through the variations of the pair potential $\Delta(r)$. Finally, there is a region that corresponds to intermediate behaviors. Seto and Van Duzer gave the fitting of their experimental data and those by Cardinne, Manhes, and Renard (1972). Of course the quality of the fitting of the latter results also depends on the value adopted for the coherence length in the semiconductor, which can be more or less realistic depending on the actual carrier concentrations and mobilities. The behavior of the supercurrent as a function of the barrier thickness for these structures produces the exponential dependence as in oxide barrier junctions if carrier concentration and mobility can be assumed to be constant. In practice this is not the case because of the lack of a suitable control of these parameters in evaporated sandwiches.

Finally, the single crystal silicon membrane structures realized by Huang and Van Duzer (1974a,b) are worth mentioning. These structures are of particular interest, since they avoid many of the problems related to the deposition of semiconductor layer (see the next chapter).

7.2.2 Light Sensitive Semiconducting Barrier Junctions. Since the pioneering experiments carried out by Giaever (1968) on light sensitive CdS barrier junctions, there has been an increasing interest in these investigations (Giaever and Zeller 1969a,b; Russo 1971; Dynes and Fulton 1971; Barone, Rissman, and Russo 1973).

Light sensitive semiconductors provide for the making of superconductive tunnel junctions with an adjustable barrier height. As we shall see, depending on the specific optical inputs, the light induced modifications of the barrier can lead to a wide number of situations for a given sample, which offers an important physical insight of the behavior of a Josephson junction. Moreover, it indicates a stimulating perspective of possible components that can be optically controlled. In practice light sensitive Josephson junctions have been obtained only by using the CdS barrier, whereas photosensitivity was observed

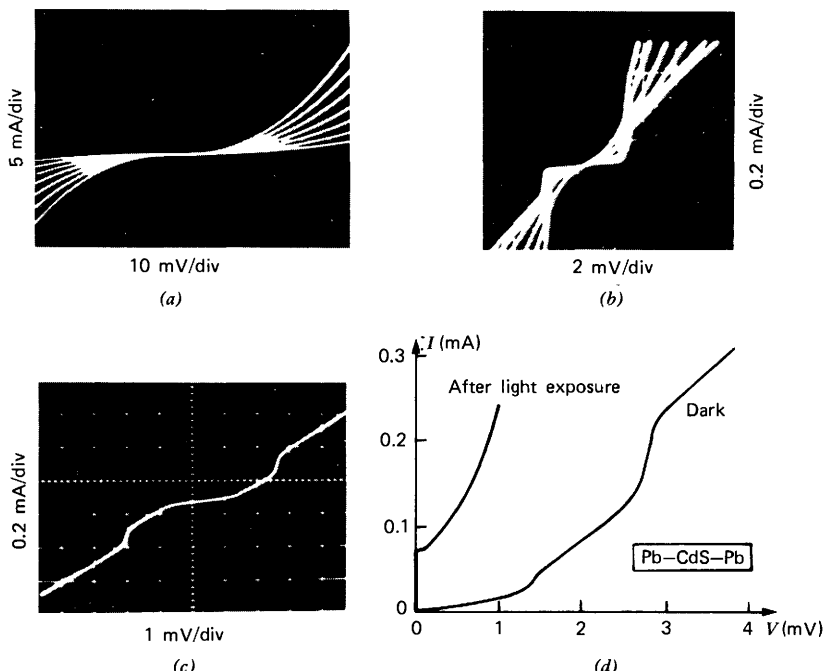


Figure 7.6 Optical response of Pb-CdS-Pb junctions. All V - I characteristics are at 4.2 K; the optical input is realized by an electronic flash. (a) Light induced resistance change on a structure with $t > 500 \text{ \AA}$. (b) Light sensitive quasiparticle tunneling. (c) "Dark" V - I characteristics of a low impedance junction. (d) Light induced Josephson effect in the junction shown in (c). (After Barone, Rissman, and Russo 1973.)

also in quasiparticle tunneling junctions employing CdSe (Rissman 1973).[†] Detailed experimental investigations were reported by Barone, Rissman, and Russo (1973) on CdS and CdSe barriers using also various electrode materials such as Sn, Pb, and Nb and by Barone and Russo (1974) using In. In Fig. 7.6 is reported the optical response of Pb-CdS-Pb sandwiches. Figure 7.6a shows light induced resistance change in a structure with a semiconductor barrier thicker than 500 \AA . In Fig. 7.6b is shown a fully developed tunneling structure ($t \sim 200 \text{ \AA}$) and its light sensitive behavior. The various curves from lower to higher resistance correspond to an increasing number of light flashes. Figure 7.6c shows V - I characteristics of a junction ($t < 150 \text{ \AA}$) in dark conditions. Figure 7.6d refers to the same junction with a light induced Josephson current. Thus exposure to light modifies the barrier characteristics leading to a decrease of the junction tunnel resistance. In Fig. 7.7 are reported more recent results using various electrode materials. Giaever and Zeller gave a rather simplified

[†]Among other works on photosensitive tunnel junctions it is worth recalling the papers by Mehbd, Thijs, and Bruynseraede (1975), Tsuboi (1976), and Deutscher and Rappaport (1979).

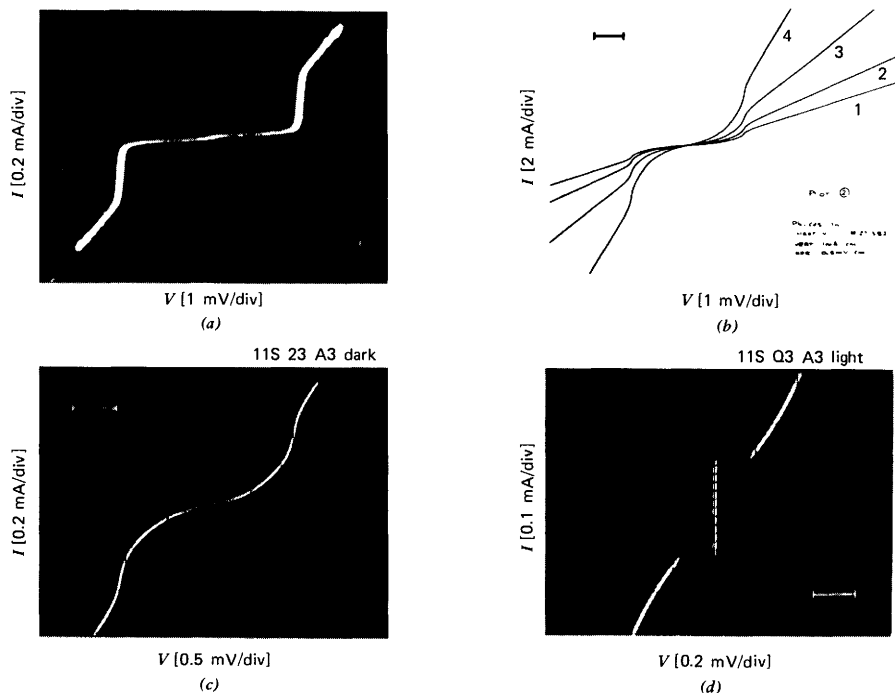


Figure 7.7 Optical response of light sensitive junctions. $V-I$ characteristics at 4.2 K. (a) Gap structure of a $\text{Pb}-\text{CdS}-\text{Pb}$ sample with a thin ($\sim 100 \text{ \AA}$) CdS barrier layer. (b) Effect of the light on the normal resistance of a $\text{Pb}-\text{CdS}-\text{In}$ sample. (c) and (d) $\text{In}-\text{CdS}-\text{In}$ junction in dark condition and after light exposure respectively. (After Barone, Russo, and Vaglio 1978.)

explanation of this behavior (see also Radhakrishnan 1970) in terms of an effective barrier lowering due to trap states for photoholes. The extremely long recombination time of these traps (Bube 1963) leads to the conductivity storage effect that is observed in the experiments. It is possible to reset the sample to its original state (dark conditions) either by pulsing it with high current or by warming it up to above 100 K. The underlying physical mechanisms are not clearly established in the two cases; it is not clear whether both effects are thermal.

It is also worth remembering that in cadmium sulfide barriers a competition of different tunneling mechanisms can occur. There can be, in fact, not only a "straightforward passage" of electrons through the semiconductor, but also an "indirect passage" through cadmium particles imbedded in the CdS. This has been clearly demonstrated by the experiments of Josefowicz and Smith (1973).

As we shall see in Chapter 8, CdS barrier junctions can employ quite different values of the semiconductor layer thickness depending on the superconducting electrode material: 100 to 200 \AA for $\text{Pb}-\text{CdS}-\text{Pb}$ junctions up to 700–800 \AA or more for $\text{In}-\text{CdS}-\text{In}$ sandwiches. This indicates that the nature of

the contact superconductor-semiconductor plays an essential role. In the case of a Pb-CdS interface, the difference in the work functions leads to the presence of a significant potential barrier, whereas interdiffusion occurring between In and CdS leads to a stable ohmic contact In-CdS (Bube 1960). Let us consider a Pb-CdS-In junction. We can assume that such a structure possesses a very asymmetric barrier which under conditions of light should be confined to the Pb-CdS boundary. The In-CdS interface can be roughly considered as a degenerate layer and to some extent approximated to a normal metal layer. Hence we can regard the Pb-CdS-In junction as a superconductor-insulator-normal metal-superconductor ($S-I-N-S'$) and discuss its behavior in the framework of the proximity effect. Such a sandwich configuration is similar to that employed by Rowell and Smith (Section 7.1.3). Following a slightly modified version of their analysis it is possible to obtain the value of the supercurrent with its explicit dependence on the temperature (Andreozzi et al. 1978). Experimental results compared with theoretical behavior predicted by this approach are reported in Fig. 7.8a, b. Similar results were obtained by Gilabert et al (1979) and interpreted by the McMillan (1968a) model. The data refer to the temperature dependence of the light induced d.c. Josephson current in In-CdS-In and Pb-CdS-In junctions (a and b respectively). We observe that in the case of asymmetric junction (Pb-CdS-In) the curve suddenly increases near T_c , whereas in the case of symmetric junction (In-CdS-In) the supercurrent increases almost linearly with temperature near T_c . Thus, within the high temperature range ($T \sim T_c$), the behavior expected for both symmetrical and asymmetrical oxide barrier structures is reproduced (see Chapter 3). However, as for other proximized structures discussed in this chapter, at lower temperatures the curves do not exhibit any saturation. Indeed, in a proximity $S-I-N-S$ structure the unobservability of current saturation can be related to the circumstance that N layers of relatively large thickness are considered in combination with not low enough temperatures (Gilabert 1979 et al.). In Fig. 7.8c the supercurrent vs. temperature dependence for a given junction is reported for two different light exposure levels.

Recently a microscopic approach to describing the behavior of this type of junctions has been discussed by Aslamazov and Fistul (1979). (See also Alfeev, 1979 and Alfeev et al. 1979).

As mentioned at the beginning, because of the possibility of adjusting the effective barrier by means of light exposure, a light sensitive junction may simulate various situations though studying a single sample. It is possible for instance, as demonstrated by Barone et al. (1975b), to observe in a given junction the behavior of both a small and a large junction (i.e., $L/\lambda_J < 1$ or $L/\lambda_J > 1$, respectively) depending on the light exposure level. The transition between the two behaviors is clearly shown in the supercurrent-magnetic field dependences reported in Fig. 7.9. We see in fact the two limiting cases of a Fraunhofer-like pattern typical of a small junction and the quasilinear dependence expected for a large cross geometry junction (see Chapter 5). The interpretation of the transition from a small to a large junction is obvious.

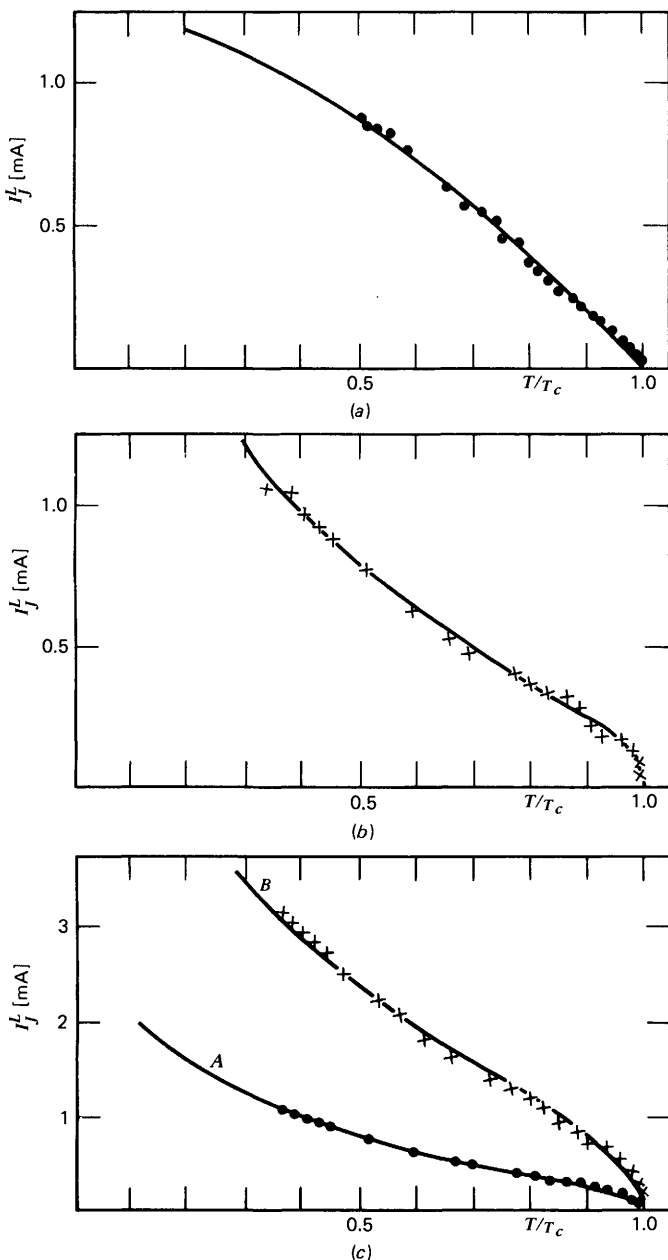


Figure 7.8 Temperature dependence of the light induced d.c. Josephson current. Experimental data are compared with the theoretical behavior (solid curve) predicted by a proximity effect model. (a) In-CdS-In structure. (b) Pb-CdS-In structure. (c) The two curves refer to two different values of the light induced critical current in the same sample (Pb-CdS-In). (After Andreozzi et al. 1978.)

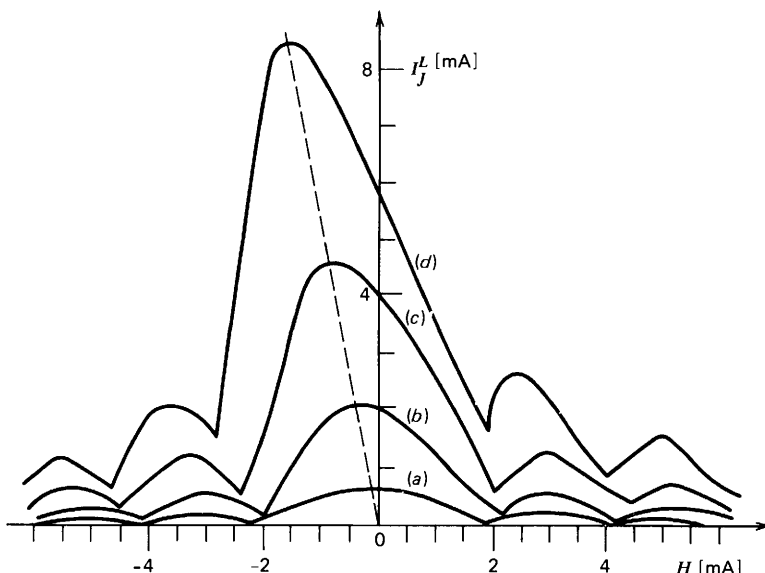


Figure 7.9 Critical current vs. externally applied magnetic field for increasing light induced current level in a given sample (Pb-CdS-In). It is interesting to observe the transition from "small" (a) to "large" junction behavior (b, c, d). (After Barone et al. 1975b.)

The increase in the light input level enhances the supercurrent; correspondingly the Josephson length decreases and the ratio L/λ_J increases.

Furthermore, by varying the transparency of the top film layer (by changing its thickness) it is possible to observe, through the I_1 vs. H dependence, a single junction behavior (Fraunhofer diffraction pattern) or a double junction behavior (interferential pattern), which correspond to situations of uniform illumination or edge localized illumination, respectively. The last circumstance also suggests the possibility of making two (or more) junction interferometers like those employed in computer circuits (see Chapter 14) by suitable selective illumination of the sample but keeping constant the physical barrier thickness. Furthermore, we mention the interest of light sensitive junctions in studying the effect of structural fluctuations in the barrier (Chapter 3, Section 4.4.2). The potential of light sensitive Josephson junctions has been discussed by Barone, Russo, and Vaglio (1978), together with a summary of the various investigations performed on these structures.

7.3 Bridge-Type Junctions

An important class of Josephson weak links is that employing planar configurations, that is, when the electrodes and the link lie in the same plane.[†] The first weak link of this kind was investigated by Anderson and Dayem (1964)

[†]For the whole section the reader is referred also to the excellent review by Likharev (1979).

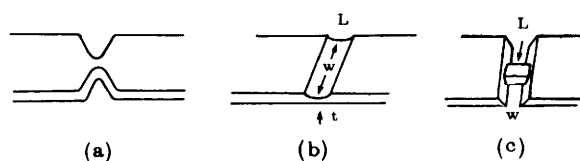
and almost simultaneously by Lambe et al. (1964) and by Parks, Mochel, and Surgent (1964). The structure is in this case a single thin film in which two relatively large superconducting regions (electrodes or banks) are linked by a narrow bridge. Such a thin film constriction-type weak link behaves as a Josephson element whenever the dimensions of the bridge linking the two electrodes are smaller than (or at least comparable with) the temperature dependent coherence length of the bridge $\xi(T)$. There is a large variety of techniques for producing these structures, including mechanical procedures, fiber masking techniques, and photo or electron beam lithography (see Chapter 8).

In Fig. 7.10 are sketched two different thin film structures: (a) constant thickness bridge (C.T.B.) or "Dayem bridge" and (b,c) variable thickness bridge (V.T.B.). The latter can be realized either by a reduction of the film thickness in the link region (b) or by both a thickness and width constriction (c).

In Fig. 7.11 is shown an actual variable thickness indium microbridge made by using a two step electron beam lithography process (Sandell, Dolan, and Lukens 1976; Lukens, Sandell, and Varmazis 1978). The bridge itself is 500 Å thick and the banks are 2000 to 3000 Å thick.

In our discussion we often use the symbol L to indicate the physical length of the bridge (spacing between the banks) although the actual parameter may be some effective length L_e larger than the geometrical length because of the extension of the modifications of the order parameter into the electrodes, which can be due to link-electrode proximity effects and to currents flowing in the electrodes. Indeed, besides geometrical ones, the lengths that characterize these weak link structures are the following: the effective length of the link L_e , the coherence length $\xi(T)$, the electron mean free path l , and the magnetic field penetration $\lambda(T)$. The relation between L_e and ξ , $L_e < \xi$, and $L_e \gtrsim \xi$ provides a classification of "short" and "long" links respectively, whereas $l \ll L_e$ and $l \geq L_e$ define "dirty" and "clean" structures.

Let us observe that the actual bridge region in the weak link structure can be either a normal metal ($S-N-S$ link) or a superconducting metal ($S-S'-S$ link) with a critical temperature T_c smaller than that T_{cB} , of the banks. Indeed even for $T_c > T_{cB}$ it is possible to realize a weak link structure by varying the



C T B

V T B

Figure 7.10 Different thin film bridge structures. (a) Constant thickness bridge (C.T.B.) or "Dayem bridge". (b), (c) variable thickness bridges (V.T.B.).

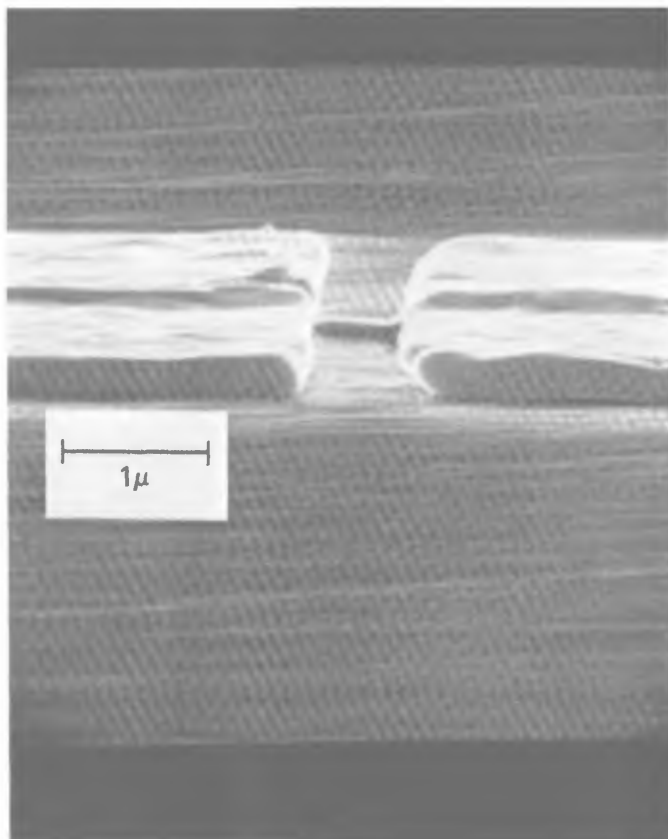


Figure 7.11 Variable thickness indium microbridge made using a two step electron beam lithography process. Bridge and banks approximately 500 and 2000 Å thick respectively. (Courtesy of R. D. Sandell, S.U.N.Y, Stony Brook.)

relative magnitudes of the critical currents of the bank I_{cB} and the bridge I_1 . In this case it has to be $I_1 < I_{cB}$.

In a C.T.B. Josephson link the conditions to be satisfied are that both the length and the width of the bridge be smaller than or of the same order as the coherence length, that is $L \approx \max[L, W] \lesssim \xi$. This condition implies that difficult technological procedures are needed to fabricate links with both planar dimensions of about, say, $\frac{1}{10} \mu\text{m}$, which is a rather typical value of the coherence length. V.T.B. link structures overcome such difficulties. In this case, in fact, the condition to be satisfied (see below) is

$$d_L \ll \min[d_B, l_B], \xi, L$$

where d_L indicates the film thickness and subscripts L and B refer to bridge and banks, respectively.

Thus in the V.T.B. link there would be no restriction in the width of the structure provided that a superconducting ground plane underlies the link, which guarantees uniform current distribution (see Chapter 5) both below and above the critical current, avoiding vortex penetration. However, when a bridge becomes very wide, it approaches a C.T.B.-like behavior since it can be regarded more like a very thick C.T.B. link turned on its side.

Another important class of weak links is represented by the Notarys-Mercereau (1969, 1973) proximity effect bridges. In these structures the link is realized by overlaying a superconducting film substrate with a normal layer (this is one possibility) and varying locally the relative thickness of the films. In this way one can use the peculiarities of the proximity effect to modify, for example, the critical temperature in a region of the superconducting film only and thus create the weak link structure. A local modification of the properties of a superconducting film can be also realized by ion etching and ion implantation techniques (Palmer, Notarys, and Mercereau 1974; Harris, 1975; Arrington and Deaver 1975; Kirshmann et al. 1976). All these links can be viewed to some extent as the $S-N-S$ structures considered in Section 7.1, but with the "barrier" fixed by the cross-section rather than the area of the metal layer.

Historically the first contribution to the theory of bridge-type weak links can be considered to have been the original investigations (e.g., Ginzburg 1958) of the infinitely long superconducting films and filaments, namely superconductor sample, in which the cross-section is small enough so that variations of the meaningful parameters can be considered only along one dimension. In actual weak links boundary conditions must be taken into account—because of the finite length of the link and the presence of the electrodes which, in practice, always have a transverse cross-section larger than that of the link itself. In the case of link and banks of equal cross-section the boundary conditions discussed in Section 7.1 can be directly applied.

For the theoretical handling of real weak links it is convenient to assume a quasi one dimensional link joining two banks very large compared with the link, namely a V.T.B. structure (Likharev 1971).[†] As discussed and justified by Likharev and Yakobson (1975a), the latter circumstance permits the consideration of the order parameter at the boundary fixed at its equilibrium value in the electrodes. Obviously this corresponds to a situation in which all variations of the order parameter are localized within the physical length of the bridge, that is, when the effective length is identical with L . The actual link configuration which well satisfies the model above is thus the variable thickness bridge (and to some extent the point contact structures). It is important to observe that such V.T.B. links also guarantee a more efficient heat removal over Dayem bridges by virtue of the "three dimensional" character of their configuration (Klapwijk and Veenstra 1974; Klapwijk and Mooij 1974; Octavio, Skocpol, and Tinkham 1976). As already pointed out this is no longer true

[†]See also early experimental work by Gubankov et al. (1973).

when a V.T.B. link is very wide. In that case the link loses its structure of a three-dimensional constriction.

As a first approach to studying the behavior of thin films and bridges (and point contact structures as well) the simple resistively shunted junction (R.S.J.) model can be used; as we shall see later it does not explain several peculiar features of these weak links, however. As discussed in Chapter 6, such a two fluid picture is described by the equation

$$I = I_1 \sin \varphi + \frac{V}{R_N}$$

or more generally by

$$I = I_1[\varphi(t)] + \frac{V}{R_N} \quad (7.3.1)$$

and

$$\frac{d\varphi}{dt} = \frac{2e}{\hbar} V$$

where the symbols have their usual meaning.

7.3.1 Static Behavior. Aslamazov and Larkin (1968) first provided a simple theoretical explanation of the Josephson behavior by these super conducting weak links (it more properly applies to V.T.B. links and point contacts), which also legitimates the picture of the R.S.J. model. Following these authors let us consider the stationary case and start from the simple time independent Ginzburg-Landau equations (valid for $T \sim T_c$ i.e., small Δ) in the form[†]

$$\xi^2 \left(\nabla - j \frac{2e}{\hbar c} \mathbf{A} \right)^2 \Delta + \left[\pm 1 - \frac{|\Delta|^2}{\Delta_0^2} \right] \Delta = 0 \quad (7.3.2)$$

$$\mathbf{J} = \frac{\pi}{4ek_B T R_N} I_m \left[\Delta^* \left(\nabla - j \frac{2e}{\hbar c} \mathbf{A} \right) \Delta \right] \quad (7.3.3)$$

assuming that the relations

$$I \ll L \quad L \ll \xi(T) \quad L \ll \lambda(T)$$

simultaneously hold. \mathbf{A} is the vector potential and Δ_0 the equilibrium value of Δ . These conditions imply that the gradient terms dominate over the other

[†]This follows from the microscopic theory (Gor'kov 1959; see also the volumes by De Gennes 1966 and Tinkham 1975).

terms so that (7.3.2) reduces to the Laplace equation (in the gauge $\mathbf{A}=0$):

$$\nabla^2 \Delta = 0$$

with the condition on the superconductor surface:

$$\frac{\partial \Delta}{\partial n} = 0$$

The solution is written as a combination of two terms:

$$\Delta = \Delta_L e^{i\varphi_L} f(\mathbf{r}) + \Delta_R e^{i\varphi_R} (1 - f(\mathbf{r})) \quad (7.3.4)$$

L and R label quantities referred to the left and right banks, respectively. The spatial function $f(\mathbf{r})$ is solution of the Laplace equation tending toward 1(0) on the left (right) side of the link.

Using the solution (7.3.4), (7.3.3) for $\mathbf{A}=0$ gives the expression of the supercurrent density:

$$J_s(\mathbf{r}) = \left[\frac{\pi}{4ek_B T R_N} \nabla f(\mathbf{r}) \Delta_L \Delta_R \right] \sin \varphi = C \nabla f(\mathbf{r}) \Delta_L \Delta_R \sin \varphi$$

To obtain the normal current density we observe that $\nabla \cdot \mathbf{E} = 0$ and $\mathbf{E} = -\nabla U$ is $\nabla^2 U = 0$ with the condition $\partial U / \partial n = 0$ on the superconductor surface. This Laplace equation for the scalar potential U admits a unique solution that can be expressed [analogously to (7.3.4)] as $U = f(\mathbf{r})V + U_R$ with $V = U_L - V_R$ being the voltage across the link so that $\nabla U = -V \nabla f(\mathbf{r})$ (U_R and U_L are spatially independent in the respective banks).

Thus we can write the “two fluid” expression for the current density as

$$\mathbf{J} = -\nabla f(\mathbf{r}) \left(\frac{V}{R_N} - C \Delta_L \Delta_R \sin \varphi \right)$$

and by integration over the cross section of the link we get for the total current the expression

$$I = \frac{V}{R_N} + I_1 \sin \varphi \quad \text{with} \quad I_1 = \frac{\pi}{4ek_B T R_N} \Delta_L \Delta_R$$

In the banks we have $d\varphi_{L,R}/dt = (\hbar/2e)U_{L,R}$ and thus we find the fundamental relation $d\varphi/dt = (2e/\hbar)V$.

Whether the current phase relation (7.3.1) is sinusoidal or not in the time independent ($V=0$) case has been discussed in detail by Baratoff, Blackburn, and Schwartz (1970) within the framework of the Ginzburg-Landau theory for a one dimensional model of the weak link structure. (See also Christiansen, Hansen and Sjöström (1971); Gregers-Hansen, Levinsen, and Pedersen 1972.)[†]

[†]See also the recent paper by Lübbig (1980).

The solutions of the time independent Ginzburg-Landau equations can be summarized as follows (Likharev et al. 1974; Likharev and Yakobson 1975a). For very short bridges $L \ll \xi$ the Aslamazov and Larkin result is reproduced apart from small corrections. If $L > \xi$, then one should distinguish the two cases $T > T_c$ and $T < T_c$ which correspond to the two situations $S - N - S$ and $S - S' - S$ respectively. In the former case as the ratio L/ξ increases there is an exponential decay of the modulus of the order parameter at the center of the bridge and the current has essentially a form that, as expected, is similar to that discussed in Section 7.1 in connection with the $S - N - S$ sandwich junction (Aslamazov, Larkin, and Ovchinnikov 1968).

For $T < T_c$ (i.e., $S - S' - S$) the supercurrent phase dependence as a function of the length of the link is reported in Fig. 7.12a for different values of the parameter $L' = L/\xi$. It is clear from the figure that $I(\varphi)$ is sinusoidal as long as the normalized length L' is smaller than unity, that is, the link is short compared to the coherence length. On increasing L , the I vs. φ dependence deviates from the sinusoidal and the maximum supercurrent (normalized) tends toward the constant value 0.385 when $L \geq 8\xi$, that is, the critical current approaches that of an infinite superconducting wire having the coherence length of the weak link (Ginzburg 1958).

The sinusoidal $I(\varphi)$ dependence has been experimentally confirmed by Fulton and Dynes (1970) at $T \sim T_c$ and for $I_1 \sim 10\mu\text{A}$ using a double weak link interferometer. Among others we recall also the recent detailed measurements performed by Jackel et al. (1976a,b).

It is interesting to observe that a convenient description of two and three dimensional constriction weak links can be obtained by choosing elliptic cylindrical (Volkov 1973) and oblate spheroidal coordinates (e.g. Klapwijk, Sepers, and Mooij 1977). The Ginzburg-Landau equations using such coordinate systems have been solved in the static limit (Mooij and Dekker 1978) leading to a sinusoidal current phase relation in the three dimensional case. This result also agrees with the detailed work by Kulik and Omel'yanchuk (1975a).

Let us observe that all these approaches, as well as the work by Aslamazov and Larkin previously discussed assume temperatures near the critical T_c , since they are based on the Ginzburg-Landau theory. To get information on the behavior of the superconducting links at arbitrary temperatures one can resort to the Eilenberger (1968) theory of superconductivity. Indeed it is possible to use in the dirty limit ($l < \xi_0$) the Usadel (1970) simple equations for the order parameter which in the one dimensional case[†] can be written (Kulik and Omel'yanchuk 1975b) as

$$2\omega F - D \frac{d}{dx} \left[(1 - |F|^2)^{1/2} \frac{dF}{dx} + \frac{1}{2} \frac{F}{(1 - |F|^2)^{1/2}} \frac{d|F|^2}{dx^2} \right] = 2\Delta(x)(1 - |F|^2)^{1/2}$$

[†]By a different choice of the functions (Kupriyanov) this restriction can be avoided (see Likharev 1979).

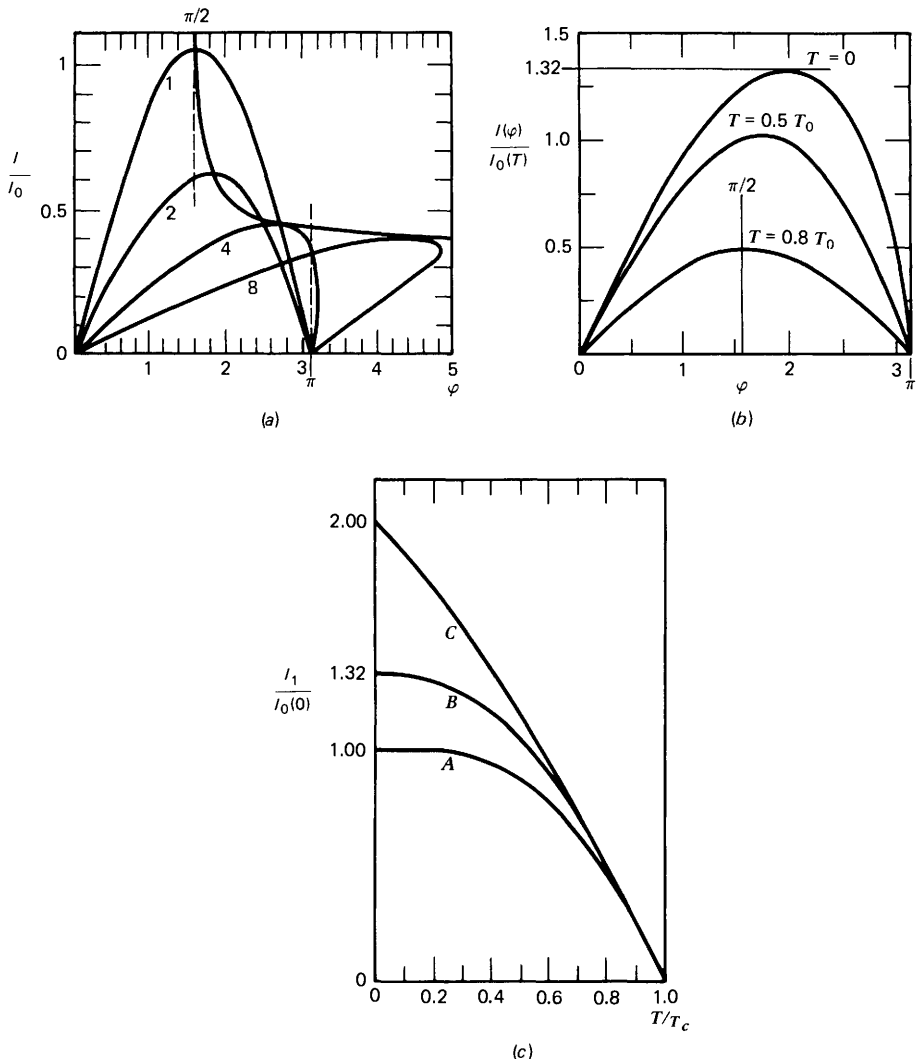


Figure 7.12 (a) Supercurrent vs. phase difference, φ , at the bridge-bank boundary in an S-S'-S bridge ($T < T_c$) for different values of L/ξ . (After Likharev and Yakobson 1975a.) (b) Supercurrent vs. phase relationship for a short dirty weak link at different temperatures obtained by the theory of Kulik and Omel'yanchuk (1975). (c) Temperature dependence of the critical current for tunnel junction (curve A), that is, Ambegaokar and Baratoff (1963) theory (see Chapter 3), and for short weak link in the dirty limit (curve B) and in the clean limit (curve C) according to the theories of Kulik and Omel'yanchuk (1975, 1977). $I_0(T)$ represents here the critical current given by the Ambegaokar and Baratoff formula. (Redrawn from Likharev 1979.)

Here $F(x, \omega)$ is the Gor'kov function, $\omega = (\pi/\hbar)k_B T(2n+1)$, and $D = \frac{1}{3}v_F l$. The supercurrent density is given by

$$J_s = -j \frac{2\pi k_B T}{R_n e} \sum_{\omega} \left(F^* \frac{dF}{dx} - F \frac{dF^*}{dx} \right)$$

Kulik and Omel'yanchuk solved the equations with the proper boundary conditions. As for the case of the Aslamazov and Larkin theory, the condition $L \ll \xi(T)$ implies that can be considered only the gradient terms, since they dominate the other terms. The final expression for the total current is found to be

$$I = \frac{2}{e} \Delta_0 \cos \frac{\varphi}{2} \pi k_B T \sum_{\omega} \frac{1}{\sqrt{\omega^2 + \Delta_0^2 \cos^2 \varphi/2}} \tan^{-1} \frac{\Delta_0 \sin \varphi/2}{\sqrt{\omega^2 + \Delta_0^2 \cos^2 \varphi/2}}$$

For $T \rightarrow T_c$ the Kulik-Omel'yanchuk theory for short bridges reproduces that by Aslamazov and Larkin. At higher temperatures, however, the current phase relationship is no longer sinusoidal and for $T=0$ tends to become markedly asymmetric (Fig. 7.12b). As far as the temperature dependence of the critical current is concerned, the theory gives a linear dependence near T_c as predicted by Ambegaokar and Baratoff for tunnel junctions (see Chapter 3) but at lower temperatures (say, below 0.85) the curves move apart (see Fig. 7.12c).

Let us observe that the Usadel equations have been used also to study the effect of the temperature on the current phase relation of a $S-N-S$ weak link when $T_{cN}=0$ (Likharev 1976). Also worth mentioning is the case of large mean free paths (clean structures, $L < l, \xi$) recently investigated by Kulik and Omel'yanchuk (1977). This theory cannot employ Usadel equations but has to resort necessarily to the more general equations by Eilenberger (1968). Figure 7.12 reports the results of this theory for the I_1 vs. T dependence.

Finally, we observe that two distinct behaviors are found in the short and long weak link limits (Skocpol 1976). In the former case the linear I_1 vs. T dependence expected by the theoretical analysis has been experimentally confirmed within a rather wide temperature range as observed by Daalmans, Klapwijk, and Mooij (1976) in aluminum microbridges, by Gregers-Hansen, Levinse, and Pedersen (1972) and Song and Rochlin (1972) in tin and indium microbridges, and by Yeh and Buhrman (1977) in lead links.[†] Some discrepancy at temperatures near T_c can be accounted for by the different temperatures of contact and banks. In addition, in the immediate vicinity of T_c thermal fluctuations, films thickness effects, specific technological fabrication procedures, and so on, can lead to deviations from the linearity of $I_1(T)$. As predicted by the Ginzburg-Landau theory (see, for instance, De Gennes 1966, Section 6-5) in the case of long one dimensional links the critical supercurrent varies with temperature as $I_1 \propto (1 - T/T_c)^{3/2}$ (e.g., Dayem and Wiegand 1967;

[†]Among others see also the early work by Wyatt et al. (1966) and the extensive article by Levinse (1973).

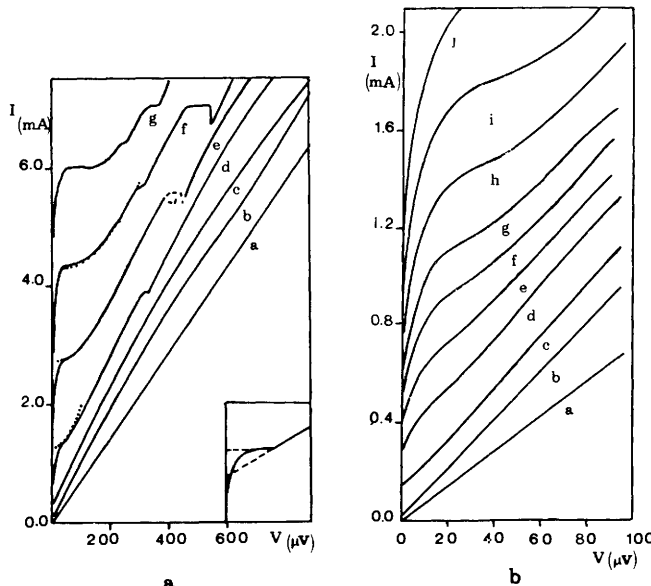


Figure 7.13 Typical voltage-current characteristics at various temperatures which refer to Sn V.T.B. samples. (Redrawn from Octavio, Skocpol, and Tinkham 1978.)

Skocpol, Beasley, and Tinkham 1974a). Such a dependence has also been found in a variety of bridge-type weak links (e.g., Kofoed and Saemark 1974; Harris 1976a; Boone et al. 1976; Kirschman et al. 1976).

7.3.2 Voltage-Current Characteristics. Let us review now the peculiar features of the voltage-current characteristics of thin films bridges. In Fig. 7.13a are reported typical V - I curves (Octavio, Skocpol, and Tinkham 1978) at different temperatures which refer to tin V.T.B. samples. Starting from $V=0$ we observe the supercurrent followed by a finite voltage branch, up to about $50 \mu\text{V}$, characterized by a small differential resistance $R_d \ll R_N$. This region, as shown in expanded scale (Fig. 7.13b), exhibits a characteristic "foot"[†] which is present at temperatures up to roughly 3.75 K. Increasing further the temperature ($T \sim T_c$) this footlike structure disappears and the curve begins rising from I_1 with a constant slope. At higher voltages the V - I characteristics follow a curve of higher resistance exhibiting a subharmonic gap structure (see, for instance, Greger-Hansen and Pickett 1973; Hasselberg, Levinsen, and Samuelsen 1974, 1975; and references cited therein). At even larger voltage values this structure is smeared out and the V - I curve shows a characteristic bending due to heating.

[†]We have chosen the word "foot" as reported in the recent literature although when, as in the figure, the current is displayed in the vertical axis, it should be rather called "knee."

We observe that the curve in the resistive region at high voltages intercepts the zero voltage state at a current value $I_e > 0$, or, in other words, the high voltage branch approaches the dependence $I = V/R + I_e$. In the pure R.S.J. model $I_e = 0$; any shift in current is usually referred to as "excess current." Furthermore, we observe that by lowering the temperature the $V-I$ curve tends progressively to increase its initial slope which, within the range of a few μV , develops into a steep linear branch. Above this branch, at low enough temperature, the characteristic exhibits also an abrupt transition to the finite voltage state. Thus a reduction of the temperature leads to a negative differential resistance which gives rise to hysteretical behavior. How the hysteresis develops and increases by decreasing the temperature is clearly shown in Fig. 7.14 where $V-I$ curves are reported which refer to the work by Daalmans, Klapwijk and Mooij (1976) on the same kind of junctions (Sn V.T.B. links). Consistently with the results of Fig. 7.13, we observe the displaced straight line in the initial portion of the characteristics at lower temperatures. At even lower temperature this branch disappears.

In Fig. 7.14*b, c* are shown $V-I$ curves of aluminum weak links corresponding to microbridge (*b*) and long strip bridge (*c*). These results show also a number of features whose interpretation has been subject to speculation (see below). Finally, we recall that there is also evidence of other phenomena that arise when investigations are performed on samples under microwave irradiation. There is in fact the occurrence of subharmonic steps, effects of frequency dependence, and enhancement of the maximum supercurrent (e.g. Levinsen 1973; Clark 1976; see also Section 11.3).

7.3.3 Interpretation of Voltage Carrying States. Thus far we have given a brief outline of the phenomenology of superconducting bridges through the inspection of their voltage-current characteristics. Let us now briefly discuss the possible interpretation of these results. Recently several effects have been invoked and various theoretical explanations proposed to account for the various phenomenological aspects of these structures, but a complete understanding of the whole subject has not yet been reached.

As we have seen, the R.S.J. picture provides a description of bridges in terms of Josephson-like behavior (at least under some conditions); however, the peculiar features of the voltage-current characteristics discussed above cannot find a satisfactory explanation within the framework of this simple two fluid model. Indeed, many attempts have been made to describe these links by a suitable equivalent circuit. In the original McCumber paper (1968a) an equivalent circuit configuration was proposed in which the link has a series inductance (self-inductance) and is driven by a constant voltage source. Sophisticated modifications of the R.S.J. scheme to explain the behavior of superconducting links as a whole have been discussed, among others, by Gregers-Hansen, Levinsen, and Pedersen (1972) and by Gregers-Hansen et al. (1972).

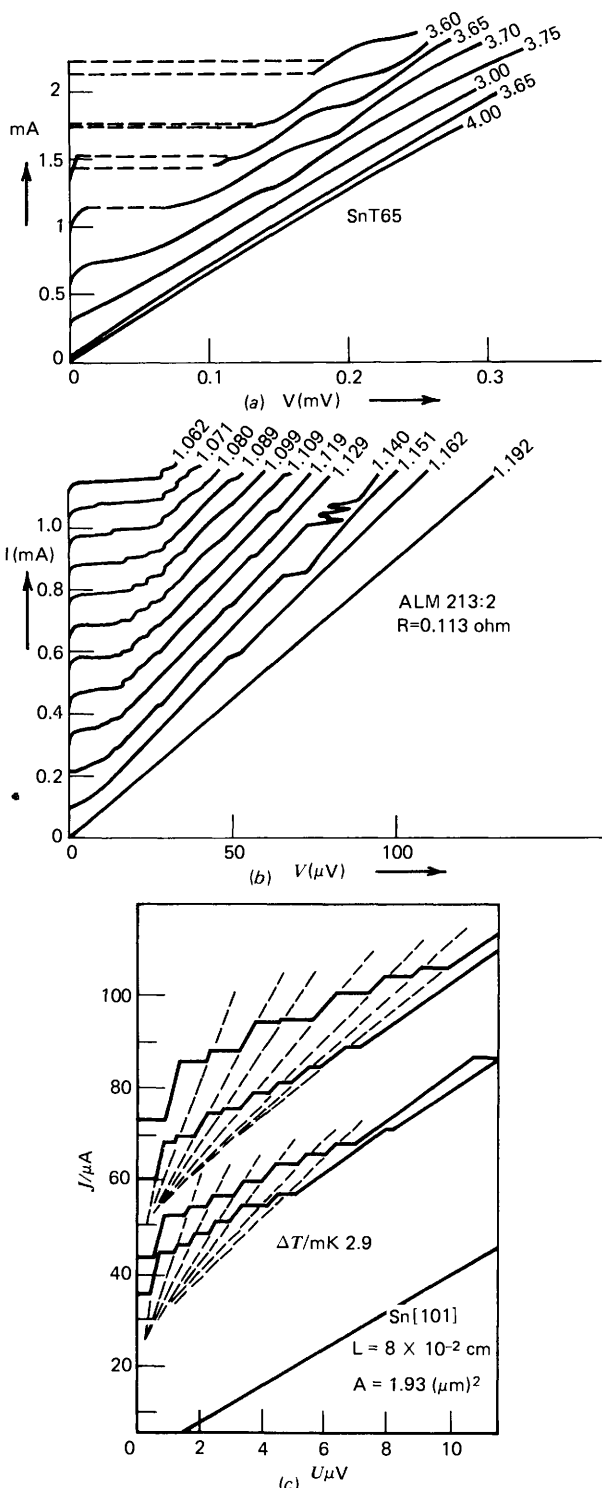


Figure 7.14 (a) Voltage-current characteristics of a variable thickness tin microbridge at various temperatures. (After Daalmans, Klopwijk, and Mooij 1976.) (b) Voltage-current characteristics of an aluminum microbridge at various temperatures. (Same reference.) (c) Voltage-current characteristics of a tin whisker. (Redrawn from Meyer 1973.)

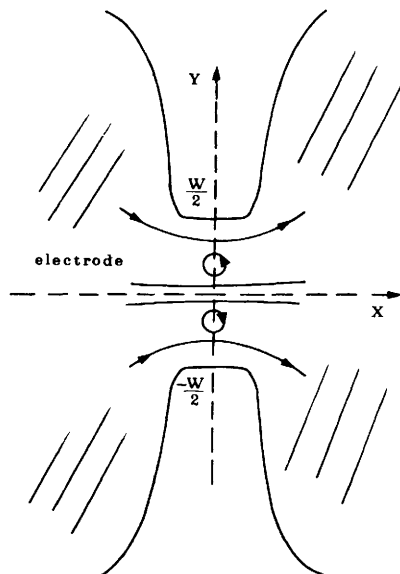


Figure 7.15 Sketch of vortex motion in a link structure.

One of the most significant phenomena that must be considered in dealing with the interpretation of the voltage carrying states is flux flow. Such a process is present also in Josephson tunneling structures (Chapter 10) both with dielectric and metal barriers. In a large bridge-type weak link without a superconducting ground plane the current is no longer uniformly distributed and, as soon as the critical supercurrent is reached, the zero voltage state becomes unstable and vortices[†] begin to move under the Lorentz force toward the center of the bridge, as sketched in Fig. 7.15. In the pioneering work by Anderson and Dayem (1964) the origin of subharmonic steps induced by microwaves was related to the occurrence of flux motion in the link. In this scheme the steps result from the synchronization of this motion by the microwave radiation. This concept has been widely developed by Likharev (1971a) and by Aslamazov and Larkin (1975).[‡]

The flux flow seems to explain very consistently the displaced linear branch in the V - I curves of the tin links reported in Fig. 7.14a (Daalmans, Klapwijk, and Mooij 1976). A similar behavior was found also for Nb V.T.B.

[†]This assumption can hold also for type 1 superconductors, since it has been demonstrated that a thin film made by this superconductor below a critical thickness behaves as a type 2 material (Burger and Saint-James 1969).

[‡]See also the paper by Golovashkin and Lykov (1978), Golovashkin, et al. (1979) and references reported therein. In that work high temperature superconducting weak links (Nb_3Sn type) are investigated and experimental results are found which are in agreement with the Aslamazov and Larkin theory. Such a theory has been also used to explain some of the unusual properties of long V.T.B. bridges formed by pulse electrical breakdown in monocrystalline silicon (Benacka et al. 1978a,b).

links (Wang, Dae, and Deaver 1978) and in this case, too, was ascribed to flux flow.[†]

A naive picture of the theoretical model can be summarized as follows (Klapwijk, Sepers, and Mooij 1977). It is assumed that the dynamics of the flux motion is governed by the presence of the Lorentz force per unit length $F_L = J\Phi_0$ because of the interaction between current and vortex and a pinning force F_p given by $F_p = J_p\Phi_0$. Moreover, the vortex moving at a constant velocity, v , undergoes viscous force F_f proportional to the velocity $F_f = \eta v$, because of the friction between normal core of the vortex and the crystal lattice.

Assuming for the viscosity parameter the expression

$$\eta = \frac{\sigma}{\pi} \left(\frac{\Phi_0}{\xi(T)} \right)^2$$

with σ being the normal state conductivity of the core the balance condition of the forces $F_L = F_p + F_f$ is

$$J\Phi_0 = J_p\Phi_0 + \frac{\sigma}{\pi} \left(\frac{\Phi_0}{\xi(T)} \right)^2 v$$

If v is the number of vortices crossing the bridge per unit time, $V = v\Phi_0$ and $v = v/W$. Thus we can write

$$I = I_p + \frac{V}{Z}$$

where $Z = \pi\xi^2(T)/\sigma W^2 d$, $I_p = J_p W d$, and $I = JW d$. Thus with the aid of this qualitative argument we found the linear relation between current and voltage above the critical current as experimentally observed and the change in the slope due to the temperature dependent impedance. Finally, among different results on flux dynamics in superconducting bridges, we recall the work by Guthmann et al. (1975) in which the plateau region of the $V-I$ curves is explained by a flux flow model.

In Fig. 7.16 the values of both length and width are given (normalized to $\xi(T)$) corresponding to the occurrence of flux motion. The region below the horizontal dashed line indicates bridge sizes which allow single valued current phase relation corresponding to the result of Fig. 7.12. The remaining region indicates the one dimensional phase slip regime (see below). It is worth observing that flux flow can exist only in the case of a multivalued I_1 vs. φ dependence (Kupriyanov, Likharev, and Maslova 1975), which in turn implies that such a phenomenon cannot take place in $S-N-S$ links which, as

[†]Extensive work on V.T.B. structures was performed by Gubankov et al. (1973) and Gubankov, Koshlets, and Ovsyannikov (1975, 1976b, 1977).

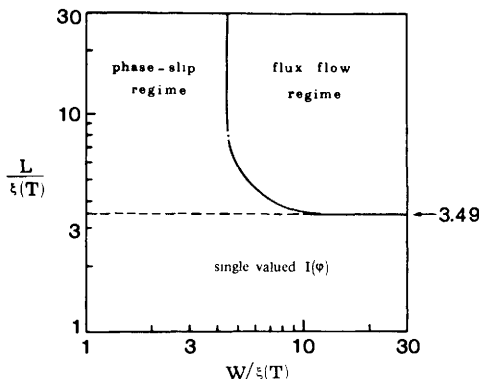


Figure 7.16 Single valued current-phase dependence, phase-slip regime, and flux flow regime. (Redrawn from Kupriyanov, Likharev, and Maslova 1975.)

previously discussed, by increasing their length exhibit only an exponential reduction of the critical current. Let us consider now the set of experimental $V-I$ characteristics of small aluminum bridges shown in Fig. 7.14b. We observe that although the curves, as a whole, are similar to those of the tin samples reported in Fig. 7.13, there are in fact significant differences in their detailed structure. The data refer to an aluminum sample whose size is too small to allow vortex penetration, making the flux flow hypothesis inapplicable. At relatively higher voltages it is evident that a temperature dependent structure can be related to the subharmonic gap structure. This should occur in fact at voltage values given by $(1/n)(2\Delta/e)$. Moreover, steps at fixed voltages are also present which can be related to self-resonant modes. This phenomenon is clearly recognized in tunneling structures (see Chapter 9) where the steps arise as a consequence of the interaction between the electromagnetic field associated with the supercurrent width and the junction cavity. In the case of bridges the "resonator" is provided by some sort of effective cavity created by the external environment of the sample. On inspecting the $V-I$ curves we see also the large values of the excess current.

In order to explain the dynamic behavior of links narrower than both ξ and λ one can resort to the time dependent superconductivity (Reiger, Scalapino, and Mercereau 1971, 1972) through the concept of relaxation oscillations of the order parameter (Notarys and Mercereau 1969) associated with the Josephson frequency. This phenomenon was interpreted as a phase slip process in which the increase in the relative phase $\varphi = \chi_L - \chi_R$ is compensated by 2π jumps in the local phase of the complex order parameter $\Psi = e^{j\chi}$ as the amplitude falls to zero. At this moment the superconducting order is destroyed and the current flows normally, then the order parameter restores itself, and the process of decay and restoration goes on. This process can be viewed as a one dimensional limit of flux flow in the sense that a vortex crossing the bridge corresponds in this situation to a collapse of Ψ at some

points along the bridge. The theory is based on the time dependent Ginzburg-Landau (T.D.G.L.) equations written in the simple form[†]

$$\xi^2 \frac{d^2 \Psi}{dx^2} + (\pm 1 - |\Psi|^2) \Psi = \tau \left(\frac{\partial}{\partial t} + j \frac{2e\mu}{\hbar} \right) \Psi \quad (A=0)$$

where Ψ is the order parameter Δ normalized to its equilibrium value and τ is the order parameter relaxation time which in the aforementioned paper was taken as zero. Later the dynamics of the links was developed and clarified by Likharev and Yakobson (1974, 1975b) under the assumption of finite τ .

Referring the reader to these papers, we observe that the analysis by the T.D.G.L. equation provides, among other things, an explanation of the presence of the excess current in the $V-I$ curves. Roughly we can say that this feature is due to a proximity effect at the bank-bridge boundary. Indeed, at high current the order parameter is vanishing into the link; however, the extension of the superconducting properties into the normal bridge, because of the proximity effect, "holds" the order parameter at the ends of the link away from zero. This circumstance allows to carry at a given voltage a higher current than expected. In connection with Likharev and Yakobson work a voltage dependent current-phase relation for short microbridges has been discussed (Hojgaard-Jensen and Lindelof 1976), considering also the effect of the relaxation parameter τ . This scheme consists basically of a resistively shunted junction model with a voltage dependent supercurrent (R.S.J. τ model).

Furthermore, an explanation of the presence of hysteresis in the $V-I$ curves has been proposed by Song (1976) in which this phenomenon is related to a temperature dependent "effective capacitance." As opposed to tunnel structures, the interelectrode capacitance of the bridge is too small to justify the hysteretical behavior of the I vs. V dependence. In this case the dominant time constant is indeed a finite relaxation time required by growth and decay processes of the order parameter that comes into play.

A further insight into the effects of the relaxation parameter in determining the essential feature of the voltage carrying states of one dimensional links has been given in the extensive works by Baratoff (B) and Kramer (K) (B and K 1976; K and B 1977). Relaxation effects have been considered also in a simple phenomenological model by Deaver, Rifkin, and Sandell (1976) which gives an account of the phase dependent conductivity expressed as $\sigma(\varphi) = \sigma_N + \sigma_1 \sin \varphi$.

For completeness we now consider the $V-I$ characteristic of Fig. 7.14c which refers to a long ($L \gg \xi(T)$) superconducting "bridge". The structure is actually a Sn crystal whisker (Meyer and Minnigerode, 1972; Meyer, 1973). The peculiar step-like shape can be explained by the existence of localized and

[†]For the time dependent generalization of the Ginzburg-Landau equation see Gor'kov and Eliashberg (1968, 1970) and other important contributions by Schmid and Schön (1975), Ovchinnikov (1977), Kramer and Watts-Tobin (1978), Baratoff and Kramer (1978), and Watts-Tobin and Kramer (1978).

essentially equal voltage units in series along the structure in agreement with the theory developed by Skocpol, Beasley, and Tinkham (1974a) and their experimental results. The basic idea is that in each of such units a relaxation oscillation process of the order parameter occurs so that these voltage drops are interpreted as voltages across quantum phase slip centers.

Indeed the presence of resistive centers along the bridge gives rise to finite voltages which in turn correspond to a different varying rates of the order parameter at the two sides of the center.

As predicted by the theory, the voltage unit V_u is found to be governed by inelastic scattering of quasiparticles. The dashed lines in Fig. 7.14c indicate the differential resistances given by nR_1 (R_1 is that relative to the first finite slope and $n=1, 2, \dots$). It is $V_u = 2\Lambda\rho_N(I - I_s)/S$ where Λ is the quasiparticle diffusion length, ρ_N the normal resistivity, S the local cross-sectional area. The various finite current slopes are given by $I = I_s + V/R_n$ with $R_n = nR_1$. This is in agreement with the theory above which predicts essentially equal voltage units, each contributing to the differential resistance with $2\Lambda\rho_n/S$. All the linear branches in the $V-I$ curve intercept the current axis at I_s which represents the time averaged supercurrent carried by the phase slip region. Dolan and Jackel (1977) using a measurement technique that employed tunnel probes near these regions in a long Sn bridge have shown experimentally the different spatial variations of the superconducting potential (almost abrupt) and normal electron potential (over a distance of many microns). The results for long strips obtained by Skocpol, Beasley, and Tinkham are obviously relevant also for short bridges, at least for the key role of the phase slip process which attains the Josephson-like behavior in the voltage carrying states. Huebener and Watson (1974) have reported interesting results which can be viewed as the outgrowth of the three dimensional case of this phenomenon of the steplike $V-I$ curve. In this case, however, the role of the single flux quanta is played by flux tubes.[†]

It is important to observe that heat dissipation related to voltage carrying processes increases the local temperature which in turn gives rise, in the limit of high dissipation, to normal "hot spots." This idea was present in early works on superconducting films and has been successfully adopted by Skocpol, Beasley, and Tinkham (1974b) to explain the hysteresis in the voltage-current characteristics at low temperatures and a voltage upper bound on the a.c. Josephson effect. A detailed quantitative analysis of self-heating effects and their influence in limiting the performances of weak link devices has also been given by the same authors (Tinkham, Octavio, and Skocpol 1977; see also the recent review by Tinkham 1978).

7.3.4 Aspects of Nonequilibrium Superconductivity.

A striking consequence of the investigations of the nonequilibrium superconductivity is the

[†]Such a magnetic flux structure has been investigated in detail also using high-resolution magneto-optical techniques (see Watson, Kampwirth, and Huebener 1974 and references cited therein).

change of superconducting parameters induced by modifications of the distribution function of quasiparticle excitations.

On the basis of these concepts Eliashberg (1970, 1971) has developed a detailed study which predicted an increase in the energy gap of a superconductor when irradiated by high frequency field (see Ivlev and Eliashberg 1971; Ivlev, Lisitsyn, and Eliashberg 1973). As a consequence, a Josephson weak link would exhibit an enhancement of the critical current.[†] This phenomenon was indeed observed many years ago on superconducting bridges (Wyatt et al 1966; Dayem and Wiegand 1967) and is referred to as the Dayem-Wyatt effect[‡] (see also Chapter 11, Section 11.3). Such an effect appears to be a true Josephson-like behavior (see, for instance, Jillie, Lukens, and Kao 1974). Moreover, it is found that at a given temperature, frequency lower and upper bounds do exist (Latyshev and Nad 1974) for the occurrence of the effect. The latter can be related to the presence of the gap; at a frequency higher than the gap frequency a pair breaking mechanism is expected which leads to a quenching rather than an enhancement of the superconductivity. More recently a modification of the theory for phonon absorption has been developed and experimentally tested by Tredwell and Jacobsen (1976). In this case the enhancement of the gap and consequently of the critical Josephson current was found by irradiating a junction with 10 GHz phonon excitation.[§]

The idea that nonequilibrium superconductivity can be considered to account for the peculiar features of $V-I$ curves has been recently discussed by Octavio, Skocpol and Tinkham (1978) in connection with detailed experimental results Fig. 7.12. Recent works by Aslamazov and Larkin (1978a,b) show that in short bridges there is a special mechanism which gives rise to a nonequilibrium electron energy distribution. Roughly, the physics of this phenomenon can be explained as follows. The value of the gap (order parameter) in the contact region (between the banks) is less than in the banks because of a larger concentration of supercurrent. Therefore, electrons with energies less than the gap in the banks are confined in the contact region (they are trapped in a potential well). When the link is in an external high frequency field the supercurrent through the link has oscillating components. As a result, the bottom and the edges of the potential well are oscillating as well. Electrons are reflected from the oscillating well and their energy (on the average) is increased. When the energy becomes larger than the gap in the banks, the electrons can diffuse from the link to the banks, where the electron distribution

[†]This effect was investigated among others by Hunt and Mercereau (1967) (see also Christiansen, Hansen, and Sjöström 1971; Dmitriev, Khristenko and Shapiro 1973). These authors ascribe such enhancement to the suppression of thermal fluctuations because of a synchronization effect by the incident microwaves.

[‡]This effect has been observed by a large number of investigators (e.g., Dmitriev et al. 1970; Greger-Hansen, and Levinsen 1971; Jahn and Kao 1973; Levinsen 1973).

[§]Excellent reviews of nonequilibrium superconductivity in connection with weak links are given by Langenberg (1975), Chang and Scalapino (1976), Schmid (1978), Lindelof (1978), Ivlev (1979), and references reported therein.

function is in equilibrium because of the small concentration of supercurrent. Therefore, the action of the h.f. field results in a reduction of the number of quasiparticles into the contact, which is equivalent to an effective cooling of the link. Thus the critical current of the link in the h.f. field is enhanced. The experimental check of this theory was made by Gubankov, Koshelets, and Ovsyannikov (1978, 1980) and by Latyshev and Nad (1979), showing that in sufficiently short contacts the energy diffusion due to oscillation of the potential well is larger than that which could result from a direct action (acceleration) of the electric field (Eliashberg mechanism for spatially homogeneous superconductor). Nonequilibrium effects are also essential to explain the shape of the V - I curves of the links. Nonequilibrium in this case is caused by the Josephson oscillations of the supercurrent and the corresponding oscillation of the order parameter in the contact region, which appear when the current exceeds the maximum. Analogously to the case when contact is in the external h.f. field, these oscillations lead to a nonequilibrium electron energy distribution, which in turn produces a superconductivity enhancement.

As a result, at low voltages (which are inversely proportional to the energy relaxation times) the supercurrent through the contact increases drastically. In the V - I curves of the link characteristic "foot" appears (Aslamazov and Larkin 1976). In Fig. 7.13a the dots correspond to this theory; it can be seen that they give a rather good fitting of the shape of the curve after the foot. At lower voltages there is agreement with the Golub (1976) theory, which also takes into account nonequilibrium effects.[†]

The theory shows that the role of the nonequilibrium effect depends essentially on the temperature. The "foot" appears only when the contact is longer than the characteristic distance $\sqrt{D/\Delta}$ (D is the diffusion coefficient). We see that this condition ($L > \sqrt{D/\Delta}$) is verified only when the temperature is far enough from the critical one. Correspondingly, only in this temperature region should the V - I curve exhibit the characteristic foot. The experimental temperature dependence of the "foot point" (Gubankov, Koshelets, and Ovsyannikov 1977) is in good agreement with the theory. Experimentally the correlation between the enhancement of the critical current by the external h.f. field and the appearance of the foot in the V - I curve of the bridge is also observed.

It should also be mentioned that very recently there has been essential progress in the understanding of the physical nature of the excess current. In the extensive theoretical work developed by Artemenko, Volkov, and Zaitsev (1978a,b; 1979a,b) the following expression for the excess current was obtained:

$$I_e = \frac{\Delta}{eR} \left(\frac{\pi^2}{4} - 1 \right) \tanh\left(\frac{V}{2k_B T} \right)$$

[†]In a very recent work Schmid, Schön, and Tinkham (1980) gave an extensive picture of the problem, pointing out some limitations of the papers quoted above and reaching quantitatively different conclusions.

which explains the proportionality between the excess current and the value of the order parameter. This expression is in good agreement with the experiments performed by Divin and Nad (1978, 1979). At voltages larger than the energy gap the normal current in the superconducting links is due to the same process as in tunnel contacts. Namely, current is caused by transition between occupied energy states in one bank and empty states in another bank. The difference between $S-S'-S$ links and the tunnel junctions is that the contribution to the current is made also by the quasiparticles whose energy corresponds to the forbidden band in the other bank. Such particles move, for instance, from the left bank, reflect, and become "holes" that move backward (Andreev-like reflection).[†] The current is carried by these electrons and holes in the left electrode, whereas in the right electrode the current is carried by Cooper pairs.

Finally, we mention that for a long one dimensional inhomogeneous superconducting bridge, which consists of parts with slightly different critical temperatures, the width of the transition (ΔT_c) changes in high frequency fields. By increasing the power of the radiation $\Delta T_c \rightarrow 0$ a step structure appears in the R vs. T curve (Lathishev and Nad 1977, 1978). This effect can be also explained by nonequilibrium phenomena, which tend to equalize the critical temperature of the various sections, as very recently proposed by Aslamazov (1978).

7.4 Point Contact Weak Links

A superconducting point contact consists, roughly, of two superconductors weakly coupled by a small area contact, which is realized by pressing a sharp superconducting point on a flat superconductor (actual configurations are discussed in Section 8.8). The resulting structure is not well defined because of the almost unpredictable actual configuration of the contact region between the two superconductors. This in fact depends strongly on the mechanical properties of the two superconductors, the pressure between them, the more or less unavoidable oxide growth, and so on. In principle, one could envisage two different cases. In one the point contact is realized exclusively by a metal contact between the electrodes thereby creating a current concentration weak link closely resembling those discussed in the preceding section.[‡] In the other the two superconductors are separated by a thin oxide layer so that the point contact structure is just a "small" tunnel-type junction. Unfortunately, these two situations have to be considered as ideal limiting cases. The most realistic picture should correspond to intermediate situations, that is, it should be assumed that in a point contact structure the actual "link" between the two

[†]See Andreev (1964).

[‡]We recall in particular the simple theoretical model by Aslamazov and Larkin outlined in Section 7.6.1.

superconductors results from several parallel paths, either metallic or through oxide barriers. In spite of the uncertain weak coupling mechanism, point contacts have found a large variety of applications in both low and high frequency devices and exhibited good properties of reliability. An excellent review on properties and applications of these structures is due to Zimmerman (1972b) Among the pioneering studies of superconducting point contacts in the context of the Josephson effect we recall those by Zimmerman and Silver (1964, 1966), Zimmerman and Mercereau (1964, 1965), Omar and De Bruyn Ouboter (1966), and Dayem and Grimes (1966).[†]

Certainly one of the reasons for the wide use of such structures lies in the simplicity of their fabrication. A drawback in the use of point contacts for years has been their lack of reproducibility and to some extent their limited stability. Significant progress has been made, as is briefly discussed in Chapter 8 (Section 8.8).

A large number of papers have been devoted to various aspects of point contact weak links. Among others we recall that by Taguchi and Yoshioka (1969, 1970) in which their basic properties are discussed, including temperature and magnetic field dependence on the critical current[‡] and details of the voltage-current characteristic effect on the microwave power level. The hysteresis that often appears in the $V - I$ curves has been ascribed to self-heating effect (Fulton and Dunklenberger 1974a). The role of fluctuations has been also investigated, among others, by Vystavkin et al. (1973, 1974) and Tolner and Andresse (1974a,b). Furthermore, a current phase relation has been investigated in detail (e.g., Jackel, Buhrman, and Webb 1974; Rifkin and Deaver 1976), and evidence of phase dependent conductivity (the "cos φ term") shown by Vincent and Deaver (1974), and more recently discussed and discussed by Callegari, Atwater, and Deaver (1976).[§]

In conclusion, we stress once more the character of a rough outline of what we called "other types of Josephson structures." Some aspects of these weak links are reconsidered throughout this book in specific contexts: fabrication, applications, and so on; details can be found in the quoted references, some of which include extensive bibliographies.

[†] Further works are reported in the bibliography to the paper by Zimmerman (1972b). The reader is also referred to the extensive articles by Vystavkin et al. (1973) and by De Bruyn Ouboter and De Waele (1967a,b).

[‡] Recently, niobium point contacts investigated by Divin and Nad (1978) have shown a temperature dependence of the critical current in very good agreement with the theory of Kulik and Omelyanchuk (1975b) developed for current constriction weak links.

[§] For the latest developments of point contact structures see also Weitz, Skocpol, and Tinkham (1978), Taur and Keer (1978a,b, and Skocpol (1978).

CHAPTER 8

Device Fabrication Technology

In this chapter we discuss the various technological aspects involved in the preparation of Josephson tunneling structures and other kinds of superconducting weak links. We attempt to give an overall view of existing technologies and to describe in some detail the fabrication steps of the more common procedures to provide simple “recipes” for the fabrication of whole samples.

8.1 Josephson Tunneling Junctions

Let us first discuss the preparation of the “sandwich” type Josephson junctions, that is, superconductor–tunnel barrier–superconductor. Such a structure consists of two superconducting electrodes made by thin film deposition techniques separated by a suitable tunneling barrier layer that can be made following various procedures. The preparation of reliable junction barriers is crucial. The best results have been generally obtained by using natural rather than artificial barriers. The former result from the growth of a dielectric oxide of the first deposited metal sheet, the base layer; the latter include barriers obtained by the “addition” of films of suitable materials such as metal oxide, carbon, organic compounds, and various kinds of semiconductors. Josephson tunneling requires an oxide barrier thickness of about 10–20 Å. Semiconductor and metal barriers are typically about 100 and 1000 Å thick, respectively. In all cases, nonuniformity can be a problem. In fact, within a relatively wide range of values the thickness of the superconducting films (a few thousand angstroms) is not critical. Conversely, even slight variations in the oxide thickness, t , drastically affect the behavior of the junction. As shown in the theory, the normal tunneling resistance R_N is exponential in the barrier thickness; hence when t is decreased, the maximum Josephson current increases exponentially. Recall (Chapter 4) that measurements of the Josephson supercurrent vs. the applied magnetic field can serve as a powerful method for checking the actual degree of uniformity of the tunneling barrier layer in the final sample. The junction pattern definition can be obtained by supporting, during evaporation, substrate slides in close contact with thin metal masks that are made either mechanically or by photoresist techniques. Sophisticated photo or electron lithography technologies, depending on the desired specification, are widely

and successfully employed in junction patterning. We discuss later some of the aspects of the various procedures for defining junction geometries also in connection with the specific film deposition technique.

8.2 Junction Electrodes

As we already know, the junction superconducting electrodes are prepared in the form of thin films by a suitable vacuum deposition technique. Various kinds of superconductors have been employed in the context of the Josephson effect. Table 8.1 lists typical superconducting materials and their most relevant parameters. Superconductors that can be employed in the preparation of tunneling junctions fall into two categories. One is that of soft metals, such as Pb, Sn, and In. These materials can be easily evaporated under vacuum from simple resistance heaters. The second category includes transition metals, such as Nb, V, and Ta. As we shall see, niobium in particular can be successfully employed (mainly as the base electrode). These materials have high melting points and their use requires sophisticated thin film deposition techniques such as electron gun evaporation or sputtering.

We discuss first some aspects of the various metals, referring to junctions that employ oxide barriers.

8.2.1 Soft Metals. Soft metals, particularly tin and lead, have been widely used since the early pioneering experiments on superconductive tunneling. They are very easy to handle and, as we have seen, result in junctions whose experimental behavior generally allows excellent and straightforward comparison with the theory. However, for applications where “long life” and “thermal cyclability”[†] are paramount, these materials are no longer recommended. In fact, soft metals during thermal cycling between room and helium operation temperatures (4–300 K) undergo mechanical stresses. These can produce dislocation flow and grain boundary deformations, which lead to hillocks and, in some cases, to one dimensional overgrowths referred to as whiskers. Ultimately these protrusions on the metal film cause substantial damages in the oxide barrier. In fact, the size of these localized nonuniformities[‡] can be orders of magnitude larger than the barrier thickness and therefore can pierce through the oxide layer. This is likely to occur when, for instance, tin or lead films are deposited onto the usual glass slides. The thermal expansion mismatch between the film and the substrate produces tensile stresses during cooling and compressive stresses during heating which are relieved through the formation of protrusions. A growing or shrinking of the

[†]These two properties are related and, to some extent, can even be identified.

[‡]The expression “localized nonuniformities” is used in contrast with the inhomogeneities related to unavoidable fluctuations of the barrier thickness (“structural fluctuations”) discussed in the last section of Chapter 4.

**TABLE 8.1 Typical parameter for superconducting metals
(Data refer to bulk samples)**

Material	Critical Temperature T_c (K)	Critical Field H_c (Oe)	Penetration Depth λ_L (Å)	Melting Point (°C)
Cd	0.56	30	1300	321
Al	1.20	99	515	659
In	3.40	293	515	156
Sn	3.72	305	510	232
Ta	4.48	830	(500)	3000
V	5.30	1020	398	1920
Pb	7.19	803	390	328
Nb	9.26	1980	440	2415

hillocks may also be observed, depending on the sign of the temperature variation (Lahiri and Wells 1969, Lahiri 1970).

Among the techniques for improving the performance of soft metal electrodes are a more controlled operation, such as better vacuum conditions during evaporation, and care in choosing the substrate material and temperature. Damage due to thermal cycling can be minimized by reducing the temperature excursion by a low temperature storage, that is, keeping the junction, when not in operation, in liquid nitrogen. Further improvements can be obtained by flooding the whole sample with a protective material such as SiO or photoresist in order to keep out unwanted atmospheric effects. Experience shows, however, that despite these precautions within the context of the applications the results are to be considered rather unsatisfactory. It appears to be most realistic to use either soft metal alloys or transition metals, among which niobium is particularly promising.

In applications, whether a junction is “good” or not strictly depends on the purpose to which the device is devoted. These specifications are discussed case by case in the chapters dedicated to applications. Here we confine our attention to more general requirements such as easily controllable procedures, great reliability, and a high degree of reproducibility.

8.2.2. Soft Metal Alloys. An IBM patent (Anacker et al. 1973) reported data on junctions in which the cyclability was definitely improved by using lead electrodes with the addition of indium or In-Sn to prevent hillock formation. These binary and ternary alloys in fact make it possible to produce very stable junctions. It is worth pointing out that such “additions” in the soft metal base layer can play a role both in the structure of the electrode and in the growing process of the oxide. It can also improve the adherence of the film to the substrate. In a subsequent IBM patent Eldridge and Matisoo (1974)

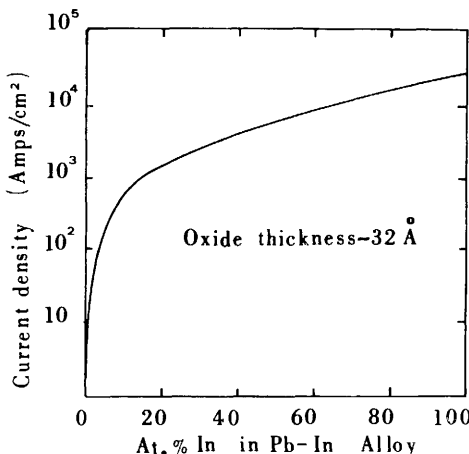


Figure 8.1 Josephson current density as a function of the indium percentage in the Pb-In alloy.
(After Anacker et al. 1973.)

reported further interesting results concerning “Pb-PbO_x-Pb” junctions made by alloying the lead base electrode with indium. Among other things it was suggested that by varying the partial concentrations of the alloy it is possible to realize an array of junctions of different barrier heights on a single chip and in a single oxidation step. The decrease of the effective barrier is indeed an essential aspect of indium alloying. It is possible to make junctions in which a thicker oxide is obtained without greatly sacrificing the value of the maximum supercurrent. This is evident from Fig. 8.1 which shows the critical supercurrent for this kind of structure as a function of the indium percentage in the alloy. The data refer to an oxide thickness of 32 Å. The role of indium in the lead superconducting electrodes has been discussed also by Emmanuel et al. (1974). In this work surface studies demonstrated the influence of the annealing temperature and sputter etching both on the quality and the quantity of hillocks, whereas no appreciable effect was found in connection with the nature of the substrate, which appears to contradict the idea of the prominent role played by the different thermal expansions of the metallic films and the substrates.

As mentioned above, good results can be achieved by using binary and ternary alloys. The thermal stability of lead alloy films improves with the use of ternary (Pb-In-Au) rather than binary alloys. Lahiri (1976) observed the onset of the first hillock in a lead film of a given area (1 cm^2) after one thermal cycle (298–4.2 K). In Pb-2%Au and Pb-8%In films the first hillock was formed after two such thermal cycles. Ternary alloy films as Pb-8%In-4%Au showed hillock growth after being cycled seven times. Furthermore, these films when subjected to high temperature (75°C) annealing clearly show the effect of the alloying against hillock formation. The effect of gold in preventing hillocks has

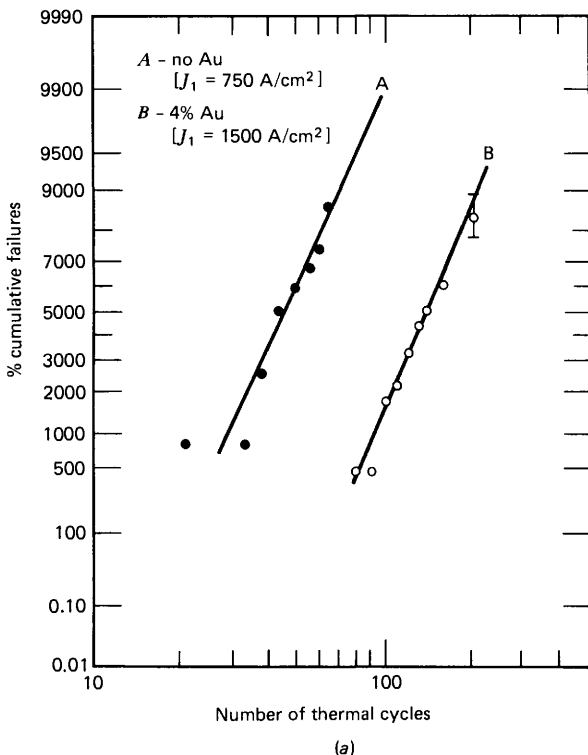


Figure 8.2 (a) Dependence of the percent cumulative failure as a function of thermal cycles (300–4.2 K) for junctions having zero and 4 wt% Au in the base electrode layer. (After Basavaiah and Greiner 1977.)

been pointed out also by Fu and Van Duzer (1976).[†] Detailed results on thermal cycling stability of Josephson junctions have been recently reported by Basavaiah and Greiner (1977) (Fig. 8.2a).

From this it is possible to infer unambiguously the improvement due, at least primarily, to the addition of gold. In both sets of data (curves A and B) the counterelectrodes were of Pb-1.7 wt% Au. It is interesting to observe that a thickness reduction of the junction electrodes can also lead to improvement (Lahiri and Basavaiah 1978 see also Chaudari 1974; Caswell, Priest, and Budo 1963). Recent investigations on the role of the thickness of the superconducting junction layers in connection with film stress and deformation provided further insight into the problem of cyclability (e.g., Murakami and Kirker 1978;

[†]As cited by Lahiri (1976), Chaudari (and other workers) independently observed the effect of the addition of gold to lead films to avoid hillocks.

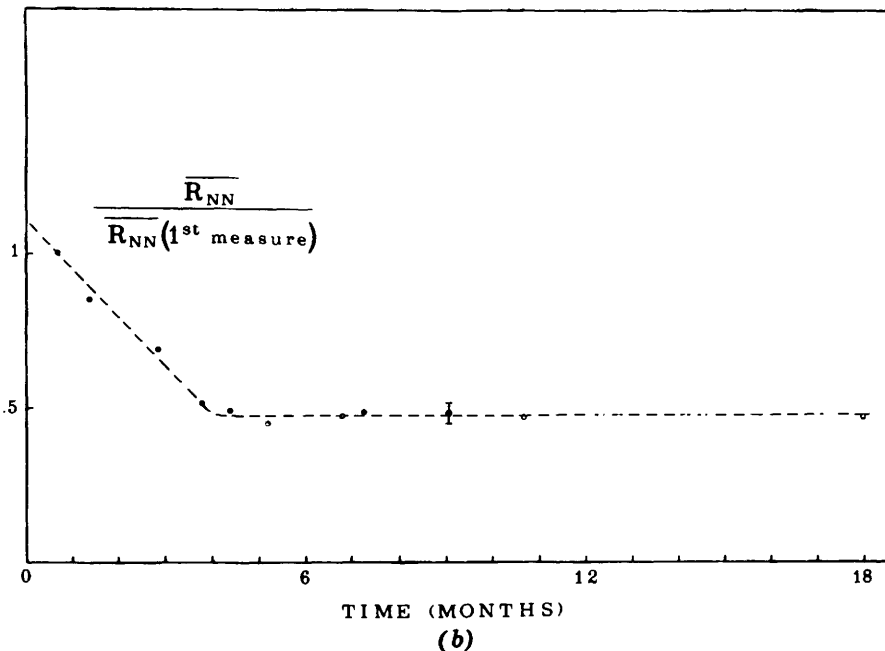


Figure 8.2 (b) Effect of room temperature storage and thermal cycling on properties of niobium-based Josephson junctions ($\text{Nb}-\text{Nb}_x\text{O}_y-\text{Pb}$). The junction normal tunneling resistance R_{NN} is used as a quality index. The resistance of each junction is normalized to the value measured in the first liquid helium test. Each point corresponds to an average over many (5-20) junctions fabricated in the same run under nominally identical conditions resulting in approximately equal maximum supercurrent densities. (Courtesy of V. Lacquaniti, G. Marullo and R. Vaglio).

Basavaiah, Murakami, and Kirker 1978). In the latest development in junction fabrication technology, gold has also been replaced by bismuth in the junction top layers. Counterelectrodes of Pb-29 wt% Bi have been successfully used not only because of their higher efficiency in preventing hillock formation, but also for the resulting junction V - I characteristics which show a lower excess current at voltages below the gap. Such a sharpness in the V - I curve is a significant property in the context of computer applications. For details and further references concerning the whole topic the reader is referred to the special issue of the *IBM Journal of Research and Development* (Vol. 24, No. 2, pp. 105-264, March 1980) describing the status of IBM's research project on Josephson computer technology.

8.2.3 Hard Materials (Transition Metals). "Hard" elemental superconductors can also be used as the base layer and possibly as the counterelectrode

in a Josephson junction. There are several reasons for considering these materials: high mechanical strength, chemical stability, high critical temperature, good adherence to glass substrates, no formation of protrusions during thermal cycling, and high stability of the oxides. A drawback lies in the high gettering action of these metals for various gaseous contaminants such as water vapor and oxygen. The latter can significantly alter the superconductive properties so that in thin films a different (lower) critical temperature with respect to that of the pure bulk can be observed. High purity thin films of Nb, Ta, and V can be deposited by electron beam evaporation (Neugebauer and Ekwall 1964; see also references cited there). In the context of tunnel junctions very good results were first reported by Nordman (1969) and by Mullen and Sullivan (1969) on Nb-NbO_x-Pb junctions. Other important works are due to Nordman and Keller (1971), Graeffe and Wiik (1971), Greiner (1971), Schwidtal (1972), and Hansma (1974). Of interest is also the paper by Hoel et al. (1972), which discusses a niobium technology for preparing junction arrays with a high pattern definition obtained by using integration circuit photoresist techniques. Among others we recall also the extensive paper by Rissman and Palholmen (1974) in which a detailed description of a simple fabrication procedure is given. More recently niobium based junction integrated arrays have been investigated by Owen and Nordman (1974) with excellent results. Thus the literature on Josephson junctions employing a niobium base layer is quite rich; moreover, other papers that refer to this kind of structure are discussed in other chapters of this book in various contexts. Such junctions exhibit a very great stability, as demonstrated also by life test measurements performed by various authors (as an example see Fig. 8.2b). Besides IBM work let us recall for instance recent work carried out by Waho, Kuroda and Ishida (1980).

In almost all the cases just considered the junctions were made by sputter deposition of the niobium base layer oxidation and an overlaying of the niobium oxide either by lead or a tin metal sheet.[†] However, it is desirable, at least for some applications, to get symmetric Nb-Nb junctions. The first successful work in this direction was carried out by Laibowitz and Cuomo (1970) and by Laibowitz and Mayadas (1972). In the former case the structure was obtained by epitaxially growing a single crystal niobium layer onto a single crystal Al₂O₃ substrate and making the tunneling barrier by sulphuric acid anodization. In the latter investigation a structure Nb-Al-Al₂O₃-Nb was realized. Broom et al. (1975) have reported excellent results on Nb-NbO_x-Nb junctions. A careful investigation of the properties of Nb-NbO_x-Pb and Nb-NbO_x-Nb junctions in the range of temperature 2–9 K has been performed by Broom (1976). Hawkins and Clarke (1976) also obtained reliable Nb-Nb junctions by overlaying the oxidized barrier (NbO_x) with a very thin (~ 10 –20 Å) copper layer before depositing the second niobium electrode.

[†]In Hansma's work the counterelectrode is actually made by a Pb-In alloy.

A very stimulating result has been obtained by Moore, Rowell, and Beasley (1976). These authors have reported experiments on Josephson junctions made by using a $\text{Nb}_3\text{-Sn}$ thin film as the base layer and lead as the counterelectrode. They reported very "clean" $V\text{-}I$ characteristics of junctions made with the Nb-Sn films of various composition. On increasing the tin concentration toward Nb_3Sn , a critical temperature of 17.2 K and a gap of 3.2 meV were observed. More recent work is due to Howard, Rudman, and Beasley (1978) (see also Beasley, 1978).

Some investigations have been reported also on vanadium based junctions. We just recall the work by Seifarth and Rentsch (1973) in which $\text{V-V}_x\text{O}_y\text{-Pb}$ Josephson junctions made by using electron beam evaporation are discussed. The dependence of the critical current vs. the magnetic field showed some discrepancy from the ideal pattern. The life test measurements for a period of more than one year indicate a rather high stability. Other investigations on vanadium based junction are due to Albrecht et al. (1974), Yanson and Rybal'chenko (1975, 1977), Dettmann (1975), Dettmann et al. (1977), Rybal'chenko and Bondarenko (1978), Dettmann and Albrecht (1979), Di Chiara, Peluso, and Russo (1979), and Barone et al. (1980).

8.3 Oxide Barriers

Metals can react more or less strongly with oxygen depending on the value of the free energy decrease that is involved in the reaction. The first requirement for making reliable barriers is to deal with nonporous oxide; in this case the oxide is protective, that is, the metal is preserved against further oxidation. Conversely, in some metals a contraction of the oxide volume with respect to the consumed metal volume occurs, causing contractive stresses that lead to porosity. A further passage of oxygen molecules is then possible, which react at the oxide-metal interface and allow the oxidation to proceed. In protective oxides the mechanisms of the oxide growth can be essentially described by a migration of positive metal ions through the oxide, which leads to a reaction at the boundary between the oxide and the oxidizing atmosphere. A competitive mechanism of oxidation can be the reaction at the metal-oxide interface produced by oxygen ions crossing the oxide film. In both cases electrons diffuse from the metal to the oxidizing atmosphere. The occurrence of the various processes is governed by transport and electrical properties such as metal and oxygen ionic diffusivity, electrical conductivity of the oxide, and effects of charge distribution at the interfaces.

The time dependence of the oxide growth can be described by different equations depending on the range of thicknesses considered (see, for instance, Kubaschewski and Hopkins 1962; Hauffe 1965). In fact, linear, parabolic, cubic, logarithmic, and inverse logarithmic relationships can hold and, for a

given metal, a combination of these dependences may be required in order to describe the oxidation rate over a wide thickness and temperature range. In the very thin film region (10–20 Å) of interest to us the situation is quite complicated and the theoretical interpretation rather incomplete. It is clear that even the assumption of a continuous oxide growth process is quite arbitrary; when oxide thicknesses of few angstroms formed in several hours are considered, a steplike rather than a continuous growth is expected. As a consequence, whatever is the measurement technique it gives some average oxide thickness value.

On the basis of an earlier idea due to Mott (see references quoted above), Hauffe and Ilschener suggested a mechanism of oxidation that straightforwardly leads to a direct logarithmic relationship for the oxidation rate. It follows from the assumption that the slowest process, which represents the rate determining step, is the tunneling of electrons instead of the ionic transfer as assumed in the Cabrera-Mott model which should be valid in the ~40–50 Å thickness region (see reference above).

The typical methods for producing oxide tunneling barriers for junction structures are (1) thermal oxidation, (2) d.c. oxygen glow discharge, and (3) r.f. glow discharge. Some other less common techniques also deserve attention.

8.3.1 Thermal Oxidation. One way, theoretically the easiest, to prepare an oxide tunneling barrier is by exposure of the first deposited superconducting layer to an oxidizing atmosphere as air or pure oxygen. Several parameters can play a role in this procedure: oxygen pressure, exposure time, substrate temperature, presence of water vapor, organic impurities, and so on. When a clean surface is exposed to the oxidizing atmosphere the oxygen can be in a first stage either chemisorbed (monoatomic layer) or combined in a stoichiometric oxide at the surface. The growth of the oxide film increases the separation between the oxygen-oxide, and oxide-metal interfaces, decreasing the effect of the oxygen ion distribution on the migration of metal ions. This leads to the peculiar self-limiting character of the thermal oxidation process. It is important to observe that although this self-limiting growth is a great advantage for the required uniformity, it implies that only relatively thin oxide films can be obtained. As we have mentioned, temperature is an important parameter in the oxidation process. Generally the rate v of a chemical reaction increases with temperature following the Arrhenius equation $v = C \exp(-E_a/T)$ (C is a constant and E_a is the activation energy). The oxidation of soft metals in the preparation of superconductive junctions can generally be done at room temperature. For junctions with a niobium base layer the oxide barriers can be obtained with the aid of high temperature (range 100–200 °C) within minutes (see below).

Figure 8.3a shows the lead oxide thickness, measured by ellipsometry, versus oxidation time. These data obtained by Eldridge and Matisoo, (1970) clearly indicate a logarithmic growth rate of the oxide. Thermal oxidation

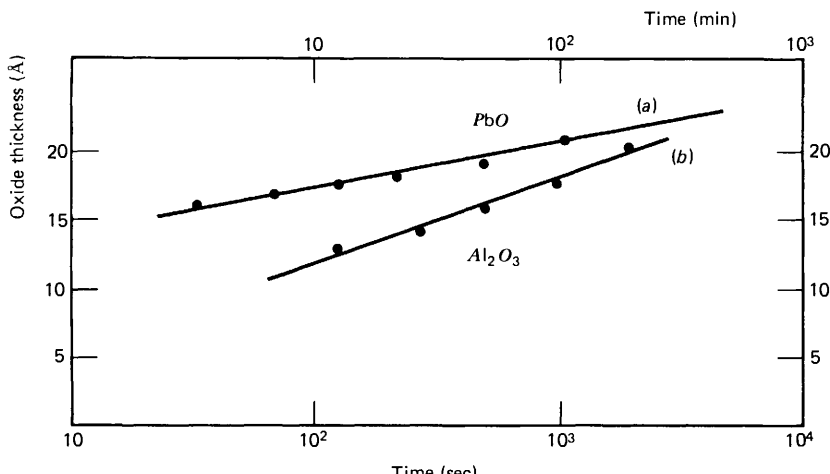


Figure 8.3 Oxide thickness vs. time. Lead oxide thermal growth (data taken from Eldridge and Matisoo 1970) and aluminum oxide d.c. glow discharge growth (data taken from Miles and Smith 1963).

requires a rather long time for the preparation of the barrier layer; this in principle permits greater control of the oxidation time and consequently of the barrier thickness. However, it increases the probability of external contaminations such as pickup of organic impurities, effect of water vapor,[†] and so on. In Fig. 8.4 the data reported in the reference above are replotted in the oxygen pressure thickness plane for a given oxidation time and at a given temperature. We recall that the oxidation can be performed using either pure oxygen or air. It is difficult to understand in detail the difference between the two cases. The presence of the "nonreactive" part of the air can in fact either decrease the oxidation rate or speed it up because of the possible effect of catalysis. In the case of oxide growth on lead alloy (Pb-In) rather than pure lead, there is a reduction in the oxidation rate and the saturation thickness (see, for instance, Donaldson and Faghihi-Nejad, 1978).

8.3.2 D.C. Glow Discharge. Let us discuss now a simple and widely employed method of oxidation. As previously mentioned, the negative charge distribution of the oxygen ions at the oxygen-oxide interface allows the migration of metal ions and produces further growth of the oxide film. As the oxide thickness increases, however, the effect of this electrical field decreases since the two interfaces, oxygen-oxide and oxide-metal, move apart. Thus the migration of metal ions can be enhanced with the aid of an externally applied electrical field.

[†]Recently a simple humidity controlled oxidation procedure was proposed by Garno (1977).

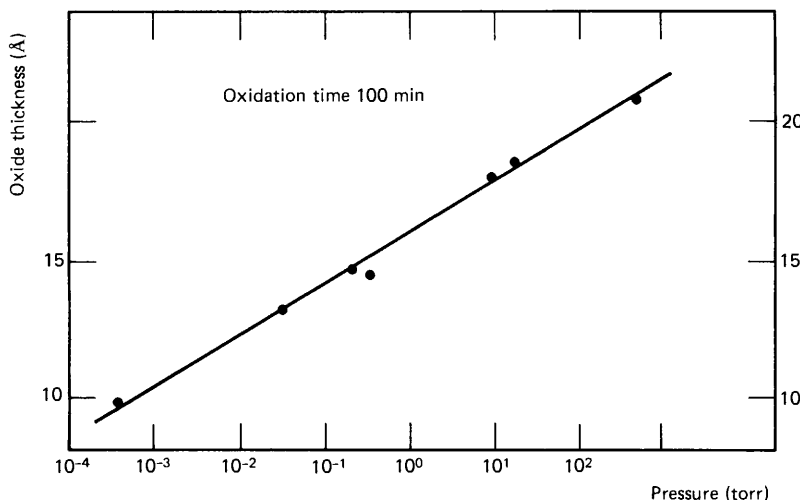


Figure 8.4 Lead oxide thickness vs. oxygen pressure (time exposure 100 min). This dependence is obtained using the data reported by Eldridge and Matisoo (1970).

In practice it is convenient to follow the plasma oxidation procedure in which the potential of the metal base layer is floating rather than the plasma anodization procedure in which the film is held at a fixed potential and the strong electrical field that is present across the thin oxide layer can lead to damages of the barrier itself. Among others, we recall here the pioneering work by Schroen (1968) and by Pritchard and Schroen (1972) on the combined technology of glow discharge oxidation and lithography for junction preparation.

To produce oxygen plasma, a negative potential of a few hundred volts is applied to a single electrode or to a set of electrodes of suitable geometry (typically cylindrical) in the oxidation chamber. The distribution of the potential near a negative cylindrical electrode can be depicted as in Fig. 8.5. Obviously in the vicinity of the negative electrode there is a high concentration

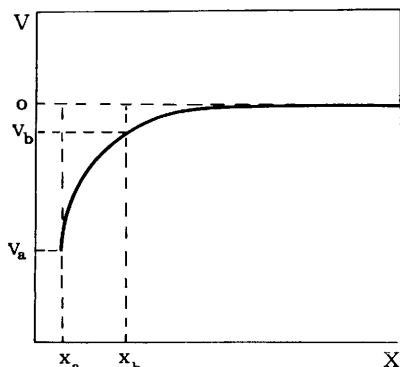


Figure 8.5 Sketch of the potential distribution near a negative electrode.

of positive ions, which decreases rapidly with distance. The quasi-neutral region corresponds to a distribution in which electrons "compensate" positive ions. The ionization mostly occurs within a transitional region via the process $e^- + O_2 \rightarrow O_2^+ + 2e^-$. A slight contribution to the oxygen ionization can derive from a process that involves slow electrons in the quasi-neutral region: $e^- + O_2 \rightarrow O_2^-$. The figure shows that the potential drop is essentially confined to the transitional region and that the potential in the quasi-neutral region is close to the ground. The samples (metal base layers) are placed in the quasi-neutral region. In Fig. 8.6 is sketched the metal-oxide-plasma system during the oxidation process in which inward diffusion of oxygen atoms and outward diffusion of oxygen vacancies are assumed.

The reason why a negative electrode potential should be preferred over a positive one is twofold: higher stability and no contamination. In fact, with positive electrode potential the ion current is much higher. The positive ions accelerated toward the walls of the oxidation chamber produce a strong sputtering action, extracting various impurities and thus introducing a dangerous contamination into the sample. In the case of a negative electrode potential the plasma is negative with respect to the chamber so that positive ions cannot be accelerated toward its walls.

Typically, oxidation by a glow discharge is performed with an oxygen pressure of tens μm of Hg. It is worth pointing out, however that the values for each parameter—discharge potential, electrode geometry, oxygen pressure, and so on—separately given, can be meaningless since these factors are intimately related. Glow discharge procedure is a much faster process with respect to thermal oxidation (Fig. 8.3b). Whether an oxidation procedure is to be preferred over another is difficult to decide. To some extent the answer is to be found in the combination of the chosen metal as base layer and the oxidation process, since all the data on quality and reliability are deduced from the behavior of the whole sample.

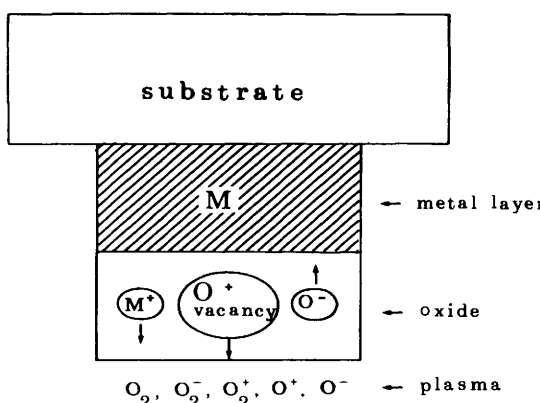


Figure 8.6 Qualitative sketch of the metal oxide plasma system.

8.3.3 R.F. Glow Discharge. Greiner (1971, 1974) has developed an oxidation procedure that consists of a glow discharge technique employing an r.f. potential. In this oxidation process two competitive mechanisms are involved which follow the half cycles of the r.f. potential: the oxide growth and the oxide reduction by sputter etching effect. The rate of the former process is roughly logarithmic, whereas the sputter etching rate is almost independent of the oxide thickness. The two mechanisms can be separately controlled by varying the oxygen pressure and the r.f. power, respectively. In this way, it is possible to reach a dynamic "equilibrium" condition between the two antagonist processes in which the oxide thickness is time independent. Fig. 8.7 reports experimental measurements of oxide growth on lead film by ellipsometry. The rotation angle of polarized light, which is proportional to the oxide thickness, is plotted as a function of time. The rapid oxide growth and its saturation at the equilibrium condition previously discussed are evident. As soon as the pressure is increased, the oxidation proceeds (growth is faster than removal). When the oxygen pressure is lowered to its initial value, the sputter etching prevails on the growth and the oxide reverts to its original thickness equilibrium value. Thus such a procedure permits one to keep the oxidation process under control and therefore to carefully "plan" the desired oxide thickness. This technique has been widely studied and employed by various authors (e.g., Emmanuel et al. 1974; Kuroda, Waho, and Ishida 1980; Karulkar and Nordman 1979, 1980; Matsuda, Inamura, and Yoshiakiyo 1980).

Furthermore, we recall the successful reactive-ion-beam oxidation procedure in the realization of submicron junctions by Kleinsasser and Buhrman (1980).

Typical data of junctions obtained using different superconducting materials and oxidation procedures are shown in Table 8.2. As far as the

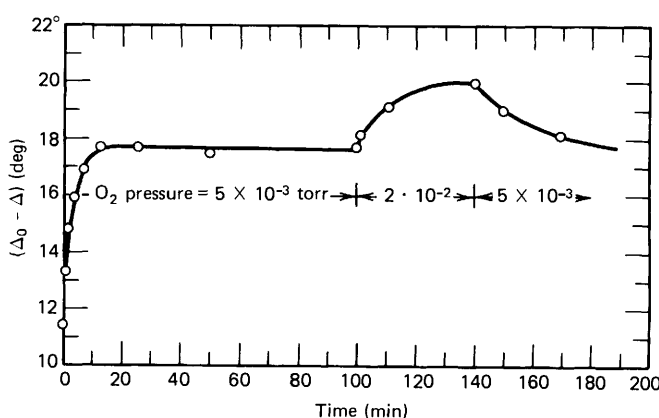


Figure 8.7 R.F. oxidation process. The rotation angle of polarized light which is proportional to the oxide thickness as function of time. It is clear the change in $\Delta_0 - \Delta$ after the achievement of steady state by first increasing and then decreasing the oxygen pressure. (After Greiner 1974.)

TABLE 8.2 Current density (J_1), magnetic field penetration depth (d), and ratio between the wave velocity in the oxide and in the empty space (\bar{c}/c) for different oxide barrier junctions. t and ϵ_r are thickness and relative dielectric permeability of the oxide. All the data refer to $T \approx 4.2$ K except the data on tin junctions, for which $T \approx 1.35$ K

Electrode Materials	J_1 (A/cm ²)	$d = \lambda_{L1} + \lambda_{L2} + t$ (Å)	$\frac{\bar{c}}{c} = \sqrt{\frac{t}{\epsilon_r d}}$	Oxidation Process
Sn-Sn ^a	0.7 ÷ 13.9	970	0.058	glow discharge
Pb-Pb ^b	$10^{-2} \div 10^2$	860	0.066	thermal
Nb-Pb ^c	3 ÷ 5	1400	0.038	thermal
Nb-Pb ^d	30 ÷ 320	1300	0.027	r.f. glow discharge
Nb-Nb ^e	524 ÷ 1570	1760	0.010	as above
PbAuIn-PbAu ^e	50 ÷ 1760	1900	0.036	as above

^aWang and Gayley (1978).

^bFinnegan, Wilson, and Toots (1976).

^cLacquaniti, Marullo, and Vaglio (1978).

^dBasavaiah and Greiner (1976).

^eBroom and Wolf (1977).

critical current density is concerned the highest values obtained so far are in the range of 10^5 A/cm² (Niemeyer and Kose 1976a,b; Howard et al. 1979) and even above 10^6 A/cm² (Kleinsasser and Buhrman 1980).

8.4 Junction Patterning

In dealing with thin film devices, one major problem is the shaping of the film into the desired pattern. We discuss here briefly only some aspects of the subject.[†] Of great importance is the goal of making the devices as small as possible, especially when large arrays of such devices are considered. For instance, in the case of logic operations, high packing densities ultimately reduce delay times related to the transfer of the information between the elements of the array. We have witnessed over the years a progressive shrinking of electronic device dimensions. So far 10,000 or more transistors can be assembled on a single chip of a few millimeters, and this limit will be soon overcome. As discussed in the final chapter, Josephson devices are very serious candidates for computer applications. Because such devices dissipate much less power than semiconductor components, their packing density limits are ultimately fixed by geometrical factors (besides "wire-in and wire-out" problems).

[†]An excellent account of this topic has been given by Smith (1974); see also references reported there.

8.4.1 Metal Masks. To prepare junctions of rather simple geometry and with electrodes of dimensions down to 0.1 mm, it is sufficient to use metal stencil masks in which the pattern is cut by a careful machine shop procedure or by conventional photoresist techniques. The film is shaped by the deposition through the mask which is put into close contact with the substrate to improve the pattern definition. The best results are obtained by using stainless steel sheets thick enough to be rigid and thin enough to be easily processed and to avoid shadowing effects; a thickness of about 0.05 mm can be a good compromise. Moreover, a large variety of more sophisticated techniques has been developed, including the high performance multilayer metal masks that are widely employed in semiconductor technology.

8.4.2 Photolithography. To achieve film dimensions in the submillimeter range down to 1–2 μm , photolithographic procedures are employed. The most commonly used technique consists of contact printing (or “shadow printing”) onto a photoresist coated substrate through a high resolution, high contrast photographic plate (photomask).[†] Two types of photoresists can be adopted depending on the specific procedure. Using positive or negative resist, either the regions exposed to light or those not exposed to light will be washed away by suitable developers.

Indeed, photolithography can be performed optically either by contact printing or, less commonly, by projection of the pattern through an optical system onto the resist layer (projection lithography). The photomask for contact printing can be prepared by starting from a suitable large size drawing of the pattern and transferring it, via a photoreduction process, onto a small (e.g., $5 \times 5 \text{ cm}^2$ is a standard size) glass photographic slide. For sophisticated patterns the usual mask fabrication facility includes an artwork cutting board. Here the desired pattern is cut through a red semitransparent plastic sheet which is supported by a thicker transparent plastic base layer. This operation can be either hand controlled or computer controlled. At this point a shrinking of the pattern is provided by a careful photoreduction process, possibly through several stages (a two step reduction is most common) depending on the required specifications. Finally the pattern (several hundred times smaller than the original) is transferred onto a glass slide that constitutes the photomask; “step and repeat” machines can provide iteration of the simple pattern to achieve more complex arrays. Presently the photomasks are straightforwardly made by means of direct computer controlled exposure.

Let us discuss the major steps in a photolithographic process assuming that a negative resist is used. These are sketched in Fig. 8.8 (on the left side). After a careful cleaning of the substrate a superconductor layer is vacuum deposited all over the substrate. The substrate with the metal film can be flooded with photoresist; by “spinning” it at high velocity a smooth, thin and

[†]To avoid a gap between the photomask and the top of the resist layer and provide intimate contact, suitable conformable photomasks can be used (see Smith reference quoted above).

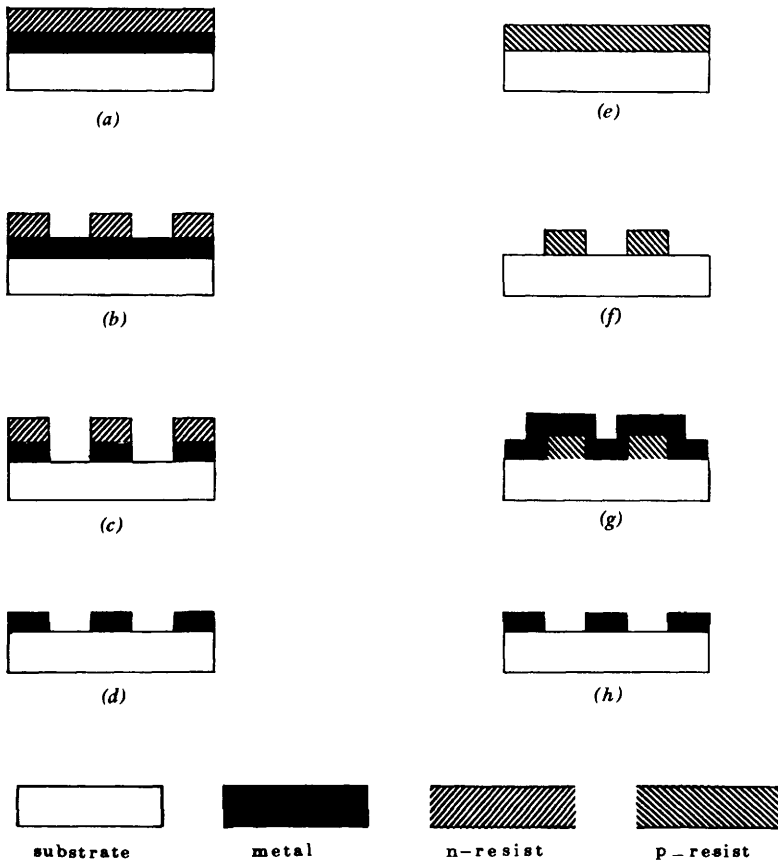


Figure 8.8 Main steps in a patterning process by photolithography. On the left negative resist is used. On the right positive resist is used in a liftoff technique (see text).

uniform layer is obtained (*a*). The parameters that govern the quality of the photoresist layer are the viscosity of the resist and the angular velocity, the acceleration, and the time of the spinning. A thinning and a higher uniformity of the layer are obtained by higher acceleration. Typical thicknesses are about 1 μm . At this point exposure through the photomask is performed using a mercury lamp. Selected areas of the photoresist layer, namely those protected by the dark areas of the photomask, are removed by the appropriate developer (*b*). For a given photoresist layer thickness, optimal exposure and developing times must be found that give the best resolution in the developed photoresist. Thus the superconductor is etched off chemically or by a sputter etching technique (*c*) and the residual resist removed by a suitable solvent (*d*).

Of course it is possible, at least in principle, to obtain the same film pattern by employing a positive resist with a complementary mask of the one used in the negative resist process.

8.4.3 Lift-Off Technique. A widely used procedure that results from the combination of lithography (not necessarily photolithography) and a metal "lift-off" process should be mentioned now. This method avoids the problems related to the etching of the superconducting film. As an example we outline a technical procedure to obtain the same film pattern as in the process previously described (Fig. 8.8) assuming the use of the same photomask but a positive resist. The first step is coating the substrate with the resist (*e*). Then, by photoprinting, the resist is shaped in the desired pattern (*f*). The superconductor film is then deposited (*g*). Finally, the developer removes the resist under the metal together with the metal itself so that there remains just the metal film in contact with the substrate (*h*). The last step, which is usually referred to as "lift-off," is rather delicate, since the desired patterned metal (or at least its edges) can easily be torn off the substrate during the process. To overcome this problem it is necessary to break the continuity of the metal layer by some means so that the patterned film is not affected by the lift-off of the metal on the photoresist. This can be realized in several ways. One possibility is profiling the photoresist by immersion in chlorobenzene after exposure (Canavello, Hatzakis, and Shaw 1977). This treatment produces a reverse bevel profile of the order of 20° in the photoresist edges. This is sufficient to produce a "clean" lift-off, if the deposition source is almost normal to the substrate (see also Hatzakis, Canavello and Shaw 1980). To get a better resolution more sophisticated methods must be employed.

We now outline two methods, which are skematically described in Figs. 8.9 and 8.10. In one method (Grebe, Ames, and Ginsberg 1974) the substrate is first coated with a positive resist approximately $1.5 \mu\text{m}$ thick; then an aluminum film of about $1 \mu\text{m}$ is evaporated, which in turn is covered by a second resist layer (equal to the first one). The top resist is then exposed to get the desired pattern (Fig. 8.9*b, c*) and the aluminum is chemically etched through the windows produced in the resist (Fig. 8.9*d*). This etching is perhaps the most critical step of the procedure. At this point by a suitable overexposure (*e*) the bottom layer of resist undercuts the aluminum by about $1 \mu\text{m}$. Thus, on developing away the resist, there remains only the patterned aluminum (Fig. 8.9*f*) which plays the role of a stencil mask on the undercut bottom resist. Now the chosen superconducting metal can be deposited without fear of tearing effects, since the desired patterned metal is not connected to the remaining part of the film.

A second procedure developed at Bell Laboratories (Dunkleberger 1976, 1978) is illustrated in Fig. 8.10. The bottom photoresist layer is first exposed (*a*). Then a suitable metal layer (say aluminum $1-2 \times 10^3 \text{ \AA}$ thick) is deposited, separating the bottom from a second resist layer (*b*). The top resist is then exposed through a mask (a negative of the desired pattern) and developed (*c, d*). Then we have the aluminum etching step (*e*) and the development of the bottom resist (exposed in the first step). In this way, playing on the exposure and development procedures, it is possible to get the appropriate undercut (*f*). In contrast to the previous method, here the deposition of the

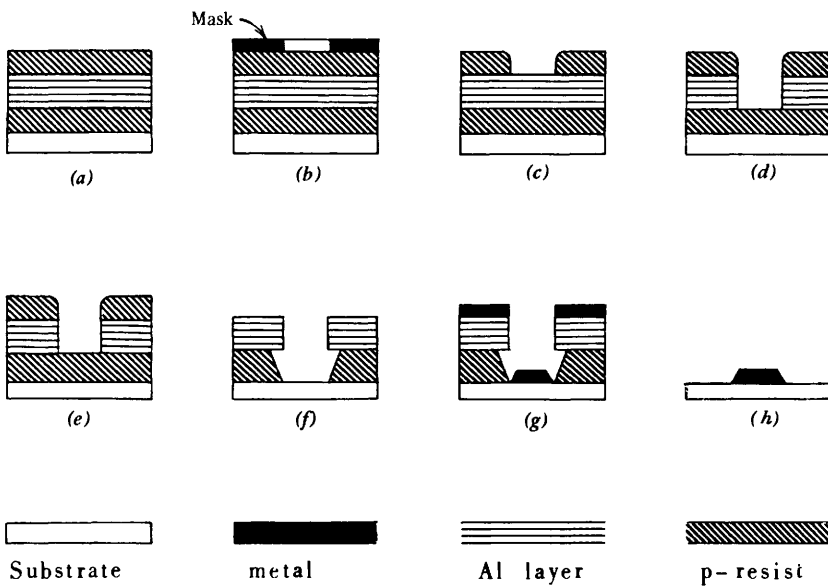


Figure 8.9 Sketch of the photolithographic process used by Grebe, Ames, and Ginsberg (1974).

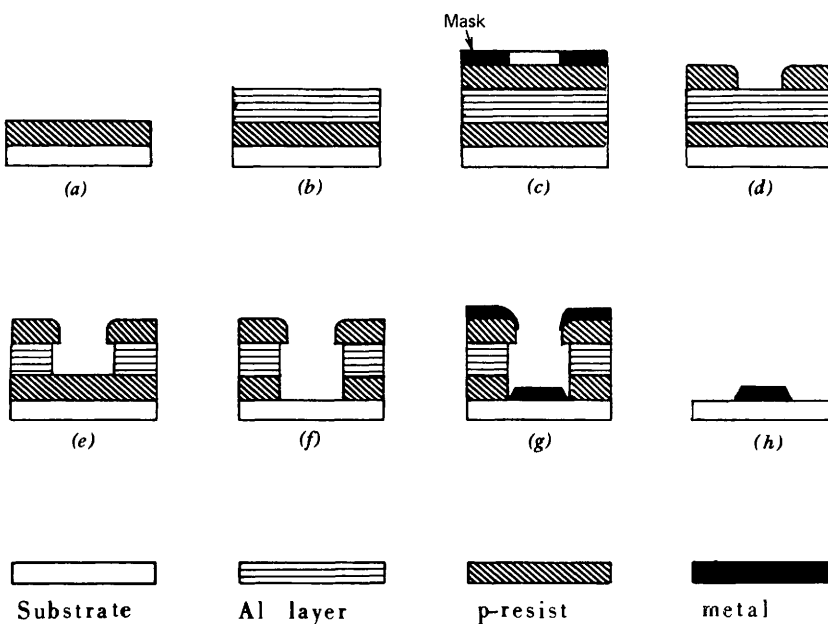


Figure 8.10 Sketch of the photolithographic process used by Dunkleberger (1978).

desired metal (*g*) occurs through the top resist rather than the aluminum. The aluminum layer serves only as a suitable separation of the two resist layers, and the ultimate resolution is related to that inherent to the resist technology. Finally, we recall that the lift-off technique can be employed also in the preparation of high T_c junctions such as Nb₃Sn (e.g., Howard 1978).

A quite different approach has been followed by Feuer, Prober, and Cogdell (1978) in the preparation of submicron bridges. This procedure consists of an optical projection lithography and a lift-off technique. It is exposure that is different—in this case it is performed from the back, that is, the light goes through the substrate and crosses the resist layer from the bottom. The projection exposure is provided by a reflected light microscope. The “back-exposure” technique permits a very sharp resist profile, and, possibly, such a “reversed path” in the resist leads to the desired undercut. The essential aspects of the whole procedure are summarized in Fig. 8.11.

Among the most important procedures developed for “lift-off” processing of thin films we recall also processes employing offset masks from the substrate and oblique angle film deposition by Nyemeyer (1974), Nyemeyer and Kose (1976a, b), Dolan (1977).

8.4.4 Electron Lithography. Regarding the best achievable geometrical resolution, let us observe that lithography is a process inherently limited by the wavelength of the source radiation. In fact, when the light wavelength and the size of the pattern lines become comparable, diffraction effects arise that lead

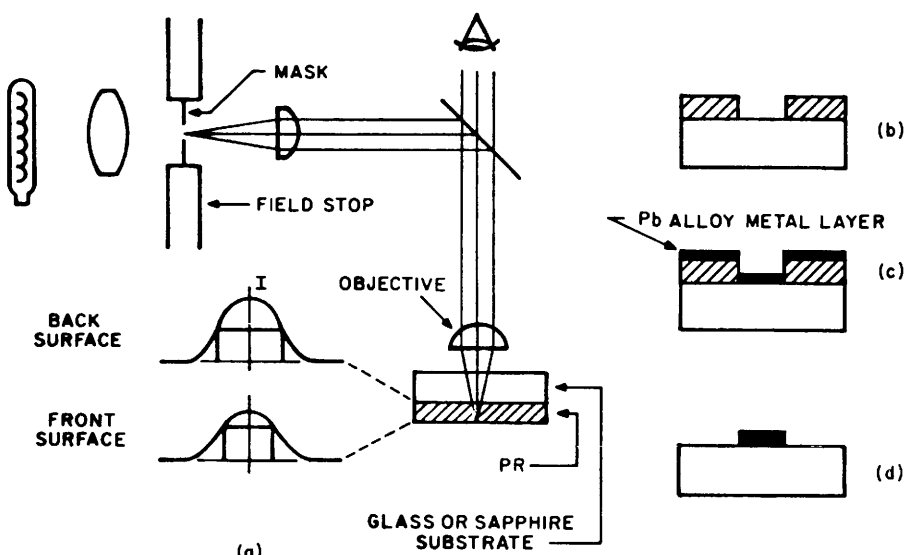


Figure 8.11 Optical projection lithography and lift-off using “back exposure” technique. (After Feuer, Prober, and Cogdell 1978.)

to a blurring of the contours of the pattern. In the most advanced photolithographic procedures this limit is about $1 \mu\text{m}$. To go down to the $0.1 - 1 \mu\text{m}$ range it is necessary to use a beam of electrons, since their associated wavelength is about a thousand times less than the wavelength of visible light.[†] Furthermore, electron beams can be "steered" by electric or magnetic deflection. This control, which can be performed by a computer, leads to the possibility of choosing and changing patterns with great flexibility, thus eliminating all the problems related to the preparation of a large number of photomasks, each one purposely made for a given specification. Thus the actual system for electron lithography consists of an electron microscope on-line with a suitable computer which controls the optical exposure following the instruction of the programmed pattern. Of course, in contrast to photolithography, the exposure is no longer made in parallel; rather, time is needed for the scanning of the beam to delineate the pattern. The exposure time in electron lithography can therefore be relatively long whenever large areas (compared with the beam size) are considered. To overcome this problem, electron optical systems with parallel exposure capability have been realized (at the University of Tübingen) which allow the simultaneous exposure of a great number of elements in a large pattern array. This procedure consists of a transmission electron microscope in which the roles of the mask and of the sample are reversed in the sense that the magnification of the object formed by the sample is replaced by the demagnification of the object formed by the mask. A striking example of the possibility of electron lithography in the context of Josephson devices is the bridge-type weak link realized by Broers and Laibowitz (1978) (see Fig. 8.20).

8.4.5 X-Ray Lithography. X-ray lithography is a very important replication technique for making high resolution patterns (Spears and Smith 1972a, b). It consists basically of a shadow printing technique, similar in principle to that of photolithography previously discussed. The associated wavelength is much shorter, however (typically soft X-rays), thus allowing much smaller limitations with respect to diffraction effects which, along with finite mask-sample separation as we have discussed, determine the ultimate pattern resolution. Moreover, X-rays, in contrast to electrons, travel in straight paths essentially unaffected by contaminations, stray fields, and deviating or scattering mechanisms. The masks for such a process consist of semitransparent membranes in which the required pattern is prepared in a thin X-ray absorbing layer. Thus the mask substrates should possess a combination of properties: transparent to X-ray radiation just in the area of the pattern, rigid enough to be self-supporting, smooth, flat, distortion free, and rugged. Successful masks have been made by using gold adsorbing patterns of silicon membrane windows supported by a

[†]Pioneering experiments have to be considered those by Buck and Shoulders (1958). Other references can be found in Smith (1974). For a simple and general account the reader is referred to Broers and Hatzakis (1972).

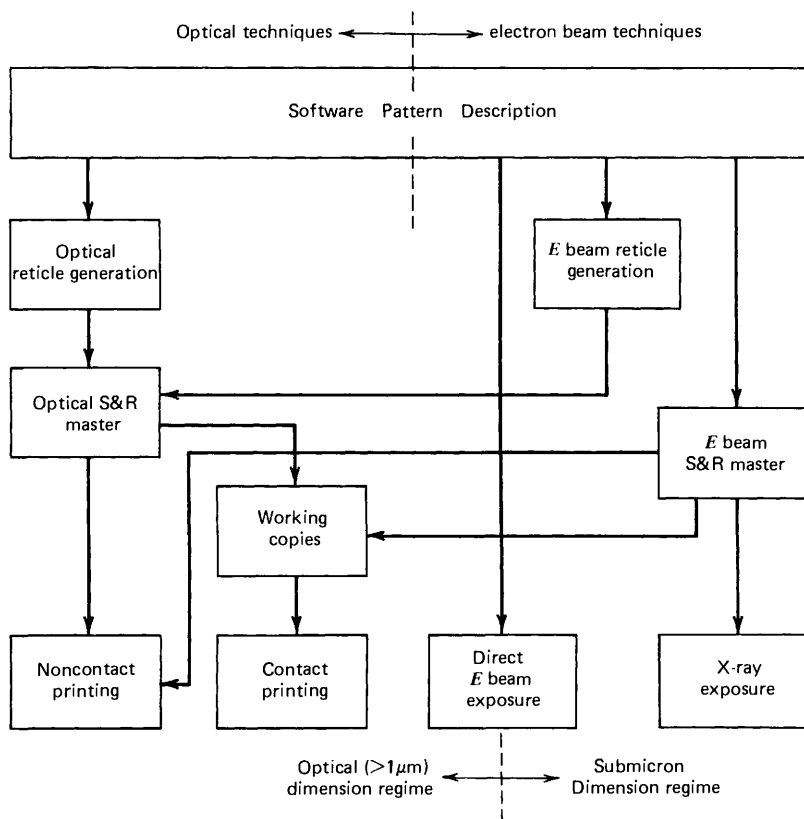


Figure 8.12 Pattern definition techniques for microelectronic devices. (After Blocker, Watts, and Holton 1978.)

silicon framework (Smith, Spears, and Bernacki 1973).[†] The resolution in X-ray lithography is limited by penumbral effects, the thickness of the absorber, and the interaction of the X-rays. Penumbral blurring as well as diffraction effects are related to the finite separation between mask and sample, which can also be a great advantage in preventing damage to both mask and sample. Therefore, again, optimal separation should result from the best compromise between these requirements. A recent overview of imaging techniques by X-rays (and electron beams as well) has been given by Blocker, Watts, and Holton (1978). Figure 8.12 summarizes pattern definition techniques.

8.5 Simple Procedures for Preparing Oxide Barrier Junctions

We outline here two simple recipes for fabricating Josephson tunnel junctions. These are only the “skeleton” of possible procedures, and the values of the

[†]Among other works we recall those by Spears, Smith, and Stern (1972), Cohen et al. (1973).

parameter are rough indications. Details of these procedures can be found in the literature and will be suggested by the necessary direct experience in the laboratory.

8.5.1 Evaporated Junctions. We do not go into the details of the specific vacuum technology. We know from previous discussion that reliable junctions require very good vacuum conditions. The vacuum system should therefore have a low ultimate pressure and should be able to keep low pressure conditions during evaporation. Furthermore, it must be as free as possible of such contaminants as organic impurities and water vapor. In the literature it is possible to find data on Josephson junctions obtained by using pressures during evaporation in a very wide range of values (10^{-5} – 10^{-9} torr) and often without information on the relative quantities of possible contaminants.

The evaporation chamber is a stainless steel box with resistance heaters that provide thin film evaporation. To select the electrode geometry, a remotely controlled mechanical system must be used for changing masks and substrate relative positions without breaking the vacuum. The films (say tin or lead) can be deposited on more or less sophisticated substrates. In the simplest procedure ordinary glass microscope slides can be used or Corning 7059 glass slides ($1 \times \frac{1}{2}$ in.) previously cleaned by conventional techniques. In addition, whenever the system is equipped for oxygen plasma glow discharge, ion cleaning in air atmosphere of low pressure (~ 10 – 20 torr) can be performed. The junction pattern definition is provided by supporting the substrates in close contact to the masks. These are preferably made of stainless steel (thickness of about 0.1 mm) by photoresist technique or, for very simple purposes, mechanically. A suitable thickness monitor provides information on growth and the final film thickness. After the first superconducting layer is deposited, the dielectric tunneling barrier can be obtained by oxidizing this film either thermally or by glow discharge. In the former procedure pure dry oxygen at atmospheric pressure is introduced in the bell jar for a period of say 1–3 hours depending on the metal. As previously discussed, these values are indicative only. In the literature it is possible to find a very wide range of values for the oxygen pressure and oxidation times. If a d.c. glow discharge procedure is adopted, pure dry oxygen at a pressure in the range of 10^{-2} – 10^{-3} torr is ionized from tens of seconds to a few minutes at a voltage in the range of 300–1000 V. These parameters, too, are rough indications only, since they are strongly interrelated and depend critically on the particular geometry of the electrode used. It is important, however, to keep the voltage reasonably low, because the ions can become energetic enough to “clean off” the oxide as it is formed, producing drastic damage in the barrier. As discussed in some detail, it is convenient to use a negative electrode potential to avoid contaminants from the walls of the oxidation chamber. After the oxidation step the system is pumped down again and the mask changer is adjusted in the correct position for the deposition of the counterelectrode. The sample is then ready; the last step in order to test the junction is making electrical connections.

8.5.2 Sputtered Base Layer Junctions. As a second example we describe a fabrication procedure of niobium based junctions following the technology developed by Hoel et al. (1972) and modified by Reible (1975). The main steps are illustrated in Fig. 8.13. A niobium film about 1000 Å thick is r.f. sputtered onto Corning 7059 substrate glass. The niobium is covered by a much thicker (order of 10^4 Å) aluminum layer also deposited by r.f. sputtering (Fig. 8.13a). The aluminum sheet with a pattern defined by photoresist technique and chemical etching (Fig. 8.13b, c) plays the role of a mask. The photoresist is removed and the niobium film is patterned by this aluminum mask using r.f. back sputtering. This process is controlled by the different rates of the sputter etching of the two metals. Residual aluminum can be removed by chemical etching. At this stage we have the desired niobium pattern on which the oxide barrier layer can be grown either thermally or by plasma oxidation (Fig. 8.13d) following the procedures previously described. At this point, in order to realize the counterelectrode a superconducting layer (in practice lead or tin) is deposited by evaporation. A photoresist pattern is developed on this layer (Fig.

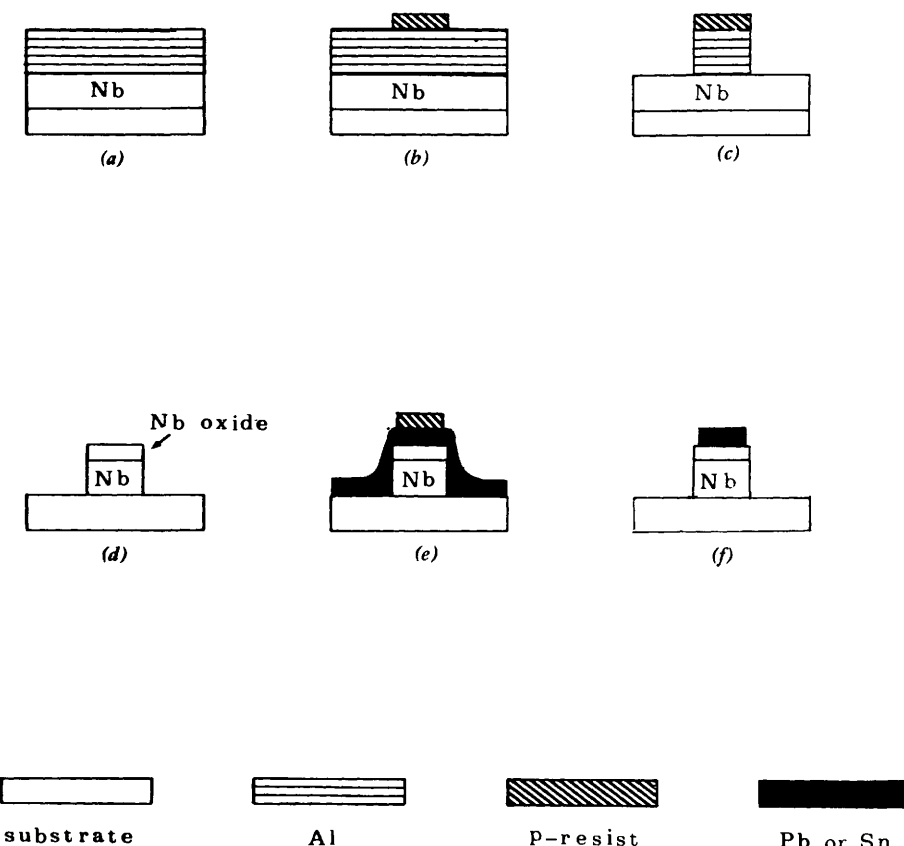


Figure 8.13 Fabrication procedure of niobium based junctions.

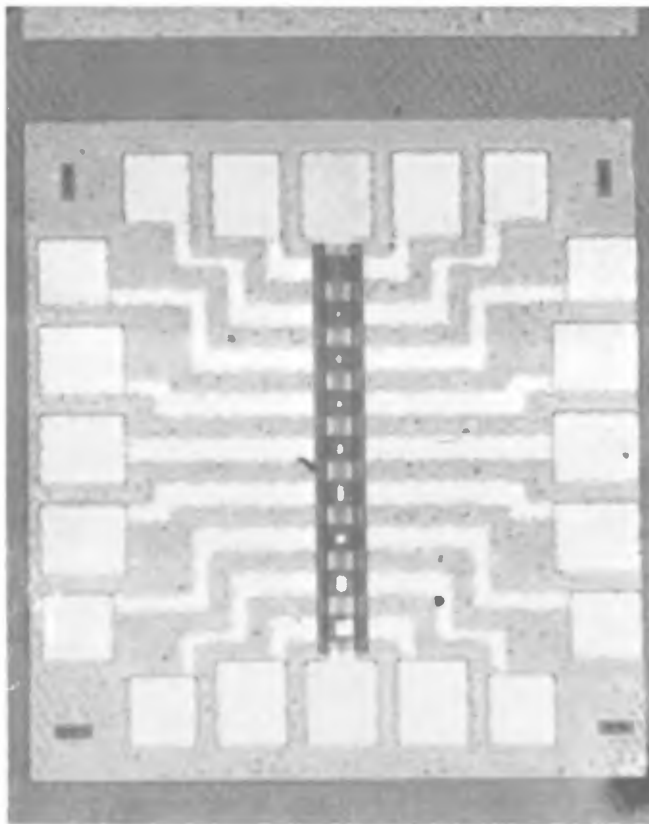


Figure 8.14 Niobium based junction technology. Integrated circuit realized by Owen and Nordman (1974).

8.13e) Figure 8.13f represents the final sample in which the pattern of the counterelectrode has been etched chemically and the photoresist removed by a suitable solvent. An outgrowth of this procedure is represented by the integrated circuit technology developed by Owen and Nordman (1974); an example is shown in Fig. 8.14.

8.5.3 Other Oxide Barrier Structures. Before concluding our necessarily incomplete discussion of oxide barrier junctions we wish to recall the preparation of samples using In_xO_y barrier layers proposed by Aspen and Goldman (1976). Furthermore, it is worthwhile to mention the simple and ingenious technique to fabricate niobium based junctions without deposition of niobium films (Cardinne and Nordman 1973). The procedure uses as base electrode the polished end of a niobium wire supported by insulating material inside a small copper cylinder. The junction is formed at the end of this niobium wire, which

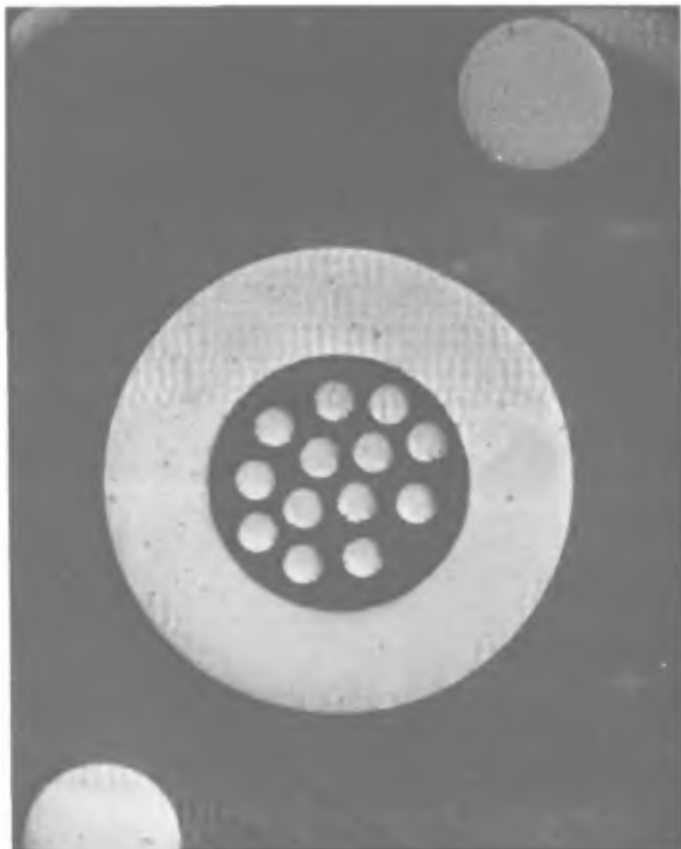


Figure 8.15 Top view of 13 niobium wire junctions. (Courtesy of J. E. Nordman.)

after a suitable sputter etching is oxidized, and then covered by an evaporated lead counterelectrode. Details of the procedure can be found in the work quoted above. Figure 8.15 shows the top view of a structure that contains 13 such junctions.

8.6 Semiconductor Barriers

Semiconducting barrier layers can be vacuum deposited by the various techniques previously discussed for metal layers. In general, however, some problems related to the nature of semiconductor materials make the fabrication process of such junctions in some cases quite hard to control. Among others, we mention the possible presence in a semiconductor film of surface states, interface problems, uncontrolled doping, occurrence of pinholes, and non-stoichiometry. It should be noted that in dealing with semiconductor thin films, in many cases amorphous, a wide variety of properties can be observed

as a consequence of slight modifications of the parameters in the deposition procedures. Once more the V - I characteristics can supply a useful "first look" indication of the actual situation. For example, among other features, a reduction of the superconducting gap may reveal the possible occurrence of interdiffusion between the semiconductor barrier material and the superconducting electrodes. A serious and rather general problem is the presence of pinholes in deposited semiconductor barriers, which result in metallic paths through the barrier. The usual way to overcome the problem is to perform an oxidation step just after the deposition of the semiconductor layer to fill the pinholes, thus avoiding shorts. However, such an oxidation step can have no trivial consequences such as altering the properties of the semiconductor. In addition, an absorbed oxygen layer on the tunneling barrier can lead to a continuation of the oxidation in the upper electrode, with a resulting additional barrier reducing the critical current density.

8.6.1 Various Semiconductors. As discussed in Chapter 7, various semiconductors can be used to make tunneling barriers. The CdS first employed by Giaever (1968) is discussed within the framework of the preparation of light sensitive junctions. Tellurium can be easily vacuum deposited (Cardinne, Marti, and Renard 1971, Seto and Van Duzer 1971) although the results are not yet satisfactory. Furthermore, Ge and InSb barriers can also be considered. Good results can be obtained by sputtering these materials as demonstrated by Keller and Nordman (1973) and Cardinne, Manhes, and Nordman (1973) in niobium based junctions (Nb-Ge-Pb and Nb-InSb-Pb sandwiches). Very thick films (above 1000 Å) can be sputtered at the same rate adopted for the preparation of the tunneling barriers in order to check, via measurements of resistivity, the nature of the films. Most likely Ge and InSb films appear to be amorphous (see the last quoted reference). Thus although these semiconductors, when in bulk form, are suitable for a controlled doping to adjust the Fermi level position in the forbidden gap, in the preparation of barrier layers, that is, films, such control is no longer possible. Deposition rate, pressure, temperature, substrate conditions, and so on, will play a role in determining the actual properties. It is interesting to observe that the life test measurements by Keller and Nordman have shown for these structures results that are rather close to those obtained for the corresponding (Hoel et al. 1972) oxide barrier junctions. Also, PbTe has been employed (Cardinne, Manhes, and Renard 1972), but junctions with high leakage current were obtained.

In almost all cases the deposited semiconductor films present the problem of pinholes; hence oxidation after deposition of the semiconductor must be performed with the drawbacks previously discussed. Regarding critical current densities, even using barrier thicknesses as thin as 50 Å, there is no conclusive evidence so far of the feasibility of high current density, low capacitance junctions. We observe that it is possible to obtain either hysteretic or nonhysteretic current voltage characteristics depending on the semiconductor thickness (Seto and Van Duzer 1971) and other parameters (Barone and Russo 1974; Balsamo et al. 1976a). Finally, we recall the evidence of the Josephson

effect in junctions using the formvar barrier reported by Faraci, Giaquinta, and Mancini (1969).[†]

8.6.2 Light Sensitive Barriers. As discussed in Chapter 7, using II-VI compounds to make photosensitive barrier junctions is of great interest. CdSe films can be more easily deposited than CdS films. In particular, CdSe layers can be deposited in ultrahigh vacuum systems without fear of contamination, whereas CdS film preparation appears to be a rather dirty process. The main problem with the latter semiconductor lies in the different vapor pressure of the constituents. In spite of it, CdS represents the most successfully employed material in light sensitive junctions. Indeed, it should be noted that the abovementioned disparity in vapor pressures of Cd and S, which makes control of the process critical, is also a great advantage, since junctions of various desirable characteristics can deliberately be prepared.

We outline some aspects of the preparation technique of Pb-CdS-Pb and Pb-CdS-Sn junctions followed by Russo (1971) (see also Barone, Rissman, and Russo 1973; Magee and Russo 1974). In this procedure a turbopump was used and all steps were performed without breaking the vacuum. After the deposition of the first superconductive electrode onto normal microscope slides at room temperature, high purity cadmium sulfide powder is evaporated. The semiconductor must be preheated for some minutes. Pressure during the evaporation of the semiconductor ranges within 10^{-5} - 10^7 torr. Among the various factors that contribute to the determination of the optoelectronics properties of light sensitive structures the pressure during the semiconductor evaporation is very critical. Before the deposition of the counterelectrode oxidation in dry air at a pressure of 1 atm for 1 hour is necessary to avoid pinholes (see below). Oxidation by glow discharge has been also employed for CdSe barrier junctions (Rissman 1973; Barone, Rissman, and Russo 1973) indicating a drastic effect on the junction impedance. We recall also the method for determining pinhole area discussed in the excellent paper by Lubberts and Shapiro (1972).

The effect of the CdS barrier thickness t in Pb-CdS-Pb structures is shown by the V - I curves in Fig. 8.16. We observe that the quasiparticle tunneling structure appears only for $t=500$ Å and the Josephson effect only for $t \leq 150$ Å. As discussed in Chapter 7, it is presently possible to realize light sensitive Josephson structures, namely Pb-CdS-In and In-CdS-In structures, using very thick CdS barriers (up to 700 Å) (Barone and Russo 1974) and up to 1000 Å (Barone, Russo, and Vaglio 1978), respectively. In this case it is also possible to avoid the oxidation step that, as mentioned, can affect the properties of the semiconductor.

In dealing with these structures, the absence of pinholes can be established in a much more controllable way. In fact, the junctions can be prepared as

[†]We do not consider here carbon barriers (MacVicar, Freake, and Adkins 1969; MacVicar 1970) since in our knowledge no Josephson tunneling has been observed in this case.

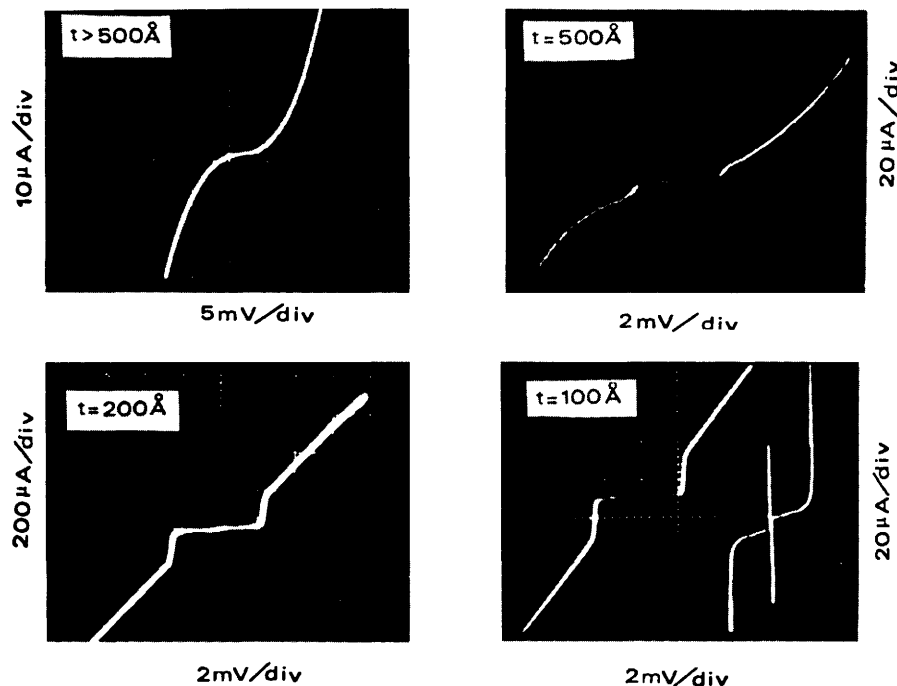


Figure 8.16 Effect of the semiconductor thickness on the V - I characteristics at 4.2 K of Pb-CdS-Pb junctions of same area. (After Barone, Rissman, and Russo, 1973.)

"non Josephson" in dark conditions so that any current contribution at zero voltage must be absent. This guarantees that, after light exposure, the zero voltage current coincides with the light induced Josephson current (see Chapter 7). Moreover, as discussed in the last section of Chapter 4, it is also possible to investigate the fluctuations of the barrier thickness with particular care in this type of junction by careful I_1 vs. H measurements (see Fig. 4.16). The result in the case of large fluctuations is reported in Fig. 8.17 where the direct record (down) very well agrees with the theoretical model (up). (For the details of this argument the reader is referred to Barone et al. 1978.)

Finally we observe that these CdS barrier structures, when employing indium electrodes, exhibit lifetime and cyclability performances that are definitely better than those observed in Pb-CdS-Pb junctions. In particular, thermal cycling up to 10 times in the range 4.2–300 K and hundred times within 4.2–100 K over a period of a few months has been performed without appreciable change in the V - I characteristics; even better results have been recently obtained using vanadium base layers by Di Chiara, Peluso, and Russo (1979) and by Barone et al. (1980).

8.6.3 Single Crystal Barrier Junctions. Huang and Van Duzer (1974a,b) developed a novel technology to make Josephson junctions that consists in the

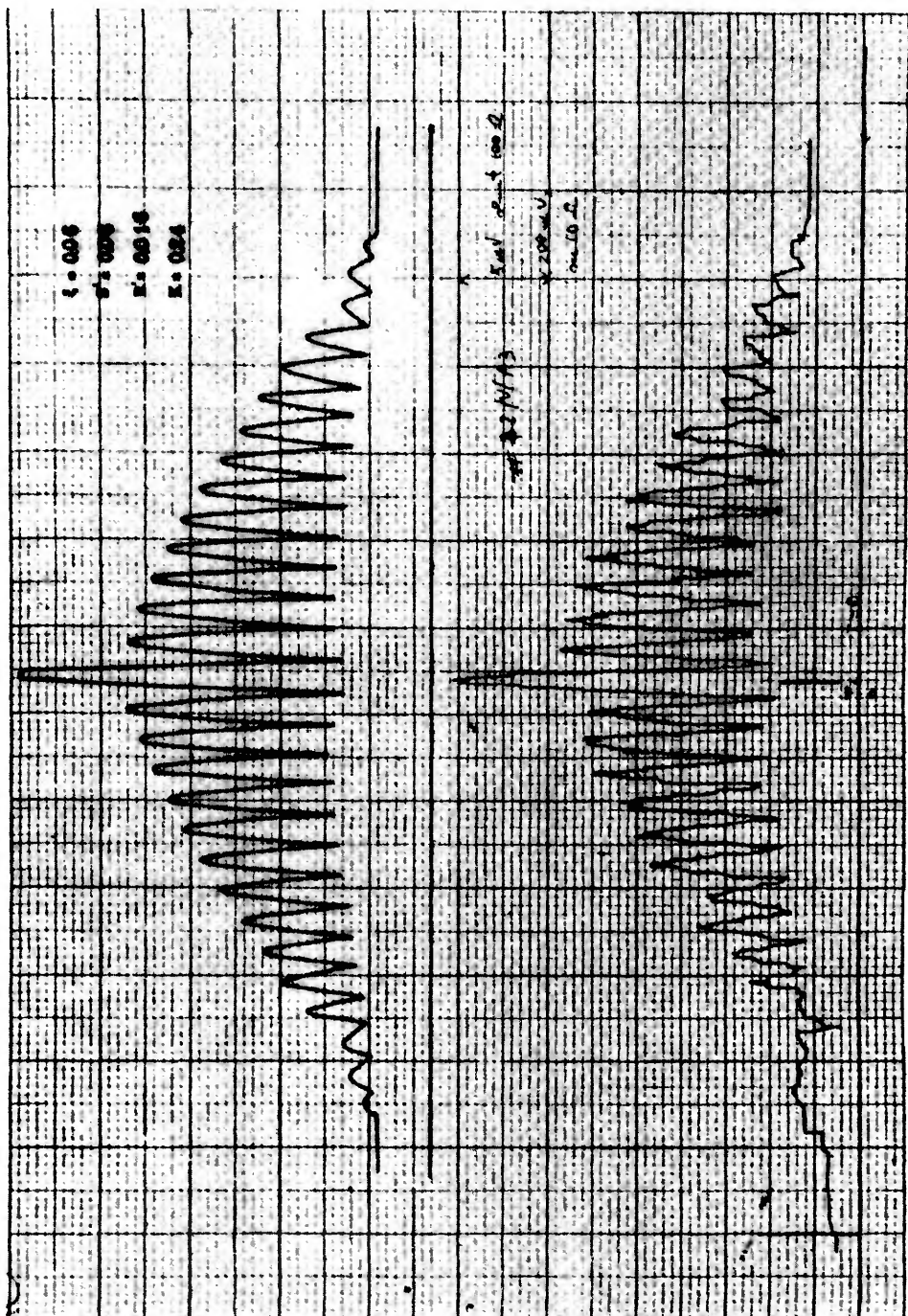


Figure 8.17 Magnetic field dependence of the d.c. Josephson current in a CdS barrier junction. Direct record (down) and theoretical model (up) assuming the presence of "structural fluctuations" (see text).

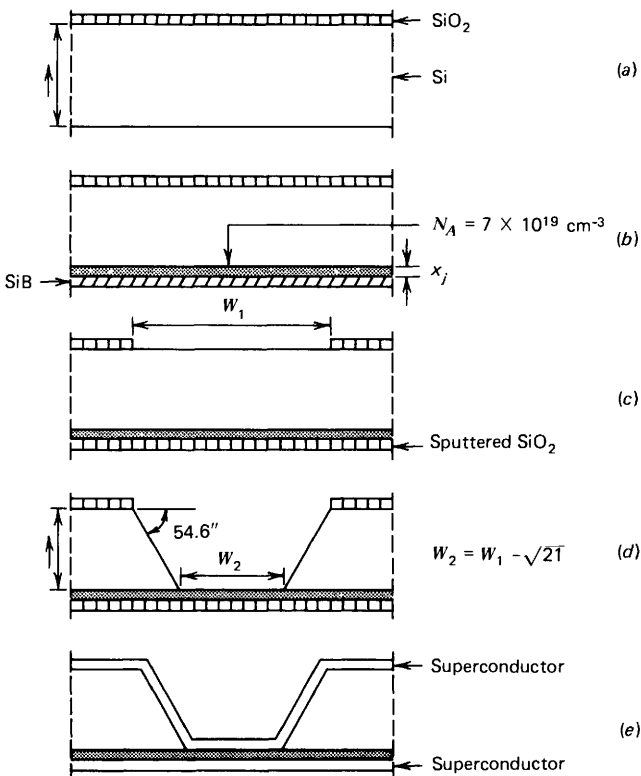


Figure 8.18 Main steps of the fabrication procedure of single crystal junctions. (After Huang and Van Duzer 1974.)

fabrication of silicon wafers in which the barrier is realized by a membrane resulting from a local thinning of a silicon crystal. The Josephson tunneling has been observed in such structure through silicon barriers with thickness of 400 and 1250 Å.

The main point of this procedure is that the barrier layer is a single crystal material. The basic steps of the technology are sketched in Fig. 8.18. A silicon ⟨100⟩ oriented wafer 250 μm thick is used as the starting material. Both polished surfaces of the wafer are thermally oxidized by wet oxidation at 1150 C. The top oxide layer (silicon dioxide, SiO₂, 7500 Å thick) is protected by photoresist, whereas the oxide on the other side is etched off (Fig. 8.18a). A saturated diborane atmosphere provides a boron diffusion from the “bottom” side, as shown in Fig. 8.18b.[†]

At this point a square window is made in the top layer by patterning with usual photoresist technique (Fig. 8.18c). Both the boron glass and the Si-B

[†]For the details of the preparation and a careful discussion of the diffusion impurity profile the reader is referred to the works by Huang and Van Duzer.

phase layer are removed by suitable techniques, and a SiO_2 layer is sputtered in order to protect the diffused layer. The wafer is now ready for the thinning process. This is done by a suitable ternary solution (ethylenediamine-water-pyrocatechol) which etches the silicon preferentially (faster) in the $\langle 100 \rangle$ direction than along the $\langle 111 \rangle$ direction. The effect of the etchant is progressively reduced as the boron concentration increases and essentially stops at a certain concentration value (Fig. 8.18d). In this way the desired membrane of boron doped silicon is obtained in the range of $\sim 400\text{--}4000 \text{ \AA}$ in thickness, depending on the parameters of the diffusion process such as time and temperature. The dimension x_j of the membrane depends on the wafer thickness. To get submicron dimensions this technology has been improved by adopting a double etching procedure (see quoted references above and the excellent reviews by Ulrich and Van Duzer 1976; Van Duzer 1976). The actual junction (Fig. 8.18e) is obtained after the removal of the SiO_2 residual silicon membrane by depositing the superconducting electrodes. With this structure a high value of the product $I_1 \text{ C}$ has been obtained, even larger than the theoretically achievable value of the corresponding oxide tunnel junction. Silicon barriers have been also employed in Josephson junctions of coplanar electrode configuration (Schyfter et al. 1976).

8.7 Bridge-Type Weak Links

The first superconducting bridges were made by Anderson and Dayem (1964), Parks, Mochel, and Surgent (1964), and Lambe et al. (1964). Their techniques, in the light of modern technology, seem naive, but even in these pioneering works bridges of a few microns were already obtained. In the simplest procedure, one can proceed by a deposition of a suitable metal layer and then obtain the desired pattern by cutting this film with a sharp point (Fulton and Dynes 1970). In the reference of Parks et al. quoted above another simple technique was employed. A thin fiber of GE7031 varnish is stretched on a glass microscope slide. A microknife provides a well defined cut of the fiber. The metal film is then deposited all over the substrate and the fiber. By a suitable technique the varnish fiber is then removed together with the metal deposited on the fiber itself, leaving the metal deposited in the region of the cut. Modifications of this method and other alternative procedures, including the use of suitable metal masks, have been successfully investigated by various authors (e.g., Wyatt et al. 1966; Dayem and Wiegand 1967; Seraphim 1970; Bondarenko et al. 1970). The reader is also referred to the important works by Gregers-Hansen and Levinsen (1971), Gregers-Hansen, Levinsen, and Fog Pedersen (1972), and Gregers-Hansen et al. (1972). Other references on bridges are quoted in Section 7.6. More recently, however, superconducting weak links have been produced by the sophisticated lithographic techniques discussed in Section 8.4 which, as we have seen, also allow the fabrication of micron and submicron metal bridges by electron beam lithography and lift-off techniques.

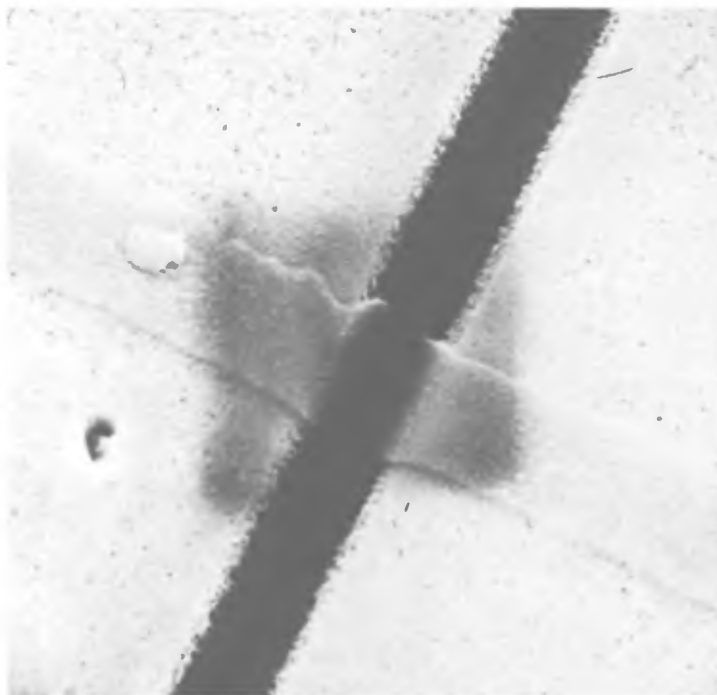


Figure 8.19 Example of V.T.B. niobium link. (Courtesy of L. K. Wang, et al., 1977.)

The first microbridge made by the electron beam lithographic technique is due to Laibowitz (1973) who made niobium bridges of uniform thickness down to the $0.3 \mu\text{m}$ size.

We saw in Chapter 7 that bridges of variable thickness (V.T.B.) are of particular importance because of their "three dimensional" configuration which permits better heat exchange (Klapwijk and Mooij, 1974; Klapwijk and Veenstra 1974) and serve as a suitable model for a theoretical description (Likharev 1971). An example of an indium V.T.B. weak link is shown in Fig. 7.11. This structure was realized by electron beam lithography.

Among the various procedures for fabricating superconducting bridges we recall also the work by Daalmans and Zwier (1978) and the technique adopted by Feuer, Prober and Cogdell (1978) outlined in section 8.4.3.

In Fig. 8.19 is shown a V.T.B. niobium link made by a rather simple procedure (Wang et al. 1977).[†] A quartz fiber of $1 \mu\text{m}$ diameter is placed on a niobium film 500 \AA thick. The surface is sputter etched and a thicker (5000 \AA)

[†]See also Boone et al. (1976), Barr et al. (1978), and Galfo, Wang and Deaver (1978). Other high quality niobium V.T.B. bridges (e.g., Octavio, Skocpol, and Tinkham 1978) have been discussed in Chapter 7. Among others it is worth to recall also the V.T.B. lead bridges made by Yeh and Buhzman (1977).

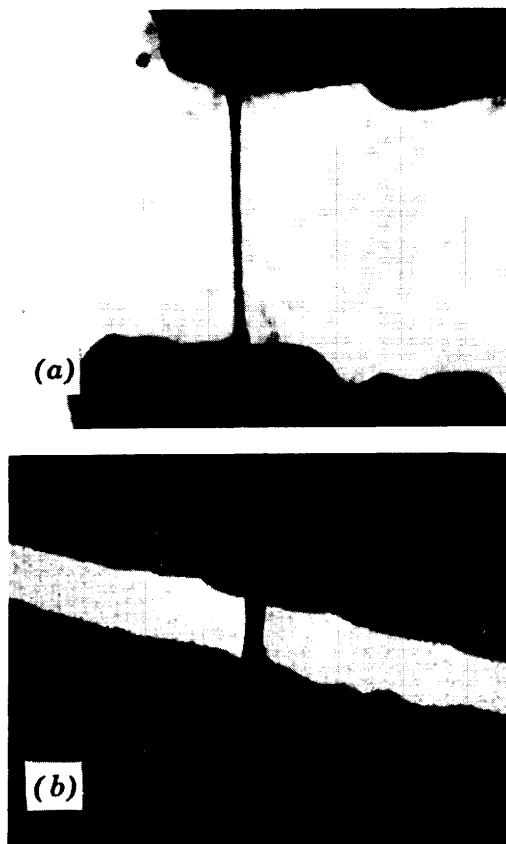


Figure 8.20 Micrograph of niobium nanobridges made at the IBM T. J. Watson Research Center, Yorktown Heights. Up: 250 Å wide nanobridge *E*-beam fabricated on window substrate. Niobium banks are separated by 0.8 μ m. Down: 600 Å wide nanobridge made with same procedure. Niobium banks are separated by 0.25 μ m. (Courtesy of A. N. Broers and R. B. Laibowitz.)

niobium layer is then deposited. The fiber is removed, leaving the variable (1:10 ratio) thickness structure. The actual bridge shape and the whole chock structure is obtained by chemical etching.

Among the latest development in the miniaturization of superconducting devices we show in Fig. 8.20 a nanobridge recently made by electron beam on window substrate by Broers and Laibowitz (1978).[‡] In the top micrograph is a niobium strip 250 Å wide and 200 Å thick with niobium banks separated by 0.8 μ m. The micrograph below represents a 600 Å wide nanobridge with banks separated by 0.25 μ m.

[‡]See also Broers (1964), Broers et al. (1976), and Laibowitz et al. (1978).

Another category of bridges of relevant importance are those based on the proximity effect (Notarys and Mercereau 1973; Mercereau 1973; Kirschman, Notarys, and Mercereau 1974). These structures are made by superimposing a normal film on a superconducting layer (or vice versa) so that the resulting *S/N* sandwich exhibits, because of the proximity effect, a critical temperature lower than that of the superconductor, whereas superconducting properties are to some extent transmitted to the normal metal across the *S/N* boundary. In the thin film limit the transition temperature of the sandwich can be adjusted, playing on the relative thickness of the normal and superconducting films. Similarly, one can consider two superconducting films *S* and *S'* of different T_c , creating a relative enhancement or reduction of the superconducting properties. Such weak links can be realized using a variety of superconductors either soft (Pb, Sn, In, and alloys) or hard metals (Nb, Ta) and using as the normal metal Au and Cu or Ta and Zr respectively. The theory of such bridges has been also discussed by Kasatkin and Volkov (1974).

An alternative to the Notarys-Mercereau proximity structures is the ion implanted bridge in which a suitable metal film is locally modified in its superconducting properties. The basic idea is to modify the order parameters in a metal film by doping it with suitable ions and thus create a region of a relatively lower transition temperature connecting two regions of higher T_c . The ion implantation technique has been successfully used by Harris (1974, 1975, 1976) to fabricate ion (N^+ and/or S^+) implanted molybdenum weak links and by Arrington and Deaver (1975) to produce niobium links by implanting iron ions into niobium films.

All these types of weak links realized by sequential layering, ion implantation, and so on, show the same superconducting quantum device behavior, provided that their lengths are appropriately scaled to the effective length.[†]

It is interesting also to mention weak links that deserve particular interest for the underlying physics involved. These are made by superconducting bridges in which the weak coupling can be created by realizing a local nonequilibrium excess quasiparticle population, which in turn tends to quench the superconducting properties. Indeed, this effect can be achieved by quasiparticle injection, phonon injection, or photoinjection. The results obtained are particularly stimulating (Wong, Yeh, and Langenberg, 1976a,b; Yeh and Langenberg 1978), suggesting the possibility of realizing weak links that can be continuously "adjusted" in their superconducting behavior. In this sense these structures recall the light sensitive sandwich junctions discussed in Chapter 7. Theoretically the weak links realized by photoexcitation of quasiparticles have been discussed since 1971 by Volkov (1971). Depression of the critical current in superconducting weak links (films and points) by laser irradiation has been reported also by Janik et al. (1974).

Finally let us observe that the research toward high temperature superconductors has been transferred into the Josephson context. Since 1972 (Janoko,

[†]A comparison of these various structures can be found in the work by Kirschman et al. (1976).

Gavaler, and Jones 1972) Dayem bridges with a T_c above 12 K were realized by using Mo-Re alloy. More recently sputtered thin films of Nb₃Ge have been realized leading to bridge structures with critical temperatures up to 21 K (Janoko, Gavaler, and Jones 1974; Laibowitz et al. 1974).[†] Moreover, NbN and Nb₃Sn[‡] have been employed (Palmer, Notarys, and Mercereau 1974) reaching T_c values of 14.7 and 17.5 K respectively.

8.8 Point Contact Structures

As discussed in the preceding chapter (Section 7.7), point contact structures deserve great attention for their important role in applications, in spite of the not well established interpretation of the underlying physics. More precisely, because of the undefined character of the contact the actual conduction mechanism is unclear. It is reasonable to assume in general the presence of metal bridgelike and tunnel junctionlike parallel "channels."

The fabrication technology of the point contacts includes numerous procedures (Zimmerman 1972b) whose differences are also strongly related to the specifications required for the particular application. In Fig. 8.21 are sketched three possible methods to make point contacts. The first is the widely employed screw-type contact, the second consists of a finely etched point realized at the end of a wire of a suitable material (e.g., Nb), and the third makes use of two superconducting sheets separated by a plastic insulation and sustained by a backing plate; these sheets are pressed together by a pushrod or a suitable screw creating the contact in a small region. Among others we recall also two types of stable point contact structures. The former (Zimmerman, Thiene, and Harding 1970) is realized by a niobium screw contact in a niobium structure (an r.f. biased SQUID; see Chapter 13) which is carefully designed to get high rigidity and to avoid problems related to expansion mismatch. Buhrman, Strait, and Webb (1971) have obtained point contacts (both single and double point structures) of high mechanical stability and with excellent properties of cyclability. Basically the structure consists of two superconducting niobium parts insulated by a glass layer. The connection between the two pieces is realized by a sharpened screw contact. The crucial point of such a structure lies in the use of an insulating glass whose thermal expansion matches that of the niobium.[§]

An excellent example of a preset, recyclable niobium point contact made by Taur at NASA/GISS is shown in Fig. 8.22. It is produced by a wire and a foil, both of niobium, between two substrates. The point of radius < 0.25 μm

[†]See also Benacka et al. (1978b) which discusses the preparation and properties of long superconducting links formed by pulse electrical breakdown in monocrystalline silicon.

[‡]We recall the values of T_c up to 18 K reported by Golovashkin et al. (1976, 1979) and Golovashkin and Lykov (1978) and in the references given there.

[§]See also the point contact structures obtained by Bondarenko et al. (1970), Dupart, Bodin, and Pech (1975), and Divin and Nad (1978).

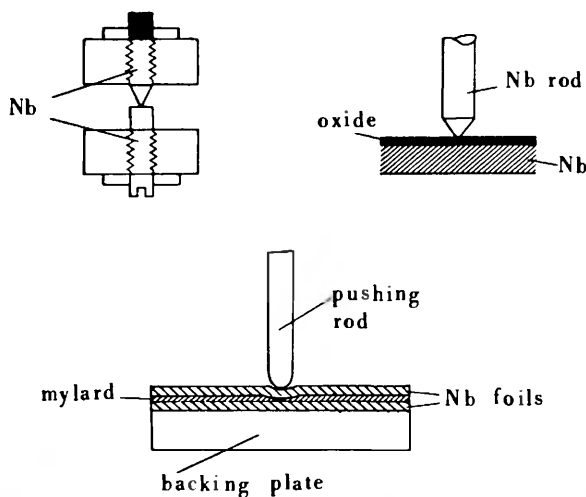


Figure 8.21 Sketch of three different point contact structures.

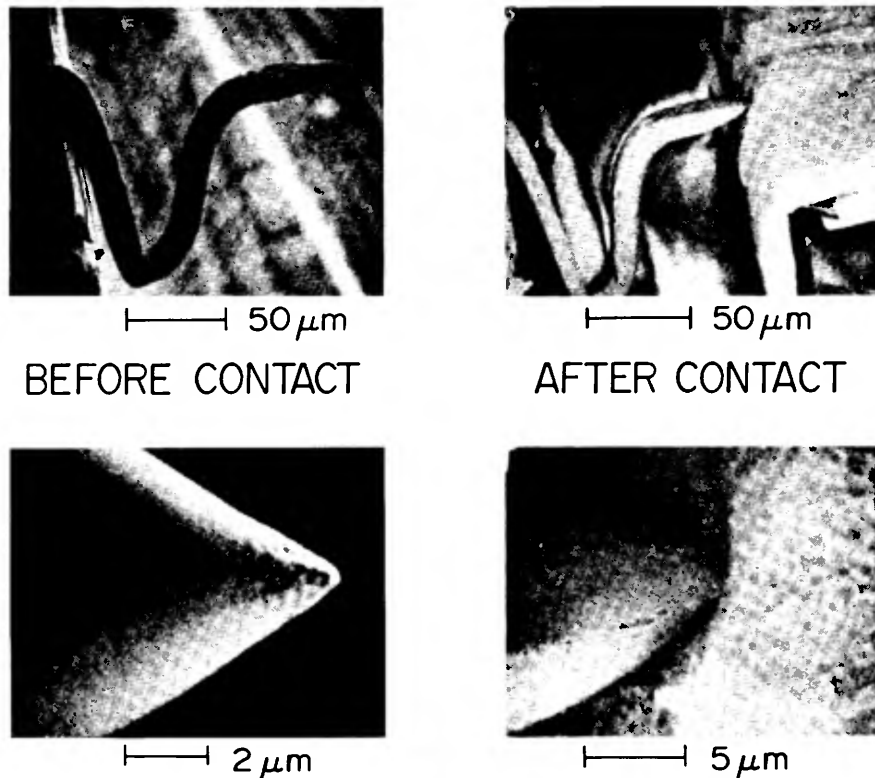


Figure 8.22 Scanning electron microscope picture of a recyclable niobium point contact made at NASA/GISS Laboratory, New York. (Courtesy of Y. Taur.)

is obtained by electrochemical etching of the niobium wire. The substrate material (Corning 8260 glass) matches, as discussed above, the thermal expansion of the niobium. For details and applications of such structures see Taur and Kerr (1978a, b).

A completely different point contact configuration is represented by the array of junctions realized by Clark (1968)—a close packed array of tin superconducting balls in which it can be assumed that point contact-like coupling is achieved where the balls touch each other. Another structure that can be regarded as pointlike has been proposed by Lum and Van Duzer (1975). This is obtained by two superconducting layers separated by a suitable resist. The two superconductors are linked through holes opened in the photoresist. The actual diameter of the hole defines the diameter of the “point,” which is therefore fixed by the possibilities of the specific lithographic process employed.

CHAPTER 9

Resonant Modes In Tunneling Structures

9.1 Josephson Junction as a Transmission Line

A tunneling junction made by two superconducting films separated by a thin dielectric layer can be regarded, as far as its electromagnetic behavior is concerned, as a transmission line. The electric field is essentially confined within the oxide region of thickness t . The magnetic field, because of the penetration into the superconductors, fills a larger region of thickness $d = t + \lambda_{L1} + \lambda_{L2}$ (λ_L are the London penetration depths in the two superconducting regions). This field configuration makes the velocity of an electromagnetic wave lower than in an equivalent stripline of nonsuperconducting films (this behavior was pointed out by Pippard in 1947). An extensive analysis of this configuration, in the absence of Josephson current, was carried out by Swihart (1961). When the two superconducting electrodes are thick compared with the corresponding penetration depths, the wave velocity for the electromagnetic radiation in such a superconducting transmission line can be very easily computed.

Let us refer to the simple configuration in Fig. 9.1. It is convenient to assume that the electric field is in the z direction, the magnetic field is in the x direction, and both are uniform in the x direction. The current density has a nonzero y component in the superconducting regions and a nonzero z component in the oxide region (quasiparticle and Josephson current). Under these assumptions the Maxwell equations reduce to

$$\frac{\partial}{\partial y} E_z(y, t) = -\frac{1}{c} \frac{\partial}{\partial t} H_x(z, y, t) \quad (9.1.1a)$$

$$-\frac{\partial}{\partial y} H_x(z, y, t) = \frac{\epsilon_r}{c} \frac{\partial}{\partial t} E_z(y, t) + \frac{4\pi}{c} J_z(y, t) \quad (9.1.1b)$$

$$\frac{\partial}{\partial z} H_x(z, y, t) = \frac{4\pi}{c} J_y(y, t) \quad (9.1.1c)$$

where ϵ_r = relative dielectric permeability and c = light velocity in free space.

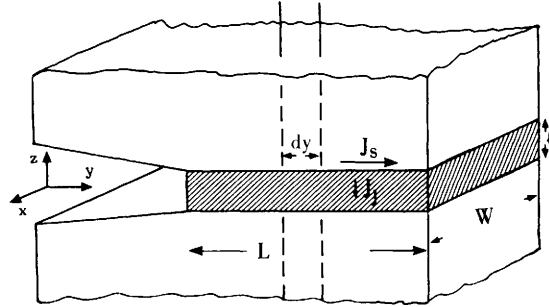


Figure 9.1 Schematic of the Josephson junction transmission line. The magnetic field H_x is in the x direction. The shaded region is the dielectric oxide.

Let us integrate (9.1.1a) on the surface S , on the y, z plane delimited by two straight lines dy apart and parallel to the z axis:

$$\int_S d\sigma \frac{\partial E_z}{\partial y} = -\frac{1}{c} \int_S d\sigma \frac{\partial H_x}{\partial t}$$

Recalling that E_z is confined to the oxide region and assuming no z dependence in that region, we get

$$-\frac{\partial}{\partial y} E(y, t) l dy = \frac{dy}{c} \left[\frac{\partial}{\partial t} H(y, t) l + \int_{+l/2}^{+\infty} dz \frac{\partial H_x}{\partial t}(z, y, t) + \int_{-l/2}^{-\infty} dz \frac{\partial H_x}{\partial t}(z, y, t) \right]$$

where $E(y, t)$ and $H(y, t)$ indicate the electric and magnetic fields in the oxide region, which are independent of z . To avoid confusion we have indicated now the oxide thickness by l . Introducing the magnetic field penetration depths defined by

$$\lambda_{L1,2} = \frac{1}{H(y, t)} \int_{\pm l/2}^{\pm \infty} dz H_x(z, y, t) \quad (9.1.2)$$

the last expression becomes:

$$l \frac{\partial E(y, t)}{\partial y} = -\frac{d}{c} \frac{\partial H(y, t)}{\partial t} \quad (9.1.3)$$

where

$$d = l + \lambda_{L1} + \lambda_{L2}$$

Let us integrate (9.1.1c) on a surface S' , which lies in a plane perpendicular to the y axis and is formed by a strip of width W extending from 0 to $+\infty$ in the

z direction. We have

$$\int_{-\frac{W}{2}}^{+\frac{W}{2}} dx \int_0^{+\infty} dz \frac{\partial H_x(z, y, t)}{\partial z} = \frac{4\pi}{c} \int_S d\sigma J_y(y, t)$$

That is,

$$W \int_0^{+\infty} dz \frac{\partial H_x}{\partial z} = \frac{4\pi}{c} I(y, t)$$

Finally:

$$H(y, t) = \frac{4\pi}{cW} I(y, t) \quad (9.1.4)$$

$I(y, t)$ is the current at point y in the superconducting electrode. From (9.1.3) and (9.1.4) it follows that

$$\frac{\partial V(y, t)}{\partial y} = - \frac{4\pi}{c^2} \frac{d}{W} \frac{\partial I(y, t)}{\partial t} \quad (9.1.5)$$

where $V(y, t) = IE(y, t)$ is the voltage across the junction. Combining (9.1.4) and (9.1.1b) we have in the dielectric region

$$\frac{\partial I(y, t)}{\partial y} = - \frac{\epsilon_r}{4\pi l} W \frac{\partial V(y, t)}{\partial t} - W J_z(y, t) \quad (9.1.6)$$

Let us neglect the current through the oxide ($J_z = 0$). Under this assumption (9.1.5) and (9.1.6) can be interpreted as the current-voltage relations of a lossless transmission line (Ramo, Whinnery, and Van Duzer 1967). By introducing the capacitance and the inductance per unit length, defined by

$$C' = \frac{\epsilon_r W}{4\pi l}; \quad L' = \frac{4\pi}{c^2} \frac{d}{W}$$

we get

$$\begin{aligned} \frac{\partial V(y, t)}{\partial y} &= - L' \frac{\partial I(y, t)}{\partial t} \\ \frac{\partial I(y, t)}{\partial y} &= - C' \frac{\partial V(y, t)}{\partial t} \end{aligned} \quad (9.1.7)$$

The wave velocity for such a transmission line is given by

$$\bar{c} = \frac{1}{\sqrt{L'C'}} = c \sqrt{\frac{l}{\epsilon_r d}} \quad (9.1.8)$$

By using typical values $l \approx 20 \text{ \AA}$, $d \approx 1000 \text{ \AA}$, $\epsilon_r = 4$, we obtain for the ratio between the wave velocity in the superconducting transmission line and in the empty space the value $\bar{c}/c \approx 0.05$. (See table 8.2.) If one of the two superconducting films has a thickness δ comparable with the London penetration depth λ_L , the expression for \bar{c} becomes (Swihart 1961):

$$\bar{c} = c \left\{ \frac{l}{\epsilon_r(l + \lambda_{L2} + \lambda_{L1} \coth \delta/\lambda_{L1})} \right\}$$

9.2 Resonant Modes for Low Q Junctions

Let us consider a tunneling junction of a finite length in the wave propagation direction. Because of reflection at the edges, it behaves like a resonant transmission line and supports self-resonant modes of the electromagnetic field. For an open ended transmission line the standing wave voltage pattern for the n th mode is

$$v_n(y, t) = A_n e^{j\omega_n t} \cos \frac{n\pi y}{L} \quad (9.2.1)$$

where L is the length of the junction, and

$$\omega_n = \frac{n\pi\bar{c}}{L} \quad (9.2.2)$$

When a Josephson current is present, for V finite, electromagnetic power of frequency $\omega = 2eV/\hbar$ is radiated into the junction. This excites the resonant modes of the cavity, which in turn interact with the Josephson current. Thus a nonlinear interaction between the cavity and the Josephson current is established. When the Josephson frequency matches the frequency ω_n of one of the junction modes, a zero frequency current appears. As we shall see, in order to have a stronger interaction the Josephson current must be spatially modulated in the y direction. For small junctions ($L \ll \lambda_J$) this is achieved only by an external magnetic field perpendicular to that direction. Therefore in an external magnetic field H_e there will be a set of current singularities in the V - I characteristic at voltages

$$V_n = \frac{\hbar}{2e} \omega_n = \frac{\hbar}{2e} \frac{\bar{c}}{2L} n \quad (9.2.3)$$

These singularities were first observed by Fiske (1964) and are generally called Fiske steps. In fact, since the junctions are current biased, these are normally observed as steps in the V - I characteristic (Fig. 9.2). However, using a variable d.c. bias superimposed on the low frequency a.c. bias employed to trace the

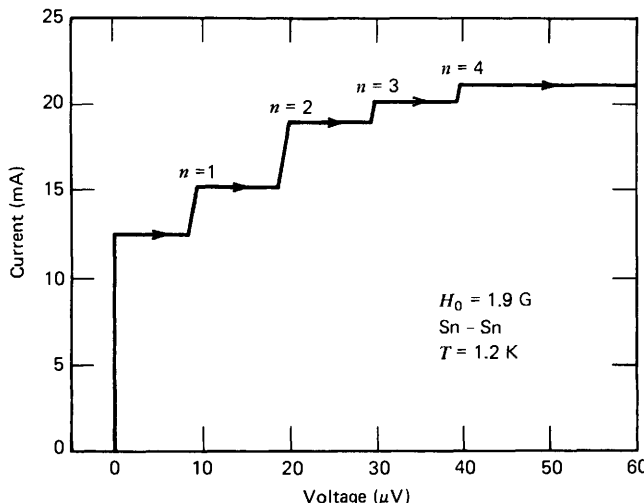


Figure 9.2 A typical V - I curve for an $\text{Sn}-\text{SnO}_x-\text{Sn}$ junction showing self-steps in the presence of a magnetic field. The curve is traced using a variable d.c. current bias. (After Langenberg, Scalapino, and Taylor 1966.)

V - I characteristic, a display like that shown in Fig. 9.3 can be obtained. In this case the picture was obtained by multiple exposure. Each singularity was selected by adjusting the value of the d.c. current bias. This procedure allows a better detection of the singularities independently of their relative amplitudes and locations.

We now derive the theoretical dependence of the step amplitude on both the voltage and the magnetic field. We assume that we are dealing with a small junction and with step amplitudes much smaller than the maximum Josephson current[†] (Eck, Scalapino, and Taylor 1964a, b; Kulik 1965a). Let us refer to the simple one dimensional junction of Fig. 9.1. In this case (9.1.5) and (9.1.6) can be written as

$$\frac{\partial V(y, t)}{\partial y} = -L' \frac{\partial I(y, t)}{\partial t} \quad (9.2.4a)$$

$$\frac{\partial I(y, t)}{\partial y} = -C' \frac{\partial V(y, t)}{\partial t} - W J_z(y, t) \quad (9.2.4b)$$

in which a nonzero current through the barrier has been assumed. These equations can be combined into a single second order equation for V :

$$\frac{\partial^2 V(y, t)}{\partial y^2} = L' C' \frac{\partial^2 V(y, t)}{\partial t^2} + L' W \frac{\partial J_z(y, t)}{\partial t}$$

[†]As we shall see, this corresponds to low Q situations.

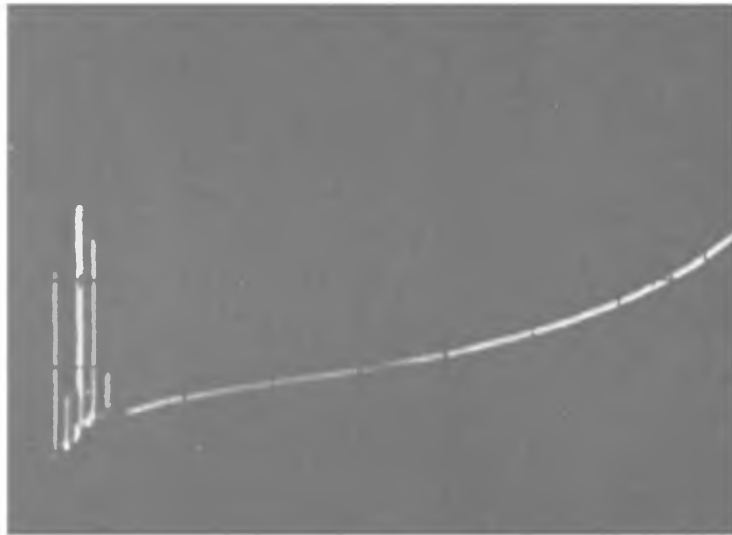


Figure 9.3 Voltage-current characteristic of an Nb-NbO_x-Pb junction showing self-steps in an applied magnetic field. Vertical scale 0.1 mA/div; horizontal scale in arbitrary units. The curve has been traced using a variable d.c. bias overimposed on a low frequency a.c. bias. The picture was taken by multiple exposure.

Using (9.1.8) and the definition of L' , it follows that

$$\frac{\partial^2 V(y, t)}{\partial y^2} - \frac{1}{c^2} \frac{\partial^2 V(y, t)}{\partial t^2} = \frac{4\pi}{c^2} d \frac{\partial J_z(y, t)}{\partial t} \quad (9.2.5)$$

We assume:

$$V(y, t) = V_0 + v(y, t) \quad (9.2.6)$$

where $v(y, t) \ll V_0$. The total current density $J_z = J_J + J_q$ is the sum of the Josephson and the quasiparticle current density. For the quasiparticle current we take the expression (see section 1.7)

$$J_q = \frac{1}{R_T(V_0)} V(y, t) \quad (9.2.7)$$

$R_T(V_0) = 1/\sigma_0(V_0)$ is the voltage dependent nonlinear tunneling resistance of the junction. The Josephson current is written as

$$J_J = J_1 \sin \varphi(y, t) \quad (9.2.8)$$

where

$$\varphi(y, t) = \omega t - ky + \varphi_1(y, t)$$

with

$$\omega = \frac{2e}{\hbar} V_0; \quad k = \frac{2\pi d}{\Phi_0} H_e$$

H_e is the external magnetic field assumed to be constant. $\varphi_1(y, t)$ is related to $v(y, t)$ by the equation

$$v(y, t) = \frac{\hbar}{2e} \frac{\partial \varphi_1(y, t)}{\partial t} \quad (9.2.9)$$

By inserting (9.2.6), (9.2.7), (9.2.8), and (9.2.9) into (9.2.5) we obtain the following equation for $\varphi_1(y, t)$:

$$\frac{\partial}{\partial t} \left\{ \frac{\partial^2 \varphi_1(y, t)}{\partial y^2} - \frac{1}{\bar{c}^2} \frac{\partial^2 \varphi_1(y, t)}{\partial t^2} - \frac{4\pi}{c^2} \frac{d}{R_T} \frac{\partial \varphi_1(y, t)}{\partial t} \right\} = \frac{\partial}{\partial t} \left[\frac{2e}{\hbar} \frac{4\pi}{c^2} d J_1 \sin \varphi \right]$$

and thus

$$\frac{\partial^2 \varphi_1(y, t)}{\partial y^2} - \frac{1}{\bar{c}^2} \left[\frac{\partial^2 \varphi_1(y, t)}{\partial t^2} + \frac{1}{CR_T} \frac{\partial \varphi_1(y, t)}{\partial t} \right] = \frac{1}{\lambda_J^2} \sin \varphi \quad (9.2.10)$$

where λ_J is the Josephson penetration depth (1.7.3b) and C is the capacitance per unit area. The integration constant is assumed to be zero. As observed by Kulik (1967), this assumption is justified since we are interested in the asymptotic ($t \rightarrow \infty$) solutions of (9.2.10) which are independent of the initial conditions because of the presence of the damping term. We can use (9.2.10) to derive an expression for $\varphi_1(y, t)$. As a first approximation we can consider φ_1 as a small perturbation and neglect it in the forcing term. Therefore we have for φ_1 the equation

$$\frac{\partial^2 \varphi_1}{\partial y^2} - \frac{1}{\bar{c}^2} \left(\frac{\partial^2 \varphi_1}{\partial t^2} + \gamma \frac{\partial \varphi_1}{\partial t} \right) = \frac{1}{\lambda_J^2} \sin(\omega t - ky) \quad (9.2.11)$$

where $\gamma = 1/CR_T$.

Furthermore, $\varphi_1(y, t)$ is directly related to $v(y, t)$ and can be expanded in terms of the normal modes of the junction (9.2.1):

$$\varphi_1(y, t) = \text{Im} \left\{ \sum_{n=0}^{\infty} g_n e^{j\omega_n t} \cos \frac{n\pi y}{L} \right\} \quad (9.2.12)$$

(g_n are complex numbers). Let us observe that this particular choice for the y dependence implies the boundary conditions for φ_1 (Kulik 1967):

$$\left(\frac{\partial \varphi_1}{\partial y} \right)_0 = \left(\frac{\partial \varphi_1}{\partial y} \right)_L = 0 \quad (9.2.13)$$

From the relation between the phase difference φ and the magnetic field,

$$H(y) = -\frac{\hbar c}{2ed} \frac{\partial \varphi}{\partial y}$$

it is easy to recognize that (9.2.13) implies that at the boundaries the magnetic field is equal to the external applied field H_e . That is, the contribution of the self-field is not taken into account. This is justified for junctions of length $L \ll \lambda_J$. The d.c. Josephson current as a function of the voltage and of the external magnetic field is given by

$$J_{dc} = \lim_{T \rightarrow \infty} \frac{1}{T} \int_0^T dt \frac{1}{L} \int_0^L dy J_1 \sin[\omega t - ky + \varphi_1(y, t)] \quad (9.2.14)$$

Since we are considering φ_1 as a perturbation, we can expand $\sin \varphi$ in terms of φ_1 . To the first order:

$$J_1 \sin(\omega t - ky + \varphi_1) = J_1 \sin(\omega t - ky) + J_1 \cos(\omega t - ky) \varphi_1(y, t) \quad (9.2.15)$$

Therefore the d.c. current is given by

$$J_{dc}(V_0, H_e) = \lim_{T \rightarrow \infty} \frac{1}{T} \int_0^T dt \frac{1}{L} \int_0^L dy J_1 \cos(\omega t - ky) \varphi_1(y, t) \quad (9.2.16)$$

where we have used the relation

$$\lim_{T \rightarrow \infty} \frac{1}{T} \int_0^T dt \frac{1}{L} \int_0^L dy J_1 \sin(\omega t - ky) = 0$$

To compute J_{dc} at a given voltage and magnetic field, we must determine $\varphi_1(y, t)$, that is, the coefficients g_n of the series expansion (9.2.12). By inserting (9.2.12) into (9.2.11) we get straightforwardly

$$\sum_{n=0}^{\infty} g_n e^{j\omega_n t} \cos \frac{n\pi y}{L} \left\{ -\left(\frac{n\pi}{L} \right)^2 + \frac{\omega_n^2}{\bar{c}^2} - j \frac{\omega_n \gamma}{\bar{c}^2} \right\} = \frac{1}{\lambda_J^2} e^{j\omega t} e^{-jk y} \quad (9.2.17)$$

in which exponential notation has been used. Let us further assume the time dependence of $\varphi_1(y, t)$ to be essentially determined by the forcing term. In this case:

$$\omega_n = \omega$$

The expression (9.2.17) becomes:

$$\sum_{n=0}^{\infty} g_n e^{j\omega t} \cos \frac{n\pi y}{L} \left\{ \frac{\omega^2}{\bar{c}^2} - \left(\frac{n\pi}{L} \right)^2 - j \frac{\omega \gamma}{\bar{c}^2} \right\} = \frac{1}{\lambda_J^2} e^{j\omega t} e^{-jk y}$$

Multiplying by $\cos(n\pi y/L)$ and integrating, we obtain for the n th coefficient g_n :

$$g_n = \frac{\bar{c}^2/\lambda_J^2}{[\omega^2 - (n\pi\bar{c}/L)^2 - j\omega\gamma]} \frac{2}{L} \int_0^L dy \cos \frac{n\pi y}{L} (\cos ky - j\sin ky) \quad (9.2.18)$$

The integrals in this expression can be easily computed. On defining the quantities:

$$B_n(k) = \frac{2}{L} \int_0^L dy \cos \frac{n\pi y}{L} \cos ky \quad (9.2.19a)$$

$$C_n(k) = \frac{2}{L} \int_0^L dy \cos \frac{n\pi y}{L} \sin ky \quad (9.2.19b)$$

(9.2.18) becomes

$$g_n = \frac{\bar{c}^2}{\omega^2 \lambda_J^2} \frac{[1 - (\omega_n/\omega)^2 + J/Q_n]}{[1 - (\omega_n/\omega)^2]^2 + 1/Q_n^2} [B_n(k) - jC_n(k)]$$

where we have introduced the quality factor $Q_n = \omega_n/\gamma = \omega_n C' R_T$. Let us remember that Q_n is voltage dependent through R_T . The real and imaginary part of g_n are

$$\operatorname{Re} g_n(\omega, k) = \frac{\bar{c}^2/\omega^2 \lambda_J^2}{[1 - (\omega_n/\omega)^2]^2 + 1/Q_n^2} \left\{ B_n(k) [1 - (\omega_n/\omega)^2] + \frac{C_n(k)}{Q_n} \right\} \quad (9.2.20a)$$

$$\operatorname{Im} g_n(\omega, k) = \frac{\bar{c}^2/\omega^2 \lambda_J^2}{[1 - (\omega_n/\omega)^2]^2 + 1/Q_n^2} \left\{ \frac{B_n(k)}{Q_n} - C_n(k) \left[1 - \left(\frac{\omega_n}{\omega} \right)^2 \right] \right\} \quad (9.2.20b)$$

Thus from (9.2.16) it follows that

$$J_{dc}(V_0, H_e) = \lim_{T \rightarrow \infty} \frac{1}{T} \int_0^T dt \frac{1}{L} \int_0^L dy J_1 [\cos \omega t \cos ky + \sin \omega t \sin ky] \varphi_1(y, t)$$

where

$$\varphi_1(y, t) = \sum_{n=0}^{\infty} [\operatorname{Re} g_n(\omega, k) \sin \omega t + \operatorname{Im} g_n(\omega, k) \cos \omega t] \cos \frac{n\pi y}{L}$$

Finally:

$$J_{dc}(V_0, H_e) = J_1 \sum_{n=0}^{\infty} \left\{ \frac{1}{4} B_n(k) \operatorname{Im} g_n(\omega, k) + \frac{1}{4} C_n(k) \operatorname{Re} g_n(\omega, k) \right\} \quad (9.2.21)$$

where we have used the relations

$$\lim_{T \rightarrow \infty} \frac{1}{T} \int_0^T dt \cos^2 \omega t = \lim_{T \rightarrow \infty} \frac{1}{T} \int_0^T dt \sin^2 \omega t = \frac{1}{2}$$

$$\lim_{T \rightarrow \infty} \frac{1}{T} \int_0^T dt \sin \omega t \cos \omega t = 0$$

Inserting (9.2.20a) and (9.2.20b) into (9.2.21), we have

$$J_{dc}(V_0, H_e) = \frac{\bar{c}^2 J_1}{4\omega^2 \lambda_J^2} \sum_{n=0}^{\infty} \frac{1/Q_n}{[1 - (\omega_n/\omega)^2]^2 + 1/Q_n^2} [B_n^2(k) + C_n^2(k)] \quad (9.2.22)$$

To get the magnetic field dependence of J_{dc} , we have to compute the coefficients B_n and C_n (9.2.19a, b). Let us observe that

$$B_n^2 + C_n^2 = \left| \frac{2}{L} \int_0^L dy e^{-jky} \cos \frac{n\pi y}{L} \right|^2 = F_n^2(k)$$

The integral can be easily calculated, and we obtain

$$F_n^2(k) = \begin{cases} \left\{ \frac{4kL \cos(kL/2)}{k^2 L^2 - (n\pi)^2} \right\}^2 & n = 1, 3, 5, \dots \\ \left\{ \frac{4kL \sin(kL/2)}{k^2 L^2 - (n\pi)^2} \right\}^2 & n = 2, 4, 6, \dots \end{cases}$$

Since $kL = 2\pi\Phi/\Phi_0 = 2\pi\phi$ it can be written as

$$F_n^2(\phi) = \begin{cases} \left\{ \frac{2\phi \cos \pi\phi}{\pi [\phi^2 - (n/2)^2]} \right\}^2 & n = 1, 3, 5, \dots \\ \left\{ \frac{2\phi \sin \pi\phi}{\pi [\phi^2 - (n/2)^2]} \right\}^2 & n = 2, 4, 6, \dots \end{cases} \quad (9.2.23)$$

and (9.2.22) becomes

$$J_{dc}(V_0, \phi) = \frac{\bar{c}^2 J_1}{4\omega^2 \lambda_J} \sum_{n=0}^{\infty} \frac{1/Q_n}{[1 - (\omega_n/\omega)^2]^2 + 1/Q_n^2} F_n^2(\phi) \quad (9.2.24)$$

This expression was derived independently by Kulik (1965a) and by Eck, Scalapino and Taylor (1964 a, b).

At a fixed value of the external field this expression is essentially a sum of many Lorentzian lines centered at voltages

$$V_n = \frac{\hbar}{2e} \omega_n = \frac{\hbar n}{2e} \bar{c} / 2L$$

However, in the usual experimental configurations because of the low impedance of the junction it is very difficult to observe the shape of the lines in the V - I characteristic. From (9.2.24) the maximum amplitude of the n th step, as a function of the external field, is given by

$$J_n^M(\phi) = J_1 \left(\frac{L}{\lambda_J} \right)^2 \frac{Q_n}{4\pi^2 n^2} F_n^2(\phi) \quad (9.2.25)$$

The index n in Q_n recalls that Q_n is voltage dependent through $R_T(V_0)$.

At this point it is worthwhile to make few remarks on the quality factor Q_n . In the present derivation it accounts only for the losses due to the quasiparticle tunneling current through the dielectric barrier. In real devices many other mechanisms contribute to these losses: surface resistance in the superconducting films, geometrical nonuniformities, radiation from the junction.

The total quality factor Q_T can be computed by the expression

$$Q_T = \frac{1}{\sum_i \left(\frac{1}{Q_i} \right)}$$

where Q_i is the quality factor and refers to each one of the abovementioned mechanisms.

Usually the most important contribution to the losses comes from the surface resistance of the electrodes. An expression for the quality factor due to this mechanism has been derived by Ngai (1969), under the approximation of short mean free path for the electrons.

First experimental investigation on the quality factor in Josephson junctions has been performed by Schwidtal and Smiley (1972) through the study of the magnetic field dependence of self-induced steps, and by Soerensen, Finnegan, and Pedersen (1973) from the response of the junction cavity to

TABLE 9.1 The absolute maxima of the function $F_n(\phi)$ and the field values ϕ_M at which they occur, for different values of n^a

	$n = 1$	$n = 2$	$n = 3$	$n = 4$	$n = 5$
$F_n(\phi_M)$	1.091	1.031	1.015	1.008	1.006
ϕ_M	0.70	1.15	1.60	2.05	2.55

external microwave radiation. Subsequent experimental investigation on this problem has been performed more recently by Broom and Wolf (1977) and Wang and Gayley (1978).

Expressions (9.2.24) and (9.2.25) are valid as long as

$$\left(\frac{L}{\lambda_J} \right)^2 \frac{Q_1}{4\pi^2} \ll 1 \quad (9.2.26)$$

Equation 9.2.23 can be equivalently written

$$F_n^2(\phi) = \left\{ \frac{2\phi}{\phi + n\pi/2} \frac{\sin(\pi\phi - n\pi/2)}{\pi\phi - n\pi/2} \right\}^2$$

In this expression $F_n(\phi)$ is written as the product of the two functions. It is easy to see that for large values of n the principal maximum tends to occur at $\phi \approx n\pi/2$. Table 9.1 gives the maxima of $F_n(\phi)$ for n from 1 to 5, together with the corresponding values ϕ_M at which they occur. The function $F_n^2(\phi)/n^2$ is reported in Fig. 9.4 for different values of n .

Figure 9.5 shows a typical experimental dependence for the d.c. Josephson current and steps 1, 2, and 3. The data refer to a Nb-Pb junction and were taken in the same experimental run. Let us remark that in the usual samples the condition (9.2.26) is generally satisfied only for higher order steps ($n \geq 2$). In Section 9.5 we discuss a more general theory developed by Kulik (1967) which is valid also for high Q junctions. Therefore we shall postpone until then the comparison between theory and experiments.

The first observation of self-resonances in tunneling junctions was reported by Fiske in 1964 on Sn-Sn and Pb-Sn junctions. The data were presented at the conference on the Science of Superconductivity held at Colgate University (Hamilton, N.Y.) in August 1963. On the same occasion Pippard (1964) suggested a possible explanation of the phenomenon.

Subsequent experimental investigations have been performed by the same Fiske (Coon and Fiske 1965) and by two groups at, respectively, the University of Pennsylvania (Eck, Scalapino, and Taylor 1964a, b; Langenberg, Scalapino, and Taylor 1966) and the Physico-technical Institute of Low Temperatures in

^a ϕ_M is in units of the flux quantum Φ_0 .

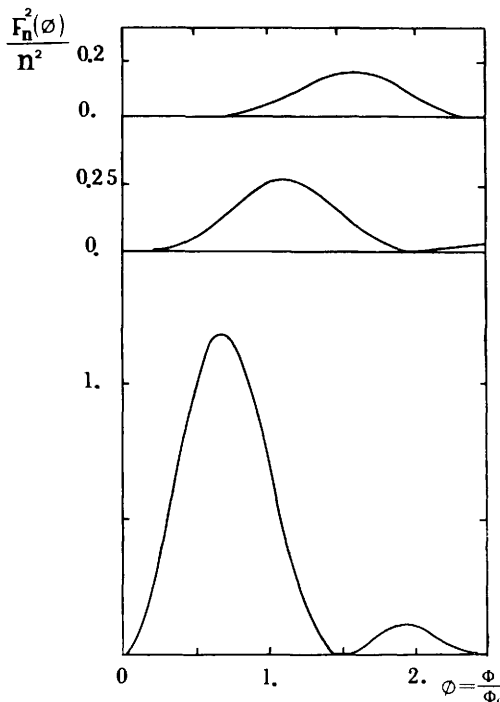


Figure 9.4 Theoretical magnetic field dependence of the Fiske steps (9.2.23)

$$\frac{F_n^2(\phi)}{n^2} = J_n^M(\phi) \left/ \left[J_1(L/\lambda_s)^2 \frac{Q_n}{4\pi^2} \right] \right. \text{ for different values of } n \text{ and for small } Q_n \text{ values.}$$

USSR (Yanson, Svistunov, and Dmitrenko 1964; Dmitrenko, Yanson, and Svistunov 1965; Dmitrenko and Yanson 1965a,b). The magnetic field dependence of resonant mode amplitudes was investigated by Dmitrenko and Yanson (1965b) on both small and large Sn-Sn cross type junctions. These authors also report data on the temperature dependence of the voltage position of a particular step, together with the theoretical dependence computed assuming the usual expression of $\lambda_L(T)$ (5.1.6). Data on the temperature dependence of the step position in Nb-NbO_x-Pb and Nb-NbO_x-In junctions were reported by Satterthwaite and coworkers (1964). In the same paper a set of V - I characteristics of a Nb-In junctions showing voltage steps, obtained using a low impedance voltage source, are also discussed. Recently experimental investigations on the magnetic field dependence of the step amplitude have been extended to semiconducting barrier junctions (Russo 1977). In particular, a light sensitive CdS barrier layer was considered and a rather good agreement was obtained with the theory for oxide barrier junctions developed in this section. Further theoretical and experimental investigation on resonances in semiconductor barrier Josephson junctions has been reported by Lum and Van Duzer (1978).

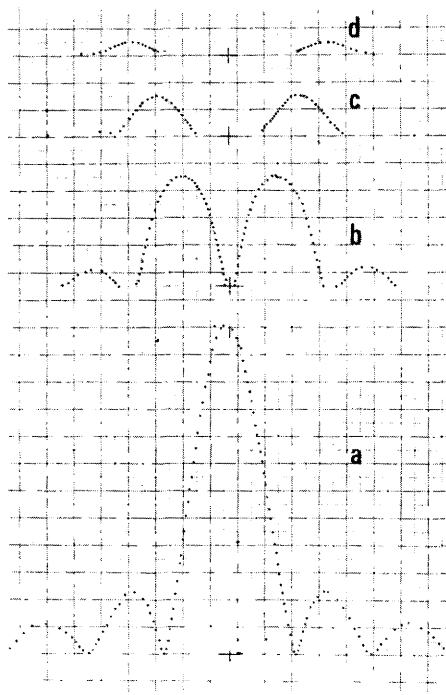


Figure 9.5 Experimental magnetic field dependence for the d.c. Josephson current (a) and the first (b), second (c), and third (d) steps. The data refer to a rectangular Nb-NbO_x-Pb junction.

Let us observe that the whole analysis so far discussed is based on an one dimensional model. Fiske modes in structures of circular geometry have been considered experimentally by Bermon and Mesak (1971) and theoretically by Neremberg and Blackburn (1974). Theoretical investigation has been performed by Neremberg, Forsyth, and Blackburn (1976) on a rectangular junction and arbitrary orientation (on the plane of the barrier) of the applied field. When the field direction is along one edge of the junction cavity the results of the linear model are obtained, whereas for an applied field with nonzero components in both directions other resonances are expected at different voltages. The effect of these new modes should be enhanced for an applied field directed corner to corner.

9.3 Junction of Infinite Length

In the case of a junction of infinite length ($L = \infty$) there are no standing waves for the electric field in the superconducting transmission line. As we have seen, (9.2.11) can be written in the form:

$$\frac{\partial^2 \varphi_1(y, t)}{\partial y^2} - \frac{1}{\bar{c}^2} \left[\frac{\partial^2 \varphi_1(y, t)}{\partial t^2} + \gamma \frac{\partial \varphi_1(y, t)}{\partial t} \right] = \frac{1}{\lambda_j^2} \operatorname{Im} e^{j(\omega t - ky)} \quad (9.3.1)$$

We look for a traveling wave solution for φ_1 as:

$$\varphi_1(y, t) = \text{Im } A(k, \omega) e^{j(\omega t - ky)} \quad (9.3.2)$$

(A is a complex number). By inserting (9.3.2) into (9.3.1) it is easy to show that

$$A(k, \omega) = \frac{1/\lambda_J^2}{\omega^2/\bar{c}^2 - k^2 - j(\omega\gamma/\bar{c}^2)}$$

Therefore:

$$\varphi_1(y, t) = \text{Im} \left\{ \frac{\bar{c}^2}{\omega^2 \lambda_J^2} \frac{(1 - k^2 \bar{c}^2 / \omega^2) - j/Q}{(1 - k^2 \bar{c}^2 / \omega^2)^2 + 1/Q^2} e^{j(\omega t - ky)} \right\} \quad (9.3.3)$$

The dc current is given, as before, by

$$J_{dc} = \lim_{\substack{T \rightarrow \infty \\ L \rightarrow \infty}} \frac{1}{T} \int_0^T dt \frac{1}{L} \int_0^L dy J_1 \cos(\omega t - ky) \varphi_1(y, t)$$

Using (9.3.3), the expression for the d.c. current becomes

$$J_{dc}(V_0, H_e) = J_1 \frac{\bar{c}^2}{2\lambda_J^2 \omega^2} \frac{1/Q}{[1 - k^2 \bar{c}^2 / \omega^2]^2 + 1/Q^2} \quad (9.3.4)$$

Thus for a junction of infinite dimensions only one resonance in the V - I characteristic is obtained.

At a given value of the external field, the maximum of this resonance occurs at a voltage such that $\omega/k = \bar{c}$. This condition implies that the phase velocity of the Josephson current density distribution ω/k matches the phase velocity \bar{c} of the electromagnetic fields in the junction. Let us define by V^M the voltage at which the peak of the resonance occurs. Since $\omega = 2eV/\hbar$, $k = (2\pi d/\Phi_0)H_e$ the relation between the applied magnetic field H_e and V^M is given by

$$V^M = d \frac{\bar{c}}{c} H_e \quad (9.3.5)$$

It is interesting to observe that in the previous case too (finite L) for n large, one finds a relation like (9.3.5). In fact, the wavelength of the electromagnetic field in the junction becomes much smaller than L (remember that $\lambda_n = \bar{c}/\omega_n = L/n\pi$). For n large the field H_e^n at which the maximum of the n th step occurs is given by

$$\phi_n^M = \frac{d L H_e^n}{\Phi_0} = \frac{n}{2} \quad (9.3.6)$$

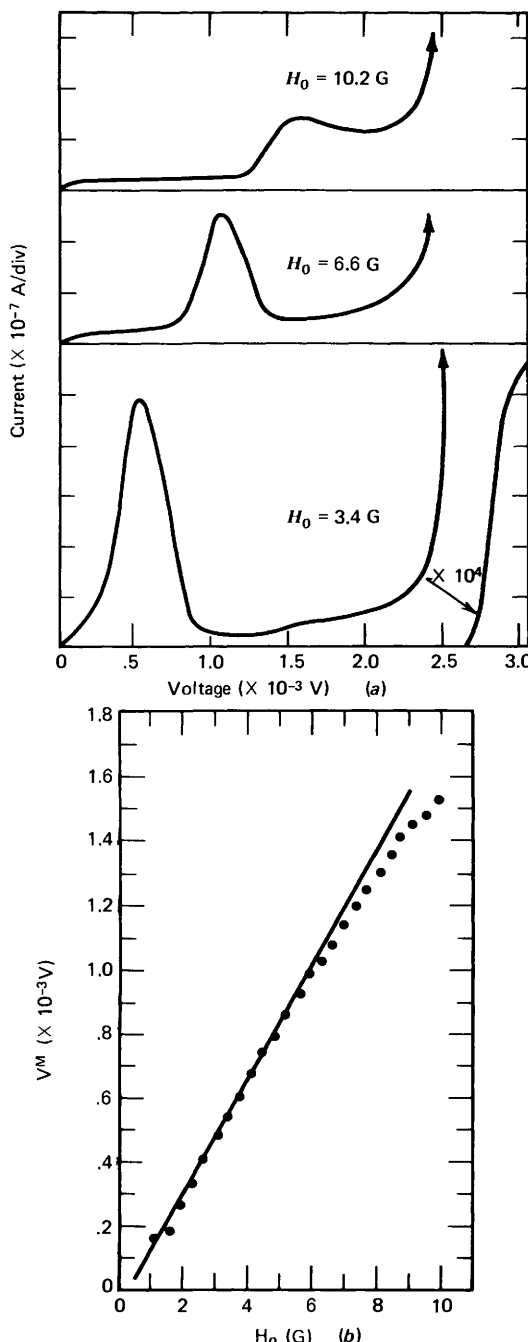


Figure 9.6 (a) Voltage-current characteristics for a $\text{Pb-PbO}_x\text{-Pb}$ junction for different value of the applied field H_0 . (b) The dependence of the peak position V^M on the applied magnetic field H_0 . The experimental data (dots) are compared with the linear relation given by (9.3.8). (After Eck, Scalapino, and Taylor 1964a.)

The corresponding voltage V_n^M is given by

$$\frac{2e}{\hbar} V_n^M = \frac{n\pi\bar{c}}{L} \quad (9.3.7)$$

and thus

$$V_n^M = d \frac{\bar{c}}{c} H_e^n \quad (9.3.8)$$

The first experimental results exhibiting a behavior typical of a junction of infinite dimensions were reported by Eck, Scalapino, and Taylor (1964). In Fig. 9.6a the V - I characteristic for different values of the applied magnetic field are shown. The data refer to a Pb-Pb junction of dimensions 0.25×0.25 mm². These results are in good agreement with the previously described model for an infinite length transmission line. However, the wavelength of the electromagnetic radiation in the junction that results from the experimental data is of the same order of magnitude as the junction length. Therefore the condition $L \rightarrow \infty$, under which the theoretical model has been derived, is not satisfied. The behavior can be related to the presence of nonuniformities in the oxide barrier. In fact, when the spacing of these oxide nonuniformities is comparable to the wavelength of the radiation, reflection at the edges is no longer effective. Thus no standing wave pattern is established, and the junction behaves like an infinite length strip line. In Fig. 9.6b the dependence of the peak position V^M on the applied magnetic field is shown. The linear relation previously derived (9.3.5) is well verified. The small discrepancy for high voltage values can be explained in terms of the frequency dependence of \bar{c} through the penetration depth (Ngay 1969).

9.4 Nonuniform Current Density Distribution

Let us consider now the effect of a nonuniform current density distribution in the y direction in a junction of finite length. We discuss this problem as an extension of the theory for low Q junctions developed in Section 9.2. In this case (9.2.11) becomes

$$\frac{\partial^2 \phi_1}{\partial y^2} - \frac{1}{\bar{c}^2} \left(\frac{\partial^2 \phi_1}{\partial t^2} + \gamma \frac{\partial \phi_1}{\partial t} \right) = \frac{J(y)}{\langle \lambda_J \rangle^2 \langle J \rangle} \sin(\omega t - ky)$$

where $\langle J \rangle$ is the mean value of the Josephson current density along the y direction and $\langle \lambda_J \rangle^2 = (\hbar c^2 / 8\pi e d \langle J \rangle)$. The expression for the dc current is

$$J_{dc} = \frac{\bar{c}^2 \langle J \rangle}{4\omega^2 \langle \lambda_J \rangle^2} \sum_{n=0}^{\infty} \frac{1/Q_n}{[1 - (\omega_n/\omega)^2]^2 + 1/Q_n^2} [B_n'^2(k) + C_n'^2(k)]$$

where now

$$B_n'^2 + C_n'^2 = \left| \frac{2}{L} \int_0^L dy e^{-jky} \frac{J(y)}{\langle J \rangle} \cos \frac{n\pi y}{L} \right|^2$$

and

$$\langle J \rangle = \frac{1}{L} \int_0^L dy J(y)$$

Therefore the maximum step height is given by

$$J_n^M(\phi) = \langle J_1 \rangle \left(\frac{L}{\langle \lambda_J \rangle} \right)^2 \frac{Q_n}{4\pi^2 n^2} F_n'(\phi) \quad (9.4.1)$$

where

$$F_n'(\phi) = \left| \frac{2}{L} \int_0^L dy e^{-j2\pi\phi \frac{y}{L}} \frac{J(y)}{\langle J \rangle} \cos \frac{n\pi y}{L} \right|$$

Let us consider the simple current density profile peaked at the junction edges that we looked at in chapter 4 (Fig. 4.11):

$$J(y) = \frac{J_1 \cosh \chi (1 - 2y/L)}{\cosh \chi}. \quad (9.4.2)$$

With the change of variables $(2/L)y = y'$ we get for the integrals

$$F_n'(\phi) = \frac{J_1}{\langle J \rangle \cosh \chi} \int_0^1 dy' \cosh(\chi y') \sin(\pi \phi y') \sin\left(\frac{n\pi y'}{2}\right) \quad \text{for } n \text{ odd}$$

and

$$F_n'(\phi) = \frac{J_1}{\langle J \rangle \cosh \chi} \int_0^1 dy' \cosh(\chi y') \cos(\pi \phi y') \cos\left(\frac{n\pi y'}{2}\right) \quad \text{for } n \text{ even}$$

Finally:

$$\begin{aligned} J_n^M(\phi, \chi) &= \frac{J_1^2}{\langle J \rangle} \left(\frac{L}{\langle \lambda_J \rangle} \right)^2 \frac{Q_n}{4\pi^2 n^2} \\ &\times \left\{ \left[\frac{\pi(\phi - n/2)}{\chi^2 + \pi^2(\phi - n/2)^2} + \frac{\pi(\phi + n/2)}{\chi^2 + \pi^2(\phi + n/2)^2} \right] \cos \pi \phi \right. \end{aligned}$$

$$\begin{aligned}
 & + \left[\frac{(-1)^n \tanh \chi}{\chi} \left(\frac{\chi^2}{\chi^2 + \pi^2(\phi - n/2)^2} \right. \right. \\
 & \left. \left. + \frac{\chi^2}{\chi^2 + \pi^2(\phi + n/2)^2} \right) \right] \sin \pi \phi \}^2 \quad \text{for } n \text{ odd} \quad (9.4.3a)
 \end{aligned}$$

$$\begin{aligned}
 J_n^M(\phi, \chi) = & \frac{J_1^2}{\langle J \rangle} \left(\frac{L}{\lambda_J} \right)^2 \frac{Q_n}{4\pi^2 n^2} \\
 & \times \left\{ \left[\frac{\pi(\phi - n/2)}{\chi^2 + \pi^2(\phi - n/2)^2} + \frac{\pi(\phi + n/2)}{\chi^2 + \pi^2(\phi + n/2)^2} \right] \sin \pi \phi \right. \\
 & \left. + \left[\frac{(-1)^n}{4} \frac{\tanh \chi}{\chi} \left(\frac{\chi^2}{\chi^2 + \pi^2(\phi - n/2)^2} \right. \right. \\
 & \left. \left. + \frac{\chi^2}{\chi^2 + \pi^2(\phi + n/2)^2} \right) \right] \cos \pi \phi \right\}^2 \quad \text{for } n \text{ even} \quad (9.4.3b)
 \end{aligned}$$

For $\chi \rightarrow 0$ the last expression reduces to our earlier expression for a uniform barrier. For $\chi \rightarrow \infty$ (current density confined at the edges) we find

$$J_n^M(\phi, \infty) = \frac{J_1^2}{\langle J \rangle} \left(\frac{L}{\langle \lambda_J \rangle} \right)^2 \frac{Q_n}{4\pi^2 n^2} \left(\frac{\tanh \chi}{\chi} \right)^2 \times \begin{cases} 4 \cos^2 \pi \phi & n = 2, 4, 6, \dots \\ 4 \sin^2 \pi \phi & n = 1, 3, 5, \dots \end{cases}$$

Since

$$\langle J \rangle = \frac{1}{L} \int_{-L/2}^{+L/2} dy J(y) = J_1 \frac{\tanh \chi}{\chi}$$

we have:

$$J_n^M(\phi, \infty) = \langle J \rangle \left(\frac{L}{\langle \lambda_J \rangle} \right)^2 \frac{Q_n}{4\pi^2 n^2} F_n'^2(\phi)$$

where

$$F_n'(\phi) = \begin{cases} 2 \sin \pi \phi & n = 1, 3, 5, \dots \\ 2 \cos \pi \phi & n = 2, 4, 6, \dots \end{cases}$$

It is interesting to observe that for $H=0$, that is, $\phi=0$ from (9.4.3 a,b), it

follows that

$$J_n^M(0, \chi) = \langle J \rangle \left(\frac{L}{\langle \lambda_J \rangle} \right)^2 \frac{Q_n}{4\pi^2 n^2} \left(\frac{2}{1 + \pi^2 n^2 / 4\chi^2} \right)^2 \quad n=2,4,6,\dots$$

$$0 \quad n=1,3,5,\dots$$

for all values of χ . Therefore as soon as $\chi \neq 0$, zero field steps for n even appear.

Figure 9.7 gives the magnetic field dependences of the Josephson current and of the first Fiske steps, computed assuming current density profiles like that of (9.4.2). In particular, the case $\chi = 5$ is considered. Data are normalized to the value of the corresponding maximum current amplitude. Recently Russo

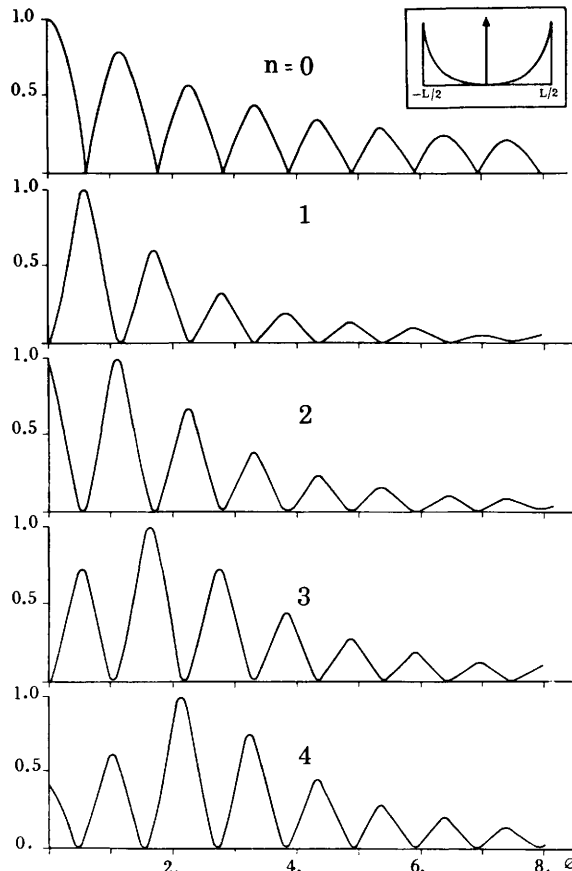


Figure 9.7 Theoretical magnetic field dependence of the maximum Josephson current ($n=0$) and of the first four self-induced steps ($n=1,2,3,4$) for a junction with a current density profile peaked at the edges (see the inset). Each curve is normalized to its maximum value.

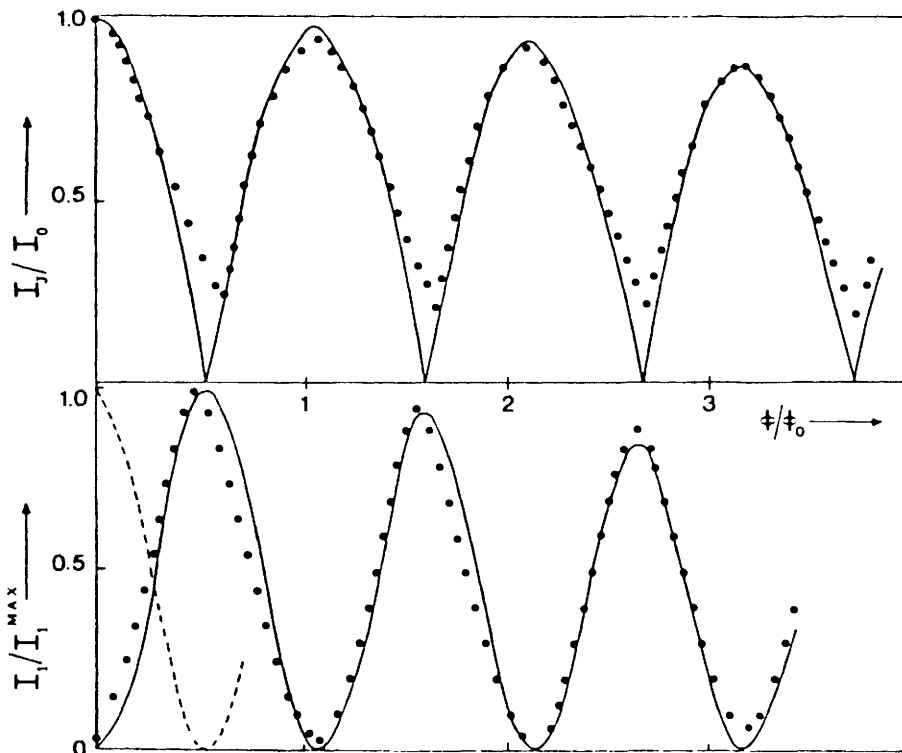


Figure 9.8 *Top:* Magnetic field dependence of the light induced maximum zero voltage Josephson current $I_j(\Phi/\Phi_0)$ of an In-CdS-In junction. The full circles are the experimental data normalized to the maximum value of the current. The solid line is the theoretical behavior of a nonuniform current density profile computed by using the one parameter model (4.4.3) for $\chi = 18$. *Bottom:* Magnetic field dependence, for the same junction, of the light induced first Fiske step amplitude. Full circles are the experimental data normalized to the maximum current value. The solid line is the behavior predicted by (9.4.3) for $\chi = 18$. The dashed line is the theoretical dependence of the second step amplitude. (After Russo and Vaglio 1978.)

and Vaglio (1978) have performed measurements on CdS barrier junctions in which the peaking of the current density at the edges of the junction was obtained by a nonuniform illumination (see below). Experimental data are reported in Fig. 9.8, together with the theoretical curve computed by using the theoretical analysis developed above.

Further experimental and theoretical analysis of the influence of barrier nonuniformities on the magnetic field dependence of self-induced steps has been carried out by Balsamo and coworkers (1978) on high Q Josephson junctions. In that work the experimental data are compared with the general Kulik's theory (see next section) modified to account for a nonuniform current density distribution. An extensive analysis on the problem has been reported by Paternò and Vaglio (1979). Further theoretical work has been reported by Wang (1979).

9.5 Resonant Modes for High Q Josephson Junctions

The theory just considered for Fiske steps is strictly valid under the restriction that

$$\frac{J_n^M(\phi_M)}{J_1} \simeq \left(\frac{L}{2\pi\lambda_J n} \right)^2 Q_n \ll 1$$

That is

$$Q_1 \ll 4\pi^2 \left(\frac{\lambda_J}{L} \right)^2$$

Kulik (1967) has considered the situation in which Q_n can assume an arbitrary large value. The starting point is (9.2.10) for the phase $\varphi_1(y, t)$; in the forcing term on the right side, the approximation of considering φ_1 as a small perturbation is not performed.

For simplicity we assume that the voltage is close to one of the resonances of the junction: $\omega \simeq \omega_n$. We write for $\varphi_1(y, t)$ the expression

$$\varphi_1(y, t) \simeq \Theta(t) \cos k_n y \quad (9.5.1)$$

where $k_n = n\pi/L$. Here we consider only one component of the Fourier expansion in the modes of the junction. Under this approximation (9.2.10) becomes

$$\frac{\partial^2 \varphi_1}{\partial y^2} - \frac{1}{\bar{c}^2} \left(\frac{\partial^2 \varphi_1}{\partial t^2} + \gamma \frac{\partial \varphi_1}{\partial t} \right) = \frac{1}{\lambda_J^2} \text{Im} \{ e^{j\omega t} e^{-jk_n y} e^{j\Theta(t)} \cos k_n y \} \quad (9.5.2)$$

For the factor $e^{j\Theta \cos k_n y}$ we take a Fourier-Bessel expansion in terms of the exponentials $e^{-jm k_n y}$ (see, for example, Jahmke and Emde 1945):

$$e^{j\Theta \cos k_n y} = \sum_{m=-\infty}^{+\infty} (j)^m J_m(\Theta) e^{-jm k_n y} \quad (9.5.3)$$

where $J_m(x)$ is a Bessel function of order m . Inserting (9.5.1) and (9.5.3) into (9.5.2) one obtains:

$$\begin{aligned} & \cos(k_n y) \left[\frac{\partial^2 \Theta(t)}{\partial t^2} + \gamma \frac{\partial \Theta(t)}{\partial t} + \bar{c}^2 k_n^2 \Theta(t) \right] \\ &= -\frac{\bar{c}^2}{\lambda_J^2} \text{Im} \left\{ e^{j\omega t} e^{-jk_n y} \sum_{m=-\infty}^{+\infty} (j)^m J_m(\Theta) e^{-jm k_n y} \right\} \end{aligned}$$

Multiplying both sides by $\cos k_n y$ and integrating between 0 and L:

$$\frac{\partial^2 \Theta}{\partial t^2} + \gamma \frac{\partial \Theta}{\partial t} + k_n^2 \bar{c}^2 \Theta = -\frac{\bar{c}^2}{\lambda_J^2} \frac{2}{L}$$

$$\times \operatorname{Im} \left\{ e^{j\omega t} \sum_{m=-\infty}^{+\infty} (j)^m J_m(\theta) \int_0^L dy e^{-jk_y} \cos(k_n y) e^{-jm k_n y} \right\}$$

where we have used the relation $\int_0^L \cos^2(k_n y) dy = L/2$. Following Kulik we define:

$$F_{n,m} = \frac{j2}{L} \int_0^L dy e^{-jk_y} \cos(k_n y) e^{-jm k_n y} \quad (9.5.4)$$

The last expression becomes

$$\frac{\partial^2 \Theta(t)}{\partial t^2} + \gamma \frac{\partial \Theta(t)}{\partial t} + \omega_n^2 \Theta(t) = \alpha \operatorname{Re} \{ e^{j\omega t} F(\Theta) \} \quad (9.5.5)$$

where $\omega_n^2 = k_n^2 \bar{c}^2$, $\alpha = \bar{c}^2 / \lambda_J^2$, and

$$F(\Theta) = \sum_{m=-\infty}^{+\infty} (j)^m J_m(\Theta) F_{n,m}$$

As observed by Kulik (1967), (9.5.5) is a standard differential equation well known in the theory of nonlinear oscillations (Bogolyubov and Mitropolskii 1961). Under the hypothesis $\alpha \rightarrow 0$, that is, $\lambda_J \rightarrow \infty$, it is possible to find an asymptotic solution for $\Theta(t)$ in the form

$$\Theta(t) = a(t) \cos(\omega t + b) + \alpha u(a, b, \omega t) + \dots$$

where $a(t)$ and $b(t)$ are slowly varying functions whose time derivative is related to the forcing term of (9.5.5). Under the assumption $da/dt = db/dt = 0$

$$\Theta(t) \approx a \cos(\omega t + b) \quad (9.5.6)$$

with a and b constants.

If we neglect the time dependence in $F(\Theta)$ taking only the time independent term it can be shown (Kulik 1967):

$$F(\Theta) \approx J_0 \left(\frac{a}{2} \right) F_{n0} \quad (9.5.7)$$

where

$$F_{n0} = \frac{2j}{L} \int_0^L dy e^{-jk_y} \cos k_n y$$

By inserting (9.5.6) and (9.5.7) into (9.5.5) it is easy to derive the relation:

$$ae^{jb} = \frac{1}{(\omega_n^2 - \omega^2) + j\omega\gamma} \alpha J_0^2\left(\frac{a}{2}\right) F_{n,0}$$

From this we get for the amplitude a :

$$\frac{a}{J_0^2\left(\frac{a}{2}\right)} = \frac{\alpha}{\sqrt{(\omega_n^2 - \omega^2)^2 + \omega^2\gamma^2}} |F_{n,0}| \quad (9.5.8)$$

where

$$|F_{n,0}| = F_n(\phi) = \frac{2}{\pi} \frac{\phi |\sin(\pi\phi - \pi(n/2))|}{|\phi^2 - n^2/4|}$$

$F_n(x)$ is the function that we introduced previously. Expression (9.5.8) can be written as

$$\frac{a}{J_0^2(a/2)} = \frac{\bar{c}^2}{\lambda_J^2} \frac{1}{\omega\gamma} \frac{\omega\gamma}{\sqrt{(\omega_n^2 - \omega^2)^2 + \omega^2\gamma^2}} F_n(\phi) \quad (9.5.9)$$

The d.c. Josephson current is:

$$J_{dc}(\omega, k) = \lim_{T \rightarrow \infty} \frac{1}{T} \int_0^T dt \frac{1}{L} \int_0^L dy J_1 \sin(\omega t - ky + \Theta(t)) \cos k_n y$$

If we take a Fourier expansion of the sine in terms of $e^{-jk_n y}$ and consider the lowest order terms, we get

$$J_{dc}(\omega, \phi) \approx J_1 J_0\left(\frac{a}{2}\right) J_1\left(\frac{a}{2}\right) F_n(\phi) \frac{\omega\gamma}{\sqrt{(\omega_n^2 - \omega^2)^2 + \gamma^2\omega^2}} \quad (9.5.10)$$

It is very easy to see that in the limit of small amplitude for the electromagnetic wave excited into the junction, that is, for $a \rightarrow 0$, we recover from (9.5.9) and (9.5.10) the expression (9.2.24) derived in the preceding section. In fact, by using the asymptotic expression for $J_0(x)$ and $J_1(x)$ for $a \rightarrow 0$ we have

$$J_0\left(\frac{a}{2}\right) \approx 1 \quad J_1\left(\frac{a}{2}\right) \approx \frac{a}{2}$$

and

$$J(\omega, \phi) \approx J_1 \frac{a}{2} F_n(\phi) \frac{\omega\gamma}{\sqrt{(\omega_n^2 - \omega^2)^2 + \gamma^2\omega^2}}$$

$$a = \frac{\bar{c}^2}{\lambda_J^2} \frac{1}{\omega\gamma} \frac{\omega\gamma}{\sqrt{(\omega_n^2 - \omega^2)^2 + \gamma^2\omega^2}} F_n(\phi)$$

Combining these expressions we obtain the n th term of (9.2.24). In the general case the maximum step amplitude as a function of the magnetic field is obtained from (9.5.9) and (9.5.10) for $\omega = \omega_n$. In this case:

$$J_n^M(\phi) = J_1 J_0\left(\frac{a}{2}\right) J_1\left(\frac{a}{2}\right) F_n(\phi) \quad (9.5.11)$$

where a is the first solution of the nonlinear equation:

$$J_0\left(\frac{a}{2}\right) = \frac{a \lambda_J^2}{\bar{c}^2} \omega_n \gamma$$

If we again introduce the Q of the junction defined by $Q_n = \omega_n / \gamma$ since $\omega_n / \bar{c} = n\pi/L$ the last expression becomes

$$J_0\left(\frac{a}{2}\right) = \frac{a}{(L/\pi n \lambda_J)^2 Q_n F_n(\phi)}$$

which is valid for arbitrary large values of Q_n , but only under the assumption that $L/\lambda_J \rightarrow 0$. Introducing the parameter

$$Z_n = \left(\frac{L}{\lambda_J}\right)^2 \frac{Q_n}{\pi^2 n^2} \quad (9.5.12)$$

the last expression can be written as

$$J_0\left(\frac{a}{2}\right) = \frac{a}{Z_n F_n(\phi)} \quad (9.5.13)$$

From (9.5.11) and (9.5.13) it is easy to see that $J_n^M/J_1 F_n$ as a function of $Z_n F_n$ is a universal function independent of n and ϕ . This function is shown in Fig. 9.9.

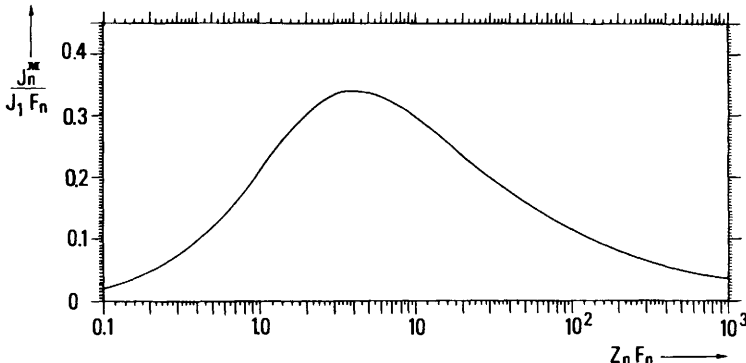


Figure 9.9 The universal function $J_n^M / (J_1 F_n)$ vs. $Z_n F_n$ (ϕ) numerically computed by (9.5.11) and (9.5.13). (After Paternò and Nordman 1978.)

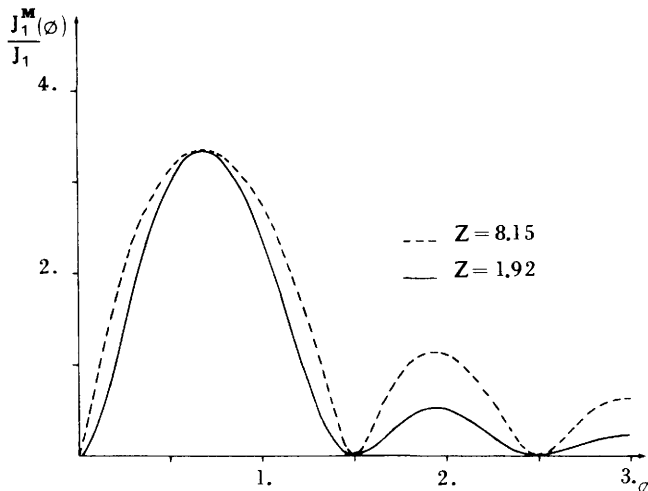


Figure 9.10 Theoretical magnetic field dependence of the first self-induced step ($n = 1$) for a high Q junction, computed by (9.5.11) and (9.5.13). The two curves refer to the two values of Z_n for which a maximum value of 0.33 for the step amplitude is obtained from the universal function of Fig. 9.9.

It is very useful to compare experimental data with the theory. Figure 9.10 shows the curves for $n = 1$ and for a given value of $\max J_1^M/J_1$ corresponding to the two particular values of Z_n that are found from the curve of Fig. 9.9.

The first comparison between experimental data and Kulik's theory previously discussed was performed by Schwidtal (1972) and Schwidtal and Smiley (1972). In this work, however, the analysis was confined to the

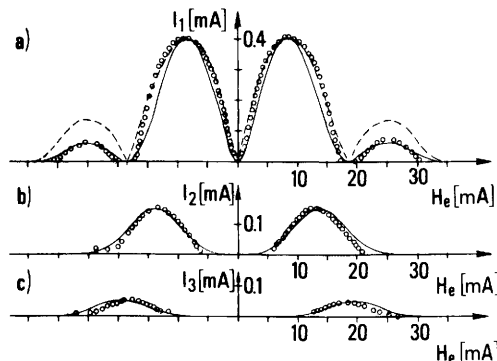


Figure 9.11 Magnetic field dependence of the first (a), second (b), and third (c) self-induced step for an $\text{Nb}-\text{NbO}_x-\text{Pb}$ junction. The experimental data (circles) refer to a sample whose dimension perpendicular to the applied field was slightly larger than the Josephson penetration depth λ_J . The theoretical dependences computed from (9.5.11) and (9.5.13) are also shown. For $n = 1$ (a) the theoretical curves corresponding to $Z_n = 1.91$ (solid line) and $Z_n = 8.15$ (dashed line) which give rise to the same maximum value for the step are shown. For $n = 2$, $Z_n = 0.51$; for $n = 3$, $Z_n = 0.16$. (After Paternò and Nordman 1978.)

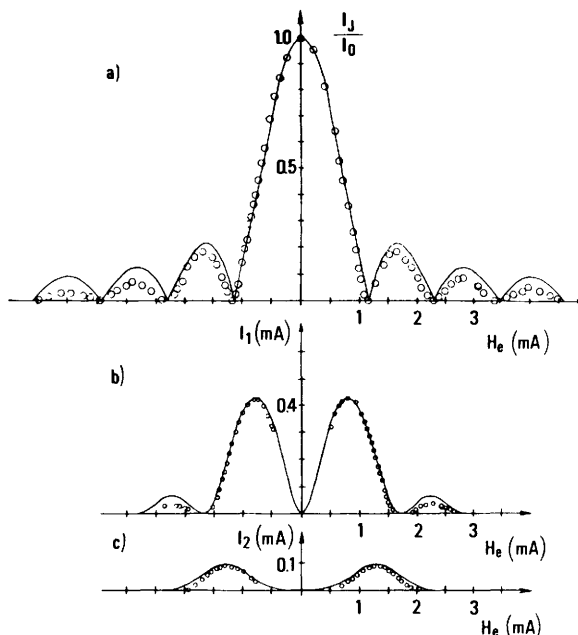


Figure 9.12 Magnetic field dependence for the maximum Josephson current $I_J(\phi)$ (a), and for the first (b) and second (c) self-induced step for an Nb-Nb O_x -Pb junction. The experimental data (circles) are compared with the theoretical dependence (solid line) computed from (4.3.1) and from (9.5.11) and (9.5.13) respectively. For this sample a ratio $L/\lambda_J = 0.6$ was estimated. (After Paternò and Nordman 1978.)

dependence of the maximum step amplitude on the corresponding Q_n value. Investigations on the magnetic field dependence of the step amplitude on high Q junctions has been reported by Gou and Gayley (1974). Recently extensive measurements on the magnetic field dependence of the "Fiske" steps have been performed by Paternò and Nordman (1978). The junction samples were of Nb-Nb O_x -Pb type with different values for the ratio L/λ_J (L perpendicular to the applied field). The experimental results are reported in Fig. 9.11 together with the theoretical curve. The data refer to a sample with a ratio L/λ_J slightly larger than unity consistently with the shape of the I vs. H pattern relative to the same sample reported in Fig. 9.5. The theoretical dependences for the step amplitudes have been numerically computed from (9.5.11) and (9.5.13). The values of Z_n were determined by means of the universal function plotted in Fig. 9.9 using the theoretical values of $F_n(\phi)$ (see Table 9.1) and using for J_n^M/J_1 the ratio I_n/I_0 between the measured maximum step amplitude and the maximum d.c. Josephson current. For $Z_n < 1$, the theoretical data were computed by using (9.2.25). The data of the Fig. 9.11 refer to steps 1, 2, and 3.

Figure 9.12 reports data for junctions with $L/\lambda_J < 1$ (~ 0.6). The agreement with the theory is excellent. In the previous case (experimental data of Fig. 9.11) the slight discrepancy is well explained by the relatively large value

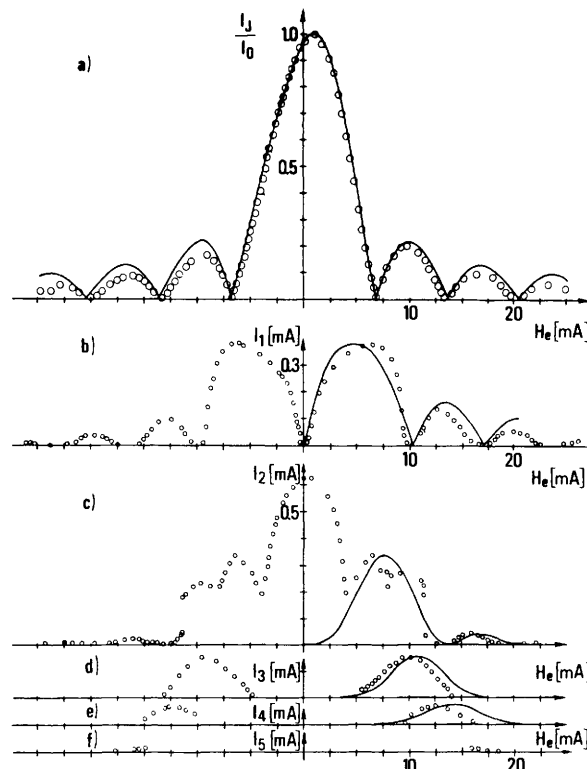


Figure 9.13 Magnetic field behavior of a rectangular junction whose maximum lateral dimension L was greater than the Josephson penetration depth λ_J ($L/\lambda_J = 1.3$). The sample was an Nb-NbO_x-Pb cross-type junction. The field was perpendicular to the larger dimension. (a) D.c. Josephson current compared with the theoretical dependence (solid line) derived by using (5.1.5). (b), (c), (d), (e), and (f) Self-induced steps 1 through 5. The solid lines are the theoretical dependences computed from (9.5.11) and (9.5.13). (After Paternò and Nordman 1978.)

of L/λ_J of the sample whereas Kulik's theory holds in the limit of $L/\lambda_J \rightarrow 0$. Figure 9.13 shows results concerning a junction with a ratio $L/\lambda_J = 1.3$.[†] As expected, there is a marked discrepancy with the theory. For $n=2$ the maximum amplitude of the current step occurs at zero external magnetic field. These singularities are the so called zero field steps first observed by Chen, Finnegan, and Langenberg (1971). Subsequent experimental results are due to Chen and Langenberg (1972), Fulton and Dynes (1973), and Gou and Gayley (1974). These zero field steps usually occur at voltages corresponding to even n Fiske modes. An explanation of the existence of these singularities has been proposed by Fulton and Dynes (1973) on the basis of vortex motion inside the

[†]The theoretical dependence of the maximum Josephson current on the applied field is computed using the approximate analysis for the self-field by Yamashita and Onodera (1967) discussed in Chapter 5 (Section 5.1.).

junction. This model predicts that these steps occur for even n and up to a limiting voltage value given by $V_0 = (\bar{c}/\lambda_J)\Phi_0$. This model, however, does not supply indications on the magnetic field dependence of these current singularities. Experimentally the step amplitude appears to be a decreasing function of the magnetic field and independent of its direction. We shall further discuss the problem of zero field steps in Section 10.4.

CHAPTER 10

Fluxon Dynamics

10.1 The Sine Gordon Equation

As we have seen, the electrodynamics of a long Josephson junction is described by the nonlinear partial differential equation (1.7.4), which in the one dimensional case can be written as[†]

$$\frac{\partial^2 \varphi}{\partial x^2} - \frac{1}{\bar{c}^2} \frac{\partial^2 \varphi}{\partial t^2} - \frac{\beta}{\bar{c}^2} \frac{\partial \varphi}{\partial t} = \frac{1}{\lambda_J^2} \sin \varphi \quad (10.1.1)$$

We have already examined particular solutions of this equation. In the preceding chapter some approximate oscillatory solutions were investigated in the presence of dissipation. Exact stationary (i.e., time independent) solutions were considered in Chapter 5.

Now we discuss general solutions of (10.1.1), neglecting dissipative effects. In this case, measuring distance x in units of λ_J and time t in units of λ_J/\bar{c} , (10.1.1) reduces to[‡]

$$\phi_{xx} - \phi_{tt} = \sin \phi \quad (10.1.2)$$

This very important equation is widely used throughout applied science (Barone et al. 1971; Scott, Chu, and McLaughlin 1973). It is referred to in the current literature as the “sine-Gordon” equation (S.G.E) (Rubinstein 1970).[§] This equation has solitary wave solutions, with the peculiar character of a particle-like or “soliton” solutions. One of the most striking features of these solutions is that when two solitons collide, they emerge after the collision with the initial speed and shape, the consequence of the collision being merely a time delay. In (10.1.2) ϕ can be interpreted either as the phase difference, φ , or as a normalized measure of the magnetic flux. This follows directly from the integration of the fundamental Josephson equation for the time dependence of the phase (1.4.5):

$$\varphi = \frac{2\pi}{\Phi_0} \int V dt = 2\pi \frac{\Phi}{\Phi_0}$$

[†]Here the x -axis is along the junction and z is perpendicular to the barrier.

[‡]The subscript notation for partial derivatives is used in this chapter.

[§]For a general account on the nonlinear wave propagation see Witham (1974).

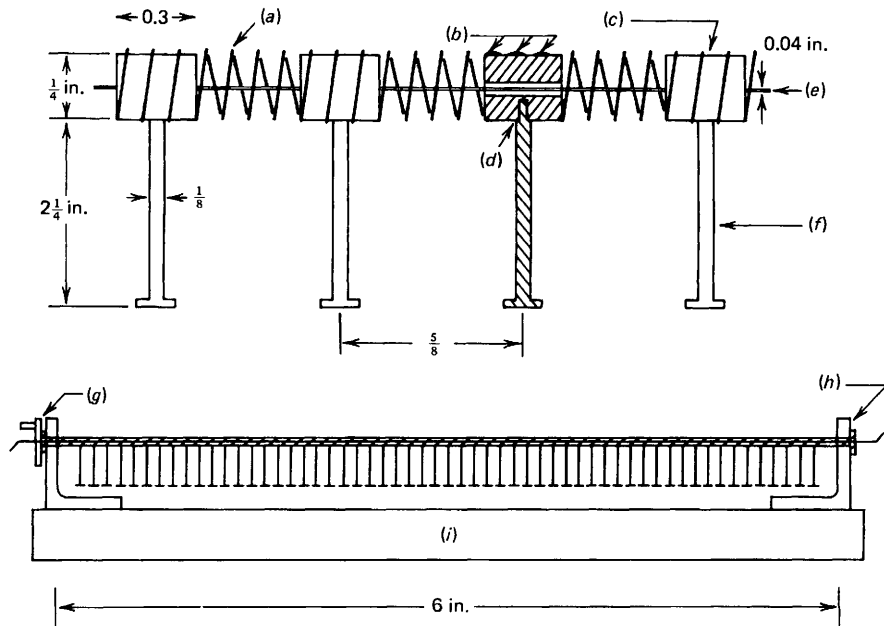


Figure 10.1 Mechanical model of the Sine-Gordon equation. (a) Spring, (b) solder, (c) brass, (d) tap and thread, (e) wire, (f) nail, (g) and (h) ball bearings, and (i) base. (After Scott 1969.)

A qualitative appreciation for solutions of the sine-Gordon equation can be obtained by playing with the mechanical model shown in Fig. 10.1 (Scott 1969). In this model the ϕ_{xx} term is represented by the restoring torque of the spring, the ϕ_{tt} term by the moments of inertia of the pendula, and the $\sin\phi$ corresponds to the gravitational torque. The reader who chooses to make a simple mechanical model (using dressmaker's pins and a rubber band) will find the experience rewarding. Such a "pocket" version of the mechanical model is shown in Fig. 10.2. A sketch of the junction is given in Fig. 10.3.

10.1.1 Traveling Wave Solutions. Time dependent solutions of (10.1.2) that are traveling waves or waves of permanent profile of the form

$$\phi = \phi(x - ut) \quad (10.1.3)$$

were investigated in connection with Josephson junctions by Kulik (1967), Scott (1967), and Lebwohl and Stephen (1967).[†] In (10.1.3) the parameter u represents an arbitrary constant velocity of propagation. If we write the argument of (10.1.3) as $\xi = x - ut$ then

$$\frac{\partial}{\partial x} \rightarrow \frac{d}{d\xi} \quad \text{and} \quad \frac{\partial}{\partial t} \rightarrow -u \frac{d}{d\xi}$$

[†]See also the volume by Scott (1970).



Figure 10.2 A "pocket" version of the mechanical model in Fig. 10.1.

and (10.1.2) becomes the original differential equation of the pendulum

$$\frac{d^2\phi}{d\xi^2} = \frac{\sin\phi}{1-u^2}$$

Multiplying by $d\phi/d\xi$ we find by integration

$$\frac{d\phi}{d\xi} = \left[\frac{2(E - \cos\phi)}{1-u^2} \right]^{1/2} \quad (10.1.4)$$

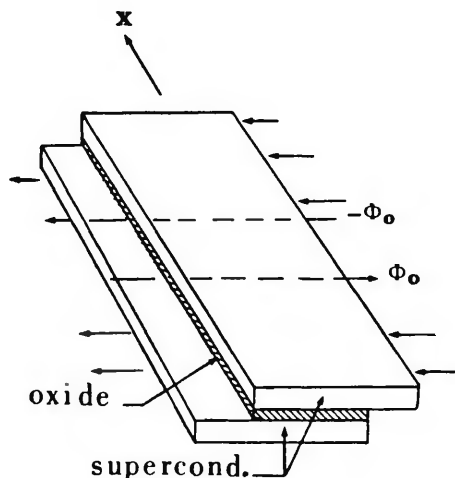


Figure 10.3 Long Josephson junction.

with E a constant of integration. Equation 10.1.4 has the following two solutions:

$$\phi = 4 \tan^{-1} \left\{ \exp \left[\pm \frac{(x - ut)}{\sqrt{1-u^2}} \right] \right\}$$

for $E=1$, and $|u|<1$ and

$$\phi = 4 \tan^{-1} \left\{ \exp \left[\frac{(x - ut)}{\sqrt{u^2 - 1}} \right] \right\} + \pi$$

for $E=-1$ and $|u|>1$.

The first solution is the single “kink” or soliton solution corresponding to a rotation in ϕ by 2π shown in the mechanical analog in Fig. 10.4a. The sign + or – indicates the sense of rotation and corresponds to a kink (soliton) or antikink (antisoliton) respectively. In the framework of the junction this solution is representative of the motion of a single fluxon or antifluxon (see Fig. 10.3). The second solution is clearly unstable because it describes a situation in which the equilibrium state has all of the pendula in the upward position.

When E is different from unity we can get periodic solutions. Equation 10.1.4 can be integrated giving

$$\xi = \sqrt{1-u^2} \int_0^\phi \frac{d\phi}{\sqrt{2E-\cos\phi}}$$

which is a typical elliptic integral. Let us consider two solutions. For $E>1$; $|u|<1$:

$$\phi = 2 \sin^{-1} \left[\pm \operatorname{cn} \left(\frac{\xi}{k\sqrt{1-u^2}} \middle| k \right) \right]$$

where cn is an elliptic function of modulus k , with $0 < k < 1$ (in the limit $k \rightarrow 1$ we recover the single kink solution). This solution corresponds to an evenly spaced array of fluxons in the junction. The mechanical analogy is depicted in Fig. 10.4b. This solution in the case of $E \gg 1$, namely high density of “kinks,” reduces to

$$\phi \simeq \sqrt{\frac{2E}{1-u^2}} \xi$$

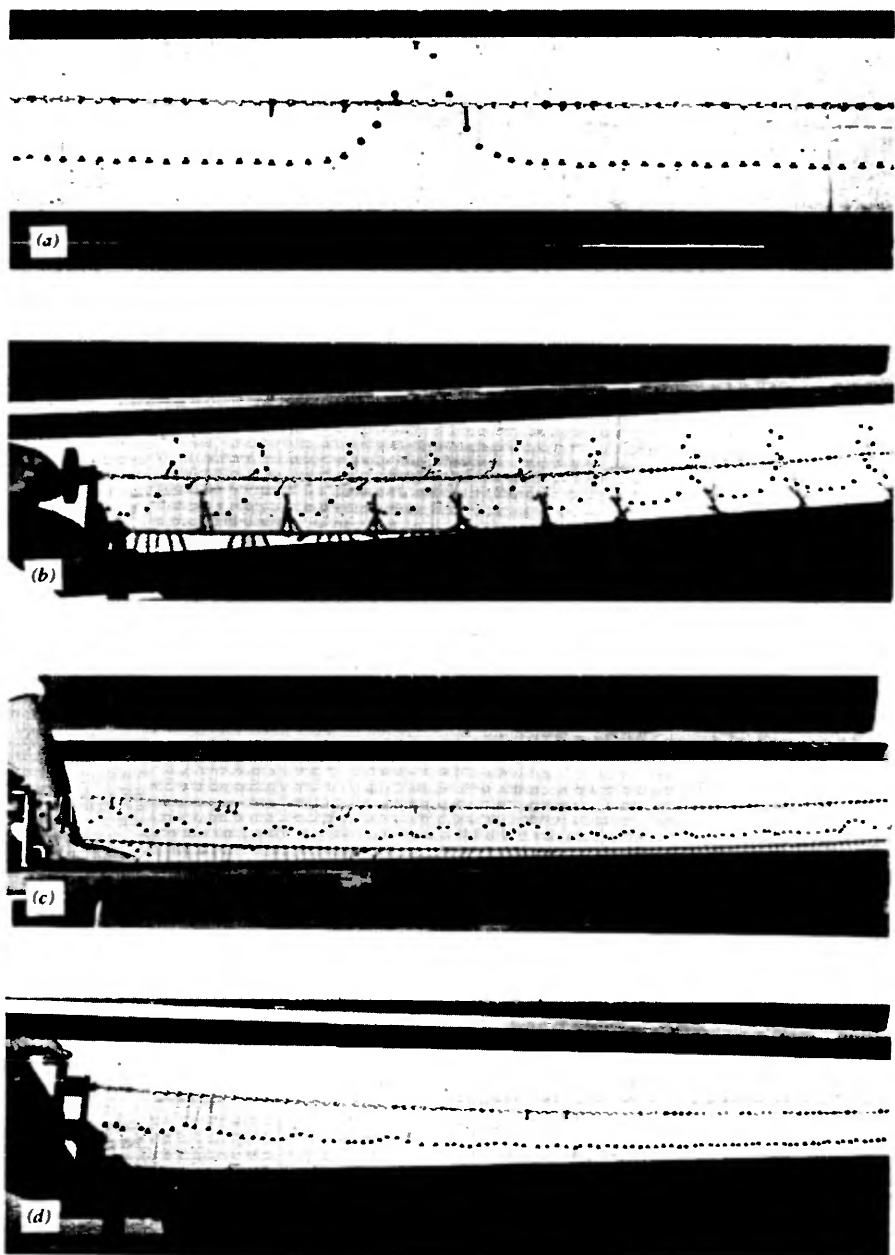


Figure 10.4 Photographs of the mechanical analog. (a) Single soliton solution; (b) evenly spaced array of solitons; (c) large amplitude waves; (d) small amplitude waves (Courtesy of A. C. Scott.)

When $-1 < E < +1$ and $|u| > 1$ the solution becomes

$$\phi = 2 \sin^{-1} \left[k \operatorname{sn} \left(\frac{\xi}{\sqrt{u^2 - 1}} \mid k \right) \right]$$

where sn is an elliptic function of modulus $k > 1$. This represents large amplitude periodic waves (see Fig. 10.4c). In the limit $E \rightarrow +1$, and $\phi \rightarrow 0$ reduces to the case of small amplitude waves reported in Fig. 10.4d. These correspond to the “plasma waves.”

10.1.2 Energy Functions. Let us observe that if the Lagrangian density function

$$\mathcal{L} = \frac{1}{2} [\phi_x^2 - \phi_t^2] + 1 - \cos \phi \quad (10.1.5)$$

is substituted into the Lagrange-Euler equation

$$\frac{\partial}{\partial x} \left(\frac{\partial \mathcal{L}}{\partial \phi_x} \right) + \frac{\partial}{\partial t} \left(\frac{\partial \mathcal{L}}{\partial \phi_t} \right) - \frac{\partial \mathcal{L}}{\partial \phi} = 0 \quad (10.1.6)$$

the sine-Gordon equation is obtained. Therefore any solution of this equation satisfies Hamilton's principle, that is, the integral

$$\int \mathcal{L} dx dt$$

is an extremum. We note that the negative of (10.1.5) also satisfies this condition; however, with the chosen sign as in (10.1.6) the stable solutions give a minimum whereas unstable ones give a maximum.

By introducing the corresponding momentum density

$$\Pi \equiv \frac{\partial \mathcal{L}}{\partial \phi_t} = -\phi_t$$

we obtain the Hamilton density \mathcal{H} through the Legendre transformation

$$\mathcal{H} \equiv \mathcal{L} - \Pi \phi_t$$

that is, the total energy is

$$H = \int_{-\infty}^{+\infty} \mathcal{H} dx = \int_{-\infty}^{+\infty} \left\{ \frac{1}{2} [(\phi_x)^2 + (\phi_t)^2] + 1 - \cos \phi \right\} dx$$

We recognize in the three terms of the Hamiltonian the various contributions, in normalized units, to the junction energy; the electric energy stored in the

insulating barrier region, the magnetic energy stored within the London penetration depth, and the energy associated with the superconducting phase difference across the junction barrier.

In analogy with the quantity Π introduced above we can define a rotation density ρ

$$\rho \equiv \frac{\partial \mathcal{L}}{\partial \dot{\phi}_x} = \phi_x$$

and we can write

$$\frac{\partial \mathcal{K}}{\partial t} + \frac{\partial \mathcal{P}}{\partial x} = 0 \quad (10.1.7)$$

where

$$\mathcal{P} = -\rho \dot{\phi}_t$$

Equation 10.1.7 can be interpreted as follows. \mathcal{K} is the density of a conserved quantity per unit length in the x direction and \mathcal{P} is the power flow of that quantity past a point per unit of time. We observe that an explicit dependence of the Lagrangian on time would lead to an additional term in (10.1.7) and consequently the conservation law for energy would no longer hold. The Lagrangian density (10.1.5) and consequently the sine-Gordon equation are invariant under a Lorentz transformation of the independent variables. Then if $\phi(x, t)$ is a solution of (10.1.2), so is $\phi(x', t')$ where

$$x \rightarrow x' = \frac{x - u_r t}{\sqrt{1 - u_r^2}} \quad \text{and} \quad t \rightarrow t' = \frac{t - u_r x}{\sqrt{1 - u_r^2}}$$

Here u_r represents the relative velocity of the two reference frames (x, t) and (x', t') .

Presently there is a wide variety of mathematical tools for constructing and analyzing soliton solutions of the sine-Gordon equation. These include Whitham's averaged Lagrangian method for computing slow variations of periodic wave parameters (Whitham 1974) and the Bäcklund transformation (Miura 1976) which can be used to create a soliton solution from the vacuum state, thus introducing a constant of the motion that can be interpreted as the velocity of the soliton (Barone et al. 1971). Moreover, the "machinery" of iteration of Bäcklund transformations allows the creation of a hierarchy of N -soliton solutions of the sine-Gordon equation and, correspondingly, additional constants of the motion (see also Lamb 1971). Solutions containing an arbitrary number of solitons have also been discussed by Hirota (1972). This analysis has been recently extended by Currie (1977), providing a further powerful technique.[†]

[†]Besides the various papers cited throughout the chapter, the reader is referred to the account on soliton theory given by Zakharov and Manakov (1979).

Exact solutions of (10.1.2) with given initial conditions can be found by using the “inverse scattering transform method” (Ablowitz et al. 1974; Calogero 1977) which can be viewed as a generalization of the Fourier transform method. More precisely, this general procedure describes a nonlinear wave in a combination of soliton and radiative components, the former being a nonlinear version of the corresponding Fourier modes in a linear wave. A discussion of both the inverse scattering and the averaged Lagrangian methods in the context of flux propagation in Josephson junctions was given by Scott, Chu, and Reible (1976). Finally, we recall the exact solution for a finite long Josephson junction by Costabile et al. (1978), the perturbation methods proposed by McLaughlin and Scott (1978), and the numerical results (for junctions with loss and bias) reported by Nakajima et al. (1974), Christiansen and Olsen (1980), and Erné and Parmentier (1980). In the remainder of this chapter we do not claim to be exhaustive on the flux flow dynamics in a Josephson junction; we merely introduce some of the possibilities emerging from the application of these powerful research tools.

10.2 Nonlinear Standing Waves on a Rectangular Junction

We have just considered solutions of the sine-Gordon equation corresponding to traveling waves of fixed shape propagating with constant velocity. The translational invariant nature of such solutions ($\phi = \phi(x - ut)$) requires for their existence, a junction of infinite length. Although the investigation of these solutions provides a deep physical insight into the nonlinear wave propagation in Josephson structures it is obvious that a more realistic approach implies a study of solutions that account for finite boundary conditions.

For waves in a one dimensional junction of finite length L , neglecting dissipation, the problem to be solved is described by (10.1.2):

$$\phi_{xx} - \phi_{tt} - \sin \phi = 0$$

with the boundary conditions

$$\phi_x(0, t) = \phi_x(L, t) = 0 \quad (10.2.1)$$

which represent open circuit ends since ϕ_x is proportional to the current. We follow here the recent approach to the problem given by Costabile et al. (1978). As shown by Lamb (1971), (10.1.2) admits solutions of the form

$$\phi(x, t) = 4 \tan^{-1}[f(x)g(t)]$$

where $f(x)$ and $g(t)$ are in general Jacobian elliptic functions defined by the relations

$$(f')^2 = af^4 + (1-b)f^2 - c$$

$$(g')^2 = cg^4 + bg^2 - a$$

with a , b , and c arbitrary constants. Such types of solutions have been qualitatively described in great detail by Fulton (1976).

In the framework of the approach outlined above the analytical solution corresponding to the plasma wave oscillation is given by

$$\phi = 4 \tan^{-1} [A \operatorname{cn}(\beta x|k_f) \operatorname{cn}(\Omega t|k_g)]$$

with

$$k_f^2 = \frac{A^2 [\beta^2(1+A^2)+1]}{\beta^2(1+A^2)^2}; \quad k_g^2 = \frac{A^2 [\Omega^2(1+A^2)-1]}{\Omega^2(1+A^2)^2}$$

where A , β , and Ω are connected by the nonlinear dispersion relation

$$\Omega^2 - \beta^2 = \frac{1-A^2}{1+A^2} \quad (10.2.2)$$

The spatial periodicity determined by (10.2.1) is given by

$$\beta = \frac{2n}{L} K(k_f)$$

$K(k_f)$ is the complete elliptic integral of the first kind; $n=1, 2, \dots$ is the number of nodes in the standing wave. The time periodicity is related to the normalized frequency

$$\omega(k_g) = \frac{\pi\Omega}{2K(k_g)}$$

For the case $n=0$, which in terms of the mechanical analog corresponds to a situation of all pendula oscillating in phase, the solution is

$$\phi = 4 \tan^{-1} [A \operatorname{sn}(\Omega t|k)]$$

where $k=A^2$ and $\Omega=(1+A^2)^{-1}$. We see that for small deviations of ϕ about zero, that is, $A \rightarrow 0$, the dispersion relation (10.2.2) reduces (in unnormalized units) to the relation

$$\left(\frac{\omega}{\omega_J}\right)^2 - (\lambda_J k)^2 = 1$$

introduced in Section 1.7 and sketched in Fig. 1.12.

Another analytical solution of (10.1.2) is a bound state oscillation of a vortex-antivortex pair (Fulton 1976). This is the so-called breather oscillation, which can be formed either by a fluxon-antifluxon pair in the central region of

the junction or by a fluxon bound to a virtual fluxon at the junction edges. Such breather oscillations are described by

$$\phi = 4 \tan^{-1} \{ A \operatorname{dn} [\beta(x - x_0) | k_f] \operatorname{sn} (\Omega t | k_g) \}$$

where

$$k_f^2 = 1 - \left[\frac{1 - \beta^2(1 + A^2)/A^2}{\beta^2(1 + A^2)^2} \right]; \quad k_g^2 = \frac{A^2 [1 - \Omega^2(1 + A^2)]}{\Omega^2(1 + A^2)^2}$$

The nonlinear dispersion equation in this case is

$$\beta = \Omega A$$

and the periodicity condition is

$$\beta_n = \frac{n}{L} (k_f)$$

with two possible values for x_0 :

$$\beta x_0 = K(k_f), \quad n \text{ even for breathers at the center of the junction}$$

$$x_0 = 0 \quad \text{for fluxon-virtual antifluxon at the junction ends}$$

It is worth observing that breather oscillations can exist only above a minimum value of amplitude A whereas plasma oscillations can occur for arbitrarily small amplitudes (Costabile et al. 1978).

A different type of oscillation is that corresponding to a single kink or fluxon traveling along the junction. After reflection at the junction end the kink moves backward and is representative of an “antifluxon.” This solution is given by

$$\phi = 4 \tan^{-1} [A \operatorname{dn}(\beta x | k_f) \operatorname{tn}(\Omega t | k_g)] \quad (10.2.3)$$

where

$$k_f = \left[\frac{(\beta^2/A^2)(A^2 - 1) - 1}{\beta^2(A^2 - 1)} \right]; \quad k_g = 1 - \left[\frac{A^2[\Omega(A^2 - 1) - 1]}{\Omega^2(A^2 - 1)} \right]$$

with $\beta = \Omega A$ and $\beta_n = (n/L)K(k_f)$. The fluxon oscillations are of particular interest because ϕ increases monotonically with time at any value of x . Thus d.c. current bias can provide a source of power to the oscillation that will sustain it in the presence of dissipation effects. The solution (10.2.3) also describes symmetric multifluxon propagation.

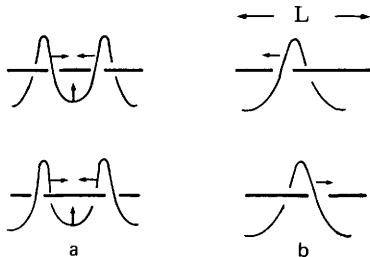


Figure 10.5 (a) Breather oscillation; (b) fluxon oscillation.

The three types of analytical solutions discussed so far—plasma, breather, and fluxon oscillation—are shown in Figs. 10.4*d* and 10.5*a, b* respectively.

10.3 Effects of Losses and Bias

Up to now we used the S.G.E. to describe the flux dynamics in the Josephson structure. However, in dealing with real junctions one must take into account losses, bias, and junction irregularities which influence the motion of real fluxons. In this section we discuss steady state propagation when bias and losses are included in the model. In Section 10.4 an important physical consequence (namely the occurrence of zero field steps) of these effects is considered and in Sections 10.5 and 10.6 a general perturbative approach is discussed together with other types of structural perturbations.

In (10.1.1) dissipation was accounted for by a first derivative term which corresponds to a linear resistive loss. So far analytic solutions of this equation have not been found; on the other hand Costabile and Parmentier (1975) have demonstrated that if the loss term is assumed to be quadratic, rather than linear, it is possible to find analytical solutions for steady propagation. The equation considered was in the form

$$\phi_{xx} - \phi_{tt} - \Gamma|\phi_t|\phi_t + \gamma = \sin \phi \quad (10.3.1)$$

where $\Gamma|\phi_t|\phi_t$ accounts for dissipation and γ represents the normalized current bias that supplies energy to sustain the fluxon oscillation. The solution representing steady propagation of fluxon array is (Parmentier and Costabile 1978):

$$\phi = \sin^{-1} \gamma_0 + 2 \sin^{-1} \left\{ \operatorname{cn} \left[\frac{1}{k} \left(\frac{\gamma_0}{2\Gamma u^2} \right)^{1/2} (\xi - \xi_0) \right] \right\}$$

where cn is a Jacobian elliptic function with modulus k given by

$$k = \left(\frac{2\gamma_0}{\gamma + \gamma_0} \right)^{1/2}$$

and

$$\gamma_0 \equiv \frac{2\Gamma u^2}{[(1-u^2)^2 + \Gamma^2 u^4]^{1/2}}$$

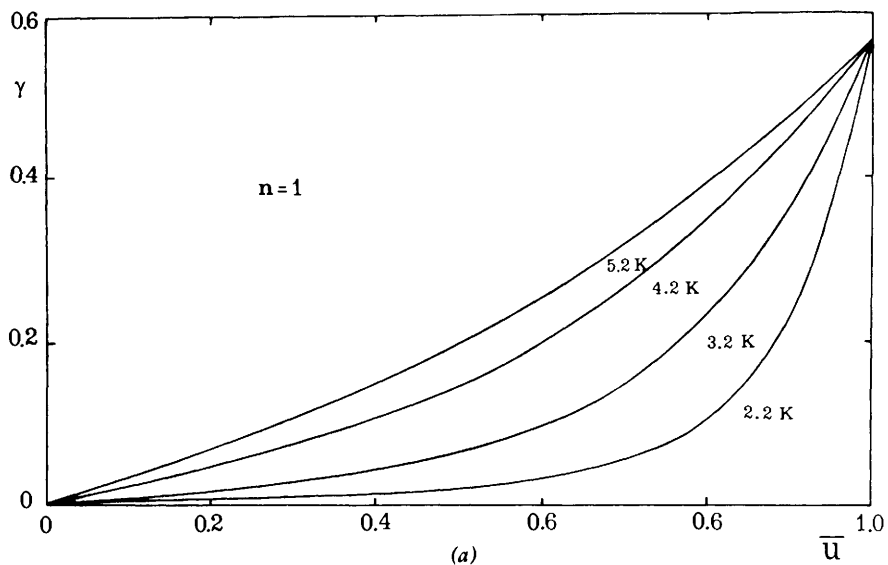
is an arbitrary constant of integration. In this solution $0 \leq \sin^{-1} \gamma \leq \pi/2$, but the second term is not limited to its principal value. In the limit $k \rightarrow 1$ this solution becomes that of a single fluxon propagating in an infinite line.

Dissipative effects and bias can be introduced in a quite general way by considering the equation

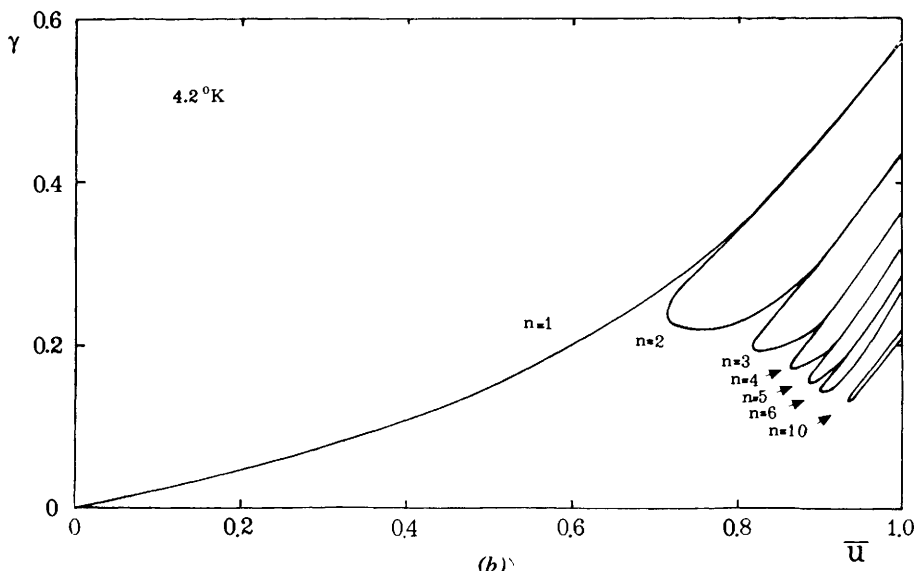
$$\beta \phi_{xx,t} + \phi_{xx} - \phi_{tt} - \alpha \phi_t - \gamma = \sin \phi \quad (10.3.2)$$

where the terms $\beta \phi_{xx,t}$ and $\alpha \phi_t$ represent normal electron current flow along and across the junction respectively (longitudinal and shunt losses). The quantity γ is the normalized current bias as before. With the restriction of considering traveling wave solutions $\phi = \phi(x - ut)$ this equation reduces to an ordinary nonlinear third order differential equation which can be integrated numerically. This has been carried out by Johnson (1968) using a hybrid (analog-digital) computer. The results suggest that traveling wave solutions exist for (10.3.2) which correspond to bundles of flux quanta propagating along the junction. These in turn give rise to voltage pulses. From this computer analysis a large number of d.s.s. solutions were found, all containing an integral number of flux quanta, the actual number depending on the initial conditions. The first order pulse solution (i.e., corresponding to one fluxon) can propagate at any velocity from 0 to $\bar{c} = (LC)^{-1/2}$ (L and C being the series inductance and shunt capacitance, both per unit length). This velocity depends on the bias (see Fig. 10.6a) and on the losses. The latter tend to reduce the velocity. Higher order pulses (i.e., containing more fluxons) propagate only at velocities near $(LC)^{-1/2}$. For pulses with more than one flux quantum the velocity is double valued in the current bias. The solution loci for various pulses in the velocity-bias plane for a lead-lead junction at 4.2 K are shown in Fig. 10.6b. Figures 10.7a, b show the change in pulse waveform as the velocity and the bias are varied along the solution locus. We observe that in both figures (actually this is true for all n) a fluxon "begins to split" from the trailing edge. Whether or not these pulses exist in the actual physical junction depends on their stability. In the lossless case (S.G.E.) the stability of the first order solution has been discussed by Scott (1969). For $n \neq 1$ the problem of the stability requires further study.

A sophisticated mechanical analogue of (10.3.2) and a detailed numerical simulation have been reported more recently by Yamashita and Onodera (1974), Nakajima et al. (1974), Nakajima, Sawada, and Onodera (1975), Cirillo, Parmentier and Savo (1981). This work indicates that flux quanta tend to attract each other. This should suggest that states on the high velocity branch



(a)



(b)

Figure 10.6 (a) Analog computer results for a $n=1$ pulse solution at various temperatures. Normalized current bias γ vs. normalized velocity $\bar{u} = u\sqrt{LC}$. (b) Loci of $n=1, 2, \dots, 10$ pulse solutions at 4.2 K . (After Johnson 1968.)

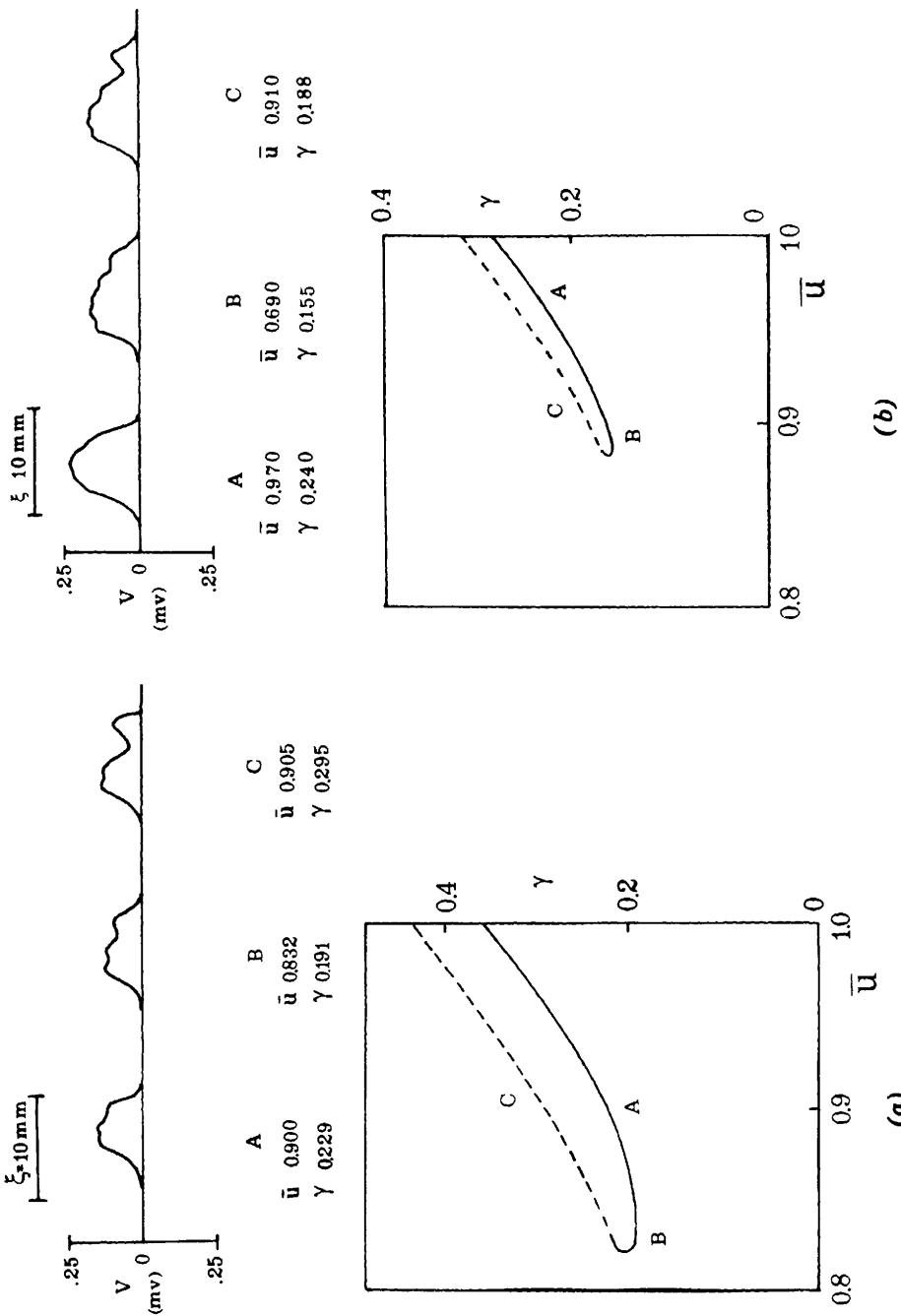
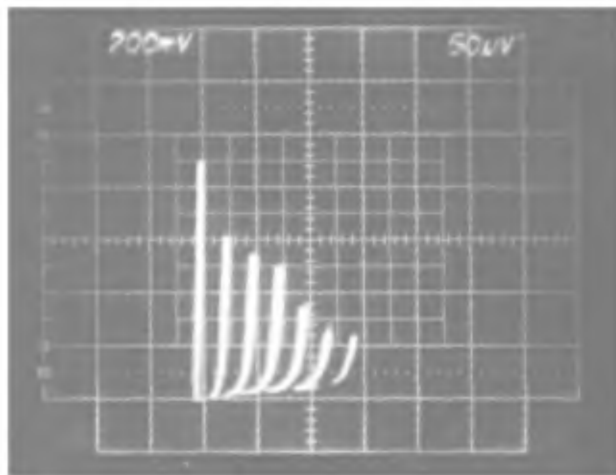


Figure 10.7 Change in $n=3$ (a) and $n=5$ (b) pulse waveforms as the velocity and bias are varied along the solution locus. (After Johnson 1968.)

in Fig. 10.7a, b (full line) are stable while those on the low velocity branch (dashed line) are unstable.

10.4 Zero Field Steps

As mentioned at the end of the preceding chapter, current singularities in the $V - I$ characteristics have been observed in the absence of external applied magnetic field. Such singularities appear in junctions of dimensions larger than λ_J . These were first observed by Chen, Finnegan, and Langenberg (1971) and



(a)

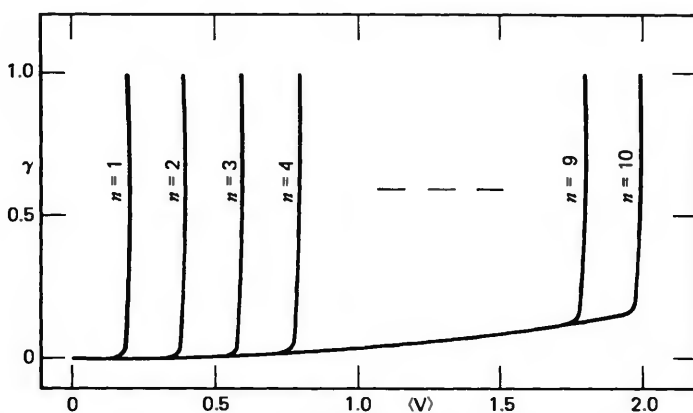


Figure 10.8 Zero field steps in voltage-current characteristics of Josephson junctions. (a) Experimental $V - I$ curve for an $\text{Nb}-\text{Nb}_x\text{O}_y-\text{Pb}$ junction of dimensions $L/\lambda_J \approx 13$. (Courtesy of R. Vaglio.) (b) Voltage-current characteristics obtained from (10.4.1). (After Parmentier 1978).

Chen and Langenberg (1972). Figure 10.8a shows experimental result obtained at the Institute of Physics of the University of Salerno for a $\text{Nb}-\text{Nb}_x\text{O}_y-\text{Pb}$ junction. As we anticipated in Chapter 9, this effect can be accounted for in terms of fluxon oscillation inside the junction (Fulton and Dynes 1973).

To calculate these singularities Costabile et al. use (10.3.1). They assume that Γ and γ are sufficiently small that $\phi(x, t)$ is still adequately described by (10.2.3), which holds strictly only in the absence of bias and dissipation.

The balance between the total power input $\gamma\phi_t$ and the power dissipation $\Gamma|\phi_t|\dot{\phi}_t^2$ gives

$$\gamma = 2A^2\Omega^2\Gamma \left[\frac{6E(k_f)}{K(k_f)} + \frac{1+(k_g)^2}{A^2} \right]$$

where $K(x)$ and $E(x)$ are the complete elliptic integrals of the first and second kind respectively. The voltage is given by

$$\bar{V} = \frac{1}{2\pi} \bar{\phi}_t = \frac{\Omega}{K(k_g)}.$$

The bar indicates the average over both space and time. The resulting current voltage characteristics, that is, the dependence of γ on V , is reported in Fig. 10.8b (Parmentier, 1978). Let us observe that n , used to indicate the order of the corresponding Fiske step, in this case represents the number of fluxons engaged in the oscillation. The curve $\gamma - u$ discussed in the preceding section is essentially the $V - I$ curve for the zero field step.

Chen and Langenberg in the reference quoted above have also measured X -band power output under various bias conditions. Under these experimental conditions a fine structure with hysteresis in the $V - I$ characteristics and significant changes in the level of power output are observed. A pure fluxon oscillation, on the other hand, has a theoretical power output that increases in a modest and monotonic way with the bias current. Finally we recall the interesting discussion by Mkrtchyan and Shmidt (1979) on the radiation produced by a single fluxon moving on a long inhomogeneous junction.

10.5 Perturbative Analysis of Fluxon Dynamics

The fluxon oscillation discussed in the preceding section can be viewed as a nonlinear standing wave arising from the interaction of two equally spaced trains of fluxons traveling to the right and left. It is also of interest to consider the propagation of a single fluxon on an infinitely long Josephson transmission line. This can be described by the sine-Gordon equation with structural perturbations to account for bias energy input, dissipation, microshorts, and so on.

As discussed in Chapter 14, these lines have possible applications for information transmission (Fulton, Dynes, and Anderson 1973; Likharev 1976), storage (Gueret 1975), and processing (Nakajima, Onodera, and Ogawa 1976).

10.5.1 Single Fluxon Dynamics. The effects of structural perturbations on the dynamics of single fluxons have been considered in some detail by Fogel et al. (1976, 1977). The perturbation scheme we describe here has been developed in the work by McLaughlin and Scott (1977, 1978) and can be readily generalized to the multifluxon case. It proceeds in two stages. In the first stage the fluxon speeds and phases are modulated in order to remove secularities (i.e., linear growth with time) from the first order perturbation. This requirement leads to a direct calculation of the acceleration or deceleration of the fluxons under the influence of the structural perturbation. In the second stage, the radiation caused by this acceleration or deceleration is calculated as a first order correction.

To undertake a perturbation analysis, it is convenient to describe the junction transmission line as a system that is first order in time:

$$\begin{pmatrix} \partial_t & 1 \\ -\partial_{xx} + \sin & \partial_t \end{pmatrix} \begin{pmatrix} \phi \\ \phi_t \end{pmatrix} = \begin{pmatrix} 0 \\ \epsilon f \end{pmatrix}.$$

Here ϵf is a general representation of a structural perturbation. If ϵ is small, we can expand the solution as a power series

$$\begin{pmatrix} \phi \\ \phi_t \end{pmatrix} = \begin{pmatrix} \phi_0 \\ \phi_{0,t} \end{pmatrix} + \epsilon \begin{pmatrix} \phi_1 \\ \phi_{1,t} \end{pmatrix} + \dots$$

whereupon ϕ_0 must satisfy the unperturbed sine-Gordon equation

$$\phi_{0,xx} - \phi_{0,tt} - \sin \phi_0 = 0 \quad (10.5.1)$$

and ϕ_1 must satisfy the *linear* equation

$$\begin{pmatrix} \partial_t & -1 \\ -\partial_{xx} + \cos \phi_0(x, t) & \partial_t \end{pmatrix} \begin{pmatrix} \phi_1 \\ \phi_{1,t} \end{pmatrix} = \begin{pmatrix} 0 \\ f \end{pmatrix}$$

or, in a more compact form,

$$L \bar{W} = \bar{F}$$

This linear equation can be solved using a Green's function $G(x, t|x', t')$ so that

$$\bar{W} \equiv \begin{pmatrix} \phi_1 \\ \phi_{1,t} \end{pmatrix} = \int_{-\infty}^{+\infty} \int_0^t G(x, t|x', t') F(x', t') dx' dt'$$

The rows of G , as functions of x' and t' , must lie in the null space $\mathcal{N}(L^+)$ of the operator

$$L^+ \equiv - \begin{pmatrix} \partial_{t'} & \partial_{x'x'} - \cos \phi_0(x', t') \\ 1 & \partial_{t'} \end{pmatrix}$$

That is, $L^+ G^T$ where G^T is the transpose of G . If the source $\bar{F}(x', t')$ is not orthogonal to $\mathcal{N}(L^+)$, \bar{W} will have (secular) components growing linearly with time. This is undesirable because it invalidates our original perturbation expansion in a time of order $1/\epsilon$. To eliminate these secular effects we can proceed as follows (Keener and McLaughlin 1977; McLaughlin and Scott 1977).

Assume ϕ_0 to represent a single fluxon:

$$\phi_0 = 4 \tan^{-1} \left[\exp \left(\frac{x - X}{\sqrt{1 - u^2(t)}} \right) \right] \quad (10.5.2)$$

where

$$X \equiv x_0(t) + \int_0^t u(t') dt'$$

Thus both the velocity of the fluxon, u , and its phase, x_0 , are allowed to be slowly varying (i.e., order ϵ) functions of time. Then additional terms appear in the first order source augmenting it to

$$\bar{F} \rightarrow \bar{\mathfrak{F}} = \begin{pmatrix} -\frac{1}{\epsilon} \frac{\partial \phi_0}{\partial u} \dot{u} - \frac{1}{\epsilon} \frac{\partial \phi_0}{\partial x_0} \dot{x}_0 \\ f - \frac{1}{\epsilon} \frac{\partial^2 \phi_0}{\partial u \partial t} \dot{u} - \frac{1}{\epsilon} \frac{\partial^2 \phi_0}{\partial x_0 \partial t} \dot{x}_0 \end{pmatrix}$$

Imposition of the abovementioned orthogonality condition

$$\bar{\mathfrak{F}} \perp \mathcal{N}(L^+)$$

then yields two ordinary differential equations for the slow variation of u and x_0 . Assuming structural perturbation of the form

$$\epsilon f = -\alpha \phi_t + \beta \phi_{xxt} - \gamma - \mu \delta(x) \sin \phi$$

which represents dissipation (α and β), bias current (γ), and a single microshort (μ) located at $x=0$, these equations are

$$\begin{aligned}\dot{u} &= \frac{1}{4}\pi\gamma(1-u^2)^{3/2} - \alpha u(1-u^2) - \frac{1}{3}\beta u \\ &\quad + \frac{1}{2}\mu(1-u^2)\operatorname{sech}^2\left(\frac{X}{(1-u^2)^{1/2}}\right)\tanh\left(\frac{X}{(1-u^2)^{1/2}}\right)\end{aligned}\quad (10.5.3a)$$

and

$$\dot{X} = u - \frac{1}{2}\mu u X \operatorname{sech}^2\left(\frac{X}{(1-u^2)^{1/2}}\right)\tanh\left(\frac{X}{(1-u^2)^{1/2}}\right). \quad (10.5.3b)$$

Such equations are obtained as follows. Let us start from (10.5.1) where ϕ_0 is given by (10.5.2). Assuming x_0 and u as parameters it is straightforward to obtain the vectors of the null space L^+ . These are given by

$$\begin{pmatrix} \psi_1^1 \\ -\psi_1^1 \end{pmatrix} \quad \text{and} \quad \begin{pmatrix} \psi_2^2 \\ -\psi_2^2 \end{pmatrix}$$

where

$$\psi^1 = \frac{\partial\phi_0}{\partial u} \quad \psi^2 = \frac{\partial\phi_0}{\partial x}$$

Equations 10.5.3 are obtained by imposing the orthogonality conditions.

Let us consider (10.5.3) by phase plane analysis in the (u, x) plane. Figure 10.9 describes a situation corresponding to the parameter values $\alpha=0.033$, $\beta=0$, and $\gamma=0.5$ (McLaughlin and Scott 1977). Different curves refer to different values of the bias current (γ). We see that in the case of small values of γ each trajectory in the phase plane encircles a given point (pinning point). From (10.5.3a) it follows for $u=\dot{u}=0$ that

$$\frac{\pi\gamma}{2\mu} + \operatorname{sech}^2 X \tanh X = 0 \quad (10.5.4)$$

Therefore coordinates of the steady state pinning point in the phase plane are $u=0$ and $X=X_0$ where X_0 is solution of the last equation. Physically this situation corresponds to a pinning of the flux at the microshort. For lower values of α (smaller dissipation) large amplitude oscillations around the pinning point can occur. The result of the calculations is a zero order (or adiabatic) acceleration or deceleration of the fluxon because of the structural

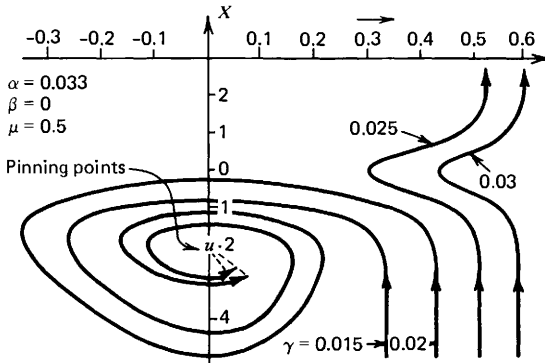


Figure 10.9 Trajectories in the (u, x) plane for a fluxon approaching a microshort of magnitude $\mu = 0.5$ with $\alpha = 0.033$ and $\beta = 0$ for various values of γ . Pinning occurs at $u = 0$ and X a solution of (10.5.4). (After McLaughlin and Scott 1977)

perturbation ϵf . McLaughlin and Scott (1978) have shown how radiation of a multifluxon interaction into the junction plasma modes can be calculated from the radiative part of the Green's function $G_R(x, t|x't')$. Thus

$$\begin{pmatrix} \phi_1 \\ \phi_{1,t} \end{pmatrix} = \int_0^t \int_{-\infty}^{+\infty} G_R(x, t|x', t') \mathcal{F}(x', t') dx' dt'$$

For ϕ_0 a single fluxon (as in 10.5.2)

$$G_R(x, t|x', t') = \frac{1}{4\pi j} \int_{-\infty}^{+\infty} \begin{bmatrix} g_{11} & g_{12} \\ g_{21} & g_{22} \end{bmatrix} \frac{\exp[-j[k(\lambda)(x-x') + \omega(\lambda)(t-t')]] d\lambda}{\lambda(\xi - \lambda^2)^2}$$

$$g_{11} \equiv (\xi^2 + \lambda^2 + 2\xi\lambda \tanh \tilde{x}) [j\omega(\xi^2 + \lambda^2$$

$$- 2\xi\lambda \tanh \tilde{x}') - 2j\xi\lambda\omega(\xi) \operatorname{sech}^2 \tilde{x}']$$

$$g_{12} \equiv (\xi^2 + \lambda^2 + 2\xi\lambda \tanh \tilde{x})(\xi^2 + \lambda^2 - 2\xi\lambda \tanh \tilde{x}')$$

$$g_{21} \equiv [-j\omega(\xi^2 + \lambda^2 + 2\xi\lambda \tanh \tilde{x}) + 2j\xi\lambda\omega(\xi) \operatorname{sech}^2 \tilde{x}]$$

$$\times [j\omega(\xi^2 + \lambda^2 - 2\xi\lambda \tanh \tilde{x}') - 2j\xi\lambda\omega(\xi) \operatorname{sech}^2 \tilde{x}']$$

$$g_{22} \equiv [-j\omega(\xi^2 + \lambda^2 + 2\xi\lambda \tanh \tilde{x}) + 2j\xi\lambda\omega(\xi) \operatorname{sech}^2 \tilde{x}]$$

$$\times (\xi^2 + \lambda^2 - 2\xi\lambda \tanh \tilde{x}')$$

In these formulas, $\omega(\xi) = \frac{2\xi+1}{8\xi}$ and $u = (16\xi^2 + 1)/(16\xi^2 - 1)$. Also

$$\bar{x}' = \frac{x' - X(t')}{\sqrt{1 - u^2(t')}}$$

and \bar{x} is given by the same equation with the primes dropped.

10.5.2 Fluxon-Antifluxon Annihilation. Another important aspect of the flux dynamics is the study of the interactions between fluxons and antifluxons. They can occur either as nondestructive collisions or as fluxon-antifluxon annihilation. Besides the fundamental interest concerning the physics of the junction these events have suggested the possibility of realizing logic functions (Nakajima, Onodera, and Ogawa 1976) (see Chapter 14).

Let us suppose that $\epsilon f = -\alpha\phi_t - \gamma$ and that a fluxon and an antifluxon are each initially moving at the velocity

$$u_\infty = \frac{1}{\sqrt{1 + (4\alpha/\pi\gamma)^2}}$$

where $u_\infty = \lim_{t \rightarrow \infty} u(t)$ is the velocity at which the power loss from dissipation is just equal to the power input from the bias current. A zero order description of the event is

$$\phi = 4 \tan^{-1} \left\{ \frac{\sinh \frac{X}{\sqrt{1 - u^2(t)}}}{u(t) \cosh \left[\frac{x - x(t)}{\sqrt{1 - u^2(t)}} \right]} \right\}$$

where

$$X \equiv x_0(t) + \int_0^t u(t') dt'.$$

Proceeding with a perturbation calculation, just as in the preceding section, McLaughlin and Scott (1977) show that $x_1 = 0$ (preserving symmetry), $\dot{x}_0 = O(\alpha)$ and

$$\dot{u} = F(\gamma, \alpha, \mu, T) \quad (10.5.5)$$

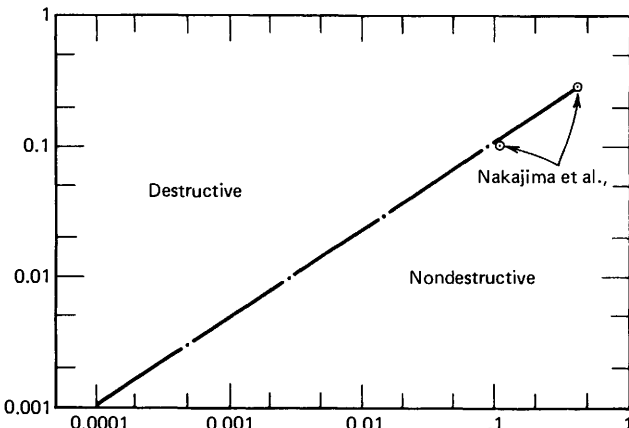


Figure 10.10 Values of bias current γ and dissipation α for destructive and nondestructive fluxon-antifluxon collision. (After McLaughlin and Scott 1977.)

where

$$F = \frac{\pi\gamma}{4} \frac{(1-u^2)^{3/2} \cosh T}{\sqrt{\sinh^2 T + u^2}} - \frac{\alpha u^3 (1-u^2) \cos^2 T}{\sinh^2 T + u^2}$$

$$\times \left(\frac{1}{u^2} - \frac{\ln \left| (1/w) \left[(\sinh^2 T + u^2)^{1/2} - \sinh T \right] \right|}{\sinh T \sqrt{\sinh^2 T + u^2}} \right)$$

with $T \equiv X[1-u^2(t)]^{-1/2}$. Since $T = u/\sqrt{1-u^2}$ to zero order in α , the last equation can be directly integrated with respect to T . A nondestructive collision between fluxon and antifluxon introduces some delay time. Indeed, the velocity during the interaction decreases to a minimum value after which it increases again so that the fluxon and the antifluxon emerge with the initial velocity u_∞ . In a destructive collision the velocity falls to zero and the fluxon-antifluxon become a "breather" (bound state). This in turn decays and finally radiates emitting photons of energy $\hbar\omega_J$.

By numerical integration (10.5.1) readily yields the threshold locus between the two types of collisions: the $\alpha-\gamma$ plane. This is shown in Fig. 10.10 together with the data obtained by Nakajima et al. (1974) integrating the full partial differential equation.

10.6 Effects of Flux Flow on D.C. Voltage-Current Characteristics

The voltage-current characteristics of a large (0.6×1.7 mm) crossed strip Josephson junction displaying a peculiar branch starting from the top of the maximum zero voltage current is reported in Fig. 10.11. This is the so-called

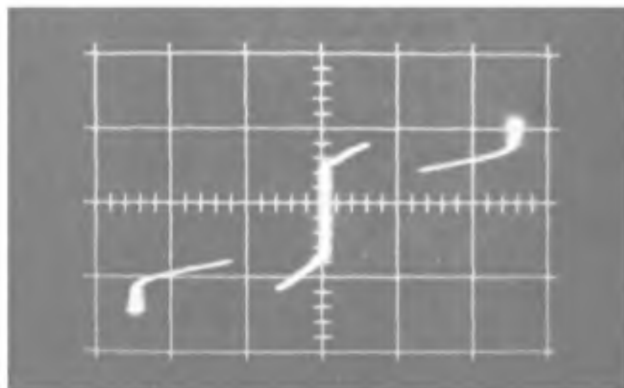


Figure 10.11 Typical-voltage current characteristics of a $\text{Pb}-\text{Pb}_x\text{O}_y-\text{Pb}$ Josephson junction exhibiting the displaced linear slope effect. Horizontal 1 mV/div; vertical 500 mA/div. (After Barone 1971.)

displaced linear slope (D.L.S.) effect (Scott and Johnson 1969; Barone and Johnson 1969; Barone 1971) which can be related to flux motion phenomena. This slope is rather independent of the temperature as long as $T < T_c$ whereas at higher temperatures it becomes markedly rounded (Barone 1971). The D.L.S. effect has been observed in a variety of junction electrode materials (both symmetrical and asymmetrical junctions) and for both "in line" and "cross" type geometry. This effect has been subsequently investigated in a number of interesting papers (e.g., Yoshida and Irie 1975, 1977; Yoshida, Irie, and Hamasaki 1977, 1978; Irie, Hamasaki, and Yoshida, 1978).

Scott and Johnson (1969) suggested an explanation based on moving fluxons interacting with longitudinal current (i.e., flowing in the direction of fluxon motion) rather than with transverse current as in the fluxon oscillations discussed in Section 10.2. The scheme is more easily understood by considering the one dimensional in-line overlap geometry (indicated in Fig. 10.1c). The current entering one end forces fluxons toward the center while the current entering the other end forces antifluxons toward the center.

The qualitative effect is readily observed on a mechanical model of the long Josephson junction shown in Fig. 10.12a. If the crank is turned very slowly (i.e., small voltage), widely spaced fluxons and antifluxons annihilate each other to form breathers near the center of the junction. As the crank is turned faster, distinct flow regions develop near the ends of the junction. This situation has recently been analyzed in some detail by Scott (1977). In the flux flow regions the longitudinal current i is related to the transverse voltage v by the characteristic impedance Z of the junction cavity. Since current flows into both ends, the volt-ampere characteristic becomes

$$i = i_1 + 2 \frac{v}{Z}$$

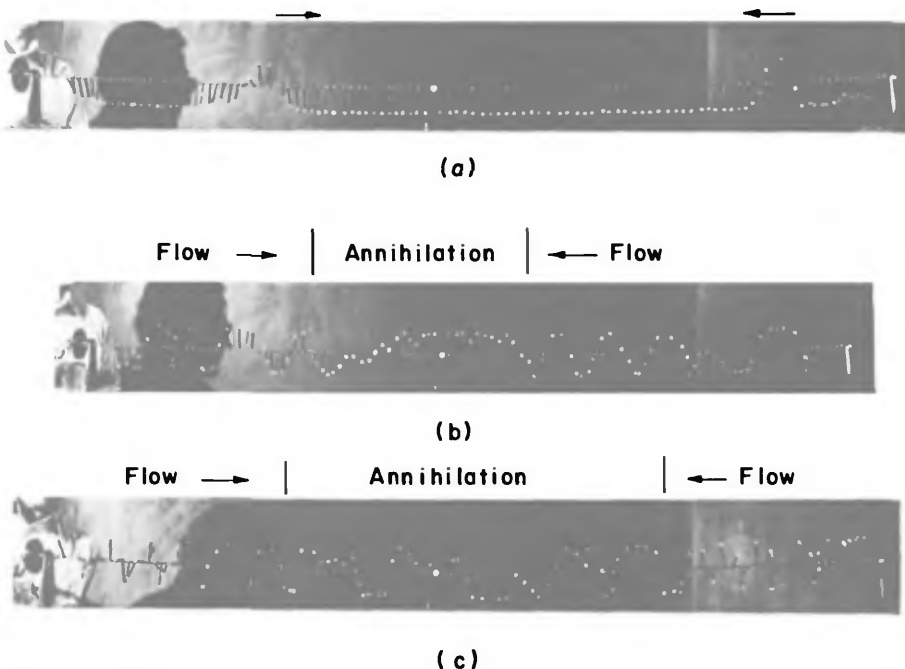


Figure 10.12 Flux flow and fluxon annihilation domain shown on a mechanical analog (Courtesy of A. C. Scott.)

where i_1 is the maximum value of current attaining to the zero voltage (i.e., no flux motion). The factor 2 accounts for current flow into both ends of the long junction.

Near the center of the junction, as modeled in Fig. 10.12, an annihilation region is observed. This region is characterized by a rather random state of activity because breathers (i.e., bound fluxon-antifluxon pairs) are continually being formed through mutual annihilation of fluxons (coming from the left) by antifluxons (coming from the right).

In general we expect the propagation of flux to be governed by a dissipative sine-Gordon equation $\phi_{xx} - \phi_{tt} - \alpha\phi_t = \sin\phi + \gamma$. In the discussion by Scott and Johnson and by Barone (1971) it is assumed that $\alpha \ll 1$ so that dissipative effects are not taken into account although they play a central role in the flux motion. The opposite limit $\alpha \gg 1$ is that of equation

$$\phi_{xx} - \alpha\phi_t = \sin\phi + \gamma$$

which describes well flux flow in metal barrier junctions. In this case, in fact, the first order time derivative term which accounts for transverse losses (normal electrons across the junction) dominates over the second order time derivative term which is related to the electric energy storage in the junction.

This situation has been considered in detail in the paper by Waldram, Pippard, and Clarke (1970).

Finally we observe that investigations of light sensitive junctions (such as those considered in Chapter 6) could supply a further insight into the flux dynamics in a Josephson junction. In fact, the possibility of adjusting by light the junction barrier height allows investigations on propagation structures with modifiable parameters and a more controllable comparison between theory and experiments.

10.7 Two Dimensional Junctions

In concluding this chapter it is worth commenting on the flux dynamics in a Josephson “surface” described by the two dimensional S.G.E.:

$$\frac{\partial^2 \phi}{\partial x^2} + \frac{\partial^2 \phi}{\partial y^2} - \frac{\partial^2 \phi}{\partial t^2} = \sin \phi \quad (10.7.1)$$

Such an equation is, as (10.1.2), invariant under the Lorentz transformation:

$$\begin{aligned} x \rightarrow x' &= \frac{x - ut}{\sqrt{1-u^2}}; & y \rightarrow y' &= y \\ t \rightarrow t' &= \frac{t - ux}{\sqrt{1-u^2}}; & \phi \rightarrow \phi' &= \phi \end{aligned} \quad (10.7.2)$$

It is of interest to see whether soliton type of solutions similar to those previously discussed exist for (10.7.1). To this purpose we can look for time independent solutions; steady motion in fact can always be introduced by the transformation (10.7.2). Furthermore, let us consider solutions having circular symmetry (i.e., flux lines closed on themselves). Thus (10.7.1) reduces to

$$\frac{d^2 \phi}{dr^2} + \frac{1}{r} \frac{d\phi}{dr} = \sin \phi \quad (10.7.3a)$$

It is easy to verify that for large values of r this equation has the asymptotic solution

$$\phi \sim \frac{1}{\sqrt{r}} e^{-r}$$

Making the change of variable $\rho \rightarrow 1/r$ (10.7.3) becomes

$$\frac{d^2 \phi}{d\rho^2} + \frac{1}{\rho} \frac{d\phi}{d\rho} = \frac{\sin \phi}{\rho^4} \quad (10.7.3b)$$

with the corresponding asymptotic solution (for $\rho \rightarrow 0$)

$$\phi \sim K\sqrt{\rho} e^{-1/\rho} \quad (10.7.4a)$$

From this we can calculate numerically on a digital computer $\phi = \phi(\rho)$ the various values of the arbitrary constant K . Such curves are reported in Fig. 10.13 for six values of K . The values of ρ ranges within the interval 0.1–10. For larger values of K the second member of (10.7.3b) becomes vanishingly small so that the equation reduces to

$$\frac{d^2\phi}{d\rho^2} + \frac{1}{\rho} \frac{d\phi}{d\rho} \sim 0$$

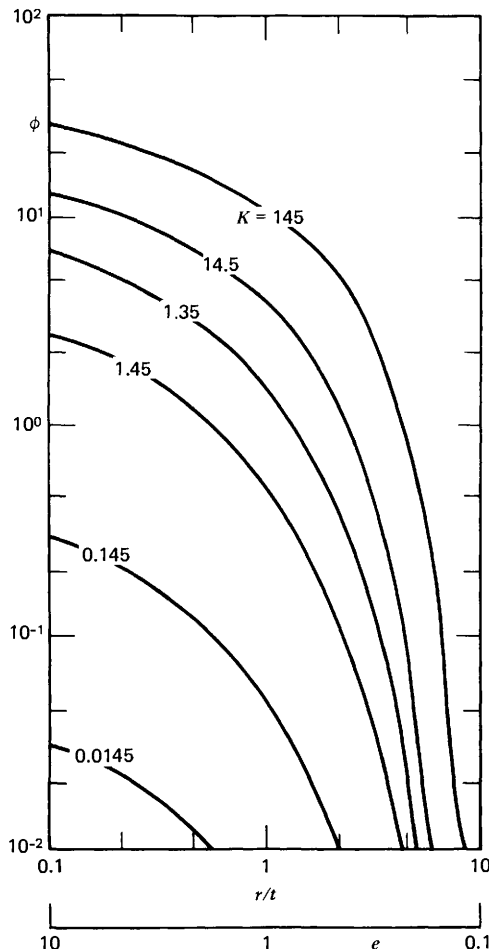


Figure 10.13 Solutions of (10.7.3b) for selected values of K in (10.7.4). (After Barone et al. 1971.)

with a solution such as

$$\phi \sim \alpha \log \rho + \beta \quad (10.7.4b)$$

The computer integration “curves” range within the two asymptotic solutions. As discussed in the reference quoted above it can be seen that solutions of (10.7.3) are found only when the boundary condition is supplied by the current through a short at the origin.

Solutions of the S.G.E. in two spatial dimensions have been investigated by various authors. Among these we recall, Ben-Abraham (1976), Zagrodzinski (1976, 1979) Leibbrandt (1977), Grella and Marinaro (1978), Grella and Parmentier (1979).

CHAPTER 11

High Frequency Properties and Applications of the Josephson Effect

11.1 Simple Voltage Source Model

In chapter 1 we briefly considered the effect of an external microwave radiation on a Josephson junction. We saw that current “steps” appear on the V - I characteristic, at voltages, related to the frequency of the applied radiation ω_r by the expression

$$V_n = \frac{\hbar}{2e} \omega_r n \quad (11.1.1)$$

For a tunneling junction it is easy to understand how this contribution to the d.c. current arises (Josephson 1962a,b, 1964). In fact, when the d.c. voltage across the junction is equal to V_n , there is a difference in energy of $2eV_n$ between the pairs on one side and those on the other side of the barrier. When external radiation is present, pair tunneling processes are possible in which a pair absorbs or radiates n photons of frequency ω_r . The maximum probability for this process is realized when the relation (11.1.1) is satisfied.

11.1.1 Microwave Induced Steps. Let us consider now in more detail how the amplitude of the current steps and their dependence on the power of the applied radiation can be computed. The starting hypothesis is the assumption that the effect of external radiation is to produce an alternating electric field of the same frequency across the junction (voltage bias model). Also, we assume both the electric field and the current density to be constant all over the sample. We consider a small junction ($L \ll \lambda_J$) and zero external magnetic field. Under this assumption the effective voltage applied to the junction is

$$V(t) = V_0 + v \cos \omega_r t \quad (11.1.2)$$

where V_0 is the d.c. voltage. From the Josephson relations (1.4.4) and (1.4.5), we get for the phase difference the expression

$$\varphi(t) = \omega_f t + \frac{\omega_f}{\omega_r} \frac{v}{V_0} \sin \omega_r t + \varphi_0$$

where we have defined

$$\omega_f = \frac{2e}{\hbar} V_0$$

For the current:

$$J(t) = J_1 \sin \left(\omega_f t + \frac{\omega_f}{\omega_r} \frac{v}{V_0} \sin \omega_r t + \varphi_0 \right)$$

This expression can be written as

$$J(t) = J_1 [\sin(\omega_f t + \varphi_0) \cos(a \sin \omega_r t) + \cos(\omega_f t + \varphi_0) \sin(a \sin \omega_r t)]$$

where

$$a = \frac{\omega_f}{\omega_r} \frac{v}{V_0} = \frac{2ev}{\hbar \omega_r}$$

Let us introduce the Fourier-Bessel expansions for $\cos(a \sin \omega_r t)$ and $\sin(a \sin \omega_r t)$. The following expressions are valid (Abramowitz and Stegun 1970):

$$\begin{aligned} \cos(a \sin \omega_r t) &= J_0(a) + 2 \sum_{k=1}^{\infty} (-1)^k J_{2k}(a) \cos(2k\omega_r t) \\ \sin(a \cos \omega_r t) &= 2 \sum_{k=0}^{\infty} (-1)^k J_{2k+1}(a) \cos[(2k+1)\omega_r t] \end{aligned} \quad (11.1.3)$$

where $J_k(x)$ are Bessel functions of the first kind of integer order. The expression for the current becomes:

$$\begin{aligned} J(t) &= J_1 \left\{ J_0(a) \sin(\omega_f t + \varphi_0) + 2 \sum_{k=1}^{\infty} J_{2k}(a) \cos(2k\omega_r t) \sin(\omega_f t + \varphi_0) + \right. \\ &\quad \left. + 2 \sum_{k=0}^{\infty} J_{2k+1}(a) \sin[(2k+1)\omega_r t] \cos(\omega_f t + \varphi_0) \right\} \end{aligned}$$

Using trigonometric relations:

$$\begin{aligned} J(t) &= J_1 \left\{ J_0(a) \sin(\omega_f t + \varphi_0) + \sum_{l=1}^{\infty} J_l(a) [\sin((l\omega_r + \omega_f)t + \varphi_0) - \right. \\ &\quad \left. - (-1)^l \sin((l\omega_r - \omega_f)t + \varphi_0)] \right\} \end{aligned} \quad (11.1.4)$$

Therefore, whenever the relation

$$\omega_f = \frac{2e}{\hbar} V_0 = \pm n \omega_r$$

is satisfied, a d.c. current component is present whose magnitude is

$$J_n = J_1 J_n \left(\frac{nV}{V_0} \right) \sin \varphi_0 \quad (11.1.5)$$

This current is added to or subtracted from the quasiparticle current, depending on the value of φ_0 , the phase difference between the Josephson radiation, $J_1(\sin \omega_f t)$, and the external microwave signal. The value of φ_0 is determined by the current feeding into the junction. A positive value of the current step corresponds to the tunneling of a pair with emission of photons, and a negative value to a tunneling process with absorption of photons (Langenberg, Scalapino and Taylor 1966). The maximum amplitude of the n th step is given by

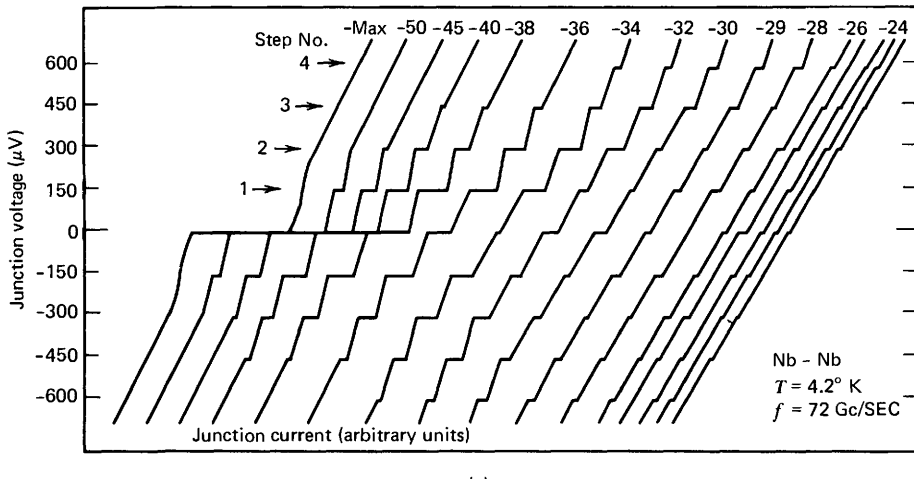
$$|J_n(v)| = J_1 \left| J_n \left(\frac{nv}{V_n} \right) \right| \quad (11.1.6)$$

which is a function of the microwave applied voltage v and therefore of the square root of the microwave power.

The first experimental data on the dependence of the induced steps on the microwave power in Al-AlO_x-Sn junctions were reported by Shapiro and coworkers in 1964 (Shapiro, Janus, and Holly 1964). However, in that case the Bessel function behavior for the step amplitude was not very well satisfied. The origin of the discrepancy can be understood by recalling that expression (11.1.6) has been derived assuming that the applied a.c. field was constant along the junction. As we have seen (Chapter 9) the wave velocity of the electromagnetic radiation in a tunneling structure is lower than in the free space. Therefore to avoid spatial variations the dimensions of the junction must be very small (Hamilton and Shapiro 1970). Another assumption was that of neglecting any frequency dependence of the Josephson current J_1 . As we shall see, this assumption for a tunneling junction holds for voltages much smaller than the energy gap of the superconductor.

Figure 11.1a, b gives data on Nb-Nb point contact (Grimes and Shapiro 1968) for which a satisfactory agreement is obtained. It is interesting to observe that for point contact structures the coupling with the waveguide is much easier.

11.1.2 Effect of Fluctuations on the Induced Voltage Steps. Stephen (1968, 1969b,c) has investigated intrinsic fluctuations in the a.c. Josephson effect both in the “autonomous” junction (1968, 1969b) and in a driven oscillator (1969c). In the last case a microwave monochromatic radiation is applied to the junction. The signal is strong enough so that the Josephson



(a)

Figure 11.1 (a) Voltage-current curves for an Nb-Nb point contact Josephson junction exposed to a 72 Gc/sec signal at various power levels. (b) Data from (a) plotted to show how the current in several constant voltage steps varies as the applied r.f. voltage is varied. The data points from the n th step are compared with the amplitude of the n th order Bessel function. The data are fitted to the theoretical curves at the two points denoted by double circles. The r.f. voltage across the junction is expressed in units of $h\nu/2e$ or $149 \mu\text{V}/\text{div}$. (After Grimes and Shapiro 1968.)

oscillator is “locked” on to the external source. In this situation the fluctuations can be treated as those on the zero voltage step previously discussed (Chapter 6). The mechanical analogy is now with a Brownian motion of a particle in a periodic potential whose maxima are related to the strength of locking (external) signal. Also in this case a “slippage” from one potential valley to the next will cause a rounding of the (finite voltage) induced step. As in the work by Ambegaokar and Halperin (1969) here too the large viscosity (negligible capacitance) hypothesis is assumed. As already discussed, Lee (1971) gives the correct criterion to establish the low capacitance limit. Furthermore, this author takes into account the effect of the finite bandwidth of the external oscillator. Detailed experimental results on the “rounding off” of the induced steps, which are in quite good agreement with Stephen’s theory, have been reported by Kose and Sullivan (1970) and by Henkels and Webb (1971).

11.2 Tunneling Junctions in External Microwave Radiation

As we saw from the microscopic theory developed in Chapter 2, the Josephson current is frequency dependent. In particular, near the gap this dependence has a singularity: the Riedel peak. This behavior is reflected in the step amplitude and, specifically, in the step microwave power dependence.

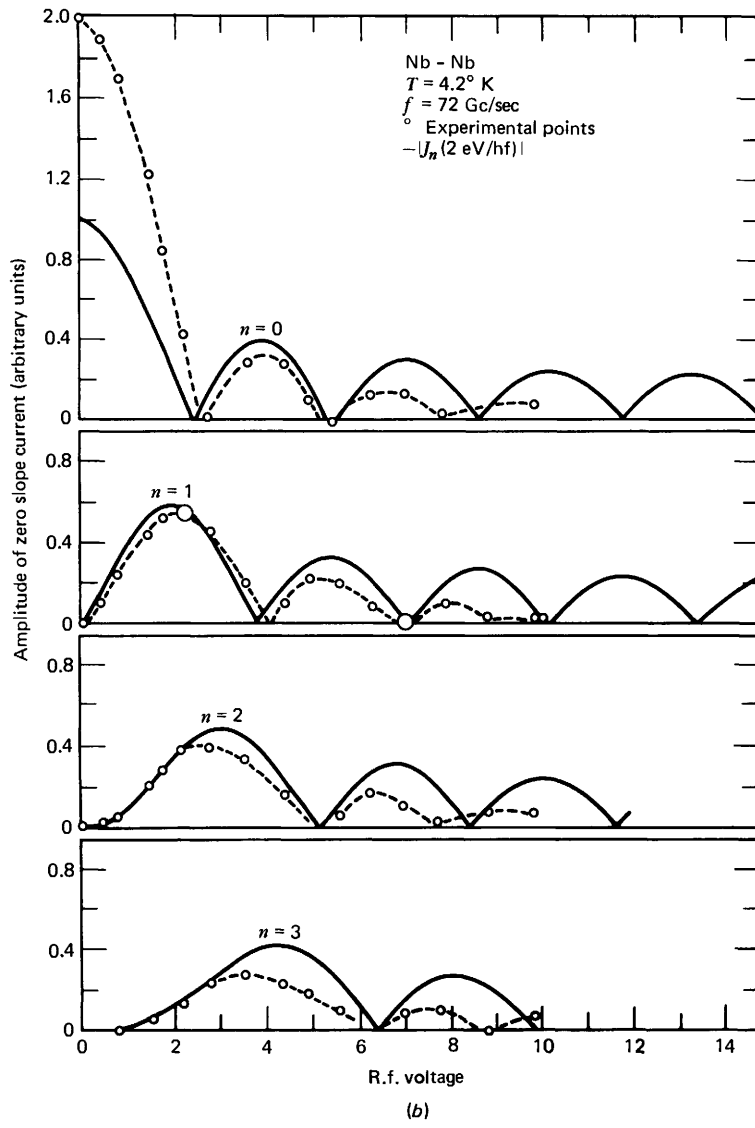


Figure 11.1 (Continued)

We know (Chapter 9) that a junction is a resonant cavity like structure with frequencies of resonance depending on the junction's dimensions and on the dielectric barrier. Furthermore, the wavelength in such a superconducting structure is related to the wavelength λ_0 in free space by the formula (Swihart 1961)

$$\lambda = \lambda_0 \sqrt{\frac{t}{\epsilon_r d}}$$

where t is the oxide thickness, ϵ_r is the dielectric permeability, and d , previously defined, is the usual magnetic field penetration in the junction. Typical values for the factor λ/λ_0 are of the order of $\sim 4 \times 10^{-2}$. Therefore for a frequency of about 30 GHz we have a wavelength $\lambda \approx 0.4$ mm, which can be of the same order of magnitude as the dimensions of junctions normally used in experiments.

We now discuss the effect of the frequency dependence of the Josephson current. We take into account the effects related to the spatial variations of the electromagnetic field and the Josephson current density inside the junction. In particular, such effects are considered for the case of a small junction in which the frequency dependence of J_1 is not included.

11.2.1 The “Riedel” Peak. The general case of a junction in a time dependent external voltage has been investigated by Werthamer (1966) and Larkin and Ovchinnikov (1966). This situation was discussed in Chapter 2 in regard to the case of an arbitrary time varying potential (2.2.7). We now consider a simplified situation in which the time dependent voltage is assumed to be sinusoidal. This particular case has been discussed by Hamilton (1971, 1972b). We start from (2.2.3) that we derived for the total current when a time dependent voltage $V(t)$ across the junction is present:

$$I(t) = \operatorname{Im}_{\eta \rightarrow 0^+} \left\{ e^{-j\Phi(t)/2} \int_{-\infty}^{+\infty} dt' e^{-\eta t'} \right. \\ \left. \times [e^{(j/2)\Phi(t-t')} S(t') + e^{-j\alpha} e^{-j/2\Phi(t-t')} R'(t')] \right\} \quad (11.2.1)$$

where

$$\frac{d\Phi}{dt} = \frac{2|e|}{\hbar} V(t)$$

$S(t)$ and $R'(t)$ were defined in Chapter 2 and are related to the quasiparticles and pair tunneling respectively. In particular, the case $V(t) = V_0 = \text{constant}$ was examined. Let us assume now that there is, in addition, an a.c. voltage $v \cos \omega_r t$. The total voltage applied to the junction is

$$V(t) = V_0 + v \cos \omega_r t$$

The expression for the phase factor $\Phi(t)$ is found by simple integration:

$$\Phi(t) = \omega_f t + a \sin \omega_r t + \Phi_0 \quad (11.2.2)$$

where

$$\omega_f = \frac{2e}{\hbar} V_0; \quad a = \frac{2ev}{\hbar \omega_r} = \frac{\omega_f}{\omega_r} \frac{v}{V_0}$$

by inserting (11.2.2) into (11.2.1) we have

$$I(t) = \operatorname{Im}_{\eta \rightarrow 0^+} \left\{ e^{-j(a/2)\sin \omega_r t} \int_{-\infty}^{+\infty} dt' e^{-\eta t'} \left[e^{-j(\omega_f/2)t'} e^{j(a/2)\sin \omega_r(t-t')} S(t') \right. \right. \\ \left. \left. + e^{-j(\omega_f t + \Phi_0)} e^{j(\omega_f/2)t'} e^{-j(a/2)\sin \omega_r(t-t')} e^{-j\alpha} R'(t') \right] \right\} \quad (11.2.3)$$

Let us introduce the Fourier expansion for the $\sin(\omega_r t)$ term:

$$e^{j(a/2)\sin \omega_r t} = \sum_{n=-\infty}^{+\infty} A_n e^{jn\omega_r t} \quad (11.2.4)$$

The coefficients are given in terms of Bessel functions of the integer order $J_n(x)$ (Mathews and Walker 1965):

$$A_n = A_n^* = J_n\left(\frac{a}{2}\right) \quad (11.2.5)$$

By inserting (11.2.4) and (11.2.5) into (11.2.3) and by introducing (as in Chapter 2) the Fourier transforms of $S(t)$ and $R'(t)$:

$$J(t) = \sum_{\eta \rightarrow 0^+} \sum_l J_n\left(\frac{a}{2}\right) J_l\left(\frac{a}{2}\right) \operatorname{Im} \left\{ e^{j(l-n)\omega_r t} S\left(j\eta - \frac{\omega_f}{2} - l\omega_r\right) \right. \\ \left. + e^{-j(l+n)\omega_r t + \omega_f t + \varphi} R'\left(j\eta + \frac{\omega_f}{2} + l\omega_r\right) \right\} \quad (11.2.6)$$

where $\varphi = \Phi_0 + \alpha$.

Let us introduce the quantities, $I_{qp}(\omega)$, $I_{qpi}(\omega)$, $I_{J1}(\omega)$, $I_{J2}(\omega)$ (2.2.8) related to the real and imaginary parts of $S(\omega)$ and $R'(\omega)$. The expression for the current becomes

$$I(t) = \sum_{n=-\infty}^{+\infty} \sum_{l=-\infty}^{+\infty} J_n\left(\frac{a}{2}\right) J_l\left(\frac{a}{2}\right) \left\{ I_{qp}\left(\frac{-\omega_f}{2} - l\omega_r\right) \cos(l-n)\omega_r t \right. \\ \left. + I_{qpi}\left(\frac{-\omega_f}{2} - l\omega_r\right) \sin(l-n)\omega_r t \right. \\ \left. + I_{J2}\left(\frac{\omega_f}{2} + l\omega_r\right) \cos\{(n+l)\omega_r + \omega_f\}t + \varphi \right\} \\ \left. + I_{J1}\left(\frac{\omega_f}{2} + l\omega_r\right) \sin\{(n+l)\omega_r + \omega_f\}t + \varphi \right\} \quad (11.2.7)$$

For $\omega_r = 0$ and $v = 0$, we recover (2.3.2). In this limit, as we have already observed, I_{qp1} gives no contribution.

The expression (11.2.7) is the general expression for the tunneling current; it includes the $\cos \varphi$ term, I_{J2} , and the contribution that arises from the real part of the quasiparticle current for an a.c. voltage applied to the junction. The effect of I_{qp1} and its interpretation has been discussed by Larkin and Ovchinnikov (1966) and by Harris (1975a). We here neglect (as usual) this term together with the $\cos \varphi$ term I_{J2} . Under this assumption the expression for the current is

$$I(t, \omega_f) = \sum_{n=-\infty}^{+\infty} \sum_{l=-\infty}^{+\infty} J_n\left(\frac{a}{2}\right) J_l\left(\frac{a}{2}\right) \left\{ I_{qp}\left(\frac{\omega_f}{2} + l\omega_r\right) \cos[(l-n)\omega_r t] + I_{J1}\left(\frac{\omega_f}{2} + l\omega_r\right) \sin[((n+l)\omega_r + \omega_f)t + \varphi] \right\} \quad (11.2.8)$$

The first term describes the quasiparticle current and the second term the pair current. From the last expression the d.c. current contribution can be easily derived. For the first term a d.c. component arises from all the terms in the sum for which the condition $l=n$ is satisfied. The quasiparticle d.c. current is given by the expression

$$\bar{I}_q(V_0) = \sum_{n=-\infty}^{+\infty} J_n^2\left(\frac{a}{2}\right) I_{qp}\left(\frac{\omega_f}{2} + n\omega_r\right) \quad (11.2.9)$$

Since $I_{qp}(\omega)$ has a strong discontinuity at $\omega=2\Delta/\hbar$,[†] the last expression predicts a set of current steps in the quasiparticle current branch. These steps occur at voltage values V_0^n given by

$$V_0^n = \frac{2\Delta}{e} \pm n \frac{\hbar\omega_r}{e}$$

and have an amplitude proportional to $J_n^2(a/2)$. They correspond to the photon assisted single particle process first observed by Dayem and Martin (1962) and theoretically described by Tien and Gordon (1963). The d.c. contribution of the pair current is derived from the second term in (11.2.8) if the condition

$$\omega_f = \pm(n+l)\omega_r$$

is satisfied. It is given by

$$\bar{I}_J(V_0) = \sum_{N=0}^{\infty} \sum_{l=-\infty}^{+\infty} J_l\left(\frac{a}{2}\right) J_{N-l}\left(\frac{a}{2}\right) I_{J1}\left[\left(l - \frac{N}{2}\right)\omega_r\right] \sin \varphi \delta(\omega_f \pm N\omega_r) \quad (11.2.10)$$

[†]We refer to the $T=0$ K case.

where

$$\delta(\omega) = \begin{cases} 0 & \omega \neq 0 \\ 1 & \omega = 0 \end{cases} \quad \text{and} \quad N = n + l$$

Therefore the maximum amplitude of the N th r.f. induced step, taking into account the frequency dependence of the Josephson current, is

$$\bar{I}_J(V_N) = \left| \sum_{l=-\infty}^{+\infty} J_l\left(\frac{a}{2}\right) J_{N-l}\left(\frac{a}{2}\right) I_{J1}\left[\left(l - \frac{N}{2}\right)\omega_r\right] \right| \quad (11.2.11)$$

where

$$V_N = \frac{\hbar N \omega_r}{2|e|}$$

Figure 11.2 gives experimental data from Hamilton (1972b). The sample investigated was a very small Sn-SnO_x-Sn junction of the in-line point overlap configuration (Hamilton and Shapiro 1970; Buckner, Chen, and Langenberg 1970a,b). In Fig. 11.2a a typical V - I characteristic is shown in the absence of microwave radiation. As the microwave amplitude v (via the microwave power) is increased, quasiparticle steps appear in the region around $V_0 = 2\Delta/e$ (see Fig. 11.2b). The Josephson steps that start to appear near $V_0 = 0$ are not observable, since the junction is current biased and they cannot be traced out. The number of observable steps increases with the applied microwave power (Fig. 11.2c), and the V - I curve tends to assume a staircase-like form (Fig. 11.2d). The power dependence of the maximum amplitude for a particular Josephson step and the corresponding quasiparticle step are shown in Fig. 11.3 (Hamilton 1972b). The solid lines are the theoretical curves computed by using (11.2.9) and (11.2.11). Because of the presence of the singularity in $I_{J1}(\omega)$, the amplitude variation of the Josephson steps has small deviations from the usual $|J_N(a)|$ dependence (11.1.6). The effect is more apparent for higher values of the applied microwave power. This behavior can be deduced also by inspecting (11.2.1). In fact, from the general properties of Bessel functions, $J_N(a) = 0$ for all $a < |N|$, it follows that in (11.2.11) the terms that give the more significant contribution are those for which $|l| < a/2$ and $|N - l| < a/2$. Thus for small value of the applied power, that is, for $v < 2\Delta/e$, the argument of $I_{J1}(\omega)$ is less than $2\Delta/\hbar$ for all significant terms.

Assuming that $I_{J1}(\omega) = I_{J1}(0) = J_1$ and using the identity (Mathews and Walker 1965)

$$\sum_{l=-\infty}^{+\infty} J_l(x) J_{N-l}(x) = J_N(2x)$$

(11.2.11) reduces to $|J_1 J_N(a)|$, which coincides with (11.1.6), previously derived. For larger values of the applied microwave voltage ($v \gtrsim 2\Delta/e$) some of the

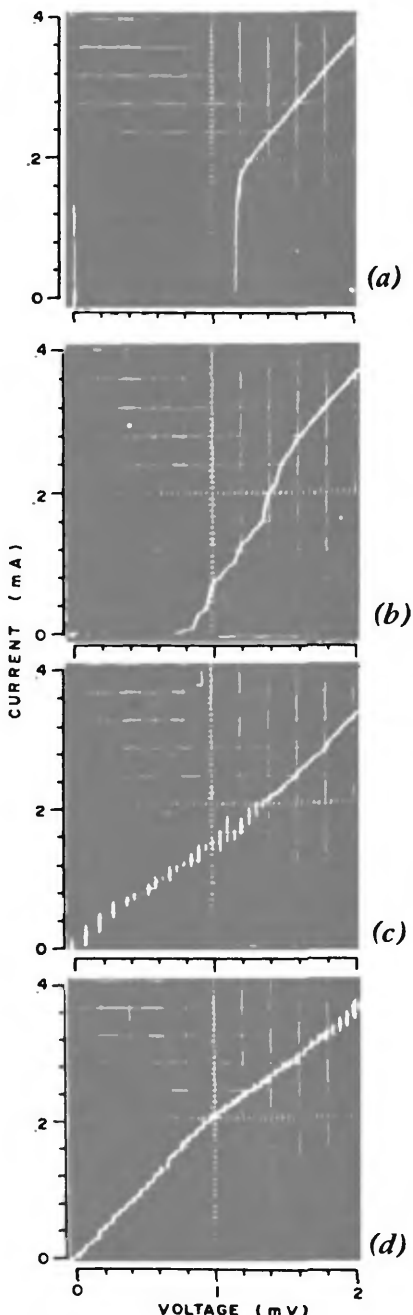


Figure 11.2 (a) Oscilloscope trace of the V - I curve for a typical superconducting $\text{Sn}-\text{SnO}_x-\text{Sn}$ junction in the absence of microwave radiation. (b), (c), and (d) V - I curves for increasing amplitude of the applied radiation at 25 GHz. The microwave voltage amplitudes are: $v \approx 0.6(\Delta/e)$ (b); $v = 2\Delta/e$ (c); $v = 3\Delta/e$ (d). (After Hamilton 1972b.)

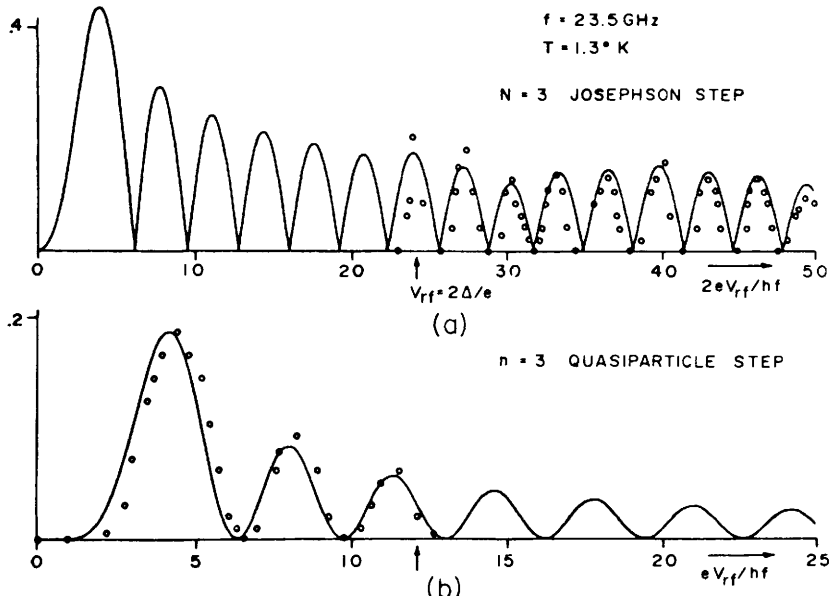


Figure 11.3 Power dependence of the maximum amplitude for the $N=3$ microwave induced Josephson step and for the corresponding quasiparticle step. The experimental data (open circles) are compared with the theoretical curves (solid lines) computed from (11.2.11) and (11.2.9). (After Hamilton 1972b).

significant terms in (11.2.5) contain values of $I_{J1}(\omega)$ near the singularity; therefore significant deviations from Bessel-function behavior are apparent for every step. An estimation of the value of v at which the effect of the Riedel singularity becomes evident can be obtained in the following way (Hamilton and Shapiro 1971). Let us assume that M is the number of the step that falls nearest the gap voltage. This means that the condition

$$M\omega_r \simeq \frac{2\Delta}{\hbar} \quad (11.2.12)$$

is satisfied. The first significant contribution of the summation in (11.2.11), for which the argument of $I_{J1}(\omega)$ is nearest the singularity, will be the n th term, where n satisfies the relations

$$\frac{a}{2} \gtrsim n; \quad \left(n - \frac{N}{2}\right)\omega_r \simeq \frac{2\Delta}{\hbar}$$

Combining these expressions with expression (11.2.12) we have

$$v \gtrsim \frac{\hbar\omega_r}{|e|} \left(M + \frac{N}{2}\right)$$

This is the value of v at which the effect of the Riedel singularity begins to be evident for the N th step. By carefully measuring the step heights as a function of the frequency and voltage amplitude of the microwave radiation, it is possible to determine the value of $I_{J1}(\omega)$ near $\omega=2\Delta/\hbar$. Experimental observations of the Riedel peak based on this method have been performed by Hamilton and Shapiro (1971) and by Hamilton (1972b). Data from the latter work are reported in Fig. 11.4. The samples investigated were very small Sn-SnO_x-Sn junctions. The frequency of the applied radiation ranged between 20 and 26 GHz and the temperature was ~ 1 K. From the figure it is apparent that the peak is broadened and has a maximum value of about $3.0I_J(0)$. A possible explanation of the rounding of the singularity can be found in terms of gap anisotropy and quasiparticle damping. Scalapino and Wu (1966) have analyzed the behavior of a Josephson junction in the presence of high frequency radiation, taking into account the effect of the quasiparticle damping in terms of a temperature dependent complex energy gap parameter $\Delta=\Delta_1+j\Delta_2$. From their theory it is possible to derive the following approximate expression for the amplitude of the N th microwave induced step which holds when the M th step occurs at a voltage near the gap (Buckner, Finnegan, and Langenberg

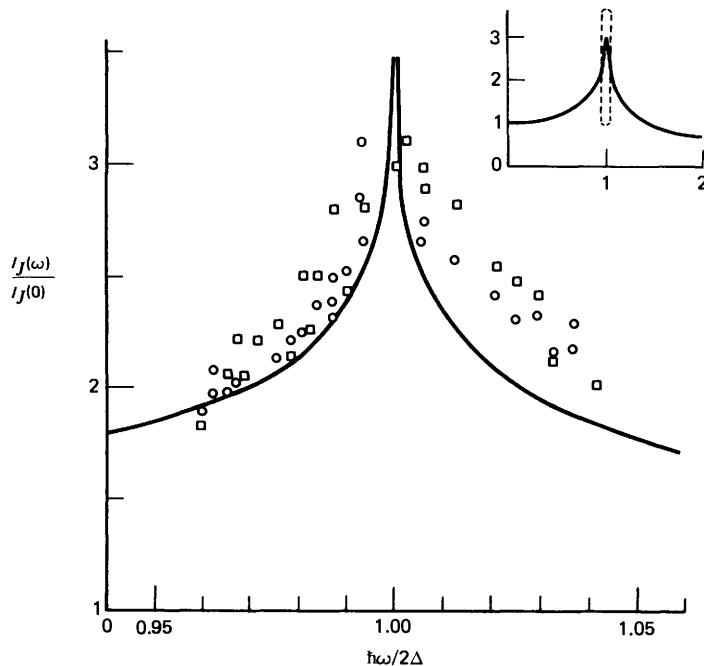


Figure 11.4 Riedel peak function $I_J(\omega)$ (solid line) and data (points) computed from experimental measurements of the Josephson step amplitudes. The dashed box in the insert shows the region plotted. (After Hamilton 1972b.)

1972):

$$I_N \simeq I_1(T) \left[F\left(\frac{a}{2}\right) - F_{N,M}\left(\frac{a}{2}\right) \ln\left(\frac{|N\hbar\omega_r - 4\Delta_0(T)|}{32\Delta_0(T)} + \frac{|\Delta_2|}{4\Delta_0(T)}\right) \right] \quad (11.2.13)$$

where $\Delta_0(T)$ is the real part of the energy gap parameter computed at the gap edge, $F(a/2)$ and $F_{N,M}(a/2)$ are two functions of the parameter $a=2ev/\hbar\omega_r$, whose analytical expressions can be given in terms of Bessel functions, and $I_1(T)$ is the temperature dependent d.c. maximum Josephson current (3.2.9) evaluated by using $\Delta_0(T)$. Expression (11.2.13) does not include effects due to gap anisotropy. Buckner, Finnegan, and Langenberg (1972) have investigated the Riedel singularity in Sn-Sn junctions, taking advantage of the temperature dependence exhibited by (11.2.13). Microwave radiation at a frequency near 135 GHz was applied to the sample. The r.f. power was held constant while the temperature was varied in order to cross the Riedel peak. Figure 11.5 presents data for the zero voltage Josephson current. By comparing experiments and theory it is possible to evaluate the damping parameter $\delta = |\Delta_2|/\Delta_0$. Further investigations on the damping mechanism of the Riedel peak have been performed by Buckner and Langenberg (1976) on Sn-Sn junctions. These authors have shown that at low temperature, effects due to gap anisotropy give

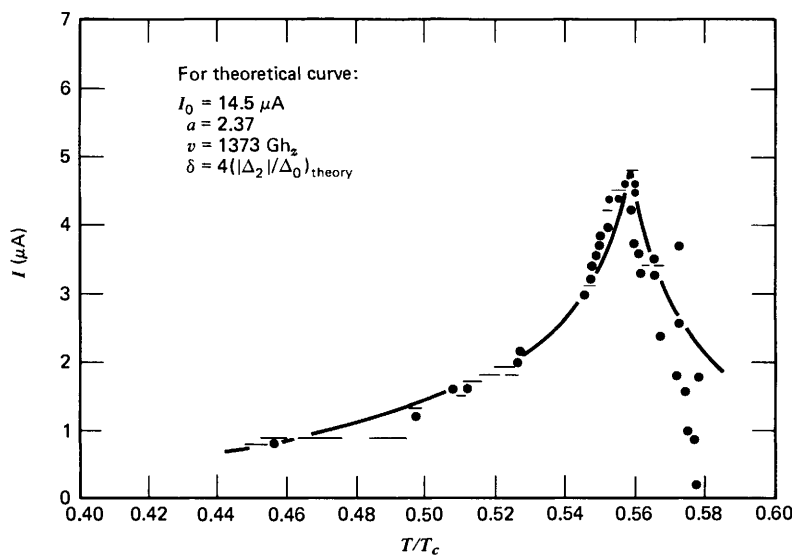


Figure 11.5 Zero voltage current versus temperature in the presence of a microwave radiation of a frequency ν related to the zero temperature energy gap of the superconducting junction electrodes Δ_0 by the expression: $\hbar\nu = \Delta_0$. The sudden drop in current near $T/T_c \approx 0.58$ is believed to be due to substrate heating when the temperature of the helium bath passes through the λ point. (After Buckner, Finnegan, and Langenberg 1972.)

the most important contribution. At high temperature a quantitative agreement is found with the Scalapino and Wu theory based only on quasiparticle damping processes.

Effects of the Riedel singularity have been observed in point contact structures too (Thome and Couder 1975). A direct observation of the maximum peak height has been performed by Vernet and Adde (1976) on Ta-Ta point contact. The value $3.5I_J(0)$ for the Riedel peak has been reported by these authors. It is of the same order of magnitude as that observed for tunneling junctions.

11.2.2 Finite Dimension Effects. Let us consider a junction whose dimensions are small compared with the Josephson penetration length λ_J , though comparable with the wavelength of the applied radiation. For the sake of simplicity we refer to a junction of in-line geometry (Fig. 5.49) of width W and length L . The direction of propagation of the microwave signal is along L , and the electric field is perpendicular to the plane of the junction. We neglect the frequency dependence of the Josephson current. ($I_{J1}(\omega)=J_1=\text{const.}$) The frequency ω_r of the external radiation is chosen so that

$$L = \frac{1}{2}n\lambda_r$$

where n is an integer and λ_r is the wavelength of the applied microwave signal inside the oxide barrier. Taking into account the existence of a standing wave pattern for the voltage along the L direction, (11.1.2) becomes

$$V(t) = V_0 + v(z)\cos\omega_r t \quad (11.2.14)$$

where

$$v(z) = V_m \cos\left[\left(\frac{n\pi}{L}\right)z\right]$$

and the z axis has been chosen along the L dimension.[†] The current density $J(t)$ is given by an expression analogous to (11.1.4) in which the variable a must be replaced by a space dependent function:

$$a(z) = \frac{2eV_m}{\hbar\omega_r} \cos\left(\frac{n\pi}{L}z\right) \quad (11.2.15)$$

The amplitude of the N th induced step is given by

$$I_N(V_m) = J_1 W \int_0^L dz J_N\left[\frac{2eV_m}{\hbar\omega_r} \cos\left(\frac{n\pi}{L}z\right)\right]$$

[†]This approach has been used by Hamilton and Shapiro (1970) to account for the discrepancies in the power dependence of the photon induced quasiparticle steps.

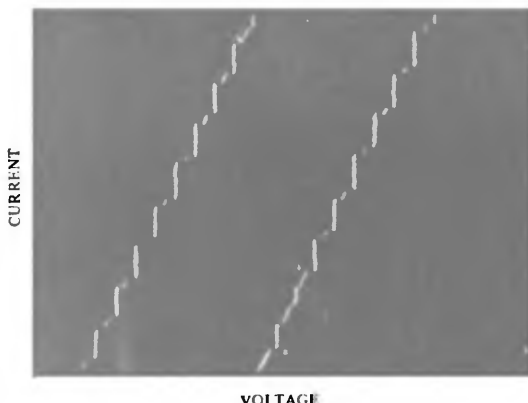


Figure 11.6 Voltage-current characteristic of an Nb-NbO_x-Pb junction in the presence of external microwave radiation ~ 10 GHz. The different amplitudes for odd and even steps, due to the junction dimensions, are clearly observable. (Courtesy of R. Vaglio, V. Lacquaniti, and G. Marullo.)

Using the Bessel functions property (Abramowitz and Stegun 1965)

$$\int_0^{\pi/2} J_{2n}(2x \sin y) dy = \frac{\pi}{2} J_n^2(x)$$

it can be shown (Pech and Saint-Michel 1975; Somervuo and Sirkeinen 1975) that

$$I_N(V_m) = J_i W L J_{N/2}^2 \left(\frac{eV_m}{\hbar \omega_r} \right) \quad \begin{cases} 0 & \text{for } N \text{ odd} \\ & \text{for } N \text{ even} \end{cases}$$

The effect is often observed in the V - I characteristic of Pb-Pb and Nb-Pb junctions, in which the odd steps exhibit smaller amplitudes and sometime disappear. Figure 11.6 gives data taken on a Nb-Pb junction. The dimensions of the sample were $W=0.2$ mm and $L=0.5$ mm, and the microwave frequency was ~ 10 GHz. By using a typical value $\bar{c}/c=0.038$, this gives $\lambda_r \simeq 1.1$ mm.

If an external magnetic field is present, the phase factor in (11.1.4) has a spatial dependence. As a consequence the expressions previously derived for the step amplitudes no longer hold. This effect has been theoretically investigated by Wu, Chi, and Liu (1978).

11.3 Current Source Model

In dealing with the properties of a junction in the presence of a.c. radiation, we have used the simplified approach of a "voltage biased" configuration. In practice, unless a matching circuit is employed, the r.f. source impedance is

higher compared with the junction impedance. Therefore a constant current source model is more realistic.

The junction can be described in terms of the R.S.J. model considered in Chapter 6, by adding to the d.c. current, I_{dc} , a time dependent current $I_{rf} \sin \omega_r t$. This case is usually referred to as the nonautonomous case. A thorough discussion in the framework of the phase plane analysis has been reported by Belykh, Pedersen, and Soerensen (1977b). In the case of zero capacitance the equation that gives the time dependence of the phase difference across the weak link is

$$\frac{I_{rf}}{I_1} \sin \Omega \tau + \frac{I_{dc}}{I_1} = \frac{d\varphi}{d\tau} + \sin \varphi \quad (11.3.1)$$

where the dimensionless time τ is now defined by

$$\tau = \left(\frac{2eRI_1}{\hbar} \right) t$$

and Ω is the dimensionless frequency given by

$$\Omega = \frac{\hbar \omega_r}{2eRI_1}$$

Equation 11.3.1 can be solved by recourse to analog computer (Hamilton 1972a; Russer 1972; Hahlbohm et al. 1972). In the case of small r.f. signal, perturbation methods have been used (Aslamazov and Larkin 1968; Kanter and Vernon 1972). A simple-to-build analog, which includes the $\cos \varphi$, term has been presented by Bak and Pedersen (1973). Recently a way to solve (11.3.1) analytically has been presented by Yao (1978). This is based on the substitution

$$e^{j\varphi} = 2 \frac{d\xi/d\tau}{\xi}$$

which leads to an equation for ξ that can be solved by standard methods of series solution. ξ can be expressed by a series whose coefficients satisfy a three term recursion formula and are given in the form of continued fractions. (Morse and Feshback 1953).

By solving (11.3.1), we can compute the dependence of the r.f. induced steps on the V - I characteristic as a function of the amplitude I_{rf} (and therefore of the power) of the applied radiation. As shown by Russer (1972), the behavior depends on the value of the normalized frequency Ω . For low values of Ω the r.f. power dependence differs markedly from the Bessel function behavior obtained by the voltage source model (see Section 11.1). In Fig. 11.7 the behavior of the zero voltage current and the first induced step, evaluated by using an electrical analog for two different values of Ω , are shown.

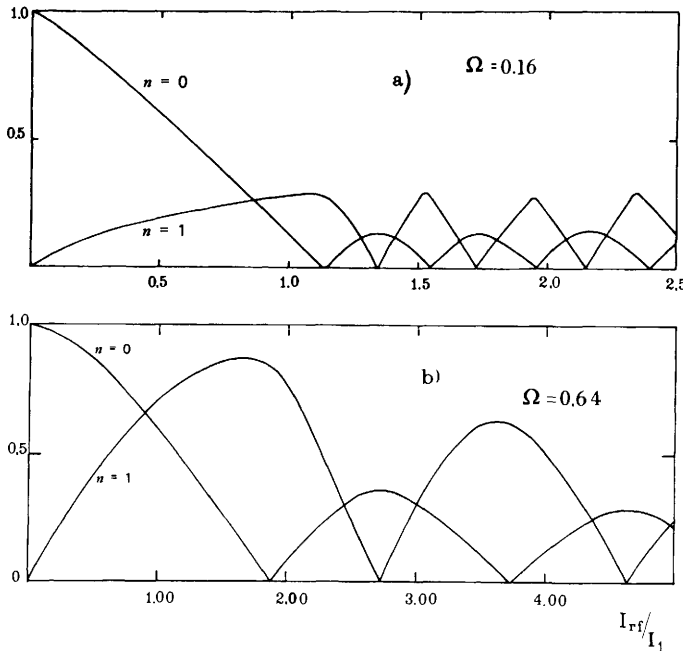


Figure 11.7 Theoretical microwave power dependence of the d.c. Josephson current ($n = 0$) and of the first step for a weak link computed by using an electrical analog. (a) $\Omega = 0.16$; (b) $\Omega = 0.64$. (Balsamo and Paternò 1981.)

Experimental data on small Dayem bridges and on point contact junctions can be accounted for in terms of this simple R.S.J. current biased model. Experimental results on Nb point contacts have been reported by Taur, Richards, and Auracher (1972). The best agreement with the theory is obtained for small values of Ω . For Dayem bridges the situation is slightly more complicated. The microwave power dependence for a cross scratched tin bridge (Greger-Hansen, Levinsen, and Fog Pedersen 1972) is shown in Fig. 11.8 (Greger-Hansen and Levinsen 1971). An enhancement effect of the zero voltage current when the microwave radiation is applied is evident. This effect was observed in the early experiments on the a.c. properties of Dayem bridges by Wyatt and coworkers (1966) and by Dayem and Wiegand (1967). This phenomenon and its interpretation have already been mentioned in Chapter 7. An explanation in terms of the microscopic theory of superconductivity has been given by Eliashberg (1970). According to this author, when a radiation of frequency too small to cause pair breaking is present, quasiparticles are pushed up in energy. The situation is described by a nonequilibrium distribution function different from the equilibrium Fermi-Dirac distribution function. Inserting this nonequilibrium distribution function in the B.C.S. integral equation for the energy gap Δ leads to a value of Δ larger than the equilibrium value.

In the V - I curves of superconducting bridges current steps are often observed at voltage values that are not an integer multiple of the frequency of

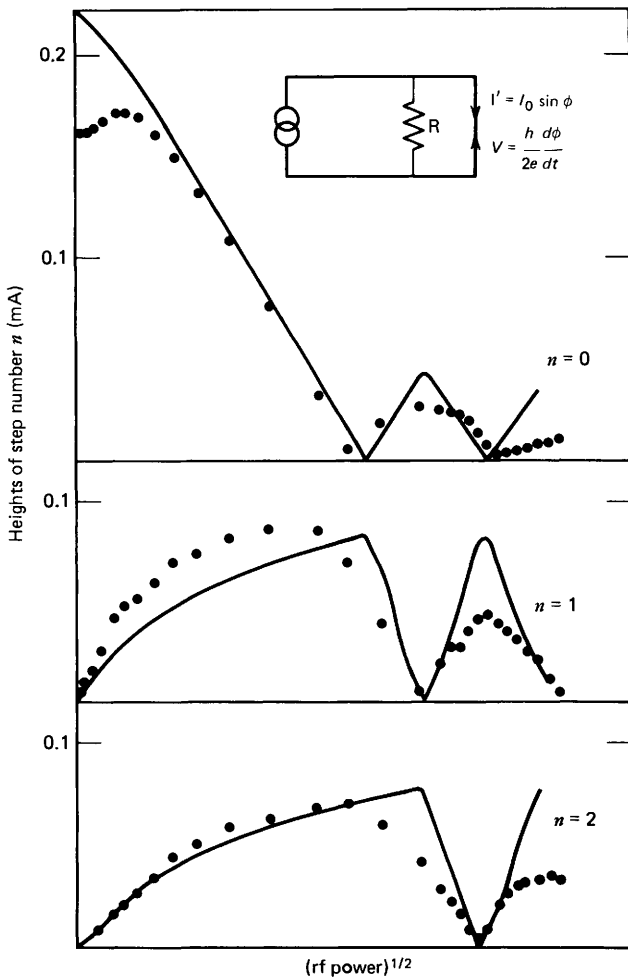


Figure 11.8 The magnitudes of the supercurrent and the first and second current steps as a function of relative microwave field amplitude for a Dayem bridge. $\omega_r/2\pi = 9.054$ GHz, $T = 3.677$ K. The solid lines are computed by using the equivalent circuit, shown in the insert, assuming for the dimensionless parameter Ω the value $\Omega = 0.22$. (After Greger-Hansen and Levinsen 1971.)

the applied radiation. These are the so-called subharmonic steps (see Section 7.6) and cannot be explained in terms of the simple R.S.J. model with a sinusoidal current phase relation as in (11.3.1). The simplest way to obtain subharmonic steps is to assume a nonsinusoidal current phase relation (Greger-Hansen, Levinsen, and Fog Pedersen 1972). Gundlach and Kadlec (1977) have considered (11.3.1) assuming for the Josephson element a linear periodic current phase relation. This gives a relatively simple way in which to obtain an analytical solution for φ . The abovementioned authors have also compared, under the same approximation, the results of the current biased and voltage

biased models (Kadlec and Gundlach 1977). Expression (11.3.1) does not contain the $\cos \varphi$ term. The effect of this term on the power dependence of the microwave induced steps has been investigated by Auracher, Richards, and Rochlin (1973).

11.4 Emission of Radiation

As mentioned in Chapter 1 and at the beginning of this chapter, in the presence of a finite d.c. voltage V_0 an alternating current flows back and forth inside the junction. Therefore a process in which d.c. energy is converted to a.c. energy takes place. In the framework of the simple voltage source model used in Section 11.1 the expression for the a.c. current is

$$I(t) = I_1 \sin(\omega_f t + \varphi_0)$$

where the frequency ω_f is related to the voltage by the fundamental relation

$$\omega_f = \frac{2e}{\hbar} V_0$$

The existence of the a.c. Josephson current was first observed experimentally by way of the effects induced on the d.c. V - I characteristics in the presence of external magnetic field (Fiske 1964) or of external microwave radiation (Shapiro 1963) in tunneling junctions. These two aspects were examined in great details in Chapter 9 and at the beginning of this chapter.

A rough estimate of the maximum available radiation power can be obtained if we assume that all the d.c. power is converted to a.c. radiation. For a device whose V - I curve can be described in terms of the R.S.J. model in the limit of $\beta_J \gg 1$ (see Fig. 6.3), a reasonable bias point can be

$$I \simeq I_1; \quad V_0 \simeq I_1 R_N$$

where I_1 is the maximum d.c. Josephson current and R_N is the normal state resistance. The maximum radiation power at this point is

$$P_\omega \simeq R_N I_1^2$$

For practical devices $R_N I_1 \sim 0.3\Delta$ where Δ is the energy gap of the material, which is of the order of $\sim 10^{-3}$ V. Assuming that $I_1 \simeq 10^{-3}$ A, we get $P_\omega \sim 10^{-7}$ W. In trying to detect this small amount of energy, a very big problem arises related to the coupling of the device to the detection system. As an example let us consider a Josephson tunneling junction. As we have previously seen (Chapter 9) this structure can be regarded as a transmission line. The characteristic impedance for electromagnetic wave propagation is

given by (Swihart 1961):

$$Z_J = \frac{c}{\bar{c}} \left(\frac{l}{\epsilon_r W} \right) Z_0$$

where $Z_0 = 377 \Omega$ is the impedance of the free space, W is the width of the junction, and the other symbols are as defined in Section 9.1. Using the typical values of $\bar{c}/c \sim 0.03$, $l \sim 3.10^{-7}$ cm, $W \simeq 10^{-2}$ cm, $\epsilon_r \sim 4$, we get

$$Z_J \sim 10^{-4} Z_0$$

The power transmission coefficient from the junction to the external circuit is given from the theory of the transmission line (Ramo, Whinnery, and Van Duzer 1965):

$$T = \frac{4Z_S Z_J}{(Z_S + Z_J)^2}$$

where Z_S is the impedance of the detection system. Assuming that $Z_S \sim Z_0$, the maximum radiation power available in the detector is

$$P_d \sim 4 \frac{Z_J}{Z_S} P_\omega \sim 4 \times 10^{-11} \text{ W}$$

An ingenious experiment to investigate qualitatively the radiation emitted by a Josephson junction has been performed by Giaever (1965). He used as a detector a tunneling junction realized on top of the radiating Josephson junction (see Fig. 11.9). The presence of the radiation was revealed by the occurrence in the V - I curve of the junction detector of the r.f. induced quasiparticle steps (Dayem and Martin 1962). The coupling in a structure like that used by Giaever and depicted in Fig. 11.9 can occur through the oxide or directly through the intermediate film, if this film is not too thick. The problem has been theoretically investigated by Owen and Scalapino (1970).

The first direct detection of emitted Josephson radiation has been reported by Yanson, Svistunov, and Dmitrenko (1965), by Dmitrenko and Yanson (1965b), and by the group at the University of Pennsylvania (Langenberg et al. 1965; Langenberg, Scalapino, and Taylor 1966). The detected power at ± 9 GHz was of the order of 10^{-12} W. A sketch of a typical experimental apparatus used in these experiments appears in Fig. 11.10. The samples used were tunneling junctions. In these structures the Josephson radiation is coupled to the resonant cavity formed by the junction. The maximum coupling is realized at the characteristic frequencies of the cavity, as is apparent from the Fiske steps exhibited in the V - I curve (Chapter 9). Therefore the maximum radiation emission occurs when the junction is biased

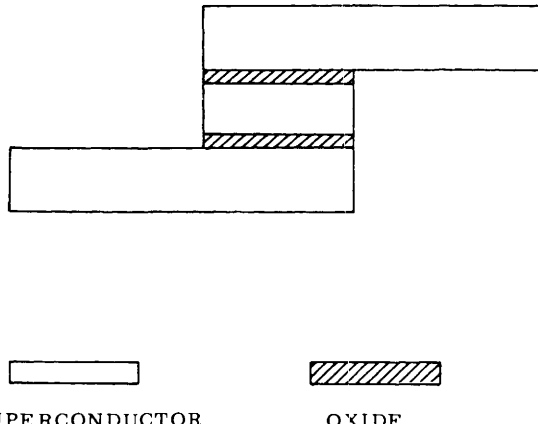


Figure 11.9 Schematic drawing of the experimental arrangement used by Giaever to detect the radiation emitted by a Josephson junction.

on these current singularities. Microwave radiation emission from point contact structures has been observed by Dayem and Grimes (1966) and Krasnopolin and Khaikin (1967). Experimental observations on thin film bridges have been carried out by Gubankov, Koshelets, and Ovsyannikov (1975, 1976a) and by Pedersen and coworkers (1976a,b). In all these experiments the Josephson element was coupled to a microwave cavity. In this case, too,

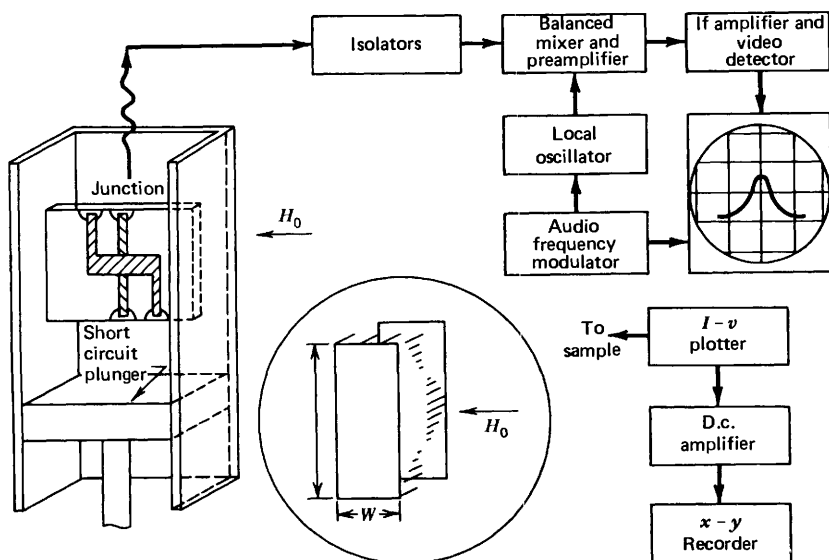


Figure 11.10 Cutaway view of the waveguide sample holder and short circuit plunger and a block diagram of one of the detection systems used. The insert shows the electric field distribution in the junction when it is biased on the $n=2$ mode. (After Langenberg et al. 1965.)

singularities are present in the V - I characteristics at voltages related to the frequencies of resonance of the cavity. The maximum output power is obtained when the Josephson radiator is d.c. biased on these singularities.

The coupling between a Josephson junction and a resonant cavity has been examined theoretically by Werthamer and Shapiro (1967) and by Smith (1974). Experimental data on a thin film microbridge (Pedersen et al. 1976a) are reported in Fig. 11.11. The bridge was mounted at the end wall of an X band rectangular microwave cavity. The receiver used was a superheterodyne detector. As clearly shown in the dV/dI curve (Fig. 11.11.b), two cavity induced steps exist in the V - I characteristic: at 17.5 and 19.9 μ V. They

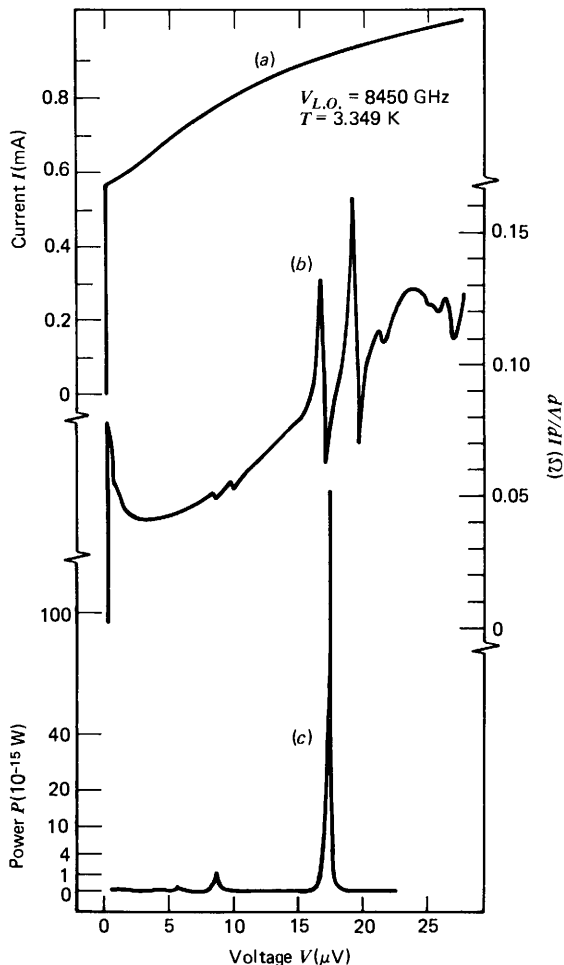


Figure 11.11 (a) Voltage current (V - I) characteristic, (b) first derivative characteristic dV/dI , and (c) detected microwave power output as a function of bias voltage V for a superconducting thin film indium microbridge. (After Pedersen et al. 1976a.)

correspond to the two cavity resonances at 8.5 and 9.7 GHz. The emitted power detected at $\nu_{L_0} = 8.450$ GHz as a function of the d.c. voltage across the bridge is shown in Fig. 11.11c. The peaks in the detected signal occur at voltages $V_n = h\nu_R/2ne$, where ν_R is the receiver central frequency and n is an integer. The signal at V_n is due to the presence of the n th harmonic of the Josephson fundamental frequency corresponding to that voltage. Since the linewidth of the radiation was comparable to the sideband separation of the receiver, the splitting of the peak in two sidebands is not observable. The maximum power detected was of the order of 10^{-13} W.

The presence of harmonics in the emitted Josephson radiation can be accounted for in terms of the R.S.J. model (Fack and Kose 1971; Vystavkin et al. 1973; Likes and Falco 1977). It is essentially due to the high nonlinearity exhibited in the voltage vs time dependence when the junction is current biased (see Fig. 6.6). Microwave harmonics generation was also observed by Shapiro (1967) under different experimental conditions. The junction was irradiated with a small power signal of frequency ν_0 and the signal induced at $2\nu_0$ and $3\nu_0$ was detected. It is interesting to observe that this author used a wideband nonresonant system to couple the junction (a solder blob of the kind described by De Bruin Ouboter et al. 1966) to the detector.

The linewidth of the radiation emitted by a Josephson junction has been theoretically investigated by Larkin and Ovchinnikov (1967), by Stephen (1968), and by Dahm and coworkers (1969). By using the simple voltage bias model, the effect of the noise can be accounted for in terms of a noise voltage which frequency modulates the Josephson radiation. For small voltage values, that is, $k_B T \gg eV_0$ where V_0 is the voltage corresponding to the central frequency, and at a temperature T it is (Dahm et al. 1969):

$$\Delta\nu = \left(4\pi R_d^2 \frac{k_B T}{V_0} \right) \left(\frac{2e}{h} \right)^2 (I_q + I_J) \quad (11.4.1)$$

$R_d = dV/dI$ is the dynamic resistance, I_q and I_J are the quasiparticle and pair currents, and k_B is the Boltzman constant. Experimental data on tunneling junctions have been reported by the same authors (Dahm et al. 1969). A qualitative agreement with the theoretical expression was found. Experimental data on point contact junction (Vernet and Adde 1971) have shown a more satisfactory agreement with the same theoretical expression. In the latter experiment the sample was coupled to the detector via a nonresonant system. It is worthwhile to point out that in linewidth measurements it is crucial to avoid resonances in the coupling system. In fact, when the device is coupled to a resonant cavity a high regenerative interaction is established. Because of this interaction, the linewidth of the Josephson radiation can be narrowed. Another phenomenon often observed in resonant systems is the presence of the so called non-Josephson radiation (Langenberg, Parker, and Taylor 1966b; Vystavkin et al. 1973, 1974; Gubankov et al. 1975). This radiation is at a frequency ν , which is not related to the voltage V across the Josephson device,

by the usual relation $\nu = 2eV/h$. Nonresonant detection of radiation from microbridges at microwave frequency has been reported by Soerensen and coworkers (1977). The coupling to the X band waveguide was realized by a broadband waveguide transformer. Experimental data for two different values of the temperature are shown in Fig. 11.12. In the same figure the I vs. V and dV/dI vs. V curves are reported. As can be noted, there are no structures in these curves, since the coupling is nonresonant. As usual, the peaks of the radiation spectrum are centered at $V_n = h\nu_R/2ne$ where n is an integer and ν_R is the detector frequency. Close to the critical temperature T_c (Fig. 11.12a) only the peak corresponding to $n=1$ is observable. On decreasing the temperature the linewidth increases considerably. The expression for the linewidth of the n th peak derived from the R.S.J. model (Vystavkin et al. 1973; Likharev and Ulrich 1978) is

$$\Delta V_n = \frac{h}{2e} \Delta \nu_n = n^2 \frac{4ek_B T^* R}{\hbar} \left(\frac{R_d^2}{R^2} \right) \left[1 + \frac{1}{2} \left(\frac{I_1}{I} \right)^2 \right] \quad (11.4.2)$$

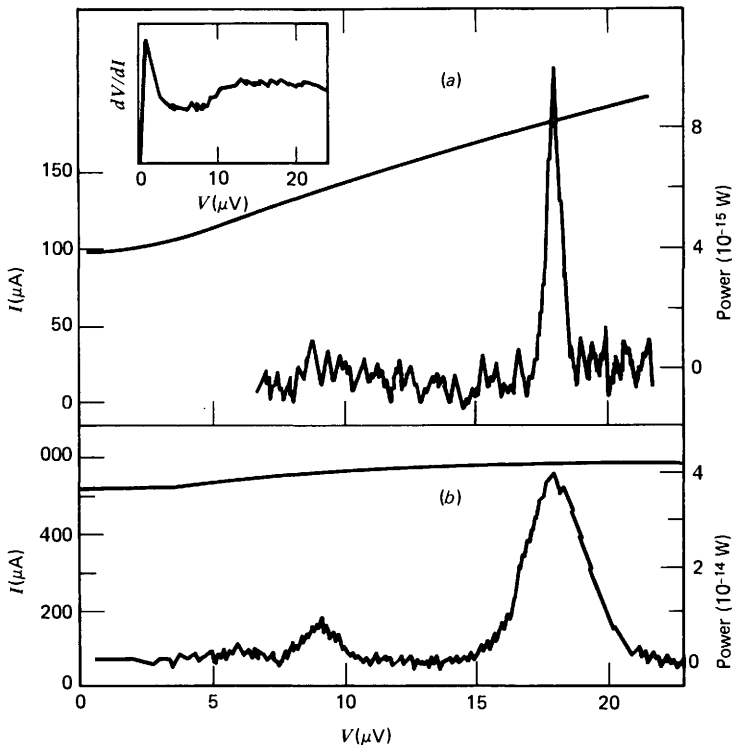


Figure 11.12 D.c. current and r.f. power as a function of d.c. voltage at two different temperatures. (a) $T = 3.42 \text{ K}$ and (b) $T = 3.35 \text{ K}$. The left and right hand vertical scales are for current and measured r.f. power, respectively. The inset in (a) shows the differential resistance dV/dI at a temperature near T_c . Local oscillator frequency $\sim 9.199 \text{ GHz}$; $T_c = 3.44 \text{ K}$. (After Soerensen et al. 1977.)

where T^* is an effective noise temperature, R is the normal state resistance, R_d the dynamic resistance, I_1 is the critical current, and I is the d.c. bias current. In Fig. 11.13 the linewidth for the principal peak ($n=1$) is reported as a function of $R_e^2 = R_d^2 [1 + \frac{1}{2}(I_1/I)^2]$. The quadratic dependence predicted by (11.4.2) is well verified for values of T not too far from T_c . From the figure an effective noise temperature $T^* = 19 \pm 3$ K is derived. A strong discrepancy is observed at lower temperatures (large values of R_d).

Varmazis, Lukens, and Finnegan (1977) have detected microwave radiation between 2 and 12 GHz for nonresonant coupling to a microbridge via a broadband microstrip geometry. The data reported by these authors for radiated microwave power and linewidth show no frequency dependence and are in disagreement with the theoretical results derived on the basis of the R.S.J. model.

The method for coupling to Josephson devices via microstripline techniques has been introduced by Finnegan, Wilson, and Toots (1973, 1974). It is particularly useful with thin film structures, as tunneling junctions or microbridges, when the integrated circuit fabrication technology is employed. The device is readily integrated into the microstrip transmission line by using the substrate itself as the dielectric of the microwave structure. Many integrated circuit components such as low pass filters and resonators can be adapted for use at low temperatures.

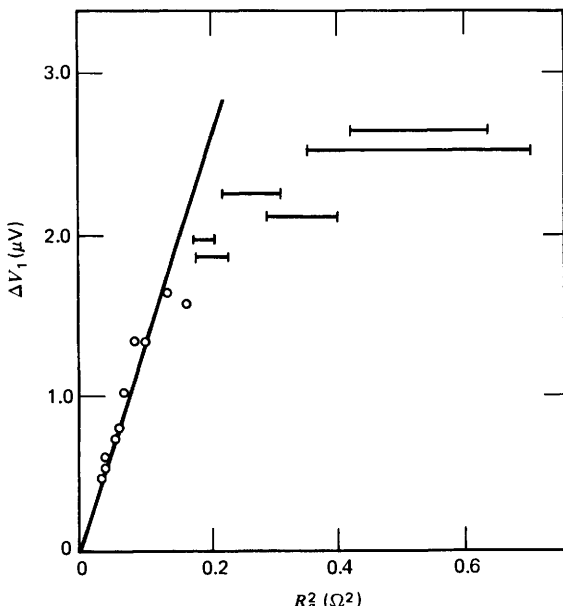


Figure 11.13 The measured line width at half-peak power ΔV_1 as a function of $R_e^2 = R_d^2 [1 + \frac{1}{2}(I_1/I)^2]$. The horizontal bars at the large values of R_e reflect the observed variation of R_d across the linewidth. The initial slope of the curve (corresponding to high temperatures) defines an effective noise temperature $T = 19 \pm 3$ K. (After Soerensen et al. 1977.)

An example of the microwave integrated circuit realized by Finnegan, Holdeman, and Wahlsten (1976) is shown in Fig. 11.37. The design, operation, and construction of a microwave integrated circuit holder for use with thin film Josephson devices have been recently intensively discussed by Finnegan (1980).

The amount of power emitted by a single Josephson junction is rather small for many applications. Recently considerable interest has been devoted to the use of arrays of junctions as generators and detectors of microwave radiation. Such structures can behave coherently if the interaction between the junctions is sufficiently strong. Experimental investigations on arrays formed by pressing together small superconducting spheres have been performed by Clark (1968, 1969, 1973a, b) and by Saxena, Crow, and Strongin (1972). The problem of an array of M junctions in series coupled to a cavity mode has been theoretically analyzed by Tilley (1970). This author has shown that all the junctions can radiate coherently, the number of photons emitted being proportional to M^2 . The first experimental observations of this "superradiant" state on a two junctions array ($M=2$) have been reported by Finnegan and Wahlsten (1972). The samples used consisted of four identical $\text{Pb-PbO}_x\text{-Pb}$, junctions connected in series. The dimensions of the junctions were 0.8×0.3 mm. The fundamental frequency of resonance ν_0 along the 0.8 mm dimensions was about 9 GHz at 4.2 K. The device was mounted in an X band waveguide holder. A sensitive superheterodyne receiver was used to detect the emitted radiation. A block diagram of the apparatus is sketched in Fig. 11.14.

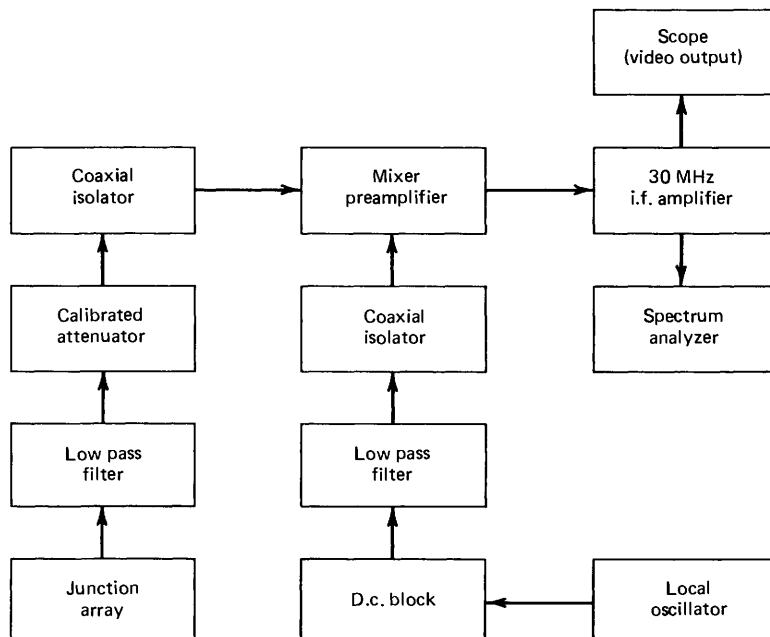


Figure 11.14 Block diagram of the experimental setup used by Finnegan and Wahlsten to detect the Josephson radiation emitted by a two junction array. (After Finnegan and Wahlsten 1972.)

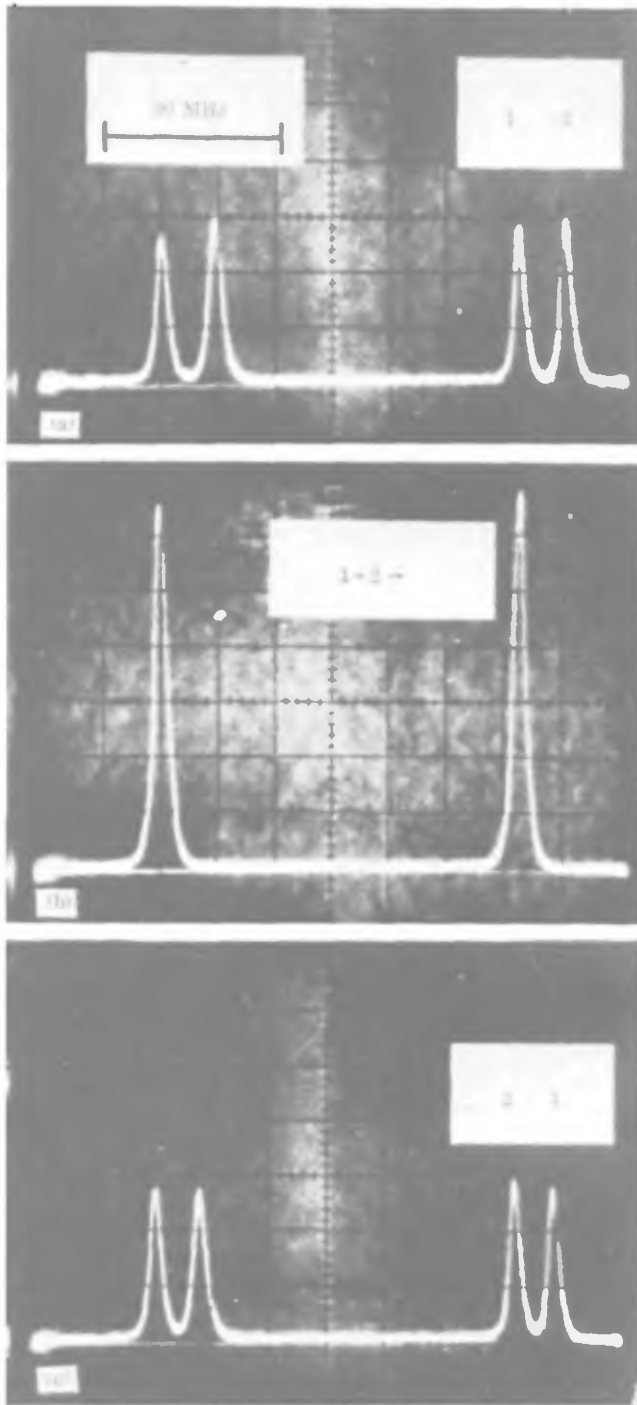


Figure 11.15 Video detected output as a function of frequency for a pair of junctions. (a) Junction frequencies ν_1 and ν_2 separated so that ν_2 is 10 MHz greater than ν_1 . (b) ν_1 equals ν_2 ; (c) ν_1 is about 10 MHz greater than ν_2 . The apparent linewidth is determined by the 2 MHz bandwidth of the filter in the intermediate frequency amplifier. (After Finnegan and Wahlsten 1972.)

The video detected output from the adjacent junctions is reported in Fig. 11.15. The two junctions were about 1 mm apart and were biased independently on the $n=2$ zero field step (Chapter 10). The output from each junction is displaced as two sidebands separated by twice the 30 MHz i.f. frequency. When the current in junction 2 is adjusted so that the frequency of the radiation from the two junctions is the same (Fig. 11.15b), the emitted signals add coherently. In fact the detected radiation power in this case is $4.2 \cdot 10^{-11}$ W and is greater than the sum of the power $P_1 + P_2$ emitted by junctions 1 and 2 separately: $P_1 = 1.05 \cdot 10^{-11}$ W and $P_2 = 1.1 \cdot 10^{-11}$ W. Sometimes, however, the interaction between the junctions manifested itself in the disappearance of the signal when the two samples were radiating at the same frequency. This behavior can be understood in terms of a phaselocking of the two signals with a shift of π . The detailed mechanism by which the phase between the two Josephson oscillators adjusts itself is not clear. Coherent radiation from thin film bridge arrays has been observed by Lindelof et al. (1977) and by Lindelof and Hansen (1977).

Varmazis and coworkers (1978) have observed tunable coherent radiation with narrowed linewidth from two identical junctions coupled via a shunt resistor. The thin film sample consisted of two microbridges in series. A gold film resistor was placed in parallel connecting the two external ends of the structure. Without this shunt resistor, coherent radiation effects were only observed for samples in which the distance between the two microbridges was less than $2 \mu\text{m}$.

Collective synchronization of arrays of superconducting weak links has been experimentally investigated by Palmer and Mercereau (1974, 1977) and Jillie, Lukens, and Kao (1974, 1976). Clark and Lindelof (1976) have investigated by analog computer the coherent behavior of multiply connected two dimensional arrays of weak links. They have also performed measures on 2×2 , 3×3 , and 4×4 indium microbridge arrays. Data on the 3×3 array show that the junctions are synchronized. However, it is not fully understood if this strong collective synchronization is due to a better impedance match with the external applied microwave source or to better coupling between the junctions.

11.5 Detection of Radiation

The high sensitivity to electromagnetic radiation makes it possible to use Josephson weak links as low noise detectors in the microwave to far infrared ranges. We now discuss briefly some of the principal configuration that have been employed. For more details the reader is referred to the review papers by Richards (1977) and Adde and Vernet (1976).

11.5.1 Wide Band Detectors. In the presence of small amplitude external radiation, the maximum zero voltage Josephson current I_1 decreases quadratically with the applied signal (see Fig. 11.7b). Assuming a current bias

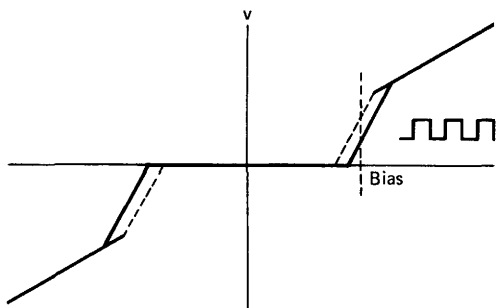


Figure 11.16 Schematic V - I curve showing how applied radiation causes a change in zero voltage current which is converted to a voltage output by constant current external bias. Dashed curve is for radiation on; solid curve for radiation off. (After Grimes, Richard, and Shapiro 1968.)

model, this dependence can be written as

$$I_1(I_{\text{rf}}) = I_1(0)(1 - \gamma I_{\text{rf}}^2) \quad (11.5.1)$$

where I_{rf} is the amplitude of the external radiation and γ is a constant. If the V - I characteristic of the weak link is nonhysteretic, the variations of the d.c. Josephson current can be detected by current biasing the device at a value slightly greater than $I_1(0)$ and by measuring the d.c. voltage developed across it (see Fig. 11.16).

This configuration is called a video square law detector; in it a Josephson device was first used to detect radiation up to the far infrared region (Grimes, Richards, and Shapiro 1968). Figure 11.17 is a schematic of the experimental setup employed in the first experiments. The sensing element is an adjustable point contact. When the input signal to be measured is amplitude modulated (by a chopper, for example), the voltage output at the modulation frequency is

$$\delta V = \delta IR_d = -\gamma I_1(0)I_{\text{rf}}^2 R_d \quad (11.5.2)$$

where $R_d = dV/dI$ is the dynamic resistance at the bias point and (11.5.1) has been used. In the limit where the source impedance R_s is much greater than the radio frequency impedance R_{rf} of the weak link, the coupled power is

$$P_c = \frac{1}{2} I_{\text{rf}}^2 R_{\text{rf}} \quad (11.5.3)$$

From (11.5.2) and (11.5.3) it follows that the responsivity of the device defined as the ratio between output voltage and applied power is

$$S = \frac{\delta V}{P_c} = -2\gamma I_1 \frac{R_d}{R_{\text{rf}}}$$

At high frequency, that is, for $\Omega = \hbar\omega_r / 2eRI_1 \gg 1$, the expression for the zero

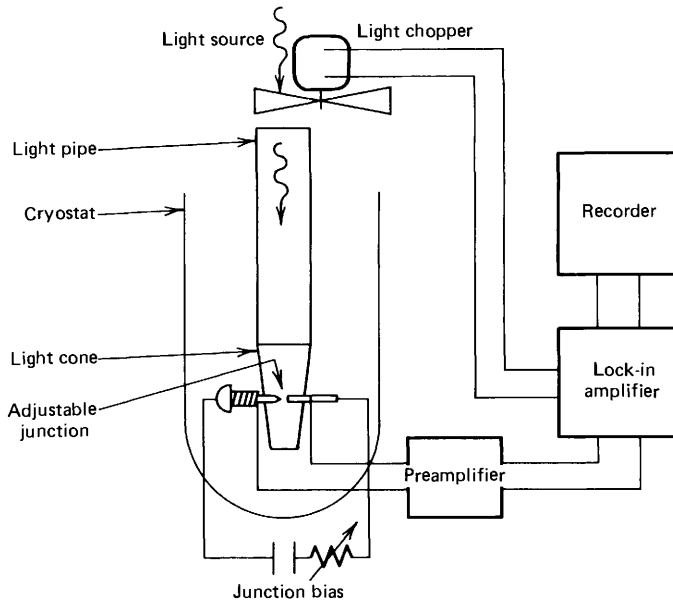


Figure 11.17 Schematic of far infrared detection experiment. (After Grimes, Richard, and Shapiro 1968.)

voltage current as a function of the applied signal approaches the Bessel function dependence derived for the simple voltage biased model (see Section 11.3.1):

$$I_1(I_{\text{rf}}) = I_1(0) J_0 \left(\frac{2ev}{\hbar\omega_r} \right) \simeq I_1(0) \left(1 - \frac{e^2 v^2}{\hbar^2 \omega_r^2} \right)$$

Comparing the last expression with (11.5.1), we obtain for γ the value

$$\gamma = \frac{e^2 R^2}{\hbar^2 \omega_r^2} = \frac{1}{4I_1^2(0)\Omega^2}$$

where it is assumed that $v = RI_{\text{rf}}$. Therefore in this limit ($\Omega \gg 1$) the responsitivity is given by

$$S = - \frac{R_a}{2I_1 R \Omega^2} \quad (11.5.4)$$

A more detailed analysis of the video detectors has been performed by Kanter and Vernon (1972), Vystavkin and coworkers (1973), Ohta and coworkers (1973), and Likharev and Ulrich (1978). By a second order perturbation calculation the expression for the d.c. voltage variation induced by the external

radiation in the absence of fluctuations is given by Kanter and Vernon (1972):

$$\delta V = \frac{I_{\text{rf}}^2}{4} \frac{R}{I_1} \left(\frac{I_b^2}{I_1^2} - 1 \right)^{-3/2} \frac{\omega_0^2}{\omega_r^2 - \omega_0^2} \quad (11.5.5)$$

where $\omega_0 = (2e/\hbar)V_0$. I_b is the d.c. current bias and $V_0 = \bar{V}(t)$ is the time averaged value of the voltage across the device. Let us introduce the expression for the dynamic resistance:

$$R_d = \frac{dV_0}{dI_b} = R \frac{I_b}{I_1} \left[\left(\frac{I_b}{I_1} \right)^2 - 1 \right]^{-1/2} \quad (11.5.6)$$

This relation follows directly from the \bar{V}, I_b dependence for $\beta_J \gg 1$ (6.2.8) in the absence of external radiation.

In the two limits $\omega_r \ll \omega_0$ and $\omega_r \gg \omega_0$ (11.5.5) reduces to a more simplified form:

- (a) For $\omega_r \ll \omega_0$ the average voltage corresponding to the bias point is greater than the voltage at which the first induced step would appear. The expression (11.5.5) reduces to

$$\delta V \approx \frac{1}{4} I_{\text{rf}}^2 \frac{d^2 V_0}{dI_b^2} \quad (11.5.7)$$

where the relation

$$\left[\left(\frac{I_b}{I_1} \right)^2 - 1 \right]^{-3/2} = \frac{I_1}{R} \frac{d^2 V_0}{dI_b^2}$$

which directly follows from (11.5.6) has been used. In this limit the value of the junction impedance R_{rf} reduces to the dynamic resistance R_d . Therefore the coupled power, assuming that the coupling factor is 1, becomes

$$P_c = \frac{1}{2} I_{\text{rf}}^2 R_d \quad (11.5.8)$$

From (11.5.7) and (11.5.8) we obtain the responsivity S for $\omega_r \ll \omega_0$:

$$S \approx \frac{1}{2 R_d} \frac{d^2 V_0}{dI_b^2}$$

Since the signal is proportional to the curvature of the current voltage characteristics, that is, to $d^2 V_0 / dI_b^2$, the detection is said to be "classical" in this case.

- (b) For $\omega_r \gg \omega_0$ (11.5.5) becomes

$$\delta V \simeq \frac{\frac{I_{rf}^2}{4} \frac{R_d}{I_b} \left(\frac{2e}{\hbar} RI_1 \right)^2}{\omega_r^2} \quad (11.5.9)$$

where (11.5.6) and (6.2.8) have been taken into account. Since $R_{rf} \rightarrow R$ in this limit, the coupled power can be written as

$$P_c = \frac{1}{2} I_{rf}^2 R$$

and the expression for the responsivity in terms of the normalized frequency $\Omega = \hbar \omega_r / 2eRI_1$ is

$$S = \frac{1}{2} \frac{R_d}{I_b R \Omega^2} \quad (11.5.10)$$

Therefore with $\omega_0 \ll \omega_r$, we have for the responsivity an expression very similar to (11.5.4) which was previously obtained in the simple approximation $\Omega \gg 1$.

- (c) For $\omega_r = \omega_0$ the response has a singularity. However, when the effect of fluctuations is taken into account, this singularity is washed out.

Experimental data obtained by Kanter and Vernon (1972) with a point contact irradiated with a 90 GHz signal are reported in Fig. 11.18. The agreement with the theoretical predictions is satisfactory. As can be observed from the figure, the maximum sensitivity for a detector operating with the zero voltage step, is obtained for $\omega_0 \ll \omega_r$.

The maximum sensitivity for a device is determined by the signal value for which the signal-to-noise ratio is 1. Assuming that the noise is due only to thermal fluctuations in the weak link normal resistance R , the r.m.s. noise voltage can be written (Likharev and Semenov 1972) as

$$\delta V_N = \frac{R_d(I_b)}{R} \left[1 + \frac{1}{2} \left(\frac{I_b}{I_1} \right)^2 \right]^{1/2} (4k_B T R \Delta\nu)^{1/2} \quad (11.5.11)$$

where $\Delta\nu$ is the bandwidth of the postdetection system. To express the sensitivity in units of incident power, the noise equivalent power is used, which is defined by

$$\text{N.E.P.} = \frac{\delta V_N}{S} \quad (11.5.12)$$

In the limit of small voltage ($\omega_0 \ll \omega_r$) from (11.5.10), (11.5.11), and (11.5.12) it

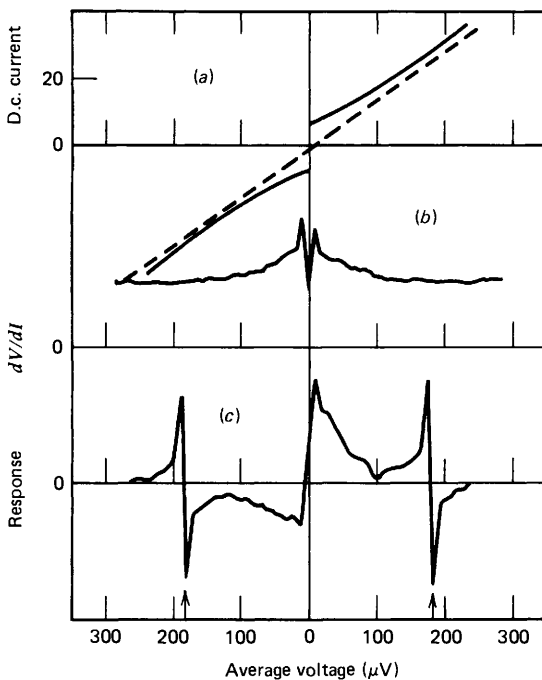


Figure 11.18 Measured V - I characteristic, dV/dI , and the voltage response at 90 GHz for a point contact. The arrows indicate the bias equivalent to applied frequency. (After Kanter and Vernon, Jr. 1972.)

is

$$\frac{\text{N.E.P.}}{\sqrt{\Delta\nu}} \simeq 2\sqrt{\frac{3}{2}} \left(\frac{\hbar}{2e}\right)^2 (4k_B T R)^{1/2} \frac{\omega_r^2}{(I_1 R)^2} \quad \text{W}/\sqrt{\text{Hz}}$$

The last expression states that in order to have optimum sensitivity (i.e., minimum value for N.E.P.), junctions with a high value of $I_1 R$ are required.

Table 11.1 compares experimental data for a Nb-Nb video detector (Kanter and Vernon 1972) and the theoretical performance of a detector biased on the step $n=1$ (i.e., for $\omega_0 = \omega_r$). Experimental data for a super-Schottky barrier detector (McColl, Millea, and Silver 1973) are also shown.

Point contact junctions as wideband detectors have been employed by Ulrich (1970, 1973) for astronomical applications and by Tolner, Andriesse, and Schaeffer (1976) as far infrared detectors. The spectral response of this kind of device has been investigated experimentally by Tolner (1977). Finally, we mention a configuration in which the point contact is coupled to the radiation via the magnetic field, which has been considered by So and Hamilton (1977). Clark (1968, 1973a,b) has investigated the behavior of square arrays of junctions made by pressing superconducting spheres. He has suggested the use of such structures as far infrared detectors.

TABLE 11.1 Video detectors performances

Characteristic Parameter	Josephson Detectors		Super-Schottky Diode Experiments ^c
	Experiments ^a	Theory ^b	
ν	90 GHz	150 GHz	10 GHz
$I_1 R$	4×10^{-4} V	9×10^{-4} V	
$S_I = S_v / R_d$	2×10^2 A/W	6×10^3 A/W	1.1×10^3 A/W
N.E.P.	5×10^{-15} W/ $\sqrt{\text{Hz}}$	4.84×10^{-16} W/ $\sqrt{\text{Hz}}$	2×10^{-15} W/ $\sqrt{\text{Hz}}$
T	4 K	2 K	1 K

^aKanter and Vernon (1972).^bOhta et al. (1973).^cMcColl, Millea, and Silver (1973).

Junction arrays can be useful to improving the matching of the source to the detector impedance. However, the impedance of square arrays is independent of their size: therefore they are more useful as detectors for multimode sources (Richards 1977).

Another way in which Josephson weak links have been used as wide band detectors is as bolometers. In these devices the output voltage is directly proportional to the temperature variation produced by the absorbed radiation. Clarke, Hoffer, and Richards (1973) taking advantage of the temperature dependence of the Josephson d.c. supercurrent have used a Pb-Cu-Al-Pb sandwich as the sensing element in a bolometer. The best sensitivity of this detector was a N.E.P. = 5×10^{-15} W/ $\sqrt{\text{Hz}}$ with a time constant $\tau = 3$ seconds.

11.5.2 Narrow Band Detectors. Josephson elements are also used as mixers in heterodyne detectors. In these devices the signal at a frequency ω_S , which has to be detected, is mixed with another signal (local oscillator) at a frequency ω_{LO} slightly different. The resulting signal at intermediate frequency ω_{IF} is detected by the intermediate frequency amplifier. Two different modes of operation are possible: with an external or an internal local oscillator. In the last configuration the local oscillator signal is generated by the Josephson element itself. Josephson junction mixer behavior has been extensively discussed in terms of the R.S.J. model by Auracher and Van Duzer (1972b, 1973); Taur, Claassen and Richards (1973, 1974a,b); Vystavkin et al. (1973); and Claassen and Richards (1978a). We now briefly describe the operating principles of a Josephson mixer with an external local oscillator. This is in fact the most often employed configuration. A simplified equivalent circuit for a Josephson mixer is sketched in Fig. 11.19. The r.f. current applied to the Josephson element is

$$I_{rf}(t) = I_S \sin \omega_S t + I_L \sin \omega_{LO} t$$

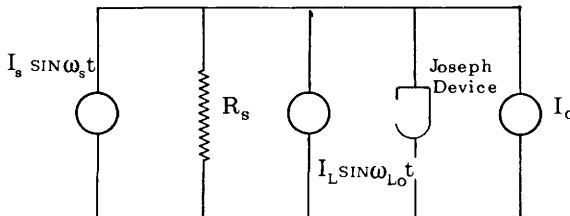


Figure 11.19 Simple equivalent circuit for a Josephson mixer.

Let us assume that the amplitude of the signal to be detected is much smaller than the local oscillator amplitude ($I_S \ll I_L$) and that $|\omega_S - \omega_{LO}| \ll \omega_{LO}$. Under this approximation the r.f. current applied to the junction is

$$I_{rf}(t) \approx [I_L + I_S \cos \omega_{IF} t] \sin \omega_{LO} t$$

where

$$\omega_{IF} = \omega_S - \omega_{LO}$$

Therefore the effect of the small signal is to amplitude modulate the local oscillator signal at a frequency that is much smaller than that of the two applied signals. Once again we can take advantage of the dependence of the zero voltage current I_1 by the external a.c. radiation (Fig. 11.7). The amplitude I_L of the local oscillator is chosen to depress the d.c. Josephson current to $\sim I_1(0)/2$. Around this point $I_1(I_{rf})$ varies linearly with the applied r.f. signal amplitude. Therefore I_1 will have a variation $\Delta I(t)$ at a frequency ω_{IF} and with an amplitude proportional to I_S . It is

$$\Delta I = I_S S \cos \omega_{IF} t$$

where

$$S = \left(\frac{\partial I_1}{\partial I_{rf}} \right)_{I_L}$$

is the slope in the I_1 vs. I_{rf} dependence (Fig. 11.7) for $I_{rf} = I_L$. If the junction is current biased between the zero voltage state and the first microwave induced step, and there is no hysteresis in the V - I curve, the amplitude of the voltage variation detected at the frequency ω_{IF} is

$$V_{IF} = R_d S I_S$$

where R_d is the dynamic resistance at the d.c. bias point. Let us observe that this mixing mode is similar to the wide band detection mechanism described in Section 11.5.1. A useful parameter to describe the mixer performances is the

overall conversion efficiency η defined as the ratio between the power P_{IF} delivered to the *IF* amplifier and available signal power P_S . The value of $\eta = P_{IF}/P_S$ computed for a nonresonant coupled junction in the R.S.J. model approximation (Auracher and Van Duzer 1972b) can be written in the form (Taur, Claassen, and Richards 1974b)

$$\eta = \frac{C_{IF}\alpha^2 R_d}{R} \quad (11.5.13)$$

where C_{IF} is the coupling efficiency at the *IF* amplifier and R_d and R are the dynamic and normal state resistances of the Josephson element. The dimensionless parameter α is defined by

$$\alpha = \frac{\partial(I_b/I_l)}{\partial[(8P_{LO}/RI_1^2)^{1/2}]}$$

where I_b is the d.c. bias current. This parameter can be computed using the R.S.J. model approximation. It is a function of P_{LO} , the source resistance R_s , and the normalized frequency $\Omega = \hbar\omega_s/2eRI_1$. Figure 11.20 gives theoretical data (Taur, Claassen, and Richards 1974a) for the values of R_s , which maximizes α^2 as a function of Ω . The dependence of α_{\max}^2 on Ω is also shown.

If we assume that $P_{LO} = I_{LO}^2 R_s / 8$ the conversion efficiency can be written as

$$\eta = C_{IF} S^2 \frac{R_d}{R_s} \quad (11.5.14)$$

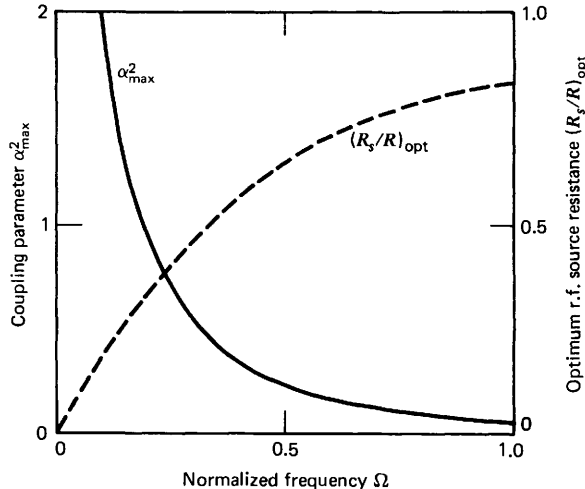


Figure 11.20 The maximum value of the mixer coupling parameter α and the optimum r.f. source impedance R_s computed from the R.S.J. model as a function of the dimensionless frequency Ω . (After Taur, Claassen, and Richard 1974.)

where S is the slope of the I_1 vs. I_{LO} dependence and has been previously defined. This is the expression for η given by Auracher and Van Duzer (1972b). Using (11.5.13), the best values for the conversion efficiency, as seen in Fig. 11.20, are obtained for $\Omega \ll 1$. This result follows also from (11.5.14). In fact (Auracher and Van Duzer 1973), S^2 approaches 1 for $\Omega \rightarrow 0$ and goes like $(0.581/\Omega)^2$ for large Ω values. The dynamic resistance for small value of Ω can be made very high by a proper choice of the local oscillator current I_L and is only noise limited. For large values of the normalized frequency Ω , R_d is noise independent and has a low value ($R_d \sim R$). Therefore, to get higher values for η , the parameter RI_1 of the device used must be very large compared to $\hbar\omega_S/2e$. Another very useful parameter for comparing mixer performances is the noise temperature T_M defined by

$$T_M = \frac{T_N C_{IF}}{\eta}$$

where T_N is the temperature at the input of the *IF* amplifier. If we assume that the only source of noise is thermal noise across the normal resistance R of the junction, T_N can be written as (Claassen, Taur, and Richards 1974)

$$T_N = \beta_N^2 T \frac{R_d}{R}$$

where β_N^2 is a dimensionless parameter, which is relatively insensitive to R_d and to the ambient temperature T . It is a function of the bias point and of the normalized frequency Ω .

The first experimental investigations of the mixing properties of Josephson devices have been carried out by Grimes and Shapiro (1968) on point contact junctions. The most extensive investigation has been performed at 36 GHz by Taur, Claassen, and Richards (1973, 1974a, 1974b). The apparatus used is sketched in Fig. 11.21. The point contacts were made of niobium or vanadium. The microwave radiation was resonantly coupled to the point

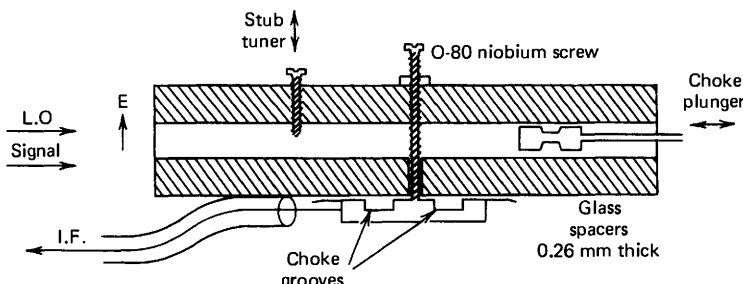


Figure 11.21 Niobium waveguide assembly for a 36 GHz Josephson junction mixer. (After Taur, Claassen, and Richards 1974.)

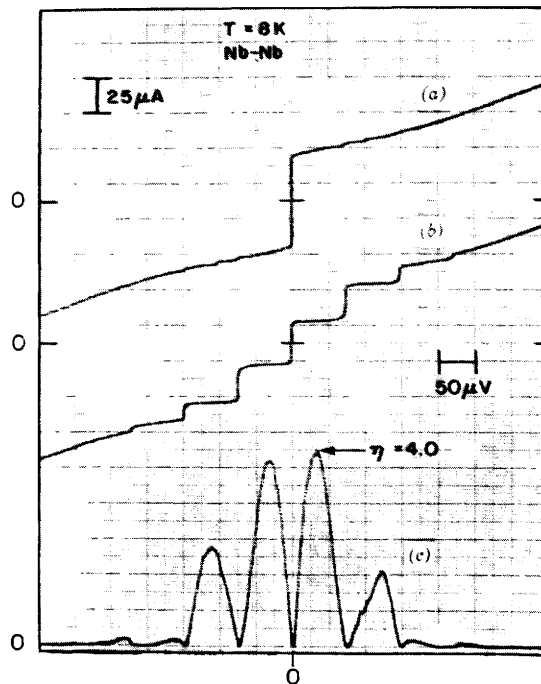


Figure 11.22 Junction current (a) without and (b) with 36 GHz r.f. local oscillator and conversion efficiency (c) for a niobium point contact mixer. (After Taur 1974.)

contact with a choke plunger and a tuning stub. In Fig. 11.22 typical experimental values of the conversion efficiency η as a function of the voltage bias are reported. As can be observed, the largest values of η are achieved between steps where R_d has its maximum value. The peak values of η range up to 4 and are in good agreement ($\pm 20\%$) with the theoretical data computed using the R.S.J. model approximation.

Table 11.2 lists typical experimental data for a vanadium point contact mixer, together with the best performance for a super-Schottky diode mixer (McColl et al. 1976).

TABLE 11.2 Comparison between Mixer performances

Material	Josephson Mixer ^a (V Point Contact)	Super-Schottky Mixer ^b (Pb-Ga As Diode)
T	1.4 K	1.1 K
ν	36 GHz	9 GHz
η	1.35	0.12
T_M	54 K	13 K
P_{LO}	10^{-9} W	2×10^{-8} W

^aClaassen, Taur, and Richards (1974).

^bMcColl et al. (1976).

Harmonic mixing has also been investigated by the abovementioned authors (Taur, Claassen, and Richards 1973). In this case the external local oscillator has a frequency much lower than the signal frequency. The mixing occurs between a harmonic component at a frequency near the signal frequency ω_s , generated inside the Josephson element by the local oscillator signal. The theory for this kind of mixing has been considered by Levinsen and Ulrich (1974) and by Claassen and Richards (1978a). Further experimental investigation has been carried out on point contacts at 95 GHz by Kanter (1973b) and at 891 GHz by Blaney (1973). Mixing experiments on niobium variable thickness bridges have been performed by Wang et al. (1977). Typical data for this kind of sample are reported in Fig. 11.23. Usually in all the experiments

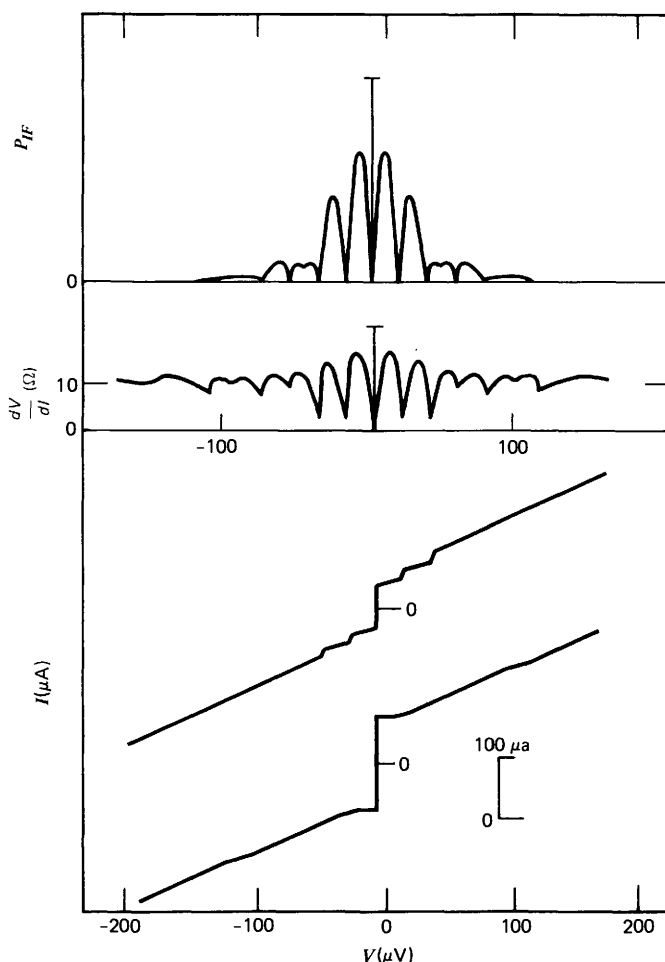


Figure 11.23 Bridge characteristics at 6.57 K showing V - I curves without and with microwaves, dynamic resistance, and intermediate frequency output at 60 MHz with local oscillator power at 9.90 GHz. (After Wang et al. 1977.)

mentioned a qualitative agreement with the R.S.J. model is found. The values obtained for the conversion efficiency are much smaller than those theoretically expected, probably because of the poor coupling or the nonideal properties of the weak links used.

Experiments at 140 GHz by Richards, Claassen, and Taur (1975) and at 130 GHz by Claassen and Richards (1978b) are in good agreement with the theory, as are the results of these authors at 36 GHz.

A Josephson mixer with a niobium point contact that is permanently adjusted has been designed by Taur and Kerr (1978a,b). The device is cyclable and exhibits a noise temperature $T_M \approx 120$ K and a conversion efficiency $\eta \sim 1$ at $\nu_s \approx 115$ GHz. Fundamental and harmonic mixing have been observed with HCN laser radiation at 891 GHz by McDonald et al. (1969). The highest frequency fundamental mixing experiments so far reported are those by McDonald et al. (1973). These authors have investigated the properties of niobium point contact junctions with $9.5 \mu\text{m}$ (32 THz) radiation from two CO₂ lasers. The data are analyzed in terms of the Werthamer theory, since the frequency used is much greater than the energy gap frequency. Although at this frequency heating is a serious problem and can be responsible for the *IF* signal observed, it is probable that mixing has been observed.

Considerable effort has been devoted to the investigation of harmonic mixing of microwave local oscillator signals with infrared laser radiation (McDonald et al. 1971; Lourtioz et al. 1977; Blaney and Knight 1974; McDonald et al. 1972). The purpose is to extend the applicability of Josephson mixers to this range. Since the devices are used mainly for frequency comparison, a relatively high input power is available and the coupling problem imposes a less severe limitation.

Finally, we mention the potential properties of series arrays to solve the problem of impedance matching between the Josephson weak link and the input and output circuit (Richards 1977; Claassen and Richards 1978a). Configurations of this kind may help to make possible the use as mixers of thin film structures, which have impedances that are too low.

11.6 Parametric Amplification

From the two expressions (1.4.4) and (1.4.5) which hold for the pure Josephson element it is easy to derive the relation

$$V = \frac{d}{dt} (L_J(I)I)$$

where V is the voltage across the junction and I the total current. The quantity L_J is defined by

$$L_J(I) = L_1 \frac{\sin^{-1}(I/I_1)}{I/I_1} \quad (11.6.1)$$

where

$$L_1 = \frac{\hbar}{2eI_1}$$

and is the equivalent inductance. I_1 as usual is the maximum d.c. Josephson current. Therefore at zero bias the Josephson element behaves as a nonlinear inductor of zero current value equal to L_1 . Equation 11.6.1 is plotted in Fig. 11.24. As can be observed, the nonlinear behavior is stronger for bias current values near I_1 . Because of the presence of this nonlinear reactance when the Josephson element is subjected to external radiation, frequency mixing can occur with consequent transfer of power from one frequency to another. In the absence of dissipation, the power flow is governed by the Manley-Rowe (1956) relations.

In the case in which only two external signals at frequencies ω_p and ω_s are applied to the device, these relations can be written as

$$\sum_{m=0}^{+\infty} \sum_{n=-\infty}^{+\infty} \frac{mP_{m,n}}{m\omega_p + n\omega_s} = 0$$

$$\sum_{n=0}^{+\infty} \sum_{m=-\infty}^{+\infty} \frac{nP_{m,n}}{m\omega_p + n\omega_s} = 0 \quad (11.6.2)$$

where $P_{m,n}$ is the power flow at a frequency $m\omega_p + n\omega_s$ and is positive or negative depending on whether it is flowing into or from the inductor. Therefore a Josephson element can be employed to realize parametric devices. Its behavior is analogous to that of varactors. The theory developed for these

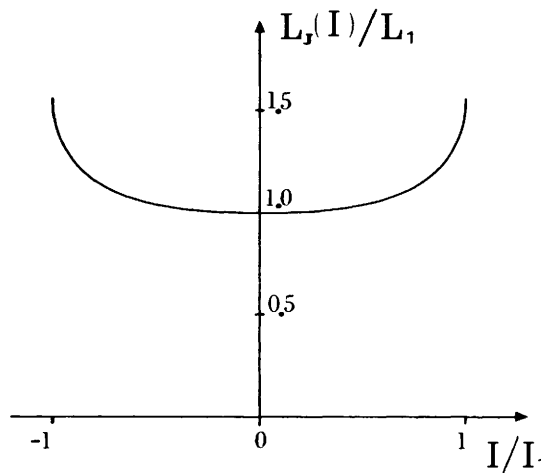


Figure 11.24 Zero d.c. voltage equivalent inductance of a Josephson element as a function of the supercurrent.

nonlinear inductors can be applied to the Josephson elements (Blackwell and Kotzebue 1961; Pennfield and Rafuse 1962). However, there are some important differences from passive elements. For example, since the Josephson element is an active element, it can convert d.c. power to a.c. power directly. Also, a dissipative term is present in parallel with the Josephson inductance.

In what follows we are concerned essentially with the properties of Josephson junction parametric amplifiers. Two different general configurations are possible depending on whether the source of the pump frequency ω_p is external or internal to the Josephson element. Since more progress has been made with externally pumped devices, this class of amplifiers is examined in more detail.

11.6.1 Parametric Amplifiers with Externally Pumped Josephson Elements. As is usual in analyzing these devices, we assume that the circuit to which the Josephson inductor is coupled is designed to be a short circuit for any frequency different from the pump, signal, and idler frequencies ω_p , ω_s , and ω_i . Depending on the relations among these three characteristic frequencies, different configurations are possible. If we assume that $2\omega_p = \omega_s + \omega_i$, we have the doubly degenerate parametric amplifier. The other configuration investigated has been the singly degenerate amplifier for which $\omega_p = \omega_s + \omega_i$. It can be shown that both kinds are negative resistance amplifiers (Blackwell and Kotzebue 1961). In fact, let us consider as an example the doubly degenerate device. The Manley-Rowe relation (11.6.2) reduces to

$$\frac{P_p}{\omega_p} + 2\frac{P_i}{\omega_i} = 0$$

$$\frac{P_s}{\omega_s} = \frac{P_i}{\omega_i} \quad (11.6.3)$$

If the power is supplied at the pump frequency only, P_p is positive and from (11.6.3) P_i and P_s are negative. Therefore power is coming out from the nonlinear Josephson reactance at the signal and idler frequency. The maximum power transfer between pump and signal is given by

$$\frac{P_s}{P_p} = \frac{\omega_s}{2\omega_p}$$

Therefore, since power at ω_s is extracted also in the absence of input power at ω_p , the power gain at the signal frequency can be infinite. As an example of this kind of behavior, Fig. 11.25 shows the spectrum analyzer pictures of the reflected power from a doubly degenerate point contact configuration (Taur and Richards 1977). Only the signal at the pump frequency (central peak at ~ 36 GHz) is applied to the device. The parametric generated signal and idler signals are clearly evident.

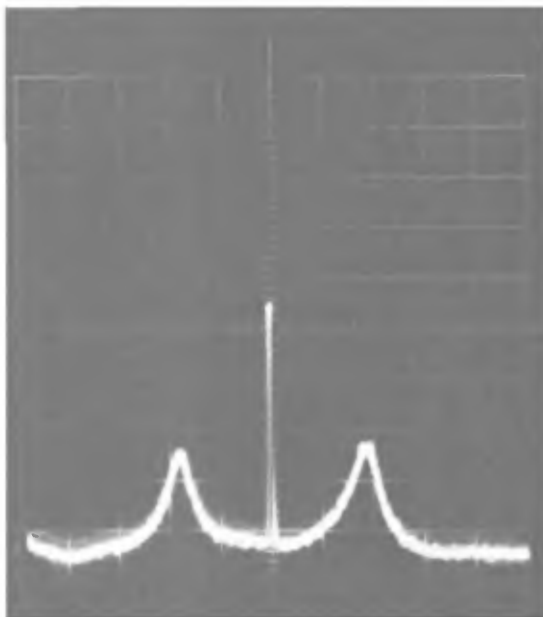


Figure 11.25 Reflected microwave power vs. frequency for a junction in the presence of radiation at the pump frequency. Parametric excitation is clearly evident. (Courtesy of Y. Taur.)

Let us consider now in more details the doubly degenerate parametric amplifier. To take advantage of the symmetry in the Josephson parametric inductance, no d.c. bias is applied. Since the relation $2\omega_p = \omega_s + \omega_i$ holds, the pump, signal, and idler frequency are close sidebands and the same resonant circuit can be used for them. The device has been called SUPARAMP (Feldman, Parrish, and Chiao 1975). The theoretical analysis can be worked out in the small signal approximation by using the simple voltage bias model for the Josephson element (Parrish et al. 1973; Feldman, Parrish, and Chiao 1975; Feldman 1975, 1977). Let us assume that the a.c. voltage across the Josephson device is

$$v(t) = v_p \cos \omega_p t + v_s \cos(\omega_s t + \theta_s) + v_i \cos(\omega_i t + \theta_i)$$

From the Josephson relation (1.4.5) the phase difference is

$$\varphi(t) = a_p \sin(\omega_p t) + a_s \sin(\omega_s t + \theta_s) + a_i \sin(\omega_i t + \theta_i)$$

where we have assumed that no d.c. voltage bias is present and have defined the normalized signal amplitudes as

$$a_p = \frac{2ev_p}{\hbar\omega_p}; \quad a_s = \frac{2ev_s}{\hbar\omega_s}; \quad a_i = \frac{2ev_i}{\hbar\omega_i} \quad (11.6.4)$$

let us assume now that the signal and idler voltages are small. This restriction is expressed by imposing

$$a_s \ll 1; \quad a_i \ll 1$$

In this “small signal” approximation the Josephson current is

$$\begin{aligned} i(t) = & I_1 \sin(a_p \sin \omega_p t) + I_1 [a_s \sin(\omega_s t + \theta_s) \\ & + a_i \sin(\omega_i t + \theta_i)] \cos(a_p \sin \omega_p t) \end{aligned}$$

By using the Fourier-Bessel expansion (11.1.3), we get for the amplitude of the currents at the three characteristic frequencies:

$$I_p = -2jI_1 J_1(a_p) \quad (11.6.5a)$$

$$I_s = -j \frac{2eI_1}{\hbar} \left[J_0(a_p) \frac{V_s}{\omega_s} - J_2(a_p) \frac{V_i^*}{\omega_i} \right] \quad (11.6.5b)$$

$$I_i = -j \frac{2eI_1}{\hbar} \left[J_0(a_p) \frac{V_i}{\omega_i} - J_2(a_p) \frac{V_s^*}{\omega_s} \right] \quad (11.6.5c)$$

where complex notation is used. $J_n(x)$ are Bessel functions of integer order. Let us observe that V_s and V_i are complex numbers and that the phase factors θ_s and θ_i with respect to the pump signal have been included in them. Equations 11.6.5b and 11.6.5c which relate the signal and idler voltages can be expressed in terms of an admittance matrix:

$$\begin{bmatrix} I_s \\ I_i^* \end{bmatrix} = \begin{bmatrix} Y_{ss} & Y_{si}^* \\ Y_{is} & Y_{ii}^* \end{bmatrix} \begin{bmatrix} V_s \\ V_i^* \end{bmatrix} \quad (11.6.6)$$

where

$$Y_{ss} = -j \frac{J_0(a_p)}{L_1 \omega_s} \quad Y_{si} = -j \frac{J_2(a_p)}{L_1 \omega_i}$$

$$Y_{is} = -j \frac{J_2(a_p)}{L_1 \omega_s} \quad Y_{ii} = -j \frac{J_0(a_p)}{L_1 \omega_i}$$

Therefore there are two contributions to the current at each frequency. One is induced by the voltage at the same frequency through the inductance $L_1/J_0(a_p)$ where L_1 is the Josephson inductance. The other is a cross coupling term induced by the other frequency signal. This process is regulated by the inductance $L_1/J_2(a_p)$ and is responsible for the parametric amplification. The terms Y_{ss} and Y_{ii} are called self-coupling susceptances, and Y_{si} and Y_{is} cross

coupling susceptances. These terms are strongly dependent on the pump power through the parameter a_p in the Bessel function argument.

So far we have examined the behavior of an ideal isolated Josephson element. To compute the properties of a real parametric amplifier the Josephson device must be coupled to an external circuit in order to supply and extract power from it. The circuit model used for the theoretical analysis is reported in Fig. 11.26. The transmission line is terminated by Y_T which is purely imaginary. G_0 represents the effect of source and load impedance which are supposed to be perfectly matched to the transmission line impedance $Z_0 = 1/G_0$. In a physical circuit a circulator would be required to separate source and load. C and R_J are the junction capacitance and equivalent shunt resistance. The index k in the figure stands for p , s , and i respectively. The transmitted and reflected traveling waves of Fig. 11.26 must satisfy the relations

$$I_k^\pm = G_0 V_k^\pm$$

The resulting current and voltage at the junction terminals are

$$\tilde{I}_k = I_k^+ - I_k^-$$

$$V_k = V_k^+ + V_k^-$$

The incident and reflected powers at the signal frequency ω_s are

$$P_s^\pm = \frac{1}{2} G_0 |V_s^\pm|^2 = \frac{1}{8G_0} |\tilde{I}_s \pm G_0 V_s|^2 \quad (11.6.7)$$

The signal power gain Γ_s can be computed by the ratio of the incident to reflected power:

$$\Gamma_s = \frac{P_s^-}{P_s^+} = \left| \frac{Y_s - G_0}{Y_s + G_0} \right|^2 \quad (11.6.8)$$

where we have defined the signal input admittance $Y_s = \tilde{I}_s / V_s$. To evaluate Γ_s ,

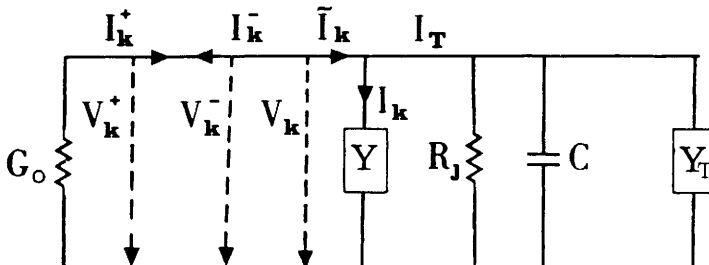


Figure 11.26 Equivalent circuit for the doubly degenerate parametric amplifier.

we must compute the expression for Y_s . This can be done by observing that the total signal current \tilde{I}_s is given by

$$\tilde{I}_s = I_s + I_T \quad (11.6.9)$$

where I_s is the signal current flowing in the Josephson admittance and can be computed by the admittance matrix (11.6.6). I_T is the current flowing in the other elements and is given by

$$I_T = V_s(G_J + j\omega_s C + Y_T)$$

Dividing (11.6.9) by V_s and inserting the expression for I_s and I_T , we get

$$Y_s = \frac{\tilde{I}_s}{V_s} = Y_{ss} + G_J + Y_T + j\omega_s C + Y_{si}^* \frac{V_i^*}{V_s} \quad (11.6.10)$$

In the case of small value of the pump power ($a_p \ll 1$), the cross coupling admittance Y_{is}^* is negligible. The junction admittance becomes

$$Y_s = G_J + j \left(\omega_s C - \frac{J_0(a_p)}{L_1 \omega_s} \right) \quad (11.6.11)$$

where the termination admittance has also been neglected and the explicit expression for Y_{ss} has been inserted.

From (11.6.11) we find the resonance condition

$$\omega_s C - \frac{J_0(a_p)}{L_1 \omega_s} = 0$$

from which the resonant frequency follows:

$$\tilde{\omega}_s^2 = \frac{2e}{\hbar} \frac{I_1}{C} J_0(a_p) = \omega_J^2 J_0(a_p)$$

If C is the intrinsic capacitance of the Josephson element, the resonance frequency is just the plasma frequency in which the dependence of the maximum Josephson current I_1 on the pump power is explicitly taken into account. In the general case, for arbitrary values of a_p the expression V_i^*/V_s in (11.6.10) can be evaluated computing the expression for \tilde{I}_s^* . The procedure is analogous to that used to compute \tilde{I}_s . By inserting (11.6.10) in (11.6.8) we get the general expression for the power signal gain valid for $\omega_p = \omega_i = \omega_s = \omega$ (Feldman 1975; Feldman, Parrish, and Chiao 1975):

$$\Gamma_s = 1 - \frac{4g\Omega^2}{D} + \Gamma_{is} \quad (11.6.12)$$

where

$$\Gamma_{is} = \frac{P_i^-}{P_s^+} = \frac{4g^2\Omega^2 J_2^2(a_p)}{D^2} \quad (11.6.13)$$

is called the idler conversion gain. The expression for D is

$$D = \Omega^2(1+g) + (J_0(a_p) - \Omega B_T)^2 - J_2(a_p) \quad (11.6.14)$$

where g and Ω are dimensionless parameters defined by

$$g = \frac{G_0}{G_J} = \frac{R_J}{Z_0}$$

$$\Omega = \omega L_1 G_J = \frac{\hbar\omega}{2eJ_1 R} \quad (11.6.15)$$

and B_T has been defined (Wahlsten, Rudner, and Claeson 1977) as

$$jB_T = R_J(j\omega C + Y_T)$$

When a series array of N identical junctions is used instead of just one junction, the dimensionless parameter g must be replaced by

$$g_N = \frac{G_0 N}{G_J} = \frac{N R_J}{Z_0}$$

Arrays of junctions are desirable for improving the matching to the transmission line. Another important point is that in order to reduce saturation problems one must require $g_N \gg 1$ (Feldman 1975, 1977), which can be more easily achieved by using a large number of junctions in series. The quantity D appears in the denominator of both Γ_s and Γ_{is} . When $D=0$, the condition of infinite gain is realized. In this limit, as can be seen from (11.6.12) and (11.6.13), the signal gain Γ_s approaches the idler conversion gain Γ_{is} . In the plane of the parameters Ω and g the curve of infinite gain $D(\Omega, g)=0$ defines two regions. In the one under the curve the gain vs. pump power is hysteretic, while in the external region the curve is nonhysteretic. The situation is illustrated in Fig. 11.27. The maximum gain condition is realized for points as close as possible to the curve $D(\Omega, g)=0$. This curve is often referred to as the I.N.G. curve (infinite, nonreentrant gain). In a real device, as shown in the inserts in Fig. 11.27, the gain is finite on the I.N.G. curve. In the theoretical analysis for the SUPARAMP we have just reported, effects of the $\cos\varphi$ term in the Josephson current have not been considered. It has been assumed that $\epsilon = \sigma_1/\sigma_0 = 0$. A complete derivation which accounts also for the $\cos\varphi$ term has been given by Feldman (1975) and by Feldman, Parrish, and Chiao (1975).

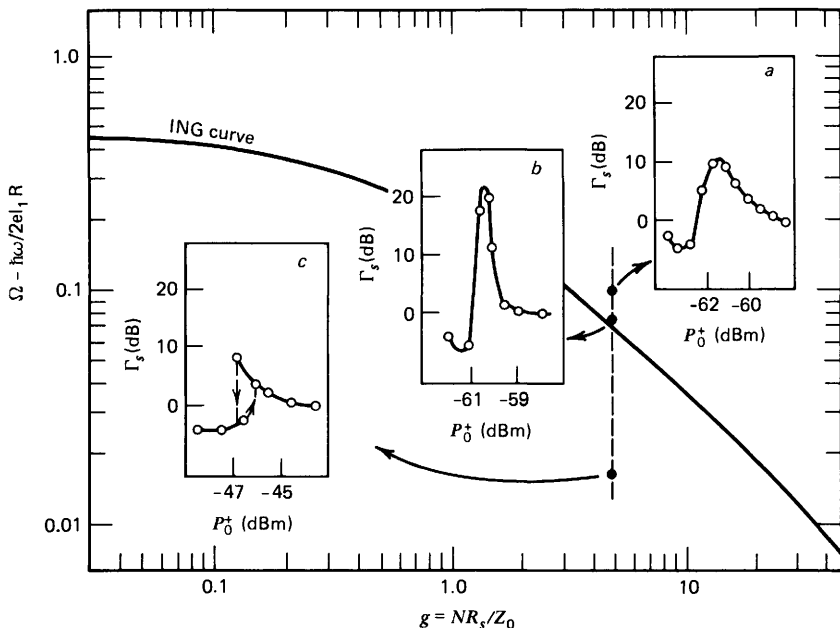


Figure 11.27 The behavior of the SUPARAMP in the plane of the two dimensionless parameters g and Ω . The curve of infinite nonreentrant gain (I.N.G.) divides the (g, Ω) plane into two regions. Above that curve, the signal gain Γ_s has a smooth maximum as a function of the applied pump power P_0^+ , with a fairly large power width. This is illustrated with data from an array of junctions in inset (a). As the I.N.G. curve is approached, the gain increases at the expense of the power width, inset (b). For values of (g, Ω) lying on the I.N.G. curve, the gain peak becomes infinitely high over a diminishing power width in the ideal case. Below the I.N.G. curve, the signal gain is a reentrant function of pump power, inset (c). It displays a hysteretic behavior, and an amplifier operated in this region is unstable. To operate the SUPARAMP with a high stable gain, g and Ω should be chosen to lie slightly above the I.N.G. curve. (After Wahlsten, Rudner, and Claeson 1978.)

Expressions for Γ_s and Γ_{is} , which include the $\cos\varphi$ dependence and the dependence of the Josephson current on the magnetic field, have been reported by Wahlsten, Rudner, and Claeson (1978).

First preliminary experimental observations of parametric effects in tunneling junctions have been reported by Zimmer (1967). The device was coupled to a rutile resonator and was working in the doubly degenerate mode. The first thorough experimental investigation on this kind of parametric amplifier has been performed by Parrish and Chiao (1974). The device employed a series array of tin Dayem bridges. The pump frequency was 10 GHz, and it was coupled to the array by a parallel plate stripline with an open circuit at a distance $\lambda/4$ from the array. The schematic of the experimental apparatus is shown in Fig. 11.28. As can be seen in the inset, a tuning stub consisting of an open ended $\lambda/12$ orthogonal stripline is employed to short out unwanted harmonics. A typical spectrum analyzer of the reflected signal from the

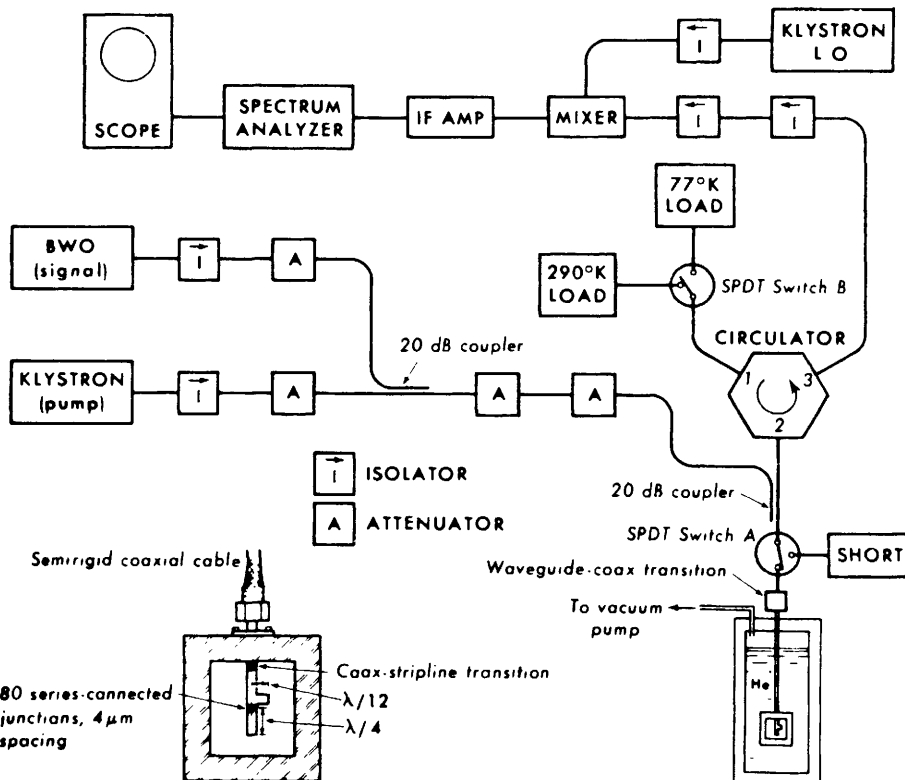


Figure 11.28 Schematic of the experimental apparatus for the parametric amplifier. X band waveguide components were used everywhere up to the Dewar inset, where coaxial and microstrip components were used. The width of the microstrip is 22 mils and the thickness of its fused quartz substrate 10 mils. (After Parrish and Chiao 1974.)

parametric amplifier is shown in Fig. 11.29. The experimental data on bridge arrays have been compared with the theory developed using the voltage bias model which is not very adequate for samples of this kind. (Feldman, Parrish, and Chiao 1975). However, a satisfactory agreement between experiments and theory has been obtained. Successful operation of a bridge array at 33 GHz (Chiao and Parrish 1976) has been reported. Experiments on point contacts at 36 GHz have been carried out by Taur and Richards (1977), who have also developed a theoretical analysis valid for current biased devices based on the R.S.J. model approximation. In these current biased devices a sharp rise in the noise output associated with the presence of gain in the parametric amplification process is often observed.

As Chiao and coworkers (1978) have shown, this phenomenon appears to be related to phase instability and does not occur in voltage biased devices. Wahlsten, Rudner, and Claeson (1977, 1978) have operated at 10 GHz a SUPARAMP with a series array of tunnel junctions (see Fig. 11.30). In this

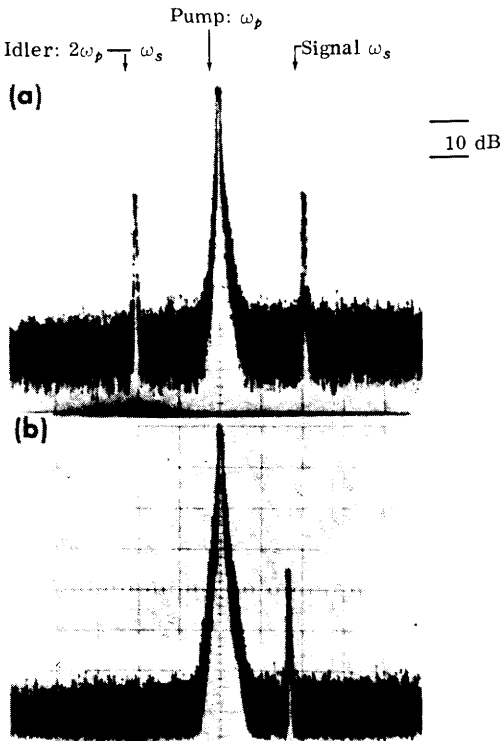


Figure 11.29 (a) Output spectrum of parametric amplifier. The vertical scale is logarithmic in power (10 dB/div); the horizontal is linear in frequency (2 MHz/div). The resolution was 0.1 MHz; the pump power was 0.17 μ W. (b) Input spectrum of parametric amplifier. (After Parrish and Chiao 1974.)

device each junction is r.f. voltage biased by the parallel capacitance. A magnetic field parallel to the junctions was used to conveniently tune the amplifier. In fact, since I_1 is magnetic field dependent, it is possible in this way to adjust the parameter Ω (11.6.15). In Fig. 11.31 experimental data for the signal gain dependence on the pump power for different input noise temperature are reported. The agreement between the performance of this tunnel junction SUPARAMP and the theoretical analysis based on the voltage biased model is excellent. Preliminary results on a junction array parametric amplifier operated at 33 GHz have been reported by Goodall and coworkers (1978). A gain greater than 13 dB has been observed.

Another very interesting configuration of an externally pumped parametric amplifier has been developed by the group at the Technical University of Denmark. This work started with the discovery made with an electrical analog that a signal at the plasma frequency ω_p was parametrically excited when the junction was biased by an r.f. signal at a frequency equal to $2\omega_p$ (Pedersen, Samuelsen, and Saermark 1973a,b). This effect was experimentally observed

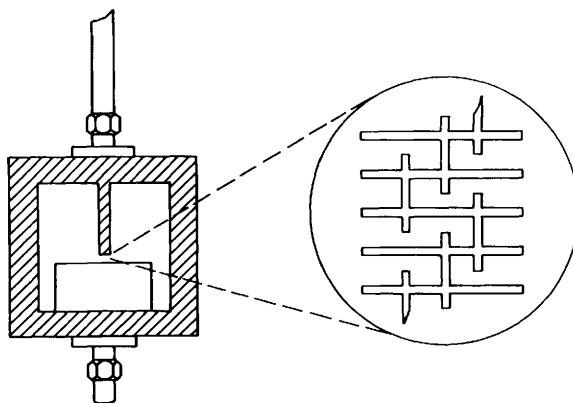


Figure 11.30 Geometry of the microstrip and tunnel junction array. Thirty tunnel junctions ($8 \times 8 \mu\text{m}$) cover a 0.8 mm space between the 50Ω , 1.2 mm wide lead microstrip and a ground plane, both 300 nm thick. The latter is grounded via a nonsuperconducting short at the lower end of the holder. A detail of the array is shown to the right. The junctions are formed in the shaded intersections between the strips. (After Wahlsten, Rudner, and Claeson 1978.)

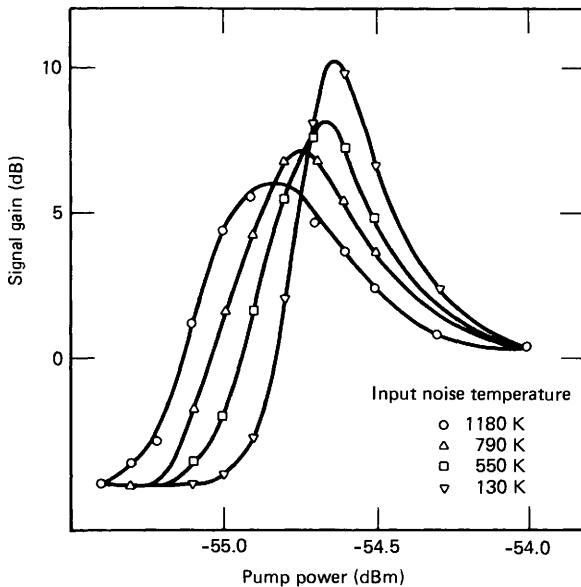


Figure 11.31 Signal gain of the junction array parametric amplifier for different input noise temperatures. Note the shift toward lower pump levels for the peak gain and the broadening of the curves as the input noise temperature increases. $\Gamma_s^{3/4} \Delta P / P_0 = 0.30 \pm 0.03$ for the four curves. (After Wahlsten, Rudner, and Claeson 1978.)

on tunneling junctions first indirectly (Bak et al. 1975) and later by direct detection of the generated plasma frequency radiation (Mygind, Pedersen, and Soerensen 1976). The device is called singly degenerate parametric amplifier. In fact, the relation between the three characteristic frequencies is

$$\omega_p = \omega_s + \omega_i$$

Therefore in this case only one pump photon decays in one signal and idler photon. A d.c. current bias is applied to the junction to tune the amplifier. The signal power conversion gain for this device, computed in the framework of the R.S.J. model, is (Soerensen, Mygind, and Pedersen 1978)

$$\Gamma_s = 1 + \frac{4\Omega^2 A^2 g^2}{\tilde{D}}$$

where now the denominator is

$$\tilde{D} = \Omega^2(1 + g^2) + \Omega^2 A^2 - B^2$$

The frequency in the dimensionless parameter Ω is $\omega = \omega_p/2$ and is half the pump frequency. The parameter A accounts for the detuning from the plasma frequency ω_j and is defined by

$$\Omega^2 A^2 = \left[\left(\frac{\omega_p}{2\omega_0} \right)^2 - \left(\frac{\omega_j}{\omega_0} \right)^2 \right]^2$$

where $\omega_0^2 = 2eI_1/\hbar C$ is the zero d.c. current value of the plasma frequency and is related to ω_j by the expression

$$\omega_j^2 = \omega_0^2 \cos \left[\sin^{-1} \frac{I}{I_1} \right]$$

in which I/I_1 is the d.c. current flowing into the junction normalized to the maximum value of the Josephson current I_1 .

The term B is responsible for the parametric amplification and is given by

$$B = J_1(a_p) \frac{I}{I_1}$$

where $J_1(x)$ is the Bessel function of order 1 and accounts for the pump power dependence.

Experimental results on a singly degenerate parametric amplifier at a pump frequency of 18 GHz have been reported by Mygind, Pedersen, and Soerensen (1978). The sample used was a single Sn-O_x-Sn junction coupled to the microwave system by a two section binomial microwave transformer. The

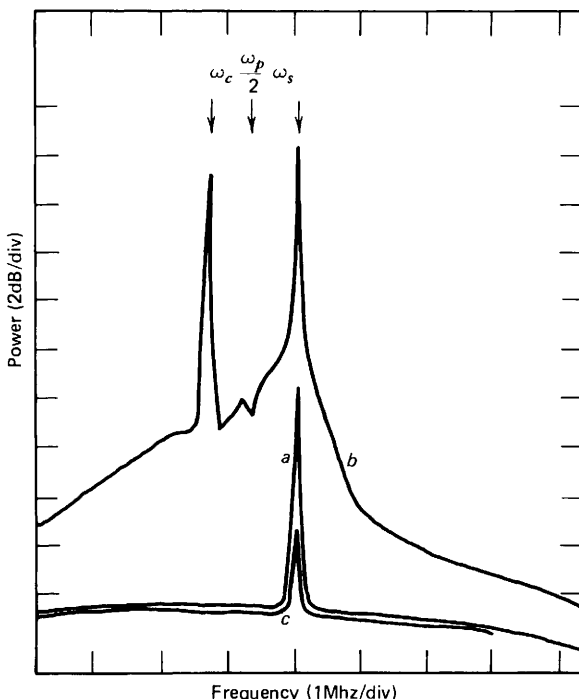


Figure 11.32 A frequency display of the singly degenerate parametric amplifier output. (a) The input signal applied directly to the receiver; (b) the signal after amplification in the junction; (c) the signal reflected from the junction in a “nonparametric” state. (After Mygind, Pedersen, and Soerensen 1978.)

signal and idler frequencies were approximately equal to $\omega_p/2$ ($\simeq 9$ GHz). The received power from the parametric amplifier as a function of the frequency is reported in Fig. 11.32. The local oscillator frequency in the detection system was 8.67 GHz, the signal frequency was 8.60 GHz, and the pump frequency was 17.20 GHz. Parametric amplification at 35 GHz has been reported by Mygind and coworkers (1979) in a single Josephson junction operating in the singly degenerate mode.

Finally, we mention a different mode of operation of an externally pumped parametric amplifier which has been theoretically investigated by Pedersen (1976). It is a zero voltage nondegenerated parametric mode in which the signal frequency is at the plasma resonance and the idler frequency at a geometrical resonance of the junction. To give an idea of the performances achieved with externally pumped Josephson parametric amplifiers, typically obtained experimental results are reported in Table 11.3.

11.6.2 Internally Pumped Parametric Amplifiers. In this class of devices the pump frequency is internally generated by voltage biasing the Josephson element. Therefore an energy conversion process in which d.c. power is

TABLE 11.3 Experimental performances of Josephson parametric amplifiers

Sample Used	Signal Frequency ω_s (GHz)	Signal Gain Γ_s (dB)	Bandwidth (MHz)	Noise Temperature (K)
80 tin microbridges ^a	10	12	$\sim 1 \times 10^3$	26
Niobium single point contact ^b	36	~ 13		$\lesssim 50$
30 lead tunnel junctions ^c	10	23	12	
10 and 40 tunnel junctions ^d	10	20	15	30 ± 20
Single tunnel junction ^e	35	4–12	15	$\gtrsim 50$

^aParrish and Chiao (1974).

^bTaur and Richards (1977).

^cWahlsten, Rudner, and Claeson (1977).

^dWahlsten, Rudner, and Claeson (1978).

^eMygind et al. (1979).

converted to a.c. power is present. The Manley-Rowe relations have been generalized to account for this process by Russer (1971) and by Thompson (1973). The properties of this kind of parametric amplifiers have been theoretically investigated for different equivalent circuit configurations (Vystavkin et al. 1970, 1973). Parametric gain of 11 dB has been measured at a signal frequency of 30 MHz by Kanter and Silver (1971). Experiments at 9 GHz have been performed by Kanter (1973a) who has reported also, with a similar apparatus, observation of parametric upconversion (1975). A thorough theoretical and experimental analysis of the performance of a nondegenerate internally pumped parametric amplifier has been carried out by Vystavkin and coworkers (1976).

11.7 The Determination of $2e/h$ and the Voltage Standard

As we saw in Chapter 1 and earlier in this chapter, when a Josephson junction is irradiated by a microwave signal at a frequency ω_r , a set of current steps appears in the V - I characteristic. The voltage at which the n th step occurs is directly proportional to the applied frequency through (11.1.1), the constant of proportionality being the fundamental constant $2e/h$. The relation (11.1.1) is quite general and follows directly from the macroscopic quantum properties of the superconducting state. It is independent of the temperature or the magnetic field and of the particular kind of weakly coupled Josephson structure used (Langenberg, Parker and Taylor 1966a; Parker et. al. 1969; Clarke 1968; Finnegan, Denestein and Langenberg 1971; Bracken and Hamilton 1972). Therefore by an independent measure of the step voltage and of the frequency ω_r of the applied radiation a very accurate determination of the value of $2e/h$

can be performed (Parker, Taylor and Langenberg 1967). Parker and co-workers (reference quoted above) using this method in 1969 found a value of $2e/h$, in absolute units, 38 ppm smaller than the previously known one. The measurement of e/h by the Josephson effect had a dramatic impact on the knowledge of the physical constants and played a prominent role in the least mean square readjustment of the fundamental constants performed in 1969 (Taylor, Parker, and Langenberg 1969, 1970). In fact, the associated errors at that time were a factor from 3 to 5 smaller than those of the previous determination performed in 1963 (Cohen and DuMond 1965). A comparison between the values of some of the physical constants obtained in the two measurements is reported in Table 11.4. It must be observed that the fine structure constant α is determined in this way independently by the quantum electrodynamic theory and therefore a more consistent comparison between that theory and the experiments is possible. Using the Josephson effect, it is now possible to get an accuracy in the measure of $2e/h$ better than 0.02 ppm in terms of the local standard voltage.

Assuming a known value for the constant $2e/h$, from (11.1.1) it follows that the voltage output from a Josephson device can be measured by simply measuring the frequency ν_r of the applied signal. Let us observe that this measurement can be done with a precision better than 10^{-3} ppm. Therefore the a.c. Josephson effect can be used to set up a voltage standard to maintain and compare the various standard reference cells (Taylor et al. 1967). At present the value adopted by most countries for $2e/h$, as suggested in October 1972 by the Comité Consultif d'Électricité, is

$$\frac{2e}{h} = 483594.0 \text{ GHz/V} \quad (11.7.1)$$

The use of an irradiated Josephson junction as a voltage reference offers many advantages. Only relatively simple experimental techniques are required. The comparison between the reference standard cells of the various countries,

Table 11.4 Comparison between the values of some important physical constant obtained by the measurement of $2e/h$ (Taylor, Parker, and Langenberg 1969) and the values resulting from the 1963 adjustment (Cohen and Du Mond 1965)^a

Constant	Units	1963 Adjustments	1969 Adjustment	Change (ppm)
Inverse of fine structure constant	α^{-1}	137.038 (6)	137.03602 (21)	-20
Electron charge	$e 10^{-19} \text{ C}$	1.60210 (2)	1.6021917 (70)	+57
Electron mass	$m 10^{-31} \text{ kg}$	9.10908 (13)	9.109558 (54)	+52
Plank's constant	$h 10^{-34} \text{ J-sec}$	6.62559 (16)	6.626196 (50)	+91

^aThe data are taken from Taylor, Parker, and Langenberg (1969).

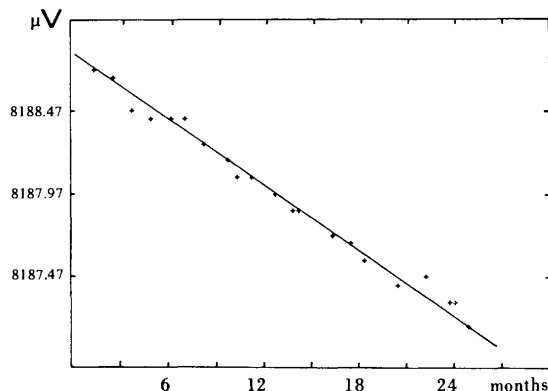


Figure 11.33 Mean voltage of a standard cell of the National Bureau of Standards measured by the a.c. Josephson effect as a function of time. The voltage values are reduced by 1.81 V. (After Document CCE/78-3, NBS, September 1978.)

which implies the transport of the cells to distant laboratories, is avoided. Finally, it becomes possible to check with high accuracy the stability of the standard cells. As an example, Fig. 11.33 gives the mean voltage of a standard cell of the National Bureau of Standards measured by the a.c. Josephson effect as a function of time. The starting value was measured in January 14, 1976. As is apparent from the figure, a drift in the voltage values is clearly evident. The data confirm the fact that the emf of standard cells in general have a tendency to decrease with time.

In conclusion, it can be said, that by using the Josephson effect to maintain the voltage standard a considerable improvement in the precision and relative accuracy of the national standards will result. It is interesting to observe that in principle a definition of the voltage units in terms of the Josephson frequency is possible; of course this step would imply a deep revision of the whole International System of Units. An excellent tutorial review on the measurement of $2e/h$ by the Josephson effect has been published by Clarke (1970).†

The basic experimental apparatus used in the measurement of $2e/h$ and for the voltage standard is essentially the same. In what follows we briefly describe this apparatus and discuss the problems associated with the measurements. Figure 11.34 is a sketch of the sample holder used by Finnegan and his coworkers (1971). The junctions are placed at the bottom of an X band waveguide immersed in the liquid helium bath. Current and voltage leads are soldered to the junctions. In order to improve the microwave coupling, a low Q cavity is formed by locating an iris a quarter wavelength above the junctions. The cavity can be tuned by an adjustable sliding short placed under the device. The entire cryogenic system is surrounded by three μ metal layers to reduce the

†More recent advances in voltage standards have been discussed by Kose (1976).

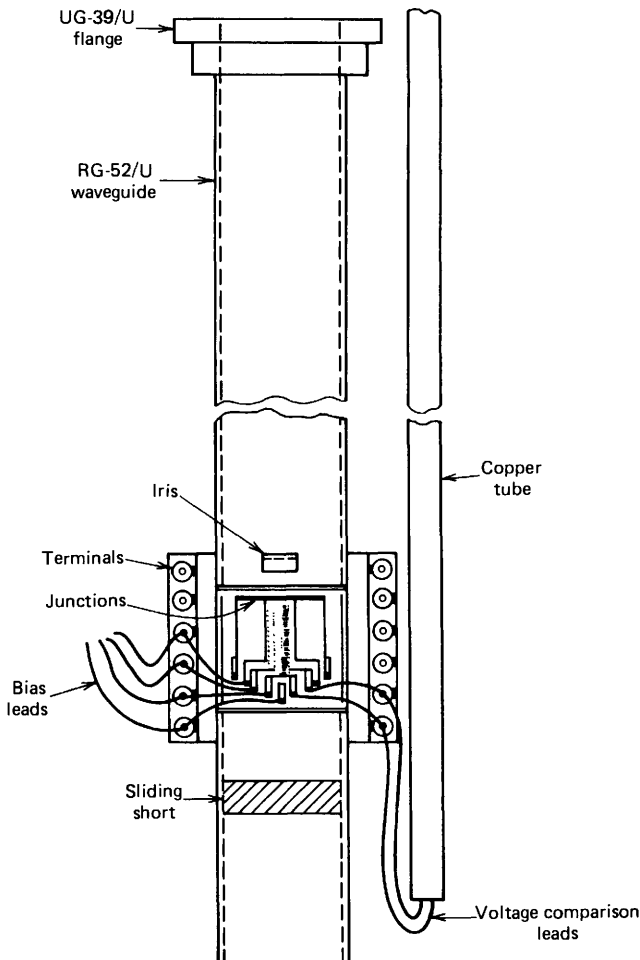


Figure 11.34 Waveguide holder, with Josephson device in place, used in the measurement of $2e/h$. Some of the bias leads have been omitted for clarity. (After Finnegan, Denenstein, and Langenberg 1971.)

effects of the earth's magnetic field. The devices used in the experiments are tunneling oxide junctions. Niobium point contacts can be used, but are less desirable because of their poor cyclability and mechanical stability. The samples typically used are Pb-Pb-O_x-Pb junctions for the high critical temperature and the good electromagnetic properties and Nb-NbO_x-Pb junctions for the extremely good cyclability and the long life characteristics (see Chapter 8). A typical sample (see Fig. 11.35) consists of more than four junctions deposited on a glass substrate. A schematic of the d.c. current bias circuit and of the voltage comparator is shown in Fig. 11.36. The junction is biased on the n th microwave induced current step, and the output voltage is compared

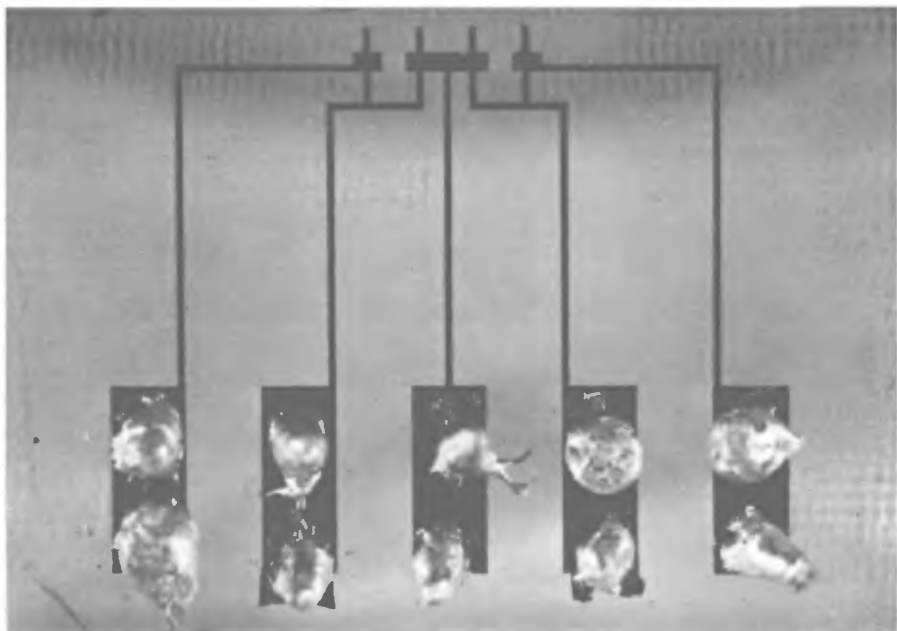


Figure 11.35 Typical sample used for the voltage standard. The device consists of four Nb-NbO_x-Pb junctions. (Courtesy of R. Vaglio, V. Lacquaniti, and G. Marullo.)

through a well calibrated resistive divider with the standard cell whose emf is equal to V_R . When both the null detectors are balanced, we have

$$\frac{V_R}{R_1} = \frac{V_n}{R_2} = n \frac{\hbar}{2e} \frac{\nu_r}{R_2}$$

The frequency $\nu_r = \omega_r / 2\pi$ of the applied microwave signal can be measured

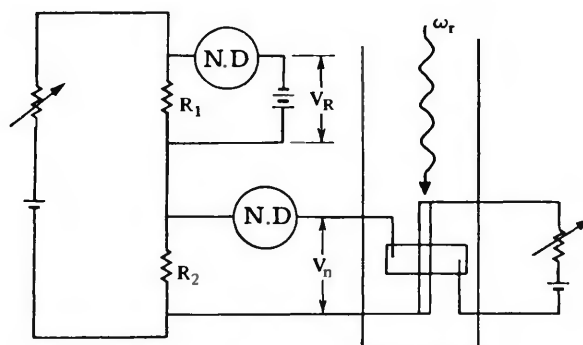


Figure 11.36 A schematic of the d.c. current bias circuit and of the voltage comparator. N.D. are null detectors.

within an accuracy of $\Delta\nu_r/\nu_r$ better than 10^{-9} . The main source of errors is related to the presence of parasitic thermal emf's and to the determination and the stability of the ratio R_1/R_2 . The effect of the thermal emf's can be compensated for by measuring both values of the n th step in the positive and negative part of the V - I characteristic (a null point can be taken with zero current and no applied microwave power). In each experimental run the same measurements are repeated a certain number of times. A least mean square method is used to get the final results. Since each experiment can take a rather long time, the temperature of the helium bath has to be carefully stabilized, otherwise the characteristics of the junction change and tiresome fine readjustments of the current are required. Another way to minimize errors is to reduce the ratio R_1/R_2 , that is, to increase the voltage output of the device. Since the stable microwave generators are most readily available in the X band (~ 10 GHz), the only way to use a lower R_1/R_2 ratio is to work with a high step number n or with more junctions connected in series. For example, working with one junction at about 10 GHz and $n=50$, a ratio $R_1/R_2=1000$ must be used, whereas when using two junctions in series and $n=250$ we have $R_1/R_2=100$. Therefore a considerable gain in the accuracy of the measure results.

As we have shown in Section 11.1 and 11.2 the amplitude I_n of the n th microwave induced current step is related to the amplitude of the applied radiation (and therefore to the power) through a Bessel function of integer order. Since these functions have the property that $J_n(x)\approx 0$ if the argument is lower than the order n ($x\lesssim n$), it follows that in order to get high amplitude current steps at large d.c. voltage values V_n , a large value for the microwave power coupled to the junction is required. An arbitrary increase of the total power supplied by the microwave source will give rise to instabilities related to local heating in the helium bath. Therefore it is the coupling between the junction and the microwave system that has to be optimized. In the apparatus shown in Fig. 11.34 the optimum coupling condition is achieved by external adjustment of the sliding short. Because of the presence of the current and voltage leads in the waveguide, spurious resonances exist. Therefore the optimal coupling condition depends critically on the particular device and the particular arrangement of the biasing leads. Better results have been obtained by the use of thin film integrated superconducting microstripline structures (Finnegan, Wilson, and Toots 1974; Finnegan, Holdeman, and Wahlsten 1976).

To have a good coupling, the junction impedance must be made as large as possible to match the external impedance of the guide (or microstripline). This suggests the use of a high normal tunneling resistance junction. However R_{NN} cannot be increased arbitrarily because the amplitude of the microwave induced step I_n is proportional to I_1 and so to $1/R_{NN}$; on the other hand, to avoid problems related to thermal fluctuations and noise I_n must be at least of the order of $20 \mu\text{A}$. Typical values of the normal tunneling resistance in the devices employed in the experiments range from 0.1 to 1Ω . When optimal coupling conditions are achieved, "useful" (i.e., $20 \mu\text{A}$) steps can be rather

easily obtained up to $V_n \simeq 10$ mV. The maximum possible value for V_n is related to the noise rounding effect of the current steps. This problem has been considered by Kose and Sullivan (1970).

For resonant junctions, a condition that must be satisfied is that the frequency of the applied signal ω_r match the frequency of one of the internal resonant modes of the junction cavity (see Section 9.2). For the first resonant mode from (9.2.2) we get the relation

$$\omega_r = \frac{\pi\bar{c}}{L} \quad (11.7.2)$$

where L is the junction dimension parallel to the direction of propagation of the applied electromagnetic radiation. For $\omega_r/2\pi=10$ GHz typical values for L are $L=0.2 \div 1.0$ mm depending on the material used for the junctions. The main difficulty that arises in trying to satisfy (11.7.2) is that the value of the Swihart velocity is not exactly predictable but can slightly vary from sample to sample and from junction to junction in the same sample. This fact can cause problems whenever more than one high Q junction in a series configuration is used to get a higher output voltage. To give a numerical example, the frequencies of resonance of different junctions on the same substrate can differ by 2%. Recently very promising results have been obtained by Lacquaniti, Marullo and Vaglio (1978). These authors have been able to adjust the resonant frequency of a Nb-NbO_x-Pb junction within an accuracy of 2%, after it had been tested at 4.2 K, by simply varying the dimension of the lead film by photolithographic techniques.

Finally, useful information on the Q of a resonant junction can be obtained by the magnetic field dependence of the Fiske steps (see Chapter 9) or by observing the frequency dependence of the junction response at a fixed microwave input power. At low temperature typical values observed are $Q=300 \div 450$ for Pb-PbO_x-Pb junctions and $Q=100 \div 250$ for Nb-NbO_x-Pb junctions (Finnegan, Wilson, and Toots 1976; Marullo, Lacquaniti, and Vaglio 1978).

At present most of the developed countries maintain the voltage standard through the Josephson effect. At the National Bureau of Standards (N.B.S.) the U.S. standard emf has been maintained since July 1, 1972, by means of an apparatus consisting of two resonant series connected Pb-PbO_x-Pb small junctions producing a 10 mV output. The precision and estimated accuracy of this system are about 0.02 and 0.04 ppm, respectively. At the Bureau International des Poids et Mésures (B.I.P.M.) essentially the same system is used while at the National Physical Laboratory (N.P.L.) a single resonant Pb-Pb tunnel junction is used with a 2.5 mV output. At the Physikalisch-Technische Bundesanstalt (P.T.B.) a nonresonant Pb-Pb junction is used at 3.2 mV level. The laboratories maintaining a Josephson voltage standard are listed in Table 11.5.

Some of the previously mentioned systems (N.P.L., P.T.B., etc.) are entirely cryogenic, characterized by the presence of cryogenic resistors with

TABLE 11.5 Some laboratories using Josephson devices for voltage standard maintenance

Laboratory	Sample Used	Output Voltage (mV)	Input Frequency (GHz)	Comments
Bureau International des Poids et Mesures—B.I.P.M. (France)	Two series connected Pb-Pb self-resonant junctions	10	9	Room temperature system; cryogenic system and microstrip line in progress
National Bureau of Standards—N.B.S. (U.S.A.)	Same as above Nb point contact	10 1	9 9.3	Same as above Same as above
National Measurement Laboratory—N.M.L. (Australia)	Single Pb-Pb self-resonant junction	2.5	10.3	Cryogenic system (microstrip line in progress)
National Physical Laboratory—N.P.L. (U.K.)	Single Nb-Pb self-resonant junction	4.5	10	Room temperature system; cryogenic system in progress
Laboratoire Central des Industries Electriques—L.C.I.E. (France)	Single Pb-Pb self-resonant junction	2.5	10	Same as above
National Research Council—N.R.C. (Canada)	Single Pb-Pb nonresonant junction	3	70	Cryogenic system
Physikalisch-Technische Bundesanstalt—P.T.B. (West Germany)	Single Pb-Pb nonresonant junction			
Electrotechnical Laboratory—E.T.L. (Japan)	Two series connected Pb-Pb self-resonant junctions	10	10	Room temperature system
Institute of Metrology "D. F. Mendelev"—I.M.M. (U.R.S.S.)	Single Pb-Pb self-resonant junction	4	8.7	Room temperature system
Istituto Elettrotecnico Nazionale "G. Ferraris"—I.E.N. (Italy)	Single Nb-Pb self-resonant junction	5	10	Room temperature system; cryogenic system and microstrip line in progress

very low temperature and load coefficients. The resistors are calibrated at low temperature by a superconducting d.c. comparator. This is a recently developed instrument based on the perfect diamagnetism of a superconducting shield (Harvey 1972). A superconducting quantum interference device (SQUID) (see Chapter 13) is used as a null detector for the various operations and superconducting switching is employed to change the operative configuration. Many of the national standards laboratories are now developing all cryogenic systems (Dziuba, Field, and Finnegan 1974) as well as improved microstrip coupled junctions. Coupling of the junctions to the microstrip via thin film superconducting resonator appears to be a particularly promising technique (Finnegan, Holdeman and Wahlsten 1976; Finnegan and Wahlsten 1978; Finnegan 1980). Integrated microwave filters can be deposited together with the junctions and the microstrip to form the current and voltage leads, to minimize interactions of the microwave radiation with the SQUID system. Figure 11.37 shows an integrated microstrip coupled device, which was made at N.B.S. (Finnegan, Wilson, and Toots 1974). An "in-line" Pb-Pb junction is

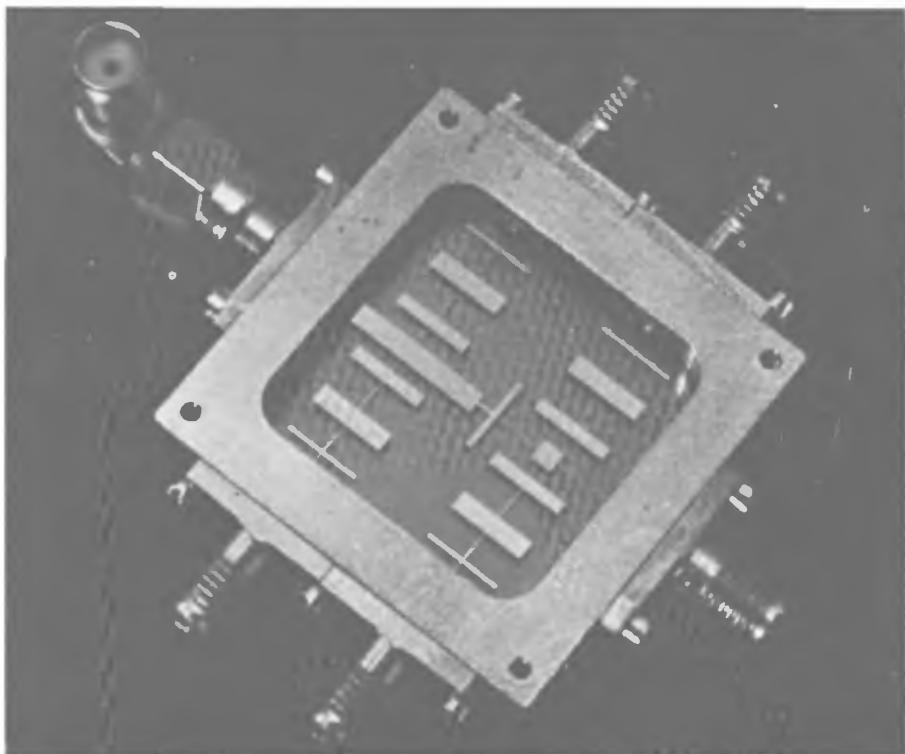


Figure 11.37 Microwave integrated circuit box with cover removed to show experimental device. A single in-line junction (near the center) and filtered bias leads are shown. (Courtesy of T. Finnegan.)

located near the center of the structure. The stripline is formed between the film deposited on the substrate and a copper ground plane under that, the glass substrate being the dielectric. Two multisection low pass filters made by evaporated gold films are inserted in the current and voltage leads.

There are also many possibilities for improving the voltage standard maintenance methods that are now being studied. Among others we can mention the design proposed by the I.E.N. (Arri 1976; Andreone et al. 1976), in which the junction biased on a current step acts as an ideal d.c. voltage generator which is loaded by a stable cryogenic resistor. An external voltage generator calibrated on the local voltage standards feeds an identical cryogenic resistor. The currents flowing in the two resistors are in the same ratio as the Josephson voltage and the standard cell voltage and are directly compared by a superconducting current comparator.

Another interesting proposal is based on the use of the so-called inverse a.c. Josephson effect (Levinsen et al. 1977, Kautz 1980). This effect is based on the fact that an unbiased Josephson tunnel junction irradiated with microwaves can spontaneously develop quantized d.c. voltages. First observations of this effect have been reported by Langenberg and coworkers (1966); subsequent experimental investigation has been performed by Chen, Todd, and Kim (1972). The voltage level is low (no more than 100 μ V) but, since no current feeding is required, several junctions exhibiting this property could be connected in series giving a high overall output voltage.

Recently a commercial prototype version of the Josephson effect voltage standard has been realized at N.B.S. (Holdeman et al. 1978). Because of its simplicity and ease of use this system is expected to be particularly suitable for use outside national standards laboratories. A single resonant $Pb-PbO_x-Pb$ Josephson junction, coupled to a 9 GHz microwave signal via a microstripline, works at 4.2 K and gives an output level of 5 mV. The reported overall accuracy is better than 1 ppm and special features of the device allow a very low power dissipation, required to reduce the liquid helium waste. Great importance is given to the development of such a class of instruments, since it has been estimated that more than 6000 laboratories need to maintain an *in situ* d.c. voltage standard in the United States alone (Holdeman and Chang 1978). Large scale use of d.c. voltage references based on the Josephson effect is also connected to the development of cryocoolers (Zimmerman 1978) if both the d.c. and r.f. power input required for the Josephson junction can be reduced to less than 1 mW and/or if high quality junctions with high T_c electrodes are developed.

A comparison between B.I.P.M. and P.T.B. was made in 1975 involving two room temperature voltage measuring systems; B.I.P.M. and N.P.L. were compared in 1978, involving the room temperature system of B.I.P.M and the cryogenic comparator of the N.P.L. (Hartland et al. 1978). The observation of small but significant differences at the parts in 10^8 level indicates the direct comparison of $2e/h$ voltage measuring systems will be useful when relative accuracies below about 1 part in 10^7 are required.

CHAPTER 12

Josephson Junctions in Superconducting Loops

In this chapter we examine the behavior of multiply connected superconducting structures that contain one or more Josephson elements. In Section 12.1 we consider the properties of simple superconducting loops in order to recall the phenomenon of fluxoid quantization. Superconducting loops with one or two Josephson elements are analyzed in Sections 12.2 and 12.3. Structures of this kind are fundamental either to their application as SQUIDs and computer elements that we consider in the next two chapters or to the investigation of the physical nature of the Josephson element itself.

12.1 Fluxoid Quantization

As we have seen, the superconducting state is characterized by the presence of bound electron pairs (Cooper pairs). All the pairs are described by the same “wave function” or “order parameter” which in general is a complex quantity of the kind: $\psi(\mathbf{r}) = \rho^{1/2}(\mathbf{r})e^{i\varphi}$. The density of pairs at a given point \mathbf{r} (in the superconductor) is given by $\psi^*(\mathbf{r})\psi(\mathbf{r}) = \rho(\mathbf{r})$. Therefore, in order to have physical meaning, the function $\psi(\mathbf{r})$ must be single valued. This implies that on a closed loop in the superconductor the phase φ can change only by a quantity $2\pi n$, where n is an integer. By using (1.1.2) it is easy to see that the phase φ is related to the supercurrent density \mathbf{J}_S and the vector potential \mathbf{A} , by the equation

$$\nabla \varphi = \frac{2\pi}{\Phi_0} \left(\mathbf{A} + \frac{m}{2e^2\rho} \mathbf{J}_S \right) \quad (12.1.1)$$

where $\Phi_0 = h/2e$ is the flux quantum and we are using MKS units.

By integration over a closed loop we have

$$2\pi n = \oint \nabla \varphi \cdot d\mathbf{l} = \frac{2\pi}{\Phi_0} \left\{ \oint \mathbf{A} \cdot d\mathbf{l} + \oint \frac{m}{2e^2\rho} \mathbf{J}_S \cdot d\mathbf{l} \right\}$$

from which it follows that

$$\int_S \int \mathbf{B} \cdot d\sigma + \frac{m}{2e^2\rho} \oint_{\Gamma} \mathbf{J}_S \cdot d\mathbf{l} = n\Phi_0 \quad (12.1.2)$$

where \mathbf{B} is the magnetic field related to the vector potential \mathbf{A} by the usual relation $\mathbf{B} = \nabla \times \mathbf{A}$ and Green's theorem of vector integration has been used. The quantity on the left side of (12.1.2) is called the "fluxoid." It is important to remark that while the system is in the superconducting state n is constant and time independent. If the closed loop Γ encircles a superconducting region (Fig. 12.1a) the only possible choice for n is $n=0$. In this case (12.1.2) states that the flux inside a bulk superconductor is zero, except in a region near the surface to which the shielding supercurrents are confined. Therefore, it represents just a more correct formulation of the Meissner-Ochsenfeld effect, which takes into account the finite penetration of the magnetic field. If the loop Γ encloses a normal spot or an empty space (Fig. 12.1b) all the values are possible for n . Expression (12.1.2) states that the fluxoid is quantized in units of Φ_0 . If the integration path in the contour integral can be taken in a region far from the surface of the superconductor where the supercurrent is negligible, (12.1.2) reduces to

$$\Phi = \int_S \int \mathbf{B} \cdot d\sigma = n\Phi_0 \quad (12.1.3)$$

which states that the flux Φ enclosed by the superconducting loop is quantized. Flux quantization was first predicted by F. London (1950) and verified experimentally later by Deaver and Fairbank (1961) and Doll and Nabauer (1961). It is interesting to note that since at that time the concept of a pair had not yet been established, the value predicted by London was twice that later observed experimentally.

To clarify the behavior of a superconducting loop, we consider the simple cylindrical geometry sketched in Fig. 12.1c. Let us assume the sample to be initially at a temperature lower than its critical temperature T_c and in the zero flux state. If an external field \mathbf{B}_e is applied, a supercurrent i starts to circulate to compensate for the increase of the geometrical flux Φ_e inside the hole. The presence of the supercurrent i , however, causes an increase of free energy. For the simple geometry assumed it can be shown that the Gibbs free energy (per unit length) is given by (Ginzburg 1962):

$$G\left(\frac{\Phi_e}{\Phi_0}\right) = G_0 \left(n - \frac{\Phi_e}{\Phi_0}\right)^2 \quad (12.1.4)$$

This expression is shown in Fig. 12.2, where each branch corresponds to a different value $n\Phi_0$ for the flux Φ in the cylinder. On increasing the applied

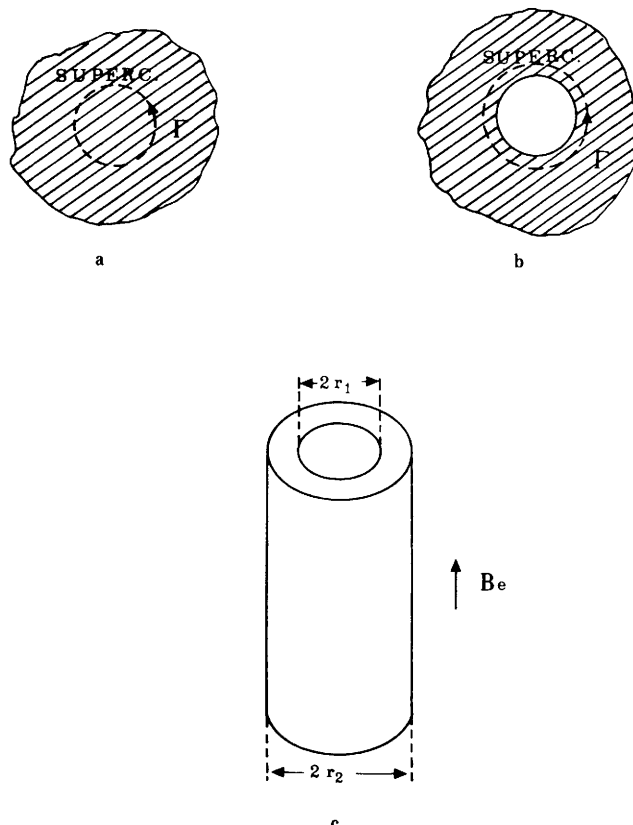


Figure 12.1 (a) Singly connected superconductor; (b) multiply connected superconductor; (c) superconducting cylinder in the presence of external field B_e .

field B_e , the value of the internal flux does not change; the free energy increases along its $n=\text{const.}$ branch ($n=0$ in our case). A transition to a state with a different number of flux quanta can occur when the free energy of the sample is equal to the one in the normal state G_N (see Fig. 12.2), that is, the system is no longer superconducting. In fact, this process requires a rearrangement of the carried momentum for all the pairs. The final state will not necessarily be the one with minimum energy value. This lowest energy state can be reached if the same field is applied to the sample in the normal state and the temperature is subsequently lowered below T_c . It is easy to see from Fig. 12.2 that the state $\Phi=n\Phi_0$ is obtained if the applied flux Φ_e is in the range $(n-\frac{1}{2})\Phi_0 < \Phi_e < (n+\frac{1}{2})\Phi_0$. Figure 12.3 gives experimental data on flux quantization obtained using this procedure (Goodman and Deaver, Jr. 1970).

If the wall thickness $r_2 - r_1$ of the cylinder becomes smaller than the London penetration depth λ_L , it is no longer possible to find a path for which

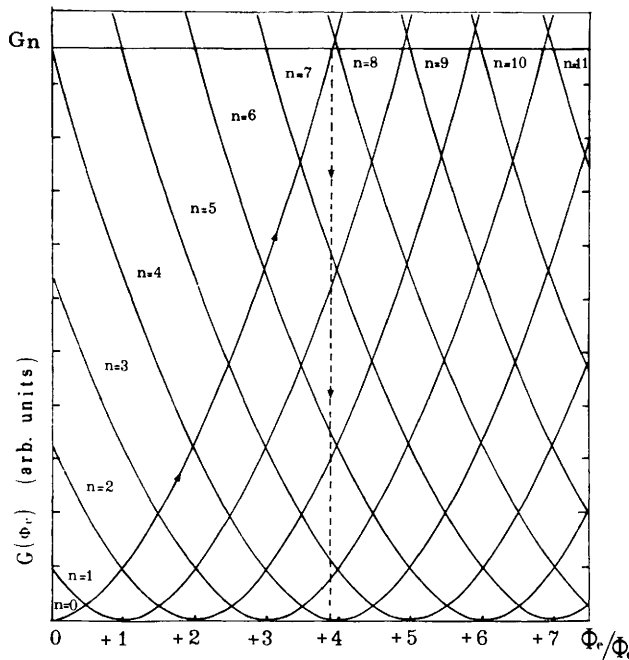


Figure 12.2 Gibbs free energy (per unit length) for the superconducting cylinder (Fig. 12.1c) as a function of the applied flux Φ_e of the applied field. Each branch corresponds to a constant value $n\Phi_0$ of the flux Φ in the cylinder.

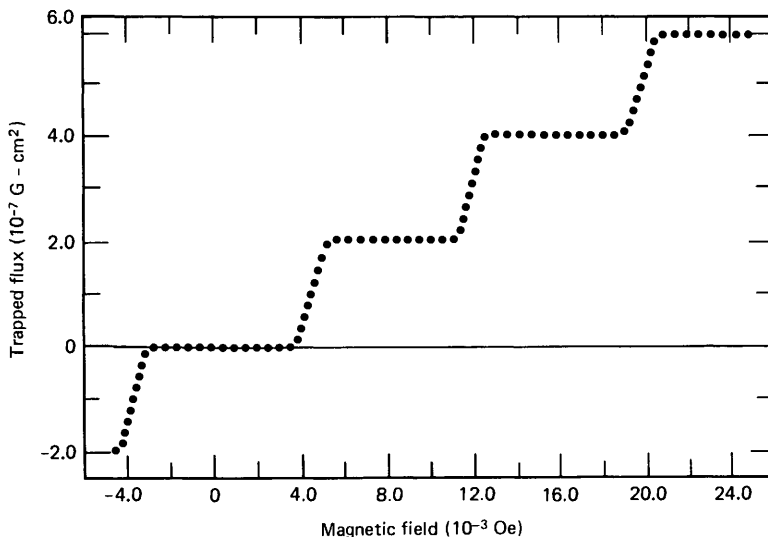


Figure 12.3 Trapped flux as a function of the magnetic field in which the cylinder was cooled below the superconducting transition temperature. (After Goodman and Deaver 1970.)

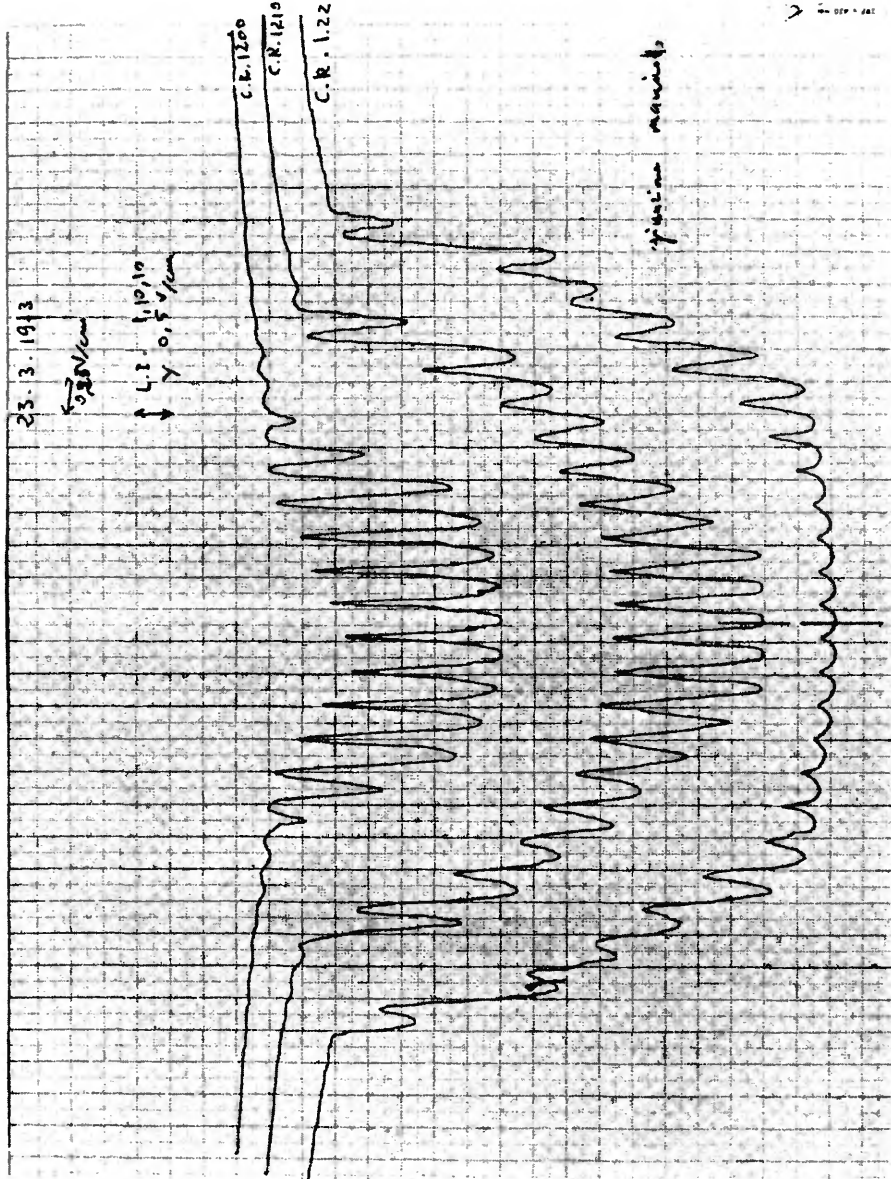


Figure 12.4 The resistance of an aluminum microcylinder as a function of the applied magnetic field. Each curve refers to a different value of the temperature in the vicinity of the critical temperature of the sample. (After Sacchetti, Ricci, and Paternó, 1973.)

the contour integral of the current density \mathbf{J}_S in (12.1.2) is negligible. In this condition the fluxoid is to be quantized rather than the flux. The main contribution to the quantization comes from the integral of the current density \mathbf{J}_S . An ingenious experiment to demonstrate the fluxoid quantization on thin walled cylinder was performed by Little and Parks (Little and Parks 1962; Parks and Little 1964). They measured the resistance R of superconducting hollow microcylinders as a function of the applied field B_e at temperatures very close to the critical temperature T_c . In this range the condition $r_2 - r_1 \ll \lambda_L$ is satisfied and the field inside the sample (parallel) is just equal to B_e . To adjust the value of the fluxoid the circulating current in the cylinder will have a periodic dependence on the external field. As Tinkham has shown (Tinkham 1964, 1975), this gives rise to the appearance of a periodic contribution in the free energy of the system, which in turn will cause a periodic variation in the $T_c - B_c$ curve. In Fig. 12.4 typical data for aluminum microcylinders are shown. The R vs. B_e dependence can be better understood by considering the shape of the surface $R(H_e, T)$. The curves in Fig. 12.4 are obtained by the interception of the R, B_e plane with this surface for different values of T . For more details the reader is referred to the paper of Groff and Parks (1968).

12.2 Superconducting Loop with a Single Junction

Let us consider now a superconducting loop in which a single Josephson junction is inserted (see Fig. 12.5). The condition for the single valuedness of the wave function ψ still holds. By integrating (12.1.1) on a closed loop we get

$$2\pi n = \varphi_J - \frac{2\pi}{\Phi_0} \int_{P_1}^{P_2} \mathbf{A} \cdot d\mathbf{l} \quad (12.2.1)$$

where φ_J is the phase difference across the junction and we have assumed that on the chosen path Γ the supercurrent density \mathbf{J}_S is negligible. By introducing the gauge invariant expression (De Bruyn Ouboter 1976) for the phase difference[†]

$$\varphi_J^* = \varphi_J - \frac{2\pi}{\Phi_0} \int_{P_1}^{P_2} \mathbf{A} \cdot d\mathbf{l}$$

we recover the missing part of the closed loop integral of \mathbf{A} in (12.2.1). Therefore we get straightforwardly the relation

$$\varphi_J^* = 2\pi n - 2\pi \frac{\Phi}{\Phi_0} \quad (12.2.2)$$

[†] The integration path is taken just across the barrier.

which relates the phase difference across the junction to the effective flux in the superconducting loop. When an external field is applied, it produces a geometrical flux Φ_e inside the loop. However, because of the flux quantization condition, a circulating current i is induced which tends to screen the applied flux. By introducing the inductance L of the loop the actual flux Φ is given by

$$\Phi = \Phi_e + Li \quad (12.2.3)$$

The circulating supercurrent i is determined by the junction. Assuming the usual sinusoidal phase dependence (1.4.4) in the static case ($d\Phi_e/dt = 0$) we get, using (12.2.2),

$$i = -I_1 \sin 2\pi \frac{\Phi}{\Phi_0} \quad (12.2.4)$$

where I_1 is the maximum Josephson current as well as the maximum value of the supercurrent which the loop can carry to adjust the fluxoid value.

12.2.1 Metastable States. At this point let us examine the behavior of the loop when there is no applied field (Goldman, Kreisman and Scalapino 1965). The effective flux is given by

$$\Phi = Li \quad (12.2.5)$$

Combining (12.2.3) and (12.2.4) we get the relation

$$-\frac{i}{I_1} = \sin \frac{2\pi Li}{\Phi_0} \quad (12.2.6)$$

The solutions of this equation correspond to the values of the circulating current which the structure can sustain in zero external field. Therefore a set of metastable states are possible. Equation 12.2.6 can be solved graphically by

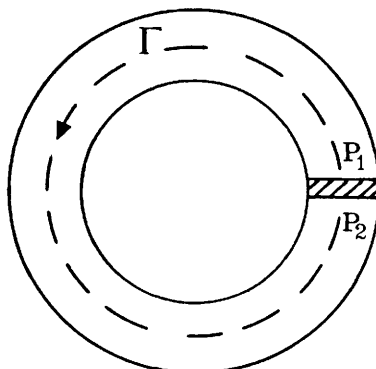


Figure 12.5 Superconducting loop interrupted by a Josephson junction.

plotting the two members as a function of i/I_1 and looking at the interceptions of the two curves. Not all the values correspond to stationary states, but only those for which the free energy has a local minimum. For a loop with a junction the free energy is given by

$$E = -\frac{\hbar I_1}{2e} \cos \varphi_j^* + \frac{1}{2} L i^2 \quad (12.2.7)$$

where the first term is the junction coupling energy and the second the magnetic energy. By using (12.2.2) and (12.2.5) we can write (12.2.7) as

$$E = -\frac{\hbar I_1}{2e} \cos\left(2\pi \frac{Li}{\Phi_0}\right) + \frac{1}{2} L i^2$$

In normalized units, the energy as a function of i/I_1 is given by

$$\frac{E(i/I_1)}{\frac{1}{2} L I_1^2} = \left(\frac{i}{I_1}\right)^2 - \frac{2}{\beta_e} \cos\left(\beta_e \frac{i}{I_1}\right) \quad (12.2.8)$$

where we have introduced the parameter $\beta_e = 2\pi L I_1 / \Phi_0$. Figure 12.6 is the graphical solution of (12.2.5) for $\beta_e = 10\pi$. The stable states are marked by circles. In the same figure the free energy as a function of the current is also shown. For $\beta_e < 3\pi/2$ only the solution corresponding to zero current in the cylinder is stable.

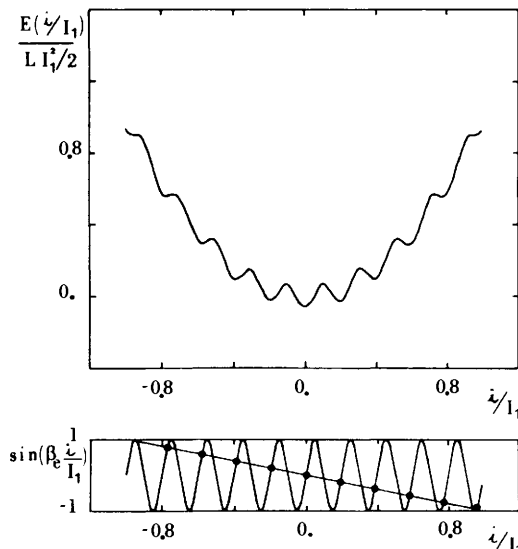


Figure 12.6 (a) Free energy function for a loop with a junction. (b) Graphical solution of (12.2.6). Both curves refer to the case $\beta_e = 2\pi L I_1 / \Phi_0 = 10\pi$. The circles indicate the metastable states of the system, which correspond to the relative minima of the free energy function.

12.2.2 Applied External Field. In the presence of external field ($\Phi_e \neq 0$) from (12.2.3) and (12.2.4) we get the relations (Silver and Zimmerman 1967)

$$\Phi_e = \Phi + \frac{\beta_e}{2\pi} \Phi_0 \sin\left(2\pi \frac{\Phi}{\Phi_0}\right) \quad (12.2.9a)$$

$$i = -I_1 \sin\left(2\pi \frac{\Phi_e}{\Phi_0} + \beta_e \frac{i}{I_1}\right) \quad (12.2.9b)$$

which give the dependence of the currents i and the effective flux Φ on the geometrical flux Φ_e . These dependences are shown in Fig. 12.7 for two different values of β_e . Let us observe that the i vs. Φ_e curve can be obtained by computing, for each value of Φ_e , the difference between the corresponding Φ vs. Φ_e curve and the dashed line $\Phi = \Phi_e$.

Two different kinds of behavior are recognized. For $\beta_e < 1$ the curves are single valued: on increasing the external flux Φ_e , the effective flux Φ increases continuously (Fig. 12.7a). Furthermore $d\Phi/d\Phi_e$ is periodic with respect to Φ_e within a period Φ_0 . The analytical expression of $\Phi(\Phi_e)$ satisfying (12.2.9a) is

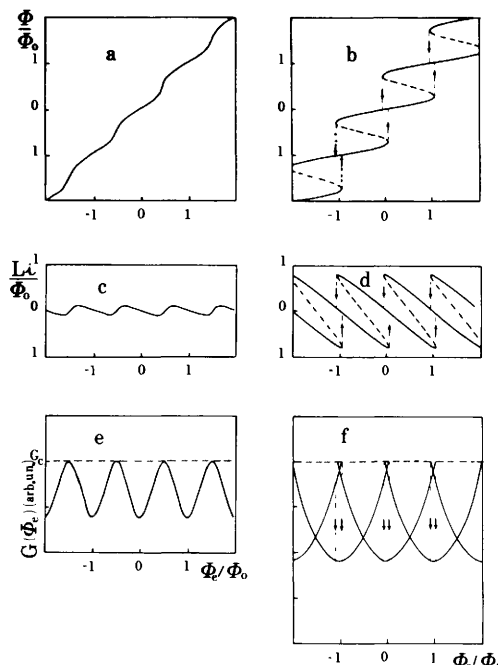


Figure 12.7 Internal flux Φ , circulating current i , and free energy G versus external flux Φ_e for a superconducting loop of inductance L with a single junction. (a), (c), and (e) $\beta_e = 2\pi LI_1/\Phi_0 < 1$. (b), (d), and (f) $\beta_e > 1$.

given by (Erné, Hahlbohm, and Lübbig 1976):

$$\frac{\Phi}{\Phi_0} = \frac{\Phi_e}{\Phi_0} + \sum_{n=1}^{\infty} M_n(\beta_e) \sin\left(2\pi n \frac{\Phi_e}{\Phi_0}\right) \quad (12.2.10)$$

where the coefficients $M_n(\beta_e)$ are determined in terms of Bessel functions of the first kind $J_n(x)$:

$$M_n(\beta_e) = \frac{(-1)^n}{n\pi} J_n(n\beta_e) \quad 0 \leq \beta_e < 1$$

In this condition the flux is not quantized inside the ring. This means that in the quantization condition (12.2.2) the contribution of the junction (i.e., φ_f^*) is not negligible and plays an important role.

For $\beta_e > 1$ the curves are multivalued: on increasing Φ_e , only the branches with positive slope are traced (solid lines in Fig. 12.7b). From (12.2.9a) it is easy to see that the slope $d\Phi/d\Phi_e$ of these regions for $\Phi_e = n\Phi_0$ is given by

$$\left(\frac{d\Phi}{d\Phi_e} \right)_{\Phi_e=n\Phi_0} = \frac{1}{(d\Phi_e/d\Phi)_{n\Phi_0}} = \frac{1}{1+\beta_e}$$

On increasing β_e this slope tends to zero; the stable regions approach horizontal lines, showing that flux quantization is more effective.

The Gibbs free energy for the ring can be computed as

$$G = - \int i d\Phi_e \quad (12.2.11)$$

The complete expression for the geometry that we consider to be valid for arbitrary values of β_e has been given by Silver and Zimmerman (1967). We now examine the two particular cases $\beta_e \ll 1$ and $\beta_e \gg 1$. For $\beta_e \ll 1$ we can make the approximation $\Phi \approx \Phi_e$, that is, the current i depends only on the applied flux Φ_e . Therefore it is

$$G = - \frac{\Phi_0 I_1}{2\pi} \cos\left(2\pi \frac{\Phi_e}{\Phi_0}\right) + G_c$$

From this, introducing the parameter β_e , we have

$$\frac{G - G_c}{\Phi_0^2 / 4\pi^2 L} = -\beta_e \left(\cos \frac{2\pi \Phi_e}{\Phi_0} + 1 \right) \quad (12.2.12)$$

where G_c is the Gibbs energy for the superconducting open loop, that is, for $i = I_1$. This dependence is shown in Fig. 12.7e for a particular value of β_e . In

the other case ($\beta_e \gg 1$), we assume that the flux quantization condition is completely satisfied, that is, $\Phi = n\Phi_0$. Therefore (12.2.3) reduces to

$$\Phi_e + Li = n\Phi_0$$

By using the last expression we get the Gibbs free energy:

$$G = \frac{1}{2L} (\Phi_e - n\Phi_0)^2 + G_c$$

From this, with our previous normalization, we get

$$\frac{G - G_c}{\Phi_0^2 / 4\pi^2 L} = 2\pi^2 \left(\frac{\Phi_e}{\Phi_0} - n \right)^2 - \frac{1}{2} \left(\beta_e + \frac{\pi}{2} \right)^2 \quad (12.2.13)$$

This expression is given in Fig. 12.7f. The zero of the Gibbs energy corresponds to the configuration in which the circulating current is just equal to the critical value I_1 . At this point the junction switches to the normal state, the superconducting loop is interrupted, and the flux quantization ceases to hold. Therefore the flux in the hole adjusts to a different value, corresponding to a lower value of the Gibbs energy. With a particular choice of the parameters of the superconductive loop and of the Josephson element, configurations can be realized in which transitions occur only between adjacent fluxoid states. In this case Φ undergoes changes of $\pm\Phi_0$ only. As we see in the next chapter, this is the range of behavior that is used in magnetometer applications. Measurements of the internal flux vs. applied field in a superconducting loop with a weak link have been performed by Zimmerman and Silver (1966b). The sample investigated was a bulk niobium cylinder in which an adjustable point contact was inserted. Figure 12.8 shows experimental data obtained with different values of the critical current I_1 of the link and therefore with different β_e values. The field was measured using a SQUID magnetometer (see Chapter 13). The axes are taken in such a way as to compensate for the field picked up by the magnetometer directly from the field coil.

12.2.3 Dynamics of Flux Transitions for $\beta_e > 1$. As we have just seen in the case $\beta_e > 1$, the Φ vs. Φ_e curve is a multiple valued function. Now we must describe the behavior of the loop when the value of the applied flux corresponds to an extreme of one of the stable regions shown in Fig. 12.7b. In this case (12.2.9), valid in the static case, no longer hold. Let us recall that in deriving these equations the Josephson element has been described by the simple sinusoidal current phase relation (1.4.4). A more suitable way to describe the junction in dynamical process is in terms of the R.S.J. model considered in Section 6.2. Combining (6.2.2) with (12.2.2) we obtain for the loop current $i(t)$ the expression

$$i(t) = -\frac{\hbar}{2e} C \frac{d^2}{dt^2} \left(\frac{\Phi}{\Phi_0} \right) - \frac{\hbar}{2e} \frac{1}{R_J} \frac{d}{dt} \left(\frac{\Phi}{\Phi_0} \right) - I_1 \sin \left(2\pi \frac{\Phi}{\Phi_0} \right) \quad (12.2.14)$$

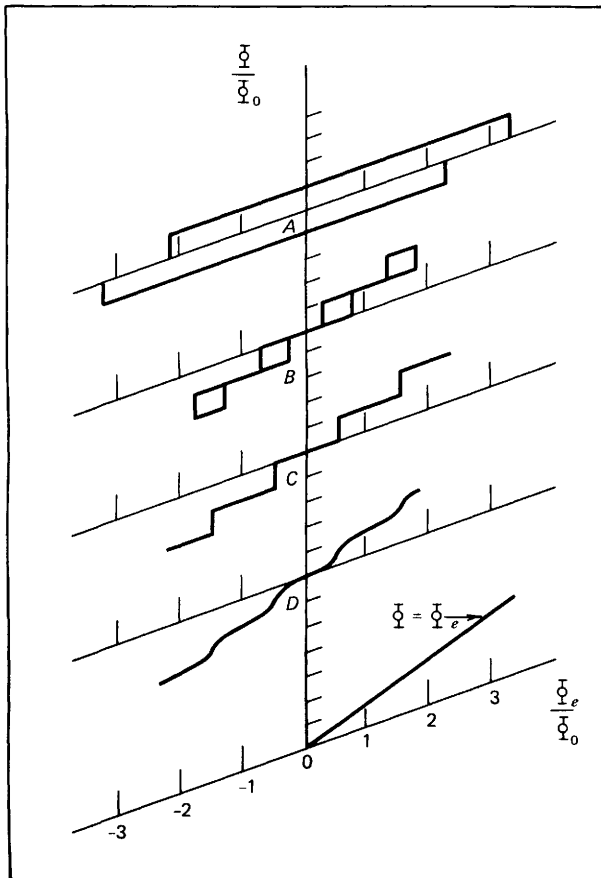


Figure 12.8 Tracing of the magnetometer output Φ/Φ_0 as a function of the applied external flux Φ_e/Φ_0 . The four tracings A through D represent decreasing values of $L I_1$ and each curve represents one full cycle of Φ_e . The axis $\Phi/\Phi_0 = \text{constant}$ is slanted to compensate for leakage coupling of the field coil to the magnetometer ring. The axes are marked in integral steps, but the absolute calibrations are arbitrary within an integral number of Φ_0 . The straight line labeled $\Phi = \Phi_e$ indicates the unity slope line expected for $I_1=0$. (After Zimmerman and Silver 1966b.)

where C and R_J are the capacitance and the normal state resistance of the Josephson element.

By inserting (12.2.14) into (12.2.3) we obtain

$$\left(LC \frac{d^2}{dt^2} + \tau_L \frac{d}{dt} + 1 \right) \frac{\Phi}{\Phi_0} + \frac{1}{2\pi} \beta_e \sin\left(\frac{2\pi\Phi}{\Phi_0}\right) = \frac{\Phi_e}{\Phi_0} \quad (12.2.15)$$

where $\tau_L = L/R_J$ and the relation $\Phi_0 = h/2e$ has been used. Equation 12.2.15 is homologous (Jackel et al. 1974), with the equation for a particle moving in a sinusoidally modulated parabolic potential and having a damping coefficient

$\eta = 1/R_J C$. The shape of the potential is similar to the $E(i)$ dependence shown in Fig. 12.6. On increasing the applied flux Φ_e the particle is carried into one of the lateral minima of the curve, until for a certain value Φ_{e0} it rolls down. The final state reached will depend on the value of the damping coefficient. For high damping it will stop in the next lowest state. This situation corresponds to flux variations of one single flux quantum Φ_0 . The problem has been analyzed (Sullivan and Zimmerman 1971) by using a mechanical analog. Smith and Blackburn (1975) have considered numerical solutions of (12.2.15) in order to investigate the problem of the final state reached by the single junction loop after the transition. These authors have shown that for large values of β_e the number of flux quanta entering the loop is a function of the parameter $\gamma_L = \eta\sqrt{LC}$ and therefore is a predictable quantity. When γ_L goes to zero this number tends to the value $(1/2\pi)\beta_e$ (Fig. 12.9). Experimental results performed by the same authors are in satisfactory agreement with the theoretical predictions. However, as Wang and Gayley (1977) have shown, this predictable behavior is only valid for γ_L greater than a critical value $\gamma_0 \approx 2$. For lower damping the flux enter the loop in an erratic way. In (12.2.14) the $\cos\varphi$ term has not been taken into account. Effects of this phase dependent conductivity term on flux transitions have been examined by Blackburn, Smith, and Keith (1977).

Let us examine in more detail the case in which a flux transition occurs between adjacent fluxoid states ($\Delta\Phi = \pm\Phi_0$). In particular, we are interested in the transition time and in the energy dissipated during this transition. This problem has been analyzed by Ernè and Lübbig (1976). The time dependence of the effective flux Φ into the loop can be found by solving (12.2.15). Numerical results are shown in Fig. 12.10 (top). The initial condition $\Phi = \Phi_0/4$ has been used and the applied flux has been set under the equilibrium conditions $d\Phi/dt = d^2\Phi/dt^2 = 0$ adding a small quantity $\delta\Phi_e$ to start the transition. In the same figure the barrier free energy (see Section 1.6) that, using (12.2.2), can be written as

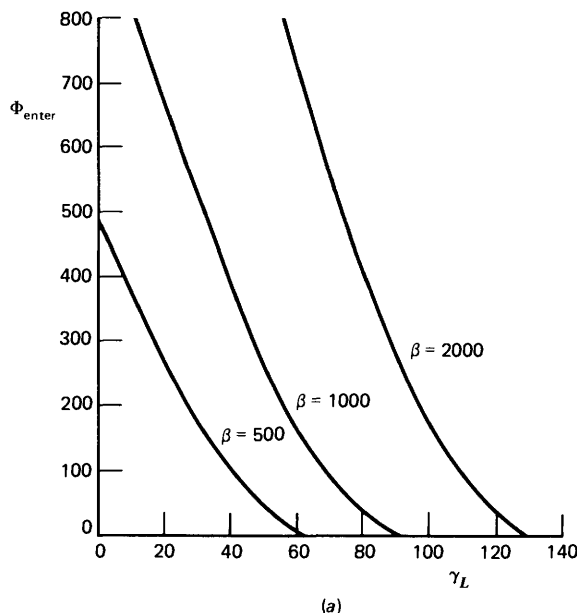
$$F(t) = \frac{I_1\Phi_0}{2\pi} \left[1 - \cos\left(2\pi \frac{\Phi}{\Phi_0}\right) \right]$$

and the magnetic energy

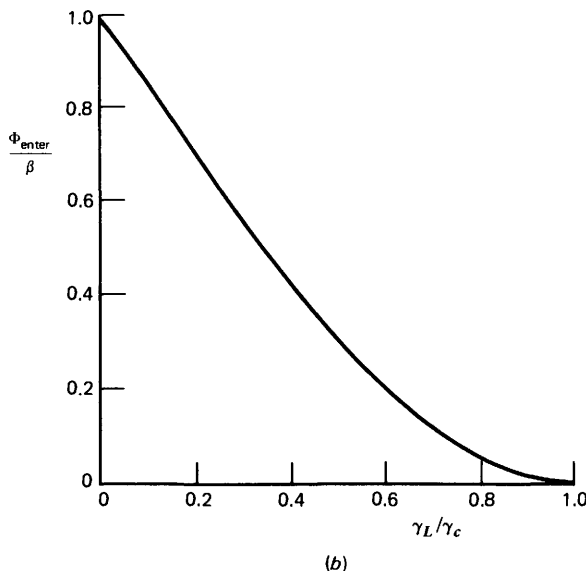
$$E_L(t) = \frac{Li^2(t)}{2}$$

are also shown.

The curves have been computed by using the numerical results shown for $\Phi(t)$ and (12.2.14) for $i(t)$. As is apparent from Fig. 12.10, two characteristic times τ_1 and τ_2 can be identified. During τ_1 only negligible dissipation occurs, and the energy of the inductance is transferred to the junction. The barrier energy drops to the next lower state energy, such as the magnetic energy, during τ_2 . Therefore the maximum dissipation occurs during this time interval.



(a)



(b)

Figure 12.9 (a) Plot of the number of flux quanta that enter a superconducting loop containing a Josephson junction as a function of the damping of the circuit ($\beta = \beta_e/2\pi$). (b) Universal curve, which may be extracted from (a). (After Smith and Blackburn 1975.)

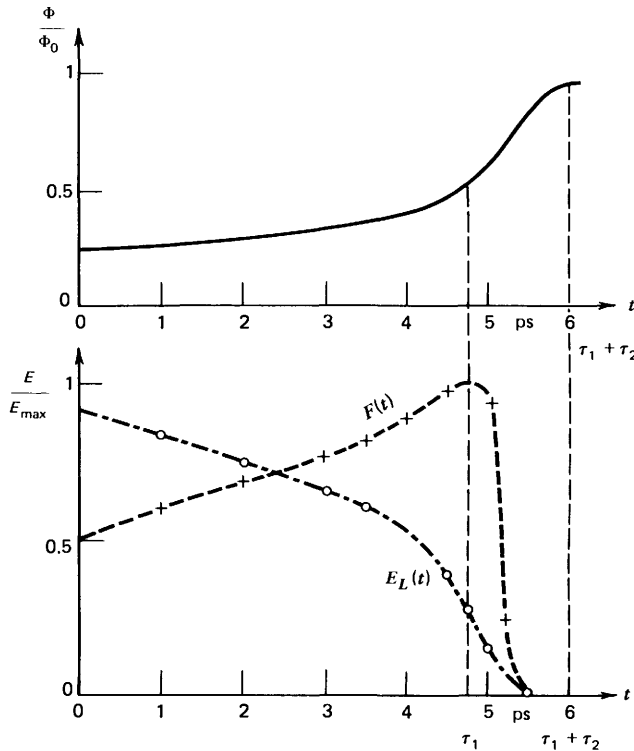


Figure 12.10 Typical time dependence of the flux in the single junction loop during a transition; the lower part contains the corresponding dependence of the barrier energy $F(t)$ and magnetic energy $E_L(t)$. (After Erné and Lübbig 1976.)

τ_1 and τ_2 are related to the characteristic parameters of the system in a different way. In the zero capacitance limit and for constant applied flux ($\Phi_e = \text{const.}$) it can be shown (Erné and Lübbig 1976) that in the range $2\pi \leq \beta_e \leq 20\pi$, τ_1 is related to the loop time constant τ_L through the expression

$$\tau_1 = \frac{2\tau_L}{0.47\beta_e - 1} \ln \left\{ \frac{[0.47\beta_e - 1]\Phi_0}{4\delta\Phi_e} + 1 \right\}$$

where $\delta\Phi_e$ is the flux variation used to start the flux transition. A typical value used is

$$\delta\Phi_e \simeq 2 \times 10^{-2}\Phi_0$$

τ_2 is related to the intrinsic gap response time $\tau_J = \Phi_0/R_J I_1$. It can be shown that increasing β_e , τ_2 becomes independent of β_e . For $\beta_e > 10\pi$ it tends to the limit value $\tau_2 \simeq 0.3\tau_J$. In the same framework the energy dissipated during the flux transition can be computed. It can be shown (Erné and Lübbig 1976) that

in the case of large values of β_e it has the expression

$$E_d = \left\{ 2\pi - 1 - \frac{\pi}{16} \left[2\pi J_0\left(\frac{\pi}{2}\right) - \frac{2\pi}{\beta_e} \right] \right\} \frac{I_1 \Phi_0}{2\pi} + \frac{1.95}{2\pi} \Phi_0 I_1 - \frac{\Phi_0^2}{2L}$$

The last expression can be reasonably approximated by

$$E_d \approx I_1 \Phi_0 - \frac{\Phi_0^2}{2L} \quad (12.2.16)$$

Therefore if β_e increases, maintaining the junction critical current I_1 constant, the energy dissipation does not increase, whereas the area of the hysteresis loop increases.

12.3 Superconducting Interferometer

Let us consider a superconducting loop interrupted by two weak links or, equivalently, two junctions in parallel. We assume a "symmetric configuration" (Fig. 12.11). In this case the two superconducting branches connecting the two weak links have the same inductance $L/2$. The two weak links generally can have different maximum critical currents. In this configuration, on increasing the current I a value I_c will be reached in which both junctions are in the normal state. At this point a voltage V is developed across the device. We now investigate the dependence of I_c on the external applied field B_e . The single valuedness condition for the phase around the loop (12.2.2) now becomes

$$\varphi_a^* - \varphi_b^* = 2\pi n - 2\pi \frac{\Phi}{\Phi_0} \quad (12.3.1)$$

where φ_a^* and φ_b^* are the gauge invariant phase differences across the junctions

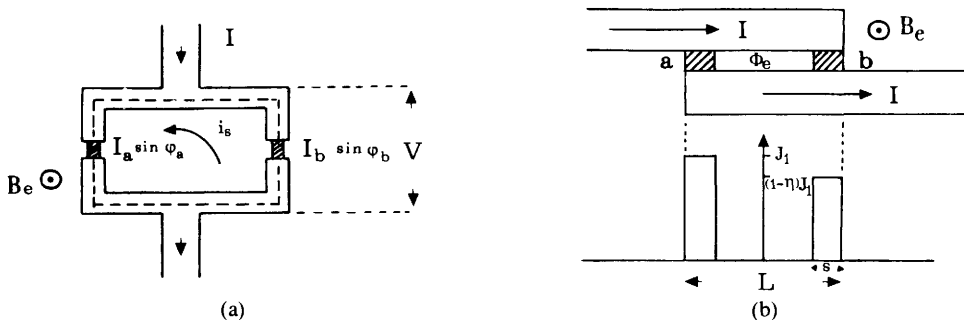


Figure 12.11 (a) Symmetric two junctions configuration. (b) Equivalence of a two junction loop with zero inductance to a single junction peaked at the edges. The current density distribution is shown in the lower part of the figure.

a and b respectively. Φ is the effective flux in the loop and is given, as before, by

$$\Phi = \Phi_e + L i_s \quad (12.3.2)$$

where L is the ring inductance and i_s indicates the shielding circulating current. The latter is related to the Josephson currents through the two weak links by the expression

$$2i_s = I_a \sin \varphi_a^* - I_b \sin \varphi_b^* \quad (12.3.3)$$

The total current I flowing into the device is given by

$$I(\varphi_a^*, \varphi_b^*) = I_a \sin \varphi_a^* + I_b \sin \varphi_b^* \quad (12.3.4)$$

12.3.1 Zero Inductance Case. Let us assume that the loop inductance can be neglected. In this case the effective flux is equal to the geometrical flux:

$$\Phi \approx \Phi_e$$

Thus combining (12.3.1) and (12.3.4) we get

$$I(\Phi_e, \varphi_a^*) = I_a \sin \varphi_a^* + I_b \sin \left(\varphi_a^* - 2\pi \frac{\Phi_e}{\Phi_0} \right) \quad (12.3.5)$$

In order to find $I_c(\Phi_e)$ we must compute the maximum value of the current with respect to φ_a^* . However, we follow a different approach. When the inductance of the ring is negligible, the double junction configuration is equivalent to a single junction with current density peaked at the edges. We discussed this problem in Chapter 4. Using the symbols introduced there, we assume the current density to be given by

$$J(x) = J_1 \left[p_{s/2} \left(x - \frac{l+s}{2} \right) + p_{s/2} \left(x + \frac{l+s}{2} \right) - \eta p_{s/2} \left(x - \frac{l+s}{2} \right) \right] \quad (12.3.6)$$

where the parameter ξ is assumed to be zero and $p_{s/2}(x)$ are the square wave function. For the sake of generality the parameter η is introduced to account for the difference in the critical currents of the two weak links (Fig. 12.11b). The equivalence with the double junction configuration is straightforward:

$$I_a = J_1 s W$$

$$I_b = J_1 s W (1 - \eta) = I_a (1 - \eta)$$

$$\Phi_e = B_e d (L - s)$$

$$\Phi_J = B_e s d \quad (12.3.7)$$

where W is the width of the junction in the direction of the applied field, d is the magnetic penetration ($d = \lambda_{L1} + \lambda_{L2} + t$), and Φ_J accounts for the coupling between the external field B_e and the junctions. The maximum Josephson current is the modulus of the Fourier transform of (12.3.6):

$$I_c(k) = W J_1 \left| \left(2 - \eta\right) \frac{2 \sin ks/2}{k} \cos k \frac{l+s}{2} + -j\eta \frac{2 \sin ks/2}{k} \sin k \frac{l+s}{2} \right|$$

This can be written as

$$I_c(\phi_e, \phi_J) = I_a \left| \frac{\sin \pi \phi_J}{\pi \phi_J} \left| (2 - \eta) \cos \pi \phi_e - j\eta \sin \pi \phi_e \right| \right| \quad (12.3.8)$$

where

$$\phi_e = \frac{\Phi_e}{\Phi_0}; \quad \phi_J = \frac{\Phi_J}{\Phi_0}$$

Assuming that $\eta = 0$, that is, $I_a = I_b$, (12.3.8) reduces to

$$I_c(\phi_e, \phi_J) = 2 I_a \left| \frac{\sin \pi \phi_J}{\pi \phi_J} \left| \cos \pi \phi_e \right| \right| \quad (12.3.9)$$

If the flux Φ_J threading the junctions is negligible, the last expression gives

$$I_c(\phi_e) = 2 I_a |\cos \pi \phi_e| \quad (12.3.10)$$

This is shown in Fig. 12.12a. Thus when the two junctions are identical, the maximum current exhibits a modulation by the external field, from zero up to $2 I_a$. The periodicity is the flux quantum Φ_0 . When the critical currents of the two junctions are different, it is easy to derive from (12.3.8) the relation

$$I_c(\phi_e) = |(I_a + I_b) \cos \pi \phi_e - j(I_a - I_b) \sin \pi \phi_e|$$

or

$$I_c(\phi_e) = \left[I_a^2 + I_b^2 + 2 I_a I_b \cos 2\pi \phi_e \right]^{1/2} \quad (12.3.11)$$

This expression is shown in Fig. 12.12c. The maximum current varies between $|I_a + I_b|$ and $|I_a - I_b|$. The general expressions that account for the effect of the field coupled to the junctions are shown in Fig. 12.12b and 12.12d for $\Phi_J/\Phi_e = s/(L-s) \approx 0.2$.

First experimental observations on double junction loops have been carried out by Jaklevic et al. (1964a, 1965). The samples investigated were formed by two tunneling junctions (see Fig. 12.13). Typical experimental data are shown in Fig. 1.10b. Effects due to the field coupled to the junction and to

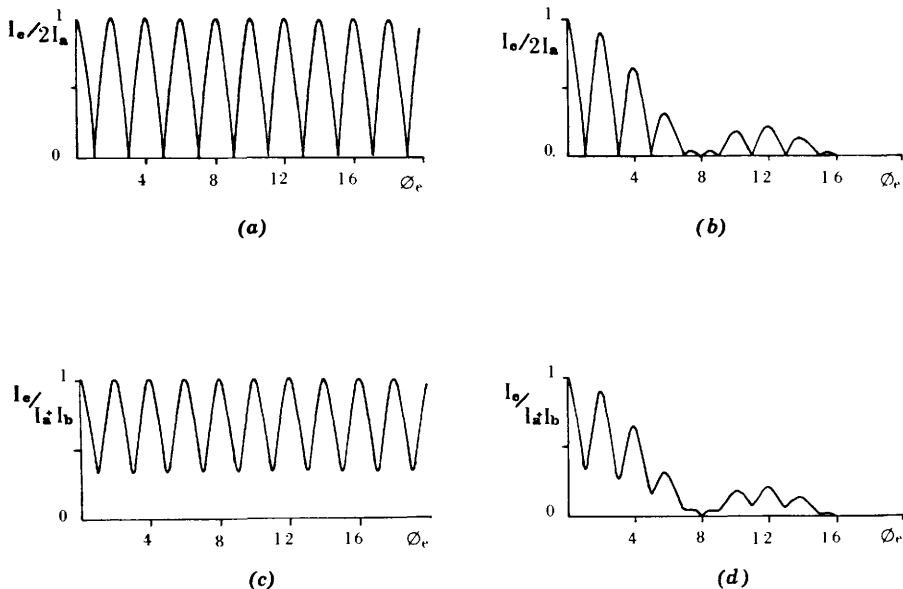


Figure 12.12 Critical current versus external flux for a two junction loop of negligible inductance. (a) $I_a = I_b, \Phi_J = 0$; (b) $I_a = I_b, \Phi_J/\Phi_e \approx 0.2$; (c) $I_a = I_{b/2}, \Phi_J = 0$; (d) $I_a = I_{b/2}, \Phi_J/\Phi_e \approx 0.2$.

the difference between the critical currents ($I_a \neq I_b$) are evident. Subsequent investigations on point contact devices have been performed by Zimmerman and Silver (1964, 1966a).

As is apparent from (12.3.9) and (12.3.10) and from the experimental results, the behavior of the double junction loop for $L=0$ can be understood in terms of the interference of the two phase differences across the junctions. This is a quantum interference phenomenon, related to the macroscopic quantum nature of the Cooper pairs. This aspect has been further demonstrated by

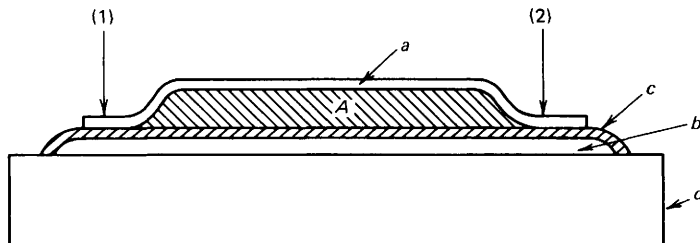


Figure 12.13 Cross section of a Josephson junction pair vacuum deposited on a quartz substrate (d). A thin oxide layer (c) separates thin ($\sim 1000 \text{ \AA}$) tin films (a) and (b). The junctions (1) and (2) are connected in parallel by superconducting thin film links forming an enclosed area (A) between junctions. Current flow is measured between films (a) and (b). (After Jaklevic et al. 1964a.)

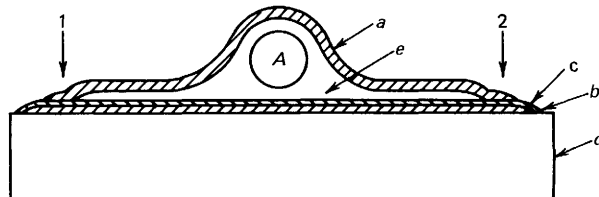


Figure 12.14 Cross-section of a Josephson junction pair vacuum deposited on a quartz substrate (*d*). A thin oxide layer (*c*) separates thin ($\sim 1000 \text{ \AA}$) tin films (*a* and *b*). The junctions (1) and (2) are connected in parallel by superconducting thin film links enclosing the solenoid (*A*) embedded in Formvar (*e*). Current flow is measured between films *a* and *b*. (After Jaklevic et al. 1964b.)

Jaklevic et al. (1964b). In their experiment a solenoid A was placed within the superconducting loop (see Fig. 12.14). In this way the field at the superconducting electrodes was negligible, while the flux inside the loop was nonzero. In varying the flux an interference pattern was observed similar to the one obtained in the case of flux produced by an external solenoid. This shows that the system was effectively sensitive to the vector potential, \mathbf{A} , which is different from zero around the superconducting loop even if the field at the junctions is zero. It is indeed the contour integral $\oint \mathbf{A} \cdot d\mathbf{l}$ which has physical meaning. This behavior is quantum mechanical in nature and can be explained in terms of the existence of a single valued wave function (Aharonov and Bohm 1959, 1961). A different experiment in which the modulation of the current was produced without applied field to the loop was performed by Jaklevic et al. (1965). In the configuration adopted, a region of the superconducting loop was thinner than the London penetration depth. When a current was flowing into this region a modulation was observed in the critical current of the device. The effect can be understood by observing that in this case it is not the flux but the fluxoid that has to be taken into account in (12.3.1) in order to compute the difference $\varphi_b^* - \varphi_a^*$. In fact, for the assumed geometry the value of the fluxoid is just determined by the line integral of the current density.

Finally, within the context of structures of negligible loop inductance, we mention the experimental and theoretical work carried out by Dmitrenko, Bondarenko and Narbut (1969) on point contact junctions.

12.3.2 Metastable States. Let us examine the case of zero external field and current applied to the two junction loops ($\Phi_e = 0, I = 0$). The inductance L is assumed to be different from zero. We restrict our analysis to the case $I_a = I_b$. From (12.3.4) it follows that

$$\sin \varphi_a^* = -\sin \varphi_b^*$$

Therefore the single valuedness condition (12.3.1) becomes

$$2\varphi_a^* = 2\pi n - 2\pi \frac{L i_s}{\Phi_0} \quad (12.3.12)$$

The circulating current (12.3.3) is given by

$$i_s = I_a \sin \varphi_a^* \quad (12.3.13)$$

Combining the last two expressions, we have

$$i_s = I_a \sin \left(\pi n - \pi \frac{L i_s}{\Phi_0} \right)$$

which can be written as

$$\pm \frac{i_s}{I_a} = \sin \left(\frac{\beta_e}{2} \frac{i_s}{I_a} \right) \quad (12.3.14)$$

where $\beta_e = 2\pi L I_a / \Phi_0$. Figure 12.15 is the graphical solution of (12.3.14). As in the previous case (single junction loop), for high β_e values a set of metastable states are possible corresponding to the local minima of the free energy of the system.

The first investigations of these metastable states have been performed by Goldman (1964, 1965). The samples consisted of two coupled, two junction loops. Thin lead films were used as the superconducting material. One of the loops was employed as a magnetometer (see Chapter 13) to measure the applied field. The technique used was to warm up the device above the critical temperature in the presence of a known magnetic field. Subsequently the sample was cooled and the field was removed. The trapped flux was detected by measuring the critical current of a tin strip placed near the lead ring.

Further investigations have been performed, by way of a simpler technique, by Goldman, Kreisman and Scalapino (1965) and Jaklevic et al. (1965). In these experiments the $V-I$ characteristic of the two junction loop was measured. In fact, if the device is in one of these metastable states, a circulating current is present. As a consequence the maximum zero voltage current is lower than the one observable when no circulating current is flowing. Figure 12.16 gives experimental data after Jaklevic et al. (1965) which show the different metastable states.

Finally, we mention the work of Wilson and Gayley (1972) on planar configurations employing Sn-SnO_x-Sn junctions. In particular, these authors present a way to preselect the quantum state of the two junction loop.

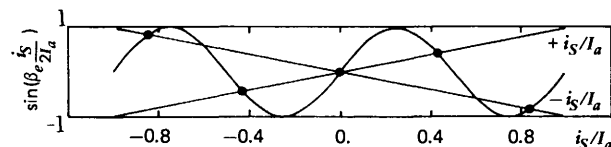


Figure 12.15 Graphical solution of (12.3.14). The circles correspond to the metastable states of the two junction loop.

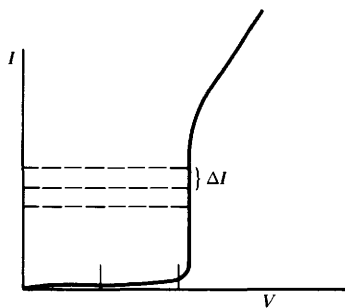


Figure 12.16 Representation of experimentally observed multiple valued maximum Josephson current displayed on an oscilloscope at 350 cps. The current at $V=0$ can attain three possible maximum values before switching along the circuit load line (dashed lines) to the normal tunneling characteristics. (After Jaklevic et al. 1965.)

12.3.3 Asymmetric Double Junction Configuration. In the preceding section the behavior of the double junction configuration was analyzed under particular restrictive assumptions. Let us consider now the general case, in which the inductance L of the loop is different from zero and an external field is applied. The only restriction we make is to assume that the field coupled to the junctions is negligible. To introduce a greater generality we consider a configuration in which the current is fed to the junctions asymmetrically (see Fig. 12.17a). In this case, as discussed by Fulton, Dunkleberger and Dynes (1972), the flux induced by the shielding current i_s can be written as

$$Li_s = L_a I_a \sin \varphi_a - L_b I_b \sin \varphi_b \quad (12.3.15)$$

where L_a and L_b are coefficients with the dimensions of an inductance. They are related to the inductance of the loop L by the expression

$$L = L_a + L_b$$

In general, L_a and L_b cannot be interpreted as the inductances of the two arms; however, they are useful parameters. The device is represented now by the equivalent circuit of Fig. 12.17b.

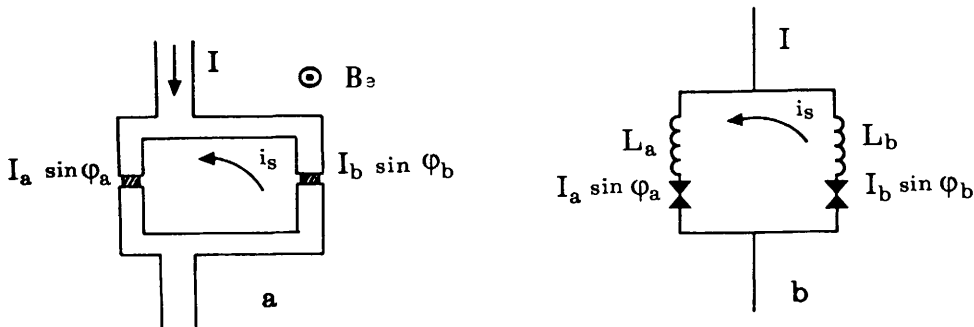


Figure 12.17 (a) Asymmetric double junction configuration. (b) Equivalent circuit for the asymmetric configuration.

By using (12.3.15) and (12.3.2) we obtain from (12.3.1):

$$2\pi n = \varphi_a - \varphi_b + 2\pi \frac{\Phi_e}{\Phi_0} + 2\pi \frac{L_a I_a}{\Phi_0} \sin \varphi_a - 2\pi \frac{L_b I_b}{\Phi_0} \sin \varphi_b \quad (12.3.16)$$

Introducing the parameters:

$$\beta_a = 2\pi \frac{L_a I_a}{\Phi_0}; \quad \beta_b = 2\pi \frac{L_b I_b}{\Phi_0}; \quad \phi_e = \frac{\Phi_e}{\Phi_0}$$

the last equation can be written as

$$2\pi n = \varphi_a - \varphi_b + 2\pi \phi_e + \beta_a \sin \varphi_a - \beta_b \sin \varphi_b \quad (12.3.17)$$

The current flowing into the device is given by (12.3.4), which is rewritten for convenience:

$$I(\varphi_a, \varphi_b) = I_a \sin \varphi_a + I_b \sin \varphi_b \quad (12.3.18)$$

Considering ϕ_e and I as external parameters, (12.3.17) and (12.3.18) form a set of two nonlinear equations in the two variables φ_a and φ_b . We are interested essentially in the critical current I_c as a function of the external field ϕ_e . The problem is reduced to a search for the maximum value of $I(\varphi_a, \varphi_b)$ with φ_a and φ_b subjected to the constrain (12.3.17). For this purpose different methods have been employed; these have been discussed and compared recently by B. Landman (1976). The most suitable method is that of Lagrange multipliers used by Tsang and Van Duzer (1975). Following these authors we introduce the new variable α , and consider the function:

$$\begin{aligned} I'(\varphi_a, \varphi_b, \alpha) &= I_a \sin \varphi_a + I_b \sin \varphi_b + \alpha(\varphi_a - \varphi_b + 2\pi \phi_e + \\ &+ \beta_a \sin \varphi_a - \beta_b \sin \varphi_b - 2\pi n) \end{aligned}$$

The problem is therefore reduced to that of finding the critical points of I' as a function of φ_a , φ_b , and α . Hence we take the derivatives of the last expression and equate them to zero:

$$\frac{\partial I'}{\partial \alpha}(\varphi_a, \varphi_b, \alpha) = \varphi_a - \varphi_b + 2\pi \phi_e + \beta_a \sin \varphi_a - \beta_b \sin \varphi_b - 2\pi n = 0$$

$$\frac{\partial I'}{\partial \varphi_a}(\varphi_a, \varphi_b, \alpha) = I_a \cos \varphi_a + \alpha(1 + \beta_a \cos \varphi_a) = 0$$

$$\frac{\partial I'}{\partial \varphi_b}(\varphi_a, \varphi_b, \alpha) = I_b \cos \varphi_b - \alpha(1 + \beta_b \cos \varphi_b) = 0$$

By eliminating α we get two equations:

$$\phi_e = \frac{1}{2\pi} (\varphi_{bc} - \varphi_{ac} + \beta_b \sin \varphi_{bc} - \beta_a \sin \varphi_{ac}) \quad (12.3.19a)$$

$$\varphi_{bc} = \cos^{-1} \left[\frac{-1}{I_b / (I_a \cos \varphi_{ac}) + \beta_T} \right] \quad (12.3.19b)$$

where the subscript c indicates that φ_a and φ_b are the values corresponding to the critical current I_c of the device and the parameter β_T , defined by

$$\beta_T = \beta_b + \beta_a \left(\frac{I_b}{I_a} \right) \quad (12.3.20)$$

has been introduced.

The integer n has been taken to be equal to zero, because we are interested in the zero flux quantum state. For a fixed value of the external applied flux, (12.3.19a) and (12.3.19b) are a set of two equations in the variables φ_{ac} , φ_{bc} . After a solution is found for the pair φ_{ac} , φ_{bc} , these values can be substituted into (12.3.18) to find the current. In this way the I_c vs. ϕ_e dependence can be computed. A numerical method, such as a multidimensional Newton-Rapson iteration, can be used (Landman 1976). However, since we are interested in the $I_c(\phi_e)$ dependence for all the values of ϕ_e , a different approach is possible (Tsang and Van Duzer 1975). First, from (12.3.19b) we find all the pairs φ_{ac} , φ_{bc} . They form a locus in the φ_a , φ_b plane. Subsequently, each pair on that locus is used in (12.3.19a) to find ϕ_e and in (3.3.4) to find the corresponding value for I_c . In a similar way the effective flux Φ as a function of the applied flux Φ_e , when the system is at its critical state, can be found. In fact, from (12.3.1) it follows that

$$\frac{\Phi}{\Phi_e} = \frac{\varphi_{ac} - \varphi_{bc}}{2\pi} + n \quad (12.3.21)$$

In Fig. 12.18a and b the $\varphi_{ac} - \varphi_{bc}$ locus and the corresponding $I_c(\phi_e)$ pattern are shown for the simple case $I_a = I_b$, $\beta_a = \beta_b = \beta_T = 0$ (i.e., $L = 0$). There is always a correspondence between the $I_c(\phi_e)$ and $\Phi(\phi_e)$ dependences and the properties of the locus.

The following general properties are valid:

- (a) The φ_{ac} , φ_{bc} locus is periodic. By the substitution

$$\varphi_{ac} \rightarrow \varphi_{ac} + 2m\pi; \quad \varphi_{bc} \rightarrow \varphi_{bc} + 2n\pi \quad (12.3.22)$$

where m and n are integers, different branches are obtained. They are

marked in Fig. 12.18a by the pair of values (m, n) . The substitution (12.3.22) has no effect on the value of I_c (12.3.18) and introduces only a shifting term $\Delta\phi_e = n - m$ in ϕ_e (12.3.19a). The different branches in Fig. 12.18b correspond to different (n, m) choices. Let us recall that (12.3.19a) is just the flux quantization condition at the critical points of the device. Therefore those branches correspond to the case of $(n - m)$ flux quanta Φ_0 inside the loop.

- (b) As can be easily verified (12.3.19b), the inversion symmetry property exists:

$$\varphi_{bc}(\varphi_{ac}) = -\varphi_{bc}(-\varphi_{ac}) \quad (12.3.23)$$

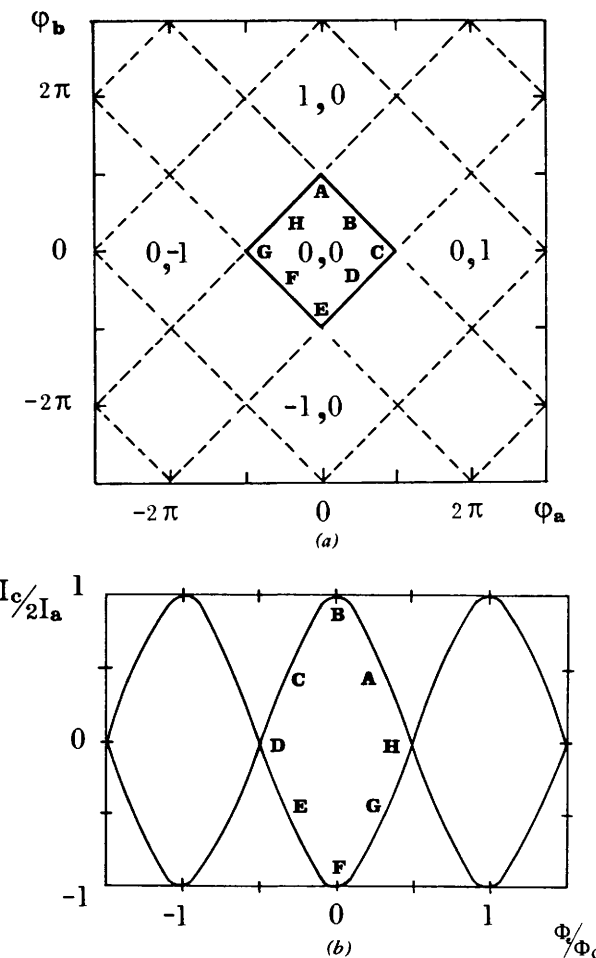


Figure 12.18 φ_{ac} - φ_{bc} loci (a) and critical current versus applied field (b) for a loop with two junctions of equal critical current ($I_a = I_b$) and in the case of negligible inductance ($L_a = L_b = 0$). The capital letters indicate the points in the locus corresponding to the points in a branch of the magnetic field pattern.

From this:

$$I_c(\phi_e) = -I_c(-\phi_e) \quad (12.3.24)$$

- (c) From (12.3.19b) it follows that for any value of β_T , I_a , I_b on the locus the values $\varphi_{ac} = 2m\pi + \pi/2$ will correspond to the values $\varphi_{bc} = 2m\pi + \pi/2$. At these points the critical current is given by $I_c = \pm(I_a \pm I_b)$. Therefore the maximum value for I_c is given by $I_a + I_b$.

In Fig. 12.19a, b, c the theoretical dependences I_c vs. ϕ_e are reported, together with the corresponding φ_{ac} , φ_{bc} locus, for different values of L . The curve refers to the case $I_a = I_b$ and to a symmetric configuration ($L_a = L_b$).

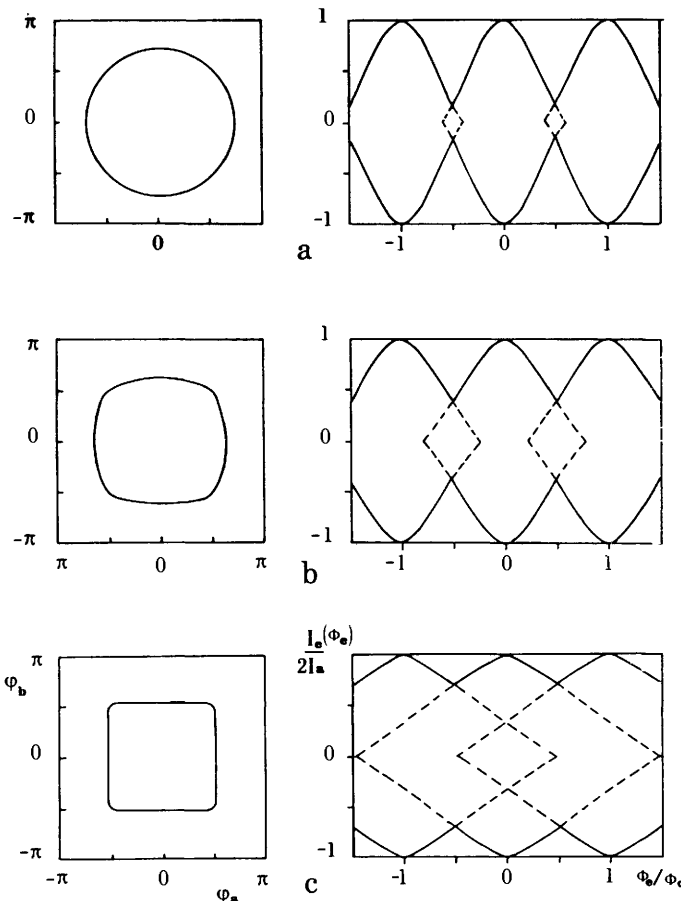


Figure 12.19 The locus in the φ_a , φ_b plane and the corresponding magnetic pattern for a two junction loop with a symmetric configuration ($L_a = L_b$) and in the case of equal critical currents ($I_a = I_b$). (a) $\beta_a = \beta_b = 0.1\pi$; $\beta_T = 0.2\pi$; (b) $\beta_a = \beta_b = 0.3\pi$; $\beta_T = 0.6\pi$; (c) $\beta_a = \beta_b = \pi$; $\beta_T = 2\pi$.

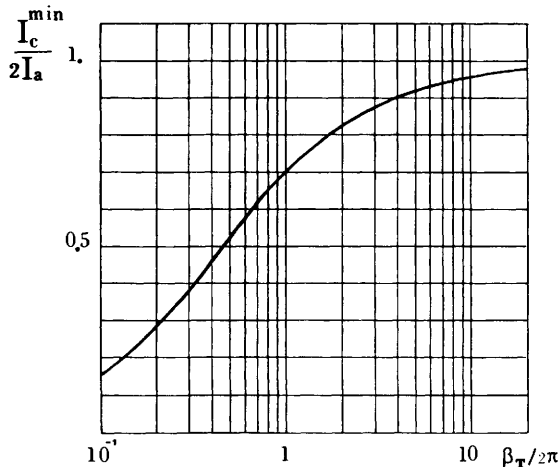


Figure 12.20 Theoretical values of the minimum modulation current I_c^{\min} in the $I_c\text{-}\Phi_e$ pattern as a function of the loop inductance ($\beta_T/2\pi = I_a L/\Phi_0$). The case refers to a symmetric double junctions configuration ($L_a = L_b$). I_a is the critical Josephson current which is assumed to be the same for both junctions.

Increasing the loop inductance, the depth of the modulation in the $I_c(\Phi_e)$ pattern decreases. In this case the minimum value of the current in the loop, I_c^{\min} , occurs for $\phi_e = (2n+1)/2$ ($n=0, \pm 1, \dots$). The dependence of I_c^{\min} on the loop inductance L , that is, on $\beta_T = 2\pi I_a L/\Phi_0$ is reported in Fig. 12.20. For $\beta_T \rightarrow \infty$, $I_c^{\min} \rightarrow 2I_a - \Phi_0/L$ (Zimmerman and Silver 1966a). The effect of the loop inductance in symmetric double junction configurations has been extensively analyzed both theoretically and experimentally by De Bruyn Ouboter and De Waele (De Waele and De Bruyn Ouboter 1969; De Bruyn Ouboter and De Waele 1970). The samples investigated were point contact devices. In Fig. 12.21 the data reported by these authors are shown. The solid line is the theoretical dependence computed by using a graphical method. Experimental

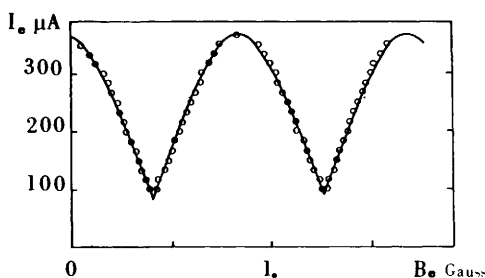


Figure 12.21 Experimental I_c vs. B_e dependence for a symmetrical double junction configuration. To get the best fit of the theoretical curve (solid line) with the experimental data (circles) the values $I_a = 185 \mu\text{A}$, $\beta_T = 1$ have been chosen. Thus $L = 1.8 \cdot 10^{-12} \text{ H}$, $I_c = 2I_a = 370 \mu\text{A}$, $I_c^{\min} = 84 \mu\text{A}$, and $\Delta B = \Phi_0/A = 0.86 \text{ G}$ where the value $A = 24 \times 10^{-8} \text{ cm}^2$ has been used for the loop area. (After De Bruyn Ouboter and De Waele 1970.)

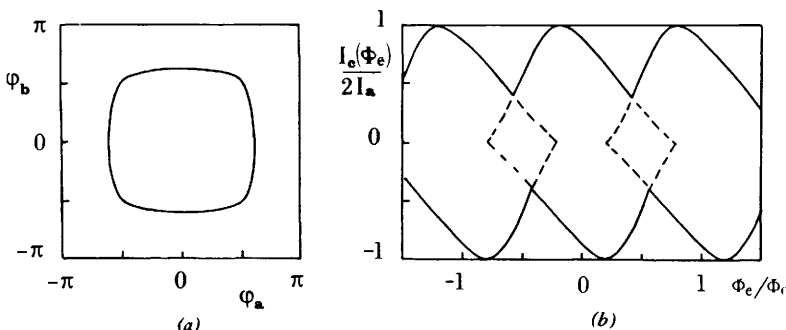


Figure 12.22 Theoretical magnetic field dependence of the maximum critical current (*b*) and the corresponding φ_a , φ_b locus (*a*) for an asymmetric configuration ($L_a \neq L_b$). The two junctions are assumed to have the same critical current ($I_a = I_b$). The values of the characteristic parameters are $\beta_a = 0.5\beta$, $\beta_b = 0.1\pi$, and $\beta_T = 0.6\pi$.

investigation of symmetric configurations has been carried out more recently by Lum and Van Duzer (1975) and Carelli and Modena (1976) using Dayem bridge structures.

When the configuration is asymmetric ($L_a \neq L_b$) the $I_c(\Phi_e)$ dependence tends to be tilted (see Fig. 12.22). The effect becomes stronger as more L_a is different from L_b . It is interesting to observe by comparing Figs. 12.22 and 12.19b that the locus φ_{ac} , φ_{bc} is the same. In fact, from (12.3.19b) it is easy to see that only the value of β_T enters in the φ_{ac} , φ_{bc} dependence. Asymmetric double junction configurations have been investigated by Clarke and Paterson (1971). The samples used were Pb-Cu/Al-Pb (*SNS*) junctions, connected by lead films. The theoretical dependence was computed by using numerical methods.

The $I_c(\Phi_e)$ dependence for the most general case $I_a \neq I_b$, $L_a \neq L_b$ is reported in Fig. 12.23. The envelope is not too different from the previous case ($I_a = I_b$); however, the shape of curve in the metastable state region is rather different.

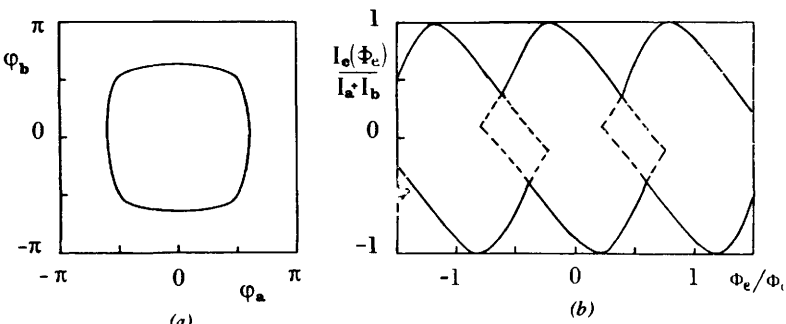


Figure 12.23 Theoretical magnetic field dependence of the maximum critical current (*b*) and the corresponding φ_a , φ_b locus (*a*) for an asymmetric configuration ($L_a \neq L_b$) in the case of junctions with different critical current ($I_a \neq I_b$). $\beta_a = 0.5\pi$, $\beta_b = 0.1\pi$, $\beta_T = 0.5\pi$, and $I_b = 0.8I_a$.

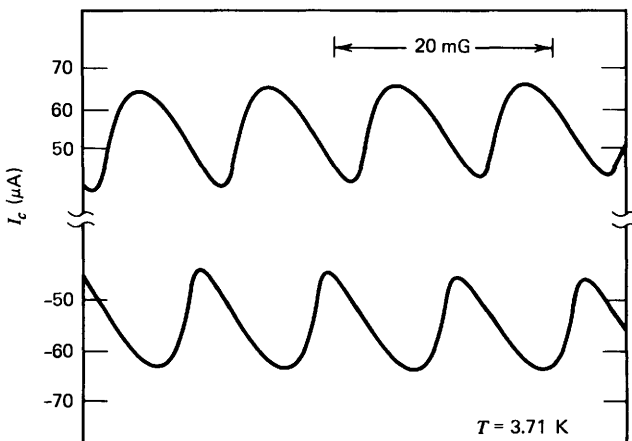


Figure 12.24 Positive and negative I_c vs. B_e pattern for an Sn-Sn double junction near T_c . (After Fulton, Dunkleberger, and Dynes 1972.)

The most complete analysis of double junctions configuration has been performed by Fulton, Dunkleberger, and Dynes (1972). These authors have carried out a theoretical analysis valid for a general current phase relation. Experimental data on Sn-Sn junctions are reported in that work, and a comparison with the theory is performed. In Fig. 12.24 some data are given for a configuration with $I_a/I_b=0.22 \pm 0.005$, $\beta_T=0.55 \pm 0.03$, $\beta_a=(0.052 \pm 0.025)\pi$, $\beta_b=(0.173 \pm 0.10)\pi$.

Further theoretical and experimental work has been carried out more recently by Peterson and Hamilton (1979).

CHAPTER 13

SQUIDS: Theory and Applications

The configurations we described in Chapter 12 are the basic elements for a class of devices that usually are referred to as SQUID. The acronym stands for “superconducting quantum interference devices.” These devices in the operating conditions give rise to an output voltage signal, which is a periodic function of the flux threading a superconducting loop in which one or two weak links are inserted. The minimum flux variation they can measure is of the order of fractions ($\sim 10^{-5}$) of the flux quantum Φ_0 ($\Phi_0 = 2.07 \times 10^{-15}$ weber).

For the single junction SQUID the junction is shorted by a superconducting path; therefore, the voltage response is obtained by coupling the loop to a radio frequency biased tank circuit. For this reason this kind of device is usually called an r.f. SQUID. In the double junction configuration the two weak links are not shorted by a superconducting path; therefore, the d.c. current-voltage characteristics can be observed. In the operating conditions the device is current biased at a value slightly greater than the critical current, and the voltage drop across it is monitored. These kinds of devices are usually called “d.c. SQUIDs.” An excellent review of both kinds of SQUIDs has been given by Clarke (1973, 1976). We here describe the basic principles of operation of both r.f. and d.c. SQUIDs. The maximum sensitivity and practical measurement techniques are discussed. Furthermore, the configuration in which the superconducting loop is interrupted by a resistive section, the so-called resistive SQUID, is briefly discussed. Some of the principal applications of the devices discussed in this chapter are also described.

13.1 Radio Frequency SQUID

An r.f. SQUID is basically made by a superconducting loop with a single junction (see Section 12.2) coupled to a radio frequency biased tank circuit.

There are essentially two different modes in which the device can operate, depending on the Φ vs. Φ_e dependence (Silver and Zimmerman 1967; Goodkind and Stolfa 1970). The parameter that characterizes the behavior is $\beta_e = 2\pi(LI_1/\Phi_0)$ (see the preceding chapter).

If $\beta_e \leq 1$, the internal flux increases monotonically with the applied external flux Φ_e (Fig. 12.7a). The mode is usually called “dispersive.”

If $\beta_e > 1$, the Φ vs. Φ_e dependence is hysteretic (Fig. 12.7b). When the amplitude of the r.f. applied flux is greater than a given value, the hysteresis loops are spanned. Therefore energy is dissipated by the system and the mode is called "dissipative."

We describe in some detail both operating modes of the SQUID for the cases $\beta_e \ll 1$ and $\beta_e \geq 1$. Before going through the analytic derivation of the behavior of the single junction loop coupled to the r.f. circuit, we examine some particular features that follow from the presence of the nonlinear element in the superconducting loop.

13.1.1 Effects of the Parametric Inductance. As we saw in Section 11.6, in the limit of zero bias the Josephson element can be described in terms of a parametric inductance. When the junction is inserted in the superconducting loop, its behavior affects the total inductance of the loop. In the case of small signal variation, that is, when the amplitude of the time varying component of the applied flux is small compared to the flux quantum Φ_0 , the expression of the effective inductance L_{eff} of the system can be obtained directly from the static characteristics discussed in Section 12.2.2.

In fact, in this approximation following Silver and Zimmerman (1967, 1975) we can define

$$L_{\text{eff}} = - \frac{d\Phi_e}{di} \quad (13.1.1)$$

Taking the derivative with respect to i of (12.2.3) we obtain the relation

$$\frac{d\Phi_e}{di} = -L + \frac{1}{di/d\Phi} \quad (13.1.2)$$

From (12.2.4) it follows that

$$\frac{di}{d\Phi} = - \frac{2\pi I_1}{\Phi_0} \cos \frac{2\pi\Phi}{\Phi_0} \quad (13.1.3)$$

Combining (13.1.1), (13.1.2), and (13.1.3) we obtain

$$L_{\text{eff}} = L \left[1 + \frac{1}{\beta_e \cos(2\pi\Phi/\Phi_0)} \right] \quad (13.1.4)$$

From the last expression we can identify the junction equivalent inductance:

$$L_J(\Phi) = \frac{L}{\beta_e \cos(2\pi\Phi/\Phi_0)} \quad (13.1.5)$$

An analogous expression for L_J has been derived by Josephson (1964) in a different way. The effect of the parametric inductance can be observed by

coupling the SQUID to a tank circuit of inductance L_T and capacitance C_T (Fig. 13.1). If L is the inductance of the superconducting loop, the system can be described by the equivalent circuit of Fig. 13.2 (Goodkind and Stofa 1970). The weak link is represented by the parametric inductance L_J and the resistance R_J . We are assuming that the resistance R_J is small enough to "shunt" the capacitance of the link. In terms of the resistively shunted model (Section 6.2) this implies that the parameter $\beta_J = 1/\omega_J CR_J$ is much greater than 1. The effective inductance of the tank circuit coupled to the SQUID, computed using the equivalent circuit of Fig. 13.2, is given by

$$\tilde{L}_T = L_T \left[1 - \kappa^2 \frac{L}{L_J(\phi) + L} \right] \quad (13.1.6)$$

where κ is the coupling coefficient defined by $M^2 = \kappa^2 L_T L$ and $\phi = \Phi/\Phi_0$.

Let us assume that $\beta_e \ll 1$. In such a case (12.2.9a) can be approximated as

$$\Phi \approx \Phi_e \quad (13.1.7)$$

Therefore (13.1.6) becomes

$$\tilde{L}_T = L_T \left[1 - \frac{\kappa^2}{1 + (1/\beta_e \cos 2\pi\phi_e)} \right] \approx L_T (1 - \kappa^2 \beta_e \cos 2\pi\phi_e)$$

The effective tank circuit inductance, because of its coupling to the SQUID, is a periodic function of the magnetic flux ϕ_e coupled to the loop. This dependence can be observed by measuring the variation of the effective resonance frequency of the tank circuit $\tilde{\nu} = 1/(\tilde{L}_T C_T)^{1/2}$ as a function of the applied magnetic field (Silver and Zimmerman 1967).

In the limit of $\kappa^2 \beta_e \ll 1$, it is easy to derive the following expression:

$$\frac{\Delta\tilde{\nu}}{\nu} \approx -\frac{1}{2} \frac{\Delta\tilde{L}_T}{L_T} \approx -\frac{1}{2} \kappa^2 \beta_e (1 - \cos 2\pi\phi_e)$$

The theoretical dependence $\Delta\tilde{\nu}/\nu$ as a function of the applied flux is shown in

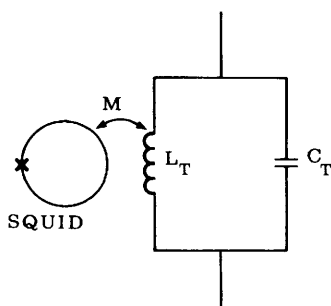


Figure 13.1 SQUID coupled to the tank circuit via a mutual inductance M .

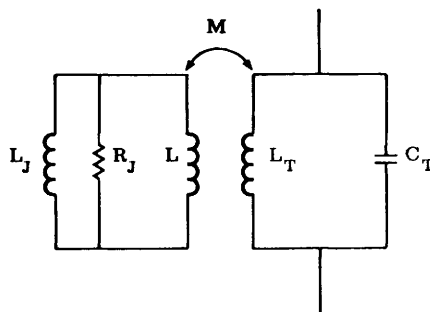


Figure 13.2 Equivalent circuit of SQUID coupled to tank circuit.

Fig. 13.3 together with experimental data (circles) after Silver and Zimmerman (1967). For the theoretical expression the value $\beta_e K^2 \simeq 10^{-2}$ has been assumed.

A different method for observing the effect of the parametric inductance in the limit $\beta_e \ll 1$ has been more recently employed by Pascal and Sauzade (1974). These authors have analyzed the noise spectrum of a preamplifier connected to the tank circuit. The preamplifier was working at a temperature of 4.2 K. The frequency at which the peak in the noise spectrum occurs varies with the applied flux Φ_e .

If $\beta_e > 1$, the situation is rather different. The static characteristics are hysteretic. The contribution of L_J becomes negligible compared to the ring inductance L . This circumstance can be easily verified by looking at (13.1.1) for L_{eff} and by observing that on increasing β_e the stable branches of the i vs. Φ_e dependence (Fig. 12.7d) approach progressively straight lines. However, at the edges of these regions where transitions between different branches occur the shape of the curve changes. This effect is more evident for β_e not much greater than 1.

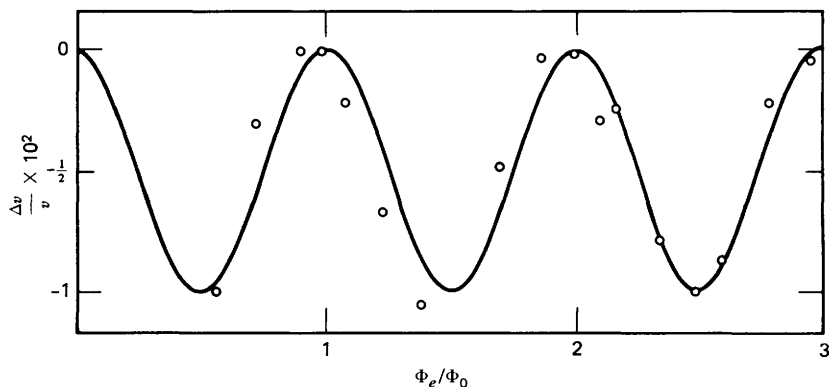


Figure 13.3 Experimental magnetic field dependence (circles) of the effective resonance frequency of the tank circuit coupled to the SQUID, for $\beta_e \ll 1$. (After Silver and Zimmerman 1967). The solid line is the theoretical dependence $\Delta \bar{v}/v$ computed in the same approximation.

The same argument holds for the Φ vs. Φ_e dependence (Fig. 12.7b). In fact, deriving (12.2.3) with respect to Φ_e we get

$$\frac{d\Phi}{d\Phi_e} = 1 + L \frac{di}{d\Phi_e}$$

Combining the last expression with (13.1.1):

$$\frac{d\Phi}{d\Phi_e} = 1 - \frac{L}{L_{\text{eff}}(\phi)}$$

Therefore the slope of the Φ vs. Φ_e curve is related to the effective inductance L_{eff} of the device. The change in this slope can be detected (Pascal and Sauzade 1974) by biasing the tank circuit by a slow varying sawtooth current with a superimposed r.f. signal of small amplitude. The r.f. signal V_T detected across the tank circuit is proportional to $d\Phi/dt$ and therefore to $d\Phi/d\Phi_e$. The slowly varying signal is proportional to the quasistatic flux. The V_T vs. Φ_e dependence is reported in Fig. 13.4. The Φ vs. Φ_e dependence is also shown. It is interesting to note that this kind of measurement supplies a way to measure the ratio LI_1/Φ_0 , that is, the value of β_e (see Fig. 13.5).

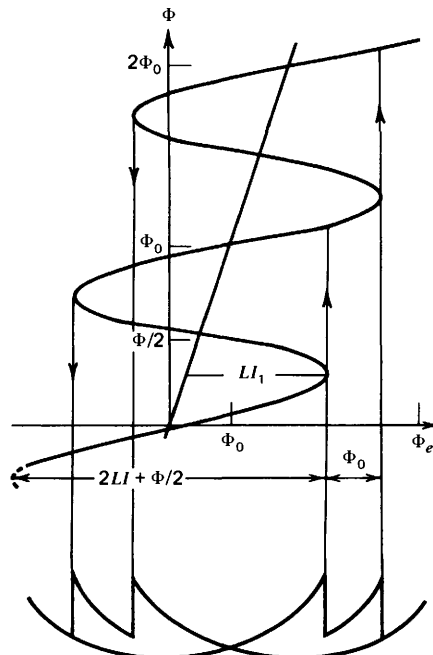


Figure 13.4 LI_1/Φ_0 measurement for a dissipative SQUID ($\beta_e > 1$). (After Pascal and Sauzade 1974.)

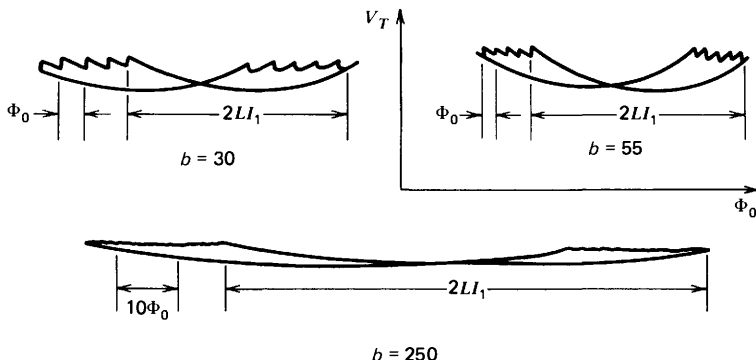


Figure 13.5 Experimental curves for measuring $LI_1/\Phi_0 = b$. (After Pascal and Sauzade 1974.)

13.1.2 R.F. SQUID in the Dispersive Mode. In the case $\beta_e < 1$ it is possible to derive an analytical solution for the single junction loop coupled to the r.f. current biased tank circuit (Ernè, Hahlbohm, and Lübbig 1976). The starting point is (12.2.15) which describes the single junction loop in dynamical conditions. The substitution is made,

$$\beta_e \sin\left(2\pi \frac{\Phi}{\Phi_0}\right) = 2\pi \sum_{n=1}^{\infty} M_n(\beta_e) \sin 2\pi n \frac{\Phi_e}{\Phi_0}$$

which directly follows from (12.2.9a), and from (12.2.10), valid for $\beta_e < 1$.

Instead of considering the general analytical solution we now examine the simplified case $\beta_e \ll 1$. This case has been analyzed by Hansma (1973). We present a simple generalization of Hansma's theory by which it is possible to derive both the in-phase and out-of-phase components of the r.f. voltage output across the tank circuit (Balsamo and Paternò 1979).

The superconducting ring is coupled to the inductance L_T via the mutual inductance M (See Fig. 13.6). An r.f. current

$$i_r = I_r \sin \omega t$$

is fed into the tank circuit. The frequency ω is near the resonant frequency of the circuit $\omega_0 = 1/\sqrt{L_T C_T}$. The r.f. current in the inductor L_T is

$$i_T = I_T \sin(\omega t + \theta)$$

The SQUID is subjected to a d.c. flux Φ_{dc} and to a r.f. flux $MI_T \sin(\omega t + \theta)$. The total flux is

$$\Phi_e(t) = \Phi_{dc} + \Phi_{rf} \sin(\omega t + \theta)$$

where $\Phi_{rf} = MI_T$.

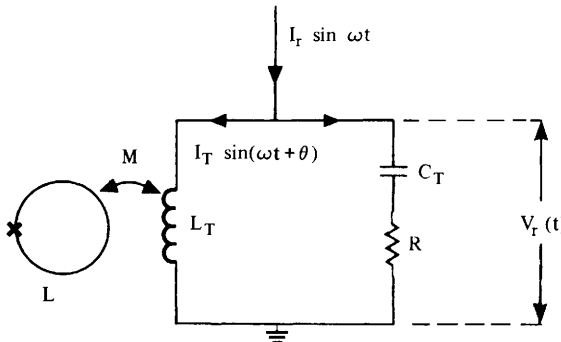


Figure 13.6 SQUID coupled to the r.f. biased tank circuit.

The assumption $\beta_e \ll 1$ ensures that the shielding current in the ring is negligible; therefore the effective flux Φ is essentially given by the external flux Φ_e . The current in the ring (12.2.9b) is

$$i(t) = -I_1 \sin \left[\frac{2\pi}{\Phi_0} (\Phi_{dc} + \Phi_{rf} \sin(\omega t + \theta)) \right] \quad (13.1.8)$$

In the presence of a time varying flux $\Phi_e(t)$ the total current in the superconducting loop includes a contribution due to the normal junction resistance R_J . In this derivation we assume this normal current, i_n , to be negligible compared to the Josephson current $i(t)$. This corresponds to the assumption that

$$|i_n| = \left| -\frac{1}{R_J} \frac{d\Phi_e}{dt} \right| \simeq \frac{\omega \Phi_0}{R_J} \ll I_1$$

The high frequency limit has been considered by Notarys, Wang and Mercereau (1973). More recently this problem has been investigated theoretically by Buhrman and Jackel (1976) and Soerensen (1976) and both theoretically and experimentally by Callegari and Deaver, Jr. (1977).

Expression (13.1.8) is a single valued function. Using trigonometric relations and Fourier-Bessel expansion (11.1.3) it can be written as

$$\begin{aligned} i(t) = & -I_1 \left\{ \sin \varphi_0 \left[J_0(\varphi_1) + 2 \sum_{n=1}^{\infty} J_{2n}(\varphi_1) \cos[2n(\omega t + \theta)] \right] \right. \\ & \left. + \cos \varphi_0 \left[2 \sum_{n=0}^{\infty} J_{2n+1}(\varphi_1) \sin[(2n+1)(\omega t + \theta)] \right] \right\} \quad (13.1.9) \end{aligned}$$

where $J_n(x)$ are Bessel functions of integer order and

$$\varphi_0 = 2\pi \frac{\Phi_{dc}}{\Phi_0}; \quad \varphi_1 = 2\pi \frac{\Phi_{rf}}{\Phi_0}$$

This oscillating current through the mutual inductance M causes an induced voltage in the tank circuit:

$$V_I = -M \frac{di}{dt}$$

This voltage in turn produces an induced current in the inductor given by

$$i_I(t) = \frac{V_I}{Z_S}$$

where

$$Z_S = R + j \left(\omega L_T - \frac{1}{\omega C_T} \right) = |Z_S| e^{j\theta_s} \quad (13.1.10)$$

is the complex series impedance of the tank circuit. We assume that $\omega \approx \omega_0$ and that the Q of the tank circuit is reasonably large. Therefore in computing the induced current $i_I(t)$ we can only consider the effect of the fundamental ω component in the expression of $i(t)$ (13.1.9). The components with frequency multiple of ω are in fact strongly attenuated. Using complex notations, the induced current into the inductor L_T is

$$i_I(t) \approx \text{Im} \left\{ \frac{j\omega M}{Z_S} I_1 \cos \varphi_0 2J_1(\varphi_1) e^{j(\omega t + \theta)} \right\} \quad (13.1.11)$$

and the total current in the inductor L_T is

$$i_T(t) + i_I(t) \approx \text{Im} \left\{ \left[I_T + j \frac{2I_1\omega M}{|Z_S|} \cos \varphi_0 J_1(\varphi_1) e^{-j\theta_s} \right] e^{j(\omega t + \theta)} \right\}$$

The voltage V_r across the tank circuit is given by

$$V_r(t) = \text{Im} \left\{ \left[j\omega L_T I_T - \frac{2\omega^2 M I_1}{|Z_S|} \cos \varphi_0 J_1(\varphi_1) e^{-j\theta_s} \right] e^{j(\omega t + \theta)} \right\}$$

At the first order, assuming that the contribution of the induced current is small, the following relations hold:

$$\omega L_T T_T = |Z_P| I_r; \quad \theta + \frac{\pi}{2} = \theta_p$$

where

$$Z_P = \frac{j\omega L_T \left(\frac{1}{j\omega C_T} + R \right)}{j\omega L_T + \frac{1}{j\omega C_T} + R} = |Z_P| e^{j\theta_p} \quad (13.1.12)$$

is the complex parallel impedance of the tank circuit. The expression for the voltage $V_r(t)$ becomes

$$V_r(t) = \text{Im} \left\{ \left[|Z_P| I_r e^{j\theta_p} + \frac{j\omega^2 M 2 I_1 L_T}{|Z_S|} \cos \varphi_0 J_1(\varphi_1) e^{j(\theta_p - \theta_s)} \right] e^{j\omega t} \right\} \quad (13.1.13)$$

An analogous expression for $V_r(t)$ was derived by Silver and Zimmerman (1975). The first term on the right side is just the contribution of the tank circuit when the coupling with the SQUID is negligible. From (13.1.13) it can be seen that at the resonance ($\omega = \omega_0$), $\theta_p = \theta_s = 0$ and the two terms are in quadrature. For $Q \gg 1$ and $\omega \approx \omega_0$ the following approximations are valid (Terman 1951):

$$|Z_S| \approx \frac{\omega L_T}{Q} (1 + \delta^2)^{1/2}; \quad \theta_s \approx -\tan^{-1} \delta$$

$$|Z_P| \approx \frac{(\omega L_T)^2}{|Z_S|}; \quad \theta_p \approx -\theta_s$$

where

$$\delta = 2Q \left(\frac{\omega}{\omega_0} - 1 \right)$$

Therefore (13.1.13) becomes

$$V_r(t) = \text{Im} \left\{ \left[\frac{Q \omega L_T I_r}{(1 + \delta^2)^{1/2}} e^{j \tan^{-1} \delta} + j \frac{\omega M 2 I_1 Q}{(1 + \delta^2)^{1/2}} \cos \varphi_0 J_1(\varphi_1) e^{2j \tan^{-1} \delta} \right] e^{j\omega t} \right\}$$

By using the dimensionless units

$$V_D = V_r / \frac{\omega L_T \Phi_0}{M}; \quad I_D = I_r / \frac{\Phi_0}{MQ}$$

the last expression can be written as

$$\begin{aligned} V_D(t) &= \text{Im}\left\{\left[I(\delta)e^{j\tan^{-1}\delta} + jA \cos \varphi_0 F(I_D, \delta)e^{2j\tan^{-1}\delta}\right]e^{j\omega t}\right\} \\ &\equiv \text{Im}\{\tilde{Z}e^{j\omega t}\} \end{aligned} \quad (13.1.14)$$

where for convenience the quantities

$$\begin{aligned} A &= \kappa^2 \frac{Q\beta_e}{\pi} = \frac{MQ\beta_e}{\pi L_T L}, \quad I(\delta) = \frac{I_D}{(\delta^2 + 1)^{1/2}}; \\ F(I_D, \delta) &= \frac{1}{(\delta^2 + 1)^{1/2}} J_1(2\pi I(\delta)) \end{aligned}$$

have been introduced. Therefore the in-phase and in-quadrature components of the output voltage are

$$\text{Re}[\tilde{Z}] = I(\delta) \cos(\tan^{-1}\delta) - A \cos \varphi_0 F(I_D, \delta) \sin(2\tan^{-1}\delta)$$

$$\text{Im}[\tilde{Z}] = I(\delta) \sin(\tan^{-1}\delta) + A \cos \varphi_0 F(I_D, \delta) \cos(2\tan^{-1}\delta)$$

In Fig. 13.7, a vector representation of the SQUID response in the plane $x = \text{Re}[\tilde{Z}]$, $y = \text{Im}[\tilde{Z}]$ is shown. Different values of the parameter δ are considered. For each value of δ the two limiting cases $\Phi_{dc} = n\Phi_0$ (triangles) and $\Phi_{dc} = [(2n+1)/2]\Phi_0$ (crosses) are shown. Each segment joining these two limiting cases corresponds to a fixed value of the current I_D . The vector joining the origin with the middle point of each segment corresponds to the SQUID response for $\Phi_{dc} = \Phi_0/4$. Since in this case $\cos \varphi_0 = 0$, this vector represents the response of the tank circuit when the coupling to the SQUID is negligible. The value used for the quantity A was $A = 0.2$. As is apparent, for $\delta = 0$ (i.e., $\omega = \omega_0$) the two contributions of the SQUID and of the tank circuit are in quadrature. The situation is symmetric around $\delta = 0$, although the Φ_{dc} dependence is reversed.

If the voltage across the tank circuit is measured by using a peak detector, the quantity of interest is the modulus of (13.1.14):

$$|V_D| = \left[I^2(\delta) + A^2 F^2(I_D, \delta) \cos^2 \varphi_0 - 2I(\delta)AF(I_D, \delta) \cos \varphi_0 \sin(\tan^{-1}\delta) \right] \quad (13.1.15)$$

In Fig. 13.8 $|V_D|$ as a function of I_D is shown for different values of δ . For each value of δ the two curves corresponding to $\Phi_{dc} = n\Phi_D$, and $\Phi_{dc} = (n + \frac{1}{2})\Phi_0$ are given. For a fixed value of I_D the depth of the d.c. field modulation ΔV_D is a function of the detuning parameter δ . This dependence is reported in Fig. 13.9

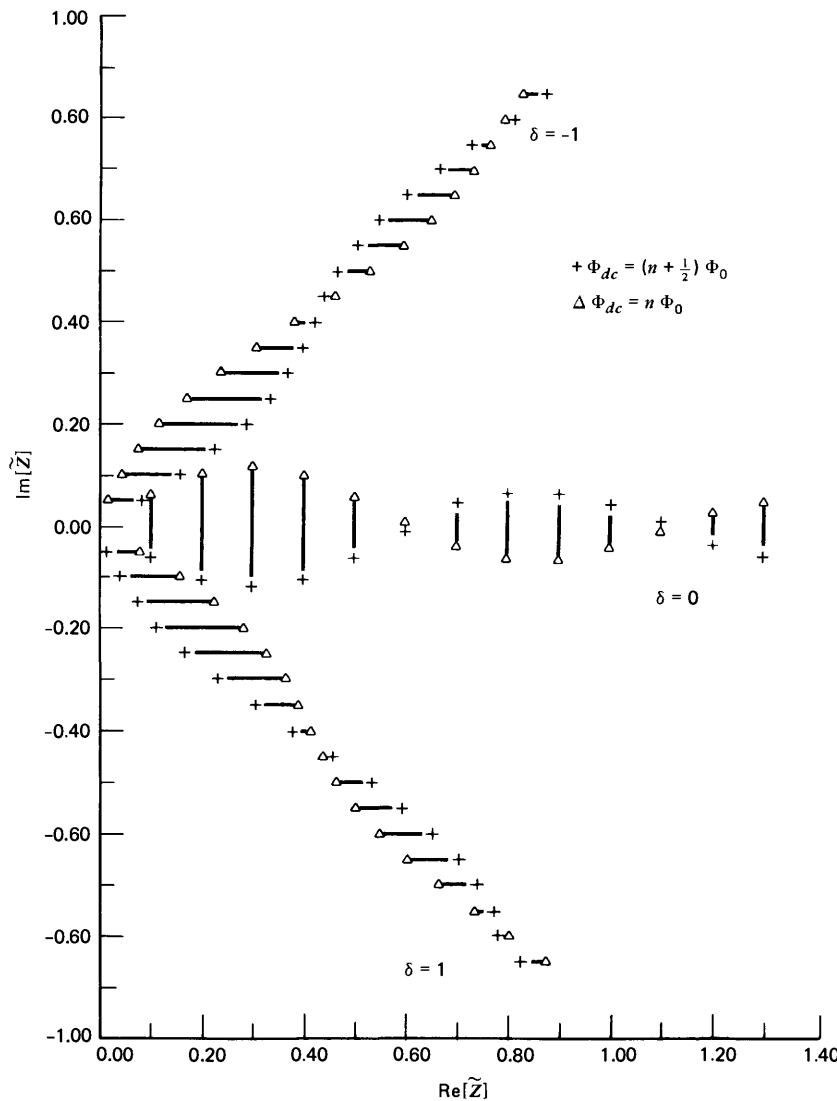


Figure 13.7 The response of the r.f. SQUID in the dispersive mode, in the complex plane for different values of the detuning parameter $\delta = 2Q(\omega/\omega_0 - 1)$. Each segment corresponds to a fixed value of the amplitude of the r.f. bias current. The value $A = 0.2$ has been assumed.

for $A = 0.2$, $I_D = 0.4$. The peak voltage across the tank circuit $|V_D|$ as a function of a d.c. field applied to the SQUID exhibits a periodic dependence. In Fig. 13.10 $|V_D|$ vs. Φ_{dc} is shown for $I_D = 0.2$ and $I_D = 0.4$, for two different values of the detuning parameter δ . It is interesting to observe that at the resonance, that is, for $\delta = 0$, the periodicity is $\Phi_0/2$ instead of Φ_0 . This “anomalous” behavior has been experimentally observed recently by Erné and Luther (1978). The

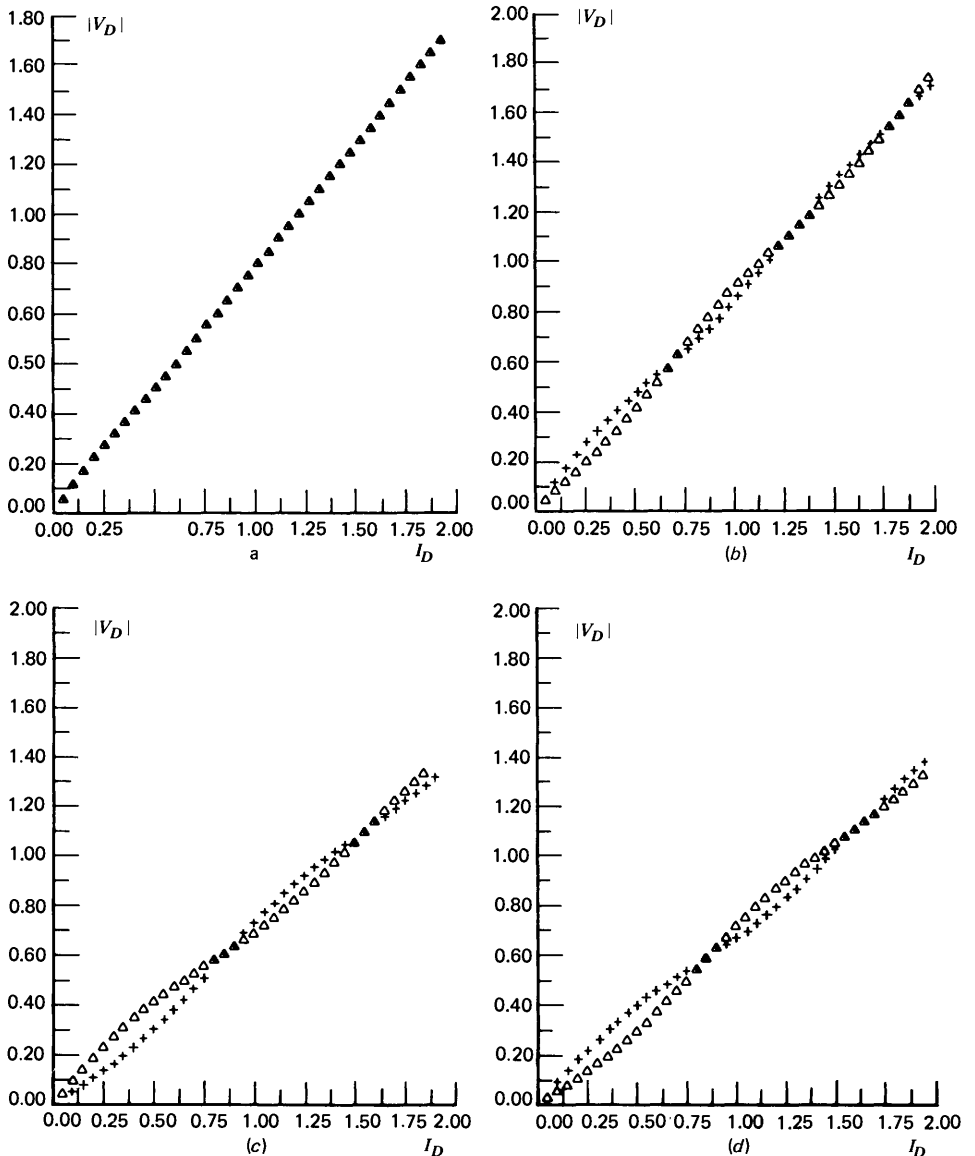


Figure 13.8 Theoretical $|V_D|$ vs. I_D dependence computed from (13.1.15) for different values of the detuning parameter δ . The two curves refer to the two limiting cases $\Phi_{dc} = (n + \frac{1}{2})\Phi_0$ and $2n\Phi_0$. (a) $\delta = 0$; (b) $\delta = 0.5$; (c) $\delta = 1 -$; (d) $\delta = -1$. The value used for A is the same as in Fig. 13.7.

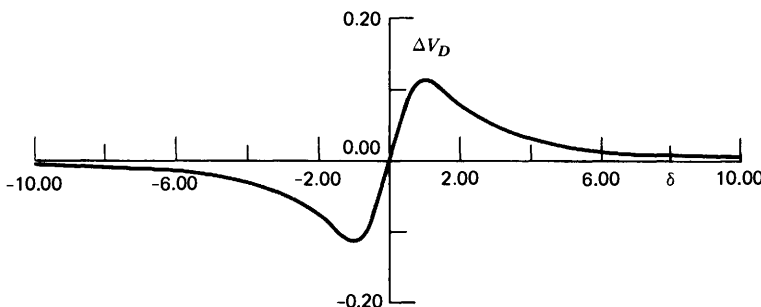


Figure 13.9 Maximum flux modulation ΔV_D as a function of δ for a fixed value of the r.f. current amplitude I_D . The curve has been computed assuming that $I_D = 0.4$, $A = 0.2$.

percentage of modulation, assuming that $F(I_D, \delta) \approx 1$, as can be derived from (13.1.15), is of the order of A . Therefore the maximum voltage variation is

$$\Delta V_D \approx A \frac{\omega L_T \Phi_0}{M} \approx \beta_e \frac{\omega L_T \Phi_0}{M} \quad (13.1.16)$$

where we have used the approximation: $\kappa^2 Q \approx \pi$.

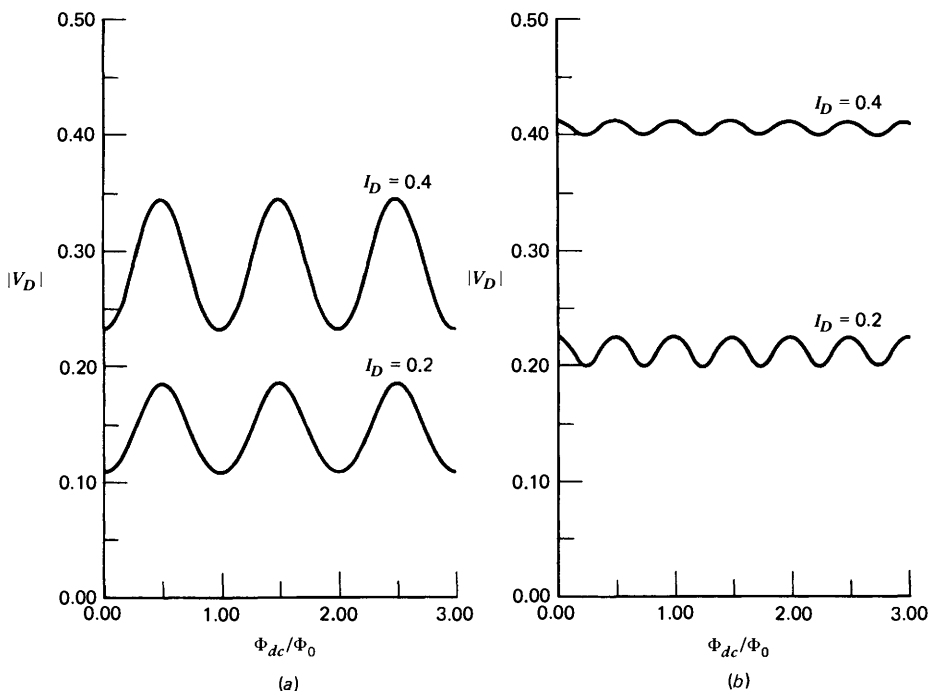


Figure 13.10 Theoretical dependence of the peak voltage across the tank circuit $|V_D|$ as a function of the external d.c. flux Φ_{dc} , for two different values of the r.f. current amplitude I_D . (a) $\delta = 1$; (b) $\delta = 0$.

If the restriction $\beta_e \ll 1$ is not imposed, it is possible to derive an expression analogous to (13.1.13) which is valid in the whole range $\beta_e \leq 1$. In this case the voltage across the tank circuit is given by (Ernè 1978a):

$$V_r(t) = \text{Im} \left\{ \left[|Z_p| I_r e^{j\theta_p} + j \frac{\omega^2 M I_1}{|Z_s|} G(\varphi_0, \varphi_1) e^{j(\theta_p - \theta_s)} \right] e^{j\omega t} \right\}$$

where $G(\varphi_0, \varphi_1)$ can be expressed in terms of Bessel functions:

$$G(\varphi_0, \varphi_1) = \sum_{n=1}^{\infty} (-1)^{n+1} \frac{2J_n(n\beta_e)}{n\beta_e} J_1(n\varphi_1) \cos n\varphi_0$$

For $\beta_e \ll 1$

$$G(\varphi_0, \varphi_1) = 2 \cos \varphi_0 J_1(\varphi_1)$$

and we recover (13.1.13).

A detailed experimental investigation of the r.f. SQUID in the dispersive regime has been performed by Rifkin et al. (1974, 1976). The sample used was a niobium point contact into a ring of toroidal configuration (see Section 13.4). The total measured inductance of the loop was $1.0 \cdot 10^{-10}$ H. Because of this low value of L , critical currents as high as $3 \mu\text{A}$ for the weak link were possible, while the condition $\beta_e \ll 1$ was satisfied. The tank circuit was tuned at a frequency of 30 MHz, and it was current biased by an r.f. oscillator coupled to it through a small capacitor and a stainless steel coaxial line. The experimental apparatus is schematically shown in Fig. 13.11a. In the same figure (Fig. 13.11b) the dependence of the tank circuit voltage vs. applied flux is reported. The data refer to the case $\beta_e \ll 1$. Circled points are theoretical data computed under this approximation using the theory developed by Hansma (1973). When the condition $\beta_e \ll 1$ is not satisfied, the screening flux cannot be neglected and the approximation $\Phi \approx \Phi_e$ is not possible. The theoretical analysis of the r.f. SQUID, taking into account the shielding current, has been carried out by Rifkin et al. (1974, 1976), Soerensen (1976), and Ernè Hahlbohm and Lübbig (1976). In this case, the $|V_D|$ vs. Φ_{dc} and $|V_D|$ vs. I_D curves are no longer symmetrical with respect to δ . Furthermore, the patterns show appreciable effects depending on the kind of dissipative terms in the link conductance. As Hansma (1973, 1975) has shown, the quasiparticle pair conductance (Section 1.7) in this case becomes important. If we write this term as $\epsilon \sigma_0 \cos \varphi$, it can be shown, for example, that the voltage modulation as a function of δ has no longer a zero crossing for $\delta=0$ but has a finite value that is positive or negative depending on the sign of ϵ . Experimental observations of the effect of the $\cos \varphi$ term have been reported by Nisenoff and Wolf (1975). These data are shown in Fig. 13.12 (cross points) together with the theoretical dependence computed by Ernè, Hahlbohm, and Lübbig (1976), taking into account the $\cos \varphi$ term and in the generalization for $\beta_e \lesssim 1$.

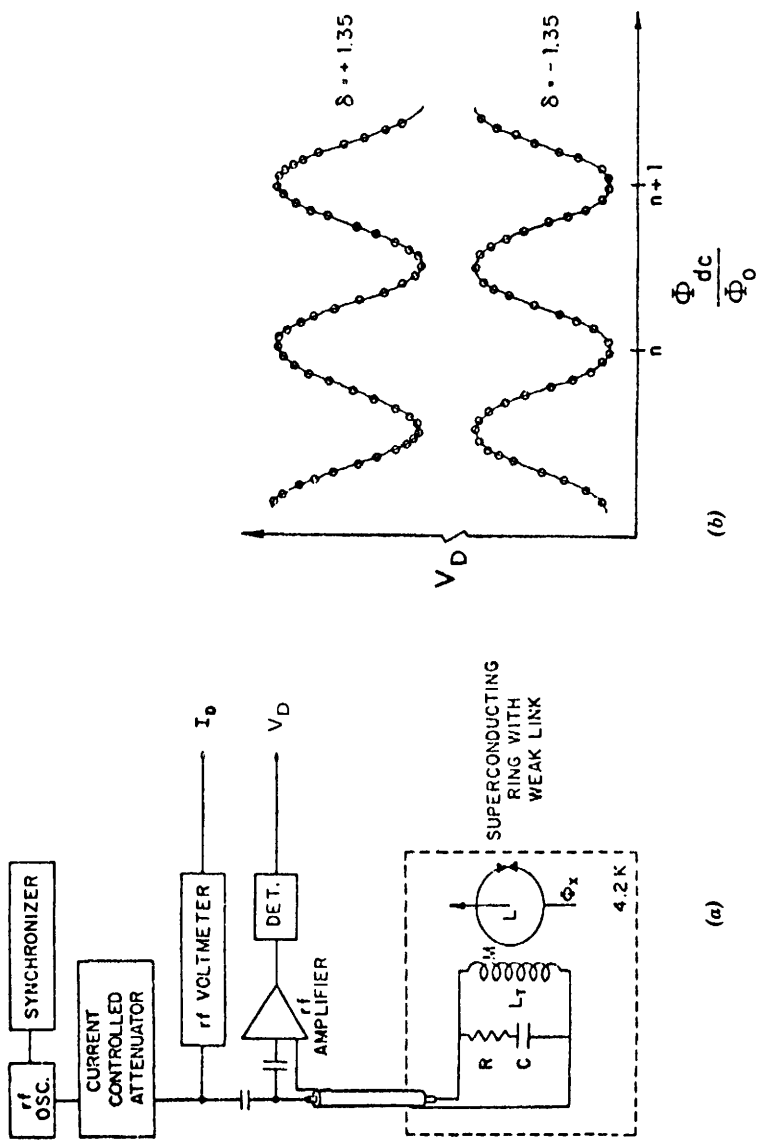


Figure 13.1 (a) Schematic diagram of experimental setup for an r.f. SQUID in the dispersive mode. (b) Experimental $|V_D|$ vs. Φ_{dc} dependence (solid line) compared with the theoretical results (circled points). (After Rifkin et al. 1976.)

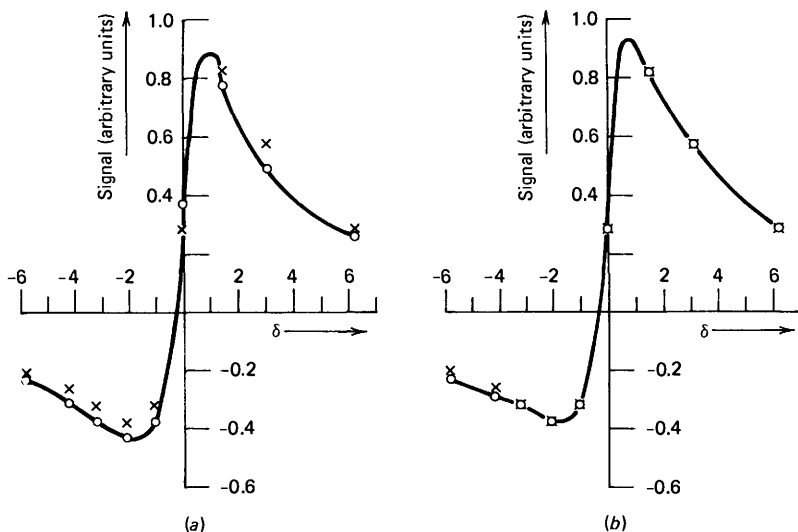


Figure 13.12 The first maximum flux modulation as a function of the detuning parameter $\delta = 2Q[(\omega/\omega_0) - 1]$. The experimental data (crosses) of Nisenoff and Wolf (1975) are compared with the theoretical dependence (circled point) which takes into account the effect of the $\cos\varphi$ term. (a) Best fit calculations under the approximation $\Phi \approx \Phi_e$. (b) General case using the first 10 terms of the series expansion (12.2.10) of the $\Phi(\Phi_e)$ term. (After Ernè, Hahlbohm and Lübbig 1976.)

13.1.3 R.F. SQUID in the Dissipative Mode ($\beta_e > 1$). When β_e is greater than 1, the Φ vs. Φ_e static characteristics are no longer single valued (see Fig. 12.7b). Therefore the analytical approach discussed so far is not suitable for this case. The problem of a SQUID coupled to the tank circuit can be solved by resorting to numerical methods or to analog computer techniques (Simmonds and Parker 1971). The operation of the r.f. SQUID in the hysteretic regime has been described in a semiquantitative way by various authors (Mercereau 1970; Nisenoff 1970; Goodkind and Stolfa 1970; Zimmerman, Thiene and Harding 1970; Webb 1972; Giffard, Webb and Wheatley 1972; Vasil'ev, Danilov and Likharev 1976; Paternò 1977, Likharev and Ulrich 1978). We follow the simple description given by Zimmerman, Thiene, and Harding (1970) in terms of energy dissipation in the tank circuit.

Let us assume the superconducting loop to have a Φ vs. Φ_e dependence as shown in Fig. 13.13a, in which, for simplicity, the stable branches have been drawn as horizontal lines. The transitions occur only between adjacent fluxoid states, $\Delta\Phi = \pm\Phi_0$. If, as before, L is the SQUID inductance and R_J the normal state resistance of the weak link, the transition time is given by $\tau_L = L/R_J$. A tank circuit of inductance L_T and capacitance C_T , r.f. excited at the resonance frequency by a current $I_{rf}\cos\omega t$, is loosely coupled by a mutual inductance M to the SQUID (Fig. 13.13b). We assume that $\omega/2\pi \ll 1/\tau_L$. By using the typical values of $L \approx 10^{-9}$ H and $R_J = 3 \Omega$, it follows that $1/\tau_L \approx 3$ GHz. In normal device operation $\omega/2\pi \approx 20 \div 30$ MHz. The value of the applied flux

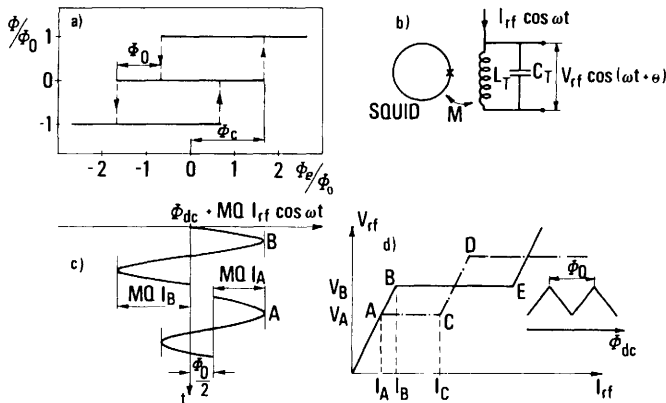


Figure 13.13 Radio frequency SQUID in the dissipative mode ($\beta_e = 2\pi L I_1 / \Phi_0 > 1$). (a) Internal flux Φ vs. external flux Φ_e for a superconducting loop with a junction. (b) Schematic of the SQUID coupled to the r.f. tank circuit. (c) Effective time varying flux applied to the SQUID. The two amplitudes A and B correspond respectively to the situation in which one or two hysteresis circles are spanned. (d) Tank circuit voltage V_{rf} vs. r.f. current amplitude I_{rf} . The two curves refer to the case $\Phi_{dc} = 2n\Phi_0/2$ (ABE branch) and $\Phi_{dc} = (2n+1)\Phi_0/2$ (ACD branch). In the inset the external flux dependence is reported, showing the characteristic triangular shape with a flux quantum Φ_0 periodicity.

Φ_e at which the first transition between the states $\Phi=0$ and $\Phi=\Phi_0$ occurs is

$$\Phi_c \simeq L I_1 \quad (13.1.17)$$

where I_1 is the weak link critical current. If Q is the quality factor of the tank circuit, the r.f. flux sensed by the SQUID is

$$\Phi_{rf} = MQ I_{rf} \cos \omega t$$

Let us consider the case in which a d.c. flux $\Phi_{dc} = \Phi_0/2$ is also applied. The r.f. voltage across the tank circuit is a linear function of I_{rf} (see Fig. 13.13c) as long as

$$I_{rf} \leq I_A = \left(\Phi_c - \frac{\Phi_0}{2} \right) / MQ$$

The peak value is given by

$$V_{rf} = \omega L_T Q I_{rf}$$

The maximum value for which this regime holds is

$$V_A = \frac{\omega L_T}{M} \left(\Phi_c - \frac{\Phi_0}{2} \right) \quad (13.1.18)$$

When $I_{\text{rf}} > I_A$, transitions to the state $\Phi = \Phi_0$ and back to the $\Phi = 0$ state begin to occur. Because of these transitions dissipation starts to occur and energy is subtracted from the tank circuit. Therefore, the amplitude of the r.f. current decreases, and a number of cycles are needed to recover its initial value. The energy dissipated depends on the number of transitions made. Since in traversing one hysteresis loop only two transitions occur, the total dissipation ΔE is twice the expression (12.2.16):

$$\Delta E \simeq \frac{2\Phi_c\Phi_0 - \Phi_0^2}{L} \quad (13.1.19)$$

where (13.1.17) has been used.

The recovery time depends on the Q of the tank circuit and the value of I_{rf} . The r.f. signal exhibits a low frequency sawtooth amplitude modulation. On increasing I_{rf} , the mean value \bar{V}_{rf} of the voltage across the circuit is constant (this is the step region from A to C in Fig. 13.13d) until $I_{\text{rf}} = I_c$. At this point one hysteresis loop is traversed during every r.f. cycle, and the energy ΔE is supplied by the tank circuit. Increasing I_{rf} further, the amplitude \bar{V}_{rf} starts to increase again and the “riser” from C to D on the $\bar{V}_{\text{rf}} - I_{\text{rf}}$ characteristics is described (Fig. 13.13d). A new “step” region is encountered when I_{rf} has a value for which more than one hysteresis is traversed by the r.f. modulation. The second step ends when three hysteresis loops are traversed during every r.f. cycle and its length is twice that of the first step. The $\bar{V}_{\text{rf}} - I_{\text{rf}}$ dependence for the case $\Phi_{\text{dc}} = 0$ is indicated by the solid line in Fig. 13.13d. The first “step” occurs for

$$\bar{V}_B = \frac{\omega L_T}{M} \Phi_c \quad (13.1.20)$$

and has a length twice the first step of the $\Phi_{\text{dc}} = \frac{\Phi_0}{2}$ case. The first “riser” occurs when two hysteresis loops are traced during each r.f. cycle. For values of the d.c. flux Φ_{dc} between 0 and $\frac{\Phi_0}{2}$ (or equivalently $M\Phi_0$ and $(n + \frac{1}{2})\Phi_0$) the $\bar{V}_{\text{rf}} - I_{\text{rf}}$ dependence is contained within the two curves shown in Fig. 13.13d. Fixing the value of I_{rf} on one step and varying the external field, one gets for \bar{V}_{rf} the triangular dependence sketched in Fig. 13.13d, whose periodicity is a flux quantum Φ_0 . The amplitude of this variation is easily computed by subtracting (13.1.20) from (13.1.18):

$$\Delta V = \frac{\omega L_T}{M} \frac{\Phi_0}{2} \quad (13.1.21)$$

On the linear branches of the triangular \bar{V}_{rf} vs. Φ_{dc} dependence the variation in \bar{V}_{rf} for a small variation $\delta\Phi_{\text{dc}}$ of the d.c. applied flux is

$$\frac{\delta\bar{V}_{\text{rf}}}{\delta\Phi_{\text{dc}}} = \frac{\omega L_T}{M} = \frac{\omega}{k} \sqrt{\frac{L_T}{L}} \quad (13.1.22)$$

By using the typical values of $\omega/2\pi = 20$ MHz, $L_T = 0.2 \mu\text{H}$, $L \approx 10^{-9} \text{ H}$, and $\kappa = 0.2$, a sensitivity of $\sim 18 \mu\text{V}/\Phi_0$ is obtained. From this expression it is evident that the flux sensitivity could be made arbitrarily high by decreasing M , that is, the coupling coefficient k between the SQUID and the inductor L_T (as usual, κ is defined by $M^2 = \kappa^2 L_T L$). However, it is obvious that for its operation the SQUID must have a finite coupling to the resonant circuit. Therefore a lower limit for κ^2 must exist.

Simmonds and Parker (1971), by analog computer techniques, have found that the condition of optimum coupling is realized when $\kappa^2 Q \gtrsim 1$. In the framework of the model just described this condition can be derived (Giffard, Webb, and Wheatley 1972) by requiring that point C on the $\bar{V}_{\text{rf}} - I_{\text{rf}}$ dependence be on the right of point B (see Fig. 13.13d). In other words, the length $I_C - I_A$ of the first step (for $\Phi_{\text{dc}} = \frac{\Phi_0}{2}$) must be greater than $I_B - I_A$. However, we have seen before that the increase in the power moving on the first step is equal to

$$\bar{V}_A(I_C - I_A) \approx \frac{\omega}{2\pi} \Delta E$$

Furthermore, it is easy to see that

$$I_B - I_A = \frac{\Phi_0}{2MQ}$$

Therefore, by using (13.1.18) and (13.1.19), it follows from the condition

$$(I_C - I_A) \geq (I_B - I_A)$$

that

$$\frac{M^2 Q}{LL_T} = \kappa^2 Q \geq \frac{\pi}{2}$$

Optimum operating conditions have been discussed by Pascal and Sauzade (1974) and Vasil'ev, Danilov and Likharev (1974).

The simple model we have used predicts an overshoot at the initial point of each step in the $\bar{V}_{\text{rf}} - I_{\text{rf}}$ dependence. Its height should be equal to half the peak-to-peak amplitude of the sawtooth modulation in the r.f. voltage. However this overshoot is much smaller than ΔV and has never been observed experimentally. For this reason, in Fig. 13.13d it has been neglected.

Our analysis of the system is valid only if the energy loss of the tank circuit per cycle is much smaller than the energy dissipated by the SQUID in describing a hysteresis loop.

In Fig. 13.14 a typical experimental arrangement for the operation of the r.f. SQUID in the hysteretic regime is shown. A stainless steel coaxial line is used to feed the tank circuit and to support the SQUID itself. This is immersed

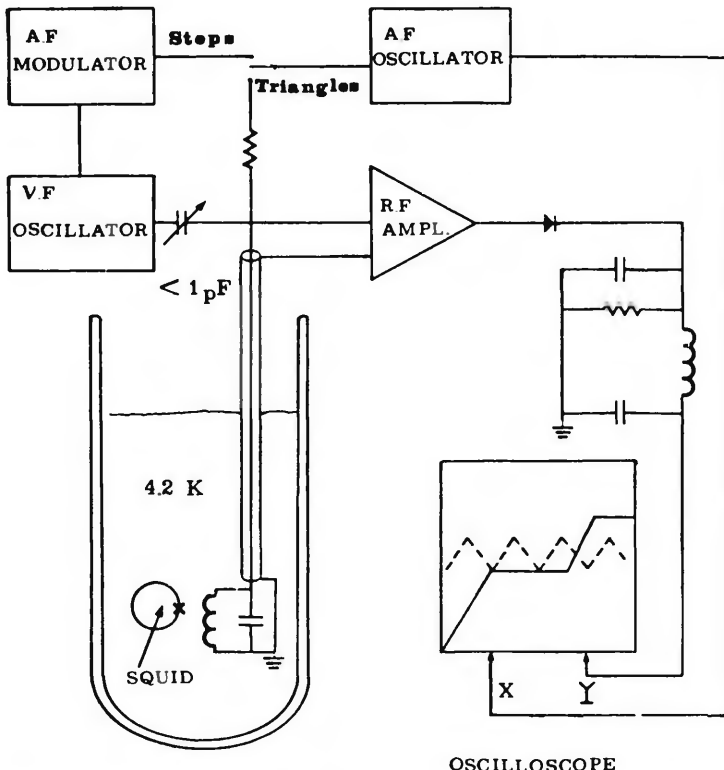


Figure 13.14 Typical experimental arrangement for r.f. SQUID operation.

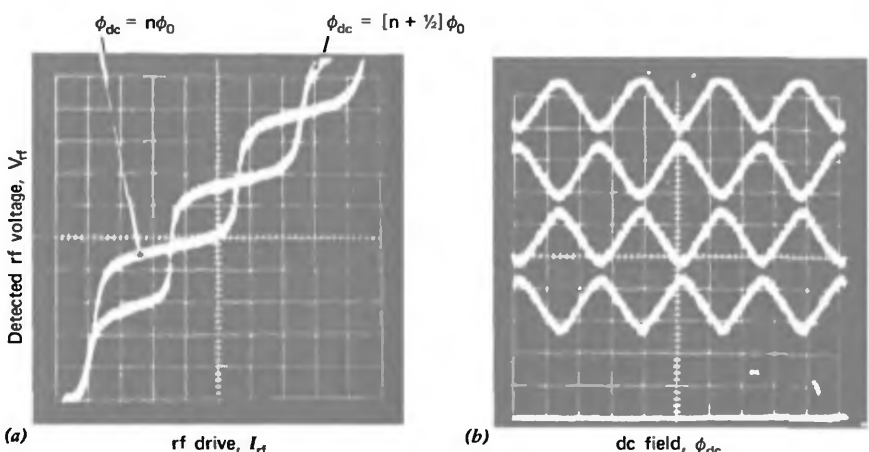


Figure 13.15 Experimental response of an r.f. SQUID in the dissipative mode. (a) Detected tank circuit voltage V_{rf} vs. r.f. current bias amplitude I_{rf} . The two curves are the two limiting cases for applied flux $\Phi_{dc} = 2n\Phi_0/2$ and $(2n+1)\Phi_0/2$. (b) Detected tank circuit voltage vs. applied magnetic field. The different curves refer to different values of the r.f. current bias I_{rf} . (After Zimmerman 1972a.)

in liquid helium at 4.2 K. The r.f. voltage is amplified by a low noise amplifier and demodulated, integrated, and displayed on the y axis of an oscilloscope. A FET preamplifier in a cascode configuration is generally used and a diode serves as a detector. When the switch is in the “step” position, the r.f. bias is amplitude modulated by the audiofrequency oscillator. Therefore this signal is proportional to the amplitude of the r.f. current. When the switch is in the “triangles” position, the low frequency signal is used to produce a quasistatic field into the SQUID in order to observe the characteristic triangular dependence. Figure 13.15a shows the characteristic “staircase” dependence for a 27 MHz operated device. The two curves correspond to the limiting cases for the static external flux. The triangular dependence is shown in Fig. 13.15b. The different curves refer to different values of the r.f. current amplitude I_{rf} .

13.2 D.C. SQUID

The double junction configuration of Section 12.3 is the basic element for the so-called d.c. SQUID. In the operational configuration the device is current biased and the voltage across it is monitored. For values of the current bias greater than the critical current I_c , a voltage signal periodic with the applied field is obtained. The problem has been considered extensively by De Waele and De Bruyn Ouboter (1969) and recently by Tesche and Clarke (1976, 1977). In order to derive the response of the device we have to compute the current voltage dependence of the two junction loop in the presence of an external flux Φ_e applied to the loop. The system is described by the equivalent circuit sketched in Fig. 13.16d. Since we are interested to the finite voltage behavior, the complete equivalent circuit for the two junctions must be considered. We use the simple R.S.J. model that we discussed in Chapter 6.

It is assumed that the parameter $\beta_J = 1/\omega_J RC$ is much greater than 1. This means that for each junction the capacitance C is completely shorted by the small resistance R . As we have seen, in this condition ($\beta_J \gg 1$) the $V - I$ characteristic for a single junction is reversible and shows no hysteresis. The same occurs for the current voltage dependence of the two junction configuration. The device is current biased by a d.c. current I . Let us indicate with $i_1(t)$, $i_2(t)$ the time dependent currents in the two arms. The following relations are valid:

$$I = i_1(t) + i_2(t) \quad (13.2.1a)$$

$$i_s = \frac{i_2(t) - i_1(t)}{2} \quad (13.2.1b)$$

where i_s is the circulating current in the loop. The two currents $i_1(t)$ and $i_2(t)$ are related to the voltage drops across the junctions, V_a and V_b , and to the

supercurrents by

$$i_1(t) = I_a \sin \varphi_a(t) + \frac{V_a}{R_a} \quad (13.2.2a)$$

$$i_2(t) = I_b \sin \varphi_b(t) + \frac{V_b}{R_b} \quad (13.2.2b)$$

The time dependence of φ_a and φ_b is given by the usual relations:

$$\frac{d\varphi_a}{dt} = \frac{2e}{\hbar} V_a \quad (13.2.3a)$$

$$\frac{d\varphi_b}{dt} = \frac{2e}{\hbar} V_b \quad (13.2.3b)$$

Let us assume that the two arms have equal inductances ($L_a = L_b = L/2$). The voltage V across the device is related to V_a and V_b by

$$V = V_a + \frac{L}{2} \frac{di_1}{dt} \quad (13.2.4a)$$

$$V = V_b + \frac{L}{2} \frac{di_2}{dt} \quad (13.2.4b)$$

where the mutual inductance between the two arms has been neglected. From (13.2.4), (13.2.3), and (13.2.1) for $I = \text{const.}$ it follows that

$$V(t) = \frac{\hbar}{2e} \frac{d}{dt} \varphi(t) \quad (13.2.5)$$

where

$$\varphi(t) = \frac{\varphi_a(t) + \varphi_b(t)}{2} \quad (13.2.5a)$$

By using (13.2.2) and (13.2.4) we can write (13.2.1a) and (13.2.1b):

$$I = I_0 [\sin \varphi_a(t) + \sin \varphi_b(t)] + 2 \frac{V(t)}{R} \quad (13.2.6a)$$

$$i_s = I_0 [\sin \varphi_a(t) - \sin \varphi_b(t)] + \frac{(V_a - V_b)}{R} \quad (13.2.6b)$$

where it has been assumed that $I_a = I_b = I_0$.

To simplify the calculations, following De Waele and De Bruyn Ouboter (1969), we neglect in (13.2.6b) the contribution due to the quasiparticles. The

last expressions become:

$$I = 2I_0 \sin\left(\frac{\varphi_a + \varphi_b}{2}\right) \cos\left(\frac{\varphi_a - \varphi_b}{2}\right) + 2 \frac{V(t)}{R} \quad (13.2.7a)$$

$$i_s = 2I_0 \cos\left(\frac{\varphi_a + \varphi_b}{2}\right) \sin\left(\frac{\varphi_a - \varphi_b}{2}\right) \quad (13.2.7b)$$

From (12.3.1)

$$\frac{\varphi_a - \varphi_b}{2} = -\pi \frac{\Phi}{\Phi_0}$$

where $\Phi = \Phi_e + Li_S$ is the effective flux into the loop and Φ_e the geometrical applied flux.

After simple manipulations (13.2.7a) and (13.2.7b) can be written as

$$I = 2I_0 \sin \varphi(t) \cos \frac{\pi \Phi}{\Phi_0} + \frac{2V(t)}{R} \quad (13.2.8a)$$

$$\frac{\Phi - \Phi_e}{\Phi_0} = \frac{\beta_T}{\pi} \sin \pi \frac{\Phi}{\Phi_0} \cos \varphi(t) \quad (13.2.8b)$$

where $\beta_T = 2\pi LI_0/\Phi_0$. When the loop inductance L is negligible, (13.2.8b) reduces ($\beta_T \rightarrow 0$) to

$$\Phi \simeq \Phi_e$$

which, inserted in (13.2.8a), gives

$$I = I_c(\Phi_e) \sin \varphi(t) + \frac{2}{R} \frac{\hbar}{2e} \frac{d\varphi(t)}{dt} \quad (13.2.9)$$

where

$$I_c(\Phi_e) = 2I_0 \cos \frac{\pi \Phi_e}{\Phi_0}$$

and (13.2.5) has been used.

Equation 13.2.9 was examined in Chapter 6. In the present case it gives

$$0 \leq |I| \leq I_c(\Phi_e) = 2I_0 |\cos \pi \phi_e| \quad \bar{V}(t) = 0$$

$$|I| > I_c(\Phi_e) \quad \bar{V}(t) = \frac{R}{2} \sqrt{I^2 - I_c^2} \quad (13.2.10)$$

When the loop inductance is nonnegligible ($\beta_T \neq 0$), the situation is more

complicated. For $|I| \leq I_c$, $V(t) = 0$ as before. The I_c vs. Φ_e dependence is the same as that computed in Chapter 12. When $|I| > I_c(\Phi_e)$ for a given value of the geometrical flux Φ_e , from (13.2.8b) Φ can be derived as a function of $\varphi(t)$. Therefore from (13.2.8a) $V(t)$ can be obtained as a function of $\varphi(t)$. $V(t)$ has a periodic dependence on φ , with a period 2π . From (13.2.5) it follows that

$$\int_0^T V(t) dt = \frac{\hbar}{2e} \int_0^{2\pi} d\varphi = \frac{\hbar}{2e} \quad (13.2.11)$$

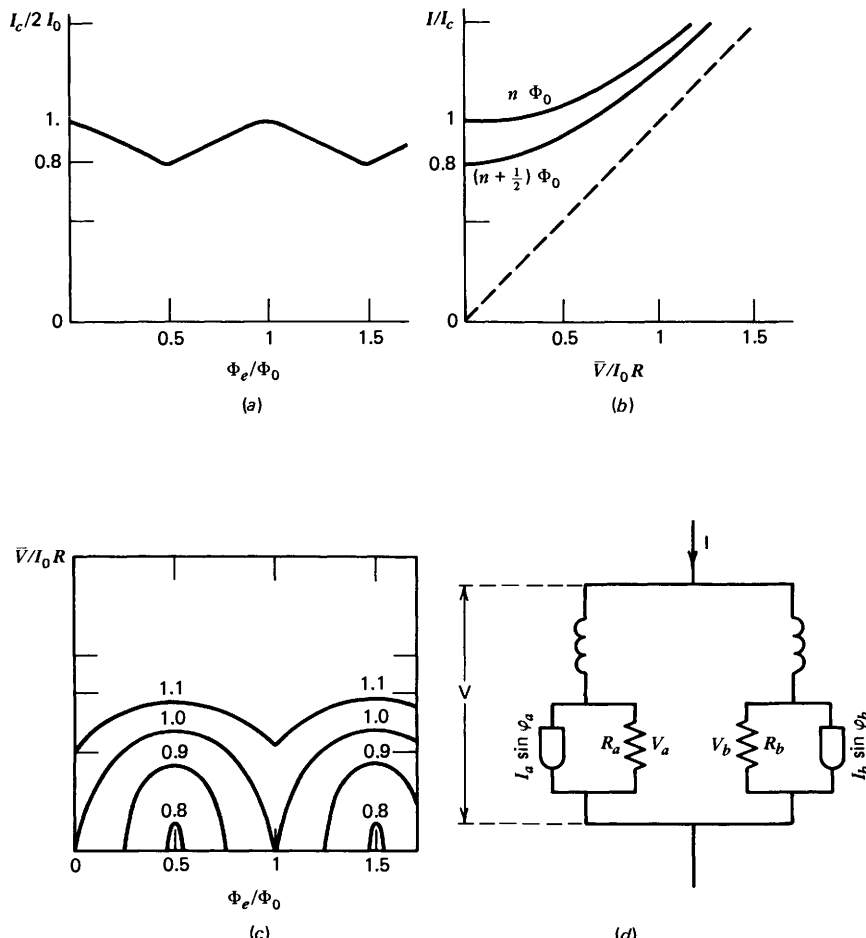
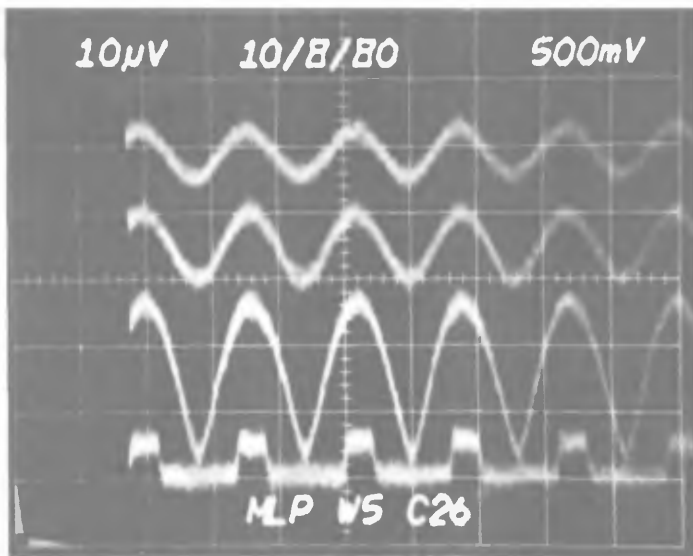
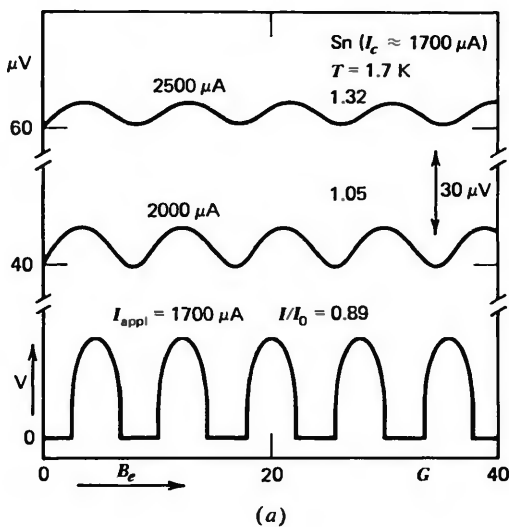


Figure 13.16 D.c. SQUID operation. (a) Typical magnetic field dependence of the supercurrent for a two junction loop. (b) Current voltage characteristic in the two limiting conditions $\Phi_e = 2n\Phi_0/2$ and $\Phi_e = (2n+1)\Phi_0/2$. (c) Detected voltage vs. applied magnetic field for different values of the d.c. current bias. (After De Bruyn Ouboter and De Waele 1970.) (d) Equivalent circuit for the two junction loops.



(b)

Figure 13.17 Voltage vs. applied magnetic field dependence of a d.c. SQUID for different values of d.c. current bias: (a) Two solder droplet junctions configuration (After De Bruyn Ouboter and De Waele 1970) (b) Thin film planar configuration with two resistively shunted lead-alloy junctions. (Courtesy of P. Carelli.)

Therefore $V(t)$ is a periodic function of t , with a period T given by

$$T = \frac{\hbar}{2e} \int_0^{2\pi} \frac{d\varphi}{V(\varphi)} \quad (13.2.12)$$

The average time of the voltage can be computed by the average over one period T :

$$\bar{V}(t) = \frac{1}{T} \int_0^T V(t) dt = \frac{2\pi}{\int_0^{2\pi} \frac{d\varphi}{V(\varphi)}} \quad (13.2.13)$$

From this expression, for a given value of the current I , the $\bar{V}-\Phi_e$ dependence can also be computed. In Fig. 13.16 the $I_c-\Phi_e$ and $\bar{V}-\Phi_e$ dependences numerically computed by De Bruyn Ouboter and De Waele (1970) are reported. The data refer to a configuration for which $\beta_T \simeq 3\pi$. The $\bar{V}-\Phi_e$ curves correspond to two different values for the current I . In the same figure the $\bar{V}-I$ dependence is shown for different values of the applied flux $\Phi_e = n\Phi_0$ and $\Phi_e = (n + \frac{1}{2})\Phi_0$.

Experimental data obtained by De Bruyn Ouboter and De Waele (1970) on solder-droplet junctions (Omar et al. 1967) are reported in Fig. 13.17a. The voltage response for a thin film planar d.c. SQUID recently designed by Cromar and Carelli (1981) is shown in Fig. 13.17b. The device is made by two resistively shunted lead alloy junctions inserted in a multiloop configuration. An order of magnitude estimate of the maximum voltage modulation in the \bar{V} vs. Φ_e dependence can be obtained as follows. For practical devices the parameter β_T is much greater than 1; therefore, the maximum critical current modulation is $\Delta I_c \simeq \Phi_0/L$ (see section 12.3.3). The maximum voltage variation across the device then is

$$\Delta V \simeq \frac{R}{2} \frac{\Phi_0}{L} \quad (13.2.14)$$

where R is the normal resistance of each weak link and L is the loop inductance. For bias current I slightly greater than I_c , the $\bar{V}-\Phi_e$ dependence can be approximated as a triangular dependence. On the linear branches of this dependence the voltage response to a small variation $\delta\Phi_e$ of the external flux is given by

$$\frac{\delta V}{\delta\Phi_e} \simeq \frac{R}{2L} \quad (13.2.15)$$

By using the typical values $R \simeq 1 \Omega$ and $L \simeq 10^{-9} \text{ H}$, a sensitivity of $\sim 1 \mu\text{V}/\Phi_0$ is obtained.

13.3 Noise and Maximum Sensitivity

The r.f. and d.c. SQUID devices we have just described are generally employed as magnetic flux detectors. It is therefore important to estimate the flux noise level generated in working conditions. This level gives the value of the minimum external signal observable by these devices. Noise contributions are due to different sources. There is the intrinsic noise due to the SQUID; the noise associated with the circuit directly coupled to the SQUID; noise generated in the preamplifier; external noise such as that peaked up by normal enclosure surrounding the device or caused by radio sources or electrical machineries. A simple estimate of the intrinsic noise for both kind of devices can be obtained if we assume that the source of the fluctuation is the Johnson noise in the normal state resistance R of the weak link in the superconducting loop (Zimmerman 1972a). At a temperature T and for a frequency bandwidth $\delta\omega/2\pi$, the mean square value of the noise voltage across R is

$$\langle \delta V_N^2 \rangle = 2k_B T R \frac{\delta\omega}{2\pi}$$

where k_B is the Boltzman constant. This voltage causes a fluctuating quasiparticle current to flow in the loop. The mean square value of this current is

$$\langle \delta I_N^2 \rangle = \frac{2k_B T R \delta\omega}{\pi(R^2 + \omega^2 L)}$$

and the mean square value of the flux noise is

$$\langle \delta\Phi_N^2 \rangle = L^2 \langle \delta I_N^2 \rangle = \frac{2k_B T L^2 \delta\omega}{\pi R (1 + \omega^2 L^2 / R^2)} \quad (13.3.1)$$

where L is the loop inductance.

By integration over all frequencies this expression gives for the total flux noise:

$$\langle \Phi_N^2 \rangle = k_B T L \quad (13.3.2)$$

If $\langle \Phi_N^2 \rangle \geq \Phi_0^2$, the periodicity in the response of the device would be completely wiped out by the noise. By imposing this restriction from (13.3.2) the following limitation for the allowed values of the SQUID inductance can be derived:

$$L < \frac{\Phi_0^2}{k_B T} \quad (13.3.3)$$

In the low frequency limit for $\omega \ll L/R$, from (13.3.1) it follows that

$$(\delta\Phi)_{\text{class}} = \langle \delta\Phi_N^2 \rangle^{1/2} = L \left(\frac{4k_B T \delta\nu}{R} \right)^{1/2} \quad (13.3.4)$$

which is the so-called classical limit for the minimum observable magnetic flux. By using the typical values of $L = 10^{-10}$ H, $R = 5$ Ω, and $T = 4$ K, a sensitivity of $3 \cdot 10^{-7} \Phi_0/\sqrt{\text{Hz}}$ is obtained. This value is a few orders of magnitude below the maximum sensitivity of real devices. In fact, there are other mechanisms that contribute to the intrinsic noise of the device. In what follows we examine in more detail the problem of the noise for the different kinds of devices that we have discussed.

13.3.1 R.F. Magnetometers. We begin with the r.f. SQUID in the hysteretic regime ($\beta_e > 1$). In fact, this has been the most used configuration in flux sensor applications of the r.f. device.

In real SQUIDs, thermal fluctuations prevent transitions between adjacent fluxoid states at a fixed value Φ_c of the external flux, as we assumed in our description (Section 13.1.3). As Kurkijärvi (1972) has shown, the distribution of applied flux at which the jump occurs has a width σ and is peaked around a value Φ'_c , which is different from Φ_c . Both Φ'_c and σ depend on how Φ_e varies with time and on the SQUID parameters. When $(d\Phi_e/dt)/\Phi_0 = \text{const.} \ll R/L$ (L =loop inductance and R is the weak link resistance), it is (Kurkijärvi 1972):

$$\sigma = \sigma_0 \left\{ L I_1 \left(\frac{k_B T}{\Phi_0 I_1} \right)^{2/3} \left(\frac{3\pi}{2\sqrt{2}} \right)^{2/3} \left[1 - \left(\frac{1}{\beta_e} \right)^2 \right]^{1/6} \right\} \quad (13.3.5)$$

where σ_0 is typically about 1, for a usual device, and T is the SQUID temperature. For $L \approx 10^{-9}$ H, $T \approx 4$ K, $L I_1 \approx \Phi_0$ it is: $\sigma \approx 0.13 \Phi_0$. The transition distribution has been experimentally investigated (Jackel et al. 1972, 1974), and the Kurkijärvi theory has been confirmed. This distribution of value has two important consequences (Kurkijärvi and Webb 1972). First, it causes a voltage noise across the tank circuit, giving in the low frequency limit an equivalent flux noise:

$$\frac{\langle \delta\Phi_i^2 \rangle^{1/2}}{\sqrt{\text{Hz}}} \approx 0.7 \sqrt{\frac{2\pi}{\omega}} \sigma \approx \sigma_0 \left(\frac{3\pi}{2\sqrt{2}} \right)^{2/3} \left(\frac{2\pi}{\omega} \right)^{1/2} L I_1 \left(\frac{k_B T}{\Phi_0 I_1} \right)^{2/3} \quad (13.3.6)$$

where $\omega/2\pi$ is the r.f. pumping frequency of the tank circuit. The last expression is the “intrinsic” noise of the device. For $\omega/2\pi = 20$ MHz and the value of $\sigma \approx 0.13 \Phi_0$ previously computed, we get $\langle \delta\Phi_i^2 \rangle^{1/2} \approx 3 \cdot 10^{-5} \Phi_0/\sqrt{\text{Hz}}$. Second, the intrinsic noise generated gives rise to a rounding and to a tilting of the “step” regions in the $V_{\text{rf}} - I_{\text{rf}}$ curve (see Fig. 13.18). The induced step slope

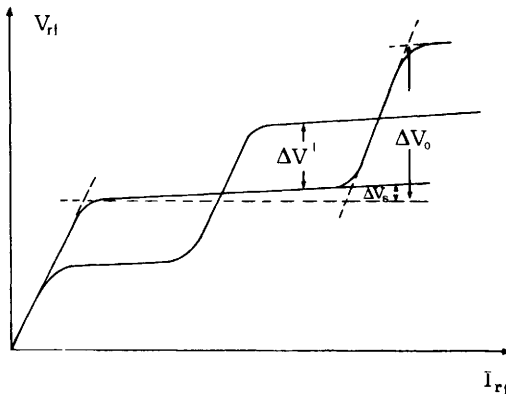


Figure 13.18 The response of an r.f. SQUID in the presence of intrinsic noise.

is proportional to the amplitude of the intrinsic noise. Because of this slope the maximum voltage amplitude ΔV (13.1.21) is reduced to

$$\Delta V' = (1 - \alpha) \frac{\omega L_T}{M} \frac{\Phi_0}{2} \quad (13.3.7)$$

where $\alpha = \Delta V_s / \Delta V_0$ is the ratio between the voltage step increase and the voltage difference at two consecutive steps (see Fig. 13.18). As Jackel and Burhman (1975) have shown, this ratio α is directly related to the intrinsic noise by the expression

$$\alpha = \frac{1}{0.7\Phi_0} \left(\frac{\omega}{2\pi} \right)^{1/2} \frac{\langle \delta\Phi_i^2 \rangle^{1/2}}{\sqrt{\text{Hz}}} \quad (13.3.8)$$

Therefore, it is possible by the experimental $\bar{V}_{rf} - I_{rf}$ curve to get a measure of the intrinsic noise of the device.

Another important source of noise, which can be optimized but not eliminated, is the tank circuit. Johnson noise currents in its load resistance cause a fluctuation of the r.f. current biasing point. Because of the finite slope this gives rise to fluctuations in the voltage \bar{V}_{rf} detected. As Kurkijärvi (1973) has shown, the tank circuit noise is related to the intrinsic noise of the device. In terms of flux it is given by the expression:

$$\frac{\langle \delta\Phi_T^2 \rangle^{1/2}}{\sqrt{\text{Hz}}} \simeq 4 \left(\frac{k_B T L}{\Phi_0^2} \right)^{1/2} (\kappa^2 Q)^{-1/2} \frac{\langle \delta\Phi_i^2 \rangle^{1/2}}{\sqrt{\text{Hz}}} \quad (13.3.9)$$

where T is the effective temperature of the tank circuit, Q is its quality factor, and κ is the coupling constant defined, as usual by, $\kappa^2 = M/(LL_T)$. In general T is higher than 4 K; a typical value can be $T \simeq 200$ K. By using the value

$L \simeq 10^{-9}$ H and assuming $\kappa^2 Q \simeq 1$, it is:

$$\frac{\langle \delta\Phi_T^2 \rangle^{1/2}}{\sqrt{\text{Hz}}} \simeq 3.2 \frac{\langle \delta\Phi_i^2 \rangle^{1/2}}{\sqrt{\text{Hz}}}$$

A detailed analysis of the noise problem and its optimization in r.f. SQUID in the hysteretic mode has been carried out by Jackel and Buhrman (1975). In particular, these authors have shown that the current phase relation of the link in the superconducting loops also plays a significant role.

For the r.f. SQUID in the dispersive mode ($\beta_e < 1$) the Φ vs. Δ_e dependence is reversible and therefore no flux jumps occur. The intrinsic noise has been computed for $\beta_e \ll 1$ by Danilov and Likharev (1975) and it is essentially due to the Johnson noise across the equivalent shunt resistance R of the weak link. For a quality factor Q of the tank circuit sufficiently large and in the low frequency limit it is:

$$\frac{\langle \delta\Phi_i^2 \rangle^{1/2}}{\sqrt{\text{Hz}}} \simeq \frac{L}{0.58\sqrt{2}\beta_e} \left[\frac{4k_B T}{R(1 + \omega^2 L^2 / R^2)} \right]^{1/2}$$

where $\omega/2\pi$ is the frequency of the r.f. biasing current. For $\omega \ll R/L$, the last expression becomes

$$\frac{\langle \delta\Phi_i^2 \rangle^{1/2}}{\sqrt{\text{Hz}}} \simeq \frac{1.22}{\beta_e} \left[\frac{4k_B T L^2}{R} \right]^{1/2} \quad (13.3.10)$$

It is interesting to compare the last expression with (13.3.4). The only difference is the factor $1.22/\beta_e$, which for β_e not much lower than 1 is of the order of unity. Therefore the intrinsic noise of the r.f. SQUID in this regime is closer to the classical limit. Assuming that $T = 4.2$ K, $R = 5$ Ω, and $L = 10^{-10}$ H (a value necessary in order to satisfy the condition $\beta_e < 1$, with a value of $I_1 \simeq 3 \mu\text{A}$) it is $\langle \delta\Phi_i^2 \rangle^{1/2}/\sqrt{\text{Hz}} \simeq (1.22/\beta_e)10^{-7}\Phi_0/\sqrt{\text{Hz}}$.

Let us observe at this point that (13.3.10) has been derived under the assumption that $\beta_e \ll 1$; however, it is at least qualitatively valid for $\beta_e \leq 1$ (Danilov and Likharev 1975; Buhrman 1976). The tank circuit noise can be computed in the framework of the Kurkijärvi theory (Kurkijärvi 1973). The only difference is that in the present case ($\beta_e < 1$) the slope of the $V_{\text{rf}} - I_{\text{rf}}$ curve is not determined by the intrinsic noise of the SQUID. The voltage noise spectral density across the tank circuit is given by (Buhrman 1976):

$$\frac{\langle \delta V_T^2 \rangle^{1/2}}{\sqrt{\text{Hz}}} \simeq \left(\frac{d|V_D|}{d|I_D|} \right)_{I_{\text{rf}}^B} \left(\frac{2k_B T_e}{\pi Q \omega L_T} \right)^{1/2} \quad (13.3.11)$$

where T_e is the effective tank circuit temperature, ω is the r.f. pumping

frequency, and $d|V_D|/d|I_D|$ is the slope of the $|V_D| - |I_D|$ curve at the particular chosen value for the r.f. biasing current. The equivalent flux noise in the case $\beta_e \ll 1$ is

$$\frac{\langle \delta\Phi_T^2 \rangle^{1/2}}{\sqrt{\text{Hz}}} \simeq \left(\frac{d|V_D|}{d|I_D|} \right)_{I_{\text{rf}}^b} \left(\frac{2k_B T_e}{\pi Q \omega L_T} \right)^{1/2} \frac{M}{2A\omega L_T}$$

where (13.1.16) has been used and $A = \kappa^2 Q \beta_e / \pi$. Assuming for the slope $d|V_D|/d|I_D|$ the value $\omega L_T Q / \sqrt{\delta^2 + 1}$ corresponding to the limit $\kappa^2 \rightarrow 0$ for the coupling between SQUID and tank circuit, we have

$$\frac{\langle \delta\Phi_T^2 \rangle^{1/2}}{\sqrt{\text{Hz}}} \simeq \frac{1}{\sqrt{\delta^2 + 1}} \frac{\pi}{2\beta_e} \left(\frac{2k_B L T_e}{\pi \kappa^2 Q \omega} \right)^{1/2} \quad (13.3.12)$$

where the usual relation $M = \kappa \sqrt{L L_T}$, in which L is the SQUID inductance, has been used.

13.3.2 D.C. Magnetometers. In these devices the source of the intrinsic noise is the Johnson noise across the shunt resistance of the Josephson element. This noise has two consequences: first, it produces a voltage noise across the two links; second, it induces a flux noise into the superconducting loop. Generally the second effect is lower than the first one and can be neglected. A detailed analysis of noise in d.c. SQUIDs has been given by Tesche and Clarke (1976, 1977). We here follow a simpler approach (Clarke, Goubau and Ketchen 1976). We start by considering the expression for the voltage noise power spectrum $S_v(0)$ for a resistively shunted junction. In the absence of hysteresis ($\beta_J \gg 1$), in the low frequency limit, and for $I_1 \Phi_0 / \pi k_B T \gg 0$ it is (Likharev and Semenov 1972):

$$S_v(0) = \frac{\langle \delta V^2 \rangle}{\text{Hz}} \simeq \left[1 + \frac{1}{2} \left(\frac{I_b}{I_1} \right)^2 \right] 4k_B T r_D^2(I_b) \quad (13.3.13)$$

where $r_D(I_b) = (d\bar{V}/dI)_{I_b}$ is the dynamic resistance of the weak link, at the bias current I_b , and I_1 is the critical current.

Using (13.3.13), for a double junction configuration we get for the intrinsic flux noise:

$$\frac{\langle \delta\Phi_i^2 \rangle^{1/2}}{\sqrt{\text{Hz}}} = \frac{S_v^{1/2}(0)}{\delta V / \delta \Phi_e} \simeq \left[1 + \frac{1}{2} \left(\frac{I_b}{I_c} \right)^2 \right]^{1/2} \left(\frac{4k_B L^2 T}{r} \right)^{1/2} \frac{r_D(I_b)}{r} \quad (13.3.14)$$

where r is the normal resistance. Assuming for the $V - I$ dependence the simple

parabolic expression derived in Section 13.2 for $L=0$ (13.2.10), it is

$$r_D(I) = r \frac{I}{\sqrt{I^2 - I_c^2}}$$

and (13.3.14) becomes

$$\frac{\langle \delta \Phi_i^2 \rangle^{1/2}}{\sqrt{\text{Hz}}} \simeq \left(1 + \frac{1}{2} i_b^2\right)^{1/2} \left(\frac{4k_B L^2 T}{r}\right)^{1/2} \frac{i_b}{\sqrt{i_b^2 - 1}} \quad (13.3.15)$$

where $i_b = I_b/I_c$. By using typical values $L=10^{-9}\text{H}$, $r \simeq 5 \Omega$, $T=4 \text{ K}$, and $i_b \simeq 1.1$ we get

$$\frac{\langle \delta \Phi_i^2 \rangle^{1/2}}{\sqrt{\text{Hz}}} \simeq 1.5 \times 10^{-6} \frac{\Phi_0}{\sqrt{\text{Hz}}}$$

A typical configuration for a d.c. magnetometer is shown in Fig. 13.19a. The bias current I_b or the flux current I_Φ is a.c. modulated, and the a.c. signal across the device is detected. A matching circuit is used between the SQUID and the preamplifier to raise the low output impedance (given by the dynamic resistance r_D) to the value of the preamplifier. The simplest circuits used for this purpose are sketched in Fig. 13.19b: tank circuit, resonant transformer, and transformer. The tank circuit configuration has been used by Clarke, Goubau, and Ketchen (1974, 1975, 1976), and its performance is extensively discussed by those authors. A typical noise power spectrum for this d.c. SQUID is shown in Fig. 13.20. All the three configurations have been theoretically analyzed by Danilov et al. (1976). The conclusion that can be

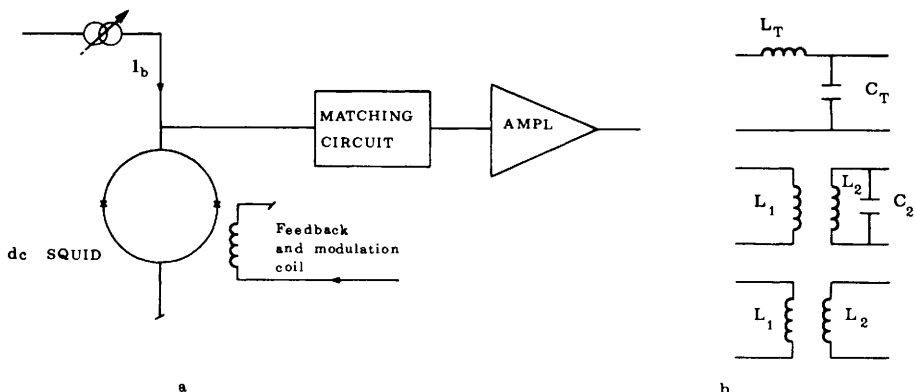


Figure 13.19 (a) Schematic circuit for a d.c. SQUID. (b) Different matching circuit configurations.

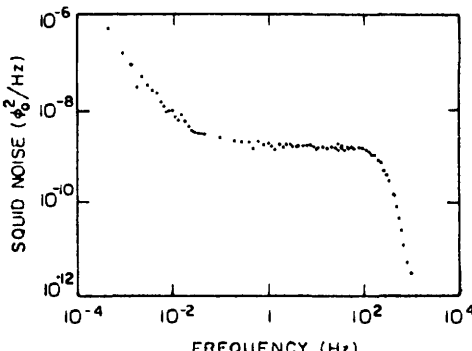


Figure 13.20 Noise power spectrum for a tunnel junction d.c. SQUID. (After Clarke, Goubau, and Ketchen 1975.)

drawn for the noise contribution of matching circuit and preamplifier is that by an appropriate choice of the parameters, such as voltage transformation factor N and quality factor Q , that contribution can be sufficiently reduced to the intrinsic flux noise level. Therefore the minimum sensitivity can be very high and is comparable with the sensitivity of r.f. SQUID in the dispersive mode.

13.3.3 Ultimate Sensitivity of Practical Devices. In practical devices the external flux is coupled to the SQUID through a superconducting coil (see Section 13.5.2). If L_s is the inductance of this coil, M_s the mutual inductance between that and the SQUID of inductance L , and $\kappa_s = M_s/\sqrt{L L_s}$ the coupling coefficient, it can be shown (Claassen 1975) that the minimum noise-to-signal ratio in optimum coupling conditions is proportional to the quantity

$$\epsilon_{SN} = \frac{L_s^{1/2} \langle \delta\Phi_T^2 \rangle^{1/2}}{M_s} = \frac{\langle \delta\Phi_T^2 \rangle^{1/2}}{\kappa_s \sqrt{L}} \quad (13.3.16)$$

where $\langle \delta\Phi_T^2 \rangle^{1/2}$ is the SQUID total noise. Therefore to get the best signal-to-noise ratio it is the quantity ϵ_{SN} that must be minimized. As observed by Claassen, the parameter ϵ_{SN} is very useful for comparing the performance of all kinds of magnetometers in the low frequency regime.

Table 13.1 lists typical values for flux noise and the figure of merit of different SQUIDS. A derivation of the minimum sensitivity of SQUIDs from uncertainty principle arguments has been recently reported by Voss (1981).

In the usual mode of operation in the r.f. SQUID in the hysteretic regime, the frequency ranges between 20 and 30 MHz. However, as is apparent from (13.1.21), the signal output is proportional to the pumping frequency. Therefore it has been speculated that increasing the frequency would in principle lead to an increase in the signal-to-noise ratio. Many experiments have operated r.f. devices in the range of hundreds of MHz (Zimmerman and

Table 13.1. Flux noise figure of merit and other characteristic parameters of different SQUIDs

SQUID	$\langle \delta\Phi_T^2 \rangle^{1/2}$	L	L_s	κ_s	$\varepsilon_{SN}^2 = \frac{\langle \delta\Phi_T^2 \rangle}{\kappa_s^2 L}$
Type	(Φ_0 / \sqrt{Hz})	(H)	(H)		(J/Hz)
D.c. cylindrical ^{a)}	3.5×10^{-5}	1×10^{-9}	356×10^{-9}	0.61	1.4×10^{-29}
D.c. planar, unlocked ^{b)}	1.6×10^{-7}	6.2×10^{-12}	1.6×10^{-6}	0.43	9.6×10^{-32}
Toroidal 19 MHz ^{c)}	7×10^{-5}		2×10^{-6}		10.4×10^{-29}
Two hole 19 MHz ^{d)}	4×10^{-5}	4×10^{-10}	18×10^{-6}	0.83	2.5×10^{-29}
430 MHz ^{e)}	4×10^{-6}	5×10^{-10}	20×10^{-6}	0.40	1.7×10^{-30}
9 GHz ^{f)}	7×10^{-6}	3×10^{-10}	28×10^{-6}	0.7	1.4×10^{-30}

^{a)} Ketchen, Clarke and Goubau (1978).

^{b)} Cromar and Carelli (1981).

^{c)} SHE Corporation Mod. 330X.

^{d)} Ernè and Romani (1980).

^{e)} Long, Clark and Prance (1980).

^{f)} Hollenorst and Giffard (1978).

Frederick 1971; Corruccini 1973; Clark and Jackel 1974, 1975; Duret, Bernard, and Zenatti 1975; Long et al 1979; Long, Clark, and Prance 1980) up to the range of a few GHz (Kamper and Simmond 1972; Pierce, Opfer, and Rorden 1974, Hollenorst and Giffard 1978, Rachford and Cukauskas 1979). However, as it is also apparent from Table 13.1 the signal-to-noise ratio is usually not too much improved. This in part is due to the fact that increasing the frequency tends to increase the noise in the amplifier and it can become necessary to use helium temperature cooled devices.

13.4 Practical Superconducting Sensor Configurations

In SQUID devices the sensing element, as we have seen, is a superconducting loop in which one or two weak links are inserted. Usually the loop is realized by evaporated thin metal films or by machined bulk metal. In thin film structures the weak links used are Dayem bridges, proximity effect bridges, or resistively shunted junctions. In bulk metal devices the most commonly employed material is niobium, for its high critical temperature (>4.2 K) and its mechanical characteristics, and the weak links are point contact devices.

13.4.1 Single Weak Link Devices. In Fig. 13.21 a variety of r.f. SQUIDS are shown. The thin film structure of Fig. 13.21a was first employed by Mercereau (1970) and Nisenoff (1970). The superconducting loop was realized by vacuum depositing a superconducting film onto a rotating dielectric rod

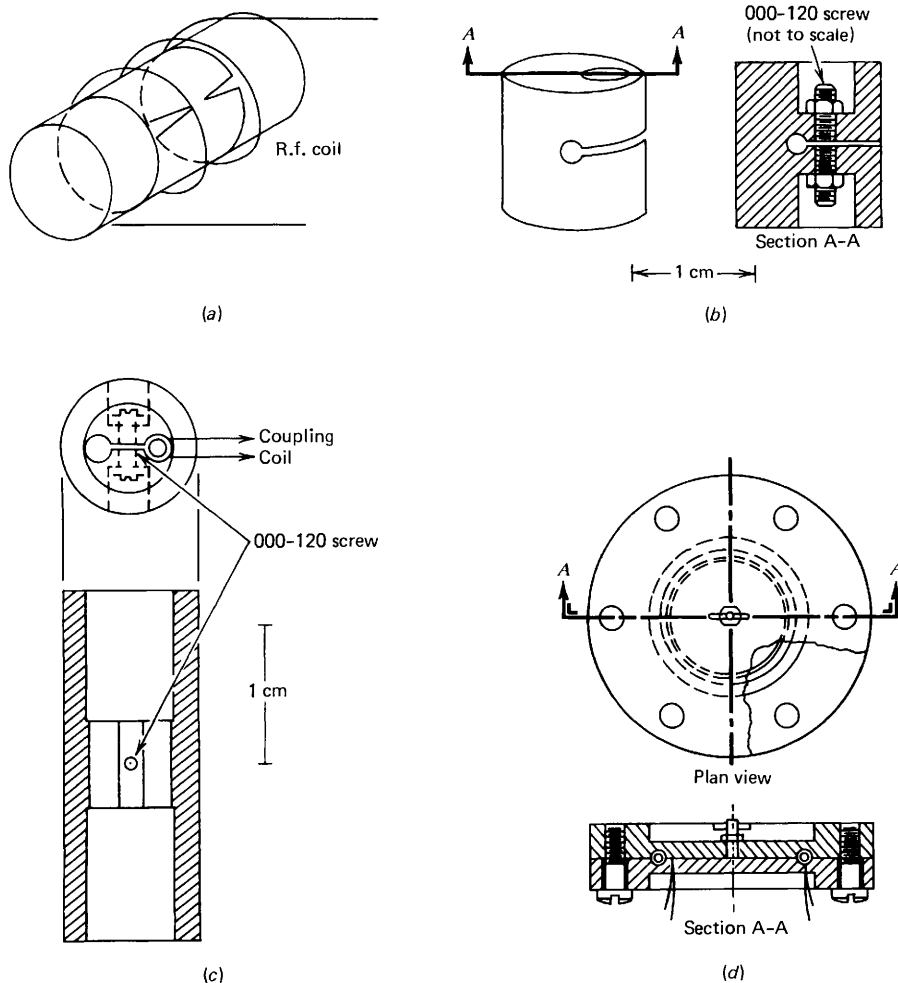


Figure 13.21 Different configuration for single junction loop devices. (a) Thin film configuration. (b) Point contact configuration. (After Zimmerman, Thiene, and Harding 1970.) (c) Two holes point contact device. (After Zimmerman, Thiene, and Harding 1970.) (d) Toroidal point contact structure. (After Rifkin et al. 1976.)

(usually of glass or quartz) of 1–2 mm in diameter. The weak link was produced by removing the undesired material by mechanical scratching or by photoresist techniques. In some configurations a Notary's proximity effect bridge was used instead of a simple Dayem bridge. These structures in fact permit the device to operate at a temperature far below the critical temperature of the film forming the superconducting loop. Furthermore, because of their larger dimensions (10–50 μm) they are easier to achieve. Thin-film r.f. biased large diameter SQUIDs have been investigated by Falco and Parker (1975).

A bulk metal structure equivalent to the thin film configuration just described is shown in Fig. 13.21*b*. It was designed by Zimmerman, Thiene and Harding (1970) and consists of a *C* shaped niobium block. The link was a point contact formed by two (000–120) niobium screws and usually was adjusted to get the correct value for the critical current while the device was in the helium bath. Figure 13.21*c* shows the very popular two hole symmetrical point contact device introduced by Zimmerman and his coworkers (Zimmerman, Thiene and Harding; Zimmerman 1973). The device is very stable with respect to thermal cycling, if moisture contamination is avoided; the point contact can be adjusted at room temperature. This structure is sensitive only to differences in the flux in the two holes, and therefore is a better shield against unwanted external fields. Usually the r.f. coil is inserted in one hole, and the field to be measured is coupled to the other one by a flux transformer (see Section 13.5.2). Recently two hole SQUID structures have been realized in planar configurations using resistively shunted tunneling junctions as a link (Ehnholm, Soini and Wiik 1975) and high critical temperature material for the loop (Fujita et al. 1974; Wu and Falko 1977, 1978). Another very interesting bulk metal structure is the toroidal SQUID sketched in Fig. 13.21*d* (Goodman et al. 1973; Rifkin et al. 1974, 1976). It has the advantage of being completely self-shielded and makes it possible to realize sufficiently low values ($\sim 10^{-10}$ H) for the loop inductance L . For these reasons this configuration has been used to study the behavior of the r.f. SQUID in the dispersive mode (Rifkin et al. 1976). With a low value of L the condition $\beta_e \ll 1$ can be satisfied with a reasonable value for the critical current of the link of the order of few μ A.

If the magnetic field to be measured is directly coupled to the SQUID, the field sensitivity is essentially determined by the area A of the superconducting loop. An increase in field sensitivity cannot be accomplished by a simple increase of that area, because this results in an increase in the SQUID inductance L . As it is apparent from (13.1.21), which in an equivalent form can be written as

$$\Delta V = \frac{\omega}{K^2} \frac{\Phi_0}{2} \sqrt{\frac{L_T}{L}}$$

an increase in L will lead to a reduction in the output voltage signal of the SQUID. An ingenious structure for overcoming this difficulty is the fractional turn configuration designed by Zimmerman (1971), in which many loops in parallel are closed by the same link.

A simple example of a fractional turn device is the two hole symmetrical SQUID we have previously considered (Fig. 13.21*c*). Let us consider the two cylindrical structures depicted in Fig. 13.22. We assume that they have the same length l and the same total cross-section A . The inductance of the double loop configuration is given by

$$L = N^2 L_0$$

where $L_0 = \mu_0 A / l$ is the single loop inductance and $N = \frac{1}{2}$. Therefore the

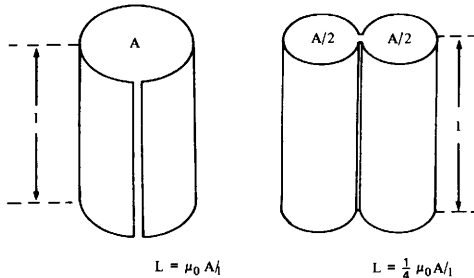


Figure 13.22 Single hole and double hole loop with the same total area A .

structure is formally equivalent to a single loop structure with equal area A and with a fractional number of turn $N = \frac{1}{2}$. To better clarify the behavior of multiturn or fractional turn structures, half turn, one turn, and two turn SQUIDs are schematically shown in Fig. 13.23. The overall dimension and the r.f. coupling are assumed to be the same for each configuration. Since L is proportional to N , the voltage amplitude ΔV is proportional to $1/N$. The field periodicity too is proportional to $1/N$. The corresponding voltage magnetic field patterns are also shown in Fig. 13.23. It is interesting to observe that the small field sensitivity that is related to the slope of the $\Delta V - H$ dependence is just the same. This result can be physically understood by observing that we expect the field sensitivity to be proportional to the effective volume, which we have assumed to be the same for the three structures.

At this point it is worthwhile to make a comment about the flux periodicity in multihole structures (Zimmerman 1978), since some authors have derived different values for it.

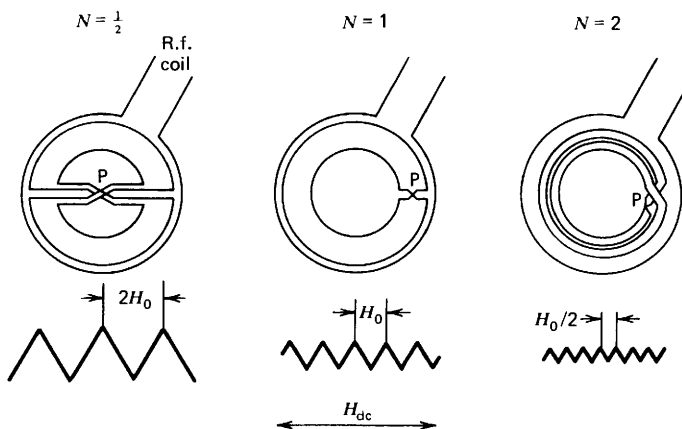


Figure 13.23 "Half-turn," one turn, and two-turn r.f. biased devices with identical overall dimensions. If the coupling coefficient of the r.f. coil is the same for all three, the relative amplitudes and periodicities of the interference patterns should be as shown. (After Zimmerman 1971.)

It is clear from the discussion in Chapter 12 that the flux periodicity of any SQUID, whether multihole, single hole, or multiturn, is the flux quantum Φ_0 . This follows if the phase integral (12.1.1) is taken once around a closed superconducting path containing the junction or junctions. Confusion results when some "projected area" is implied but not specified or when the area through which the flux is measured is the area of an external coil rather than the area bounded by the superconducting path. In the latter case, the "flux periodicity" might have any value whatever, and the concept loses the elegant simplicity of (12.1.2). In the case of a multihole SQUID, if one considers the area bounded by any one hole and the junction, the periodicity is precisely Φ_0 ,

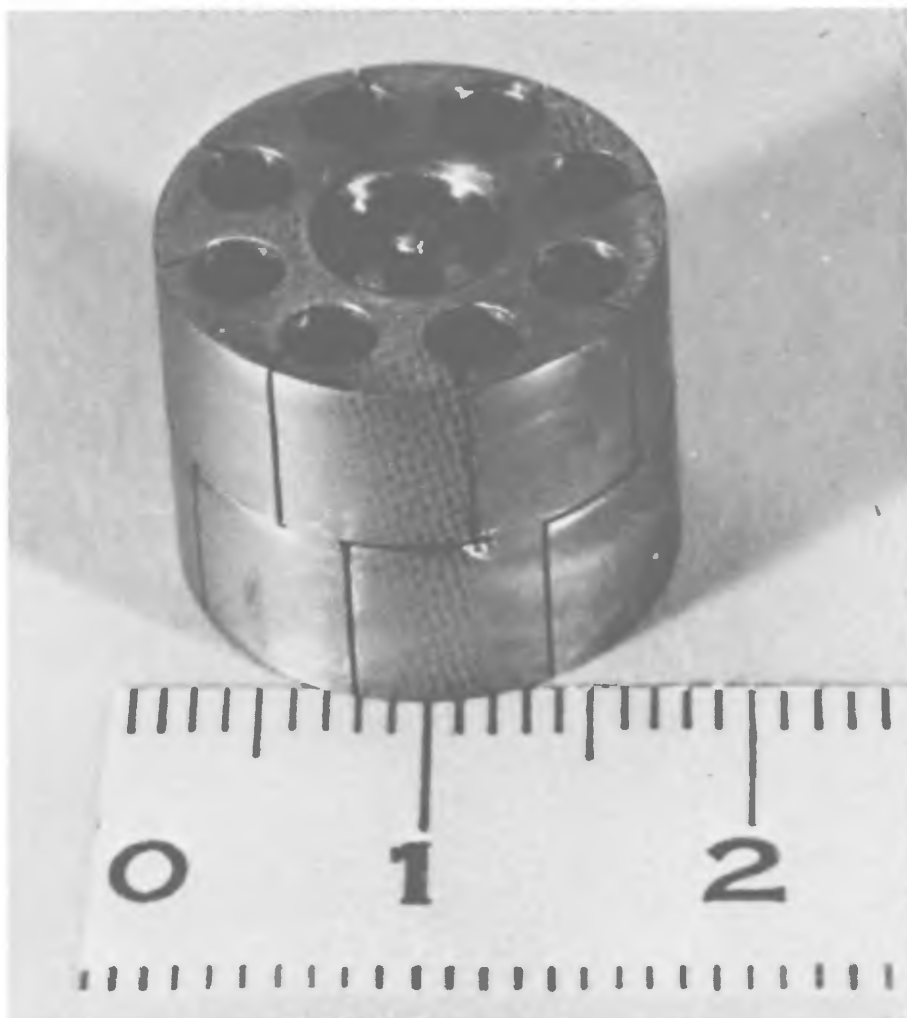


Figure 13.24 Eight hole SQUID configuration. (Courtesy of J. E. Zimmerman.)

even if the holes are unequal in size and geometrically distorted in any way whatever. On the other hand, if one takes the total projected area, the periodicity might be approximately $N\Phi_0$, but not precisely because of flux leakage between holes or overlap of holes, depending on geometry. By the use of a fractional turn configuration, the dimension of the device can be increased without increasing the value of the inductance. In this way the magnetic field sensitivity can be enhanced while the signal-to-noise ratio is the same. In Fig. 13.24 an eight hole SQUID is shown.

A 24 hole bulk configuration has been recently operated by Zimmerman (1977). A planar configuration in which eight holes are closed in parallel across a Nb-Nb-O_x-Pb resistively shunted junction has been realized by Ehnholm, Soini, and Wiik (1975).

13.4.2 Two Weak Link Configurations. The first configurations developed were the two tunneling junction loops we discussed in Chapter 12 (Jaklevic et al. 1964a, b). However, this kind of device is not suitable as a magnetometer because the loop area is very small, the coupling of the external field is difficult, and the $V-I$ characteristic exhibited is markedly hysteretic. The first practical configurations for a d.c. SQUID were point contact structures (see Fig. 13.25a) (Zimmerman and Silver 1966, Silver and Zimmerman 1966a). The device was made by two niobium bulk pieces, insulated by a mylar sheet. After the two pieces were clamped together (by a nylon thread, for example) the two niobium screws were inserted in such a way as to make two point contact regions with the other niobium flat surface. The current adjustment is made while the device is at helium temperature, and only after a certain number of thermal cycles is a readjustment necessary.

Another type of bulk metal structure is shown in Fig. 13.25b, (Beasley and Webb 1967); here the point contact is realized by pressing together two niobium foils insulated by a mylar foil in which a small hole has been made.

Among the earliest versions, of SQUIDS a rather different structure was the SLUG, designed by Clarke (1966). The name stands for superconducting low-inductance undulating galvanometer. The device (Fig. 13.25c) was made by immersing a niobium wire (0.004 in. in diameter) in a melted Sn-Pb solder. A solder blob, a few mm large, is formed around the wire. The natural oxide present on the niobium surface forms an insulating layer between niobium and the outer blob. However, at the edges two weak link regions are formed. The loop is the annular portion in which niobium oxide is present. The device is completely shielded from outside disturbances; however, a flux can be applied to the area enclosed by the superconducting loop by passing a current through the niobium wire.

It is interesting to observe that for a long time no great effort has been spent on improving two junction configuration devices. The first sophisticated d.c. magnetometer was realized in 1967 by Forgacs and Warnick (1966, 1967). After that, interest was focused more on single junction loops and r.f. magnetometers. Recently attention is again being devoted to this kind of device. Planar configurations have been developed by different authors (Decker and

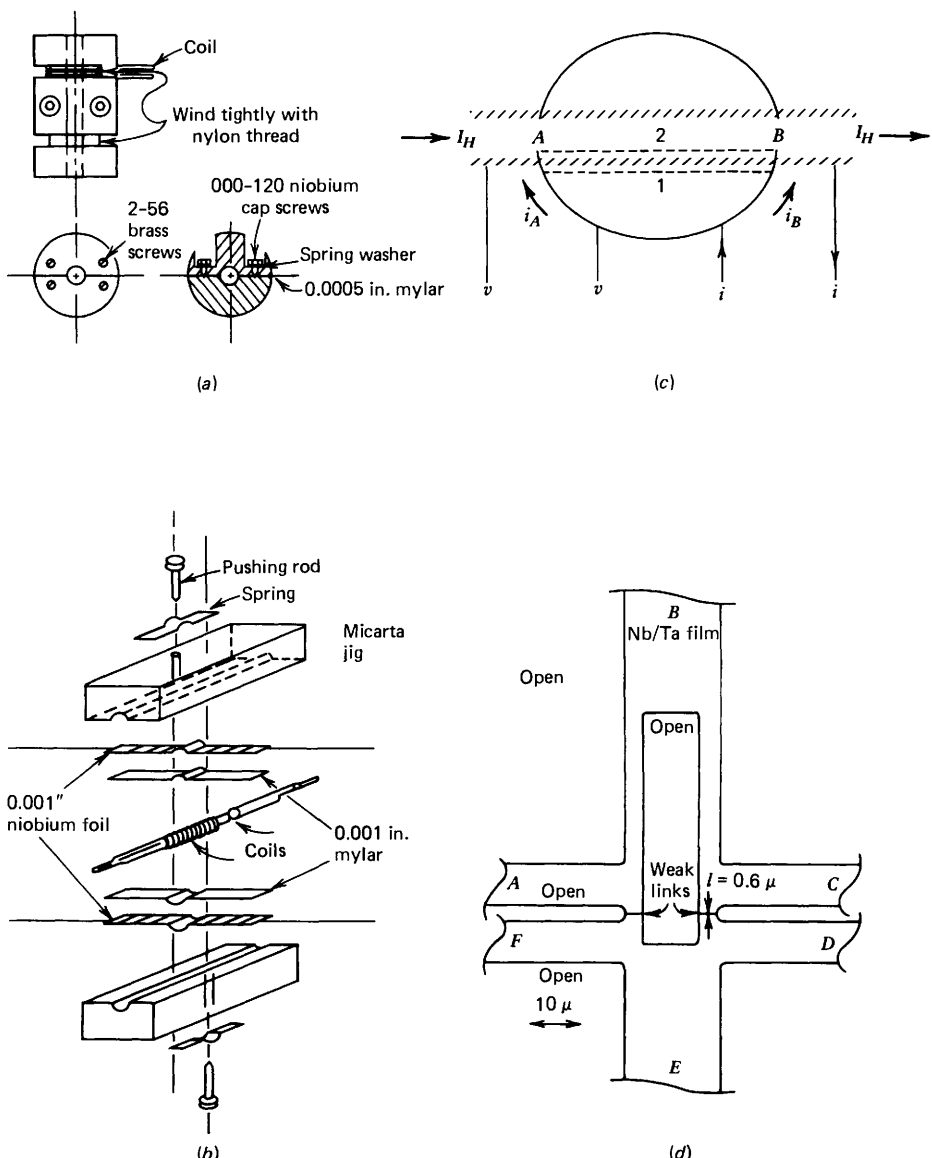


Figure 13.25 Different two junction loop configurations. (a) Point contact device. (After Silver and Zimmerman 1967.) (b) Niobium foil structure. (After Beasley and Webb 1967.) (c) Solder blob configuration. (After Clarke 1966.) (d) Thin film configuration. (After Decker and Mercereau 1973.)

Mercereau 1973; Palmer, Notarys, and Mercereau 1974; Kirschman, Notarys, and Mercereau 1974; Richter and Albrecht 1975). However, these planar structures, because of the small area enclosed by the superconducting loop, are more suitable as galvanometers than magnetometers. Figure 13.25d shows schematically the device designed by Decker and Mercereau (1973).

A thin film structure in which resistively shunted junctions are used as weak links has been developed by Clarke, Goubau, and Ketchen (1974, 1975). The superconducting loop is made by a 10 mm long Pb (5% In) film evaporated on a 3 mm outer diameter quartz tube (see Fig. 13.26). Two Nb-Pb junctions of an area $\sim 10^{-2} \text{ mm}^2$ are inserted inside the loop. To have a nonhysteretic $V-I$ curve, the junctions are shunted by a gold film. To minimize the film's inductance and to reduce flux leakage a lead ground plane (not shown in the figure) insulated from the structure by a cement layer is deposited on the front side of the device. In the figure the matching circuit used is also shown; it consists of a tank circuit resonant at the frequency of the low modulation signal. Since the performances of the shunted junctions d.c. SQUID of Clarke and coworkers are comparable and to some extent even superior to those of R.F. SQUIDS (see Table 13.1), new effort is presently devoted to the fabrication of devices of this kind. Planar gradiometer configurations have been developed by Ketchen and coworkers (1978). Small area planar d.c. SQUIDs employing $100 \mu\text{m}^2$ Nb-Nb₃O₇-Pb shunted junctions (Koch and Clarke 1979) and $3 \mu\text{m}^2$ junctions with GeSn barrier (Hu et al. 1978) have been realized. Ketchen and Voss (1979) have employed the Pb alloy fabrication process (Greiner Basavaiah and Ames 1974) developed at IBM Laboratory in the context of logic circuits to realize low noise d.c. SQUIDs with $10 \mu\text{m}^2$ junctions. Recently, electron-beam lithography (see Section 8.4.4) has been used to fabricate devices with $1 \mu\text{m}$ tunnel junctions with both

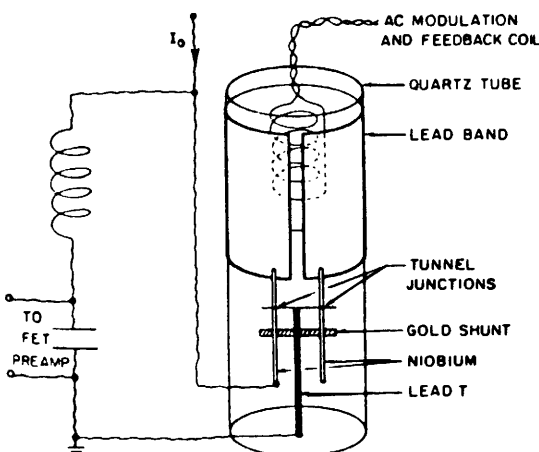


Figure 13.26 Cylindrical d.c. SQUID with tank circuit and modulation coil. (After Clarke, Goubau, and Ketchen 1975.)

niobium electrodes (Voss, Laibowitz, and Raider 1980) and niobium nano-bridges (Voss, Laibowitz, and Broers 1980; Voss et al. 1980). All the planar configurations realized so far are in general not well coupled to the primary coil of a superconducting transformer (see Section 13.5.2). A well coupled ($\kappa_s \approx 0.43$) planar d.c. SQUID configuration has been realized at the National Bureau of Standards by Cromar and Carelli (1981). The compromise between small total inductance and good coupling is achieved by using a fractional turn configuration (Zimmerman 1971) with 68 large inductance loops in parallel.

13.5 Measurement Techniques

The d.c. SQUID, and the r.f. SQUID in the dissipative regime, are employed to measure magnetic flux variations. As we saw in Section 13.3, the maximum achievable flux sensitivity is of the order of $10^{-6} \Phi_0 / \sqrt{\text{Hz}}$ where $\Phi_0 = 2.07 \times 10^{-15} \text{ Wb}$ ($2.07 \times 10^{-7} \text{ G cm}^2$) is the flux quantum. When the device is used as a magnetometer, a magnetic field sensitivity as fine as $10^{-14} \text{ T} / \sqrt{\text{Hz}}$ ($10^{-10} \text{ G} / \sqrt{\text{Hz}}$) is possible. Under normal operating conditions a flux locked configuration is used for the detecting system, and the flux to be measured is coupled to the SQUID via a “superconducting transformer.”

13.5.1 Flux Locked Configuration. The principal characteristic of both r.f. and d.c. SQUIDs, which makes possible their use as practical instruments for the detection of magnetic flux variations, is the output voltage response which exhibits a periodic dependence with the applied flux. To increase the sensitivity and to “linearize” the response of the instrument, a low frequency (1–50 kHz) flux modulation is used. The a.c. modulation is realized by a sinusoidal or square wave signal which generates a peak-to-peak flux into the SQUID of the order of $\Phi_0/2$. In the r.f. device this modulation appears as a sideband of the r.f. pumping frequency. It is recovered at the output of the peak detector. A feedback configuration, such as that reported in Fig. 13.27, is usually employed. The synchronous detector peaks up only the component at the frequency ω_m of the modulation signal. In our discussion we refer to a r.f. device; however, an analogous circuit can be used with a d.c. SQUID. In fact, the closed loop configuration has been operated for the first time on a device of this kind (Forgacs and Warnick 1966, 1967). In order to briefly sketch the principle of operation of the circuit depicted in the Fig. 13.27 let us assume that initially the feedback loop is open. If the ambient field generates in the SQUID a flux $\Phi_e = (n + \frac{1}{2})\Phi_0$ corresponding to a minimum in the \bar{V}_{rf} vs. Φ_e curve (see Fig. 13.28a), the low frequency signal at the input of the lock-in detector will have only a $2\omega_m$ component, where ω_m is the frequency of the modulation signal. If the static external field is increased or decreased and the working point is shifted on the quasi-linear regions of the \bar{V} vs. Φ_e curve, the amplitude of the first harmonic component produced by the modulation

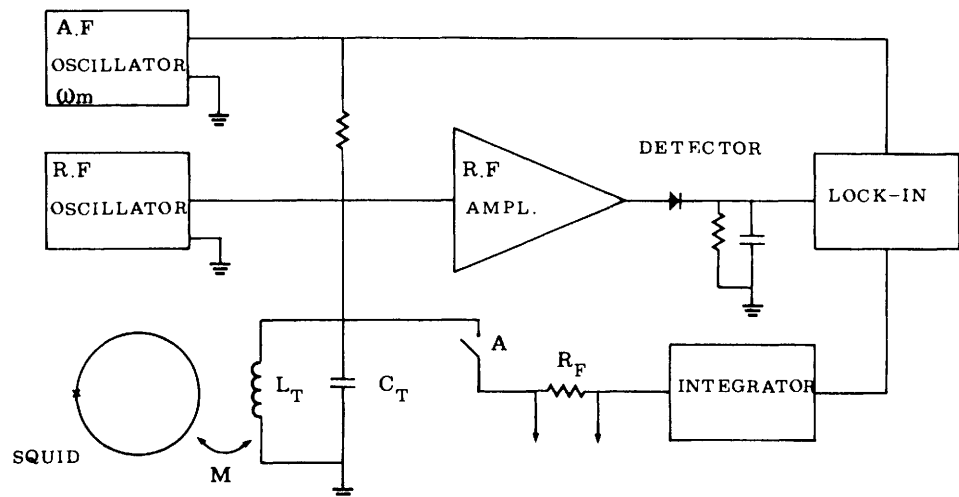


Figure 13.27 Simplified schematic of r.f. SQUID in the flux locked loop configuration.

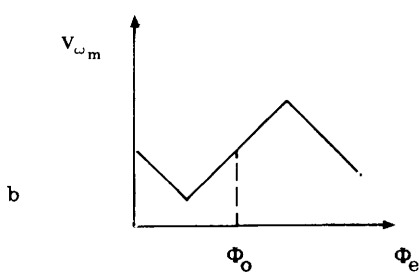
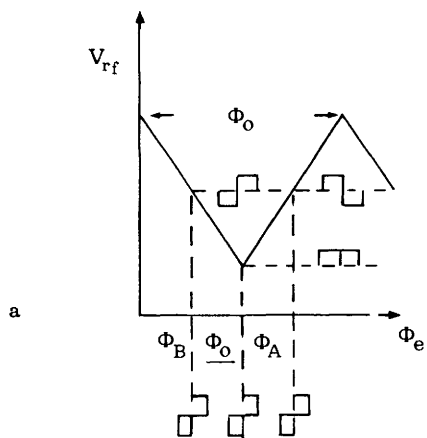


Figure 13.28 (a) Voltage response of the SQUID produced by the a.c. modulation flux.
 (b) Voltage output at the modulation frequency, V_{ω_m} as a function of external flux.

increases. This component has a maximum value in the two points Φ_A and Φ_B corresponding to the external d.c. flux $\Phi_e = (n + \frac{3}{4})\Phi_0$ and $\Phi_e = (n + \frac{1}{4})\Phi_0$.

At this point the amplitude of the second harmonic is zero. Let us observe that the signals in Φ_A and Φ_B are 180° out of phase. The d.c. signal at the output of the integrator (see Fig. 13.27) as a function of the external applied flux Φ_e is shown in Fig. 13.28b. For $\Phi_e \approx (n + \frac{1}{2})\Phi_0$ the voltage response is linear with the applied field. When the feedback loop is closed, the output of the integrator is connected by a resistor to the modulation coil. Under equilibrium conditions the system will be locked at a value corresponding to a minimum or a maximum in the $V-\Phi_e$ curve depending on the sign of the feedback.

When the external flux is varied, the current in the control loop will change in order to produce a counterflux in the SQUID, which will compensate the flux variation $\delta\Phi_e$. The voltage variation produced across the feedback resistance R_F is proportional to $\delta\Phi_e$.

The feedback configuration, in addition to giving an output signal proportional to the flux variation, has the advantage of minimizing the effect of the low frequency noise in the preamplifier, of the drift in the temperature or in other SQUID's parameters such as the weak link critical current, and so on.

An important characteristic of the system is the maximum dynamic range, that is, the maximum "slewing rate" of flux which is possible while the feedback loop is locked. If V_0^M is the maximum output voltage of the integrator, the maximum flux variation that can be measured is

$$(\delta\Phi_e)_{\max} = \frac{M_F}{R_F} V_0^M$$

where M_F is the mutual inductance between the SQUID and the modulation coil and R_F is the feedback resistance. (For the circuit of Fig. 13.27 $M_F = M$) Typical values of the dynamic range are $(\delta\Phi_e)_{\max} \approx \pm 500\Phi_0$.

The slewing rate is determined by the maximum rate at which the feedback loop can generate the counterflux into the SQUID. Its value depends on the frequency ω_m of the modulation signal. When the system is optimized the maximum "slewing rate" is given by (Giffard, Webb and Wheatley 1972):

$$\frac{d}{dt} \left(\frac{\delta\Phi_e}{\Phi_0} \right) \approx \frac{\pi}{16} \omega_m$$

The values of the modulation frequency in practical devices usually range between $\omega_m/2\pi \approx 1$ kHz and $\omega_m/2\pi \approx 50$ kHz. This corresponds to slewing rates of $\sim 10^3 - 10^4 \Phi_0/\text{second}$. An extensive discussion of the operation of the feedback configuration can be found in the paper of Giffard, Webb and Wheatley (1972).

13.5.2 Superconducting Transformers. To increase the magnetic field sensitivity, to decouple the SQUID from the region in which the sample to be

measured is placed, or when the sample is too large to be inserted directly into the SQUID, it is of fundamental importance to use a superconducting transformer. This consists essentially of a closed loop of superconducting wire (insulated niobium wire 100 μm in diameter is generally used). Let us indicate by L_p the inductance of the pickup coil coupled to the external field and by L_s the inductance of the secondary coil tightly coupled to the SQUID (See Fig. 13.29a). If a flux $\Delta\Phi$ is applied to the primary coil L_p , because of flux quantization a circulating current i_s will be established in order to maintain unchanged the flux enclosed by the entire superconducting loop. If N_p is the number of turns in the primary coil and the flux couples in the same way to each turn, the value of the shielding current is

$$i_s = \frac{N_p \Delta\Phi}{L_p + L_s}$$

The flux sensed by the SQUID is

$$\Delta\Phi_e = M_s i_s = \frac{K_s \sqrt{L_s L_p}}{L_p + L_s} N_p \Delta\Phi \quad (13.5.1)$$

where $M_s = K_s \sqrt{L_s L_p}$ is the mutual inductance between the secondary coil L_s and the SQUID of inductance L . Let us observe, in passing, that the last equation is valid for static field variations too. To achieve maximum flux transfer conditions (13.5.1) must be maximized. By taking the derivative with respect to L_s , it is easy to see that this maximum condition is realized when

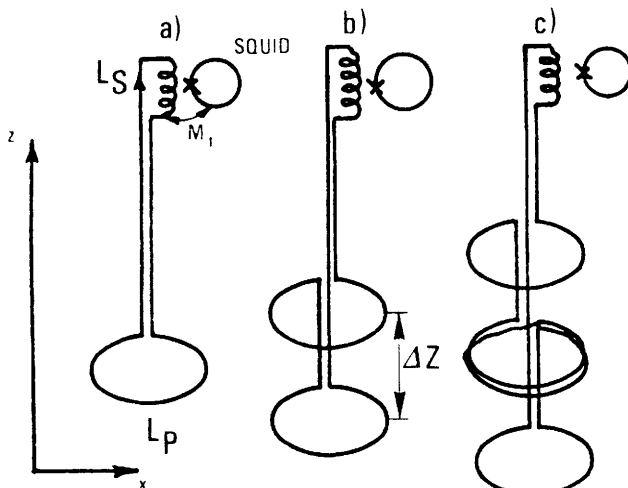


Figure 13.29 Superconducting transformer configurations. (a) Magnetometer configuration. (b) First derivative gradiometer. (c) Second derivative gradiometer.

$L_s = L_p$ (Zimmerman 1971). Therefore the optimum flux transfer coefficient is

$$\frac{\Delta\Phi_e}{\Delta\Phi} = \frac{\kappa_s}{2} N_p \sqrt{\frac{L}{L_s}} \quad (13.5.2)$$

In the presence of the superconducting transformer the minimum flux resolution of the system is determined by the value of the flux in the primary coil L_p which generates in the secondary coil L_s a flux equal to the total flux noise $\langle \delta\Phi_T^2 \rangle^{1/2}$ of the SQUID. Therefore in the optimum coupling condition ($L_p = L_s$) from (13.5.2) it follows for the maximum flux sensitivity that

$$\Delta\Phi_m = \frac{2\sqrt{L_s}}{N_p} \frac{\langle \delta\Phi_T^2 \rangle^{1/2}}{\kappa_s \sqrt{L}} \quad (13.5.3)$$

Let us observe that $\Delta\Phi_m$ is proportional to the parameter ϵ_{SN} (13.3.16) which we introduced in Section 13.3.3 in order to compare the performances of different SQUIDS.

A detailed discussion of optimum coupling conditions with superconducting transformers has been given by Claassen (1975).

Let us observe that in those applications that require a large inductance primary coil, the matching condition ($L_p = L_s$) is hardly achievable. In fact the value of L_s is generally limited by the geometrical dimensions of the SQUID cavity. One way to overcome this problem, at least partially, is by using ferromagnetic cores for the secondary inductance L_s . (Cerdonio, Romani, and Pace 1975; Cerdonio, Ricci, and Romani 1977).

Other configurations can be used for the primary coil L_p . If it is made by two identical coils wound in opposition and Δz apart (see Fig. 13.29b) it will be sensitive only to field gradients in the z direction and insensitive to uniform fields in that direction. This configuration is called the first derivative gradiometer configuration and was first introduced by Zimmerman and Frederick (1971) and by Rosen, Indue and Morse (1971). In real devices it can occur that, for example, the two loops in the primary coil are not perfectly identical or parallel; therefore, care must be taken in balancing them. This can be done either by inserting a superconducting bulk piece in one coil or by adding small coils oriented along different directions. All these procedures have been described by Wynn et al. (1974). Balance factors of 10^{-6} ppm are achieved. The sensitivity of first derivative gradiometers can be as high as 10^{-13} T/m $\sqrt{\text{Hz}}$ (10^{-11} G/cm $\sqrt{\text{Hz}}$).

If the primary coil is made by two first derivative gradiometers in opposition (see Fig. 13.29c) a second derivative gradiometer (Opfer et al. 1974; Brenner Williamson and Kaufman 1975 Barbanera et al. 1978a, 1980c) is obtained that is sensitive only to second derivative field variations along z . Also in the gradiometer configuration, the optimum coupling condition is achieved when the primary and secondary inductances are matched. Therefore

the magnetic field sensitivity of a gradiometer is lower than that of a magnetometer configuration (with the same L_p value for the primary coil). In fact, the magnetic energy picked up by the primary coil is now shared by all of the inductances from which it is made. For example, in the first derivative configuration the reduction factor would be $1/\sqrt{2}$. As observed by Zimmerman (1977), this inconvenience can be virtually eliminated by resorting to nonsymmetric configurations in which the area enclosed by each coil in the primary inductance is the same but the inductances are different.

13.6 The Resistive SQUID

In another very interesting class of SQUID devices the superconducting loop in which the Josephson element is inserted is interrupted by a small resistive section. These devices are usually referred to as resistive SQUIDs. A practical configuration for a point contact device is shown in Fig. 13.30. The resistive section is realized by a dilute Cu-Ge alloy inserted into the niobium block in which the superconducting loop is formed.

These structures were originally designed to maintain a fixed voltage bias across a Josephson junction employed as a radiation generator (Zimmerman, Cowen, and Silver 1966). When the structure is coupled to an r.f. circuit such as that used for the radio frequency SQUID (see Section 13.1) the behavior is formally identical (Ernè 1978b) to that of a superconducting loop device in the presence of a steadily increasing flux. A schematic representation of a resistive SQUID coupled to a typical electronic circuit appears in Fig. 13.32. We briefly discuss here the properties of the resistive loop devices. For further details the reader is referred to the papers by Silver and Zimmerman (1975) and by Park (1974, 1976).

13.6.1 The Resistive Loop Device in the Presence of a D.C. Bias. The equivalent circuit for a resistive SQUID in the absence of r.f. bias is that given in Fig. 13.31. The voltage bias is $V_0 = I_0 R_0$. By applying Kirchhoff's voltage

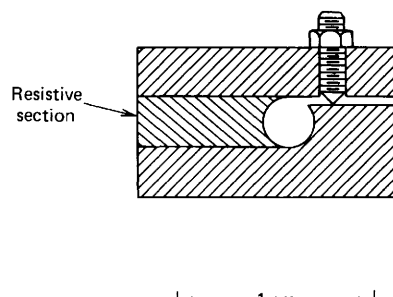


Figure 13.30 A resistive loop device. Material is niobium with a copper alloy resistive section. (After Zimmerman, Thiene, and Harding 1970.)

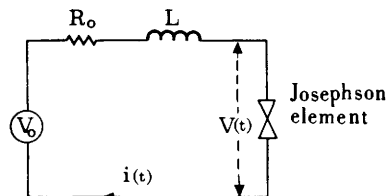


Figure 13.31 Equivalent circuit for the resistive loop SQUID.

law we obtain the relation

$$V_0 - i(t)R_0 - L \frac{di}{dt} - V(t) = 0 \quad (13.6.1)$$

where $i(t)$ and $V(t)$ are the time dependent current and voltage in the Josephson element. Using the fundamental Josephson relation (1.4.5) and assuming that the circulating current $i(t)$ is determined only by the pair current in the point contact, (13.6.1) reduces to (Zimmerman, Cowen, and Silver 1966):

$$\frac{d\varphi}{dt}(1 + \beta_e \cos \varphi) - \omega_0(1 - \alpha \sin \varphi) = 0$$

where φ is the phase difference across the Josephson element and

$$\beta_e = \frac{LI_1}{2e/\hbar} = 2\pi \frac{LI_1}{\Phi_0}$$

$$\alpha = \frac{I_1}{I_0} = \frac{R_0 I_1}{V_0}$$

$$\omega_0 = \frac{V_0}{2e/\hbar} = 2\pi \frac{V_0}{\Phi_0}$$

Φ_0 is the flux quantum.

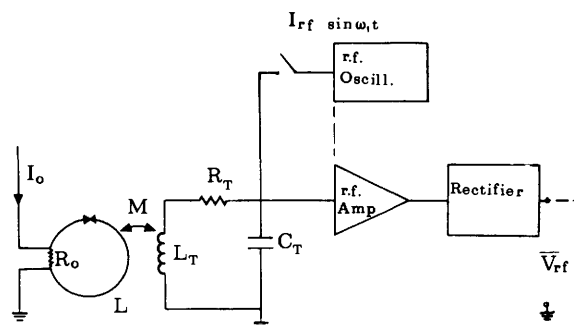


Figure 13.32 Schematic circuit configuration for a resistive SQUID.

Equation 13.6.1 can be integrated and gives for the current $i(t)$ the exact solution

$$\frac{i - \alpha I_1}{|I_1 - \alpha i|} = \sin \left\{ \omega_0 \sqrt{1 - \alpha^2} \left[t + \frac{\beta_e \alpha}{\omega_0} \cos \left(1 - \alpha \frac{i}{I_1} \right) \right] \right\} \quad (13.6.2)$$

Let us observe that this expression is valid only for $\alpha = I_1/I_0 < 1$, because only in this range is it possible to neglect the quasiparticle conductance $G = 1/R_J$. For $\alpha \gg 1$ it is reasonable in (13.6.1) to neglect the term $i(t)R_0$, in which case that expression reduces to

$$V_0 = L \frac{di}{dt} + V(t)$$

This case has been analyzed by McCumber (1968b), assuming also a finite value for the quasiparticle conductance $1/R_J$. In the other extreme limit, $\alpha \rightarrow 0$, (13.6.2) reduces to

$$\frac{i}{I_1} \simeq \sin \left(\omega_0 t - \beta_e \frac{i}{I_1} \right) \quad (13.6.3)$$

Comparing the last expression with (12.2.9b), it can be seen that the solution is identical to that of a superconducting ring with an applied external flux $\Phi_e = V_0 t$. For $\beta_e \ll 1$ the oscillations tend to be sinusoidal and their frequency is ω_0 . Increasing α causes a reduction of a factor $\sqrt{1 - \alpha^2}$ in their frequency. Both when β_e becomes greater than 1 or α approaches 1, the harmonic content increases. The d.c. biased resistive loop device can be used as a generator of radiation. The circuit used to detect such radiation is sketched in Fig. 13.32. In this case no r.f. is sent to the tank circuit. Coherent radiation at 30 MHz and 10 GHz has been detected by Zimmerman, Cowen, and Silver (1966). The device used had characteristic values for the parameters $R_0 \simeq 26 \mu\Omega$, $L \simeq 10^{-10} \text{ H}$. Oscillations corresponding to multiple flux transitions have been reported by Zimmerman and Silver (1967). In the resistive loop, Johnson noise across the resistance gives rise to an additional voltage which adds to the applied voltage V . The linewidth of the emitted radiation, due to this voltage noise, is given by (Burgess 1967):

$$\delta\nu = \frac{4\pi k_B T R_0}{\Phi_0^2}$$

The validity of the last expression has been verified by Silver, Zimmerman, and Kamper (1967) in resistive ring oscillating at 30 MHz.

13.6.2 The Resistive Loop Device in the Presence of an R.F. Bias. Let us assume that an r.f. current $I_{rf} \sin \omega_r t$ is applied to the resonant circuit coupled

to the device (see Fig. 13.32). This will cause a time varying flux in the loop given by

$$\Phi_e = MI_{\text{rf}} \sin \omega_1 t$$

where M is the mutual inductance between the tank circuit coil and the SQUID. As shown by Harding and Zimmerman (1970), the device responds to the flux modulation in a way very similar to that of the superconducting loop SQUID.

Let us derive the equation that determines the time dependence of the phase difference φ across the Josephson element. Following Ernè (1978b) we start from the equation for the voltage drop in the resistive loop (13.6.1) which, including the effect of the applied flux $\Phi_e(t)$, is written as

$$L \frac{di}{dt} + R_0 i(t) + V(t) - V_0 + \frac{d\Phi_e}{dt} = 0 \quad (13.6.4)$$

Let us assume that the junction is described in terms of the R.S.J. model shown in Fig. 6.2. The current-phase relation is

$$i[\varphi(t)] = I_1 \sin \varphi + \frac{1}{R_J} \frac{\hbar}{2e} \frac{d\varphi}{dt} + C \frac{\hbar}{2e} \frac{d^2\varphi}{dt^2} \quad (13.6.5)$$

By integrating (13.6.4) we obtain

$$i(t) = \left[i(0) - \frac{V_0}{R_0} \right] e^{-t/\tau} + \frac{V_0}{R_0} - \frac{1}{L} e^{-t/\tau} \int_0^t e^{t'/\tau} \left[\frac{\hbar}{2e} \frac{d\varphi}{dt'} + \frac{d\Phi_e}{dt'} \right] dt'$$

where $\tau = L/R_0$ and the fundamental Josephson equation (1.4.5) has been used. The integral in the last expression can be transformed into

$$\begin{aligned} e^{-t/\tau} \int_0^t dt' e^{t'/\tau} \left[\frac{\hbar}{2e} \frac{d\varphi}{dt'} + \frac{d\Phi_e}{dt'} \right] &= \frac{\hbar}{2e} \varphi(t) + \Phi_e(t) - \frac{\hbar}{2e} \varphi(0) - \Phi_e(0) \\ &\quad - \frac{1}{\tau} e^{-t/\tau} \int_0^t dt' e^{t'/\tau} \left[\frac{\hbar}{2e} \varphi(t') + \Phi_e(t') \right] \end{aligned}$$

If we consider only stationary states with periodic voltage at the junction, we can write

$$\varphi(t) = \frac{2e}{\hbar} \bar{V} t + \sum_{n=1}^{\infty} \varphi_n \sin(\omega_n t + \delta_n)$$

Under the conditions $\omega_1 \tau \gg 1$ and $\omega \tau \gg 1$, we obtain for the resistive loop

SQUID the equation

$$LC \frac{d^2\varphi}{dt^2} + \frac{L}{R_J} \frac{d\varphi}{dt} + \frac{2e}{\hbar} LI_1 \sin \varphi + \varphi = \frac{2e}{\hbar} \Phi_e(t) + \frac{2e}{\hbar} (V_0 - R_0 \bar{i})t \quad (13.6.6)$$

Comparing the last equation with (12.2.15):

- (a) Under dynamical conditions the resistive loop device is described by an equation which is identical to that for the superconducting loop SQUID.
- (b) The effect of the d.c. bias V_0 is equivalent to the application of a linearly increasing flux given by

$$\Phi_{eq} = (V_0 - R_0 \bar{i})t$$

to a superconducting loop SQUID.

The term $R_0 \bar{i}$ accounts for the fact that the current in the junction has a nonvanishing d.c. component. Assuming the typical values of $L \approx 10^{-9}$ H and $R_0 = 10^{-5}$ Ω, a lower limit of frequency of a few KHz in which (13.6.6) is still valid can be estimated. The properties of r.f. biased resistive SQUID have been experimentally investigated by Zimmerman, Thiene, and Harding (1970). Figure 13.33 shows the \bar{V}_{rf} vs. I_{rf} response for a device biased at $\omega/2\pi = 30$ MHz. The resistance of the normal region was $R_0 = 18 \mu\Omega$ and the condition $\omega_1 \gg R_0/L$ was satisfied. The corresponding \bar{V}_{rf} vs. I_{rf} curves for a superconducting loop of the same geometry are sketched in Fig. 13.33c. When a fixed d.c. voltage is present across the normal section the response of the resistive SQUID oscillates between the two limiting curves $\varphi = 0$ and $\varphi = \pi$ (that is, $\Phi_e = n\Phi_0$ and $\Phi_e = (n + \frac{1}{2})\Phi_0$). This behavior is clearly observable in Fig. 13.33a. In this case the d.c. bias was provided by a thermal emf in the circuit. When a d.c. bias is applied in order to compensate for the thermal emf, the curve of Fig. 13.33b is obtained. In this case on increasing I_{rf} the system goes from point A to point B of the curves of Fig. 13.33c. The oscillations observed are due to Johnson noise in the $18 \mu\Omega$ resistance in the loop. Their amplitude is maximum when the device is biased at point C in the middle of a plateau. The behavior of a resistive SQUID in the absence of d.c. current bias has been investigated by Park and Kendall (1975), by a computer model, neglecting the effect of voltage noise across R_0 . Experiments on resistive loop devices of toroidal configuration have been performed by Park, Farrell, and Kendall (1973). The behavior of this type of SQUID was independent of the frequency even though it was made entirely of normal metal, apart from the niobium point contact. This is a consequence of the fact that the dynamical behavior of SQUIDs is due to the interaction of weak link $I = I_1 \sin \varphi$ and ring inductance L .

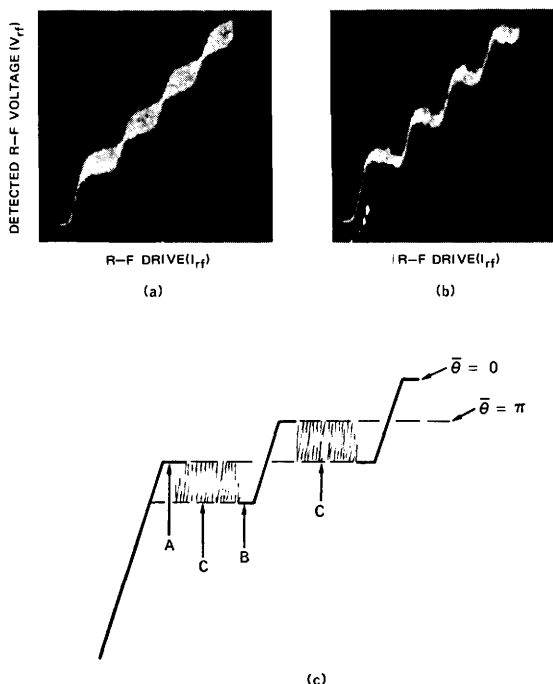


Figure 13.33 R.f. voltage-current curves for a resistive loop device. (After Zimmerman, Thiene, and Harding 1970.)

13.7 Applications

The devices we have just described have been employed in many different areas. Usually r.f. and d.c. SQUIDs have been the most widely used. The field of applications has been growing and at present there are few small companies manufacturing commercial devices. As magnetometers and gradiometers SQUIDs have been used in geophysics to measure the magnetic field fluctuations at the earth's surface (Clarke, Gamble, and Goubau 1978).

The extremely low sensitivity has allowed to detect the magnetic field variations associated with heart and brain activity in humans. Another important application has been to measure small variations of magnetic field susceptibility. As laboratory instruments these devices have shown a great versatility and have been used as high sensitivity voltmeters and amperometers and in measuring very small resistances. A striking example of the application of a SQUID in fundamental research is its use as ultrahigh sensitive transducer in the antenna for the detection of gravitational waves (Amaldi and Pizzella 1979). Resistive SQUIDs have been used as radiation generators and in noise thermometry to measure temperatures in the microkelvin range (Kamper and Zimmerman 1971).

We now discuss briefly a few of the most important applications of the SQUIDs. For a more detailed discussion the reader is referred to the proceedings of the IC SQUID conferences (1976, 1980), to the proceedings of the conference on Future Trends in Superconductive Electronics (FTSE 1978), and the references cited there.

13.7.1 Measurements of Current, Voltage and Resistance. If the flux coupled to the SQUID is generated by a current flowing into an inductance coupled to the device, the system operates as a galvanometer (Fig. 13.34a). If the current is produced by a voltage applied to the inductance through a resistor, the output is proportional to the applied voltage and the system is essentially a voltmeter (Fig. 13.34b). If the voltage is generated by a current flowing into a resistance R_x , the device can operate as an ohmmeter (Fig. 13.34c). Galvanometers have been realized by Clarke (1966) and Decker and Mercereau (1973). Sensitivities of $10^{-9} \text{ A}/\sqrt{\text{Hz}}$ are achieved.

Recently Barbanera and coworkers (1978) have designed a device that is capable of measuring a.c. currents with a possible sensitivity of 10^{-14} A . By using a tuned input circuit it is possible to measure a.c. currents down to 8.10^{-15} A in 1 Hz bandwidth (Bordoni et al. 1978). Measurements of voltage

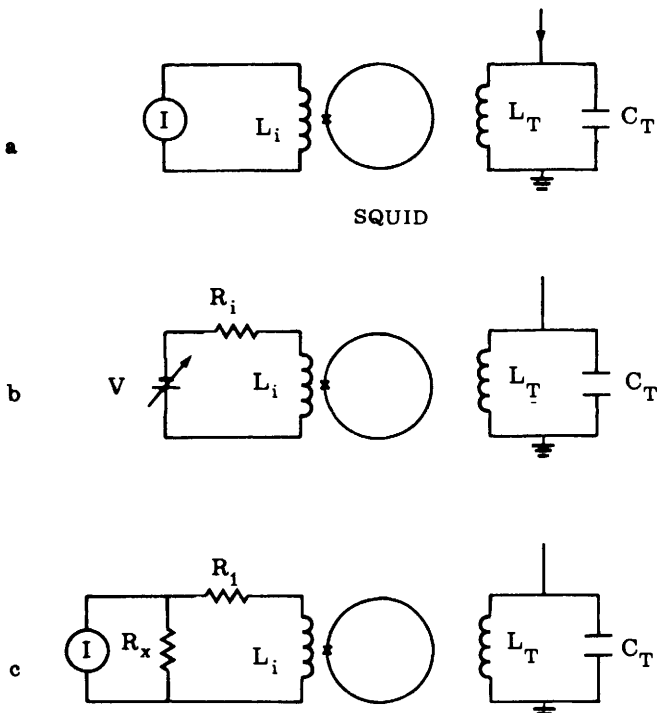


Figure 13.34 Simplified circuits for galvanometer (a), voltmeter (b), and ohmmeter (c).

and resistance have been performed by Lukens, Warburton, and Webb (1971) and Giffard, Webb, and Wheatley (1972). A typical configuration of voltmeter is depicted in Fig. 13.35. The voltage output V_0 of the magnetometer produced by the error current I_E in the inductor L_i is used to generate a feedback current $I_F = V_0/R_F$. Writing the Kirchoff voltage law for the input loop we get

$$V_x + R_1 I_E = R_2 \frac{V_0}{R_F}$$

At balance $I_E = 0$ and therefore the output voltage is related to the input voltage by

$$V_0 = \frac{R_F}{R_2} V_x$$

Usually $R_F \gg R_2$: therefore a voltage gain is realized. The last expression is valid only in the zero frequency limit.

For sinusoidally varying signal at frequency ω the relation between output and input voltage is given by (Davidson, Newbower, and Beasley 1974)

$$\frac{V_0}{V_x} = \frac{R_F}{R_2} \left[\frac{1}{1 + j\omega(\tau_F + \tau_T R_T / K_g R_2)} \right]$$

where $K_g = I_F/I_E$ is the current gain of the system and $R_T = R_1 + R_2$ and τ_F and τ_T are the feedback loop and input loop time constants. In the limit $\tau_T R_T / K_g R_2 \ll \tau_F$ the bandwidth is governed by τ_F . The ultimate sensitivity of the instrument is determined by the voltage noise, which in the low frequency limit is given by

$$\langle V_N^2 \rangle^{1/2} \simeq \frac{\langle \Phi_N^2 \rangle^{1/2}}{K} \left(\frac{R_1}{L \tau_T} \right)^{1/2} \frac{V}{\sqrt{\text{Hz}}}$$

where $\langle \Phi_N^2 \rangle^{1/2}$ is the noise at the SQUID input, L is the SQUID inductance K

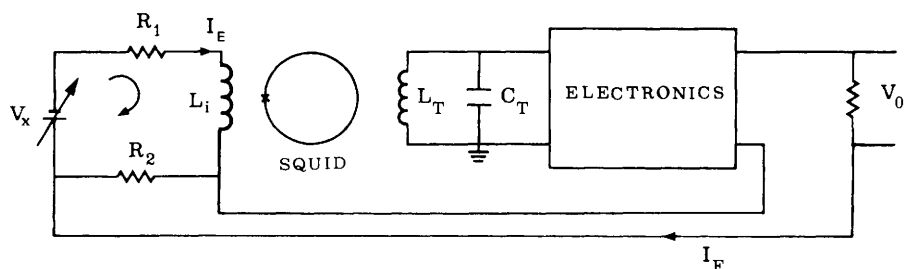


Figure 13.35 Schematic of a voltmeter configuration.

is the coupling constant between L_1 and L_2 , and we have assumed that $R_T \simeq R_1$. By taking the usual values $\langle \Phi_N^2 \rangle^{1/2} \simeq 10^{-4} \Phi_0 / \sqrt{\text{Hz}}$ and $L \simeq 10^{-9}$ and assuming that $R_1 \simeq 10 \Omega$ we get for a time constants $\tau_T \simeq 1$ second:

$$\langle V_N^2 \rangle^{1/2} \simeq 2 \times 10^{-14} \frac{\text{V}}{\sqrt{\text{Hz}}}$$

An extensive analysis of the noise characteristics of superconducting voltmeters, compared to conventional preamplifiers, has been reported by Davidson, Newbower, and Beasley (1974). Their analysis indicates that SQUID voltmeters are superior for source impedance at liquid helium temperature lower than 10Ω .

13.7.2 Magnetic Susceptibility Measurements. SQUIDs can be employed for the study of the magnetic susceptibility of very weakly magnetic materials or of samples containing small amounts of magnetic impurities. Susceptometers have been used to measure the electronic and nuclear magnetism of solids at low temperature and under low magnetic field; Hirschkoff, Symko, and Wheatley 1970, 1971; Giffard, Webb, and Wheatley 1972; Goodking and Stolfa 1970).

Mercereau and coworkers (Hoenig et al. 1972; Cerdonio et al. 1972) have employed SQUID susceptometers in the investigation of the magnetochemistry of metalloproteins in biological samples. The magnetic moment of a metal ion in a molecule is related to the geometrical arrangement of its nearest neighbors. From a measurement of the susceptibility as a function of temperature and magnetic field, information can be derived about the geometric arrangement of the molecule. Since a metalloprotein usually contains just one or a few metal ions for a molecule of molecular weight of 10^5 and is usually available in small amounts (of the order of a few tens of milligrams), a very high sensitivity instrument is needed. Superconducting susceptometers seem to be the most promising instruments for such measurements. In fact, at least for low field measurements, their ultimate sensitivity can be at least one or two orders of magnitude greater than that of conventional instruments. A sensitivity of 10^{-10} emu for a 1 cm^3 sample in a field of 100 G, has been achieved by Cukauskas, Vincent, and Deaver, Jr. (1974). Cerdonio and Messana (1974) have achieved a resolution of $6 \cdot 10^{-11}$ emu for a 0.5 cm^3 sample in a field of 200 G.

We now briefly discuss the susceptibility system of Cerdonio and co-workers (1976). Figure 13.36 depicts the experimental apparatus designed by those authors. The magnetic field H_e is generated by a superconducting solenoid operating in the persistent mode. The maximum field used is well below the critical field H_{c1} of the superconducting wire. The sample is inserted into the primary coil of a superconducting gradiometer whose secondary coil is coupled to an r.f. SQUID. When the sample is moved through the pickup coils,

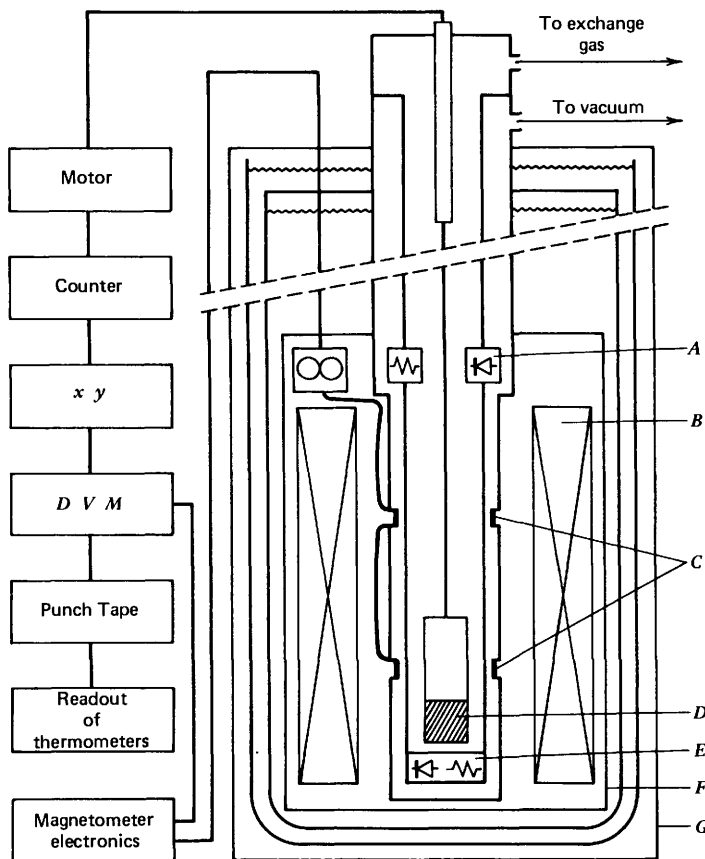


Figure 13.36 Schematic of the experimental apparatus for magnetic susceptibility measurements including the detection and recording system. *A*—thermometers; *B*—magnet; *C*—pickup coils; *D*—sample; *E*—heaters; *F*—lead shield; *G*—mu-metal shield. (After Cerdonio et al. 1976.)

a flux variation is generated which is a function of the position of the sample. The magnetometer output and a signal proportional to the sample position are sent to the *y* and *x* axes of an *xy* recorder. Typical experimental curves for different values of the temperature are reported in Fig. 13.37. The two peaks correspond to the sample at the center of the two oppositely wound coils forming the pickup coil. Care must be taken with the residual signal due to the sample holder. The system is calibrated by using a sample of known magnetic susceptibility. After the magnetometer output at the two peaks is measured by a digital voltmeter, from the peak-to-peak magnetometer reading $N\Phi_0$ (Φ_0 is the flux quantum) the magnetic susceptibility of the sample is derived by using the following relation:

$$N = \zeta H_e (2n\chi_M + Q)$$

where ζ is a calibration constant, H_e is the applied magnetic field, n and χ_M are

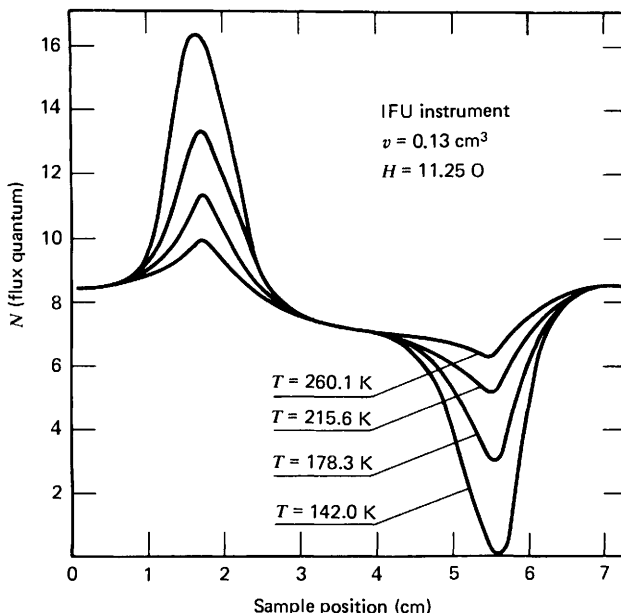


Figure 13.37 Typical plots of the magnetometer signal in units of flux quantum versus sample position for a 475 mM NiCl solution in a quartz holder at various temperatures. (After Cerdonio et al. 1976.)

the total number of moles and the molar susceptibility, and Q is the contribution from the sample holder.

To reduce noise due to vibrations the overall system was placed on an antivibration platform. To reduce electrical noise the apparatus and the electronics were operated in an electromagnetically shielded room. The sensitivity achieved was $\Delta\chi = 2.2 \times 10^{-9} \text{ emu/cm}^3$ at a field $H_e = 11.25 \text{ Oe}$ in the temperature range between 100 and 300 K.

An improved version of the apparatus just described has been recently designed by Cerdonio and coworkers (1977). In this system the sample executes small amplitude oscillations at a frequency of 5 Hz while it is moved across the pickup coils. The signal from the SQUID magnetometer is fed to a lock-in amplifier using the 5 Hz oscillation signal as a reference. The ratio between the rms magnetic flux change to the rms oscillation amplitude can be directly related through a calibration constant to the value of the volume susceptibility.

13.7.3 Medical Applications. A very interesting field in which superconducting magnetometers have found application is that related to the measurement of magnetic fields produced by humans. Among the phenomena that have been observed are magnetic field produced by heart activity (magnetocardiogram), muscle action (Magnetomyogram), and brain activity (magnetencephalogram). An excellent review on this subject has been given by Cohen

(1974) and by Williamson, Kaufman, and Brenner (1976, 1978). In Fig. 13.38 typical values of the magnetic fields involved in these kinds of measurements (after Cohen 1974) are shown. For comparison the limiting sensitivities for SQUIDS and fluxgate magnetometers and the intensity of some typical external disturbances are also indicated. The use of superconducting magnetometers in M.C.G. was introduced by Cohen, Edelsack, and Zimmerman (1970). Data reported by these authors are shown in Fig. 13.39. A simple single loop configuration (see Fig. 13.29a) was used for the sensing superconducting transformer. To minimize the effect of the earth's magnetic field, the measurement was performed in the shielded room designed by Cohen (1970) at the Francis Bitter National Magnet Laboratory at the Massachusetts Institute of Technology. The shielded room, shown in Fig. 13.40 is roughly spherical in shape and is made by three high permeability layers for magnetic shielding and two aluminum layers to provide electrical shielding. The static field in it is reduced to a few nanoteslas ($1 \text{ nT} = 10^{-5} \text{ G}$), with gradients of 1 nT/m . For comparison, the amplitude of the slowly varying M.C.G. signal is about $3 \cdot 10^{-11} \text{ T}$ ($3 \cdot 10^{-7} \text{ G}$). Subsequently, the use of the gradiometer configuration (Zimmerman and Frederick 1971; Rosen, Induye and Morse 1971) has made possible the elimination of these expensive facilities. Not many laboratories have a shielded room like that at M.I.T. As an example, the group at the University of Technology at Otaniemi (Finland) has its measurement room in a wooden cottage in a suburban area about 70 m away from an apartment block (Saarinen et al. 1974). No shield is used, a fact permitted by the first derivative gradiometer configuration used for the sensing coil. This group has applied the magnetocardiogram techniques to the detection of the heart activity of a fetus (Kariniemi et al. 1974; Ahopelto et al. 1975). It is interesting to observe that the magnetometer is an external probe and can be positioned near the abdomen of the mother, allowing to see better the contribution of the fetus. As experienced by Opfer and coworkers (1974), the use of a second derivative gradiometer (see Fig. 13.29c) makes it possible to conduct measurements in an urban environment as well. A similar configuration has been used to detect biomagnetic activity without any magnetic shield at the Instituto di Elettronica dello Stato Solido of C.N.R in Rome. (Barbanera et al. 1978a, 1980a,b, Romani 1979). To give an idea of how the gradiometer configuration might compensate for ambient noise, Figure 13.41a shows a magnetocardiogram of one of the authors of this book. It was done at the aforementioned

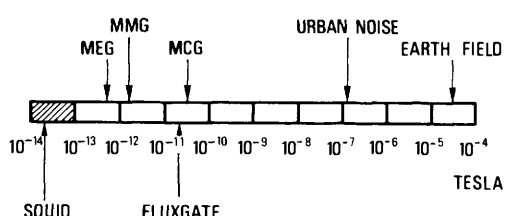


Figure 13.38 Typical magnetic field values produced by the human body.

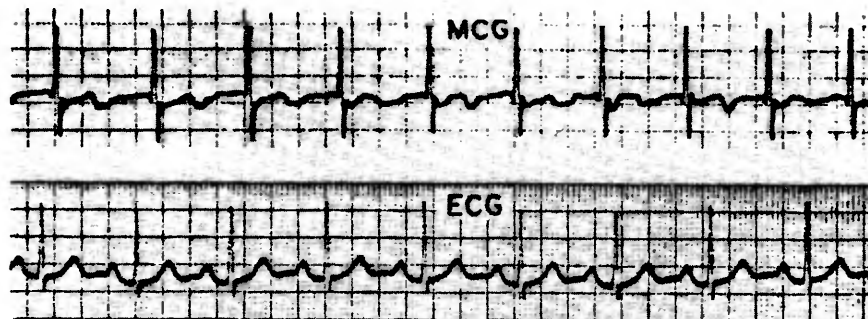


Figure 13.39 Upper trace: an M.C.G. taken inside the shielded room with the point contact magnetometer: the *T* wave is visible but the *P* wave seems masked by detector noise. Lower trace: for comparison, an E.C.G. of good medical quality taken the next day on the same subject. The chart speed for both traces was 25 mm/sec and bandwidth was about 0.5 to about 40 Hz. Assuming 3×10^{-7} G at the peak of Q.R.S., the magnetometer noise is estimated to be about 1×10^{-9} G (rms per root cycle). (After Gohen, Edelsack, and Zimmerman 1970.)

Institute. The pickup coil was a second derivative gradiometer. No shields were used, the only precaution requested being the removal of belt, buckles, and the contents of the left shirt pocket.

An example of a typical standard 36-spot MCG map of a normal subject is reported in Fig. 13.41*b*. Such maps are usually recorded during rush hours on normal and pathological subjects (Barbanera et al. 1980c).

An interesting possibility for providing low frequency shielding at a medium cost is the use of thick walled enclosures of very high conducting nonmagnetic materials, such as that recently designed by Zimmerman (1977) at the National Bureau of Standards in Boulder (Colorado). The majority of the magnetocardiograms reported have been made by measuring only one of the components of the heart's magnetic field around the chest. Recently Wikswo and Fairbank (1976) have designed at Stanford University a system to make a vector Magnetocardiogram. The gradiometer they used has the two coils in the primary inductance tilted at an angle of 55° with respect to its axis. Simple successive 120° rotations allow measuring the three orthogonal component of the field. A linear transformation is used to reduce the data to a body related coordinate system. The measurements are made in a shielded enclosure, and the data are recorded and processed by an online minicomputer (Wikswo et al. 1976).

The sensitivity achievable by means of superconducting magnetometer is good enough to study much weaker biological signals; indeed, neuromagnetic fields generated by the spontaneous brain activity are of the order of a few picoteslas ($1 \text{ pT} = 10^{-8}$ G), while the amplitude of magnetically evoked responses may even be 10 times lower. These signals were previously investigated in shielded environments (Cohen 1972, 1974). The use of more and more sophisticated spatial discriminating gradiometers allowed the investigation of these phenomena even without the aid of magnetic shielding. Williamson and

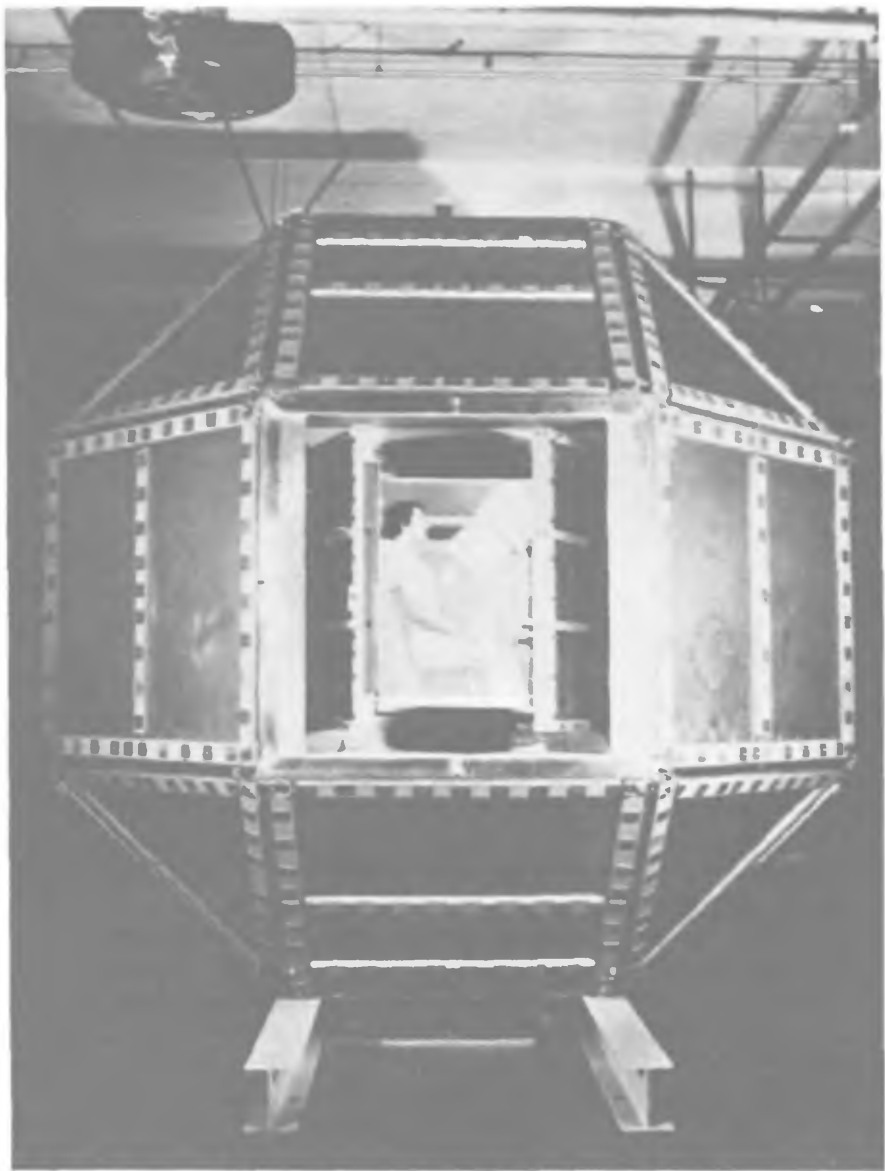


Figure 13.40 The shielded room at the Francis Bitter National Magnet Laboratory of Massachusetts Institute of Technology. (Courtesy of D. Cohen.)

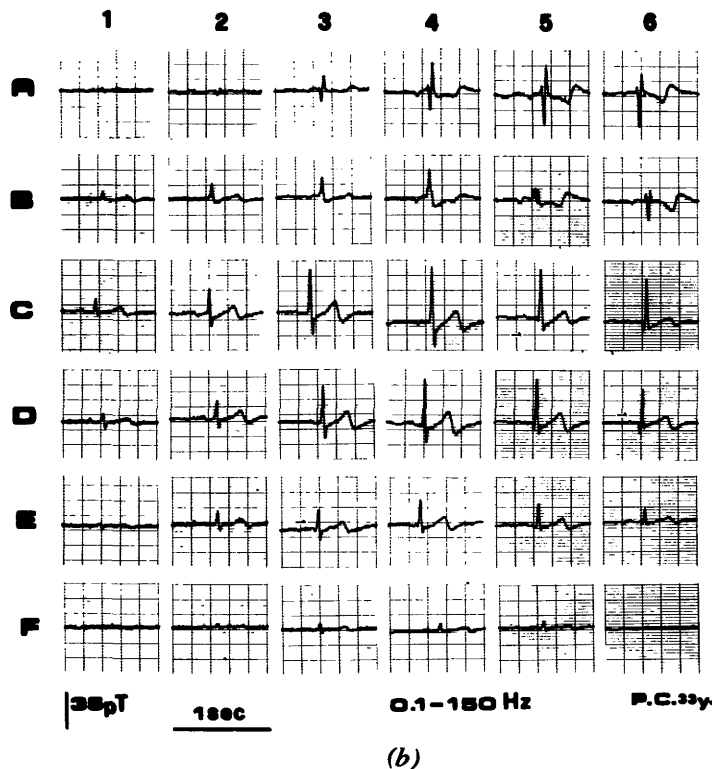
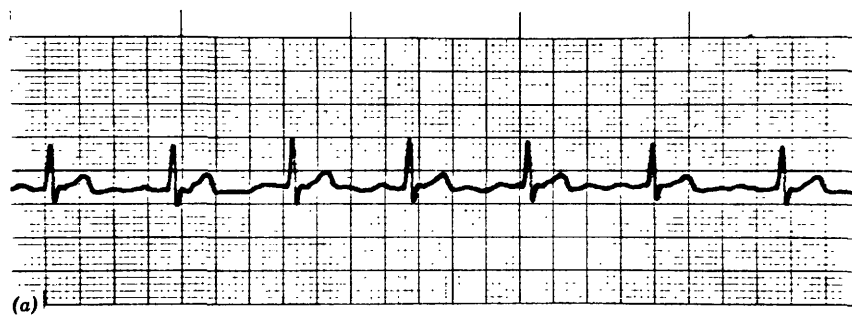


Figure 13.41 (a) The magnetic cardiogram of one of the authors of the present book. (G.P.) (b) Typical 36-spot M.C.G. map of a normal subject. The data were recorded by a second derivative gradiometer at the Istituto di Elettronica dello Stato Solido of the Consiglio Nazionale delle Ricerche (Rome). (Courtesy of S. Barbanera, P. Carelli, I. Modena, and G. L. Romani.)

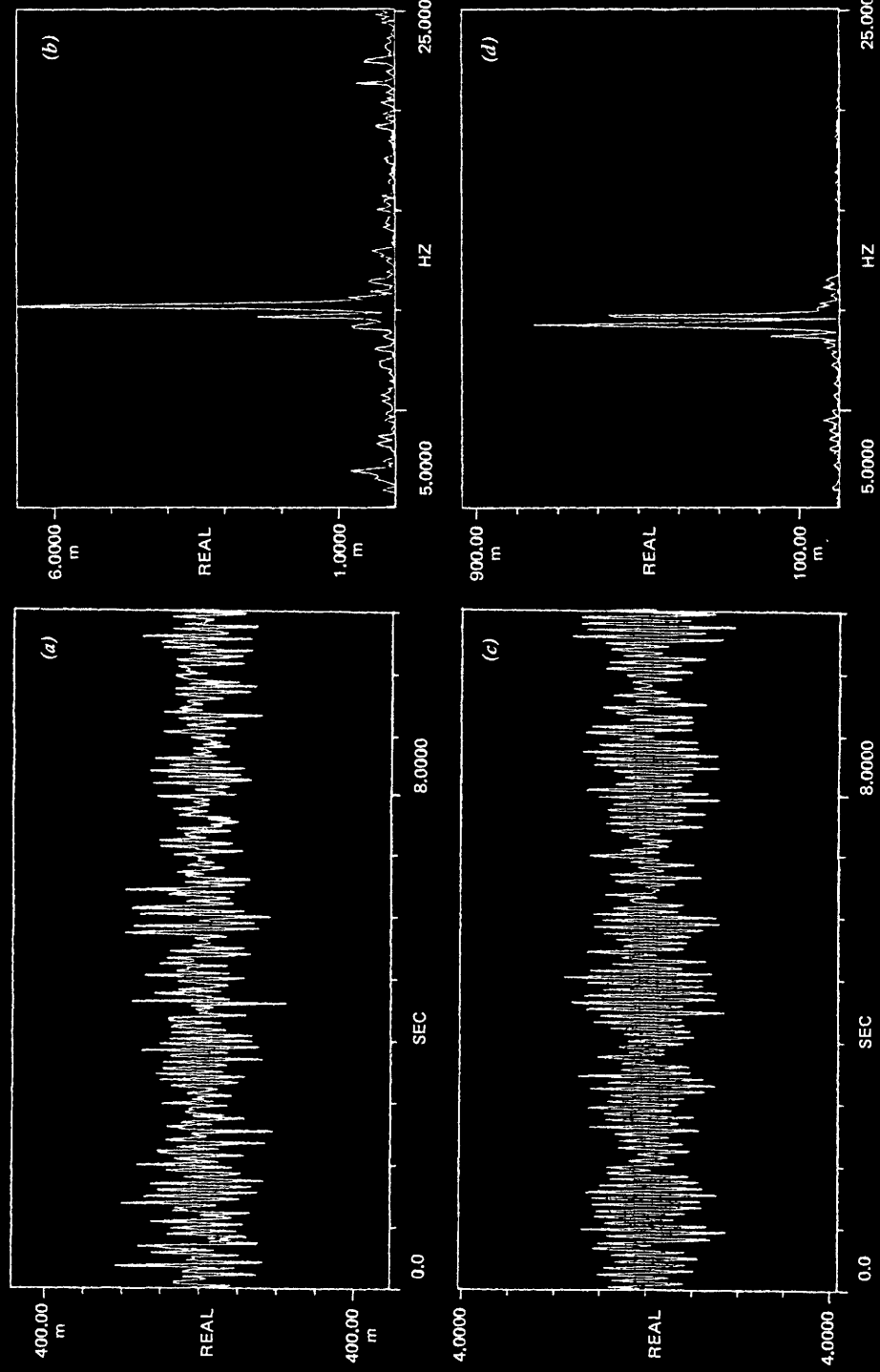


Figure 13.42 Simultaneous M.E.G. (a) and E.E.G. (c) tracings and the corresponding Fourier analysis (b), (d), of a normal subject recorded at the Istituto di Elettronica dello Stato Solido of Consiglio Nazionale delle Ricerche (Rome). (Courtesy of G. L. Romani.)

coworkers studied neuromagnetically evoked responses in urban environments since 1975 (Brenner, Williamson, and Kaufman, 1975; Williamson and Kaufman 1980).

Detailed studies about visually and auditory evoked signals have been carried out by the Helsinki group as well (Aittoniemi et al. 1979). At the Instituto di Elettronica dello Stato Solido del C.N.R. in Rome systematic investigations of the spontaneous brain activity of normal and pathological subjects are preformed by means of a simultaneous recording of the magnetic signal and of a standard (8-lead) electroencephalogram (Barbanera et al. 1980b).

Tracings are studied both in the time and in the frequency domain. An example of such an analysis for a normal subject is shown in Fig. 13.42. The high-resolution Fourier analysis clearly shows that different components constitute the electric and magnetic signals. This circumstance suggests that electrical and magnetic activities are at least partially uncorrelated; therefore different generators may be responsible for the two phenomena.

13.7.4 Magnetotellurics. Among the various applications of SQUID there is the measurement of the surface impedance of the earth through the simultaneous detection of both magnetic and electric field fluctuations. This topic, namely *magnetotellurics*, is indeed a tool of increasing interest and perspective, also in connection with investigations on petroleum and geothermal sources as well as for the study of seismic activity. The technique involves the evaluation of the impedance tensor Z as function of frequency from the relations

$$E_x(\omega) = Z_{xx}(\omega)H_x(\omega) + Z_{xy}(\omega)H_y(\omega)$$

$$E_y(\omega) = Z_{yx}(\omega)H_x(\omega) + Z_{yy}(\omega)H_y(\omega)$$

where $E_i(\omega)$ and $H_i(\omega)$ are the Fourier transforms of the horizontal orthogonal components of electric and magnetic field fluctuations $E_i(t)$, $H_i(t)$, ($i=x, y$) which are the actual quantities that have to be measured. Moreover, measurements of the vertical component $H(t)$ can also be performed, obtaining further useful informations.

Without going into detail, the role of the SQUID is to substitute successfully the conventional induction coils typically employed to improve sensitivity. In this direction 3-axis SQUID magnetometers can be used, as in the work by Clarke, Gamble, and Goubau (1978) (for early studies see the work by Frederick et al. cited therein).

Clarke and coworkers have analyzed and compared data using a standard least-squares method with a novel technique that employs a remote reference magnetometer. The high level reached with this technique improves the control of long-term variations in the apparent resistivity that can be used in the perspective of the prediction of seismic events.

CHAPTER 14

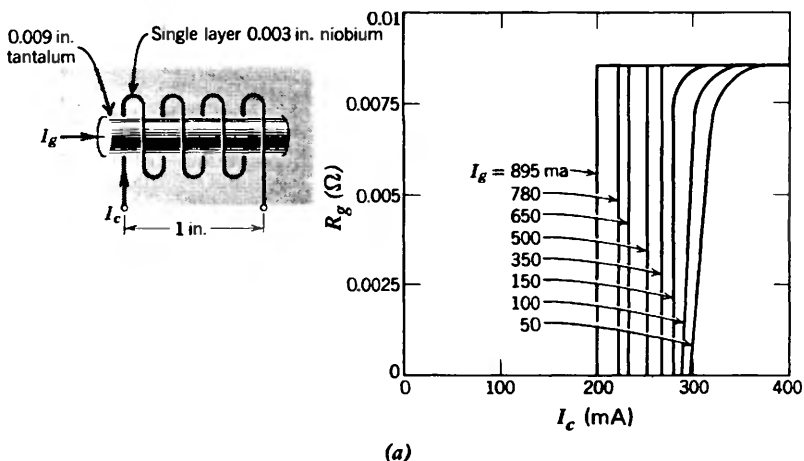
Computer Elements

Increasing computer performance is a well known example of one continuous objective in applied science. In the past three decades progress in semiconductor integrated circuit technology has led to an extremely rapid growth in computer capabilities. New approaches based on other technological solutions are also being investigated in various laboratories; in particular, the Josephson effect has stimulated new ideas and perspectives. As we shall see throughout the chapter, various junction configurations have been considered for digital Josephson technology. We follow a somewhat historical track, beginning with early attempts to make computer components based on the properties of a superconductor.

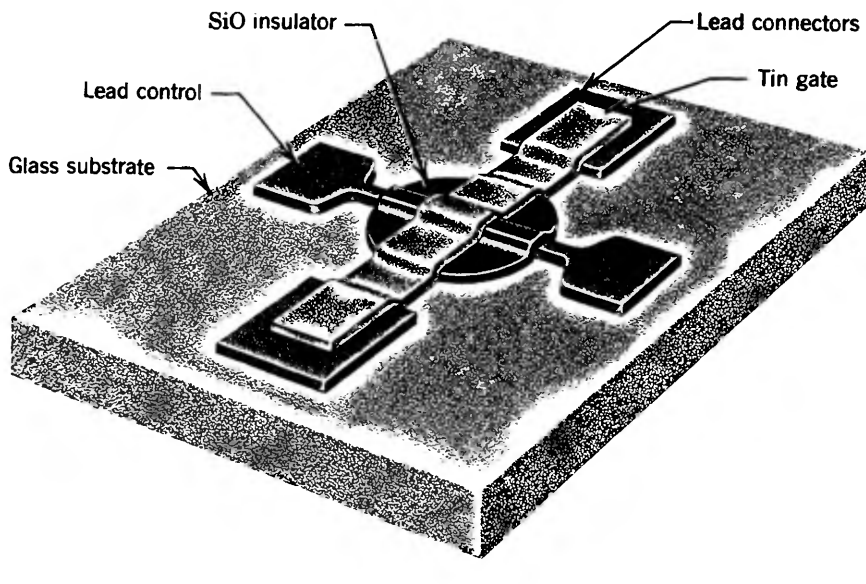
14.1 Cryotrons

The idea of employing a superconductor in computer devices is rather old. Buck (1956) proposed a new component, called the cryotron, which operates as a superconducting current switch. This simple system is shown in Fig. 14.1a. The superconductor S , acting as a gate, can be changed to the normal state by means of an applied magnetic field produced by a current I_c in the winding control. The characteristic time of operation for this device was in the range of tens of microseconds.

Newhouse and Bremer (1959) discussed a higher speed superconductive component using thin film technology. A crossed film configuration was adopted (Fig. 14.1b). The gate was a thin superconducting line (of width W) insulated from a perpendicular film control line (of width W_c). Unfortunately, in this case as well the gain-speed problem remained unsolved, since higher gain was obtained at a cost of longer operating time. In fact, an increase in the ratio W_g/W_c necessary to achieve a larger gain leads also to a longer time constant L/R (L is the total inductance of the loop and R the gate resistance). A further improvement was achieved by Brennemann (1963) who adopted an in-line geometry (the in-line cryotron). In this device the widths of gate and control lines are equal ($W_g = W_c$) see Fig. 14.2a. The main advantage of the in-line over the cross-line cryotron is a substantial increase of R , since the

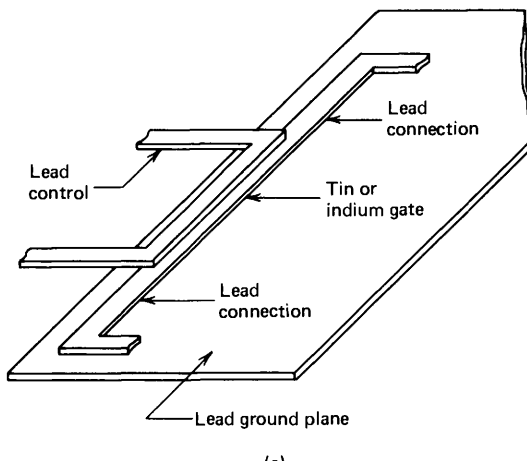


(a)

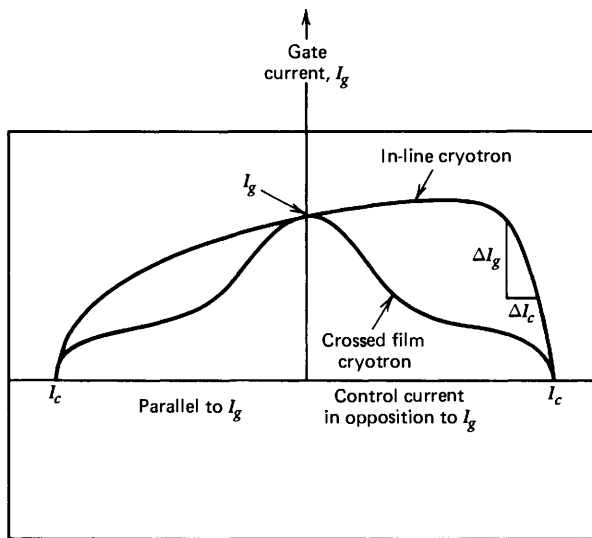


(b)

Figure 14.1 (a) Gate resistance vs. control current for a Ta-Nb wire wound cryotron at 4.2 K (Buck 1956). (b) Schematic of a crossed film cryotron (Newhouse and Bremer 1959). (After Newhouse 1964.)



(a)



(b)

Figure 14.2 (a) Sketch of an in-line cryotron. (b) Comparison of characteristic curves of crossed films and in-line cryotrons. (After Brennemann 1963.)

whole gate line is involved in the transition to the normal state. A reduction in L is also obtained by increasing W_c (up to W_g).

Figure 14.2b compares gain curves of the cross-line and in-line cryotrons for a given ratio W_g/W_c (equal to unity). It is clear that the curve referring to the in-line device has a higher slope (higher gain). It is possible, in fact, biasing the gate with an additional control line, to achieve an incremental gain ($\Delta I_g/\Delta I_c$ ratio) up to 10.

Although the cryotron technology (Newhouse 1964), including high geometrical resolution, seemed for several years to be rather promising, it did not achieve competitive levels of performance. Also, this early generation of cryotrons had strong limitations (Brenneman, McNichol and Seraphym 1963) related to the normal-superconducting phase transition which is inherent in their basic functioning. Two factors limited the speed of the operation: the presence of latent heat in the superconductive-normal transition and the finite propagation time of the phase boundary between nucleation sites. To conclude our brief outline of the state of the art "before Josephson tunneling," we recall the application of superconductive tunneling to switching elements proposed by Giaever and Megerle (1962).

14.2 Matisoo's Experiments

The double valued structure of the current-voltage characteristics of a Josephson junction, together with the possibility of switching between zero voltage and quasiparticle tunneling states by means of applied magnetic field, suggested a new potential logic element. This is a new cryotron the so-called tunneling cryotron (Matisoo 1967a). Such a device (Fig. 14.3a) does not involve, in its operation, problems connected with the superconductive-normal phase transition.

14.2.1 Tunneling Cryotron. Matisoo (1966) first reported experimental results on the transition between the two stable states at $V=0$ and $V=2\Delta/e$, with switching times of less than 1 nsec. We now outline some aspects of these pioneering experiments. The measurements were performed using in-line $\text{Sn}-\text{Sn}_x\text{O}_y-\text{Sn}$ tunneling structures with dimensions of 0.13×0.13 mm and displaying a maximum Josephson current of about 1 mA (at 1.7 K). A lead ground plane under the junction provided a substantial reduction of the inductance of the films. The scheme of the measuring apparatus is shown in Fig. 14.3b. Matisoo observed both transitions from the zero voltage state to the quasiparticle tunneling state and vice versa. In Fig. 14.3c the former process is shown as observed on the oscilloscope. The measured rise time established an upper limit for the switching time of 0.8 nsec. For the inverse transition, a switching time of about 1 nsec was measured. The larger value of the latter transition time is due to the less sharp threshold involved. In fact, it was necessary to reach, approximately, the value $V=\Delta/e$ in order to switch from the quasiparticle to the zero voltage state. As will be discussed later, this "reverse" switching presents rather complicated aspects. As predicted by Matisoo, much lower values of the transition time have been found in subsequent experiments (Zappe and Grebe 1971, 1973; Jutzi et al. 1972).

In practice, in order to "drive" the switching, the gate junction is overlaid by a superconductive control line which is electrically insulated from it. The magnetic field produced by the control current I_c modulates the maximum

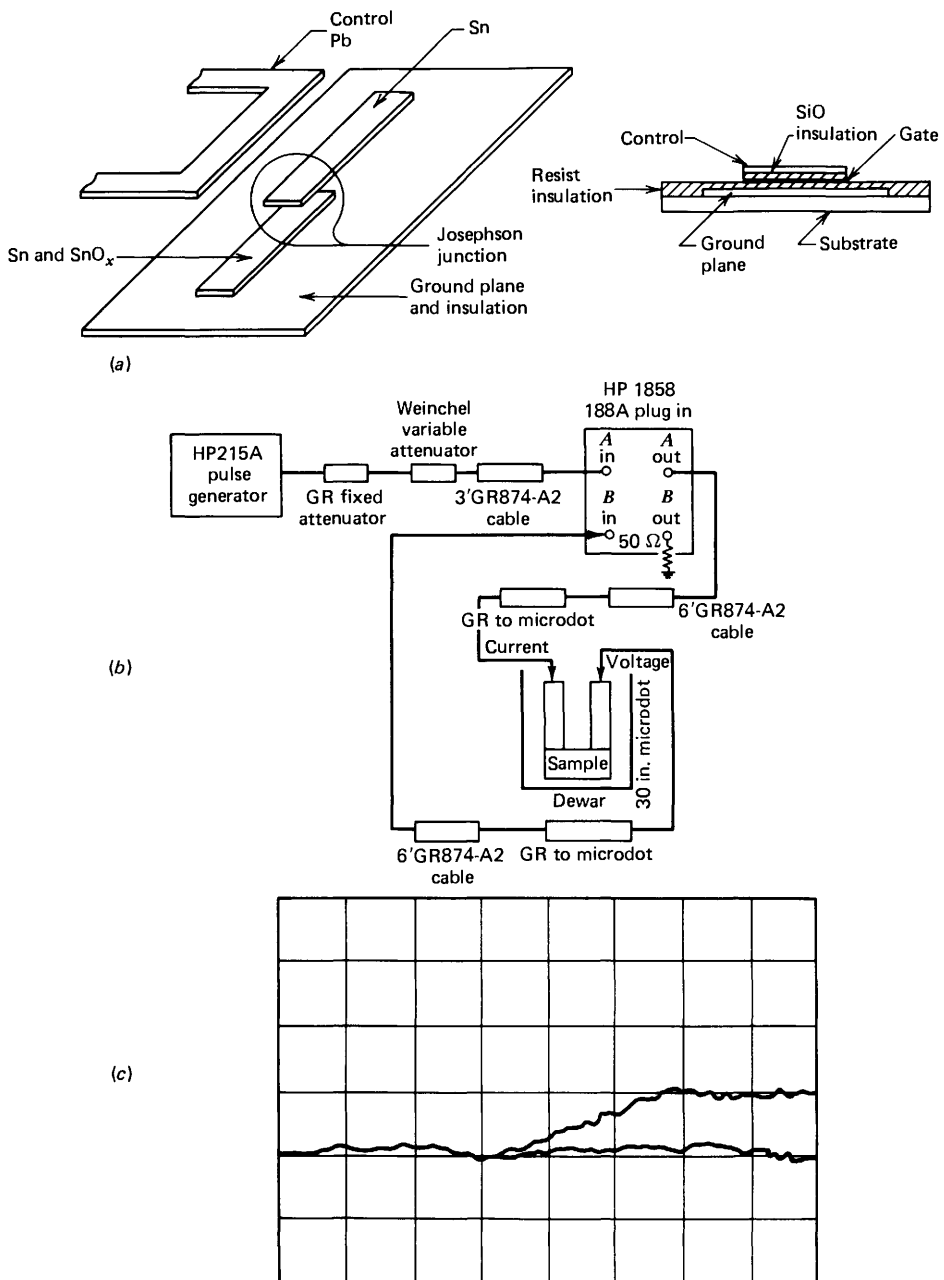


Figure 14.3 (a) Schematic of tunneling cryotron geometry. (After Matisoo 1967a.) (b) Block diagram of apparatus used for measurements. (c) Oscilloscope trace showing voltage across the $\text{Sn}-\text{Sn}_{x}\text{O}_y-\text{Sn}$ junction below threshold (lower trace) and the transition from pair tunneling state (zero voltage) to single particle voltage state (finite voltage). Horizontal scale 0.4 nsec/div; vertical scale 1 mV/div; $H_a=0$; $T=1.7$ K. (After Matisoo 1966.)

Josephson current, I_1 . When this threshold current I_1 is reduced just below I_g , the junction switches to the finite voltage curve at $V=2\Delta/e$, or, more precisely, to the intersection of the quasiparticle curve with the external load line (see Section 14.4). The dependence of the gate current I_g on the control current I_c , that is, the gain curve, for an in-line configuration is shown in Fig. 14.4a. Data points in the figure are obtained by coincident pulses in control and gate. It represents the locus of gate and corresponding control amplitudes at which the transition was observed (Matisoo 1967a). We note that the shape of the curve is the typical one of a large Josephson junction (in this particular case $L/\lambda_J \approx 10$). The asymmetry is produced by the presence of the ground plane. Pritchard and Schroen (1968) investigated a cross-control gate configuration with a "window" geometry and found the I_g vs. I_c dependence reported in Fig. 14.4b. We do not extend here the interpretation of the results, since these are essentially contained in the discussion given in Chapters 4 and 5 on the applied and self-generated magnetic field in Josephson junctions, ground plane effect, and so on.

14.2.2 Flip-Flop Circuit. A basic mode of operation of cryotrons in the context of the processing and storage of information is current steering. This

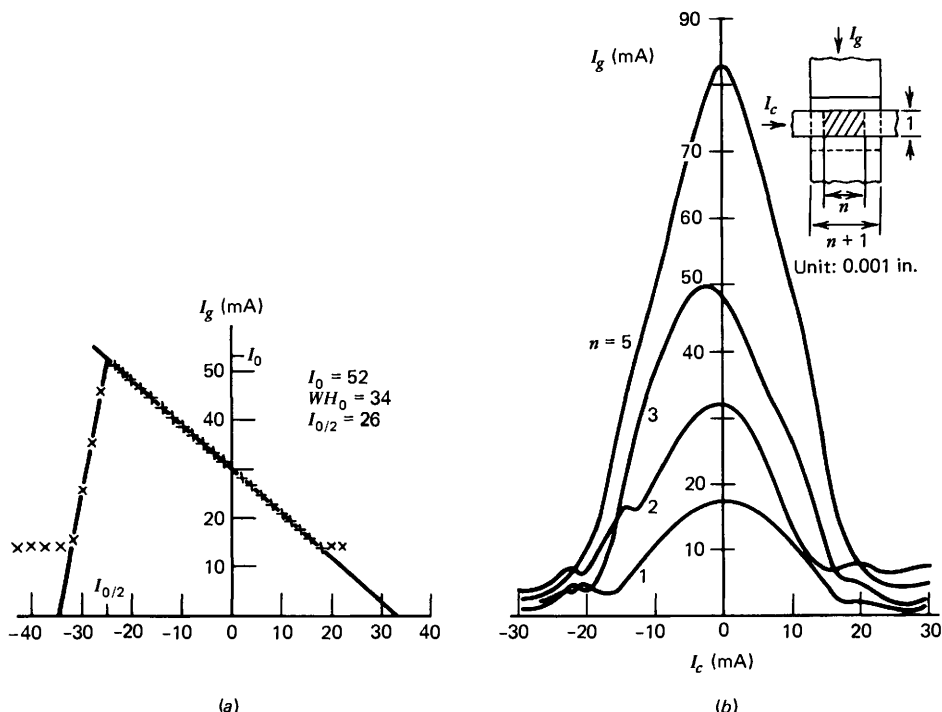


Figure 14.4 (a) Gate vs. control current for an in-line configuration with a ground plane. (After Matisoo 1967a.) (b) Same for a "window" geometry. (After Pritchard and Schroen 1968.)

kind of operation was investigated by Matisoo (1967b, 1969), who considered two tunneling cryotrons in a "flip-flop" configuration. The sketch of Matisoo's original flip-flop circuit is given in Fig. 14.5. The incoming current can be steered from one branch of the superconductive loop to the other, acting alternatively on the two switching gates with the aid of suitable control lines. A bistable logic circuit behavior is thus obtained. The various steps of the device operation can be roughly described as in Fig. 14.6. Let us consider first a superconducting film loop. Under conditions of complete symmetry (equal inductances) the current will be equally divided in the two branches of the loop. It is the same if we consider two identical Josephson junctions *A* and *B* inserted in the circuit as in Fig. 14.6*a*. The current I_0 entering the device splits into two parallel paths and crosses the two junctions which operate in the Josephson current region (zero voltage state). The maximum Josephson current I_1 is supposed to be such that $I_0 < I_1$. Now we can apply through the control line of junction *A* a current pulse I_{ca} which, by the effect of the associated magnetic field, reduces the maximum Josephson current to a value less than $I_0/2$. This produces the switching from $V=0$ to $V_0=2\Delta/e$, that is, to the only other possible state at the current level $I_0/2$. Thus, because of the appearance of resistance (in *A*), the current across junction *A* decreases and across junction *B* increases. Current is therefore diverted from one side to the other ("current steering"). As soon as the current reduces to I_m junction *A* switches back to a Josephson state at a lower current level (I_m) with respect to the initial state (Fig. 14.6*b, c*). Even when the control pulse is removed, the system remains in this new state, which is also stable because of the fluxoid conservation in superconducting loop. Acting on the control line of *B* it is possible to follow the symmetric operation. In conclusion, in this circuit, current can be steered from one branch to the other by means of an external control pulse. The control current can steer a significantly larger gate current, which is important for low power logic system operation. The gain of this device is given by the

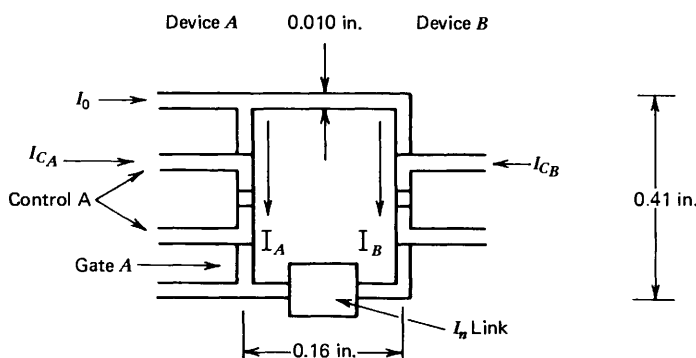


Figure 14.5 Sketch of a tunneling cryotron flip-flop circuit. The junctions are indicated by circles. Under the loop but insulated from it (typically by several thousand Å thick SiO layer) there is a ground plane. (After Matisoo 1967b.)

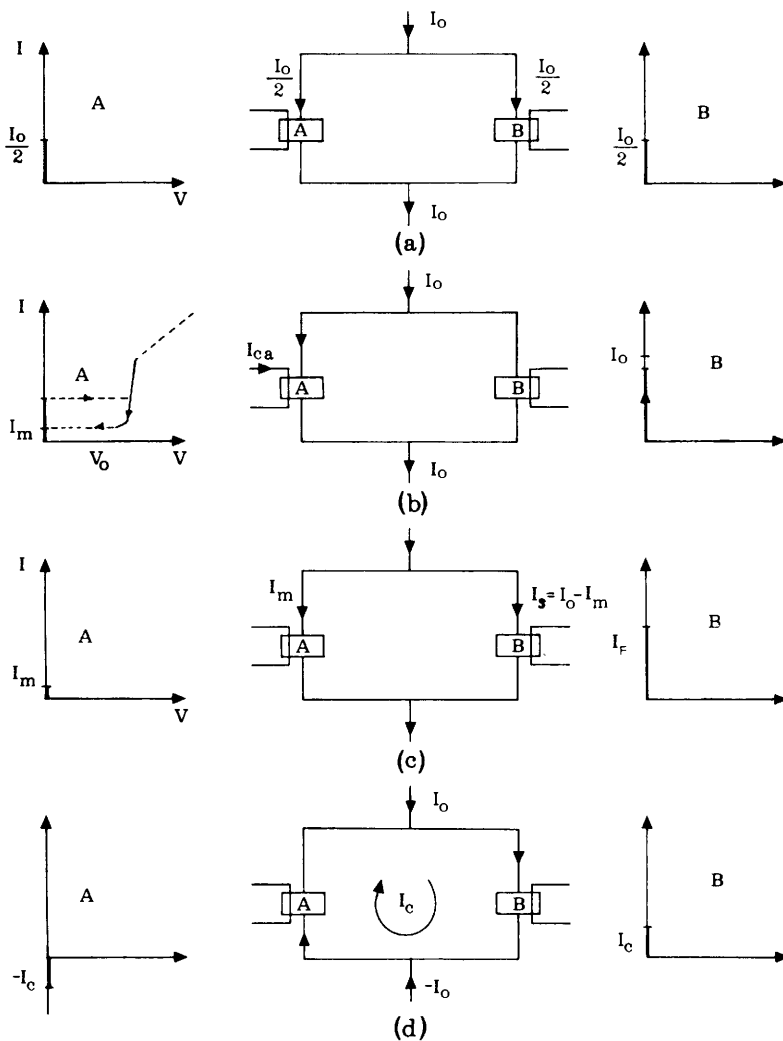


Figure 14.6 Various steps in the operation of two tunneling cryotrons in a flip-flip configuration.

ratio of the current steered to the control current necessary to produce the gate transition between the zero and finite voltage states. To evaluate the current steering time it is possible to measure the time during which junction A is in the resistive state (it is during this time that current is diverted to B). If we are in the condition that the current transferred I_s is sufficient to switch B (that is, $I_s = I_0 - I_m > I_1$), then the steering time is given by the delay between the switching of the two gates. In the last quoted reference both methods have been employed and steering of 20 mA in a time $\Delta t \leq 2$ nsec has been observed from which a junction transition time less than 0.8 nsec was also deduced.

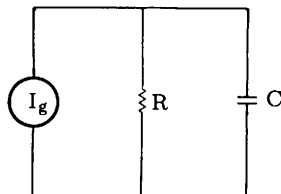
14.3 Operation Times

As we have seen, two different operation times must be taken into account: the switching time and the steering time. For a rough evaluation of the switching time from $V=0$ to $V_0=2\Delta/e$ it is possible to refer to the time necessary to charge the junction capacitance C to a voltage V_0 by a constant current source I_g . The simple electronic equivalent circuit is sketched in Fig. 14.7a. Let us assume that the resistance R is in the region $0 < V < 2\Delta/e$, as the average resistance value, $R=(2/e)(\Delta/I_m)$ (see Fig. 14.7b). Therefore V tends toward $I_g R$ with a time constant RC , that is:

$$V(t) = I_g R (1 - e^{-t/RC})$$

However, because of the drastic change in the resistance, a voltage clipping at $V=V_0$ occurs, so that the junction switching time is given by

$$t = -RC \log \left(1 - \frac{V}{I_g R} \right)$$



(a)

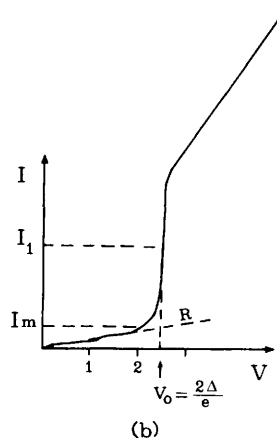


Figure 14.7 (a) Equivalent circuit for a Josephson tunnel junction. (b) Voltage-current characteristics.

and since $V_0 \ll I_g R$, it follows that

$$t \approx \frac{V_0 C}{I_g} \quad (14.3.1)$$

From this we observe that, since V_0 is fixed by the gap of the superconductor, the enhancement of switching speed can be achieved by reducing the junction capacitance and increasing I_g . This is obtained, for a given optimized miniaturization, by reducing the barrier thickness t . In fact, the capacitance is proportional to t^{-1} , whereas the Josephson current increases exponentially with decreasing t . Thus, minimum junction size and maximum current density are the two conditions to be satisfied. Using the approximate relation (14.3.1) we can roughly estimate the order of magnitude of the switching time. Assuming the rather typical values of $V_0 = 1$ mV, $C = 10^{-10}$ F, and $I_g = 10$ mA, we have $t \approx 10$ psec.

Experiments performed by Zappe and Grebe (1971, 1973) on large junctions established a switching time of 60 psec. Jutzi et al. (1972), investigating a small junction, $1 \times 3 \mu\text{m}$, observed a switching time of ~ 38 psec. These values are larger than expected since measurements were limited by instrument resolution. We note that with respect to the earlier "historical" (non-Josephson) cryotrons, a reduction of a factor of eight orders of magnitude in the switching time can be presently achieved.

Let us consider now the simple equivalent circuit of the flip-flop shown in Fig. 14.8 in order to evaluate the current steering time. In this case we have a constant voltage source V_0 in series with the dynamic resistance of the junction. L indicates the loop inductance. Therefore the current in the circuit is

$$I(t) = \frac{V_0}{R_d} (1 - e^{-(R_d/L)t})$$

Let us note that V_0/R_d is much larger than the current transferred ΔI because R_d represents the small dynamic resistance (typically less than a 10^{-3} Ω) of the junction at $V \approx V_0$. Thus

$$t \approx \frac{\Delta I L}{V_0}$$

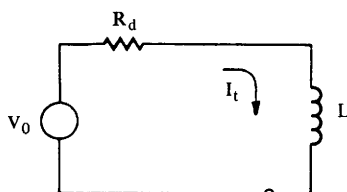


Figure 14.8 Simple flip-flop equivalent circuit.

If we assume, for example, as typical values $I = 10 \text{ mA}$, $V_0 = 1 \text{ mV}$, and $L = 5 \times 10^{-11} \text{ H}$, a steering time of 500 psec follows in agreement with experimental values reported in the literature (Matisoo 1966, 1967b; Zappe and Grebe 1971).

14.4 Different Switching Modes

We now discuss some aspects of the switching operation of a single gate in connection with the external junction loading conditions. This includes the problem, previously mentioned, of the reverse switching from the finite voltage to the zero voltage state. We can state roughly that the junction undergoes such a transition as soon as the instantaneous voltage given by the addition of d.c. and a.c. contributions is equal to zero.

When a resistive loading is considered such that the load line intersects the quasiparticle branch at a voltage value lower than V_m (see Fig. 14.9), the junction switches back to the zero voltage state independently of the control current I_c . This "self-resetting" behavior is accounted for by the instability of the V - I characteristics for finite voltages below V_m as discussed in Chapter 6. A second mode of operation occurs when the load resistance is larger than a certain value R_L (Fig. 14.9). In this case the voltage does not switch back to zero but remains at a finite value corresponding to the intercept of the load line with the quasiparticle branch. This process is usually referred to as the latching mode. The resetting in this case can be accomplished by lowering the gate current I_g to a value for which the load line intercepts the quasiparticle branch in the self-resetting region. Intermediate values of the loading ($R_r < R < R_L$) lead to a "nonlatching" behavior. In this case the resetting occurs as soon as the control current I_c is removed. This can be understood by considering that the removal of the control current implies an increase of the maximum Josephson current and consequently an increase of the amplitudes of the a.c. Josephson voltage oscillations. Of course these oscillations are present also in the two previous cases; however in the "nonlatching" situation the instantaneous voltage reaches the zero value causing the locking of the junction into the zero voltage state. The dynamic switching characteristics corresponding to

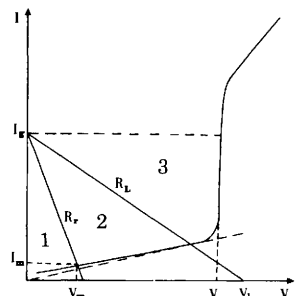


Figure 14.9 Different resistive loading for various switching modes.

these three modes of operation described by the instantaneous junction V - I curve are reported in the detailed paper by Lum, Chan, and Van Duzer (1976). The reader is also referred to the fundamental articles by Zappe (1973, 1975a, 1976) and Henkels (1974). A discussion of the switching dynamics has been also given by Chan, Ulrich, and Van Duzer (1977) in terms of the R.S.J. model with a shunt capacitance, including the effect of an output line connecting the junction to a load.

In dealing with switching problems it should also be observed that in real junctions self-resonant modes can be excited which manifest themselves as current peaks superimposed on the quasiparticle current branch. As discussed in Chapter 9, the amplitudes of these current steps can be rather large compared with the maximum zero voltage current especially when large junctions ($L > \lambda_j$) are considered. When the load line intersects such current steps, problems can arise in the resetting process. Taking advantage of the geometry of the junction (Matisoo and Zappe 1975), it is possible to avoid the presence of these current steps. Another possibility is connected with the development of Josephson devices that employ semiconducting barriers. In this case the inherent low Q character of these structures can remove such current singularities. High speed unlatching-type circuits, of this kind are discussed by Chan, Lum, and Van Duzer (1974). Moreover, Barone, Russo, and Vaglio (1978) have reported some preliminary results regarding the possibility of using devices with light sensitive semiconductor tunnel barrier.

Another effect that arises in the switching from the finite to the zero voltage state, especially in small junctions, is the so-called punchthrough effect (Fulton 1971; Fulton and Dynes 1971). This occurs when, in order to get a fast reset, the current is lowered to negative values ("overdrive") such that $|I_g| > |I_1|$. In this case, in fact, the junction voltage can go to negative values along the quasiparticle branch "punching through" the $V=0$ state.

In considering the flip-flop circuit of Fig. 14.10, it is clear that the current steering operation will be determined by the switching properties of the gates just discussed and by the effect of the loop. This problem was discussed in an

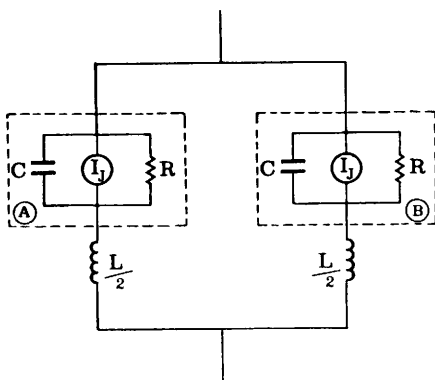


Figure 14.10 Flip-flop circuit.

earlier paper by Gueret (1973). In a first approximation it is possible to neglect one junction (say, junction *B*) and consider junction *A* and the loop inductance. It is clear that even with this assumption we may observe an oscillatory behavior. The probability of locking into the $V=0$ state will be related to the occurrence of the zeros (of voltage) during such *LC* oscillations. This, of course, will produce problems in the current steering. The amount of the transferred current will depend more or less randomly on the specific cycle at which V will jump to zero. It is possible that, as soon as the average voltage $\langle V \rangle$ across the junction reduces to a value such that $\langle V_A \rangle < \langle V_L \rangle$, a punchthrough effect occurs because of the presence of the energy storage element (inductance *L*), which "forces" the junction into a voltage state of opposite polarity. Figure 14.11 shows $\langle V_A \rangle$ vs. time. The voltage locking value is indicated as the amplitude of the damped sinusoid envelope corresponding to V_L . The damping factor is $\eta = LG^2/4C$.

Let us consider now the effect of the Josephson term previously neglected. In this case the effective inductance *L* of the equivalent circuit is given by the parallel combination of *L* and the Josephson inductance L_J . *L* is a constant fixed by geometrical factors of the loop. The total feeding current is related to the effect of the flux Φ as follows (see Chapter 12):

$$LI = LI_1 \sin 2\pi \frac{\Phi}{\Phi_0} + \Phi$$

and therefore the equivalent inductance is

$$L_e = \frac{\Phi}{I} = \frac{L}{1 + (LI_1/\Phi) \sin 2\pi(\Phi/\Phi_0)}$$

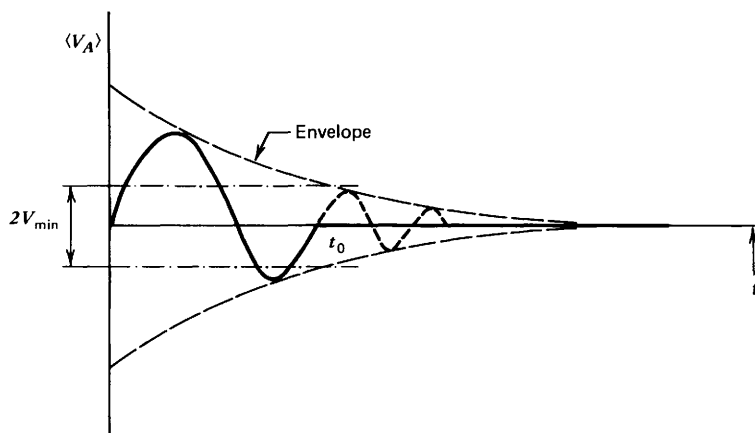


Figure 14.11 Average junction voltage locks to zero at $t = t_0$ when the amplitude of the envelope becomes $< V_{\min}$. (After Gueret 1973.)

That is, the damping factor becomes

$$\eta_e = \frac{\eta}{1 + (LI_1/\Phi) \sin 2\pi(\Phi/\Phi_0)}$$

Therefore, the presence of the sine leads to the possibility of changing from an underdamped behavior ($\eta_e < 1$) when L is neglected to an overdamped behavior ($\eta_e > 1$) when the Josephson inductance is included. Gueret (1973) investigated this aspect and found that, taking into account the effect of the Josephson current, variations of just 0.25% of the loop inductance can lead to drastic differences in the current transfer process. As discussed by this author, the effect is related to the flux quantization which becomes important even when large inductance loops (many flux quanta) are considered.

14.5 Interference Switching Devices

Increasing packing density in logic circuits implies a further reduction of linewidth and correspondingly an increase of the impedances values. Ultimately for the given junction voltages this imposes a severe limitation in the current levels. It is important therefore to conceive switching devices requiring low control currents. This argument suggests the adoption of interference devices that exhibit a higher sensitivity to magnetic field. In a single in-line gate (large junction, i.e., $L > \lambda_J$) the magnetic field dependence on the critical current is fixed by the junction dimensions, whereas in interferometer structures magnetic field sensitivity is independent of junction size, which permits a greater flexibility in the loop design of the component. We observe that with this device configuration a drastic reduction of the capacitance can be achieved, the limit being related to the minimum junction size that can be realized with the available technology. The threshold curve I_g vs. I_c of two interferometers and a simple equivalent circuit for each are reported in Fig. 14.12a together with a sketch of the device. The shape of the threshold curve of these interferometer devices is fixed just by the product LI_0 . Increasing such a product increases the magnetic field sensitivity of I_1 .

As previously mentioned, a reduction of the product LI_0 in the two junction interferometer configuration leads to a reduction in the sensitivity of the device. On the other hand, an increase in LI_0 to get higher sensitivity leads to an increasing overlap of the lobes in the threshold curve. The latter circumstance implies a reduction of the region (in the $I_c - I_g$ plane) where logic devices switch to the finite voltage state and imposes operations at higher current values. This problem has been successfully overcome by a three junction interferometer originally described by Zappe (1975). In this case the spacing between lobes drastically increases (Fig. 14.12b) (Stuehm and Wilmsen 1972). The configuration employs three junctions having threshold current

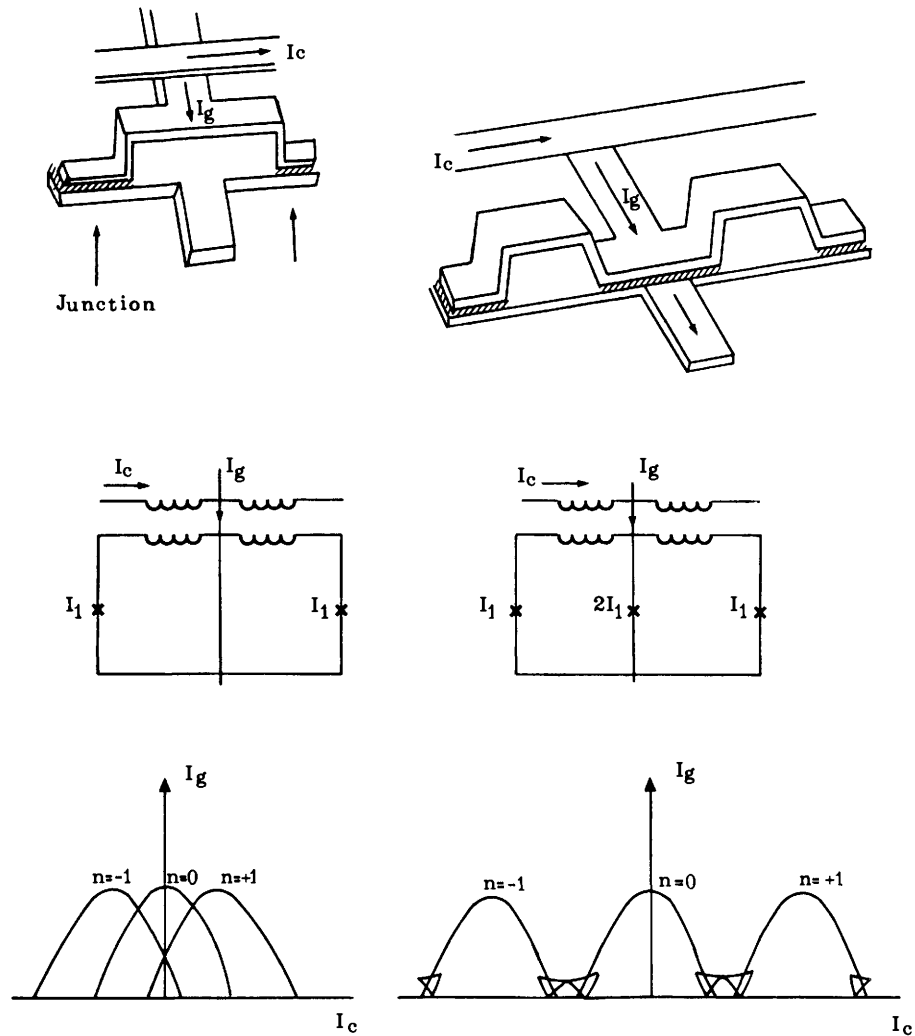


Figure 14.12 Two and three junction interferometer configurations with equivalent circuits and threshold curves I_g vs. I_c .

values in the ratio 1-2-1. Latching and nonlatching circuits with such interference devices have been discussed in detail from both theoretical and experimental points of view (Zappe 1975a, 1976).

A different switching device has been proposed by Faris and Davidson (1979) in which the switching operation does not occur between the lobes and the open region above quantum modes but uses the extremely asymmetric critical points beneath such modes.

14.6 Memory Cells

The persistence of circulating current in superconductive rings (Quinn and Ittner 1962) has suggested the possibility of new memory elements (Matisoo 1967a; Clark and Baldwin 1967; Anacker 1969).

14.6.1 Flip-Flop Memory Configuration. In practice the operation of such devices is based on both the switching properties of the Josephson junction and the flux quantization in the superconducting loop. We can roughly divide the memory elements into two categories depending on the value of the critical supercurrent I_1 and the loop inductance L . In the former, the condition $LI_1 \gg \Phi_0$ is satisfied and, because of the large number of flux quanta into the loop, the discreteness of the flux value is unimportant. In the latter category is $LI_1 \sim \Phi_0$ and the flux is stored in the cell as a single flux quantum.

The flip-flop circuit discussed in Section 14.2.2 represents a potential memory cell; the storage of the information is realized in the last step of Fig. 14.6. The clockwise or counterclockwise circulating current gives the binary representation of Boolean 1 and 0 respectively. Many years ago Anacker (1969, 1972) discussed extensively the possibility of employing such a structure in high performance computers. The memory cell he proposed also includes two junctions for writing and one for nondestructive readout (see Fig. 14.13). Zappe (1975b) successfully realized such a memory using a superconductive loop of 20×25 mils. The current transfer time in such device was about 600 psec. The writing repetition rate was larger than 1 GHz and the energy dissipation less than 2 fJ per writing cycle. For a discussion of the device and

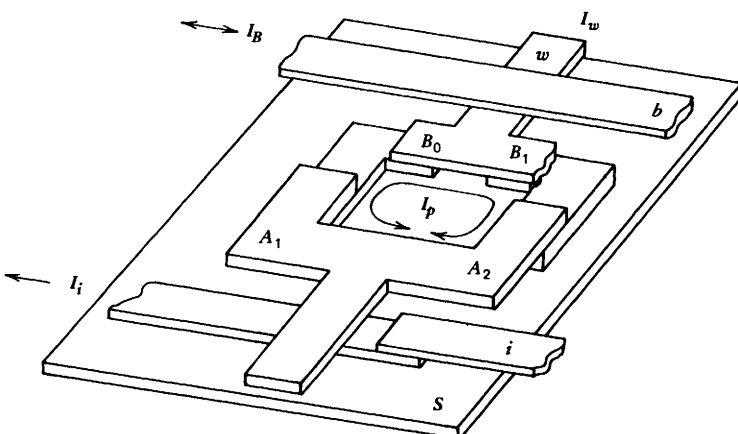


Figure 14.13 Memory cell comprising Josephson tunneling gates (B_0 and B_1) for coincidence selection and nondestructive readout (S). (After Anacker 1969.)

its details the reader is referred to the article. A Josephson memory cell made with a high degree of miniaturization was made by Broom, Jutzi, and Mohr (1974). The cell area in this case is $5 \times 5 \mu\text{m}^2$ and the Josephson current density is 30 kA/cm^2 . An upper bound of 80 psec for the transfer time, during the writing operation, was estimated. This memory differs from the one previously discussed not only in size but also in the actual design; this difference concerns in particular a new technical solution for the writing lines.

14.6.2 Single Flux Quantum Storage Devices. The peculiar features of the overlapping vortex modes that arise in other Josephson devices suggest a different approach to the storing of information (Guèret 1974a, b; Zappe 1974; Guèret, Mohr, and Wolf 1976). In this case a single bit can be stored in the form of a fluxon. Let us refer to the configuration sketched in Fig. 14.12a. The static behavior of such structures has been extensively discussed in Chapter 12. For the condition $\beta_e = 2\pi L I_1 / \Phi_0 \approx 1$ the I_g vs. I_c threshold curves display an overlapping vortex mode structure as depicted in this figure. In the overlap regions two states corresponding to the values $n\Phi_0$ and $(n+1)\Phi_0$ for the flux are possible. In order to describe the operation of the device let us refer to the first overlapping region, in which the 0 and 1 vortex states will correspond to the binary representation of the two memory states 0 and 1 (see Fig. 14.14).

When the information is stored in the cell, the device is biased in such a region by a suitable control current I_{cb} . Let us assume that the cell is in the 0 state; in order to write 1 (WR1) the control current must be varied in such a way that the threshold line of the $n=0$ mode is crossed. The result of this operation is that the value of the flux in the loop has changed by one unit, Φ_0 .

Restoring the control current to the initial value I_{cb} , the device goes back to the original point in the overlapping zone; however, the cell now is in the state $n=1$. Conversely, if the original state was $n=1$ the previous operation would not produce any change in the state of the cell since the operation point remains within the threshold line corresponding to $n=1$ vortex state. Obviously in order to write 0 (WR0) the procedure is the same except for the sign of the change in the control current which must be reversed. Let us observe that in the writing process we are describing, associated with the transition between the two different vortex states in the cell, a voltage spike across the device occurs as soon as the threshold curve is crossed. This voltage decays within a time that depends on the specific features of the device and is of the order of tens of psec. By using a small junction as the sensor it is possible to detect the occurrence of this voltage spike providing a reading mechanism.

When the vortex-to-vortex transition is performed at a value of the gate current, I_g , larger than a critical value I_{cr} (see Fig. 14.14) the cross of the threshold curve brings the cell permanently into the finite voltage state. This effect has been observed and explained by Fulton, Dunkleberger, and Dynes (1972) and provides another possible method of reading (Zappe 1974). Details of the operation of the memory cells just described and experimental data can be found in the paper by Gueret, Mohr, and Wolf (1976). The whole subject of

single flux quantum memory cells discussed so far is reviewed in the extensive paper by Wolf (1976).

Obviously the simplest structure which exhibits overlapping vortex modes is represented by a single "long" Josephson junction (see Chapter 5). Therefore such devices could also be employed as single flux memory cells. However, the two junction configurations must be preferred over these single junction cells for various aspects. In fact, as we have seen, the former show threshold curves, corresponding to different modes, of almost equal shape and offer more possibilities as far as the reading mechanism is concerned.

A different kind of single flux quantum (SQF) memory element has been recently proposed by Likharev (1976a); see also Likharev and Ulrich (1978). This device, called the "parametric quantron," uses a superconducting loop interrupted by a single junction (Fig. 14.15a, b). As we saw in Chapter 12, the

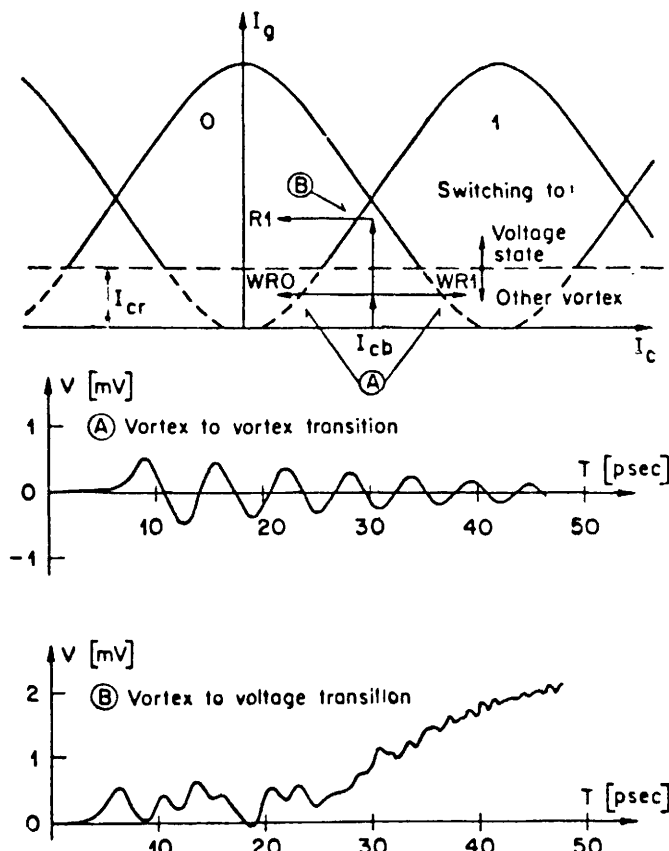


Figure 14.14 Vortex modes and vortex transitions in a two junction SQUID used for single flux quantum storage. Operating currents for writing (WR_0 and WR_1) are given. Computer simulations of voltage transients for vortex-to-vortex transitions and vortex-to-voltage transitions are also shown. (After Wolf 1976.)

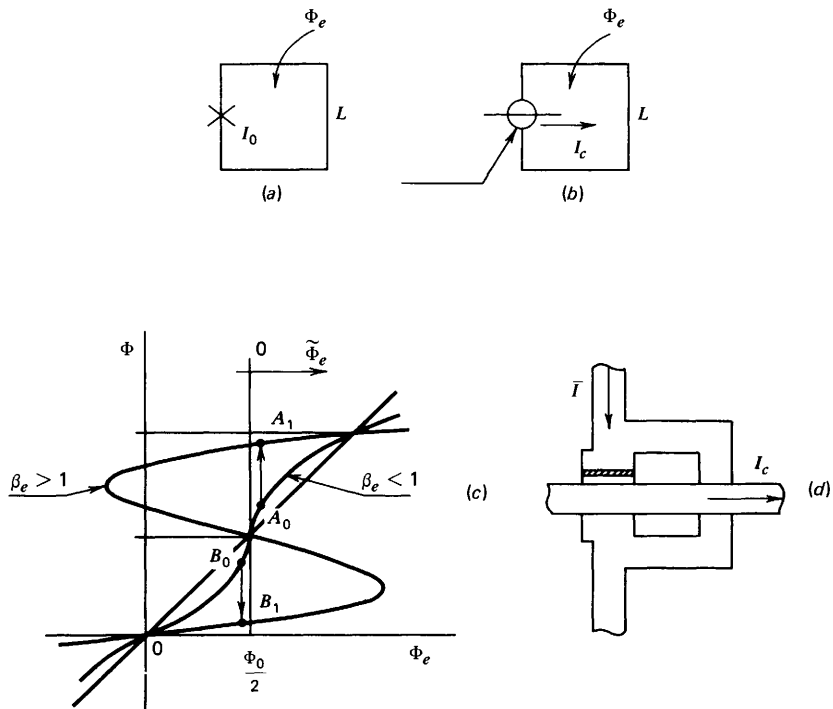


Figure 14.15 Parametric quantron. Equivalent circuits of simple (a) and parametric (b) quantrons; (c) dependence of Φ on Φ_e in quantrons. (d) possible design of a parametric quantron with a variable thickness bridge as a Josephson gate. (After Likharev 1976a.)

dependence of the internal flux, Φ vs. the applied flux Φ_e , is related to the value of the characteristic parameter β_e . If β_e is greater than unity a set of stable states, corresponding to different numbers of fluxons in the loop, is possible for a fixed value of Φ_e . If β_e is smaller than unity the Φ vs. Φ_e dependence is single valued (see Fig. 14.15c). Let us refer to the configuration sketched in Fig. 14.15d. The control current produces a net zero flux in the loop. Its role is to reduce the critical supercurrent of the junction and therefore the value of the parameter β_e . This suggests the name “parametric quantron” for this device. The external flux Φ_e is produced by the current I . Let us assume a control current applied such that $\beta_e < 1$. If $\Phi_e = \Phi_0/2$, the system will be in the state $\Phi = \frac{1}{2}\Phi_0$ (point A). By a slight increase of the current I it is possible to reach point A on the nonhysteretic curve. By removing the control current the parameter β_e will increase to a value larger than unity and the system will reach point A corresponding to a stable state at $\Phi = \Phi_0$ on the hysteretic curve. As is clear from the figure, symmetric operation can be performed to bring the quantron into the $\Phi = 0$ state. These two stable states ($\Phi \sim 0$ and $\Phi \sim \Phi_0$) will represent the 0 and 1 in the binary memory description. As discussed by Likharev, a single logic operation in this device involves an extremely small energy dissipation.

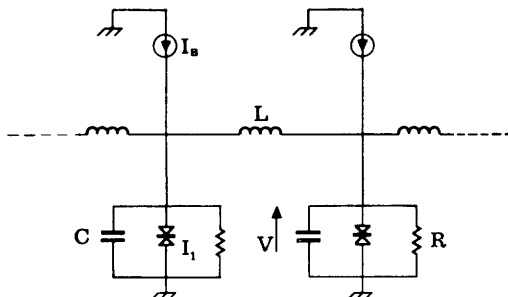


Figure 14.16 Equivalent electronic circuit of the “flux shuttle” discussed by Anderson, Dynes, and Fulton.

As a matter of fact, a logic element operating on the principle of a single flux quantum storage was already proposed in a different context (Anderson 1970). The so-called flux shuttle (Anderson, Dynes, and Fulton 1971; Fulton and Dunkleberger 1973) has been widely discussed in connection with its application as a shift register (Fulton, Dynes, and Anderson 1973). In this system each flux quantum represents a bit of information. The equivalent electronic circuit for the flux shuttle is reported in Fig. 14.16. The parameters are such that the condition

$$LI_1 = \Phi_0$$

is satisfied, so that a single flux quantum can be stored in the inductor between two adjacent junctions. A current bias I_B of about $0.7I_1$ “drives” the flux quantum from one loop to the next. For a typical Josephson current density of 2×10^2 A/cm² with a junction area of $10 \times 10 \mu\text{m}^2$, which is well within the capabilities of the present photoresist technology, it follows that $I_1 = 0.2$ mA and $L = 10^{-11}$ H. A few tens of picoseconds per single shift should be expected with an energy dissipation of the order of 10^{-19} J/shift. A different version of the single flux quantum shift register in which the parameters vary periodically along the structure has been recently proposed by Likharev (1977b); see also Lapir, Likharev, and Semenov (1977). A different sort of “manipulation” of fluxons has been also proposed in a computing network by Nakajima, Onodera, and Ogawa (1976) which employs interaction of fluxons and antifluxons on a Josephson transmission line (J.T.L.) to realize the logic functions AND, OR, and NOT. Finally, Josephson vortices have been considered (playing the role of electric charge carriers in the conventional transistor) in a “vortex transistor” configuration by Likharev et al. (1978).

14.7 Examples of Josephson Logic and Memory Circuits

Toward the objective of a computer entirely based on the Josephson junction technology, rather complex circuits have been realized which include the

various devices previously discussed. We can refer schematically to two main categories: logic and memory circuits.

Let us begin by recalling the logic circuits of fundamental importance which have been investigated in the last few years and are still under study. These include circuits employing Josephson junction gates which can perform the basic logic functions of AND, OR, INVERT, and CARRY. It is easy to understand the principle of operation of such devices. Superconductive lines are arranged in such a way that (for instance) the gate switches only when all inputs are simultaneously present (AND), that is, when the sum of the control currents (actually the resulting magnetic field) is sufficient to drive the junction gate transition. Incidentally let us observe that gate switching can be also realized by adding current in the junction, to the bias current I_g (Fulton, Magerlein, and Dunkleberger 1976). Details of the design of various logic circuits based on Josephson gates can be found in the papers by Herrel 1974a, b).

A superconducting logic circuit of a remarkable complexity is that by Herrel (1975). It consists of a 4 bit multiplier ("add and shift" multiplier) whose multiplication time, limited by the testing apparatus, was of ~ 27 nsec and is expected to be as low as 12 nsec. Among the logic circuits recently designed and tested we recall those based on Josephson three junction interferometers operating in a latching mode (Section 14.4) (Klein and Herrel 1978); see also Herrell, Arnett, and Klein (1978); Davidson (1978). The scheme of the device, which is essentially Zappe's three junction interferometer discussed in Section 14.5, is more accurately sketched in Fig. 14.17 and indicated by the symbol in the inset. The role of the resistors is to introduce a damping to remove self-resonant steps as suggested by Zappe and Landman (1978a, b). In fact, such Josephson interferometers exhibit the same resonant behavior as

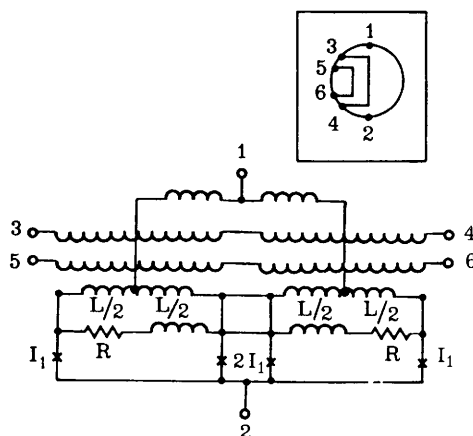
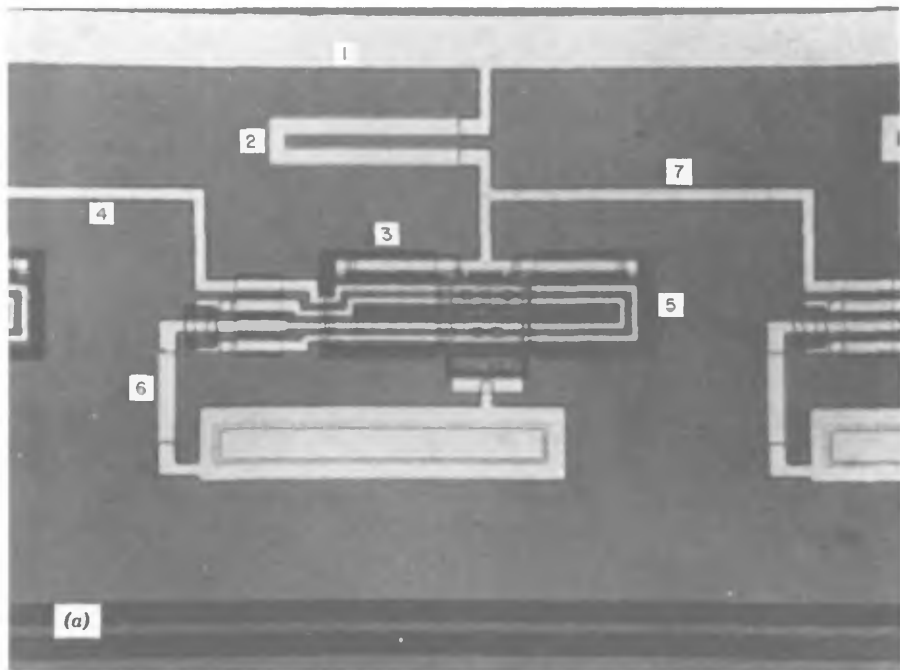
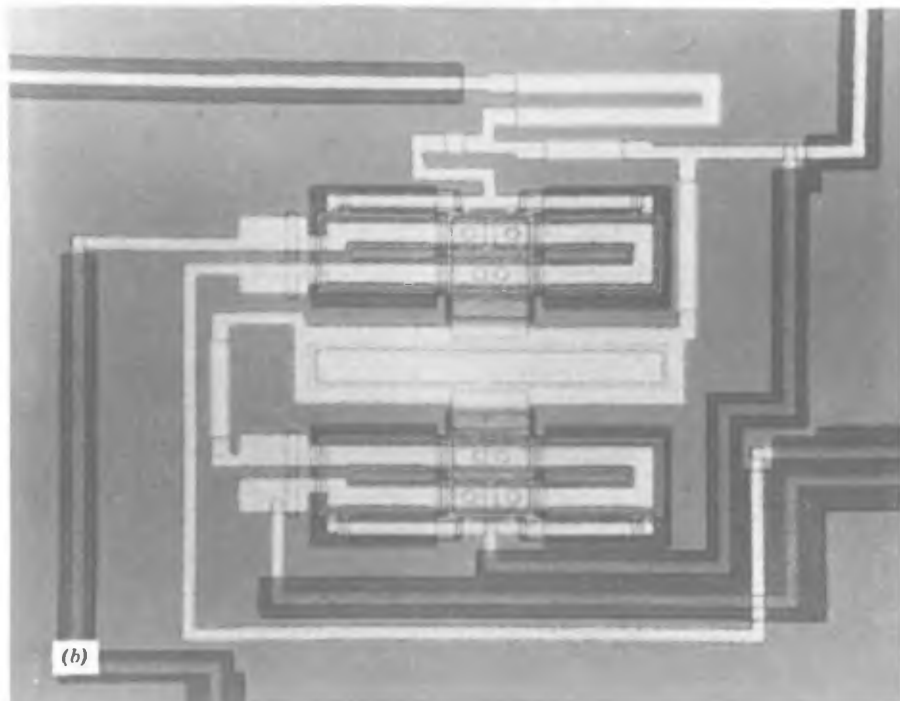


Figure 14.17 Scheme of Zappe's three junction interferometer. (After Herrell, Arnett, and Klein, 1978.)



(a)



(b)

Figure 14.18 (a) Actual interferometer device made at the IBM T. J. Watson Research Center, Yorktown Heights, as it appears in a micrograph of a section of an OR chain. The circuit includes power supply bus (1), dropping resistor (2), current dividing inductor (3), control line (4), interferometer (5), load resistor (6), and output line (7). (b) Interferometer structures inserted in an AND chain. (Courtesy of D. J. Herrell and M. Klein.) For details see Klein and Herrell (1978) and Herrell, Arnett, and Klein (1978).

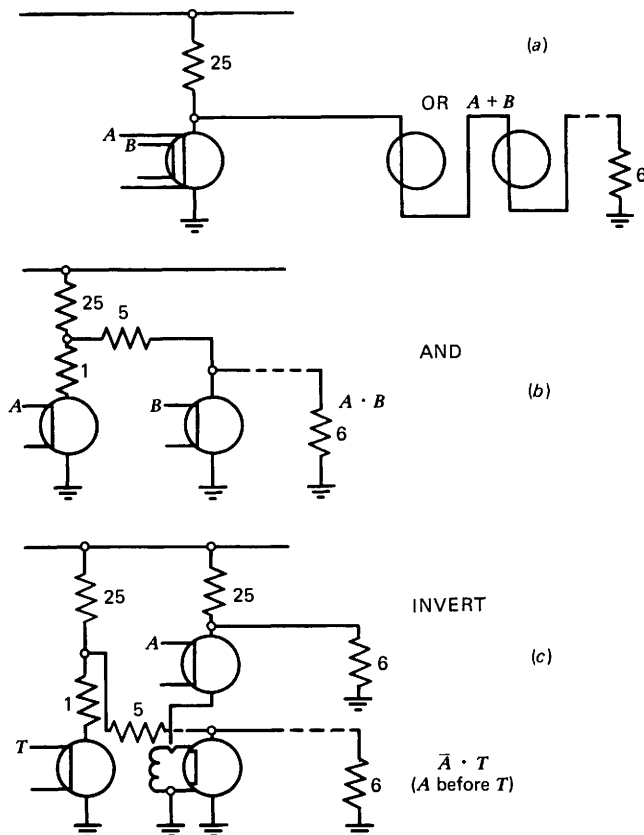


Figure 14.19 A logic family. (a) Two input OR circuit. (b) Two input AND circuit. (c) Timed INVERTER. (After Klein and Herrell 1978.)

long junctions. There are as many resonances in the current voltage characteristic as meshes in the device. Theoretical and experimental investigation on these phenomena has been performed by Zappe and Landman (1978a,b). A simple theory of resonance amplitudes has been presented by Gueret (1979). The actual device as it appears in a photo micrograph is shown in Fig. 14.18. Figure 14.19 shows the schematics of three different logic gates: OR, AND, INVERT. The first operation (OR) is achieved by a single interferometer with two control lines so that the switching occurs when either of these lines is activated. To realize the AND we see from the figure that there are two interferometers connected in parallel, each with a single control line. The AND gate operates only if both input control currents are applied. The INVERT gate consists, as shown in the figure, of an OR gate which basically plays the role of an inhibitory circuit; this in combination with an AND gate allows a timed inversion function. Fanout from a logic gate (Fig. 14.19a) is serial via terminated superconducting lines. The average logic delay per stage of gauge

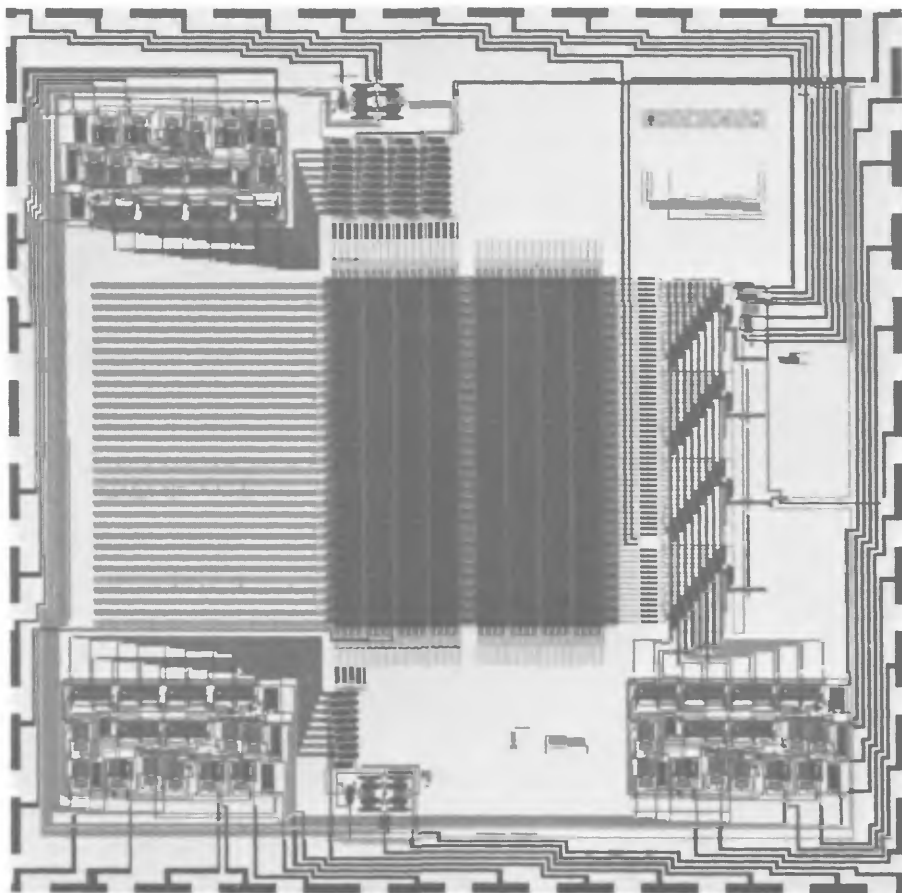


Figure 14.20 SFQ cell memory array realized at the IBM Zurich Research Laboratory. (After Broom et al. 1978.) It contains 2048 SFQ memory cells including drivers and decoders to address read (DRO) the memory array. (Courtesy of P. Wolf.)

operations can be a few tens of psec. In the abovementioned work by Klein and Herrel a value of 55 psec was found and analysis of the results leads to an evaluation of a whole machine cycle time $t_m \gtrsim 5$ nsec. The power dissipation was about 2.6 pW per gate from which can be extrapolated an average power density for a LSI chip less than 10 mW/cm².

Among the latest developments, of Josephson logic devices we mention the outstanding performances of a new family of logic circuits referred to as current injection logic (CIL) circuits obtained by Gheewala (1978, 1979, 1980). Among other results is a logic delay of 13 psec/stage in a chain of a 2 input OR gate with a power dissipation of 2.6 μ W.

In regard to the development of memory circuits we recall some of the recent work carried out at the IBM Laboratories. Henkels and Zappe (1978)

have demonstrated the feasibility of a fully decoded Josephson memory. In their experiments a 8×8 bit nondestructive readout, random access memory was successfully investigated. The device was built on a 6.35×6.35 mm chip using in-line gates. The individual cells were basically those originally described by Zappe (Section 14.6). The access to memory cells was achieved by three decoders.[†] Full memory cycle times were between 5 and 3.5 nsec.

A different type of memory circuit is that employing the single flux quantum (SFQ) cells previously described. In Fig. 14.20 is shown an array consisting of 2048 SFQ memory cells along with the necessary decode and drive circuits (about 4500 Josephson junctions in total) (Broom et al. 1978). The 2048 cells are located on the lower part of the chip. The upper half shows 2048 dummy cells. This memory circuit was purposely made to demonstrate the feasibility of a 16 K memory. The experimental results indicate an access time for such a memory of ~ 15 nsec and a cycle time of ~ 30 nsec. Moreover, the power dissipation is expected to be about $40 \mu\text{W}$.

14.8 Systems Performance and Requirements

In Chapter 8 we discussed the various technological procedures to fabricate junctions and complex circuits. Hence we do not reconsider here the problems of the barrier preparation or the sophisticated lithographic technique for the pattern definition; instead we comment on the Josephson digital technology with respect to operation speed, power dissipation, heat removal, and cryogenics requirements. Figure 14.21 summarizes the dependence of the response time of a Josephson tunnel junction when limited by $R_N C$ for lead alloy junction (also the values normalized to the intrinsic response time τ_i) upon the critical current density; the corresponding barrier thickness values (Harris and Hamilton 1978) are also indicated.

Let us observe that a signal propagating at the speed of the light would cover a distance of 3 mm in 10 psec. On the other hand, such a time is of the order of the expected logic delay so that we should, at least in principle, look toward the objective of having the whole logic array within ~ 1 cm, say, as the maximum dimension in order to remain within such limits of delay times.

Thus ultrafast logic operation requires, besides the intrinsic high speed device, small size of individual components and high packing density to reduce delay when the information is transmitted between individual elements of the circuit. In the existing semiconductor technology the packing density is indeed limited by power dissipation. Figure 14.22 shows the power dissipation per logic gate as a function of the propagation delay for a Josephson junction and a variety of semiconductor devices (roughly indicated by the dashed area). Gallium arsenide transferred electron devices (TEDs) exhibit comparable

[†]Among other circuits let us recall the successful decoder for Josephson memory arrays proposed by Faris (1979).

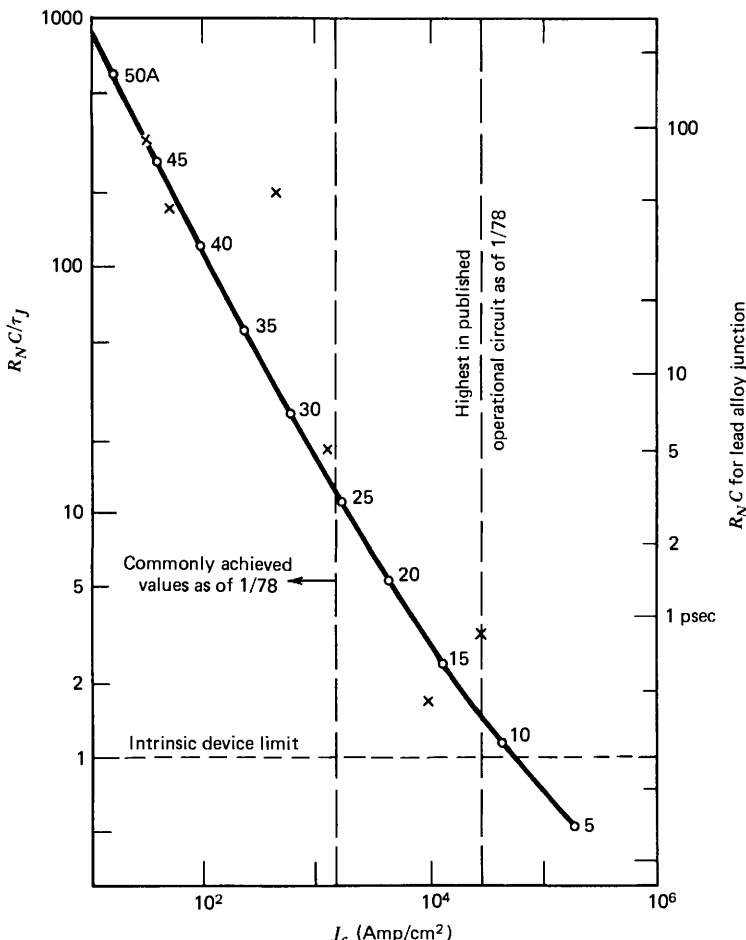


Figure 14.21 Response time of a Josephson tunnel junction when limited by $R_N C$, as a function of the critical current density. (After Harris and Hamilton 1978.)

speed operation performances. However, even in this case the drastic advantage offered by the Josephson devices over semiconductor devices arises as soon as we compare the power dissipation levels. In the former case a dissipation below 1 $\mu\text{W}/\text{gate}$ can be achieved which is several orders of magnitude less than the limits reached by semiconductor devices (Bosh 1979).

High packing density leads in turn to problems of heat removal. To compare the entity of this problem in conventional (e.g., silicon) and in the potential Josephson technologies let us refer to Table 14.1 (Anacker 1977) where the peak power density (P_{\max}) and the chip temperature (T_{chip}) for various coolants are reported. P_{\max} substantially indicates the limiting power value that permits heat transfer. Water has a more favorable peak power, but the corresponding chip temperature is too high (in practice fluorocarbon is the

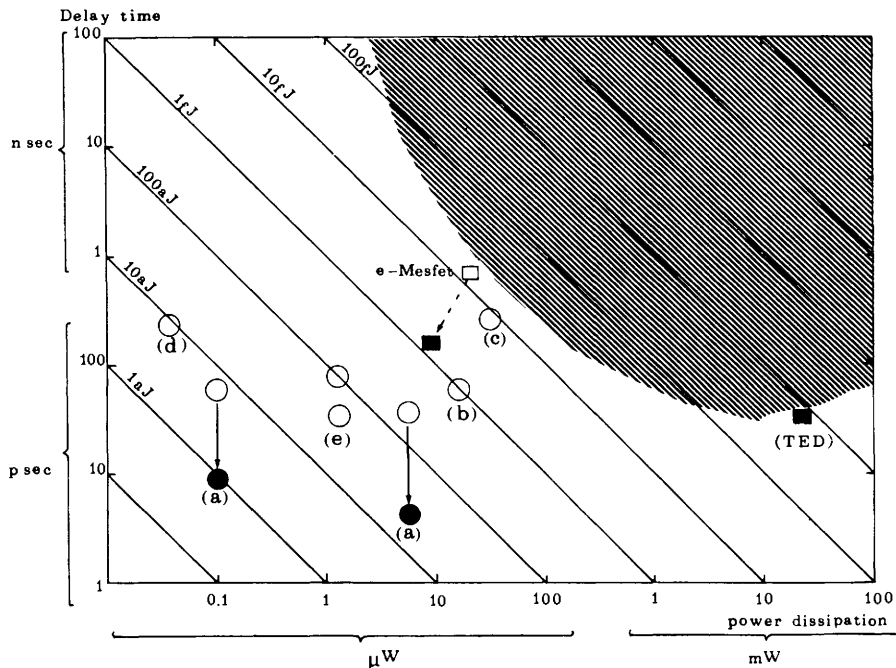


Figure 14.22 Sketch of the power dissipation per logic gate as a function of the propagation delay for Josephson and semiconductor devices. Squares and circles refer to semiconductor and Josephson devices respectively. Empty and full symbols indicate measurements and theoretical extrapolations. Dashed region (roughly above the $10 F_J$ line) corresponds to "non-Josephson" devices. (a) Jutzi et al. (1972); (b) Baechtold (1975); (c) Herrel (1975); (d) Zappe (1975b); (e) Klein and Herrel (1978).

most suitable for silicon). Assuming a power dissipation per gate of 10 mW a silicon circuit density of $2 \times 10^3/\text{cm}^2$ would reach the prohibitive limit of 20 W/cm^2 . Conversely we see that with an equal Josephson gates density of $2 \times 10^3/\text{cm}^2$, the power dissipation is just 3% of the P_{\max} for liquid helium at 4.6 K and 2% at temperatures below the lambda point.

Regarding the implications of the liquid helium environment necessary for a potential Josephson computer it should be noted that, in spite of the typical problems inherent in the actual cryogenic system or those that derive from

TABLE 14.1 Liquid Cooling

Coolant	P_{\max}	T_{chip}
Water	100 W cm^{-2}	$\sim 138^\circ\text{C}$
Freon	20 W cm^{-2}	$\sim 32^\circ\text{C}$
Helium	0.6 W cm^{-2}	$\sim 4.6 \text{ K}$
Superfluid helium	8 W cm^{-2}	$\sim 2 \text{ K}$

thermal cycling up to room temperature, the low temperature requirements are well within the capabilities of modern technology.

14.9 Conclusions and Perspectives

In this chapter we illustrated the main steps in the evolution of the original concept of the cryotron from its infant state to today. We hope that we have given at least the "flavor" of the potential of Josephson device technology in the context of computer applications.

As we have seen, the most serious limiting factor in the operational speed of a Josephson device lies in its intrinsic capacitance. However, the highly developed technology for achieving micron and submicron dimensions (see Chapter 8) together with the possibility of making devices with high critical current densities ($\gtrsim 10^4$ A/cm²) should allow switching times down to about 1 psec. Perhaps subpicosecond values for the *RC* time of the junctions can be reached approaching the intrinsic (not limited by the *RC*) response time τ_i of a Josephson junction. Such a value is expected to be given by the uncertainty principle $\Delta E \Delta t \sim \hbar$ where $\Delta t = \tau_i$ and $\Delta E = 2\Delta$ (e.g., Harris 1976a; McDonald, Peterson, and Bender 1977).

For a system with a large number of components the "overall" operating speed depends also on the time involved in the communication between the elements of the array. Again this leads naturally to the objective of a size reduction of the components and to a high packing density in the system.[†] The microminiaturization of superconductive devices can be obtained by using, essentially, all the advanced semiconductor technologies. In conventional technology a limiting factor in increasing the component packing density is heat removal. As we have seen, the power dissipation involved in the operation of Josephson devices is extremely low. Hence the three fundamental factors, strongly related, that is, high speed, small size, and low power dissipation, appear to be very encouraging and, in spite of the required cryogenic facilities, indicate the Josephson junction technology as a promising candidate for application in a future computer.[‡]

Of course, a concrete discussion of the perspectives for this new technology deserves great attention and requires a careful analysis of the actual competitiveness from a cost versus performance standpoint. Such a discussion of the actual marketplace of these Josephson devices exceeds the competence of the authors. They can only give a prediction that lies halfway between caution and optimism.

[†]In a recent article Anacker (1979) has illustrated the overall packing of the ultrahigh speed Josephson computer in a compact card-on-board tridimensional configuration.

[‡]A collection of articles devoted to the various aspects of the IBM research project concerning the Josephson computer technology is contained in a recent special issue of the *IBM Journal of Research and Development* (Vol. 24, No. 2, March 1980).

APPENDIX

Systems of Units

A.1 Comments on Systems of Units

Since the material treated in this book covers a very wide spectrum (from microscopic theory to modern applications), the appropriate units of measurements must be carefully chosen. It would be just as impractical to use MKS units in a discussion of microscopic theory as it would be to use gaussian units for engineering applications. Therefore, instead of imposing an artificial uniformity, we adopt gaussian units for Chapters 1 through 9 and MKSA units for the chapters devoted to applications. For the convenience of the reader we give a list of the expressions for some of the main quantities in both systems of units.

A.2 Conversion Tables

Conversion Table 1^a

Quantity	Symbol	M.K.S.A.	Gaussian
Flux quantum	Φ_0	$\frac{h}{2e}$	$\frac{hc}{2e}$
Josephson penetration depth	λ_J	$\left(\frac{\hbar}{2\mu_0 e J_1 d}\right)^{1/2}$	$\left(\frac{\hbar c^2}{8\pi e J_1 d}\right)^{1/2}$
Swihart velocity	\bar{c}	$\left(\frac{1}{\mu_0 C d}\right)^{1/2}$	$c \left(\frac{1}{4\pi C d}\right)^{1/2}$
Plasma frequency	$\omega_J = \frac{\bar{c}}{\lambda_J}$	$\left(\frac{2eJ_1}{\hbar C}\right)^{1/2}$	$\left(\frac{2eJ_1}{\hbar C}\right)^{1/2}$
Lower critical field	B_{c1}	$\frac{4}{\pi} \left(\frac{\mu_0 \Phi_0 J_1}{2\pi d}\right)^{1/2}$	$2\Phi_0 / \pi^2 d \lambda_J$
Phase gradient into the superconductor	$\nabla \varphi$	$\frac{2\pi}{\Phi_0} \left(\frac{m}{2e^2 \rho} \mathbf{J}_s + \mathbf{A}\right)$	$\frac{2\pi}{\Phi_0} \left(\frac{mc}{2e^2 \rho} \mathbf{J}_s + \mathbf{A}\right)$
Capacitance per unit area	C	$\frac{\epsilon_r \epsilon_0}{t}$	$\frac{\epsilon_r}{4\pi t}$

^a e =electron charge; h =Plank's constant; c =speed of light in vacuum; μ_0 =permeability of free space; ϵ_0 =dielectric constant of free space; ϵ_r =relative dielectric constant; $d=t+\lambda_{L_1}+\lambda_{L_2}$ =magnetic field depth; λ_L =London penetration depth; t =oxide barrier thickness; C =capacitance per unit area; J_1 =maximum Josephson current density; and \mathbf{A} =vector potential.

Conversion Table 2. Conversion table for symbols and formulas^a

The symbols for mass, length, time, force, and other not specifically electromagnetic quantities are unchanged. To convert any equation in Gaussian variables to the corresponding equation in MKS quantities, on both sides of the equation replace the relevant symbols listed below under "gaussian" by the corresponding "MKS" symbols listed on the right. The reverse transformation is also allowed. Since the length and time symbols are unchanged, quantities that differ dimensionally from one another only by powers of length and/or time are grouped together where possible.

Quantity	Gaussian	MKS
Velocity of light	c	$(\mu_0 \epsilon_0)^{-1/2}$
Electric field (potential, voltage)	$\mathbf{E}(\Phi, V)$	$\sqrt{4\pi\epsilon_0} \mathbf{E}(\Phi, V)$
Displacement	\mathbf{D}	$\sqrt{\frac{4\pi}{\epsilon_0}} \mathbf{D}$
Charge density (charge, current density, current, polarization)	$\rho(q, \mathbf{J}, I, \mathbf{P})$	$\frac{1}{\sqrt{4\pi\epsilon_0}} \rho(q, \mathbf{J}, I, \mathbf{P})$
Magnetic induction	\mathbf{B}	$\sqrt{\frac{4\pi}{\mu_0}} \mathbf{B}$
Magnetic field	\mathbf{H}	$\sqrt{4\pi\mu_0} \mathbf{H}$
Magnetization	\mathbf{M}	$\sqrt{\frac{\mu_0}{4\pi}} \mathbf{M}$
Conductivity	σ	$\frac{\sigma}{4\pi\epsilon_0}$
Dielectric constant	ϵ	$\frac{\epsilon}{\epsilon_0}$
Permeability	μ	$\frac{\mu}{\mu_0}$
Resistance (impedance)	$R(Z)$	$4\pi\epsilon_0 R(Z)$
Inductance	L	$4\pi\epsilon_0 L$
Capacitance	C	$\frac{1}{4\pi\epsilon_0} C$

^aAfter J. D. Jackson (1967).

PHYSICAL CONSTANTS (MKSA units)

Vacuum permittivity	ϵ_0	$= 8.854 \times 10^{-12}$ Farad/m
Vacuum permeability	μ_0	$= 4\pi \times 10^{-7}$ Henrys/m
Velocity of light ^a	c	$= 2.99792 \times 10^8$ m/sec
Electron charge ^a	e	$= 1.60219 \times 10^{-19}$ Coulombs
Electron rest mass ^a	m	$= 9.1095 \times 10^{-31}$ Kg
Magnetic flux quantum ^a	Φ_0	$= 2.06785 \times 10^{-15}$ Weber
Planck's constant ^a	h	$= 6.6262 \times 10^{-34}$ Joule × sec
	$\hbar = \frac{h}{2\pi}$	$= 1.05459 \times 10^{-34}$ Joule × sec
Boltzmann's constant ^a	k_B	$= 1.3806 \times 10^{-23}$ Joule/K

^aValues resulting from the 1969 adjustment. (After Taylor, Parker, and Langenberg 1969.)

Conversion Table 3. Conversion Table for given amounts of physical quantities^a

Physical Quantity	Symbol	Rationalized MKS	Gaussian
Length	l	1 meter (m)	10^2 centimeters (cm)
Mass	m	1 kilogram (kg)	10^3 grams (g)
Time	t	1 second (sec)	1 second (sec)
Force	F	1 newton	10^5 dynes
Work Energy	W U	1 joule	10^7 ergs
Power	P	1 watt	10^7 ergs sec ⁻¹
Charge	q	1 coulomb	3×10^9 statcoulombs
Charge density	ρ	1 coulomb m ⁻³	3×10^3 statcoulombs cm ⁻³
Current	I	1 ampere (coulomb sec ⁻¹)	3×10^9 statamperes
Current density	J	1 ampere m ⁻²	3×10^5 statamperes cm ⁻²
Electric field	E	1 volt m ⁻¹	$\frac{1}{3} \times 10^{-4}$ statvolt cm ⁻¹
Potential	V	1 volt	$\frac{1}{300}$ statvolt
Polarization	P	1 coulomb m ⁻²	3×10^5 dipole moment cm ⁻³
Displacement	D	1 coulomb m ⁻²	$12\pi \times 10^5$ statvolt cm ⁻¹ (statcoulomb cm ⁻²)
Conductivity	σ	1 mho m ⁻¹	9×10^9 sec ⁻¹
Resistance	R	1 ohm	$\frac{1}{9} \times 10^{-11}$ sec cm ⁻¹
Capacitance	C	1 farad	9×10^{11} cm
Magnetic flux	Φ	1 weber	10^8 gauss cm ² or maxwells
Magnetic induction	B	1 weber m ⁻²	10^4 gauss
Magnetic field	H	1 ampere-turn m ⁻¹	$4\pi \times 10^{-3}$ oersted
Magnetization	M	1 ampere m ⁻¹	$\frac{1}{4\pi} \times 10^{-3}$ magnetic moment cm ⁻³
Inductance	L	1 henry	$\frac{1}{9} \times 10^{-11}$

^aAfter J. D. Jackson (1967).

References

Abbreviations

- LT 8 *Proceedings of the 8th International Conference on Low Temperature Physics*, London, September 1962 (R. D. Davies, Ed.), Butterworths, London, 1963.
- LT 9 *Proceedings of the 9th International Conference on Low Temperature Physics*, Columbus, August 1964 (J. G. Daunt, D. O. Edwards, F. J. Milford, and M. Yaqub, Eds.), Plenum, New York, 1965.
- LT 10 *Proceedings of the 10th International Conference on Low Temperature Physics*, Moscow, August 1966 (M. P. Malkov, Ed.), Viniti, Moscow, 1967.
- LT 11 *Proceedings of the 11th International Conference on Low Temperature Physics*, St. Andrews, 1968 (J. F. Allen, D. M. Finlayson, and D. M. McCall, Eds.), University of St. Andrews, St. Andrews, 1968.
- LT 12 *Proceedings of the 12th International Conference on Low Temperature Physics*, Kyoto, September 1970 (E. Kanda, Ed.), Keigaku, Tokyo, 1971.
- LT 13 *Proceedings of the 13th International Conference on Low Temperature Physics*, Boulder, August 1972 (K. D. Timmerhaus, W. J. O'Sullivan, and E. F. Hammel, Eds.), Plenum, New York, 1974.
- LT 14 *Proceedings of the 14th International Conference on Low Temperature Physics*, Otaniemi, August 1975 (M. Krusius and M. Vuorio, Eds.), North-Holland, Amsterdam, 1975, Vol. 4.
- LT 15 *Proceedings of the 15th International Conference on Low Temperature Physics*, Grenoble, August 1978, *J. Phys.*, Colloque C-6 Suppl., **39** (8) (1978).
- SPSD *Proceedings of the Symposium on the Physics of Superconducting Devices*, Charlottesville, April 1967, University of Virginia, Charlottesville, 1967.
- FTSE *Proceedings of the Conference on Future Trends in Superconductive Electronics*, Charlottesville, March 1978 (B. S. Deaver, Jr., C. M. Falco, J. H. Harris, and S. A. Wolf, Eds.), AIP Conf. Proc. no. **44**, American Institute of Physics, New York, 1978.

- ICSS-69 *Proceedings of the International Conference on the Science of Superconductivity*, Stanford, August 1969 (F. Chilton, Ed.), *Physica*, **55**, 1971.
- DEJJ *Proceedings of the Conference Internationale sur la Detection et l'Emission d'Ondes Electromagnetiques par des Jonctions Josephson*, Perros-Guirec, September 1973 (H. A. Combet and B. T. Ulrich, Eds.) *Rev. Phys. Appl.*, **9** (1) (1974).
- IC-SQUID 76 *Proceedings of the International Conference on Superconducting Quantum Devices*, Berlin (West), October 1976. *SQUID, Superconducting Quantum Interference Devices and Their Applications* (H. D. Hahlbohm and H. Lübbig, Eds.), W. de Gruyter, Berlin, 1977.
- IC-SQUID 80 *Proceedings of the International Conference on Superconducting Quantum Devices*, Berlin (West), May 1980 *SQUID' 80 Superconducting Quantum Interference Devices and Their Applications* (H. D. Hahlbohm and H. Lübbig, Eds.), W. de Gruyter, Berlin, 1981.
- ASC72 *Proceedings of the Applied Superconductivity Conference*, Annapolis, May 1972, IEEE Pub. no. 72CH0682-5-TABSC, Institute of Electrical and Electronics Engineers, New York, 1972.
- ASC74 *Proceedings of the Applied Superconductivity Conference*, Oakbrook, September 1974, *IEEE Trans. Magn.*, **MAG-11** (2) (1975).
- ASC76 *Proceedings of the Applied Superconductivity Conference*, Stanford, August 1976, *IEEE Trans. Magn.*, **MAG-13** (1) (1977).
- ASC78 *Proceedings of the Applied Superconductivity Conference*, Pittsburgh, September 1978, *IEEE Trans. Magn.*, **MAG-15** (1) (1979).
- ASC80 *Proceedings of the Applied Superconductivity Conference*, Santa Fe, September 1980-*IEEE Trans. Mag.* (in press).
- NASI67 Nato Advanced Study Institute, Risö, July 1967, *Tunneling Phenomena in Solids* (E. Burstein and S. Lundquist, Eds.), Plenum, New York, 1969.
- NASI73 Nato Advanced Study Institute, Entreves, September 1973, *Superconducting Machine and Devices: Large System Applications* (S. Foner and B. B. Schwartz, Eds.), Plenum, New York, 1974.
- NASI76 Nato Advanced Study Institute, Gardone, Riviera, September 1976, *Superconductor Applications: SQUIDS and Machines* (B. B. Schwartz and S. Foner, Eds.), Plenum, New York, 1977.
- NASI80 Nato Advanced Study Institute, Acquafridda di Maratea, 1980. *Nonequilibrium Superconductivity, Phonons and Kapitza Boundaries* (K. E. Gray, Ed.), Plenum, New York, 1981.

The year of a citation in the text refers to original publication. The list of references includes both the original and English translations when available.

- Ablowitz M. J., D. J. Kaup, A. C. Newell, and H. Segur. The inverse scattering transform-Fourier analysis for nonlinear problems. *Studies Appl. Math.*, **53**, 249–315 (1974).
- Abramowitz M. and I. Stegun. *Handbook of Mathematical Functions*. 9th ed., Dover, New York, 1970, p. 361.
- Abrikosov A. A. On the magnetic properties of superconductors of the second group. *Zh. Eksp. Teor. Fiz.*, **32**, 1442–1452 (1957). *Sov. Phys. JETP*, **5**, 1174–1182 (1957).
- Abrikosov A. A. and L. P. Gor'kov. Contribution to the theory of superconducting alloys with paramagnetic impurities. *Zh. Eksp. Teor. Fiz.*, **39**, 1781–1796 (1960). *Sov. Phys. JETP*, **12**, 1243–1253 (1961).
- Adde R. and G. Vernet. High frequency properties and applications of Josephson junctions from microwave to far-infrared. NASI 76, (1976), chap. 6.
- Aharonov Y. and D. Bohm. Significance of electromagnetic potentials in the quantum theory. *Phys. Rev.*, **115**, 485–491 (1959).
- Aharonov Y. and D. Bohm. Further considerations on electromagnetic potentials in the quantum theory. *Phys. Rev.*, **123**, 1511–1521 (1961).
- Ahopelto J., P. J. Karp, T. E. Katila, R. Lukander, and P. Mäkipää. An UHF SQUID gradiometer for biomagnetic measurements. *LT* **15**, *4*, 262–265 (1975).
- Aittoniemi K., R. Hari, T. Katila, M. L. Kuusela, and T. Varpula. Magnetic fields of human brain evoked by long auditory stimuli. In *Proceedings of the 3rd National Meeting on Biophysics and Medical Engineering in Finland*, Lappeenranta (Finland), June 1979.
- Albrecht G., K. Blüthner, K. Dettman, and P. Pertsch. Properties of tunnel junctions with niobium and vanadium base films. In *Proceedings of the 5th International Cryogenic Engineering Conference*, **E7**, 121–123 (1974).
- Alfeev B. H. Semiconductors, superconductors, paraelectrics in cryoelectronics. *Sovietskaia Radio*, 1979.
- Alfeev V. N., A. V. Verbilio, D. P. Kolesnikov and V. A. Ryzhkov. Josephson effect in film structures with degenerate semiconducting barrier. *Fiz. Tekh. Poluprovodn.* **13**, 164–166 (1979). *Sov. Phys. Semicond.* **13**, 93–94 (1979).
- Amaldi E. and G. Pizzella. Search for gravitational waves. In *Relativity Quanta and Cosmology*, Johnson Reprint Corporation, **1**, 9–139 (1979).
- Ambegaokar V. and A. Baratoff. Tunneling between superconductors. *Phys. Rev. Lett.*, **10**, 486–489 (1963). Errata, *Phys. Rev. Lett.*, **11**, 104 (1963).
- Ambegaokar V. and B. J. Halperin. Voltage due to thermal noise in the d.c. Josephson effect. *Phys. Rev. Lett.*, **22**, 1364–1366 (1969).
- Anacker W. Potential of superconductive Josephson tunneling technology for ultrahigh performance memories and processors. *IEEE Trans. Magn.*, **MAG-5**, 968–975 (1969).
- Anacker W. Josephson tunneling devices—A new technology with potential for high performance computers. In *Proceedings of the Fall Joint Computer Conference*, Vol. 41, AFIPS Press, Montvale, 1972, 1269–1277.
- Anacker W. Josephson junctions as computer elements. In *ESSDERC Proceedings of Conference Series No. 32*, Institute of Physics, London, 1977, 39–55.
- Anacker W. Computing at 4 degrees Kelvin. *IEEE Spectrum*, **16**, 26–37 (1979).
- Anacker W., K. R. Grebe, J. H. Greiner, S. K. Lahiri, K. C. Park, and H. H. Zappe. Lead alloy Josephson junctions. U.S. Patent 3,733,526, May 15, 1973.
- Anderson J. T. and A. M. Goldman. Thermal fluctuations and the Josephson supercurrent. *Phys. Rev. Lett.*, **23**, 128–131 (1969a).

- Anderson J. T. and A. M. Goldman. Thermal fluctuations and the Josephson supercurrent. ICSS, 256–264 (1969b).
- Anderson P. W. Theory of dirty superconductors. *J. Phys. Chem. Solids*, **11**, 26–30 (1959).
- Anderson P. W. Special effects in superconductivity. In *Lectures on the Manybody Problem*, Ravello, 1963 (E. R. Caianiello, Ed.). Vol. 2, Academic, 1964, pp. 113–135.
- Anderson P. W. Flow of superfluid helium. *Rev. Mod. Phys.*, **38**, 298–310 (1966).
- Anderson P. W. The Josephson effect and quantum coherence measurements in superconductors and superfluids. In *Progress in Low Temperature Physics* (C. J. Gorter, Ed.). Vol. 5, North-Holland, Amsterdam, 1967, pp. 1–43.
- Anderson P. W. How Josephson discovered his effect. *Phys. Today*, **23**, 29 (1970).
- Anderson P. W. and A. H. Dayem. Radio-frequency effects in superconducting thin film bridges. *Phys. Rev. Lett.*, **13**, 195–197 (1964).
- Anderson P. W. and J. M. Rowell. Probable observation of the Josephson superconducting tunnel effect. *Phys. Rev. Lett.*, **10**, 230–232 (1963).
- Anderson P. W., R. C. Dynes, and T. A. Fulton. Josephson flux quantum shuttle. *Bull. Am. Phys. Soc.*, **16**, 399 (1971).
- Anderson P. W., N. R. Werthamer, and J. M. Luttinger. An additional equation in the phenomenology of superconductivity resistive effects. *Phys. Rev.*, **138**, A1157–A1159 (1965).
- Andreev A. F. The thermal conductivity of the intermediate state in superconductors. *Zh. Eksp. Teor. Fiz.*, **46**, 1823–1828 (1964). *Sov. Phys. JETP*, **19**, 1228–1229 (1964).
- Andreone D., E. Arri, G. Boella, and G. Marullo. A novel cryogenic voltage standard. *IEEE Trans. Instrum. Meas.*, **IM-25**, 512–515 (1976).
- Andreozzi F., A. Barone, M. Russo, G. Paternò, and R. Vaglio. Measurements of the dc Josephson current in light-sensitive junctions. *Phys. Rev.*, **B18**, 6035–6040 (1978).
- Andronov A. A. and C. E. Chaikin. *Theory of Oscillation*. Princeton University Press, Princeton, 1949.
- Arnold G. B. Theory of tunneling in superconductors. *Phys. Rev.*, **B17**, 3576–3588 (1978).
- Arri E. Proposal for a cryogenic voltage comparator for $2e/h$ measurement. *Alta Freq.*, **45**, 53E–55E (1976).
- Arrington C. H. and B. S. Deaver, Jr. Superconducting weak links formed by ion implantation. *Appl. Phys. Lett.*, **26**, 204–206 (1975).
- Artemenko S. N. and A. F. Volkov. Stationary electric field in superconductors with nonzero energy gap. *Phys. Lett.*, **55A**, 113–114 (1975).
- Artemenko S. N., A. F. Volkov, and A. V. Zaitsev. Josephson effect and collective excitations in thin-film superconducting bridges. *Pis. Zh. Eksp. Teor. Fiz.*, **27**, 122–125 (1978a). *JETP Lett.*, **27**, 113–117 (1978).
- Artemenko S. N., A. F. Volkov, and A. V. Zaitsev. The excess current in superconducting point junctions. *Pis. Zh. Eksp. Teor. Fiz.*, **28**, 637–640 (1978b); *Sov. Phys. JETP*, **28**, 589–591 (1979).
- Artemenko S. N., A. F. Volkov, and A. V. Zaitsev. Theory of nonstationary Josephson effect in short superconducting contacts. *Zh. Eksp. Teor. Fiz.*, **76**, 1816–1833 (1979a). *Sov. Phys. JETP*, **49**, 924–931 (1979a).
- Artemenko S. N., A. F. Volkov, and A. V. Zaitsev. On the excess current in microbridges S-c-S and S-c-N. *Solid State Comm.*, **30**, 771–773 (1979b).
- Aslamazov L. G. Superconducting transition of an inhomogeneous bridge in a microwave field. *Zh. Eksp. Teor. Fiz.*, **75**, 1778–1785 (1978). *Sov. Phys. JETP*, **48**, 896–899 (1978).
- Aslamazov L. G. and A. I. Larkin. Josephson effect in superconducting point contacts. *Zh. Eksp. Teor. Fiz. Pis. Red.*, **9**, 150–154 (1968). *JETP Lett.*, **9**, 87–91 (1969).

- Aslamazov L. G. and A. I. Larkin. Josephson effect in wide superconducting bridges. *Zh. Eksp. Teor. Fiz.*, **68**, 766–775 (1975). *Sov. Phys. JETP*, **41**, 381–386 (1975).
- Aslamazov L. G. and A. I. Larkin. Superconducting contacts with a nonequilibrium electron distribution function. *Zh. Eksp. Teor. Fiz.*, **70**, 1340–1349 (1976). *Sov. Phys. JETP*, **43**, 698–703 (1976).
- Aslamazov L. G. and A. I. Larkin. The critical current of superconducting contacts in a microwave field. *Phys. Lett.*, **67A**, 226–228 (1978a).
- Aslamazov L. G. and A. I. Larkin. Influence of microwave field on the critical current of superconducting contacts. *Zh. Eksp. Teor. Fiz.*, **74**, 2184–2195 (1978b). *Sov. Phys. JETP*, **47**, 1136–1142 (1978).
- Aslamazov L. G. and M. V. Fistul. Critical current of Josephson junctions with a semiconductor layer. *Pis'ma Zh. Eksp. Teor. Fiz.*, **30**, 233–236 (1979). *JETP Lett.*, **30**, 213–217 (1979).
- Aslamazov L. G., A. I. Larkin, and Yu. N. Ovchinnikov. Josephson effect in superconductors separated by a normal metal. *Zh. Eksp. Teor. Fiz.*, **55**, 323–335 (1968). *Sov. Phys. JETP*, **28**, 171–176 (1969).
- Aspen F. and A. M. Goldman. Superconducting tunnelling junctions with In_xO_y barriers. *Cryogenics*, **16**, 721–722 (1976).
- Auracher F. and T. Van Duzer. Influence of the current-phase relationship on the I - V characteristics of superconducting weak links. *Appl. Phys. Lett.*, **21**, 515–518 (1972a).
- Auracher F. and T. Van Duzer. Numerical calculations of mixing with superconducting weak links. *ASC* 72, 603–607 (1972b).
- Auracher F. and T. Van Duzer. Mixing in superconducting weak links: Numerical calculations and experimental results. *DEJJ*, 233–241 (1973a).
- Auracher F. and T. Van Duzer. RF impedance of superconducting weak links. *J. Appl. Phys.*, **44**, 848–851 (1973b).
- Auracher F., P. L. Richards, and G. I. Rochlin. Observability of quasiparticle-pair interference current in superconducting weak links. *Phys. Rev.*, **B8**, 4182–4185 (1973).
- Baechtold W. A flip-flop and logic gate with Josephson junctions. *IEEE Int. Solid State Circuits Conf.*, February 1975. *Digests of Technical Papers* **18**, 164–165 (1975).
- Bak C. K. An electric equivalent scheme of a Josephson junction. *DEJJ* 15–18 (1973).
- Bak C. K. and N. F. Pedersen. Josephson junction analog and quasiparticle-pair current. *Appl. Phys. Lett.*, **22**, 149–150 (1973).
- Bak C. K., B. Kofoed, N. F. Pedersen, and K. Saermark. Parametric excitation of plasma oscillations in a Josephson tunnel junction. *J. Appl. Phys.*, **46**, 886–889 (1975).
- Baker K. and G. Paternò. Numerical calculation of the zero bias conductivity for a superconducting tunnel junction in the presence of depairing. CNEN Internal Rep. LNF-72/10, February 1972.
- Balkashin O. P. and J. K. Yanson. Nonlinear plasma oscillations in Josephson tunnel junctions. *Fiz. Nizk. Temp.*, **2**, 289–298 (1976). *Sov. J. Low Temp. Phys.*, **2**, 143–147 (1976b).
- Balsamo E. P. and G. Paternò. R.F. SQUID in the dispersive mode. In *Proceedings of XV International Congress of Refrigeration*, Venezia, 1979 (edited by the Organizing Committee), the Istituto Tecnica del Freddo C.N.R., Padova, Vol. 1, 275–279 (1979).
- Balsamo E. P. and G. Paternò. Electrical analog simulation of a superconducting Josephson weak link. CNEN Internal Report (1981).
- Balsamo E. P., G. Paternò, A. Barone, P. Rissman, and M. Russo. Temperature dependence of the maximum (dc) Josephson current. *Phys. Rev.*, **B10**, 1881–1884 (1974).
- Balsamo E. P., G. Paternò, A. Barone, M. Russo, and R. Vaglio. Supercurrent interference patterns in a tunneling junction structure. IC-SQUID 76, 193–197 (1976a).

- Balsamo E. P., G. Paternò, A. Barone, M. Russo, and R. Vaglio. Temperature and magnetic field dependence of the critical current in Sn-Sn_xO_y-In Josephson junctions. *Phys. Status Solidi (a)*, **35**, K173-175 (1976b).
- Balsamo E. P., G. Paternò, A. Barone, M. Russo, and R. Vaglio. Influence of barrier nonuniformities on the resonance amplitudes of high Q Josephson tunnel junctions. LT 15, 571-572 (1978).
- Bano W. T. Superconducting tunneling devices. *Thin Solid Films*, **34**, 225-228 (1976).
- Baratoff A. Tunneling between superconductors the Josephson effect. Ph.D. Thesis, Cornell University, Ithaca (1964).
- Baratoff A. and L. Kramer. Order parameter relaxation and Josephson effects in superconducting weak links. IC-SQUID 76, 51-62c (1976).
- Baratoff A. and L. Kramer. Dynamics of gapless superconducting weak links. LT 15, 548-549 (1978).
- Baratoff A., J. A. Blackburn, and B. B. Schwartz. Current-phase relationship in short superconducting weak links. *Phys. Rev. Lett.*, **25**, 1096-1099 (1970).
- Barbanera S., P. Carelli, I. Modena, and G. L. Romani. A gradiometer for the study of magnetic fields generated by the human heart in a magnetically unshielded environment: Preliminary results. *J. Phys. E: Sci. Instrum.*, **11**, 297-298 (1978a).
- Barbanera S., P. Carelli, I. Modena, and G. L. Romani. A SQUID device for ac current measurements down to 10^{-14} A. *J. Appl. Phys.*, **49**, 905-909 (1978b).
- Barbanera S., P. Carelli, R. Leoni, G. L. Romani, F. Bordoni, I. Modena, R. Fenici, and P. Zeppilli. Magnetocardiographic study of some human cardioelectrophysiological phenomena: preliminary observations. IC-SQUID 80, (1980a, in press).
- Barbanera S., P. Carelli, R. Fenici, I. Modena, and G. L. Romani. Use of a superconducting instrumentation for biomagnetic measurements performed in a hospital. ASC 80, (1980b, in press).
- Barbanera S., P. Carelli, R. Fenici, I. Modena, and G. L. Romani. Biomagnetism measurements in unshielded, normally noisy environments. IC-SQUID 80, (1980c).
- Bardeen J. Tunneling from a many-particle point of view. *Phys. Rev. Lett.*, **6**, 57-59 (1961).
- Bardeen J., L. N. Cooper, and J. R. Schrieffer. Theory of superconductivity. *Phys. Rev.*, **108**, 1175-1204 (1957).
- Barone A. Flux flow effect in Josephson tunnel junctions. *J. Appl. Phys.*, **42**, 2747 (1971).
- Barone A. Thermal effect in U - I characteristics of large Josephson junctions. *Phys. Status Solidi (a)*, **13**, K93-95 (1972).
- Barone A. and W. J. Johnson. Some aspects in the preparation and measurements of Josephson junctions. *Vuoto Sci. Tec.*, **2**, 215-225 (1969).
- Barone A. and Yu. N. Ovchinnikov. Boundary conditions and critical current of SNS junctions. *Zh. Eksp. Teor. Fiz.*, **77**, 1463-1470 (1979). *Sov. Phys. JETP*, **50**, 735-738 (1979).
- Barone A. and M. Russo. Observation of light induced Josephson current through "thick" CdS barriers. *Phys. Lett.*, **49A**, 45-46 (1974).
- Barone A., W. J. Johnson, and R. Vaglio. Current flow in large Josephson junctions. *J. Appl. Phys.*, **46**, 3628-3632 (1975).
- Barone A., P. Rissman, and M. Russo. Effect of preparation parameters on light sensitivity in superconductive tunnel junctions. DEJJ, 73-77 (1973).
- Barone A., M. Russo, and R. Vaglio. Light-sensitive Josephson junctions: Ten years ago, ten years from now. FTSE, 340-344 (1978).
- Barone A., F. Esposito, C. J. Magee, and A. C. Scott. Theory and application of the sine-Gordon equation. *Riv. Nuovo Cimento*, **1**, 227-267 (1971).

- Barone A., G. Paternò, M. Russo, and R. Vaglio. Experimental results on temperature and magnetic field dependence of light induced Josephson current. *LT* 14, 88–91 (1975a).
- Barone A., G. Paternò, M. Russo, and R. Vaglio. Light-induced transition from “small” to “large” Josephson junctions. *Phys. Lett.*, **53A**, 393–394 (1975b).
- Barone A., G. Paternò, M. Russo, and R. Vaglio. Differentiation and interference phenomena in single Josephson junctions. *Phys. Status Solidi (a)*, **41**, 393–401 (1977).
- Barone A., G. Paternò, M. Russo, and R. Vaglio. Experimental results and analysis of structural fluctuations in photosensitive Josephson junctions. *Zh. Eksp. Teor. Fiz.*, **74**, 1483–1488 (1978). *Sov. Phys. JETP*, **47**, 776–778 (1979).
- Barone A., A. Di Chiara, G. Peluso, and M. Russo. Preparation parameters and characterization of vanadium based Josephson junctions. IC-SQUID 80 (1980).
- Barr D. W., R. J. Mattauch, L.-K. Wang, and B. S. Deaver, Jr. Millimeter wave response of Nb variable thickness bridges. FTSE, 345–348 (1978).
- Basavaiah S. and R. F. Broom. Characteristics of in-line Josephson tunneling gates. ASC 74, 759–762 (1974).
- Basavaiah S. and J. H. Greiner. Capacitance and ellipsometrically determined oxide thickness of Nb-oxide-Pb Josephson tunnel junctions. *J. Appl. Phys.*, **47**, 4201–4202 (1976).
- Basavaiah S. and J. H. Greiner. An investigation of the thermal cycling of Pb-alloy Josephson tunneling gates. *J. Appl. Phys.*, **48**, 4630–4633 (1977).
- Basavaiah S., J. M. Eldridge, and J. Matisoo. Tunneling in lead-lead oxide-lead junctions. *J. Appl. Phys.*, **45**, 457–464 (1974).
- Basavaiah S., M. Murakami, and C. J. Kircher. Strain relaxation effects in Pb-alloy Josephson tunnel junctions. *LT* 15, 1247–1249 (1978).
- Beasley M. R. Improved materials for superconducting electronics. FTSE, 389–396 (1978).
- Beasley M. R. and W. W. Webb. Operation of superconducting interference devices in appreciable magnetic fields. PSD, 1–8 (1967), paper V.
- Bedard F. and H. Meissner. Measurements of contact resistance between normal and superconducting metals. *Phys. Rev.*, **101**, 26–30 (1956).
- Belykh V. N., N. F. Pedersen, and O. H. Soerensen. Shunted-Josephson-junction model. I. The autonomous case. *Phys. Rev.*, **B16**, 4853–4859 (1977a).
- Belykh V. N., N. F. Pedersen and O. H. Soerensen. Shunted-Josephson-junction model. II. The non-autonomous case. *Phys. Rev.*, **B16**, 4860–4871 (1977b).
- Ben-Abraham S. I. Exact solution to the sine-Gordon equation in two space dimensions. *Phys. Lett.*, **55A**, 383–384 (1976).
- Benacka S., L. Bezakova, S. Gazi, and S. Takacs. Properties of long superconducting variable thickness bridges. I. DC and AC Josephson effect. *Czech. J. Phys. B*, **28**, 192–202 (1978a).
- Benacka S., L. Bezakova, S. Gazi, and S. Takacs. Properties of long superconducting variable thickness bridges. II. Influence of static magnetic field. *Czech. J. Phys. B*, **28**, 203–215 (1978b).
- Bermon S. and R. M. Mesak. Observation of cylindrical cavity modes in circular Josephson weak-link junctions. *J. Appl. Phys.*, **42**, 4488–4492 (1971).
- Bernard W. and H. B. Callen. Irreversible thermodynamics of nonlinear processes and noise in driven systems. *Rev. Mod. Phys.*, **31**, 1017–1044 (1959).
- Bishop A. R. and S. E. Trullinger. Josephson junction threshold viewed as a critical point. *Phys. Rev.*, **B17**, 2175–2182 (1978).
- Biswas A. C. and S. Jha. Effect of thermal noise on the d.c. Josephson effect. *Phys. Rev.*, **B2**, 2543–2547 (1970).
- Blackburn J. A. and M. A. H. Nerenberg. Relative self-phase in resonant Josephson junctions. *Phys. Lett.*, **46A**, 15–16 (1973).

- Blackburn J. A. and H. J. T. Smith. Flow penetration into doubly connected loops containing two Josephson junctions. *J. Appl. Phys.*, **48**, 2961–2964 (1977).
- Blackburn J. A., J. D. Leslie, and H. J. Smith. Self-resonant current peaks in Josephson junctions. *J. Appl. Phys.*, **42**, 1047–1054 (1971).
- Blackburn J. A., B. B. Schwartz, and A. Baratoff. Single and multiple superconducting weak-link systems. *J. Low Temp. Phys.*, **20**, 523–543 (1975).
- Blackburn J. A., H. J. T. Smith, and V. Keith. Probing the phase-dependent conductance and nonequilibrium properties of Josephson junctions by means of flux entry into weakly closed loops. *Phys. Rev.*, **B15**, 4211–4213 (1977).
- Blackburn J. A., H. J. T. Smith, and N. L. Rowell. Proximity effects and the generalized Ginzburg-Landau equation. *Phys. Rev.*, **B11**, 1053–1058 (1975).
- Blackwell L. A. and K. L. Kotzebue. *Semiconductors-Diode Parametric Amplifiers*. Prentice Hall, Englewood Cliffs, 1961.
- Blaney T. G. Heterodyne laser radiation detection at 891 GHz using Josephson point contact. *DEJJ*, 279–284 (1973).
- Blaney T. G. and D. J. E. Knight. Direct 825th harmonic mixing of a 1 GHz source with an HCN laser in a Josephson junction. *J. Phys. D: Appl. Phys.*, **7**, 1882–1886 (1974).
- Blaquiere A. *Nonlinear System Analysis*. Academic, New York, 1966.
- Bloch F. Josephson effect in a superconducting ring. *Phys. Rev.*, **B2**, 109–121 (1970).
- Blocker T. G., R. K. Watts, and W. C. Holton. Advanced imaging techniques for submicrometer devices. *FTSE*, 280–288 (1978).
- Bogoliubov N. N. and Y. A. Mitropolsky. *Asymptotic Methods in the Theory of Non-Linear Oscillations*. Hindustan, Delhi, and Gordon and Breach, New York, 1961.
- Bondarenko S. I., I. M. Dmitrienko, and T. P. Narbut. Intrinsic steps on the current-voltage characteristics of Josephson point contacts. *Fiz Tverd. Tela*, **14**, 354–359 (1972). *Sov. Phys. Solid State*, **14**, 295–299 (1972).
- Bondarenko S. I., E. I. Balanov, L. E. Kolinko, and T. P. Narbut. A superconducting point contact having the properties of a Josephson junction. *Cryogenics*, **10**, 508–510 (1970).
- Bondarenko S. I., V. A. Matveeva, N. M. Loboda, K. B. Loganov, and A. S. Shulman. Stable Josephson junctions fabricated by fritting. *Zh. Tekh. Fiz.*, **46**, 2440–2443 (1976). *Sov. Phys. Tech. Phys.*, **21**, 1440–1442 (1976).
- Bonifacio R., M. Milani, and M. Scully. Use of a coherent-state formalism in superconductivity and Josephson-junction calculations. *Nuovo Cimento*, **B50**, 152–160 (1979).
- Boone B. G., C. H. Arrington, III, L.-K. Wang, and B. S. Deaver, Jr. Properties of new types of niobium weak links. *ASC* **76**, 735–738 (1976).
- Bordoni F., P. Carelli, I. Modena, and G. L. Romani. Narrow-band ultra-low current measurements with a r.f. SQUID. *LT* **15**, 1213–1214 (1978).
- Bosch B. G. Gigabit electronics. A review. *Proc. IEEE*, **67**, 340–379 (1979).
- Brachen T. D. and W. O. Hamilton. Comparison of microwave-induced constant-voltage steps in Pb and Sn Josephson junctions. *Phys. Rev.*, **B6**, 2603–2609 (1972).
- Brennemann A. E. The in-line cryotron. *Proc. IEEE*, **51**, 442–451 (1963).
- Brennemann A. E., J. J. McNichol, and D. P. Seraphim. Delay times for switching in-line cryotrons. *Proc. IEEE*, **51**, 1009–1014 (1963).
- Brenner D., L. Kaufman, and S. J. Williamson. Applications of a SQUID for monitoring magnetic response of the linear brain. *ASC* **76**, 365–368 (1976).
- Brenner D., S. J. Williamson, and L. Kaufman. SQUID system for detecting evoked magnetic fields of the human brain. *LT* **14**, 266–269 (1975).
- Broers A. N. Electron beam fabrication. *J. Vac. Sci. Tech.*, **8**, 550–551 (1971).
- Broers A. N. and M. Hatzakis. Microcircuits by electron beam. *Sci. Am.*, **227**, 34–44 (1972).

- Broers A. N. and R. B. Laibowitz. High resolution electron beam lithography and applications to superconducting devices. FTSE, 289–297 (1978).
- Broers A. N., W. Molzen, J. Cuomo, and W. Wittels. Electron beam fabrication of 80 Å metal structures. *Appl. Phys. Lett.*, **29**, 596–598 (1976).
- Broom R. F. Some temperature-dependent properties of niobium tunnel junctions. *J. Appl. Phys.*, **47**, 5432–5439 (1976).
- Broom R. F. and P. Wolf. *Q* factor and resonance amplitude of Josephson tunnel junctions. *Phys. Rev.*, **B16**, 3100–3107 (1977).
- Broom R. F., W. Jutzi, and T. O. Mohr. A 1.4 mil² memory cell with Josephson junctions. ASC 74, 755–758 (1974).
- Broom R. F., W. Kotyczka, and A. Moser. Modeling of characteristics for Josephson junctions having nonuniform width or Josephson current density. *IBM J. Res. Develop.*, **24**, 178–187 (1980).
- Broom R. F., R. Jaggi, R. B. Laibowitz, and W. Walter. Thin-film Josephson junctions with niobium electrodes. LT 14, **4**, 172–175 (1975).
- Broom R. F., P. Gueret, W. Kotyczka, T. O. Mohr, A. Moser, A. Oosenbrug, and P. Wolf. Model for a 15 ns 16 K RAM with Josephson junctions. In *IEEE International Solid State Circuits Conference*, February 1978, pp. 60–62; in *IEEE J. Solid State Cir.*, **SC-14**, 690–699 (1979).
- Bube R. H. *Photoconductivity of Solids*. Wiley, New York (1960).
- Buck D. A. The cryotron—A superconductive computer component. *Proc. IRE*, **44**, 482–493 (1956).
- Buck D. A. and K. R. Shoulder. An approach to microminiature printed systems. In *Proceedings of the Eastern Joint Computer Conference*, (special publication, T114), 1958.
- Buckner S. A. and D. N. Langenberg. Riedel singularity in tin-tin oxide-tin tunnel junctions. *J. Low Temp. Phys.*, **22**, 569–596 (1976).
- Buckner S. A., J. T. Chen, and D. N. Langenberg. Electrodynamic and noise properties of very small Josephson tunnel junctions. LT 12, 453–454 (1970a).
- Buckner S. A., J. T. Chen, and D. N. Langenberg. Current-voltage characteristics of small Josephson tunnel junctions. *Phys. Rev. Lett.*, **25**, 738–741 (1970b).
- Buckner S. A., T. F. Finnegan, and D. N. Langenberg. Riedel singularity in Sn-Sn oxide-Sn Josephson tunnel junctions. *Phys. Rev. Lett.*, **28**, 150–154 (1972).
- Buhrman R. A. Noise limitation of rf Squid's. IC-SQUID 76, 395–431 (1976).
- Buhrman R. A. and L. D. Jackel. Performance factors in rf SQUIDs, high frequency limit. ASC 76, 879–882 (1976).
- Buhrman R. A., S. F. Strait, and W. W. Webb. Stable superconducting point-contact weak links. *J. Appl. Phys.*, **42**, 4527–4528 (1971).
- Buhrman R. A., J. E. Lukens, L. D. Jackel, S. F. Strait, J. M. Warlaumont, and W. W. Webb. SQUID techniques. I. Obtaining reliability in Point-contact SQUID's. *J. Appl. Phys.*, **45**, 4045–4048 (1974).
- Bulaevskii L. N., V. V. Kuzii, and A. A. Sobyanin. On possibility of the spontaneous magnetic flux in a Josephson junction containing magnetic impurities. *Solid State Comm.*, **25**, 1053–1057 (1978).
- Burger J. P. and D. Saint-James. Boundary effects and small specimens. In *Superconductivity* (R. D. Parks, Ed.). Vol. II, Marcel Dekker, New York, 1969, Chap. 16.
- Burgess R. E. Quantization and fluctuations in superconductors. SPSD, H1–12 (1967).
- Callegari A. and B. S. Deaver, Jr. Temperature dependence of microwave SQUID response. *J. Appl. Phys.*, **48**, 5328–5333 (1977).
- Callegari A., H. A. Atwater, and B. J. Deaver, Jr. Phase dependent conductance of superconducting point contacts at microwave frequencies. *Phys. Lett.*, **A59**, 55–58 (1976).

- Callen H. B. and T. A. Welton. Irreversibility and generalized noise. *Phys. Rev.*, **83**, 34–40 (1951).
- Calogero F. Nonlinear evolution equations solvable by the inverse spectral transform. *Proceedings of the International Conference on Mathematical Problems in Theoretical Physics*, Rome, June 1977 (G. Dell'Antonio, J. Doplicher, and G. Jona Lasinio, Eds.), in *Lecture Notes in Physics* **80**, 235–269 (1978).
- Canavello B. J., M. Hatzakis, and J. M. Shaw. Process for obtaining undercutting of photoresist to facilitate lift-off. *IBM Tech. Disc. Bull.*, **19**, 4048– (1977).
- Cardinne P. and J. E. Nordman. A simple technique for fabrication of tunnel junctions using Nb wire. *Rev. Phys. Appl.*, **8**, 467–470 (1973).
- Cardinne P., B. Manhes, and J. E. Nordman. Récents progrès dans la fabrication de jonctions Josephson. Utilisation de niobium obtenu par pulvérisation cathodique. *Rev. Phys. Appl.*, **8**, 463–466 (1973).
- Cardinne P., B. Manhes, and M. Renard. Josephson and Giaever effects with a semiconducting barrier of variable height. *ASC* **72**, 565–569 (1972).
- Cardinne P., M. Marti, and M. Renard. Jonctions Josephson à barrière semiconductrice. *Rev. Phys. Appl.*, **6**, 547–550 (1971).
- Cardinne P., J. Nordmann, and M. Renard. On the use of low barrier potential materials to improve high frequency coupling to Josephson tunnel junctions. *DEJJ*, 167–171 (1973).
- Carelli P. and I. Modena. Josephson-like behavior in double Dayem bridge structures. *J. Appl. Phys.*, **47**, 4649–4652 (1976).
- Caroli C., R. Combescot, P. Nozieres, and D. Saint-James. Direct calculation of the tunneling current. *J. Phys. C: Solid State Phys.*, **4**, 916–929 (1971a).
- Caroli C., R. Combescot, D. Lederer, P. Nozieres, and D. Saint-James. A direct calculation of the tunneling current. II. Free electron description. *J. Phys. C: Solid State Phys.*, **4**, 2598–2610 (1971b).
- Caroli C., R. Combescot, P. Nozieres, and D. Saint-James. A direct calculation of the tunneling current: IV: Electron-phonon interaction effects. *J. Phys. C: Solid State Phys.*, **5**, 21–42 (1972).
- Caswell H. L., J. R. Priest, and Y. Budo. Low-temperature properties of evaporated lead films. *J. Appl. Phys.*, **34**, 3261–3266 (1963).
- Cerdonio M. and C. Messana. Superconducting magnetometer for high resolution susceptibility measurements. *ASC* **74**, 728–731 (1974).
- Cerdonio M., F. F. Ricci, and G. L. Romani. Toroidal SQUID with ferromagnetic core superconducting transformer. *J. Appl. Phys.*, **48**, 4799–4802 (1977).
- Cerdonio M., G. L. Romani, and S. Pace. SQUID operation with ferromagnetic core superconducting d.c. transformers. *Cryogenics*, **15**, 278–282 (1975).
- Cerdonio M., R. H. Wang, G. R. Rossman, and J. E. Mercereau. Magnetochemical measurements of biochemical compounds with a superconducting magnetometer. *LT* **12**, **4**, 525–534 (1972).
- Cerdonio M., C. Cosmelli, G. L. Romani, C. Messana, and C. Gramaccioni. Superconducting magnetometer for high resolution susceptibility measurements. *Rev. Sci. Instrum.*, **47**, 1–5 (1976).
- Cerdonio M., F. Mogno, G. L. Romani, C. Messana, and C. Gramaccioni. Oscillating sample superconducting magnetometer. *Rev. Sci. Instrum.*, **48**, 300–306 (1977).
- Chan H. W., W. Y. Lum, and T. Van Duzer. High speed switching and logic circuits using Josephson devices. *ASC* **74**, 770–773 (1974).
- Chan H. W., B. T. Ulrich, and T. Van Duzer. Switching dynamics of Josephson junction logic circuits. *IC-SQUID* **76**, 555–565 (1976).
- Chandrasekhar S. Stochastic problem in physics and astronomy. *Rev. Mod. Phys.*, **15**, 1–89 (1943).
- Chang J. J. and D. J. Scalapino. Hot superconductors: The physics and applications of nonequilibrium superconductivity. *NASI* **76**, 447–485 (1976).

- Chaudhari P. Hillock growth in thin films. *J. Appl. Phys.*, **45**, 4339–4346 (1974).
- Cheishvili O. D. Theory of a cylindrical Josephson junction. *Fiz. Tverd. Tela*, **11**, 185–186 (1968). *Sov. Phys. Solid State*, **11**, 138–139 (1969).
- Chen J. T. and D. N. Langenberg. Fine structure in the anomalous d.c. current singularities of a Josephson tunnel junction. LT 13, **3**, 289–292 (1972).
- Chen J. T., T. F. Finnegan, and D. N. Langenberg. Anomalous d.c. current singularities in Josephson tunnel junctions. ICSS, 413–420 (1969).
- Chen J. T., R. J. Todd, and Y. W. Kim. Investigation of microwave induced dc voltages across unbiased Josephson tunnel junctions. *Phys. Rev.*, **B5**, 1843–1849 (1972).
- Chiao R. Y. and P. T. Parrish. Operation of the SUPARAMP at 33 GHz. *J. Appl. Phys.*, **47**, 2639–2644 (1976).
- Chiao R. Y., M. J. Feldman, D. W. Peterson, B. A. Tucker, and M. T. Levinsen. Phase instability noise in Josephson junctions. FTSE, 259–263 (1978).
- Christiansen P. L. and O. H. Olsen. Fluxons on a Josephson line with loss and bias. *Wave Motion*, **2**, 185–196 (1980).
- Christiansen P. V., E. B. Hansen, and C. J. Sjöstrom. Negative self-inductance in superconducting thin wires and weak links. *J. Low Temp. Phys.*, **4**, 349–389 (1971).
- Cirillo M., R. D. Parmentier, and B. Savo. Mechanical analog studies of a perturbed Sine-Gordon equation. *Physica D* (1981, in press).
- Claassen J. H. Coupling considerations for SQUID devices. *J. Appl. Phys.*, **46**, 2268–2275 (1975).
- Claassen J. H. and P. L. Richards. Performance limits of a Josephson junction mixer. *J. Appl. Phys.*, **49**, 4117–4129 (1978a).
- Claassen J. H. and P. L. Richards. Point-contact Josephson mixers at 130 GHz. *J. Appl. Phys.*, **49**, 4130–4140 (1978b).
- Claassen J. H., Y. Taur, and P. L. Richards. Noise in Josephson point contacts with and without rf bias. *Appl. Phys. Lett.*, **25**, 759–761 (1974).
- Claeson T. Gapless superconductor tunneling experiment. NASI 67, 443–459 (1967).
- Clark T. D. Experiments on coupled Josephson junctions. *Phys. Lett.*, **27A**, 585–586 (1968).
- Clark T. D. Generation and detection experiments using point contact junction arrays. ICSS, 432–438 (1969).
- Clark T. D. Electromagnetic properties of point-contact Josephson junction array. *Phys. Rev.*, **B8**, 137–162 (1973a).
- Clark T. D. Detection and emission of radiation by arrays of junctions. DEJJ, 207–216 (1973b).
- Clark T. D. Frequency dependence of the a.c. Josephson effect in small Dayem bridges. *Phys. Rev. Lett.*, **37**, 368–371 (1976).
- Clark T. D. and J. P. Baldwin. Superconducting memory device using Josephson junctions. *Electron. Lett.*, **3**, 178–179 (1967).
- Clark T. D. and L. D. Jackel. Low noise, permanently adjusted UHF SQUID magnetometer. ASC 74, 736–738 (1974).
- Clark T. D. and L. D. Jackel. Simple, low-noise uhf SQUID magnetometer. *Rev. Sci. Instrum.*, **46**, 1249–1252 (1975).
- Clark T. D. and P. E. Lindelof. Collective synchronization of arrays of superconducting thin film microbridges. *App. Phys. Lett.*, **29**, 751–753 (1976).
- Clarke J. A superconducting galvanometer employing Josephson tunneling. *Phil. Mag.*, **13**, 115–127 (1966).
- Clarke J. Experimental comparison of the Josephson voltage-frequency relation in different superconductors. *Phys. Rev. Lett.*, **21**, 1566–1569 (1968).
- Clarke J. Supercurrents in lead-copper-lead sandwiches. *Proc. Roy. Soc.*, **A308**, 447–471 (1969).
- Clarke J. The Josephson effect and e/h . *Am. J. Phys.*, **38**, 1071–1095 (1970).

- Clarke J. Finite-voltage behavior of lead-copper-lead junctions. *Phys. Rev.*, **B4**, 2963–2976 (1971).
- Clarke J. Low-frequency applications of superconducting quantum interference devices. *Proc. IEEE*, **61**, 8–19 (1973).
- Clarke J. Superconducting quantum interference devices for low frequency measurements. NASI 76, 67–124 (1976).
- Clarke J. and T. A. Fulton. Origin of low-voltage structure and asymmetry in the I - V characteristics of multiply connected superconducting junctions. *J. Appl. Phys.*, **40**, 4470–4476 (1969).
- Clarke J. and G. Hawkins. Low frequency noise in Josephson junctions. ASC 74, 841–844 (1974).
- Clarke J. and G. Hawkins. Flicker ($1/f$) noise in Josephson tunnel junctions. *Phys. Rev.*, **B14**, 2826–2831 (1976).
- Clarke J. and J. L. Paterson. Josephson junction amplifier. *Appl. Phys. Lett.*, **19**, 469–471 (1971).
- Clarke J. and R. F. Voss. $1/f$ noise from thermal fluctuations in metal films. *Phys. Lett.*, **33**, 24–27 (1974).
- Clarke J., T. D. Gamble, and W. M. Goubau. SQUIDS and magnetotellurics with a remote reference. FTSE, 87–94 (1978).
- Clarke J., W. M. Goubau, and M. B. Ketchen. A reliable d.c. SQUID made with tunnel junctions. ASC 74, 724–727 (1974).
- Clarke J., W. M. Goubau, and M. B. Ketchen. Thin-film d.c. SQUID with low noise and drift. *Appl. Phys. Lett.*, **27**, 155–156 (1975).
- Clarke J. W. M. Goubau, and M. B. Ketchen. Tunnel junction d.c. SQUID: Fabrication, operation and performance. *J. Low Temp. Phys.*, **25**, 99–144 (1976).
- Clarke J., G. I. Hoffer, and P. L. Richards. Superconducting tunnel junction bolometers. DEJJ, 69–71 (1973).
- Clarke J., W. E. Tenant, and D. Woody. Impedance matching a Josephson galvanometer by means of a superconducting transformer. *J. Appl. Phys.*, **42**, 3859–3865 (1971).
- Cohen D. Large volume conventional magnetic shields. *Rev. Phys. Appl.*, **5**, 53–58 (1970).
- Cohen D. Magnetoencephalography: detection of the brain's electrical activity with a superconducting magnetometer. *Science*, **175**, 664–666 (1972).
- Cohen D. Measurements of the magnetic fields produced by the human heart, brain and lungs. ASC 74, 694–700 (1974).
- Cohen D., E. A. Edelsack, and J. E. Zimmerman. Magnetocardiograms taken inside a shielded room with a superconducting point-contact magnetometer. *Appl. Phys. Lett.*, **16**, 278–280 (1970).
- Cohen E. R. and J. W. M. Dumond. Our knowledge of the fundamental constants of physics and chemistry in 1965. *Rev. Mod. Phys.*, **37**, 537–594 (1965).
- Cohen M. H., L. M. Falicov, and J. C. Phillips. Superconductive tunneling. *Phys. Rev. Lett.*, **8**, 316–318 (1962).
- Cohen R. A., R. W. Mountain, H. I. Smith, M. A. Lemma, D. L. Spears, and S. E. Bernacki. Fabrication procedure for silicon membrane X-ray lithography masks. M.I.T. Lincoln Lab., Lexington, Tech. Note 1973-38, September 20, 1973.
- Consadoli F., A. A. Fiee, R. E. Frindt, and S. Gygax. Construction and properties of weak-link detectors using superconducting layer structures. *Appl. Phys. Lett.*, **18**, 233–235 (1971).
- Coon D. D. and M. D. Fiske. Josephson ac and step structure in the supercurrent tunneling characteristic. *Phys. Rev.*, **A138**, 744–746 (1965).
- Corruccini L. R. Helical resonator for VHF SQUID operation. *Rev. Sci. Instrum.*, **44**, 1256–1257 (1973).
- Costabile G. and R. D. Parmentier. Analytic solution for fluxon propagation in Josephson junctions with bias and loss. LT 14, **4**, 112–115 (1975).

- Costabile G., R. D. Parmentier, B. Savo, D. W. McLaughlin, and A. C. Scott. Exact solutions of the sine-Gordon equation describing oscillations on a long (but finite) Josephson junction. *Appl. Phys. Lett.*, **32**, 587–589 (1978).
- Cromar M. W. and P. Carelli. Low noise tunnel junction d.c. SQUIDs. *Appl. Phys. Lett.* (1981, to be published).
- Cucolo A. M., S. Pace, and R. D. Parmentier. Surface effects on the tunneling characteristics of Nb-Pb Josephson junctions. *Phys. Status Solidi (a)*, **42**, K111–114 (1977).
- Cucolo A. M., S. Pace, and R. Vaglio. Measurements of physical properties of superconductors by Josephson devices. *Proceedings of XV International Congress of Refrigeration*, Venezia 1979 (edited by the Organizing Committee), the Istituto Tecnica del Freddo del C.N.R., Padova, Vol. 2, 224–227 (1979).
- Cukauskas E. I., D. A. Vincent, and B. S. Deaver, Jr. Magnetic susceptibility measurements using a superconducting magnetometer. *Rev. Sci. Instrum.*, **45**, 1–6 (1974).
- Currie J. F. Aspects of exact dynamics for general solutions of the sine-Gordon equation with applications to domain walls. *Phys. Rev.*, **A16**, 1692–1699 (1977).
- Daalmans G. M. and J. Zwier. Alternatives in fabricating submicron niobium Josephson junctions. *FTSE*, 312–316 (1978).
- Daalmans G. M., T. M. Klapwijk, and J. E. Mooij. Superconducting microbridges in Delft. *ASC* **76**, 719–723 (1976).
- Dahm A. J. and D. N. Langenberg. Nonlinear effects in the Josephson plasma resonance. *J. Low Temp. Phys.*, **19**, 145–167 (1975).
- Dahm A. J., A. Denenstein, T. F. Finnegan, D. N. Langenberg, and D. J. Scalapino. Study of the Josephson plasma resonance. *Phys. Rev. Lett.*, **20**, 859–863 (1968). Errata. *Phys. Rev. Lett.*, **20**, 1020 (1968).
- Dahm A. J., A. Denenstein, D. N. Langenberg, W. H. Parker, D. Rogovin, and D. J. Scalapino. Linewidth of the radiation emitted by a Josephson junction. *Phys. Rev. Lett.*, **22**, 1416–1420 (1969).
- Danilov V. V. and K. K. Likharev. Limiting characteristics of a superconducting quantum magnetometer. *Zh. Tekh. Fiz.*, **45**, 1110–1116 (1975). *Sov. Phys. Tech. Phys.*, **20**, 697–700 (1976).
- Danilov V. V., K. K. Likharev, D. V. Snigiriev, and E. S. Soldatov. Limit characteristics of two-junction magnetic flux detector. *ASC* **76**, 240–241 (1976).
- Davidson A. A Josephson lach. *IEEE J. Solid State Cir.*, **SC-43**, 583–590 (1978).
- Davidson A., R. S. Newbower, and M. R. Beasley. An ultra-low-noise preamplifier using superconducting quantum devices. *Rev. Sci. Instrum.*, **45**, 838–846 (1974).
- Dayem A. H. and C. C. Grimes. Microwave emission from superconducting point-contacts. *Appl. Phys. Lett.*, **9**, 47–49 (1966).
- Dayem A. H. and R. J. Martin. Quantum interaction of microwave radiation with tunneling between superconductors. *Phys. Rev. Lett.*, **8**, 246–248 (1962).
- Dayem A. H. and J. J. Wiegand. Behavior of thin-film superconducting bridges in a microwave field. *Phys. Rev.*, **155**, 419–428 (1967).
- Deaver B. S., Jr. and W. M. Fairbank. Experimental evidence for quantized flux in superconducting cylinders. *Phys. Rev. Lett.*, **7**, 43–46 (1961).
- Deaver B. S., Jr., R. G. Boone, and R. Rifkin. Nonequilibrium effects in superconducting weak links. *Phys. Lett.*, **A57**, 186–188 (1976).
- Deaver B. S., Jr., R. Rifkin, and R. D. Sandell. A simple phenomenological model of the Josephson effects in superconducting weak-links. *J. Low Temp. Phys.*, **25**, 409–419 (1976).
- Deaver B. S., Jr., R. D. Sandell, and D. A. Vincent. A simple phenomenological approach to the phase-dependent conductivity of a superconducting weak link. *Phys. Lett.*, **A46**, 411–412 (1974).

- De Bruyn Ouboter R. Macroscopic quantum phenomena in superconductors. *NASI* 76, 21–65 (1976).
- De Bruyn Ouboter R. and A. T. A. M. De Waele. Superconducting point contacts weakly connecting two superconductors. In *Progress in Low Temperature Physics* (C. J. Gorter, Ed.). North-Holland, Amsterdam, 1970, chap. 6, pp. 243–290.
- De Bruyn Ouboter, R., M. H. Omar, P. T. Arnold, T. Guinan, and K. W. Taconis. Oscillations in the voltage between two weakly connected current carrying superconductors, as a function of the applied magnetic field. *Physica*, **32**, 1448–1458 (1966).
- Decker S. K. and J. E. Mercereau. Superconducting thin-film quantum galvanometer. *Appl. Phys. Lett.*, **23**, 347–349 (1973).
- Decker S. K. and J. E. Mercereau. Noise measurements on proximity effect bridges. *ASC* 74, 848–851 (1974).
- Decker S. K. and J. E. Mercereau. Noise measurements in superconducting proximity bridges. *Appl. Phys. Lett.*, **27**, 466–469 (1975).
- De Gennes P. G. Self-consistent calculation of the Josephson current. *Phys. Lett.*, **5**, 22–24 (1963).
- De Gennes P. G. Boundary effects in superconductors. *Rev. Mod. Phys.*, **36**, 225–237 (1964).
- De Gennes P. G. *Superconductivity of Metals and Alloys*. Benjamin, New York, 1966.
- De Gennes P. G. and E. Guyon. Superconductivity in “normal” metals. *Phys. Lett.*, **3**, 168–169 (1963).
- De Gennes P. G. and S. Mauro. Excitation spectrum of superimposed normal and superconducting films. *Solid State Comm.*, **3**, 381–384 (1965).
- Dettman F. Hysteresis of vanadium-insulation-lead Josephson tunnel junctions. *Phys. Status Solidi*, (a)**28**, K, 21–24 (1975).
- Dettman F. Properties of quantum interference with V- VO_x -Pb tunnel junctions. *Phys. Status Solidi*, (a)**49**, 193–298 (1978).
- Dettman F. and G. Albrecht. The influence of vanadium oxide on the properties of Josephson tunnel junctions. *Phys. Status Solidi*, (a)**53**, 541–548 (1979).
- Dettman F., K. Blüthner, P. Pertsch, P. Weber, and G. Albrecht. A study of V- VO_x -Pb Josephson tunnel junctions. *Phys. Status Solidi*, (a)**44**, 577–581 (1977).
- Deutscher G. and P. G. De Gennes. Proximity effects. In *Superconductivity* (R. D. Parks, Ed.). Vol. 2, Marcel Dekker, New York, 1969, chap. 17, pp. 1005–1034.
- Deutscher G. and M. L. Rappaport. A granular photo-superconductor. *Phys. Lett.*, **71A**, 471–472 (1979).
- De Waele A. T. A. M. and R. De Bruyn Ouboter. Quantum-interference phenomena in point contacts between two superconductors. *Physica*, **41**, 225–254 (1969).
- Di Chiara A., G. Peluso, and M. Russo. Vanadium-based light-sensitive Josephson junctions. *Phys. Lett.*, **73A**, 218–220 (1979).
- Di Renzo A., D. Rogovin, M. Scully, R. Bonifacio, L. Lugjato, and M. Milani. Superconductivity and quantum optics. In *Proceedings of NATO Advanced Study Institute on Coherence in Spectroscopy and Modern Physics*, Villa Le Pianore, Italy, July 1977 (F. T. Arecchi, R. Bonifacio, and M. O. Scully, Eds.), Plenum, New York, 1978, p. 231.
- Divin Yu. Ya. and F. Ya. Nad. On conduction mechanism of high-quality superconducting point contacts. *LT* 15, 599–601 (1978).
- Divin Yu. Ya. and F. Ya. Nad. Dependence of the excess current in superconducting point contacts on temperature and voltage. *Pis. Zh. Eksp. Teor. Fiz.*, **29**, 567–570 (1979). *JETP Lett.*, **29**, 516–519 (1979).
- Dmitrenko I. M. and I. K. Yanson. Certain singularities of electromagnetic radiation generated by a superconducting tunnel structure. *Pis. Zh. Eksp. Teor. Fiz.*, **2**, 242 (1965a); *JETP Lett.*, **2**, 154–156 (1965a).

- Dmitrenko I. M. and I. K. Yanson. Investigation of the high-frequency Josephson current. *Zh. Eksp. Teor. Fiz.*, **49**, 1741–1753 (1965b). *Sov. Phys. JETP*, **22**, 1190–1197 (1966).
- Dmitrenko I. M., S. I. Bondarenko, and T. P. Narbut. A superconducting interferometer with resistive point contacts. *Zh. Exp. Teor. Fiz.*, **57**, 1513–1523 (1969). *Sov. Phys. JETP*, **30**, 817–822 (1970).
- Dmitrenko I. M., I. K. Yanson, and V. M. Svistunov. Interaction of the alternating Josephson current with resonant modes in a superconducting tunnel structure. *Pis. Zh. Eksp. Teor. Fiz.*, **2**, 17 (1965). *JETP Lett.*, **2**, 10–13 (1965).
- Dmitriev V. M., E. V. Christenko, and S. Shapiro. Microwave enhanced critical parameters of superconducting weakly coupled contacts. *Fiz. Kond. Sost.*, **28**, 3–15 (1973).
- Dmitriev V. M., E. V. Christenko, A. V. Trubitsyn, and F. F. Mende. Influence of the microwave radiation on the behaviour of thin film superconducting bridges. *Fiz. Kond. Sost.*, **28**, 128–138 (1970).
- Dolan G. J. Offset masks for lift-off photoprocessing. *Appl. Phys. Lett.*, **31**, 337–339 (1977).
- Dolan G. J. and L. D. Jackel. Voltage measurements within the nonequilibrium region near phase-slip centers. *Phys. Rev. Lett.*, **39**, 1628–1631 (1977).
- Doll R. and M. Näßauer. Experimental proof of magnetic flux quantization in a superconducting ring. *Phys. Rev. Lett.*, **7**, 51–52 (1961).
- Donaldson G. B. and H. Faghihi-Nejad. RF sputter anodization of lead-indium. FTSE, 407–411 (1978).
- Dunkleberger L. N. A stencil technique for the preparation of thin film Josephson devices. Bell Laboratories, Rep. TM-76-1151-25, 1976.
- Dunkleberger L. N. Stencil technique for the preparation of thin-film Josephson devices. *J. Vac. Sci. Tech.*, **15**, 88–90 (1978).
- Dupart J. M. and J. Baixeras. New effects observed in the dynamical behaviour of wide S-N-S junctions in series. LT 14, **4**, 132–135 (1975).
- Dupart J. M. and J. Baixeras. Series arrays of superconducting-normal-superconducting junctions in the Pb-Sn lamellar eutectic alloy. *Appl. Phys. Lett.*, **30**, 123–125 (1977).
- Dupart J. M., C. Bodin, and T. Pech. Reliable point contact preparation and adjustment for SQUIDs. *Cryogenics*, **15**, 227 (1975).
- Duret D., Bernard P., and D. Zenatti. A uhf superconducting magnetometer utilizing a new thin film sensor. *Rev. Sci. Instrum.*, **46**, 474–480 (1975).
- Dynes R. C. and T. A. Fulton. Supercurrent density distribution in Josephson junctions. *Phys. Rev.*, **B3**, 3015–3023 (1971).
- Dziuba R. F., B. F. Field, and T. F. Finnegan. Cryogenic voltage comparator system for $2e/h$ measurements. *IEEE Trans. Instrum. Meas.*, **IM-23**, 264–267 (1974).
- Eck R. E., D. J. Scalapino, and B. N. Taylor. Self-detection of the ac Josephson current. *Phys. Rev. Lett.*, **13**, 15–18 (1964a).
- Eck R. E., D. J. Scalapino, and B. N. Taylor. Tunnel junction rf modes driven by the ac Josephson current. LT 9, part A, 415–420 (1964b).
- Ehnholm G. J., J. K. Soini, and T. Wiik. Thin film SQUIDs using superconducting tunnel junctions. LT 14, **4**, 234–237 (1975).
- Eilenberger G. Transformation of Gor'kov equation for type II superconductors into transport-like equations. *Z. Phys.*, **214**, 195–213 (1968).
- Eldridge J. M. and J. Matisoo. Measurement of tunnel current density in a metal-oxide-metal system as a function of oxide thickness. LT 12, 427–428 (1970).
- Eldridge J. M. and J. Matisoo. Fabrication of variable current density Josephson junctions. U.S. Patent No. 3, 816, 173, June 11, 1974.

- Eliashberg G. M. The low temperature specific heat of metals. *Zh. Eksp. Teor. Fiz.*, **43**, 1005–1007 (1962). *Sov. Phys. JETP*, **16**, 780–781 (1963).
- Eliashberg G. M. Films superconductivity stimulated by high frequency field. *Zh. Eksp. Teor. Fiz. Pis. Red.*, **11**, 186–188 (1970). *JETP Lett.*, **11**, 114–116 (1970).
- Eliashberg G. M. Inelastic electron collisions and nonequilibrium stationary states in superconductors. *Zh. Eksp. Teor. Fiz.*, **61**, 1254–1272 (1971). *Sov. Phys. JETP*, **34**, 668–676 (1972).
- Emmanuel A., G. B. Donaldson, W. T. Band, and D. Dew-Hughes. Barriers formation in lead-based tunnel junctions studied by surface techniques. *ASC* **74**, 763–765 (1974).
- Ernè S. N. Private communication (1978a).
- Ernè S. N. On the theory of the resistive-SQUID-thermometer. In *Proceedings of the 5th International Conference on Noise in Physical System* (D. Wolf, Ed.). Springer, Berlin, Heidelberg, New York, 1978b, pp. 260–265.
- Ernè S. N. and H. Lübbig. Dynamics of flux transitions in the SQUID for the hysteretic case. *IC-SQUID* **76**, 579–585 (1976).
- Ernè S. N. and H. Lübbig. Private communication, 1979.
- Ernè S. N. and H. Lübbig. A solution of the Werthamer equation for superconducting tunneling junctions at vanishing temperature ($T=0$). *J. Appl. Phys.*, **51**, 4927–4929 (1980a).
- Ernè S. N. and H. Lübbig. Influence of self-coupling in small Josephson tunnel junction on the lower threshold of the hysteretic I-V characteristic. *ASC* **80** (1980b).
- Ernè S. N. and H. Luther. Anomalous behavior of the rf-SQUID in the non-hysteretic case: dc flux dependence of the output signal with period $\phi_0/2$. *LT15*, 1208–1209 (1978).
- Ernè S. N. and R. D. Parmentier. Microwave oscillators based on the resonant propagation of fluxons in long Josephson junctions. *J. Appl. Phys.*, **51**, 5025–5029 (1980).
- Ernè S. N. and G. L. Romani, private communication, 1980.
- Ernè S. N., H. D. Hahlbohm, and H. Lübbig. Theory of rf-biased superconducting quantum interference device for nonhysteretic regime. *J. Appl. Phys.*, **47**, 5440–5442 (1976).
- Esposito F. Computation of V-I characteristics of Josephson junctions in the presence of fluctuations. Laboratorio di Cibernetica CNR, Arco Felice, Italy, Internal Report LC78, April 23, 1978.
- Fack H. and V. Kose. Maximal output power of point-contact Josephson junctions. *J. Appl. Phys.*, **42**, 322–323 (1971).
- Falco C. M. Phase-space of a driven, damped pendulum (Josephson weaklink). *Am. J. Phys.*, **44**, 733–740 (1976).
- Falco C. M. and W. H. Parker. Operating Characteristics of thin film r.f. biased SQUID's. *J. Appl. Phys.*, **46**, 3238–3243 (1975).
- Falco C. M., W. H. Parker, and S. E. Trullinger. Observation of a phase-modulated quasi-particle current in superconducting weak links. *Phys. Rev. Lett.*, **31**, 933–936 (1973). Erratum. *Phys. Rev. Lett.*, **31**, 1476 (1973).
- Falco C. M., W. H. Parker, S. E. Trullinger, and P. K. Hansma. Effect of thermal noise on current-voltage characteristics of Josephson junctions. *Phys. Rev.*, **B10**, 1865–1873 (1974).
- Faraci G., G. Giaquinta, and N. A. Mancini. Superconducting tunnel junctions with a nonconventional insulator. *Phys. Lett.*, **30A**, 400–401 (1969).
- Faris S. M. Loop decoder for Josephson memory arrays. *IEEE J. Sol. State Circ.*, **SC-14**, 699–707 (1979).
- Faris S. M. and A. Davidson. Josephson edge detector, a novel switching element. *IEEE Trans. Mag.*, **MAG-15**, 416–419 (1979).
- Feldman M. J. Theory of the unbiased Josephson junction parametric amplifier. Ph.D. Thesis, University of California, Berkeley (1975).
- Feldman M. J. The thermally saturated SUPARAMP. *J. Appl. Phys.*, **48**, 1301–1310 (1977).

- Feldman M. J., P. T. Parrish, and R. Y. Chiao. Parametric amplification by unbiased Josephson junctions. *J. Appl. Phys.*, **46**, 4031–4042 (1975).
- Ferrell R. A. and R. E. Prange. Self-field limiting of Josephson tunneling of superconducting electron pairs. *Phys. Rev. Lett.*, **10**, 479–481 (1963).
- Fetter A. L. and M. J. Stephen. Fluctuations in a Josephson junction. *Phys. Rev.*, **168**, 475–480 (1968).
- Feuchtwang T. E. Tunneling theory without the transfer Hamiltonian formalism. I. *Phys. Rev.*, **B10**, 4121–4134 (1974a).
- Feuchtwang T. E. Tunneling theory without the transfer Hamiltonian formalism. II. Resonant and inelastic tunneling across a junction of finite width. *Phys. Rev.*, **B10**, 4135–4150 (1974b).
- Feuchtwang T. E. Theory of tunneling without transfer Hamiltonian: Relation between continuum and discrete formalisms, and equivalence with elementary theory for noninteracting systems. *Phys. Rev.*, **B12**, 3979–3983 (1975).
- Feuchtwang T. E. Tunneling theory without the transfer Hamiltonian formalism. IV. The abrupt (zero-width) three-dimensional junction. *Phys. Rev.*, **B13**, 517–530 (1976). Errata. *Phys. Rev.*, **B13**, 3665 (1976).
- Feuer M. D., D. E. Prober, and J. W. Cogdell. Fabrication of submicron Josephson microbridges using optical projection lithography and liftoff technique. FTSE, 317–321 (1978).
- Feynman R. P., R. B. Leighton, and M. Sands. The Schrödinger equation in a classical context: A seminar on superconductivity. In *The Feynman Lectures on Physics*. Vol. III, Addison-Wesley, 1965, chap. 21.
- Finnegan T. F. Versatile microwave integrated circuit holder for thin film superconducting devices. *J. Phys. E: Sci. Instrum.*, **13**, 49–52 (1980).
- Finnegan T. F. and S. Wahlsten. Observation of coherent microwave radiation emitted by coupled Josephson junctions. *Appl. Phys. Lett.*, **21**, 541–544 (1972).
- Finnegan T. F. and S. Wahlsten. Electromagnetic properties of small Josephson junctions coupled to microstrip resonators. *Physica*, **94B**, 219–222 (1978).
- Finnegan T. F., A. Denenstein, and D. N. Langenberg. AC-Josephson effect determination of e/h : A standard of electrochemical potential. *Phys. Rev.*, **B4**, 1487–1522 (1971).
- Finnegan T. F., L. B. Holdeman, and S. Wahlsten. Microwave phenomena on thin film Josephson junctions coupled to a contiguous microstrip resonator. ASC 76, 392–395 (1976).
- Finnegan T. F., J. Wilson, and J. Toots. Interactions in small system of coupled Josephson junction, at microwave frequencies. DEJJ, 199–205 (1973).
- Finnegan T. F., J. Wilson, and J. Toots. Coupling between Josephson junctions and microstrip-lines. ASC 74, 821–824 (1974).
- Finnegan T. F., J. Wilson, and J. Toots. High frequency properties of stable Nb-Nb oxide-Pb Josephson tunnel junctions. IC-SQUID 76, 381–394 (1976).
- Fiske M. D. Temperature and magnetic field dependence of the Josephson tunneling current. *Rev. Mod. Phys.*, **36**, 221–222 (1964).
- Fogel M. B., S. E. Trullinger, A. R. Bishop, and J. A. Krumhansl. Classical particle-like behavior of sine-Gordon solitons in scattering potentials and applied fields. *Phys. Rev. Lett.*, **36**, 1411–1414 (1976).
- Fogel M. B., S. E. Trullinger, A. R. Bishop, and J. A. Krumhansl. Dynamics of sine-Gordon solitons in the presence of perturbations. *Phys. Rev.*, **B15**, 1578–1592 (1977).
- Folens G., K. Schwidtal, and Y. Bruynseraede. Study of superconducting proximity effect in the aluminium-lead system by electron tunnelling. *Thin Solid Films*, **34**, 255–258 (1976).
- Forgacs R. L. and A. Warnick. Lock-on magnetometer utilizing a superconducting sensor. *IEEE Trans. Instrum. Meas.*, **IM-15**, 113–120 (1966).
- Forgacs R. L. and A. Warnick. Digital-analog magnetometer utilizing superconducting sensor. *Rev. Sci. Instrum.*, **38**, 214–220 (1967).

- Fu C. Y. and T. Van Duzer. Thermally cyclable lead-alloy Josephson junctions. *Bull. Am. Phys. Soc.*, **21**, 339 (1976).
- Fujita T., S. Kosaka, T. Ohtsuka, and Y. Onodera. Fabrication and performance of NbN thin film planar SQUIDs. *ASC* 74, 739–742 (1974).
- Fulde P. Tunneling density of states for a superconductor carrying a current. *Phys. Rev.*, **A137**, 783–787 (1965).
- Fulde P. and K. Maki. Gapless superconductivity induced by metallic contacts. *Phys. Rev. Lett.*, **15**, 675–677 (1965).
- Fulton T. A. Punchthrough and the tunneling cryotron. *Appl. Phys. Lett.*, **19**, 311–313 (1971).
- Fulton T. A. Externally shunted Josephson junctions. *Phys. Rev.*, **B7**, 1189–1193 (1973).
- Fulton T. A. Equivalent circuits and analogs of the Josephson effect. *NASI* 76, 125–187 (1976).
- Fulton T. A. and L. N. Dunkleberger. Experimental flux shuttle. *Appl. Phys. Lett.*, **22**, 232–233 (1973).
- Fulton T. A. and L. N. Dunkleberger. Origin of hysteresis in the I - V curves of point-contact junctions. *J. Appl. Phys.*, **45**, 2283–2285 (1974a).
- Fulton T. A. and L. N. Dunkleberger. Lifetime of the zero-voltage state in Josephson tunnel junctions. *Phys. Rev.*, **B9**, 4760–4768 (1974b).
- Fulton T. A. and R. C. Dynes. Current-phase relations in superconducting bridges. *Phys. Rev. Lett.*, **25**, 794–797 (1970).
- Fulton T. A. and R. C. Dynes. Switching to zero voltage in Josephson tunnel junctions. *Solid State Comm.*, **9**, 1069–1073 (1971).
- Fulton T. A. and R. C. Dynes. Single vortex propagation in Josephson tunnel junctions. *Solid State Comm.*, **12**, 57–61 (1973).
- Fulton T. A. and D. E. McCumber. DC Josephson effect for strong-coupling superconductors. *Phys. Rev.*, **175**, 585–586 (1968).
- Fulton T. A., L. N. Dunkleberger, and R. C. Dynes. Quantum interference properties of double Josephson junctions. *Phys. Rev.*, **B6**, 855–875 (1972).
- Fulton T. A., R. C. Dynes, and P. W. Anderson. The flux shuttle. A Josephson junction shift register employing single flux quanta. *Proc. IEEE*, **61**, 28–35 (1973).
- Fulton T. A., J. H. Magerlein, and L. N. Dunkleberger. A Josephson logic design employing current-switched junctions. *ASC* 76, 56–58 (1976).
- Galaiko V. P., A. V. Svidzinskii, and V. A. Slyusarev. *Zh. Eksp. Teor. Fiz.*, **56**, 835–840 (1969). *Sov. Phys. JETP*, **29**, 454–456 (1969).
- Gallo C. H., L.-K. Wang, and B. S. Deaver, Jr. Properties of variable thickness bridges on GaAs substrates. *FTSE*, 349–353 (1978).
- Galkin, A. A., B. U. Borodai, V. M. Svistunov, and V. N. Tarasenko. Concerning certain features of the stationary Josephson effect. *Zh. Eksp. Teor. Fiz. Pis. Red.*, **8**, 521–524 (1968). *JETP Lett.*, **8**, 318–320 (1968).
- Galkin A. A., B. I. Borodai, L. A. Zilberman, Yu. M. Ivanchenko, and V. M. Svistunov. Influence of low-frequency fluctuations on superconducting tunneling. *Zh. Eksp. Teor. Fiz.*, **60**, 651–658 (1971). *Sov. Phys. JETP*, **33**, 354–357 (1971).
- Garno J. P. Oxidation of lead tunnel barriers in a humidity-controlled oxygen-regulated atmosphere. *J. Appl. Phys.*, **48**, 4627–4629 (1977).
- Gheewala T. R. Josephson logic circuits based on nonlinear current injection in interferometer device. *Appl. Phys. Lett.*, **33**, 781–783 (1978).
- Gheewala T. R. A 30-ps Josephson current injection logic (CIL). *IEEE J. Solid State Cir.*, **SC-14**, 787–793 (1979).
- Gheewala T. R. Design of 2.5-micrometer Josephson current injection logic (CIL). *IBM J. Res. Develop.*, **24**, 130–142 (1980).

- Giaever I. Energy gap in superconductors measured by electron tunneling. *Phys. Rev. Lett.*, **5**, 147–148 (1960a).
- Giaever I. Electron tunneling between two superconductors. *Phys. Rev. Lett.*, **5**, 464–466 (1960b).
- Giaever I. Detection of the ac Josephson effect. *Phys. Rev. Lett.*, **22**, 904–906 (1965).
- Giaever I. Photosensitive tunneling and superconductivity. *Phys. Rev. Lett.*, **20**, 1286–1289 (1968).
- Giaever I. and K. Megerle. Study of superconductors by electron tunneling. *Phys. Rev.*, **122**, 1101–1111 (1961).
- Giaever I. and K. Megerle. The superconducting tunnel junction as an active device. *IRE Trans. Electron Devices*, ED-9, 459–461 (1962).
- Giaever I. and H. R. Zeller. Subharmonic gap structure in superconducting tunnel junctions. ICSS, 455–461 (1969a).
- Giaever I. and H. R. Zeller. Tunneling into and through evaporated semiconducting films. *J. Vac. Sci. Tech.*, **6**, 502–508 (1969b).
- Giaever I. and H. R. Zeller. Subharmonic structure in superconducting tunneling. *Phys. Rev.*, **B1**, 4278–4288 (1970).
- Giffard R. P., R. A. Webb, and J. C. Wheatley. Principles and methods of low-frequency electrical and magnetic measurements using an rf-biased point-contact superconducting device. *J. Low Temp. Phys.*, **6**, 533–611 (1972).
- Gilbert A. Effect de proximité entre un métal normal et un supraconducteur. *Ann. Phys.*, **2**, 203–252 (1977).
- Gilbert A., J. P. Romagnan, and E. Guyon. Determination of the energy gap of a superconducting tin-lead sandwich by electron tunneling. *Solid State Comm.*, **9**, 1295–1297 (1971).
- Gilbert A., J. P. Romagnan, and E. Guyon. Tunneling and Josephson experiments in normal-superconducting sandwiches. LT 13, **3**, 312–315 (1972).
- Gilbert A., C. Van Haesendonck, L. Van den Dries, and Y. Bruynseraede. Temperature dependence of the maximum d.c. Josephson current in superconducting proximity junctions. *Solid State Comm.*, **31**, 109–111 (1979).
- Ginzburg V. L. Critical current for superconducting films. *Dokl. Adad. Nauk SSSR*, **118**, 464 (1958). *Sov. Phys. Dokl.*, **3**, 102–105 (1958).
- Ginzburg V. L. Magnetic flux quantization in a superconducting cylinder. *Zh. Eksp. Teor. Fiz.*, **42**, 299–302 (1962). *Sov. Phys. JETP*, **15**, 207–209 (1962).
- Ginzburg V. L. and L. G. Landau. On the theory of superconductivity. *Zh. Eksp. Teor. Phys.*, **20**, 1064 (1950). Also in *Collected Papers of L. D. Landau* (D. Ter Haar, Ed.). Gordon and Breach, New York, 1965, pp. 546–568.
- Goldman A. M. Persistent currents and flux quantization in superconducting rings interrupted by Josephson junctions. LT 9, part A, 421–423 (1964).
- Goldman A. M. Macroscopic quantum effects in superconducting rings interrupted by Josephson junctions. Ph.D. Thesis, Stanford University, Stanford (1965).
- Goldman A. M. and P. J. Kreisman. Meissner effect and vortex penetration in Josephson junctions. *Phys. Rev.*, **164**, 544–547 (1967).
- Goldman A. M., P. J. Kreisman, and D. J. Scalapino. Metastable current-carrying states of weakly coupled superconductors. *Phys. Rev. Lett.*, **15**, 495–499 (1965).
- Golovashkin A. I. and A. N. Lykov. Investigation of bridge junctions made of the high temperature superconductor Nb₃Sn. *Zh. Eksp. Teor. Fiz.*, **74**, 214–223 (1978). *Sov. Phys. JETP*, **47**, 110–115 (1978).
- Golovashkin A. I., I. S. Levchenko, A. N. Lykov, and A. N. Makhashvili. Quantum interference on Nb₃Sn film contacts at hydrogen temperatures. *Pis. Zh. Eksp. Teor. Fiz.*, **24**, 565–569 (1976). *JETP Lett.*, **24**, 521–525 (1976).
- Golovashkin A. I., A. N. Lykov, V. I. Novikov, and B. G. Zhurkin. AC Josephson effect in Nb₃Sn thin film bridges. *J. Phys. Lett.*, **40**, L77–L79 (1979).

- Golub A. A. Dynamic properties of short superconducting filaments. *Zh. Eksp. Teor. Fiz.*, **71**, 341–347 (1976). *Sov. Phys. JETP*, **44**, 178–181 (1976).
- Goodall F., F. Bale, S. Rudner, T. Claeson, and T. F. Finnegan. Parametric amplification in Josephson tunnel junction arrays at 33 GHz. *ASC* 78, 458–461 (1978).
- Goodkind J. M. and D. L. Stolfa. The superconducting magnetic flux detector. *Rev. Sci. Instrum.*, **41**, 799–807 (1970).
- Goodman W. L. and B. S. Deaver, Jr. Detailed measurements of the quantized flux states of hollow superconducting cylinders. *Phys. Rev. Lett.*, **24**, 870–873 (1970).
- Goodman W. L., V. W. Hesterman, L. H. Rorden, and W. S. Goree. Superconducting instrument systems. *Proc. IEEE*, **61**, 20–27 (1973).
- Gor'kov L. P. On the energy spectrum of superconductors. *Zh. Eksp. Teor. Fiz.*, **34**, 735–739 (1958). *Sov. Phys. JETP*, **34**, 505–508 (1958).
- Gor'kov L. P. Microscopic derivation of the Ginzburg-Landau equations in the theory of superconductivity. *Zh. Eksp. Teor. Fiz.*, **36**, 1918–1923 (1959). *Sov. Phys. JETP*, **36**, 1364–1367 (1959).
- Gor'kov L. P. and G. M. Eliashberg. Generalization of the Ginzburg-Landau equations for non-stationary problems in the case of alloys with paramagnetic impurities. *Zh. Eksp. Teor. Fiz.*, **54**, 612–625 (1968). *Sov. Phys. JETP*, **27**, 328–334 (1968).
- Gor'kov L. P. and G. M. Eliashberg. Dynamical properties of gapless superconductors. *J. Low Temp. Phys.*, **2**, 161–172 (1970).
- Gorter C. J. and H. B. G. Casimir. On Supraconductivity. *Physica*, **1**, 306–320 (1934).
- Gou Y. S. and R. I. Gayley. Self-resonant modes in high- Q Josephson tunnel junctions. *Phys. Rev.*, **B10**, 4584–4592 (1974).
- Gradshteyn I. S. and I. M. Ryshik. *Table of Integrals, Series and Products*, Academic Press, 1980.
- Graeffe R. and T. Wiik. Preparation of Josephson junctions by plasma oxidation of Nb. *J. Appl. Phys.*, **42**, 2146–2147 (1971).
- Gray K. E. ISS depth profile analysis of anodized niobium. *Appl. Phys. Lett.*, **27**, 462–464 (1975).
- Grebe K., I. Ames, and A. Ginzberg. Making of deposited thin films by means of an aluminium-photoresist composite. *J. Vac. Sci. Tech.*, **11**, 458–460 (1974).
- Greenspoon S. and H. J. T. Smith. Study of the superconducting proximity effects by Josephson tunneling. *Can. J. Phys.*, **49**, 1350–1360 (1971).
- Greger-Hansen P. E. and M. T. Levinsen. Normal-state resistance as the determining parameter in the behaviour of Dayem bridges with sinusoidal current-phase relations. *Phys. Rev. Lett.*, **27**, 847–849 (1971).
- Greger-Hansen P. E. and G. R. Pickett. Subharmonic energy gap structure and gap-enhancement by the Josephson radiation in small Dayem bridges. *DEJJ*, 145–152 (1973).
- Greger-Hansen P. E., M. T. Levinsen, and G. F. Pedersen. A sinusoidal current-phase relation for superconducting thin-film microbridges. *J. Low Temp. Phys.*, **7**, 99–117 (1972).
- Greger-Hansen P. E., E. Hendriks, M. T. Levinsen, and G. F. Pedersen. Equivalent circuits for small Dayem bridges. *ASC* 72, 597–607 (1972).
- Greiner J. H. Josephson tunneling barriers by rf sputter etching in an oxygen plasma. *J. Appl. Phys.*, **42**, 5151–5155 (1971).
- Greiner J. H. Oxidation of lead films by sputter etching in an oxygen plasma. *J. Appl. Phys.*, **45**, 32–37 (1974).
- Greiner J. H., S. Basavaiah, and I. Ames. Fabrication of experimental tunneling circuits. *J. Vac. Sci. Tech.*, **11**, 81–84 (1974).
- Grella G. and M. Marinaro. Special solutions of the Sine-Gordon equation in 2+1 dimensions. *Lett. Nuovo Cimento*, **23**, 459–464 (1978).

- Grella G. and R. D. Parmentier. Solutions of the Sine-Gordon equation in 2+0 dimensions. *Lett. Nuovo Cimento*, **25**, 294–296 (1979).
- Grimes C. C. and S. Shapiro. Millimeter-wave mixing with Josephson junctions. *Phys. Rev.*, **169**, 397–406 (1968).
- Grimes C. C., P. L. Richards, and S. Shapiro. Josephson-effect far-infrared detector. *J. Appl. Phys.*, **39**, 3905–3912 (1968).
- Groff R. P. and R. D. Parks. Fluxoid quantization and field induced depairing in a hollow superconducting microcylinder. *Phys. Rev.*, **176**, 567–580 (1968).
- Gubankov V. N., V. P. Koshelets, and G. A. Ovsyannikov. Observation of microwave Josephson radiation in thin-film superconducting bridges. *Zh. Eksp. Teor. Fiz. Pis. Red.*, **21**, 489–494 (1975). *JETP Lett.*, **21**, 226–227 (1975).
- Gubankov V. N., V. P. Koshelets, and G. A. Ovsyannikov. Experimental investigation of the microwave-impedance peculiarities of superconducting thin-film bridges. *ASC* 76, 228–232 (1976a).
- Gubankov V. N., V. P. Koshelets, and G. A. Ovsyannikov. Coherent effects in superconducting bridges of variable thickness. *Zh. Eksp. Teor. Fiz.*, **71**, 348–358 (1976b). *Sov. Phys. JETP*, **44**, 181–186 (1976).
- Gubankov V. N., V. P. Koshelets, and G. A. Ovsyannikov. Properties of Josephson thin film variable-thickness microbridges. *Zh. Eksp. Teor. Fiz.*, **73**, 1435–1444 (1977). *Sov. Phys. JETP*, **46**, 755–760 (1977).
- Gubankov V. N., V. P. Koshelets, and G. A. Ovsyannikov. Nonequilibrium phenomena in variable thickness bridges of submicron dimensions. *LT* 15, 535–536 (1978).
- Gubankov V. N., V. P. Koshelets, K. K. Likharev, and G. A. Ovsyannikov. Coherent motion of vortices in superconducting bridges of large dimensions. *Zh. Eksp. Teor. Fiz. Pis. Red.*, **18**, 292–295 (1973). *JETP Lett.*, **18**, 171–173 (1973).
- Gubankov V. N., L. S. Kuz'min, K. K. Likharev, and V. K. Semenov. Non-Josephson generation in a resonator with a superconducting Josephson junction. *Zh. Eksp. Teor. Fiz.*, **68**, 2301–2314 (1975). *Sov. Phys. JETP*, **41**, 1150–1156 (1975).
- Gueret P. Flux-quantization effects in large inductance loops containing Josephson junctions. *J. Appl. Phys.*, **44**, 1771–1773 (1973).
- Gueret P. Experimental observation of the switching transients resulting from single flux quantum transitions in superconducting Josephson devices. *Appl. Phys. Lett.*, 426–428 (1974a).
- Gueret P. Storage and detection of a single flux quantum in Josephson junction devices. *ASC* 74, 751–754 (1974b).
- Gueret P. A simple theory of resonance amplitudes in Josephson interferometers. *Appl. Phys. Lett.*, **35**, 889–891 (1979).
- Gueret P., T. O. Mohr, and P. Wolf. Single flux-quantum memory cells. *ASC* 76, 52–55 (1976).
- Gundlach K. H. and J. Kadlec. a.c. Josephson-like effect with linear periodic current phase relation. *J. Low Temp. Phys.*, **26**, 603–612 (1977).
- Gundlach K. H. and J. Kadlec. Resistively shunted Josephson tunnel junctions. *Solid State Comm.*, **25**, 1149–1151 (1978).
- Guthmann C., J. Maurier, M. Berlin, J. Bok, and A. Libchaber. Dynamic behavior of superconducting microbridges. *Phys. Rev.*, **B11**, 1909–1913 (1975).
- Hahlbohm H. D., H. Lübbig, and H. Luther. Possible influence of the voltage dependence of the Josephson tunneling current $I[V, \varphi]$ on the corresponding current-voltage characteristic. *LT14*, **4**, 140–143 (1975).
- Hahlbohm H. D., A. Hoffmann, H. Lübbig, H. Luther, and S. Seeck. Calculation of rf-induced current-voltage characteristics of a measured Josephson tunnel junction. *Phys. Status Solidi (a)*, **13**, 607–612 (1972).

- Halse M. R. and J. C. Taunton. Measurement of the $\cos\varphi$ term in Josephson tunneling. IC-SQUID 76, 171–178 (1976).
- Hamilton C. A. R.F. induced effects in Josephson tunnel junctions. Ph.D. Thesis, University of Rochester, Rochester (New York) (1971), unpublished.
- Hamilton C. A. Analog simulation of a Josephson junction. *Rev. Sci. Instrum.*, **43**, 445–447 (1972a).
- Hamilton C. A. Frequency dependence of the Josephson current. *Phys. Rev.*, **B5**, 912–923 (1972b).
- Hamilton C. A. and S. Shapiro. RF-induced effects in superconducting tunnel junctions. *Phys. Rev.*, **B2**, 4494–4503 (1970).
- Hamilton C. A. and S. Shapiro. Experimental demonstration of the Riedel peak. *Phys. Rev. Lett.*, **26**, 426–428 (1971).
- Hansma P. K. Superconducting single-junction interferometer with small critical currents. *J. Appl. Phys.*, **44**, 4191–4194 (1973).
- Hansma P. K. A new method for fabricating niobium oxide barrier Josephson junctions. *J. Appl. Phys.*, **45**, 1472–1473 (1974).
- Hansma P. K. and G. I. Rochlin. Josephson weak links: Shunted-junction and mechanical-model results. *J. Appl. Phys.*, **43**, 4721–4727 (1972).
- Hansma P. K., G. I. Rochlin, and J. N. Sweet. Externally shunted Josephson junctions: Generalized weak links. *Phys. Rev.*, **B4**, 3003–3014 (1971).
- Harding J. I. and J. E. Zimmerman. Quantum phase fluctuations in resistive circuits containing weakly superconducting junctions. *J. Appl. Phys.*, **41**, 1581–1588 (1970).
- Harris E. P. Preparation of superconducting weak links in molybdenum films by ion implantation. *ASC* 74, 785–788 (1974).
- Harris E. P. Properties of superconducting weak links produced by ion implantation. *J. Vac. Sci. Tech.*, **12**, 1383–1386 (1975).
- Harris E. P. Transition from Josephson behavior to depairing behavior in ion-implanted molybdenum weak links. *Solid State Comm.*, **20**, 449–451 (1976).
- Harris R. E. Cosine and other terms in the Josephson tunneling current. *Phys. Rev.*, **B10**, 84–94 (1974a).
- Harris R. E. Comments on the roles of the cosine term and the reactive part of the quasiparticle term in the Josephson tunneling current. *ASC* 74, 856–857 (1974b).
- Harris R. E. Josephson tunneling current in the presence of a time-dependent voltage. *Phys. Rev.*, **B11**, 3329–3333 (1975a).
- Harris R. E. Intrinsic response time of a Josephson tunnel junction. *Phys. Rev.*, **B13**, 3818–3821 (1976a).
- Harris R. E. Numerical evaluation of the response of a Josephson tunnel junction in an arbitrary circuit. *J. Appl. Phys.*, **48**, 5188–5190 (1977).
- Harris R. E. and C. A. Hamilton. Fast superconducting instruments. FTSE, 448–458 (1978).
- Hartland A., T. J. Witt, D. Reymann, and T. F. Finnegan. An international direct comparison of two Josephson-effect voltage standards. *IEEE Trans. Instrum. Meas.*, **IM-27**, 470–474 (1978).
- Harvey I. K. A precise low temperature dc ratio transformer. *Rev. Sci. Instrum.*, **43**, 1626–1629 (1972).
- Hasselberg L. E., M. T. Levinsen, and M. R. Samuels. Theories of subharmonic gap structures in superconducting junctions. *Phys. Rev.*, **B9**, 3757–3765 (1974).
- Hasselberg L. E., M. T. Levinsen, and M. R. Samuels. Subharmonic gap structure and subharmonic Josephson steps. *J. Low Temp. Phys.*, **21**, 567–587 (1975).
- Hatzakis M., B. J. Canavello, and J. M. Shaw. Single-step optical lift-off process. *IBM J. Res. Develop.*, **24**, 452–460 (1980).
- Hauffe K. *Oxidation of Metals*. Plenum, New York, 1965.

- Hauser J. J. Gapless superconductivity induced by the proximity effect. *Phys. Rev.*, **164**, 558–565 (1967).
- Hawkins G. and J. Clarke. Nb-Nb thin-film Josephson junctions. *J. Appl. Phys.*, **47**, 1616–1619 (1976).
- Henkels W. H. An elementary logic circuit employing superconducting Josephson tunneling. *ASC* **74**, 860–863 (1974).
- Henkels W. H. and W. W. Webb. Intrinsic fluctuations in the driven Josephson oscillator. *Phys. Rev. Lett.* **26**, 1164–1167 (1971).
- Henkels W. H. and H. H. Zappe. An experimental 64-bit decoded Josephson NDRO random access memory. *IEEE J. Solid State Cir.*, **SC-13**, 591–599 (1978).
- Herrel D. J. A Josephson tunneling logic adder. *ASC* **74**, 864–867 (1974a).
- Herrel D. J. Femtojoule Josephson tunneling logic gates. *IEEE J. Solid State Cir.*, **SC-9**, 277–282 (1974b).
- Herrel D. J. An experimental multiplier circuit based on superconducting Josephson devices. *IEEE J. Solid State Cir.*, **SC-10**, 360–368 (1975).
- Herrel D. J., P. C. Arnett, and M. Klein. High-performance Josephson interferometer latching logic and power supplies. *FTSE*, 470–478 (1978).
- Hida K. and Y. Ono. Theory of the $\cos \varphi$ term in the Josephson tunneling current. *J. Low Temp. Phys.*, **29**, 355–367 (1977).
- Hilsh P. Zumverhalten von Supraleitern im kontakt mit Normalleitern. *Z. Phys.*, **167**, 511–524 (1962).
- Hirota R. Exact solution of the sine-Gordon equation for multiple collisions of solitons. *J. Phys. Soc. (Japan)*, **33**, 1459–1463 (1972).
- Hirschkoff E. C., O. G. Symko, and J. C. Wheatley. Magnetization of dilute Cu-Mn alloys at very low temperatures. *Phys. Lett.*, **33A**, 19–20 (1970).
- Hirschkoff E. C., O. G. Symko, and J. C. Wheatley. Magnetic behaviour of dilute Cu (Mn) alloys at very low temperatures. *J. Low Temp. Phys.*, **5**, 155–176 (1971).
- Hoel L. S., W. H. Keller, J. E. Nordman, and A. C. Scott. Niobium superconductive tunnel diode integrated circuit arrays. *Solid State Electron.*, **15**, 1167–1173 (1972).
- Hoening H. E., R. M. Wang, G. R. Rossman, and J. E. Mercereau. Magnetochemical studies with a new ultrasensitive superconducting quantum magnetometer. *ASC* **72**, 570–574 (1972).
- Hoegaard Jensen H. and P. E. Lindelof. Comparison between the resistively shunted Josephson junction model incorporating a voltage-dependent current-phase relation and experiments on superconducting thin-film microbridges. *J. Low Temp. Phys.*, **23**, 469–476 (1976).
- Holdeman L. B., and C. C. Chang. Josephson voltage standards: An application for cryocoolers? In *Applications of Closed-Cycle Cryocoolers to Small Superconducting Devices* (J. E. Zimmerman and T. M. Flynn, Eds.). N.B.S., Washington, 1978, pp. 243–245.
- Holdeman L. B., B. F. Field, J. Toots, and C. C. Chang. Prototype for a commercial Josephson-effect voltage standard. *FTSE*, 182–186 (1978).
- Hollenhorst J. N. and R. P. Giffard. High sensitivity microwave SQUID. *ASC* **78**, 474–477 (1978).
- Holm R. and W. Meissner. Messungen mit hilfe von flüssigem helium XIII. kontaktwiderstand zwischen supraleitern und nichtsupraleitern. *Z. Phys.*, **74**, 715–736 (1932).
- Howard R. E. A refractory lift-off process with applications to high TC superconducting circuits. *Appl. Phys. Lett.* **33**, 1034–1035 (1978).
- Howard R. E., D. A. Rudman, and M. R. Beasley. Josephson properties of Nb_3Sn/Pb tunnel junction. *Appl. Phys. Lett.*, **33**, 671–673 (1978).
- Howard R. E., E. L. Hu, L. D. Jackel, L. A. Fetter, and R. H. Bosworth. Small area high-current-density Josephson junctions. *Appl. Phys. Lett.* **35**, 879–881 (1979).

- Hsiang T. Y. and D. K. Finnemore. Superconducting critical currents for thick, clean superconductor normal metal-superconductor junctions. *Phys. Rev.* **B22**, 154–163 (1980).
- Hu E. L., L. D. Jackel, and R. W. Epworth. Josephson tunneling through Ge-Sn barriers. FTSE, 380–388 (1978).
- Hu E. L., L. D. Jackel, R. W. Epworth, and L. A. Fetter. Experiments on Ge-Sn barrier Josephson junctions. ASC 78, 585–588 (1978).
- Huang C. L. and T. Van Duzer. Single-crystal silicon-barrier Josephson junctions. ASC 74, 766–769 (1974a).
- Huang C. L. and T. Van Duzer. Josephson tunneling through locally thinned silicon wafers. *Appl. Phys. Lett.*, **25**, 753–756 (1974b).
- Huebener R. P. and H. L. Watson. Voltage steps in the current-induced resistive state of thin-film type-I superconductors. *Phys. Rev.* **B9**, 3725–3729 (1974).
- Hunt T. K. and J. E. Mercereau. Quantum phase correlation in small superconductors. *Phys. Rev. Lett.* **18**, 551–553 (1967).
- Irie F., K. Hamasaki, and K. Yoshida. Current-steps in large Josephson tunnel junctions. LT 15, 1236–1237 (1978).
- Ishii C. Josephson current through a junction with normal metal barrier. LT 12, 435–436 (1970).
- Ishii C. Thermodynamical properties of Josephson junction with a normal metal barrier. *Prog. Theor. Phys.*, **47**, 1466–1481 (1972).
- Ivanchenko Yu. M. and L. A. Zil'berman. Destruction of Josephson current by fluctuations. *Zh. Eksp. Teor. Fiz. Pis. Red.*, **8**, 189–192 (1968a). *JETP Lett.*, **8**, 113–115 (1968).
- Ivanchenko Yu. M. and L. A. Zil'berman. The Josephson effect in small tunnel contacts. *Zh. Eksp. Teor. Fiz.*, **55**, 2395–2402 (1968b). *Sov. Phys. JETP*, **28**, 1272–1276 (1969).
- Ivanchenko Yu. M., A. V. Svidzinskii, and V. A. Slyusarev. Electrodynamics of the Josephson effect. *Zh. Eksp. Teor. Fiz.*, **51**, 194–200 (1966). *Sov. Phys. JETP*, **24**, 131–135 (1967).
- Ivanov Z. G., M. Yu. Kupriyanov, K. K. Likharev, and O. V. Snigrev. Boundary conditions for the Usadel equations and properties of dirty S-N-S sandwiches. LT 15, 556–557 (1978).
- Ivlev B. I. Resistive states in superconductor junctions. *Zh. Eksp. Teor. Fiz.*, **75**, 1771–1777 (1978). *Sov. Phys. JETP*, **48**, 893–895 (1978).
- Ivlev B. I. Nonequilibrium phenomena in superconductors. *Physics Reviews—Sov. Sci. Rev. A* (I. M. Khalatnikov, Ed.), Vol. 1, pp. 85–132 (1979).
- Ivlev B. I. and G. M. Eliashberg. Influence of nonequilibrium excitations on the properties of superconducting films in a high-frequency field. *Zh. Eksp. Teor. Fiz. Pis. Red.*, **13**, 464–468 (1971). *JETP Lett.*, **13**, 333–336 (1971).
- Ivlev B. I., S. G. Lisitsyn, and G. M. Eliashberg. Nonequilibrium excitations in superconductors in high-frequency fields. *J. Low Temp. Phys.*, **10**, 449–468 (1973).
- Jackel L. D. and R. A. Buhrman. Noise in the rf SQUID. *J. Low Temp. Phys.*, **19**, 201–246 (1975).
- Jackel L. D., R. A. Buhrman, and W. W. Webb. Direct measurement of current-phase relations in superconducting weak links. *Phys. Rev.*, **B10**, 2782–2785 (1974).
- Jackel L. D., J. Kurkijärvi, J. E. Lukens, and W. W. Webb. Intrinsic fluctuations in a superconducting “flux detector” ring closed by a Josephson junctions: Theory and experiment. LT 13, 3, 705–708 (1972).
- Jackel L. D., W. W. Webb, J. E. Lukens, and S. S. Pei. Measurement of the probability distribution of thermally excited fluxoid quantum transitions in a superconducting ring closed by a Josephson junction. *Phys. Rev.*, **B9**, 115–118 (1974).
- Jackel L. D., J. M. Warlaumont, T. D. Clark, J. C. Brown, R. A. Buhrman, and M. T. Levinsen. Superconducting weak-link current-phase relations. *Appl. Phys. Lett.*, **28**, 353–355 (1976a).
- Jackel L. D., W. H. Henkels, J. M. Warlaumont, and R. A. Buhrman. Current-phase relations as determinants of superconducting thin-film weak-link I - V characteristics. *Appl. Phys. Lett.*, **29**, 214–216 (1976b).

- Jackson J. D. *Classical Electrodynamics*. John Wiley, New York, 1967.
- Jacobson D. A. Ginzburg-Landau equations and the Josephson effect. *Phys. Rev.*, **A138**, 1066–1070 (1965).
- Jahn M. T. and Y. H. Kao. Temperature dependence and microwave enhancement of the critical current of superconducting microbridges. *J. Low Temp. Phys.*, **13**, 175–183 (1973).
- Jahnke E. and F. Emde. *Tables of Functions*. 4th ed., Dover, New York, 1945.
- Jaklevic R. C., J. Lambe, A. H. Silver, and J. E. Mercereau. Quantum interference effects in Josephson tunneling. *Phys. Rev. Lett.*, **12**, 159–160 (1964a).
- Jaklevic R. C., J. J. Lambe, A. H. Silver, and J. E. Mercereau. Quantum interference from a static vector potential in a field-free region. *Phys. Rev. Lett.*, **12**, 274–275 (1964b).
- Jaklevic R. C., J. Lambe, J. E. Mercereau, and A. H. Silver. Macroscopic quantum interference in superconductors. *Phys. Rev.*, **A140**, 1628–1637 (1965).
- Janik R., L. Morelli, N. C. Cirillo, Jr., J. N. Lecheyet, W. D. Gregory, and W. L. Goodman. Effects of laser irradiation on weak link devices. *ASC* **74**, 687–689 (1974).
- Janocko M. A., J. R. Gavalier, and C. K. Jones. Observation of microwave induced steps in the I - V characteristics of Mo-Re Dayem bridges at temperatures above 12 K. *ASC* **72**, 608–612 (1972).
- Janocko M. A., J. R. Gavalier, and C. K. Jones. Observation of the Josephson effect in Nb₃Ge Dayem bridges. *ASC* **74**, 880–882 (1974).
- Jillie D. W., J. E. Lukens, and Y. H. Kao. Observation of microwave synchronization of thin film microbridge arrays. *ASC* **74**, 671–673 (1974).
- Jillie D. W., J. E. Lukens, and Y. H. Kao. Voltage locking in two coupled microbridges Josephson junctions. *ASC* **76**, 578–580 (1976).
- Johnson W. J. Nonlinear wave propagation on superconducting tunneling junctions. Ph.D. Thesis, University of Wisconsin, Madison (1968).
- Johnson W. J. and A. Barone. Effect of junction geometry on maximum zero-voltage Josephson current. *J. Appl. Phys.*, **41**, 2958–2960 (1970).
- Josephowicz J. and H. J. T. Smith. Tunneling in junctions with CdS barriers. *J. Appl. Phys.*, **44**, 2813–2815 (1973).
- Josephson B. D. The relativistic shift in the Mössbauer effect and coupled superconductors. Dissertation for the annual election of fellows, Trinity College, Cambridge (1962a).
- Josephson B. D. Possible new effects in superconductive tunneling. *Phys. Lett.*, **1**, 251–253 (1962b).
- Josephson B. D. Coupled superconductors. *Rev. Mod. Phys.*, **36**, 216–220 (1964).
- Josephson B. D. Supercurrents through barriers. *Adv. Phys.*, **14**, 419–451 (1965).
- Josephson B. D. Superconducting barriers: The plasma resonance and related properties. In *Quantum Fluids* (D. F. Brewer, Ed.). North Holland, Amsterdam, 1966, pp. 174–179.
- Josephson B. D. Weakly coupled superconductors. In *Superconductivity* (R. D. Parks, Ed.). Vol. 1, Marcel Dekker, New York, 1969, chap. 9, pp. 423–448.
- Josephson B. D. The discovery of tunneling supercurrents. *Rev. Mod. Phys.*, **46**, 251–254 (1974).
- Jutzi W. An inductively coupled memory cell for NDRO with two Josephson junctions. *Cryogenics*, **16**, 81–88 (1976).
- Jutzi W., T. O. Mohr, M. Gasser, and H. P. Gschwind. Josephson junctions with 1 μ m dimensions and with picosecond switching times. *Electron. Lett.*, **8**, 589–591 (1972).
- Kadanoff L. P. and G. Baym. *Quantum Statistical Mechanics*. Benjamin, New York, 1962.
- Kadlec J. and K. H. Gundlach. Current versus voltage source model in Josephson effect. *Phys. Lett.*, **63A**, 149–150 (1977).
- Kalashnik L. I., A. M. Kislov, I. O. Kulik, E. M. Livshits, K. V. Maslov, and A. A. Motornaya. Influence of fluctuations on the electromagnetic properties of the Josephson tunnel junction. *Zh. Tekh. Fiz.*, **42**, 1296–1305 (1972). *Sov. Phys. Tech. Phys.*, **17**, 1029–1035 (1972).

- Kamper R. A. and M. Simmonds. Broadband superconducting quantum magnetometer. *Appl. Phys. Lett.*, **20**, 270–272 (1972).
- Kamper R. A. and J. E. Zimmerman. Noise thermometry with the Josephson effect. *J. Appl. Phys.*, **42**, 132–136 (1971).
- Kanter H. A novel parametric negative-resistance effect in Josephson junctions. *Appl. Phys. Lett.*, **23**, 350–352 (1973a).
- Kanter H. Josephson junction mixer using an external local oscillator. DEJJ, 255–262 (1973b).
- Kanter H. Low noise parametric upconversion with a self-pumped Josephson junction. *J. Appl. Phys.*, **46**, 2261–2263 (1975).
- Kanter H. and A. H. Silver. Self-pumped Josephson parametric amplification. *Appl. Phys. Lett.*, **19**, 515–517 (1971).
- Kanter H. and F. L. Vernon, Jr. Shot noise in Josephson point contacts. *Appl. Phys. Lett.*, **16**, 115–117 (1970a).
- Kanter H. and F. L. Vernon, Jr. Noise voltage in Josephson junctions. *Phys. Lett.*, **32A**, 155–156 (1970b).
- Kanter H. and F. L. Vernon, Jr. Current noise in Josephson point contacts. *Phys. Rev. Lett.*, **25**, 588–590 (1970c).
- Kanter H. and F. L. Vernon. High-frequency response of Josephson point contacts. *J. Appl. Phys.*, **43**, 3174–3183 (1972).
- Kariniemi V., J. Ahopelto, P. J. Karp, and T. E. Katila. The fetal magnetocardiogram. *J. Perinat. Med.*, **2**, 214–216 (1974).
- Karulkar P. C. and J. E. Nordman. Fabrication of Nb-NbO_x-Pb Josephson tunnel junctions using rf glow discharge oxidation. *J. Appl. Phys.*, **50**, 7051–7059 (1979).
- Karulkar P.C. and J. E. Nordman. Study of thin Nb oxide films., *J. Vac. Sci. Technol.* **17**, 462–465 (1980).
- Kasatkin A. L. and A. F. Volkov, Theory of the Josephson effect in Notarys Mercereau bridges, Report on ASC 74 (1974), unpublished.
- Kautz R. L. On a proposed Josephson-effect voltage standard at zero current bias. *Appl. Phys. Lett.*, **36**, 386–388 (1980).
- Keener J. P. and D. W. McLaughlin, A Green's function for a linear equation associated with solitons. *J. Math. Phys.*, **14**, 2008–2013 (1977).
- Keller W. H. and J. E. Nordman. Sputtered thin-film superconductor-semiconductor tunnel junctions. *J. Appl. Phys.*, **42**, 137 (1971) (abstract only).
- Keller W. H. and J. E. Nordman. Niobium thin-film Josephson junctions using a semiconductor barrier. *J. Appl. Phys.*, **44**, 4732–4738 (1973).
- Ketchen M. B. and R. F. Voss. An ultra-low-noise tunnel junction d.c. SQUID. *Appl. Phys. Lett.* **35**, 812–815 (1979).
- Ketchen M. B., J. Clarke, and W. M. Goubau. Present status and future of the d.c. SQUID. FTSE, 22–27 (1978).
- Ketchen M. B., W. M. Goubau, J. Clarke, and G. B. Donaldson. Superconducting thin-film gradiometer. *J. Appl. Phys.*, **49**, 4111–4116 (1978).
- Kirschman R. K. and J. E. Mercereau. Current noise in weak superconductors. *Phys. Lett.* **35A**, 177–178 (1971).
- Kirschman R. K., H. A. Notarys, and J. E. Mercereau. Advances in superconducting quantum electronic microcircuit fabrication. ASC 74, 778–781 (1974).
- Kirschman R. K., J. A. Hutchby, J. W. Burgess, R. P. McNamara, and H. A. Notarys. Comparative studies of ion-implant Josephson effect structures. ASC 76, 731–734 (1976).
- Klapwijk T. M. and J. E. Mooij. Extension of the operating range of superconducting micro-bridges. ASC 74, 858–859 (1974).

- Klapwijk T. M. and T. B. Veenstra. Superconducting Al microbridges with reduced self-heating. *Phys. Lett.*, **47A**, 351–352 (1974).
- Klapwijk T. M., M. Sepers, and J. E. Mooij. Regimes in the behavior of superconducting microbridges. *J. Low Temp. Phys.*, **27**, 801–835 (1977).
- Klapwijk T. M., J. N. Van den Bergh, and J. E. Mooij. Radiation-stimulated superconductivity. *J. Low Temp. Phys.*, **26**, 385–405 (1977).
- Klein M. and D. J. Herrel. Sub-100 ps experimental Josephson interferometer logic gates. *IEEE J. Solid State Cir.*, **SC-13**, 577–583 (1978).
- Kleinsasser A. W. and R. A. Buhrman. High-quality submicron niobium tunnel junctions with reactive ion-beam oxidation. *Appl. Phys. Lett.*, **37**, 841–843 (1980).
- Koch R. and J. Clarke. Small area tunnel junction d.c. SQUID. *Bull. Amer. Phys. Soc.*, **24**, 264 (1979).
- Kofoed B. and K. Saermak. A note on superconducting weak-links. *Phys. Lett.*, **49A**, 91–92 (1974).
- Kose V. Recent advances in Josephson voltage standards. *IEEE Trans. Instrum. Meas.*, **IM-25**, 483–489 (1976).
- Kose V. E. and D. B. Sullivan. Influence of external noise on microwave-induced Josephson steps. *J. Appl. Phys.*, **41**, 169–174 (1970).
- Kramer L. and A. Baratoff. Lossless and dissipative current-carrying states in quasi one-dimensional superconductors. *Phys. Rev. Lett.*, **38**, 518–521 (1977).
- Kramer L. and R. J. Watts-Tobin. Theory of dissipative current-carrying states in superconducting filaments. *Phys. Rev. Lett.*, **40**, 1041–1044 (1978).
- Kramers H. Brownian motion in a field of force and the diffusion model of chemical reactions. *Physica*, **7**, 284–304 (1940).
- Krasnopolin I. Ya. and M. S. Khaikin. Generation and detection of microwave radiation by a superconducting point contact of tin electrodes. *Zh. Eksp. Teor. Fiz. Pis. Red.*, **6**, 533–637 (1967). *JETP Lett.*, **6**, 129–132 (1967).
- Kubaschewski O. and B. E. Hopkins. *Oxidation of Metals and Alloys*. Butterworths, London, 1962.
- Kulik I. O. Theory of “steps” of voltage-current characteristics of the Josephson tunnel current. *Zh. Eksp. Teor. Fiz. Pis. Red.*, **2**, 134 (1965a). *JETP Lett.*, **2**, 84–87 (1965).
- Kulik I. O. Magnitude of the critical Josephson tunnel current. *Zh. Eksp. Teor. Fiz.*, **49**, 1211–1214 (1965b). *Sov. Phys. JETP*, **22**, 841–843 (1966).
- Kulik I. O. The Josephson tunnel effect in superconductors with paramagnetic impurities. *Zh. Eksp. Teor. Fiz.*, **50**, 799–806 (1966a). *Sov. Phys. JETP*, **23**, 529–533 (1966).
- Kulik I. O. Wave propagation in a Josephson tunnel junction in the presence of vortices and the electrodynamics of weak superconductivity. *Zh. Eksp. Teor. Fiz.*, **51**, 1952–1969 (1966b). *Sov. Phys. JETP*, **24**, 1307–1317 (1967).
- Kulik I. O. Theory of resonance phenomena in superconducting tunneling. *Zh. Tekh. Fiz.*, **37**, 157–166 (1967). *Sov. Phys. Tech. Phys.*, **12**, 111–116 (1967).
- Kulik I. O. and A. N. Omel'yanchuk. Current flow in long superconducting junctions. *Zh. Eksp. Teor. Fiz.*, **68**, 2139–2148 (1975a). *Sov. Phys. JETP*, **41**, 1071–1075 (1976).
- Kulik I. O. and A. N. Omel'yanchuk. Contribution to the microscopic theory of the Josephson effect in superconducting bridges. *Zh. Eksp. Teor. Fiz. Pis. Red.*, **21**, 216–219 (1975b). *JETP Lett.*, **21**, 96–97 (1975).
- Kulik I. O. and A. N. Omel'yanchuk. Properties of superconducting microbridges in the pure limit. *Fiz. Nizk. Temp.*, **3**, 945–948 (1977). *Sov. J. Low Temp. Phys.*, **3**, 459–461 (1978).
- Kulik I. O. and I. K. Yanson. *The Josephson Effect in Superconductive Tunneling Structures*. Izdatel'stvo "Nauka", Moskow, 1970. Israel Program for Scientific Translations, Jerusalem, 1972.
- Kupriyanov M. Yu., K. K. Likharev, and L. A. Maslova. The $J_s(\varphi)$ relationship, Abrikosov vortices, and Josephson vortices in variable thickness bridges. *LT 14*, **4**, 104–107 (1975).

- Kurdyumov N. N. Low-frequency fluctuations at superconducting point junctions. *Pis. Zh. Tekh. Fiz.*, **2**, 973–976 (1976). *Sov. Tech. Phys. Lett.*, **2**, 381–382 (1976).
- Kurkijärvi J. Intrinsic fluctuations in a superconducting ring closed with a Josephson junction. *Phys. Rev.*, **B6**, 832–835 (1972).
- Kurkijärvi J. Noise in the superconducting quantum flux detector. *J. Appl. Phys.*, **44**, 3729–3733 (1973).
- Kurkijärvi J. and V. Ambegaokar. Numerical calculations of thermal noise-voltage in a Josephson junction of finite capacitance. *Phys. Lett.*, **31A**, 314–315 (1970).
- Kurkijävi J. and W. W. Webb. Thermal fluctuation noise in a superconducting flux detector. ASC **72**, 581–587 (1972).
- Kuroda K., T. Waho, and A. Ishida. Ellipsometric study on rf-plasma oxidized tunnel barriers for In/Pb/Au-alloy Josephson junctions. *J. Appl. Phys.*, **51**, 4513–4517 (1980).
- Kuznetsov P. I., R. L. Stratovich, and V. I. Tikhonov. *non-linear Transformations of Stochastic Processes*. 1st English ed., Pergamon, Oxford, 1965.
- Lacquaniti V., G. Marullo, and R. Vaglio. A.C. properties of Nb-Nb_xO_y-Pb Josephson tunnel junctions. ASC **78**, 593–594 (1978).
- Lahiri S. K. Stress relief and hillock formation in thin lead film. *J. Appl. Phys.*, **41**, 3172–3176 (1970).
- Lahiri S. K. Metallurgical considerations with respect to electrodes and interconnection lines for Josephson tunneling circuits. *J. Vac. Sci. Tech.*, **13**, 148–151 (1976).
- Lahiri S. K. and S. Basavaiah. Lead alloy Josephson tunneling gates with improved stability upon thermal cycling. *J. Appl. Phys.*, **49**, 2880–2884 (1978).
- Lahiri S. K. and O. C. Wells. Reversible hillock growth in thin films. *Appl. Phys. Lett.*, **15**, 324–325 (1969).
- Lahiri S. K., S. Basavaiah, and C. J. Kircher. Lead alloy Josephson junctions with Pb-Bi counterelectrodes. *Appl. Phys. Lett.*, **36**, 334–336 (1980).
- Laibowitz R. B. Properties of Nb Josephson microbridges. *Appl. Phys. Lett.*, **23**, 407–408 (1973).
- Laibowitz R. B. and J. J. Cuomo. Tunneling sandwich structures using single-crystal niobium films. *J. Appl. Phys.*, **41**, 2748–2750 (1970).
- Laibowitz R. B. and A. F. Mayadas. Josephson junctions with Nb/Al composite electrodes. *Appl. Phys. Lett.*, **20**, 254–256 (1972).
- Laibowitz R. B., C. C. Tsuei, J. C. Cuomo, J. F. Ziegler, and M. Hatzakis. Fabrication and Josephson properties of Nb₃Ge. ASC **74**, 883–884 (1974).
- Laibowitz R. B., A. N. Broers, J. M. Viggiano, J. J. Cuomo, and W. W. Molzen. Fabrication and properties of superconducting Nb nanostripes. *Bull. Am. Phys. Soc.*, **23**, 357 (1978).
- Lamb G. L., Jr. Analytical descriptions of ultrashort optical pulse propagation in a resonant medium. *Rev. Mod. Phys.*, **43**, 99–124 (1971).
- Lambe J., A. H. Silver, J. E. Mercereau, and R. C. Jaklevic. Microwave observation of quantum interference effects in superconductors. *Phys. Lett.*, **11**, 16–17 (1964).
- Landman B. S. Calculation of threshold curves for Josephson quantum interference devices. ASC **76**, 871–874 (1976).
- Langenberg D. N. Physical interpretation of the $\cos \varphi$ term and implication for detectors. DEJJ, 35–40 (1973).
- Langenberg, D. N. Nonequilibrium phenomena in superconductivity. LT **14**, 223–263 (1975).
- Langenberg D. N., W. H. Parker, and B. N. Taylor. Experimental test of the Josephson frequency-voltage relation. *Phys. Rev.*, **150**, 186–188 (1966a).
- Langenberg D. N., W. H. Parker, and B. N. Taylor. “Non-Josephson” radiation from Josephson tunnel junctions. *Phys. Lett.*, **22**, 259–260 (1966b).

- Langenberg D. N., D. J. Scalapino, and B. N. Taylor. Josephson-type superconducting tunnel junctions as generators of microwave and submillimeter wave radiation. *Proc. IEEE*, **54**, 560–575 (1966).
- Langenberg D. N., D. J. Scalapino, B. N. Taylor, and R. E. Eck. Investigation of microwave radiation emitted by Josephson junctions. *Phys. Rev. Lett.*, **15**, 294–297 (1965).
- Langenberg D. N., D. J. Scalapino, B. N. Taylor, and R. E. Eck. Microwave-induced dc voltages across Josephson junctions. *Phys. Lett.*, **20**, 563–565 (1966).
- Lapir G. M., K. K. Likharev, and V. K. Semenov. Magnetic flux dynamics in inhomogeneous distributed Josephson structures. *Zh. Tekh. Fiz.*, **47**, 1069–1072 (1977). *Sov. Phys. Tech. Phys.*, **22**, 638–639 (1977).
- Larkin A. I. and Yu. N. Ovchinnikov. Tunnel effect between superconductors in an alternating field. *Zh. Eksp. Teor. Fiz.*, **51**, 1535–1040 (1966). *Sov. Phys. JETP*, **24**, 1035–1040 (1967).
- Larkin A. I. and Yu. N. Ovchinnikov. Radiations line width in the Josephson effect. *Zh. Eksp. Teor. Fiz.*, **53**, 2159–2163 (1967). *Sov. Phys. JETP*, **26**, 1219–1221 (1968).
- Latyshev Yu. I. and F. Ya. Nad. Enhancement of the critical current of superconducting bridges by microwave radiation. *ASC* **74**, 877–879 (1974).
- Latyshev Yu. I. and F. Ya. Nad. Steplike structure produced on the superconducting transition of a tin film by microwave radiation. *Pis Zh. Eksp. Teor. Fiz.*, **26**, 488–491 (1977). *JETP Lett.*, **26**, 354–357 (1978).
- Latyshev Yu. I. and F. Ya. Nad. Nonequilibrium phenomena in superconducting Al bridges under the microwave radiation. *LT* **15**, 531–532 (1978).
- Latyshev Yu. I. and F. Ya. Nad. On the dependence of UHF radiation stimulated superconductivity in film bridges on their length. *Pis Zh. Eksp. Teor. Fiz.*, **29**, 54–58 (1979). *JETP Lett.*, **29**, 49–53 (1979).
- Lavenda B., private communication, 1979.
- Lebwol P. and M. J. Stephen. Properties of vortex lines in superconducting barriers. *Phys. Rev.*, **163**, 376–379 (1967).
- Lee P. A. Effect of noise on the current-voltage characteristics of a Josephson junction. *J. Appl. Phys.*, **42**, 325–334 (1971).
- Lee Y. W. *Statistical Theory of Communication*. Wiley, New York, 1960.
- Leibbrandt G. Exact solutions of the elliptic sine equation in two space dimensions with applications to the Josephson effect. *Phys. Rev.*, **B15**, 3353–3361 (1977).
- Leplae L., F. Mancini, and H. Umezawa. New approach to the Josephson effect. *Lett. Nuovo Cimento*, **4**, 963–968 (1970).
- Leplae L., H. Umezawa, and F. Mancini. Derivation and application of the boson method in superconductivity. *Phys. Rep.*, **10**, 151–272 (1974).
- Levinson M. T. Electromagnetic properties of the Dayem bridge. *DEJJ*, 135–144 (1973).
- Levinson M. T. and B. T. Ulrich. Perturbation treatment of mixing in Josephson junctions. *ASC* **74**, 807–810 (1974).
- Levinson M. T., R. Y. Chiao, M. J. Feldman, and B. A. Tucker. An inverse ac Josephson effect voltage standard. *Appl. Phys. Lett.*, **31**, 776–778 (1977).
- Levinstein H. J. and J. E. Kunzler. Observation of energy gaps in β -tungstens and other superconductors using a simplified tunneling technique. *Phys. Lett.*, **20**, 581–583 (1966).
- Likes R. S. and C. M. Falco. Power spectrum of radiation from a Josephson junction. *J. Appl. Phys.*, **48**, 5370–5371 (1977).
- Likharev K. K. Vortex motion and the Josephson effect in superconducting thin bridges. *Zh. Eksp. Teor. Fiz.*, **61**, 1700–1711 (1971); *Sov. Phys. JETP*, **34**, 906–912 (1972).
- Likharev K. K. Dynamics of some single flux quantum devices: I. Parametric quantron. *ASC* **76**, 242–244 (1976a).

- Likharev K. K. Dynamics of some single flux quantum devices: II. Inhomogeneous flux shuttle. *ASC* 76, 245–247 (1976).
- Likharev K. K. The relation $J_s(\phi)$ for SNS bridges of variable thickness. *Pis. Zh. Tekh. Fiz.*, **2**, 29–34 (1976); *Sov. Tech. Phys. Lett.*, **2**, 12–14 (1976).
- Likharev K. K. Private communication, 1978.
- Likharev K. K. Superconducting weak links. *Rev. Mod. Phys.*, **51**, 101–159 (1979).
- Likharev K. K. and V. K. Semenov. Fluctuation spectrum in superconducting point junctions. *Zh. Eksp. Teor. Fiz. Pis. Red.*, **15**, 625–629 (1972). *JETP Lett.*, **15**, 442–445 (1972).
- Likharev K. K. and V. K. Semenov. The effect of fluctuations on the microwave impedance of superconducting point contacts. *Radiotekhnika i Elektronika*, **18**, 2390–2397 (1973). *Radio Engin. Electron. Phys.*, **18**, 1290–1297 (1973).
- Likharev K. K. and B. T. Ulrich. Josephson Junction Circuits and Applications. Izd. Mosk. Universiteta, Moscow, 1978. (English edition to be published.)
- Likharev K. K. and L. A. Yakobson. Dynamic properties of variable thickness bridges. *ASC* 74, 860–865 (1974).
- Likharev K. K. and L. A. Yakobson. Steady-state properties of superconducting bridges. *Zh. Tech. Fiz.*, **45**, 1503–1509 (1975a). *Sov. Phys. Tech. Phys.*, **20**, 950–954 (1976).
- Likharev K. K. and L. A. Yakobson. Dynamical properties of superconducting filaments of finite length. *Zh. Eksp. Teor. Fiz.*, **68**, 1150–1160 (1975b). *Sov. Phys. JETP*, **41**, 570–575 (1976).
- Likharev K. K., G. M. Lapir, V. K. Semenov, and L. A. Yakobson. Some properties of variable thickness bridges. Report on *ASC* 74 (1974) (unpublished).
- Likharev K. K., V. K. Semenov, O. V. Snigirev, and B. N. Tedorov. Josephson junction with lateral injection as a vortex transistor. *ASC* 78, 420–423 (1978).
- Lim C. S., J. D. Leslie, H. J. T. Smith, P. Vashishta, and J. P. Carbotte. Temperature variation of the dc Josephson current in Pb-Pb tunnel junctions. *Phys. Rev.*, **B2**, 1651–1656 (1970).
- Lindelof P. E. Non-equilibrium effects in constricted superconductors. *LT* 15, 1411–1420 (1978).
- Lindelof P. E. and J. B. Hansen. Coherent behavior of two interacting Dayem bridges. *J. Low Temp. Phys.*, **29**, 369–396 (1977).
- Lindelof P. E., J. B. Hansen, J. Mygind, N. F. Pedersen, and O. H. Sørensen. Coherent Josephson radiation from an array of two Dayem bridges. *Phys. Lett.*, **60A**, 451–452 (1977).
- Lipson S. G. and M. M. Stupel. Induced superconductivity in germanium films. *Phys. Lett.*, **33A**, 493–494 (1970).
- Little W. A. and R. D. Parks. Observation of quantum periodicity in the transition temperature of a superconducting cylinder. *Phys. Rev. Lett.*, **9**, 9–12 (1962).
- Lo S. C. and A. D. S. Nagi. Josephson tunnel effect and the order parameter of superconducting alloys containing paramagnetic impurities with local states within the gap. *Phys. Rev.*, **B9**, 2090–2096 (1974).
- London F. Macroscopical interpretation of supraconductivity. *Proc. Roy. Soc.*, **152**, 23–24 (1935).
- London F. *Superfluids*. Vol. I, Wiley, New York, 1950.
- London F. and H. London. The electromagnetic equations of the superconductors. *Proc. Roy. Soc.*, **A149**, 71 (1935a).
- London F. and H. London. Supraleitung und Diamagnetismus. *Physica*, **2**, 341 (1935b).
- Long A. P., T. D. Clark, and R. J. Prance. Varactor tuned ultrahigh frequency SQUID magnetometer. *Rev. Sci. Instrum.*, **51**, 8–13 (1980).
- Long A., T. D. Clark, R. J. Prance, and M. G. Richards. High-performance UHF SQUID magnetometer. *Rev. Sci. Instrum.*, **50**, 1376–1381 (1979).
- Lourtioz J. M., R. Adde, G. Vernet, and J. C. Henaux. Harmonic mixing with Josephson point contacts. *Rev. Phys. Appl.*, **12**, 487–492 (1977).

- Lubberts G. and S. Shapiro. Cadmium selenide films deposited at high substrate temperature as tunneling barriers between tin electrodes. *J. Appl. Phys.*, **43**, 3958–3963 (1972).
- Lübbig H. Progress in physics of Josephson junctions. IC-SQUID 80 (1980) (in press).
- Lugiatto L. A. and M. Milani. On the quantum mechanical description of Josephson junctions. *Nuovo Cimento* **B55**, 417–434 (1980).
- Lukens J. E., R. D. Sandell, and C. Varmazis. Fabrication of microbridge Josephson junctions using electron beam lithography. FTSE, 298–311 (1978).
- Lukens J. E., R. J. Warburton, and W. W. Webb. Versatile superconducting femtovolt amplifier and multimeter. *J. Appl. Phys.*, **42**, 27–30 (1971).
- Lum W. Y. and T. Van Duzer. New configuration for a superconducting weak link. *J. Appl. Phys.*, **46**, 3216–3218 (1975).
- Lum W. Y. and T. Van Duzer. Resonances in semiconductor-barrier Josephson junctions. *J. Appl. Phys.*, **49**, 4560–4563 (1978).
- Lum W. Y., H. W. Chan, and T. Van Duzer. Memory and logic circuits using semiconductor-barrier Josephson junctions. ASC 76, 48–51 (1976).
- Lum W. Y., H. W. K. Chan and T. Van Duzer. Switching measurements on Josephson memory loops. *J. Appl. Phys.*, **49**, 4302–4303 (1978).
- MacVicar M. L. A. Amorphous carbon films: Conduction across metal/carbon/metal sandwiches. *J. Appl. Phys.*, **41**, 4765–4768 (1970).
- MacVicar M. L. A., S. M. Freake, and C. J. Adkins. Thin semiconducting films as tunneling barriers. *J. Vac. Sci. Tech.*, **6**, 717–719 (1969).
- Magee C. J. and M. Russo. Some aspects in the preparation of light-sensitive superconducting tunnel junctions. *Vuoto Sci. Tec.*, **7**, 4–13 (1974).
- Mahutte C. K., J. D. Leslie, and H. J. T. Smith. Self-field limiting of Josephson tunnel current. *Can. J. Phys.*, **47**, 627–629 (1969).
- Maki K. Gapless superconductivity. In *Superconductivity* (R. D. Parks, Ed.). Vol. 2, Marcel Dekker, New York, 1969, chap. 18, pp. 1035–1105.
- Manley J. M. and H. E. Rowe. Some general properties of nonlinear elements—Part I. General energy relations. *Proc. IRE*, **44**, 904–913 (1956).
- Maple M. B. Paramagnetic impurities in superconductors. In *Magnetism* (G. T. Rado and H. Suhl, Eds.). Vol. V, Academic, New York, 1973, pp. 289–325.
- Mathews J. and R. L. Walker. *Mathematical Methods of Physics*. Benjamin, New York, 1965.
- Matisoo J. Sub-nanosecond pair tunneling to single-particle tunneling transition in Josephson junctions. *Appl. Phys. Lett.*, **9**, 167–168 (1966).
- Matisoo J. The tunneling cryotron—A superconductive logic element based on electron tunneling. *Proc. IEEE*, **55**, 172–180 (1967a).
- Matisoo J. Measurement of current transfer time in a tunneling cryotron flip-flop. *Proc. IEEE*, **55**, 2052–2053 (1967b).
- Matisoo J. Critical currents and current distributions in Josephson junctions. *J. Appl. Phys.*, **40**, 1813–1820 (1969).
- Matisoo J. Josephson tunnel junctions. ASC 72, 535–543 (1972).
- Matisoo J. Josephson computer technology. LT 15, 1590–1597 (1978).
- Matisoo J. and H. H. Zappe. Techniques for minimizing resonance amplitudes of Josephson junction. U. S. Patent 3,906,538, Sept. 16, 1975.
- Matsuda A., T. Inamura, and H. Yoshikiyo. Study of Nb-based Josephson tunnel junctions. *J. Appl. Phys.*, **51**, 4310–4316 (1980).
- McColl M., M. F. Millea, and A. H. Silver. The superconductor-semiconductor Schottky barrier diode detector. *Appl. Phys. Lett.*, **23**, 263–264 (1973).

- McColl M., R. J. Pedersen, M. F. Bottjer, M. F. Millea, A. H. Silver, and F. L. Vernon, Jr. The super-Schottky diode microwave mixer. *Appl. Phys. Lett.*, **28**, 159–162 (1976).
- McCumber D. E. Tunneling and weak-link superconductor phenomena having potential device applications. *J. Appl. Phys.*, **39**, 2503–2508 (1968a).
- McCumber D. E. Effect of ac impedance on dc voltage-current characteristics of superconductor weak-link junctions. *J. Appl. Phys.*, **39**, 3113–3118 (1968b).
- McDonald D. G., E. G. Johnson, and R. E. Harris. Modeling Josephson junctions. *Phys. Rev.*, **B13**, 1028–1031 (1976).
- McDonald D. G., R. L. Peterson, and B. K. Bender. Design of a Josephson-junction picosecond pulser. *J. Appl. Phys.*, **48**, 5366–5369 (1977).
- McDonald D. G., V. E. Kose, K. M. Evenson, J. S. Wells, and J. D. Cupp. Harmonic generation and submillimeter wave mixing with the Josephson effect. *Appl. Phys. Lett.*, **15**, 121–122 (1969).
- McDonald D. G., A. S. Risley, J. D. Cupp, and K. M. Evenson. Harmonic mixing of microwave and far-infrared laser radiation using a Josephson junction. *Appl. Phys. Lett.*, **18**, 162–164 (1971).
- McDonald D. G., A. S. Risley, J. D. Cupp, K. M. Evenson, and J. R. Ashley. Four-hundredth-order harmonic mixing of microwave and infrared laser radiation using a Josephson junction and a maser. *Appl. Phys. Lett.*, **20**, 296–299 (1972).
- McDonald D. G., F. R. Petersen, J. D. Cupp, B. L. Danielson, and E. G. Johnson. Detection mechanisms in superconducting point contacts at frequencies of 44 times the energy gap. DEJJ, 273 (1973) (abstract only).
- McLaughlin D. W. and A. C. Scott. Fluxon interaction. *Appl. Phys. Lett.*, **30**, 545–547 (1977).
- McLaughlin D. W. and A. C. Scott. Perturbation analysis of fluxon dynamics. *Phys. Rev.*, **A18**, 1652–1680 (1978).
- McMillan W. L. Tunneling model of the superconducting proximity effect. *Phys. Rev.*, **175**, 537–542 (1968a).
- McMillan W. L. Theory of superconductor-normal-metal interfaces. *Phys. Rev.*, **175**, 559–568 (1968b).
- McMillan W. L. and J. M. Rowell. Tunneling and strong-coupling superconductivity. In *Superconductivity* (R. D. Parks, Ed.) Vol. 1, Marcel Dekker, New York, 1969, chap. 11, pp. 561–613.
- Mehbod M., W. Thijss, and Y. Bruynseraeede. Electron tunneling through semiconducting barriers. *Phys. Status Solidi (a)*, **32**, 203–211 (1975).
- Meissner H. Measurements on superconducting contacts. *Phys. Rev.*, **109**, 686–694 (1958).
- Meissner H. Superconductivity of contacts with interposed barriers. *Phys. Rev.*, **117**, 672–680 (1960).
- Mercereau J. E. Macroscopic quantum phenomena. In *Superconductivity* (R. D. Parks, Ed.). Vol. 1, Marcel Dekker, New York, 1969, chap. 8, pp. 393–421.
- Mercereau J. E. Superconducting magnetometers. *Rev. Phys. Appl.*, **5**, 13–20 (1970).
- Mercereau J. E. Physical processes in proximity microbridges. DEJJ, 47–52 (1973).
- Meyer J. D. Spannungsstufen in den U(T)-Übergangskurven und U(I)-Kennlinien stromtragender Zinn-Whisker. *Appl. Phys.*, **2**, 303–320 (1973).
- Meyer J. and G. v. Minnigerode. Instabilities in the transition curve of current-carrying one-dimensional superconductors. *Phys. Lett.*, **38A**, 529–530 (1972).
- Minnigerode G. v. Zur Kontaktwirkung in supraleitenden Doppelschichten aus Cu/Pb. *Z. Phys.*, **192**, 379–408 (1966).
- Miles J. L. and P. H. Smith. The formation of metal oxide films using gaseous and solid electrolytes. *J. Electroch. Soc.*, **110**, 1240–1245 (1963).
- Minorsky N. *Nonlinear Oscillations*. Van Nostrand, Princeton, 1962.

- Mkrtyan G. S. and V. V. Shmidt. On the radiation from inhomogeneous Josephson junction. *Solid State Comm.*, **30**, 791–793 (1979).
- Mooij J. E. and P. Dekker. Static properties of two and three-dimensional superconducting constrictions. *J. Low Temp. Phys.*, **33**, 551–576 (1978).
- Moore D. F., J. M. Rowell, and M. R. Beasley. Superconductive tunneling into niobium-tin thin films. *Solid State Comm.*, **20**, 305–308 (1976).
- Mori M., S. Kodama, and H. Ozaki. The d.c. Josephson effect for superconducting proximity systems. LT 15, 6561–6562 (1978).
- Morse P. M. and H. Feshbach. *Methods of Theoretical Physics*. Vol. 32, McGraw-Hill, New York, 1953, p. 555.
- Moser A. Logic gates with shaped Josephson junctions. *IEEE J. Sol. St. Circuits SC* **14**, 672–679 (1979).
- Muhlschlegel B. Z. Die thermodynamischen funktionen des supraleiters. *Z. Phys.*, **155**, 313–327 (1959).
- Mullen L. O. and D. B. Sullivan. Fabrication of tunnel junctions on niobium films. *J. Appl. Phys.*, **40**, 2115–2117 (1969).
- Murakami M. and C. J. Kircher. Strain relaxation in Pb alloy Josephson junction electrode material. ASC 78, 443–445 (1979).
- Mygind J., N. E. Pedersen, and O. H. Soerensen. Direct detection of the parametrically generated half-harmonic voltage in a Josephson tunnel junction. *Appl. Phys. Lett.*, **29**, 317–319 (1976).
- Mygind J., N. F. Pedersen, and O. H. Soerensen. X-band singly degenerate parametric amplification in a Josephson tunnel junction. *Appl. Phys. Lett.*, **32**, 70–72 (1978).
- Mygind J., N. F. Pedersen, O. H. Soerensen, B. Dueholm, and M. T. Levinsen. Low noise parametric amplification at 35 GHz in a single Josephson tunnel junction. *Appl. Phys. Lett.*, **35**, 91–93 (1979).
- Nagi S. A. D. and S. C. Lo. Josephson tunnel effect in superconducting alloy with local states within the gap. *Phys. Lett.*, **42A**, 387–388 (1973).
- Nakajima K., Y. Onodera, and Y. Ogawa. Logic design of Josephson network. *J. Appl. Phys.*, **47**, 1620–1627 (1976).
- Nakajima K., Y. Sawada, and Y. Onodera. Nonequilibrium stationary coupling of solitons. *J. Appl. Phys.*, **46**, 5277–5279 (1975).
- Nakajima K., T. Yamashita, and Y. Onodera. Mechanical analogue of active Josephson transmission line. *J. Appl. Phys.*, **45**, 3141–3145 (1974).
- Nakajima K., Y. Onodera, T. Nakamura, and R. Sato. Numerical analysis of vortex motion on Josephson structure. *J. Appl. Phys.*, **45**, 4095–4099 (1974).
- Nam S. B. Theory of electromagnetic properties of superconducting and normal systems. I. *Phys. Rev.*, **156**, 470–486 (1967a).
- Nam S. B. Theory of electromagnetic properties of strong-coupling and impure superconductors. *Phys. Rev.*, **156**, 487–493 (1967b).
- Nerenberg M. A. H. and J. A. Blackburn. Self-resonance in cylindrical Josephson junctions. *Phys. Rev.*, **B9**, 3735–3738 (1974).
- Nerenberg M. A. H., P. A. Forsyth, Jr. and J. A. Blackburn. Excitation of cavity modes in rectangular Josephson junctions. *J. Appl. Phys.*, **47**, 4148–4150 (1976).
- Neugebauer C. A. and R. A. Ekvall. Vapor-deposited superconductive films of Nb, Ta and V. *J. Appl. Phys.*, **35**, 547–553 (1964).
- Newhouse V. L. *Applied Superconductivity*. Wiley, New York, 1964.
- Newhouse V. L. and J. W. Bremer. High-speed superconductive switching element suitable for two-dimensional fabrication. *J. Appl. Phys.*, **30**, 1458–1459 (1959).
- Newhouse V. L., J. W. Bremer, and H. H. Edwards. An improved film cryotron and its application to digital computers. *Proc. IRE*, **48**, 1395–1404 (1960).

- Ngai K. L. Interaction of ac Josephson currents with surface plasmons in thin superconducting films. *Phys. Rev.*, **182**, 555–568 (1969).
- Nicol J., S. Shapiro, and P. H. Smith. Direct measurement of the superconducting energy gap. *Phys. Rev. Lett.*, **5**, 461–464 (1960).
- Niemeyer J. Eine einfache methode zur herstellung kleinster Josephson-elemente. *PTB-Mitt.*, **84**, 251–253 (1974).
- Niemeyer J. and V. Kose. Effects in high critical current density Josephson tunnel junctions. IC-SQUID 76, 179–191 (1976a).
- Niemeyer J. and V. Kose. Observation of large dc supercurrents at non zero voltages in Josephson tunnel junctions. *Appl. Phys. Lett.*, **29**, 380–382 (1976b).
- Niemeyer J. and G. v. Minnigerode. Effects of nonmagnetic and magnetic impurities in the normal metal layer of SNS junctions. *Z. Phys.*, **B36**, 57–66 (1979).
- Nisenoff M. Superconducting magnetometers with sensitivities approaching 10^{-10} Gauss. *Rev. Phys. Appl.*, **5**, 21–24 (1970).
- Nisenoff M. and S. Wolf. Observation of a $\cos\phi$ term in the current phase relation for “Dayem”-type weak link contained in an rf-biased superconducting quantum interference device. *Phys. Rev.*, **B12**, 1712–1714 (1975).
- Nordman J. E. Thin-film Josephson junctions using getter-sputtered niobium. *J. Appl. Phys.*, **40**, 2111–2115 (1969).
- Nordman J. E. and W. H. Keller. Controlled fabrication of Nb superconductive tunnel junctions with anomalous negative resistance. *Phys. Lett.*, **36A**, 52–53 (1971).
- Notarys H. A. and J. E. Mercereau. Dynamics of small superconductors. ICSS-69, 424–431 (1969).
- Notarys H. A. and J. E. Mercereau. Proximity effect bridge and superconducting microcircuitry. *J. Appl. Phys.*, **44**, 1821–1830 (1973).
- Notarys H. A., R.H. Wang, and J. E. Mercereau. Weakly superconducting circuits. *Proc. IEEE*, **61**, 79–84 (1973).
- Octavio M., W. J. Skocpol, and M. Tinkham. Improved performance of tin variable-thickness superconducting microbridges. ASC 76, 739–742 (1976).
- Octavio M., W. J. Skocpol, and M. Tinkham. Nonequilibrium-enhanced supercurrents in short superconducting weak links. *Phys. Rev.*, **B17**, 159–169 (1978).
- Ohta H. Sensitivity of Josephson junctions in video detection of microwave and millimeter-wave radiation. *J. Appl. Phys.*, **43**, 5161–5163 (1972).
- Ohta H. A self-consistent model of the Josephson junction. IC-SQUID 76, 35–49 (1976).
- Ohta H., M. J. Feldman, P. T. Parrish, and R. Y. Chiao. Sensitivity of Josephson-effect millimeter-wave radiometer. DEJJ, 61–64 (1973).
- Omar M. H. and R. de Bruyn Ouboter. Oscillations on the voltage between two weakly connected current-carrying superconductors as a function of the applied magnetic field. *Physica*, **32**, 2044–2050 (1966).
- Omar M. H., W. H. Kraan, A. T. A. M. de Waele, and R. de Bruyn Ouboter. On the existence of a corrugated surface representing the relationship between current, voltage and magnetic field for weakly-connected superconductors. *Physica*, **34**, 525–533 (1967).
- Opfer J. E., Y. K. Yeo, J. M. Pierce, and L. H. Rorden. A superconducting second-derivative gradiometer. *IEEE Trans. Magn.*, **MAG-10**, 536–539 (1974).
- Ovchinnikov Yu. N. Penetration of an electrical field into a superconductor. *J. Low Temp. Phys.*, **28**, 43–60 (1977).
- Owen S. and J. E. Nordman. Application of integrated circuit technology to the fabrication of large numbers of niobium based Josephson junctions. ASC 74, 774–777 (1974).
- Owen C. S. and D. J. Scalapino. Vortex structure and critical currents in Josephson junctions. *Phys. Rev.*, **164**, 538–544 (1967).

- Owen C. S. and D. J. Scalapino. Inductive coupling of Josephson junctions to external circuits. *J. Appl. Phys.*, **41**, 2047–2056 (1970).
- Paley S., J. Wilson, and R. I. Gayley. Studies of the Josephson junctions of anomalously high supercurrent. *Phys. Rev.*, **B12**, 157–162 (1975).
- Palmer D. W. and J. E. Mercereau. Coherent effects in large arrays of superconducting bridges. *Appl. Phys. Lett.*, **25**, 467–469 (1974).
- Palmer D. W. and J. E. Mercereau. Mode locking in arrays of superconducting weak-links. *Phys. Lett.*, **61A**, 135–137 (1977).
- Palmer D. W., H. A. Notarys, and J. E. Mercereau. Quantum interference effects in high-transition-temperature thin-film materials. *Appl. Phys. Lett.*, **25**, 527–528 (1974).
- Pankove J. J. New effect at superconducting contacts. *Phys. Lett.*, **21**, 406–407 (1966).
- Papoulis A. *The Fourier Integral and its Applications*. McGraw-Hill, New York, 1962.
- Park J. G. The physics of resistive SQUIDS modulated at low frequency. *J. Phys. F: Metal Phys.*, **4** 2239–2263 (1974).
- Park J. G. Resistive devices. NASI 76, chap. 10, 415–446 (1976).
- Park J. G. and J. P. Kendall. Resistive SQUIDS in the absence of modulation current. *LT* **14**, **4**, 164–167 (1975).
- Park J. G., D. E. Farrell, and J. P. Kendall. The response of a toroidal resistive SQUID to modulation by magnetic flux. *J. Phys. F: Metal Phys.*, **3**, 2169–2173 (1973).
- Parker W. H., B. N. Taylor, and D. N. Langenberg. Measurement of $2e/h$ using the ac Josephson effect and its implications for quantum electrodynamics. *Phys. Rev. Lett.*, **18**, 287–291 (1967).
- Parker W. H., D. N. Langenberger, A. Denenstein, and B. N. Taylor. Determination of e/h using macroscopic quantum phase coherence in superconductors, I. Experiment. *Phys. Rev.*, **177**, 639–664 (1969).
- Parks R. D. and W. A. Little. Fluxoid quantization in a multiply connected superconductor. *Phys. Rev.*, **133A**, 97–103 (1964).
- Parks R. D., J. M. Mochel, and L. V. Surgent, Jr. Critical-field behavior at a microscopic superconducting bridge. *Phys. Rev. Lett.*, **13**, 331–333 (1964).
- Parmenter R. H. Theory of superconducting contacts. *Phys. Rev.*, **118**, 1174–1182 (1960).
- Parmentier R. D. Fluxons in long Josephson junctions. In *Solitons in Action* (K. Lonngren and A. C. Scott, Eds.). Academic, New York, 1978, pp. 173–199.
- Parmentier R. D. and G. Costabile. Fluxon propagation and d.c. current singularities in long Josephson junctions. *Rocky Mountain J. Math.*, **8**, 117–124 (1978).
- Parrish P. T. and R. Y. Chiao. Amplification of microwaves by superconducting microbridges in a fourwave parametric mode. *Appl. Phys. Lett.*, **25**, 627–629 (1974).
- Parrish P. T., M. H. Feldman, H. Ohta, and R. Y. Chiao. Four photon parametric amplification. *DEJJ*, 229–232 (1973).
- Pascal D. and M. Sauzade. Experimental determination of optimum operating conditions of a superconducting interferometer. *J. Appl. Phys.*, **45**, 3085–3090 (1974).
- Paternò G. Techniques for very low magnetic fields: Superconducting magnetometer. In *Proceedings of the 6th International Conference on Magnet Technology (MT-6)*, Bratislava, August 1977, Alfa Bratislava, 1978, pp. 917–928.
- Paternò G. and J. Nordman. Self-resonant modes in Nb-NbO_x-Pb Josephson junctions. *J. Appl. Phys.*, **49**, 2456–2460 (1978).
- Paternò G. and R. Vaglio. On the magnetic field dependence of dc Josephson current in tunneling junctions. CNEN, Rep. LNF-75/20(R), October 1975.
- Paterno G. and R. Vaglio. On the theory of resonant modes in Josephson junctions. CNEN, Centro di Frascati, Rep. 79.4, 1979. Available from: CNEN—Edizioni Scientifiche, C.P. 65-00044 Frascati, Rome, Italy.

- Paternò G., M. V. Ricci, and N. Sacchetti. Experimental test of the microscopic theory of a current-carrying superconductor by measurement of the zero-bias conductivity of tunnel junctions. *Phys. Rev.*, **B3**, 3792–3796 (1971).
- Paternò G., P. Rissman, and R. Vaglio. Temperature dependence of the maximum Josephson current for Nb-NbO_x-Pb. *J. Appl. Phys.*, **46**, 1419–1420 (1975).
- Pech T. and J. Saint-Michel. Design of stable thin-film Josephson tunnel junctions for the maintenance of voltage standards. *ASC 74*, 817–820 (1974).
- Pedersen N. F. Zero-voltage nondegenerate parametric mode in Josephson tunnel junctions. *J. Appl. Phys.*, **47**, 696–699 (1976).
- Pedersen N. F. and K. Saermark. Analytical solution for a Josephson junction model with capacitance. *Physica*, **69**, 572–578 (1973).
- Pedersen N. F. and O. H. Sørensen. An introductory course in the compound pendulum. *Am. J. Phys.*, **45**, 994–998 (1977).
- Pedersen N. F., T. F. Finnegan, and D. N. Langenberg. Magnetic field dependence and Q of the Josephson plasma resonance. *Phys. Rev.*, **B6**, 4151–4159 (1972a).
- Pedersen N. F., T. F. Finnegan, and D. N. Langenberg. Evidence for the existence of the Josephson quasiparticle-pair interference current. *LT 13*, **3**, 268–271 (1972b).
- Pedersen N. F., M. R. Samuels, and K. Saermark. Parametric excitation of plasma oscillations in Josephson junctions. *J. Appl. Phys.*, **44**, 5120–5124 (1973a).
- Pedersen N. F., M. R. Samuels, and K. Saermark. Parametric excitation of plasma oscillations in Josephson junctions. *DEJJ*, 223–225 (1973b).
- Pedersen N. F., O. H. Sørensen, and J. Mygind. Temperature dependence of the $\cos \varphi$ conductance in Josephson tunnel junctions determined from plasma resonance experiments. *Phys. Rev.*, **B18**, 3220–3230 (1978).
- Pedersen N. F., O. H. Sørensen, J. Mygind, P. E. Lindelof, M. T. Levinsen, and T. D. Clark. Direct detection of the Josephson radiation emitted from superconducting thin-film microbridges. *Appl. Phys. Lett.*, **28**, 562–564 (1976a).
- Pedersen N. F., O. H. Sørensen, J. Mygind, P. E. Lindelof, M. T. Levinsen, T. D. Clark, and M. Danielsen. Microwave generation and complex microwave responsivity measurements on small Dayem bridges. *ASC 76*, 248–251 (1976b).
- Pedersen N. F., J. Mygind, O. H. Sørensen, and B. Dueholm. A simple qualitative determination of Josephson tunnel junction parameters near the transition temperature. *LT 15*, 1232–1233 (1978).
- Penfield P., Jr and R. P. Rafuse. *Varactor Applications*. MIT Press, Cambridge, 1962, pp. 160–177.
- Peterson R. L. and C. A. Hamilton. Analysis of threshold curves for superconducting interferometers. *J. Appl. Phys.*, **50**, 8135–8142 (1979).
- Pierce J. M., J. E. Opfer, and L. H. Rorden. A broadband thin-film SQUID magnetometer pumped at 10 GHz. *IEEE Trans. Magn.*, **MAG-10**, 599–602 (1974).
- Pippard, A. B. The surface impedance of superconductors and normal metals at high frequencies. III. The relation between impedance and superconducting penetration depth. *Proc. Roy. Soc., A191*, 399–415 (1947).
- Pippard A. B. *Rev. Mod. Phys.*, **36**, 225 (1964), discussion 34.
- Pippard A. B. The historical context of Josephson's discovery. *NASI 76*, 1–20 (1976).
- Poulsen U. K. Quasiparticle interference current in Josephson junctions. *Phys. Lett.*, **41A**, 195–196 (1972).
- Poulsen U. K. On the $\cos \varphi$ term in Josephson's expression for the tunneling current. *DEJJ*, 41–44 (1973a).
- Poulsen U. K. A theoretical treatment of tunneling currents in superconducting junctions. Technical University of Denmark, Lyngby, Internal Rep. 121, 1973b.

- Prange R. E. Tunneling from a many-particle point of view. *Phys. Rev.*, **131**, 1083–1086 (1963).
 See also: *Lectures in the Many-body Problem*, Ravello 1963 (E. R. Caianiello, Ed.). Vol. 2, Academic, 1964, p. 139.
- Pritchard J. P. and W. H. Schroen. Superconductive tunneling device characteristics for array applications. *IEEE Trans. Magn.*, **MAG-4**, 320–323 (1968).
- Pritchard J. M., Jr., and W. H. Schroen. Process for preparation of tunneling barriers. U.S. Patent 3,673,071, June 27, 1972.
- Quinn D. J. and W. B. Ittner. Resistance in superconductor. *J. Appl. Phys.*, **33**, 748–749 (1962).
- Rachford F. J. and J. Cukauskas. High Tc refractory thin-film microwave SQUID's. *Appl. Phys. Lett.*, **35**, 881–884 (1979).
- Radhakrishnan V. Photosensitive tunneling in superconductivity. *Can. J. Phys.*, **48**, 630–631 (1970).
- Ramo S., J. R. Whinnery, and T. Van Duzer. *Fields and Waves in Communication Electronics*. Wiley, New York, 1967.
- Reible S. A. Pulse propagation on superconductive tunnel transmission lines. Ph.D. Thesis, University of Wisconsin, Madison, 1975.
- Reiger T. J., D. J. Scalapino, and J. E. Mercereau. Charge conservation and chemical potentials in time-dependent Ginzburg-Landau theory. *Phys. Rev. Lett.*, **27**, 1787–1790 (1971).
- Reiger T. J., D. J. Scalapino, and J. E. Mercereau. Time-dependent superconductivity and quantum dissipation. *Phys. Rev.*, **B6**, 1734–1743 (1972).
- Richards P. L. The Josephson junction as a detector of microwave and far-infrared radiation. In *Semiconductors and Semimetals*, (R. K. Willardson and A. C. Beer, Eds.). Vol. 12, Academic, New York, 1977, chap. 6.
- Richards P. L., J. H. Claassen, and Y. Taur. Josephson effect mm-wave receivers. *LT* **14**, **4**, 238–241 (1975).
- Richter J. and P. Seidel. Theoretical studies of the influence of barrier inhomogeneities on the behavior of Josephson junctions. *Exp. Tech. Physk.*, **26**, 217–228 (1978), in German.
- Richter W. and G. Albrecht. Thin film superconducting quantum interferometers. *Cryogenics*, **15**, 148–149 (1975).
- Rickayzen G. *Theory of Superconductivity*. Wiley-Interscience, New York, 1975, chap. 10.
- Riedel E. Zum tunneleffekt bei supraleitern in mikrowellenfeld. *Z. Naturforsch.*, **19A**, 1634–1635 (1964).
- Rifkin R. and B. S. Deaver, Jr. Current-phase relation and phase-dependent conductance of superconducting point contacts from rf impedance measurements. *Phys. Rev.*, **B13**, 3894–3901 (1976).
- Rifkin R., D. A. Vincent, P. K. Hansma, and B. S. Deaver, Jr. Detailed measurements of the response of an rf SQUID in the regime $\angle I_c < \Phi_0 / 2\pi$. *ASC* **74**, 873–876 (1974).
- Rifkin R., D. A. Vincent, B. S. Deaver, Jr., and P. K. Hansma. R.F. SQUID's in the nonhysteretic mode. Detailed comparison of theory and experiment. *J. Appl. Phys.*, **47**, 2645–2650 (1976).
- Rissman P. Photosensitivity in superconducting tunnel junctions with cadmium selenide barrier. *J. Appl. Phys.*, **44**, 1893–1894 (1973).
- Rissman P. and T. Palholmen. Preparation and lifetest of niobium Josephson junction tunnel diodes and arrays. *Solid State Comm.*, **17**, 611–615 (1974).
- Rochlin G. I. and P. K. Hansma. Inexpensive mechanical model of a Josephson weak-link. *Am. J. Phys.*, **41**, 878–887 (1973).
- Rogovin D. The Josephson junction as a macroscopic radiating atom. *Ann. Phys.*, **90**, 18–47 (1975a).
- Rogovin D. Electrodynamics of Josephson junctions. *Phys. Rev.*, **B11**, 1906–1908 (1975b).

- Rogovin D. Josephson tunneling: an example of steady-state superradiance. *Phys. Rev.*, **B12**, 130–133 (1975c).
- Rogovin D. Further studies on the two-level-atom picture of the Josephson effect. *Phys. Rev.*, **B13**, 1980–1991 (1976).
- Rogovin D. and D. J. Scalapino. Power spectrum for superconducting tunnel junction. *Bull. Am. Phys. Soc.*, **13**, 475 (1968).
- Rogovin D. and D. J. Scalapino. Tunnel junction current fluctuations. ICSS, 399–404 (1969).
- Rogovin D. and D. J. Scalapino. Fluctuation phenomena in tunnel junctions. *Ann. Phys.*, **86**, 1–90 (1974).
- Rogovin D. and M. O. Scully. Does the two-level atom picture of a Josephson junction have a theoretical foundation in B.C.S.? *Ann. Phys.*, **88**, 371–396 (1974).
- Romagnan J. P., A. Gilabert, J. C. Noiray, and E. Guyon. Study of superconducting tin-lead proximity sandwich by Josephson tunneling. *Sol. State Comm.*, **14**, 83–86 (1974).
- Romani G. L. Superconducting instrumentation for biomagnetism. *Int. J. of Refrigeration*, **2**, 215–219 (1979).
- Rosen A., G. T. Induye, and A. L. Morse. Magnetic recordings of the heart's electrical activity with a cryogenic magnetometer. *J. Appl. Phys.*, **42**, 3682–3684 (1971).
- Rowell J. M. Magnetic field dependence of the Josephson tunnel current. *Phys. Rev. Lett.*, **11**, 200–202 (1963).
- Rowell N. L. and H. J. T. Smith. Investigation of the superconducting proximity effect by Josephson tunneling. *Can. J. Phys.*, **54**, 223–226 (1976).
- Rubinstein J. Sine-Gordon equation. *J. Math. Phys.*, **11**, 258–266 (1970).
- Rudner S., T. Claeson, and S. Wahlsten. Temperature and magnetic field variations in the resistance, $\cos \varphi$ conductance, and effective capacitance of small Josephson junctions. *Solid State Comm.*, **26**, 953–956 (1978).
- Rusinov A. I. Superconductivity near a paramagnetic impurity. *Zh. Eksp. Teor. Fiz. Pis. Red.*, **9**, 146–149 (1969a). *JETP Lett.*, **9**, 85–87 (1969).
- Rusinov A. I. On the theory of gapless superconductivity in alloys containing paramagnetic impurities. *Zh. Eksp. Teor. Fiz.*, **56**, 2047–2056 (1969b). *Sov. Phys. JETP*, **29**, 1101–1106 (1969).
- Russer P. General energy relations for Josephson junctions. *Proc. IEEE (Lett.)*, **59**, 282–283 (1971).
- Russer P. Influence of microwave radiation on current-voltage characteristic of superconducting weak links. *J. Appl. Phys.*, **43**, 2008–2010 (1972).
- Russo M. Fotosensibilità in giunzioni tunnel superconduttrici. *Atti Congresso Cibernetica*, GRC, Casciana Terme, Pisa, 1971, pp. 424–435, in Italian.
- Russo M. Self-resonant modes in light-sensitive Josephson tunnel junctions. *Phys. Lett.*, **61A**, 191–192 (1977).
- Russo M. and R. Vaglio. Self-resonant modes in Josephson junctions exhibiting a nonuniform maximum current distribution. *Phys. Rev.*, **B17**, 2171–2174 (1978).
- Rybal'chenko L. F. and S. I. Bondarenko. SQUID with two $V-V_xO_y-Pb$ tunnel junctions. *Zh. Tech. Fiz.*, **48**, 578–582 (1978). *Sov. Phys. Tech. Phys.*, **23**, 339–349 (1978).
- Saarinen M., P. J. Karp, T. E. Katila, and P. Siltanen. The magnetocardiogram in cardiac disorders. *Cardiovasc. Res.*, **8**, 820–834 (1974).
- Sacchetti N., M. V. Ricci, and G. Paternò. Unpublished, 1973.
- Samuelson M. R. Unpublished (1978).
- Sandell R. D., G. J. Dolan, and J. E. Lukens. Preparation of variable thickness microbridges using electron beam lithography and ion etching. IC-SQUID 76, 93–100 (1976).

- Satterthwaite C. B., M. G. Crawford, R. N. Peacock, and R. P. Ries. D.C. pair tunneling between two superconductors at finite voltages. LT 9, Part A, 443–445 (1964).
- Saxena A., J. E. Crow, and M. Strongin. Coherent behavior in Josephson junction arrays. LT 13, 3, 696–700 (1972).
- Scalapino D. J. Current fluctuation in superconducting tunnel junctions. SPSD, G1–G19 (1967).
- Scalapino D. J. and T. M. Wu. Radiation-induced structure in the dc Josephson current. *Phys. Rev. Lett.*, **17**, 315–318 (1966).
- Schlup W. Possible influence of the quasiparticle-pair interference term on the current-voltage characteristics of oxide barrier Josephson junctions. *Solid State Comm.*, **12**, 631–634 (1973).
- Schlup W. A. I-V characteristics and stationary dynamics of a Josephson junction including the interference term in the current phase relation. *J. Phys. C. Solid State Phys.*, **7**, 736–748 (1974).
- Schlup W. A. Solution of the Werthamer equation at finite temperatures. *Phys. Rev.*, **B18**, 6132–6138 (1978a).
- Schlup W. A. Adiabatic and pendulum approximations to the retarded Josephson equation. *J. Appl. Phys.*, **49**, 3011–3017 (1978b).
- Schmid A. Superconductors out of thermal equilibrium. LT 15, 1360–1367 (1978).
- Schmid A. and G. Shön. Linearized kinetic equations and relaxation processes of a superconductor near T_c . *J. Low Temp. Phys.*, **20**, 207–227 (1975).
- Schmid A., G. Schön, and M. Tinkham. Dynamic properties of superconducting weak links. *Phys. Rev.*, **B21**, 5076–5086 (1980).
- Schroen W. Physic of preparation of Josephson barriers. *J. Appl. Phys.*, **39**, 2671–2678 (1968).
- Schroen W. and J. P. Pritchard, Jr. Maximum tunneling supercurrents through Josephson barriers. *J. Appl. Phys.*, **40**, 2118–2122 (1969).
- Schulz-Du Bois E. O. and P. Wolf. Static characteristics of Josephson interferometers. *Appl. Phys.*, **16**, 317–338 (1978).
- Schwidtal K. Type I and type II superconductivity in wide Josephson junctions. *Phys. Rev.*, **B2**, 2526–2532 (1970).
- Schwidtal K. Dc and ac Josephson effect in sputtered $\text{Nb}-\text{NbO}_x-\text{Pb}$ junctions. *J. Appl. Phys.*, **43**, 202–208 (1972).
- Schwidtal K. and R. D. Finnegan. Barrier-thickness dependence of the dc quantum interference effect in thin-film lead Josephson junctions. *J. Appl. Phys.*, **40**, 2123–2127 (1969).
- Schwidtal K. and R. D. Finnegan. Maximum dc Josephson current in $\text{Pb}-\text{PbO}_x-\text{Pb}$ junctions. *Phys. Rev.*, **B2**, 148–154 (1970).
- Schwidtal K. and C. F. Smiley. Magnetic field and Q dependence of self-induced current peaks in resonant Josephson tunnel junctions. LT 13, 4, 575–579 (1972).
- Schyfter M., J. Maah-Sango, N. Raley, R. Ruby, B. T. Verich, and T. Van Duzer. Silicon-barrier Josephson junctions in coplanar and sandwich configuration. ASC 76, 862–865 (1976).
- Scott A. C. Steady propagation of long Josephson junctions. *Bull. Am. Phys. Soc.*, **12**, 308 (1967).
- Scott A. C. A nonlinear Klein-Gordon equation. *Am. J. Phys.*, **37**, 52–61 (1969).
- Scott A. C. *Active and Nonlinear Wave Propagation*. Wiley-Interscience, New York, 1970.
- Scott A. C. Magnetic flux annihilation in large Josephson junctions. 1978. *Proc. Conference on Stochastic Systems* (J. Ford, Ed.), Como, June 1977.
- Scott A. C. and W. J. Johnson. Internal flux motion in large Josephson junctions. *Appl. Phys. Lett.*, **14**, 316–318 (1969).
- Scott A. C., F. Y. F. Chu, and D. W. McLaughlin. The soliton: A new concept in applied science. *Proc. IEEE*, **61**, 1443–1483 (1973).

- Scott A. C., F. Y. F. Chu, and S. A. Reible. Magnetic flux propagation on a Josephson transmission line. *J. Appl. Phys.*, **47**, 3272–3286 (1976).
- Scott W. C. Hysteresis in the dc switching characteristics of Josephson junctions. *Appl. Phys. Lett.*, **17**, 166–169 (1970a).
- Seifarth H. and W. Rentsch. V-V_xO_y-Pb Josephson tunnel junctions of high stability. *Phys. Status Solidi, (a)* **18**, 135–146 (1973).
- Seraphim G. R. S. Weak links between superconductors. Ph.D. Thesis, St. Catherine's College, Oxford University, Oxford (1970).
- Seto J. and T. Van Duzer. Supercurrent tunneling junctions with tellurium barriers. *Appl. Phys. Lett.*, **19**, 488–491 (1971).
- Seto J. and T. Van Duzer. Theory and measurements on lead-tellurium-lead supercurrent junctions. *LT 13, 3*, 328–333 (1972).
- Shapiro S. Josephson currents in superconducting tunneling: The effect of microwaves and other observations. *Phys. Rev. Lett.*, **11**, 80–82 (1963).
- Shapiro S. Microwave harmonic generation from Josephson junctions. *J. Appl. Phys.*, **38**, 1879–1884 (1967).
- Shapiro S., P. H. Smith, J. Nicol, J. L. Miles, and P. F. Strong. Superconductivity and electron tunneling. *IBM J. Res. and Develop.*, **6**, 34–43 (1962).
- Shapiro S., A. R. Janus, and S. Holly. Effect of microwaves on Josephson currents in superconducting tunneling. *Rev. Mod. Phys.*, **36**, 223–225 (1964).
- Shen L. Y. L. Superconductivity of tantalum, niobium and lanthanum studied by electron tunneling: Problems of surface contamination. In *Superconductivity in d and f band metals* (D. H. Douglass, Ed.), AIP Conference Proceedings No. 4, American Institute of Physics, New York, 1972.
- Shiba H. Classical spins in superconductors. *Prog. Theor. Phys.*, **40**, 435–451 (1968).
- Silver A. H. and J. E. Zimmerman. Quantum states and transitions in weakly connected superconducting rings. *Phys. Rev.*, **157**, 317–341 (1967).
- Silver A. H. and J. E. Zimmerman. Josephson weak-link devices. In *Applied Superconductivity* (V. L. Newhouse, Ed.), Vol. 1, Academic, New York, 1975, chap. 1, pp. 1–112.
- Silver A. H., J. E. Zimmerman, and R. A. Kamper. Contribution of thermal noise to the line-width of Josephson radiation from superconducting point contacts. *Appl. Phys. Lett.*, **11**, 209–211 (1967).
- Silvert W. Variational solution of the superconducting proximity effect for arbitrary mean free path. *Solid State Comm.*, **14**, 635–638 (1974).
- Simmonds M. and W. H. Parker. Thermal fluctuations in superconducting weak links. *Phys. Rev. Lett.*, **24**, 876–879 (1970).
- Simmonds M. B. and W. H. Parker. Analog computer simulation of weakly connected superconducting rings. *J. Appl. Phys.*, **42**, 38–45 (1971).
- Skocpol W. J. Critical currents of superconducting microbridges. *Phys. Rev.*, **B14**, 1045–1051 (1976).
- Skocpol W. J. High-frequency properties of microbridge and point contact Josephson junctions. *FTSE*, 335–339 (1978).
- Skocpol W. J., M. R. Beasley, and M. Tinkham. Phase-slip centers and nonequilibrium processes in superconducting tin microbridges. *J. Low Temp. Phys.*, **16**, 145–167 (1974a).
- Skocpol W. J., M. R. Beasley, and M. Tinkham. Self-heating hotspots in superconducting thin-film microbridges. *J. Appl. Phys.*, **45**, 4054–4066 (1974b).
- Smith H. I. Fabrication techniques for surface-acoustic-wave and thin-film optical devices. *Proc. IEEE*, **62**, 1361–1387 (1974).

- Smith H. I., D. L. Spears, and S. E. Bernacki. X-Ray lithography: A complementary technique to electron beam lithography. *J. Vac. Sci. Tech.*, **10**, 913–917 (1973).
- Smith H. J. T. and J. A. Blackburn. Multiple quantum flux penetration in superconducting loops. *Phys. Rev.*, **B12**, 940–942 (1975).
- Smith H. J. T. and N. L. Rowell. Proximity effects and the generalized Ginzburg-Landau equation. *Phys. Rev.*, **B11**, 1053–1058 (1975).
- Smith P. H., S. Shapiro, J. L. Miles, and J. Nicol. Superconducting characteristics of superimposed metal films. *Phys. Rev. Lett.*, **6**, 686–688 (1961).
- Smith T. I. Observation of persistent currents in a superconducting circuit containing a Josephson junction. *Phys. Rev. Lett.*, **15**, 460–462 (1965).
- Smith T. I. Superconducting microwave cavities and Josephson junctions. *J. Appl. Phys.*, **45**, 1875–1878 (1974).
- So C. K. and W. O. Hamilton. Untuned Josephson detectors of microwave and millimeterwave radiation. *J. Appl. Phys.*, **48**, 2037–2042 (1977).
- Sørensen O. H. Unpublished (1971).
- Sørensen O. H. Analysis of the ac-SQUID with low inductance and low critical current. *J. Appl. Phys.*, **47**, 5030–5037 (1976).
- Sørensen O. H., T. F. Finnegan and N. F. Pedersen. Study of the geometrical resonances of superconducting tunnel junctions. *Appl. Phys. Lett.*, **22**, 129–131 (1973).
- Sørensen O. H., J. Mygind and N. F. Pedersen. Measured temperature dependence of the $\cos \varphi$ conductance in Josephson tunnel junctions. *Phys. Rev. Lett.*, **39**, 1018–1021 (1977).
- Sørensen O. H., J. Mygind, and N. F. Pedersen. Microwave parametric amplifiers using externally pumped Josephson junctions. FTSE, 246–253 (1978).
- Sørensen O. H., B. Kofoed, N. F. Pedersen, and S. Shapiro. Microwave dependence of sub-harmonic gap structure in superconducting junctions. *Phys. Rev.*, **B9**, 3746–3756 (1974).
- Sørensen O. H., J. Mygind, N. F. Pedersen, V. N. Gubankov, M. T. Levinsen and P. E. Lindelof. Nonresonant detection of Josephson radiation from thin-film microbridges. *J. Appl. Phys.*, **48**, 5372–5374 (1977).
- Solymar L., *Superconductive Tunnelling and Applications*, Chapman and Hall, London, 1972.
- Somervuo P. and Y. Sirkeinen. Simple method of determining the external signal voltage in Josephson junctions. *J. Appl. Phys.*, **46**, 1415–1416 (1975).
- Song Y. Origin of “capacitance”, in superconducting microbridges. *J. Appl. Phys.*, **47**, 2651–2655 (1976).
- Song Y. and G. I. Rochlin. Transition from bulk-like behavior to Josephson-junction-like behavior in superconducting microbridges. *Phys. Rev. Lett.*, **29**, 416–419 (1972).
- Spears D. L. and H. I. Smith. High-resolution pattern replication using soft x-rays. *Electron. Lett.*, **8**, 102–104 (1972a).
- Spears D. L. and H. I. Smith. X-ray lithography—A new high resolution replication process. *Solid State Tech.*, **15**, 21–26 (1972b).
- Spears D. L., H. I. Smith, and E. Stern. X-ray replication of scanning electron microscope generated patterns. In *Proc. 5th International Conference on Electron and Ion Beam Science and Technology*, Houston 7–11 May 1972 (R. Bakish, Ed.) published by The Electrochemical Society, Princeton, N.J., 1972, pp. 80–91.
- Stephen M. J. Theory of a Josephson oscillator. *Phys. Rev. Lett.*, **21**, 1629–1632 (1968).
- Stephen M. J. Lectures on Josephson tunneling. In *Superconductivity* (Wallace, Ed.), Vol. I, Gordon and Breach, New York, 1969a, pp. 297–326.
- Stephen M. J. Noise in the a.c. Josephson effect. *Phys. Rev.*, **182**, 531–538 (1969b).
- Stephen M. J. Noise in a driven Josephson oscillator. *Phys. Rev.*, **186**, 393–397 (1969c).

- Stewart J. L. The power spectrum of a carried frequency modulated by Gaussian noise. *Proc. IRE*, **42**, 1539–1542 (1954).
- Stewart W. C. Current-voltage characteristics of Josephson junctions. *Appl. Phys. Lett.*, **12**, 277–280 (1968).
- Stewart W. C. Current-voltage characteristics of superconducting tunnel junctions. *J. Appl. Phys.*, **45**, 452–456 (1974).
- Strassler S. and H. R. Zeller. Subharmonic structure in superconducting tunnel junctions. *Phys. Rev.*, **B3**, 226–228 (1971).
- Stratonovich R. L. Oscillator synchronization in the presence of noise. *Radiotekh. Elektron.*, **3**, 497 (1958). Also in *Nonlinear Transformations of Stochastic Processes* (P. I. Kuznetsov, R. L. Stratonovich, and V. I. Tikhonov, Eds.). Pergamon, 1965, pp. 269–282.
- Stratonovich R. L. *Topics in the Theory of Random Noise*. Gordon and Breach, New York, 1967.
- Stuehm D. L. and C. W. Wilmsen. Geometrical dependence of the maximum dc Josephson current. *J. Appl. Phys.*, **42**, 869–870 (1971).
- Stuehm D. L. and C. W. Wilmsen. Diffraction patterns and vortex structure of asymmetrical and cross Josephson junctions. *J. Appl. Phys.*, **45**, 429–433 (1974).
- Sullivan D. B. and J. E. Zimmerman. Mechanical analogs of time dependent Josephson phenomena. *Am. J. Phys.*, **39**, 1504–1517 (1971).
- Svidzinskii A. V., T. N. Antsygina, and E. N. Bratus. Superconducting current in wide S-N-S junctions. *Zh. Eksp. Teor. Fiz.*, **61**, 1612–1619 (1971). *Sov. Phys. JETP*, **34**, 860–863 (1972).
- Swihart J. C. Field solution for a thin-film superconducting strip transmission line. *J. Appl. Phys.*, **32**, 461–469 (1961).
- Taguchi I. and H. Yoshioka. Josephson effect like behavior of point contacts between normal and superconducting metals. *J. Phys. Soc. (Japan)*, **27**, 1074 (1969).
- Taguchi I. and H. Yoshioka. Properties of superconducting point contacts. *J. Phys. Soc. (Japan)*, **29**, 371–379 (1970).
- Taur Y. Josephson junctions as microwave heterodyne detectors. Ph.D. Thesis, University of California, Berkeley (1974).
- Taur Y. and A. R. Kerr. Progress on millimeter wave Josephson junction mixers. FTSE, 254–258 (1978a).
- Taur Y. and A. R. Kerr. Low-noise Josephson mixers at 115 GHz using recyclable point contact. *Appl. Phys. Lett.*, **32**, 775–777 (1978b).
- Taur Y. and P. L. Richards. Parametric amplification and oscillation at 36 GHz using a point-contact Josephson junction. *J. Appl. Phys.*, **48**, 1321–1326 (1977).
- Taur Y., J. H. Claassen, and P. L. Richards. Conversion gain and noise in a Josephson mixer. DEJJ, 263–268 (1973).
- Taur Y., J. H. Claassen, and P. L. Richards. Conversion gain in a Josephson effect mixer. *Appl. Phys. Lett.*, **24**, 101–103 (1974a).
- Taur Y., J. H. Claassen, and P. L. Richards. Josephson junctions as heterodyne detectors. *IEEE Trans. Micr. Theory Tech.*, **MTT-22**, 1005–1009 (1974b).
- Taur Y., P. L. Richards, and F. Auracher. Application of the shunted junction model to point-contact Josephson junctions. LT 13, **3**, 276–280 (1972).
- Taylor B. N., E. Burstein, and D. N. Langenberg. Electron tunneling between identical superconductors. *Bull. Am. Phys. Soc.*, **7**, 190 (1962).
- Taylor B. N., D. N. Langenberg, and W. H. Parker. The fundamental physical constants. *Sci. Am.*, **223** (4), 62–78 (1970).
- Taylor B. N., W. H. Parker, and D. N. Langenberg. Determination of e/h using macroscopic quantum phase coherence in superconductors: Implications for quantum electrodynamics and the fundamental physical constants. *Rev. Mod. Phys.*, **41**, 375–496 (1969).

- Taylor B. N., W. H. Parker, D. N. Langenberg, and A. Denestein. On the use of the ac Josephson effect to maintain standards of electromotive force. *Metrologia*, **3**, 89–98 (1967).
- Terma F. E. *Radio Engineering*. McGraw-Hill, New York, 1951.
- Tesche C. D. and J. Clarke. A computer model for noise in the d.c. SQUID. ASC 76, 859–861 (1976).
- Tesche C. D. and J. Clarke. D.c. SQUID: noise and optimization. *J. Low Temp. Phys.*, **29**, 301–331 (1977).
- Tholfsen P. and H. Meissner. Flux flow in thin type-I superconducting films. *Phys. Rev.*, **185**, 653–663 (1969).
- Thomé H. and Y. Couder. High frequency Josephson effect and Riedel anomaly at the gap frequency. LT 14, **4**, 156–159 (1975).
- Thompson E. D. Power flow for Josephson elements. *IEEE Trans. Electron Dev.*, **ED-20**, 680–683 (1973).
- Tien P. K. and J. P. Gordon. Multiphoton process observed in the interaction of microwave fields with the tunneling between superconductor films. *Phys. Rev.*, **129**, 647–651 (1963).
- Tikhonov V. I. The effect of noise on the operation of a phase AFC circuit. *Autom. Telemekh.*, **20**, 1188 (1959). Also in *Nonlinear Transformations of Stochastic Processes* (P. I. Kuznetsov, R. L. Stratonovich, and V. I. Tikhonov, Eds.). Pergamon, Oxford, 1965, pp. 298–309.
- Tilley D. R. Superradiance in arrays of superconducting weak links. *Phys. Lett.*, **33A**, 205–206 (1970).
- Tinkham M. Consequence of fluxoid quantization in the transitions of superconducting films. *Rev. Mod. Phys.*, **36**, 268–276 (1964).
- Tinkham M. *Introduction to superconductivity*. McGraw-Hill, New York, 1975.
- Tinkham M. Junctions—Types, properties and limitations. FTSE, 269–279 (1978).
- Tinkham M., M. Octavio, and W. J. Skocpol. Heating effects in high-frequency metallic Josephson devices: Voltage limit, bolometric mixing, and noise. *J. Appl. Phys.*, **48**, 1311–1320 (1977).
- Tolner H. Spectral response of point-contact Josephson junctions. *J. Appl. Phys.*, **48**, 691–701 (1977).
- Tolner H. and C. D. Andriesse. Microwave response of Josephson junctions in the presence of strong fluctuations. *Phys. Lett.*, **49A**, 255–256 (1974a).
- Tolner H. and C. D. Andriesse. High impedance point contact Josephson junctions. ASC 74, 866–869 (1974b).
- Tolner H., C. D. Andriesse, and H. H. A. Schaeffer. Wide-band detection with high impedance Josephson junctions. *Infrared Phys.*, **16**, 213–223 (1976).
- Tredwell T. J. and E. H. Jacobsen. Phonon-induced increase in the energy gap of superconducting films. *Phys. Rev.*, **B13**, 2931–2942 (1976).
- Truong V. K. and J. Baixeras. Comportement type Josephson d'un alliage eutectique lamellaire In₂Bi–In(Bi) formant une structure SNS périodique. LT 15, 195–203 (1978).
- Tsang W.-T. and T. Van Duzer. D.C. analysis of parallel arrays of two and three Josephson junctions. *J. Appl. Phys.*, **46**, 4573–4580 (1975).
- Tsubo T. Photosensitive tunnel junctions and photosensitive granular films with Te or Se barriers. *Phys. Lett.*, **56A**, 472–474 (1976).
- Ulrich B. T. Josephson junctions in astronomy. LT 12, 867–869 (1970).
- Ulrich B. T. Josephson junction detector for astronomical applications. DEJJ, 111–118 (1973).
- Ulrich B. T. and T. Van Duzer. Fabrication of Josephson junctions. NASI 76, 321–353 (1976).
- Usadel K. D. Generalized diffusion equation for superconducting alloys. *Phys. Rev. Lett.*, **25**, 507–509 (1970).
- Vaglio R. Approximate analysis for stationary current flow in two-dimensional Josephson tunnel junctions. *J. Low Temp. Phys.*, **25**, 299–315 (1976).

- Van den Dries L., C. Van Haesendonck, Y. Bruynseraede, and A. Gilabert. Thickness dependence of the maximum D.C. Josephson current in superconducting proximity junctions. *Phys. Lett.*, **72A**, 45–47 (1979).
- Van Duzer T. Junction fabrication techniques. IC SQUID 76, 63–92 (1976).
- Vant-Hull L. Effects of fluctuations on junction characteristics. In *Proceedings of the Conference on Fluctuations in Superconductors*, Asilomar Conference Grounds, Pacific Grove, California, March 1968 (W. S. Gorel and F. Chilton, Eds.), pp. 291–203. Stanford Research Institute, Palo Alto, 1968.
- Vant-Hull L. L. and J. E. Mercereau. Normal Josephson junctions and quantum coherence. *Phys. Rev. Lett.*, **17**, 629–631 (1966).
- Varmazis C., J. E. Lukens, and T. F. Finnegan. Broadband generation of tunable Josephson radiative at microwave frequencies. *Appl. Phys. Lett.*, **30**, 660–661 (1977).
- Varmazis C., R. D. Sandell, A. K. Jain, and J. E. Lukens. Generation of coherent tunable Josephson radiation at microwave frequency with narrowed linewidth. *Appl. Phys. Lett.*, **33**, 357–359 (1978).
- Vasenko S. A. and G. F. Zharkov. Passage of current through a Josephson barrier of finite dimensions. *Zh. Eksp. Teor. Fiz.*, **75**, 180–190 (1978). *Sov. Phys., JETP* **48**, 89–94 (1979).
- Vasil'ev B. V., V. V. Danilov, and K. K. Likharev. On some aspects of superconducting quantum interferometer optimization. ASC 74, 743–748 (1974).
- Vasil'ev B. V., V. V. Danilov, and K. K. Likharev. SQUID signal in the hysteresis mode. *Zh. Tekh. Fiz.*, **46**, 2409–2414 (1976). *Sov. Phys. Tech. Phys.*, **21**, 1419–1421 (1976).
- Vernet G. and R. Adde. Linewidth of the radiation emitted by a Josephson point contact. *Appl. Phys. Lett.*, **19**, 195–197 (1971).
- Vernet G. and R. Adde. Direct observation of the Riedel singularity in a superconducting point contact. *Appl. Phys. Lett.*, **28**, 559–561 (1976).
- Vincent D. A. and B. S. Deaver, Jr. Observation of a phase-dependent conductivity in superconducting point contacts. *Phys. Rev. Lett.*, **32**, 212–215 (1974).
- Volkov A. F. Weak coupling produced in superconductors by irradiation. *Zh. Eksp. Teor. Fiz.*, **60**, 1500–1508 (1971). *Sov. Phys. JETP*, **33**, 811–815 (1971).
- Volkov A. F. Critical current in narrow superconducting links. *Fiz. Tverd. Tela.*, **15**, 1364–1368 (1973). *Sov. Phys. Solid State*, **15**, 925–927 (1973).
- Volkov A. F. Nonequilibrium states in superconducting tunnel structures. *Sov. Phys. JETP*, **41**, 376–380 (1975). *Zh. Eksp. Teor. Fiz.*, **68**, 756–765 (1975).
- Voss R. F. Uncertainty principle limit to the energy sensitivity of SQUID's and other linear amplifiers. *Appl. Phys. Lett.*, **38**, 182–184 (1981).
- Voss R. F. and J. Clarke. Flicker ($1/f$) noise: Equilibrium temperature and resistance fluctuations. *Phys. Rev.*, **B13**, 556–573 (1976).
- Voss R. F., R. B. Laibowitz, and A. N. Broers. Niobium nanobridges d.c. SQUID. *Appl. Phys. Lett.*, **37**, 656–658 (1980).
- Voss R. F., R. B. Laibowitz, and S. I. Raider. All-Nb low-noise d.c. SQUID with $1 \mu\text{m}$ tunnel junctions. *J. Appl. Phys.*, **51**, 2306–2309 (1980).
- Voss R. F., R. B. Laibowitz, M. B. Ketchen, and A. N. Broers. Ultra low noise d.c. SQUIDs. IC SQUID 80, (1980, to be published).
- Vrba J. and S. B. Woods. Tunneling into weakly coupled films of tin and aluminum in proximity II from the tin side. *Phys. Rev.*, **B4**, 87–94 (1971a).
- Vrba J. and S. B. Woods. Tunneling into weakly coupled films of aluminum and tin in proximity. *Phys. Rev.*, **B3**, 2243–2252 (1971b).
- Vystavkin A. N., V. N. Gubankov, G. F. Leshchenko, K. K. Likharev, and V. V. Migulin. Parametric conversion and amplification using the superconducting point contacts. *Radiotekhnika i Elektron.*, **15**, 2404–2407 (1970). *Radio Engin. Electron. Phys.*, **15**, 2121–2124 (1970).

- Vystavkin A. N., V. N. Gubankov, L. S. Kuzmin, K. K. Likharev, V. V. Migulin, and V. K. Semenov. S-c-S junctions as nonlinear elements of microwave receiving devices. DEJJ, 79–109 (1973).
- Vystavkin A. N., V. N. Gubankov, L. S. Kuzmin, K. K. Likharev, V. V. Migulin, and V. K. Semenov. Non-Josephson radiation from the cavity containing superconducting point contact junction. ASC 74, 834–837 (1974).
- Vystavkin A. N., V. N. Gubankov, L. S. Kuzmin, K. K. Likharev, V. V. Migulin, and V. K. Semenov. One-frequency parametric amplifier using self-pumped Josephson junction. ASC 76, 233–236 (1976).
- Wahlsten S., S. Rudner, and T. Claeson. Parametric amplification in arrays of Josephson tunnel junctions. *Appl. Phys. Lett.*, **30**, 298–300 (1977).
- Wahlsten S., S. Rudner, and T. Claeson. Arrays of Josephson tunnel junctions as parametric amplifiers. *J. Appl. Phys.*, **49**, 4248–4263 (1978).
- Waho T., K. Kuroda, and A. Ishida. Aging phenomena of plasma oxidized Pb-alloy Josephson junctions. *J. Appl. Phys.*, **51**, 4508–4512 (1980).
- Waldrum J. R., A. B. Pippard, and J. Clarke. Theory of current-voltage characteristics of SNS junctions and other superconducting weak links. *Phil. Trans. Roy. Soc.*, **A268**, 265–287 (1970).
- Wang L. K., D. J. Hyun, and B. S. Deaver, Jr. Heating and flux flow in niobium variable-thickness bridges. *J. Appl. Phys.*, **49**, 5602–5609 (1978).
- Wang L. K., A. Callegari, and B. S. Deaver, Jr., D. W. Barr and R. J. Mattauch. Microwave mixing with niobium variable thickness bridges. *Appl. Phys. Lett.*, **31**, 306–308 (1977).
- Wang T. C. Current-density distribution in Josephson tunnel junctions. *J. Appl. Phys.*, **50**, 2859–2862 (1979).
- Wang T. C. and R. I. Gayley. Erratic behaviour of superconducting loops with Josephson junctions. *Phys. Rev.*, **B15**, 3401–3404 (1977).
- Wang T. C. and R. I. Gayley. High-frequency losses in tin Josephson tunnel junctions. *Phys. Rev.*, **B18**, 293–300 (1978).
- Watson, H. L., R. T. Kampwirth, and R. P. Huebener. Current-induced magnetic-flux structures in a type-I superconducting constriction. *J. Appl. Phys.*, **45**, 3634–3637 (1974).
- Watts-Tobin R. J. and L. Kramer. Theory of the phase-slip state in superconducting filaments. LT 15, 554–555 (1978).
- Webb W. W. Superconducting quantum magnetometers. *IEEE Trans. Magn.*, **MAG-8**, 51–60 (1972).
- Weihnacht M. Influence of film thickness on dc Josephson current. *Phys. Status Solidi*, **32**, K169–172 (1969).
- Weitz D. A., W. J. Skocpol, and M. Tinkham. High-frequency behavior of “ideal” superconducting point contacts. *Phys. Rev. Lett.*, **40**, 253–256 (1978).
- Werthamer N. R. Theory of the superconducting transition temperature and energy gap function of superposed metal films. *Phys. Rev.*, **132**, 2440–2445 (1963).
- Werthamer N. R. Nonlinear self-coupling of Josephson radiation in superconducting tunnel junctions. *Phys. Rev.*, **147**, 255–263 (1966).
- Werthamer N. R. and S. Shapiro. Analog-computer studies of Josephson radiation effects. *Phys. Rev.*, **164**, 523–535 (1967).
- Whittaker E. T. and G. N. Watson. *A Course of Modern Analysis*. Cambridge University Press, Cambridge, 1952.
- Wikswo J. P., Jr. and W. M. Fairbank. Application of superconducting magnetometers to the measurement of the vector magnetocardiogram. ASC 76, 354–357 (1976).
- Wikswo J. P., Jr., G. E. Crawford, W. H. Barry, W. M. Fairbank, and D. C. Harrison. Computer data acquisition and signal processing techniques for magnetocardiography. In *Proceedings of the Conference: Computers in Cardiology*, St Louis, October 1976.

- Williamson, S. J. and L. Kaufman. Magnetic field of the cerebral cortex. IC SQUID 80, (1980 in press).
- Williamson S. J., D. Brenner, and L. Kaufman. Biomedical applications of SQUIDS. FTSE, 106–116 (1978).
- Williamson S. J., L. Kaufman, and D. Brenner. Biomagnetism. NASI 76, 355–402 (1976).
- Wilson J. and R. I. Gayley. Behaviour of multiple-quantum-state superconducting ring with Josephson tunnel junctions. *Solid State Comm.*, **11**, 1183–1185 (1972).
- Witham G. B. *Linear and Nonlinear Waves*. Wiley-Interscience, New York, 1975.
- Wolf P. SQUIDS as computer elements. IC-SQUID 76, 519–540 (1976).
- Wong T. W., J. T. C. Yeh, and D. N. Langenberg. Quasiparticle-injection-induced superconducting weak links. *Phys. Rev. Lett.*, **37**, 150–153 (1976).
- Wong T. W., J. T. C. Yeh, and D. N. Langenberg. Controllable superconducting weak links. ASC 76, 743–746 (1976).
- Wu C. T. and C. M. Falco. High-temperature Nb₃Sn thin-film SQUIDS. *Appl. Phys. Lett.*, **30**, 609–613 (1977).
- Wu C. T. and C. M. Falco. Fabrication and properties of high-temperature weak links and SQUID's. *J. Appl. Phys.*, **49**, 361–365 (1978).
- Wu H. S., K. T. Chi, and F. S. Liu. The effect of the magnetic field on the height of microwave-induced step of a Josephson tunneling junction. Presented at LT 15, 1978 (unpublished).
- Wyatt A. F. G., V. M. Dmitriev, W. S. Moore, and F. W. Sheard. Microwave-enhanced critical supercurrents in constricted films. *Phys. Rev. Lett.*, **16**, 1166–1169 (1966).
- Wynn W. M., C. P. Frahm, P. J. Carroll, R. H. Clark, J. Wellhoner, and M. J. Wynn. Advanced superconducting gradiometer/magnetometer arrays and a novel signal processing technique. ASC 74, 701–707 (1974).
- Yamashita T. and Y. Onodera. Magnetic field dependence of Josephson current influenced by self-field. *J. Appl. Phys.*, **38**, 3523–3525 (1967).
- Yamashita T. and L. Rindereer. Magnetization and pinning effect of a Josephson junction. *J. Low Temp. Phys.*, **21**, 153–167 (1975).
- Yamashita T., M. Kunita, and Y. Onodera. Magnetic field dependence of Josephson current modified by self-field. *J. Appl. Phys.*, **39**, 5396–5400 (1968a).
- Yamashita T., M. Kunita, and Y. Onodera. Josephson current limited by self-field. *Japan J. Appl. Phys.*, **7**, 288–290 (1968b).
- Yanson I. K. Effect of fluctuations on the dependence of the Josephson current on the magnetic field. *Zh. Eksp. Teor. Fiz.*, **58**, 1497–1510 (1970a). *Sov. Phys. JETP*, **31**, 800–807 (1970).
- Yanson I. K. Influence of barrier inhomogeneities on the Josephson critical current. *Tr. Fiz. Tekh. Inst. Nizk. Temp. N.* **8**, 19–26 (1970b).
- Yanson I. K. and L. F. Rybal'chenko. Tunnel effect in films of vanadium and its oxides. *Phys. Status Solidi*, (a) **28**, 663–671 (1975).
- Yanson I. K. and L. F. Rybal'chenko. Josephson effect in tunnel junctions with vanadium and vanadium oxide. *Fiz. Nizk. Temp.*, **3**, 44–56 (1977). *Sov. J. Low Temp. Phys.*, **3**, 21–27 (1977).
- Yanson T. K., V. M. Svistunov, and I. M. Dmitrenko. Experimental observation of Cooper pair tunneling between thin layers of superconducting tin. *Zh. Eksp. Teor. Fiz.*, **47**, 2091–2094 (1964). *Sov. Phys. JETP*, **20**, 1404–1406 (1965).
- Yanson I. K., V. M. Svistunov, and I. M. Dmitrenko. Experimental observation of the tunnel effect for Cooper pairs with the emission of photons. *Zh. Eksp. Teor. Fiz.*, **48**, 976–979 (1965). *Sov. Phys. JETP*, **21**, 650–653 (1965).
- Yao S.-S. Analytical solution of resistively shunted Josephson junctions. Presented at LT 15, 1978 (unpublished).

- Yeh J. T. C. and R. A. Buhrman. Superconducting lead variable-thickness microbridges. *J. Appl. Phys.*, **48**, 5360–5361 (1977).
- Yeh, J. T. C. and D. N. Langerberg. Light-induced superconducting weak-links. *Appl. Phys. Lett.*, **32**, 191–192 (1978).
- Yoshida K. and F. Irie. Frequency conversion in a long Josephson junction with a moving vortex array. *Appl. Phys. Lett.*, **27**, 469–470 (1975).
- Yoshida K. and F. Irie. Driving of a single vortex in a long Josephson junction. *Phys. Lett.*, **61A**, 253–255 (1977).
- Yoshida K., F. Irie, and K. Hamasaki. Current-voltage characteristics of large Josephson tunnel junctions. *Phys. Lett.*, **63A**, 144–146 (1977).
- Yoshida K., F. Irie, and K. Hamasaki. Flux flow characteristics of a large Josephson junction, *J. Appl. Phys.*, **49**, 4468–4474 (1978).
- Zagrodzinski J. The solutions of the two dimensional sine-Gordon equation. *Phys. Lett.*, **57A**, 213–214 (1976).
- Zagrodzinski J. Particular solutions of SGE in 2+1 dimensions. *Phys. Lett.* **A72**, 284–286 (1979).
- Zaikin A. D. and G. F. Zharkov. Contribution to the theory of weak superconductivity in SNINS systems. *Zh. Eksp. Teor. Fiz.* **78**, 721–732 (1978). *Sov. Phys. JETP* **51**, 364–369 (1980).
- Zaitsev R. O. Boundary conditions for the superconductivity equations at temperatures close to critical. *Zh. Eksp. Teor. Fiz.*, **48**, 1759–1771 (1965). *Sov. Phys. JETP*, **21**, 1178–1185 (1965).
- Zaitsev R. O. Boundary conditions and surface superconductivity. *Zh. Eksp. Teor. Fiz.*, **50**, 1055–1063 (1966). *Sov. Phys. JETP*, **23**, 702–707 (1966).
- Zakharov, V. E. and S. V. Manakov. Soliton theory. *Physics Reviews-Sov. Sci. Rev. A* (I. M. Khalatnikov, Ed.), Vol. 1, pp. 133–190 (1979).
- Zappe H. H. Evaluation of tunnel junction barriers using the magnetic field dependence of the dc Josephson current. IBM, Research Rep. RC 2974 (13854), July 23, 1970.
- Zappe H. H. Minimum current and related topics in Josephson tunnel junction devices. *J. Appl. Phys.*, **44**, 1371–1377 (1973).
- Zappe H. H. A single flux quantum Josephson junction memory cell. *Appl. Phys. Lett.*, **25**, 424–426 (1974).
- Zappe H. H. Quantum interference Josephson logic devices. *Appl. Phys. Lett.*, **27**, 432–434 (1975a).
- Zappe H. H. A subnanosecond Josephson tunneling memory cell with nondestructive readout. *IEEE J. Solid State Cir.*, **SC-10**, 12–19 (1975b).
- Zappe H. H. Determination of the current density distribution in Josephson tunnel junctions. *Phys. Rev.*, **B11**, 2535–2538 (1975c).
- Zappe H. H. Josephson quantum interference computer devices. ASC 76, 41–47 (1976).
- Zappe H. H. and K. R. Greebe. Ultra-high-speed operation of Josephson tunneling devices. *IBM J. Res. Develop.*, **15**, 405–407 (1971).
- Zappe H. H. and K. R. Greebe. Dynamic behavior of Josephson tunnel junctions in the subnanosecond range. *J. Appl. Phys.*, **A4**, 865–874 (1973).
- Zappe H. H. and B. S. Landman. Analysis of resonance phenomena in Josephson interferometer devices. *J. Appl. Phys.*, **49**, 344–350 (1978a).
- Zappe H. H. and B. S. Landman. Experimental investigation of resonances in low Q Josephson interferometer devices. *J. Appl. Phys.*, **49**, 4149–4154 (1978b).
- Zharkov G. F. and S. A. Vasenko. Penetration of a magnetic field into a Josephson junction. *Zh. Eksp. Teor. Fiz.* **74**, 665–680 (1978). *Sov. Phys. JETP*, **47**, 350–357 (1978).
- Zilberman L. A. The stability of the dc Josephson current. *Phys. Lett.*, **51A**, 95–96 (1975).
- Zilberman L. A. and Yu. M. Ivanchenko. Josephson coupling energy in the presence of thermal fluctuations. *Fiz. Tverd. Tela.* **12**, 1922–1930 (1970). *Sov. Phys. Solid State*, **12**, 1530–1535 (1971).

- Zil'berman L. A. and Yu. M. Ivanchenko. Effect of external fluctuations on the properties of superconducting microjunctions near critical temperature. *Zh. Eksp. Teor. Fiz.*, **60**, 2286–2295 (1971). *Sov. Phys. JETP*, **33**, 1229–1233 (1971).
- Zimmer H. Parametric amplification of microwaves in superconducting Josephson tunnel junctions. *Appl. Phys. Lett.*, **10**, 193–195 (1967).
- Zimmerman J. E. Sensitivity enhancement of superconducting quantum interference devices through the use of fractional-turn loops. *J. Appl. Phys.*, **42**, 4483–4487 (1971).
- Zimmerman J. E. Josephson effect devices and low-frequency field sensing. *Cryogenics*, **12**, 19–31 (1972a).
- Zimmerman J. E. A review of the properties and applications of superconducting point contacts. *ASC* 72, 544–561 (1972b).
- Zimmerman J. E. Superconductive quantum interference device having two cavities isolated by a superconductive weak link. U.S. Patent 3,758,854, September 11, 1973.
- Zimmerman J. E. SQUID instruments and shielding for low-level magnetic measurements. *J. Appl. Phys.*, **48**, 702–710 (1977).
- Zimmerman J. E. Private communication (1978a).
- Zimmerman J. E. Cryocoolers for superconductive electronics. FTSE, 412–420 (1978b).
- Zimmerman J. E. and N. V. Frederick. Miniature ultrasensitive superconducting magnetic gradiometer and its use in cardiography and other applications. *Appl. Phys. Lett.*, **19**, 16–19 (1971).
- Zimmerman J. E. and J. E. Mercereau. Compton wavelength of superconducting electrons. *Phys. Rev. Lett.*, **14**, 887–888 (1965).
- Zimmerman J. E. and A. H. Silver. Quantum effects in type II Superconductors. *Phys. Lett.*, **10**, 47–48 (1964).
- Zimmerman J. E. and A. H. Silver. Macroscopic quantum interference effects through superconducting point contacts. *Phys. Rev.*, **141**, 367–375 (1966a).
- Zimmerman J. E. and A. H. Silver. Flux entry in macroscopic superconducting rings. *Solid State Comm.*, **4**, 133–136 (1966b).
- Zimmerman J. E. and A. H. Silver. Coherent radiation from high-order quantum transitions in small-area superconducting contacts. *Phys. Rev. Lett.*, **19**, 14–16 (1967).
- Zimmerman J. E., J. A. Cowen, and H. Silver. Coherent radiation from voltage-biased weakly connected superconductors. *Appl. Phys. Lett.*, **9**, 353–355 (1966).
- Zimmerman J. E., P. Thiene, and J. T. Harding. Design and operation of stable rf-biased superconducting point-contact quantum devices, and a note on the properties of perfectly clean metal contacts. *J. Appl. Phys.*, **41**, 1572–1580 (1970).
- Zorin A. B. and K. K. Likharev. Current-voltage characteristics of low-capacitance Josephson junctions. *Fiz. Nizk. Temp.*, **3**, 148–151 (1977). *Sov. J. Low Temp. Phys.*, **3**, 70–71 (1977).
- Zorin A. B., I. O. Kulik, K. K. Likharev, and J. R. Schrieffer. On the sign of the quasiparticle-pair interference current in superconducting tunnel junctions. *Fiz. Nizk. Temp.*, **5**, 1138–1157 (1979). *Sov. J. Low Temp. Phys.*, **5**, 537–546 (1979).

Index

- A.C. Josephson effect, 12, 291–318
 inverse, 353
- Adiabatic approximation, 137, 139
- Analog:
 long junction, mechanical, 265–268,
 272–275, 286–287
 small junction, mechanical, 123–126
- Array structures, 234, 316, 318
 microwave radiation in, 316
 mixing and, 330
- Bäcklund transformation, 270
- Bolometers, 324
- Bridge structures:
 of constant thickness (C.T.B.), 177–179
 fabrication of, 228–232
 Ginzburg Landau theory of, 181–185
 proximity effect, 23, 180
 R.S.J. model in, 181, 187
 variable thickness (V.T.B.), 23, 177–181
 see also Dayem bridges
- Coherence length:
 for degenerate semiconductor layer, 172
 for superconductor-normal metal interface,
 162
- Computer elements, 446–473
 power dissipation for, 471–472
 logic circuits, 465–469
 memory cells, 461–465
- “Cos φ ” term, 39, 47–49, 153
- Coupling of Josephson junction:
 to microstripline, 315, 349, 352, 353
 to resonant cavity, 312
- Critical fields for large junction, 106, 108, 109
- Cryotron:
 thin film, 446–449
 tunneling junction, 449–451
- Cryotron tunneling:
 current steering for, 455, 457
 flip-flop configuration, 451–453
- Current density and vector potential, 2
- Current distribution in large junctions:
 effects of geometrical configurations in,
 112–120
 of one-dimensional geometry, 96–112
- Current phase relation:
 for bridge structures, 182–185, 191
 piecewise linear, 114
 sinusoidal, 11, 19, 69
- Current steps:
 microwave induced:
 current source model for, 305–309
 fluctuations effects on, 293–294, 350
 voltage source model for, 291–293
 voltage standard and, 347
 self-induced, *see* Self-resonant modes
- Cyclability:
 junctions thermal, 199–205, 225
 point contact, 232
- Dayem bridges, 23, 178, 228, 229
 see also Bridge structures
- Detection of electromagnetic radiation, 318–330
 see also Radiation detectors
- Double-junction configuration, *see* Interferometer
- Electrodynamics of Josephson junction, 19–22, 235–290
- Electron-beam lithography, 178, 216–217
- Energy functions for long junction, 269–271
- Energy gap, 4, 40, 41
 current biased junction and, 136, 138, 140
 enhancement of, 194, 307
 paramagnetic impurities effects, 60, 63
 single particle tunneling and, 8
 strong coupling effects on, 57
 sub-harmonic structures, 186, 191
- Fabrication technology, 198–234
- Fluctuations:
 structural, 91–95, 225–226
 thermal, 143–158

- Flux flow:
 in bridge structures, 189–191
 effects on voltage current characteristics,
 285–288
 in long junctions, 264–271, 273–288
 in metal barrier junctions, 287, 288
- Fluxoid, 355
 quantization of, 354–359, 361, 369
- Fluxon dynamics, 264–290
 losses and bias effects on, 274–278, 287,
 288
 perturbative analysis of, 279–285
 see also Flux flow
- Flux quantum, 17, 71, 108, 110, 354, 366,
 400, 420, 462
- Flux shuttle, 465
- Free energy for junction barrier, 18–19
 flux line and, 108–109
- Galvanometer, 435
- Gauge invariance, 2–3, 14–15
 and broken symmetry, 32
- Ginzburg-Landau theory, 1, 167, 169,
 181–183, 185
 time-dependent, 192
- Green functions, 30, 162
 Fourier transform of, 31
- Ground plane effects, 112, 113, 118
- Inductance, equivalent, for Josephson junction,
 22, 331, 384, 458
- Interferometer, 369–382
 of asymmetric two-junction configuration,
 375–382
 critical current for, 18, 371–372, 376–382,
 406
 fluxoid quantization in, 369
 magnetic field patterns for, 17, 378–382,
 406, 460
 as magnetometers, 403–408
 as memory cells, 461–463
 metastable states in, 373–375
 practical configurations for, 421–424, 467
 self-resonant steps in, 466, 467
 as switching devices, 459–460
- Inverse scattering transform method, 271
- Jacobian elliptic functions, 101, 102, 103,
 267, 269, 272, 273
- Josephson current:
 enhancement of, 187, 194–195, 307
 magnetic field dependence of:
- in large junctions, 96–120, 175, 177
 for nonuniform current density
 distribution, 79–95
 in small junctions, 69–95
 for uniform current density distribution,
 74–79
- measurement techniques of, 66–68
 with paramagnetic impurities, 59–65
- temperature dependence of,
 B.C.S. approximation, 50–56
 in bridge structures, 183–185
 in light-sensitive junctions, 175–176
 and paramagnetic impurities, 62–64
 in proximity effect structures, 164,
 167–168
 strong coupling effects for, 56–58
- Josephson current density:
 in magnetic field, 14–17, 70–72
 self field effects, 102–103, 106, 107
- Josephson effect:
 constitutive relations of, 11, 15
 discovery of, 1
 gapless superconductivity and, 62
 microscopic theory of, 25–39
 phenomenological theory of, 9–14, 181–182
- Josephson junctions:
 characteristic impedance for electromagnetic
 radiation, 309–310
 different geometrical configurations of, 112–120
 long, electrodynamics of, 264–290
 mechanical analog, *see Analog*
 mixing in, 324–330
 Josephson penetration depth, 20, 69–70
 temperature dependence of, 99
- Josephson radiation:
 detection of, 13–14, 318–330
 emission of, 309–318
 emitted, harmonics in, 313
 linewidth of, 313–315, 317
- Junction electrodes, *see Superconductors*
- Kramers-Kronig relations, 34, 37, 47
- Lift-off technique, 214–216
- Light-sensitive junctions:
 optical response of, 173–174
 preparation of, 224–225
 temperature dependence of, 175–176
- Logic functions, 284, 465–470
 see also Computer elements
- London penetration depth, 15, 16, 20
 measure of, 76
 temperature dependence of, 99
 typical values of, 200

- Magnetic susceptibility measurements, 437–439
- Magnetocardiogram, 439–441, 443
- Magnetoencephalogram, 441, 444, 445
- Magnetometers:
- applications of, 434–445
 - coupling to superconducting transformer, 428
 - d.c.-biased, 403–408
 - in feedback configuration, 424–426
 - noise in, 409–415
 - r.f.-biased, 398–403
 - sensor configurations for, 416–424
- Magnetotellurics, 445
- Manley-Rowe relations, 331, 332
- Memory cells, 461–465
- flip-flop circuit as, 461, 469
 - flux quantization and, 462, 465
 - single flux quantum, 462–465, 469–470
- Metal barrier junctions, 161–169
- Mixers, Josephson junction as, 324–330
- Mixing between harmonics, 329–330
- Noise power spectrum, 158–160, 413
- Nonequilibrium superconductivity, 191, 193–195, 307
- Oxide tunneling barrier:
- d.c. glow discharge for, 207–209, 219–220
 - r.f. glow discharge for, 210–211
 - thermal oxidation for, 206–207, 219–220
- Pair current, microscopic expression for, 38–39
- Pair current density, *see* Josephson current density
- Pair density, 9, 36
- B.C.S. approximation of, 39, 40, 41
 - with paramagnetic impurities, 59, 60, 62
 - and strong coupling, 57
- Pair tunneling, energy momentum diagram for, 12
- Parametric amplification, 330–344
- Parametric amplifiers:
- doubly degenerate, 333–340
 - externally pumped, 332–343
 - internally pumped, 343–344
 - singly degenerate, 340, 342–343
- Parametric inductance, Josephson junction, 22, 331, 384, 458
- Parametric quantron, 463–464
- Penetration depth:
- Josephson, 20, 69–70, 99
 - London, 15, 16, 20, 76, 99, 200
 - magnetic, 16, 69, 235, 238
- Phase plane analysis, 128–131, 282, 283
- Phase slip process, 191, 193
- Photolithography, 178, 212–216
- Physical constants determination of, 345
- Plasma frequency, 21–22, 48, 123, 336, 340, 342
- parametric excitation of, 340
- Point contact devices, 24, 196–197
- fabrication of, 232–234
 - phenomenological theory for, 181–182
- Power dissipation, in Josephson devices, 465, 469, 470–473
- Preparation procedure, *see* Fabrication technology
- Proximity effect, 23, 141, 161–169, 175
- Proximity-effect bridges, fabrication of, 231
- Quantum interference, 18, 369–382
- Quantum interference devices, *see* Interferometers; SQUID
- Quasiparticle current:
- microscopic expression of, 37–38
 - phenomenological expression of, 7
- Quasiparticle density, 36
- B.C.S. approximation of, 40
 - with paramagnetic impurities, 59–61
- Quasiparticle tunneling:
- energy momentum diagrams, 4, 6, 8
 - microscopic theory of, 25–47
 - phenomenological theory of, 4–9
 - photon-assisted, 298, 310
- Radiation detectors:
- narrow-band, 324–330
 - wide-band, 318–324
- Resistive loop devices:
- d.c.-biased, 429–431
 - r.f.-biased, 431–433
- Resistively shunted junction model (R.S.J.):
- autonomous case, 122–123, 126–128, 145
 - for bridges and point contacts, 181–182
 - nonautonomous case, 306
- Resonant modes in tunneling junctions, 235–263, 350
- see also* Self-resonant modes
- Riedel peak, 41, 47
- broadening of, 49, 303
 - in current-biased junctions, 138, 139
 - microwave-induced steps and, 296–304
- Self field, in large junctions:
- approximate analysis of, 96–100
 - theoretical analysis of, 100–112

- Self-resonant modes:**
- in bridge structures, 188, 191
 - in high Q junctions, 256–263
 - for junction of infinite length, 248–251
 - in low Q junctions, 238–248
 - non-uniform current density effects in, 251–255
 - in zero magnetic field, *see* Zero field step
- Semiconducting barrier junctions**, 169–177
- light-sensitive, 172–177
- Semiconductor barrier**, fabrication of, 222–228
- Sine Gordon equation**, 264
- solutions for finite boundary conditions of, 271–274
 - in two-dimensional junctions, 288–290
- Single-junction loop:**
- in applied magnetic field, 362–364
 - free energy for, 361
 - fluxoid quantization in, 359
 - flux transitions in, 364–369
 - Gibbs free energy for, 363, 364
 - as magnetometers, 401
 - as memory elements, 463–464
 - metastable states in, 360–361
 - parametric inductance effect in, 384–388
 - practical configurations for, 416–421
 - r.f.-biased, 383–403
- Singularities current**, microwave-induced, *see* Current steps
- Solder blob**, 24, 421–422
- Soliton solution of Sine Gordon equation**, 267, 270, 271
- SQUID:**
- d.c.-biased, 403–408
 - flux sensitivity of, 408, 415–416
 - r.f.-biased, 383–403
 - in dispersive mode, 388–398
 - in dissipative mode, 398–403
 - flux sensitivity of, 401, 415–416
- Subharmonic gap structure**, 186, 191
- SUPARAMP**, 333–340
- Superconducting loop**, 354–382
- fractional turn configuration for, 418–419
 - Gibbs free energy for, 355
 - with single junction, *see* Single-junction loop
 - with two junctions, *see* Interferometers
- Superconducting pairs**, macroscopic wave function, 2
- Superconducting transformer**, 426–429
- Superconductor-insulator-normal metal-superconductor (S-I-N-S) structures**, 166–169
- Superconductor-normal metal-superconductor (S-N-S) junctions**, 164–166
- Superconductors:**
- hard materials, 204–205, 220–221
 - soft-metal alloys, 200–204
 - soft metals, 199–200, 219
 - typical parameters of, 200
- Switching devices**, interferometer as, 459–460
- Switching time:**
- external load effects on, 456, 457
 - Josephson inductance effects on, 458–459
 - for junction gate, 449–451, 454–457
 - self-resonant modes and, 457
- Thermal fluctuations**, *see* Fluctuations
- Thin-film patterning**, 211–218
- Thin films**, superconducting, *see* Superconductors
- Time reversal symmetry**, 27, 59, 65
- Transmission line:**
- Josephson junction as, 235–238, 264–290
 - wavelength for electromagnetic radiation in, 295
 - wave velocity in, 237
- Tunneling**, Hamiltonian for, 10, 25–27
- Tunneling current**, microscopic expression of, 21, 28–34
- B.C.S. approximation**, 39–47
- for constant voltage, 35
- Tunneling junction:**
- capacitance, 20, 237
 - with current bias, 136–143
 - inductance, 237
 - in external microwave radiation, 294–305
 - preparation of, 198–211, 218–222
 - quality factor Q for, 245, 350
 - with shunt resistance, 135, 153
 - switching time of, 449–451, 454, 455, 471, 473
 - wave velocity in, 20, 237
- Voltage current characteristics**, 121–160
- for bridge structures, 122, 186–188
 - of high-current density junctions, 141
 - for Josephson junction, 13, 134, 285, 286
 - for light-sensitive junctions, 173, 174, 224, 225
 - measurement of, 66–68
 - for metal barrier junctions, 165, 166
 - in presence of thermal fluctuations, 150–153
 - and R.S.J. model, 127, 131–135
- Voltage standard**, 344–352

Voltmeter, 436
Vortex motion, *see* Flux flow
Vortex structure:
 in bridges, 189–191
 in large junctions, 105–111

Wave velocity in superconducting transmission
 line, 237
Weak superconductivity, 3, 20
Zero field step, 262, 278–279